

**EVOLUTION OF THE HYDROTHERMAL ALTERATION
AT THE
CHUQUICAMATA PORPHYRY COPPER SYSTEM,
NORTHERN CHILE**

by

Alexandra M. Arnott

Submitted in partial fulfillment of the requirements
for the degree of Doctor of Philosophy

at

Dalhousie University
Halifax, Nova Scotia
January 2003

© Copyright by Alexandra M. Arnott, 2003



National Library
of Canada

Acquisitions and
Bibliographic Services

395 Wellington Street
Ottawa ON K1A 0N4
Canada

Bibliothèque nationale
du Canada

Acquisitions et
services bibliographiques

395, rue Wellington
Ottawa ON K1A 0N4
Canada

Your file Votre référence

Our file Notre référence

The author has granted a non-exclusive licence allowing the National Library of Canada to reproduce, loan, distribute or sell copies of this thesis in microform, paper or electronic formats.

The author retains ownership of the copyright in this thesis. Neither the thesis nor substantial extracts from it may be printed or otherwise reproduced without the author's permission.

L'auteur a accordé une licence non exclusive permettant à la Bibliothèque nationale du Canada de reproduire, prêter, distribuer ou vendre des copies de cette thèse sous la forme de microfiche/film, de reproduction sur papier ou sur format électronique.

L'auteur conserve la propriété du droit d'auteur qui protège cette thèse. Ni la thèse ni des extraits substantiels de celle-ci ne doivent être imprimés ou autrement reproduits sans son autorisation.

0-612-79410-5

Canada

DALHOUSIE UNIVERSITY
FACULTY OF GRADUATE STUDIES

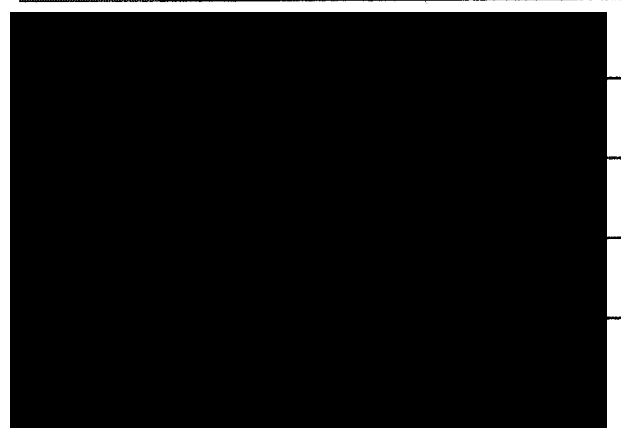
The undersigned hereby certify that they have read and recommend to the Faculty of Graduate Studies for acceptance a thesis entitled "Evolution of the Hydrothermal Alteration at the Chuquicamata Porphyry Copper System, Northern Chile" by Alexandra Arnott in partial fulfilment for the degree of Doctor of Philosophy.

Dated: November 25, 2002

External Examiner:

Research Supervisor:

Examining Committee:



DALHOUSIE UNIVERSITY

DATE: December 13, 2002

AUTHOR: Alexandra M. Arnott

TITLE: Evolution of the Hydrothermal Alteration at the Chuquicamata

Porphyry Copper System, Northern Chile

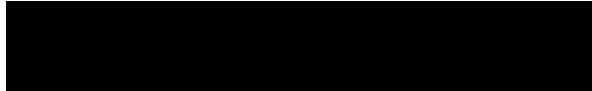
DEPARTMENT OR SCHOOL: Earth Sciences

DEGREE: Ph.D.

CONVOCATION: May

YEAR: 2003

Permission is herewith granted to Dalhousie University to circulate and to have copied for non-commercial purposes, at its discretion, the above title upon the request of individuals or institutions.



Signature of Author

The author reserves other publication rights, and neither the thesis nor extensive extracts from it may be printed or otherwise reproduced without the author's written permission.

The author attests that permission has been obtained for the use of any copyrighted material appearing in the thesis (other than the brief excerpts requiring only proper acknowledgement in scholarly writing), and that all such use is clearly acknowledged.

For mum and dad, who always insisted I do whatever made me happy;
For Don, who sustained me even when I wasn't happy doing it; and
For Cameron, who made doing it worthwhile.

non reagent nisi soluti

-Agricola 1556

Table of Contents

Dedication	iv
Table of Contents	v
List of figures	x
List of tables	xvi
Abstract	xviii
Acknowledgements	xix
Chapter 1. <u>Introduction</u>	
1.1 General Statement	1
1.2 Introduction	2
1.3 Location and geography	2
1.4 Porphyry copper deposits	5
1.5 Objectives of this study	8
1.6 Previous work	9
1.7 Organization of this thesis	9
Chapter 2. <u>Hydrothermal Alteration</u>	
2.1 Introduction	14
2.2 Source and nature of magmas in porphyry systems	14
2.3 Hydrothermal solutions	19
2.3.1 Sources of solutions in hydrothermal alteration	21
2.2.1.1 Hydrous magmas	21
2.2.1.2 Meteoric fluids	23
2.2.1.3 Metamorphic fluids	25
2.2.1.4 Connate waters	25
2.2.1.5 Seawaters	26
2.2.1.6 Hydrothermal solutions in porphyry copper deposits	26
2.3.2 Composition and precipitation of minerals from hydrothermal solutions	27
2.3.2.1 Base metals and ligands	27
2.3.2.2 Silica	29
2.3.2.3 Alkalies	30
2.3.2.4 Sulphur	31
2.3.2.5 Redox	31

2.3.3	Reactive replacement and hydrolysis by hydrothermal solution	32
2.4	Hydrothermal alteration in porphyry copper systems	33
2.4.1	Propylitic alteration	34
2.4.2	Potassic alteration	34
2.4.3	Quartz-sericite alteration	37
2.4.4	Intermediate argillic alteration	38
2.5	Structural and tectonic constraints on hydrothermal alteration	38
2.5.1	Phase separation and volume expansion of hydrothermal fluids	41
2.5.2	Tectonically induced failure	43
2.6	Models for porphyry copper systems	44
2.7	Distinguishing primary and secondary assemblages	47
2.7.1	Biotite	47
2.7.2	Feldspar	51
2.7.2.1	Albite	51
2.7.2.2	Megacrysts	54
2.7.2.3	Microcline versus orthoclase	55
2.7.2.4	Perthite	56
2.7.3	White Mica	57
2.7.4	Anhydrite	59
2.8	Glossary of terms	59

Chapter 3. Geological background and previous work

3.1	Introduction	61
3.2	The Domeyko Cordillera	61
3.3	The protoliths	66
3.3.1	Fortuna Intrusive Complex and the West Fault	66
3.3.2	The 'Chuqui' Porphyries	74
3.3.2.1	Este Porphyry	77
3.3.2.2	Banco Porphyry	79
3.3.2.3	Oeste Porphyry	81
3.4	Structural and mineralization evolution	82
3.5	Alteration and mineralization	83
3.5.1	Early stage	87
3.5.2	Quartz-molybdenite stage	90
3.5.3	Main stage	90
3.5.4	Late stage	93
3.5.5	Supergene enrichment	93

Chapter 4. Petrology and Geochemistry of the Fortuna and Chuquicamata Intrusive Complexes

4.1 Introduction	96
4.2 Petrology and mineralogy	102
4.2.1 The Fiesta Granodiorite of the Fortuna Intrusive Complex	102
4.2.1.1 Observations	102
4.2.1.2 Discussion	110
4.2.2 The Este Porphyry of the Chuquicamata Intrusive Complex	110
4.2.2.1 Observations	111
4.2.2.2 Discussion	119
4.2.3 The Banco Porphyry of the Chuquicamata Intrusive Complex	120
4.2.3.1 Observations	120
4.2.3.2 Discussion	123
4.2.4 The Oeste Porphyry of the Chuquicamata Intrusive Complex	126
4.2.4.1 Observations	127
4.2.4.2 Discussion	127
4.2.5 Interpretation	129
4.3 Geochemistry of the Fortuna and Chuquicamata Intrusive complexes	130
4.3.1 Whole-rock geochemistry	131
4.3.2 Trace- and rare-earth element geochemistry	134
4.3.3 Discussion of geochemistry	138
4.4 Geochronology	142
4.4.1 $^{40}\text{Ar}/^{39}\text{Ar}$ of the Fiesta Granodiorite	142
4.4.1.1 Hornblende	143
4.4.1.2 Biotite	143
4.4.1.3 K-feldspar	146
4.4.1.4 Discussion of $^{40}\text{Ar}/^{39}\text{Ar}$ ages	146
4.5 Two-feldspar geothermometry	147
4.6 Hornblende geobarometry	153
4.7 Stable isotopes of the Este Porphyry	155
4.7.1 Isotope thermometry	156
4.7.2 Isotope composition of crystallizing fluids	158
4.8 Summary	160

Chapter 5. Petrology and Geochemistry of the Potassic Alteration Zone

5.1 Introduction	162
5.2 Petrology of the potassic zone of the Este Porphyry	162
5.2.1 Mineralogy	166
5.2.1.1 Plagioclase	166
5.2.1.2 Biotite	166
5.2.1.3 K-feldspar	172
5.2.1.4 Quartz	178

5.2.1.5 Chlorite	183
5.2.1.6 Ti-minerals	183
5.2.1.7 Accessory Minerals	183
5.2.2 Interpretation	186
5.3 The Banco Porphyry	189
5.4 Geochemistry	189
5.4.1 Whole-rock geochemistry	190
5.4.2 Trace- and rare-element geochemistries	190
5.4.3 Interpretation	192
5.5 Geochronology and timing	197
5.6 Stable Isotopes	198
5.6.1 Oxygen Isotopes	199
5.6.1.1 Data from the potassic alteration zone	199
5.6.1.2 Isotopic Equilibrium	201
5.6.1.3 Temperature of Equilibration	202
5.6.1.4 Isotopic composition of the fluids	205
5.6.1.5 Interpretation	206
5.6.2 Hydrogen Isotopes	208
5.7 Summary	208

Chapter 6. Petrology and Geochemistry of the Quartz-Sericite (Qser) Alteration Zone

6.1 Introduction	212
6.2 Petrology	214
6.2.1 Textures	214
6.2.2 Mineralogy	217
6.2.2.1 Plagioclase	217
6.2.2.2 Mafic minerals	217
6.2.2.3 K-feldspar	217
6.2.2.4 Quartz	219
6.2.2.5 Sericite	219
6.2.2.6 Ti-minerals	223
6.2.2.7 Accessory Minerals	227
6.2.2.8 Sulphate	227
6.2.3 Interpretation	230
6.3 Geochemistry	236
6.3.1 Whole-rock geochemistry of the Qser zone	236
6.3.2 Interpretation of whole-rock geochemistry	238
6.3.3 Trace-element and rare-earth element geochemistries	240
6.3.4 Comparison of the geochemistries in the potassic and Qser zones	244
6.4 Geochronology	247
6.4.1 White mica	247
6.4.2 Potassic overprinted by Qser	253

6.4.2.1 K-feldspar	253
6.4.2.2 Biotite	258
6.4.3 Interpretation	260
6.5 Stable Isotopes	261
6.5.1 Isotope geothermometry	262
6.5.2 Isotopic equilibrium	263
6.5.3 Isotopic fractionation	264
6.5.4 Interpretation of the quartz-mica isotopic study	264
6.6 Summary	266
Chapter 7. <u>Discussion</u>	
7.1 The relationship between the Fortuna and Chuquicamata Intrusive complexes ...	270
7.2 The age of the Banco Porphyry	276
7.3 The nature of the potassic alteration zone	277
7.4 The nature of the Qser alteration zone	284
7.5 The formation of anhydrite	287
Chapter 8. <u>Conclusions</u>	289
Appendix A Sample Information	293
Appendix B Petrography	313
Appendix C Microprobe Data	345
Appendix D X-ray Diffractometry	378
Appendix E Geochemistry	385
Appendix F Isotope Data	400
Appendix G Radiometric Dating	404
References	433

List of Figures

Figure 1.1	The Chuquicamata porphyry copper deposit has been mined as an open-pit since the early 1900's.	3
Figure 1.2	Chuquicamata is located in northern Chile, along the Domeyko Fault System which host other giant porphyry copper deposits.	4
Figure 1.3	The 'onion-skin' model of porphyry copper deposits (after Lowell and Guilbert 1970)	7
Figure 2.1	The involvement of the subducted slab in magma evolution (Hedenquist and Lowenstern 1994).	16
Figure 2.2	Using $\delta^{18}\text{O}$ and δD to identify source fluids	17
Figure 2.3	Oxygen fugacity of mineralizing granitoids	18
Figure 2.4	Wall-rock-fluid interaction classification (after Giggenbach 1997)	20
Figure 2.5	The fluid-rock interaction diagram (after Reed 1997)	22
Figure 2.6	Multiple intrusion model of Hedenquist and Lowenstern (1994)	24
Figure 2.7	Geophysical studies have identified magma chambers at depth (Wigger et al. 1994)	40
Figure 2.8	Hydraulic fracturing of the carapace (Burnham 1979)	42
Figure 2.9	Porphyry copper deposits are part of a volcanic system (Sillitoe 1973) .	45
Figure 2.10	Alteration a protracted event in porphyry systems (Sillitoe 1993)	46
Figure 2.11	Feldspar stability at various water pressures	52
Figure 3.1	The geology of northern Chile	62
Figure 3.2	The regional geology	65
Figure 3.3	Proposed relationship between the Fortuna and Chuquicamata Intrusive complexes (Sillitoe 1973)	68
Figure 3.4	Regional geology of the El Abra-Fortuna region	69

Figure 3.5	Age-elevation diagram for apatite (U-Th/He) and fission track data (McInnes et al. 1999)	71
Figure 3.6	Tonnage versus initial $^{187}\text{Os}/^{186}\text{Os}$ ratio	73
Figure 3.7	Age versus initial $^{187}\text{Os}/^{186}\text{Os}$ ratio	75
Figure 3.8	Variations in the abundance of the porphyries over time	78
Figure 3.9	Structural domains at Chuquicamata	84
Figure 3.10	Simplified map of alteration zoning at Chuquicamata	86
Figure 3.11	Sulphur isotope diagram	94
Figure 3.12	Average temperatures of homogenization and salinity for fluid inclusion studies	95
Figure 4.1	Simplified geology map of the pit showing the Chuquicamata and Fortuna Intrusive complexes	97
Figure 4.2	The Fortuna Intrusive Complex distribution map	98
Figure 4.3	The Chuquicamata Intrusive Complex distribution map	100
Figure 4.4	Hand specimen of the Fiesta Granodiorite	103
Figure 4.5	Thin section of Fiesta Granodiorite	104
Figure 4.6	Amphibole compositions	106
Figure 4.7	Feldspar ternary diagram	107
Figure 4.8	Ba-zonation in K-feldspar of the Fiesta Granodiorite	108
Figure 4.9	Chemical variations in trace elements in titanite	109
Figure 4.10	Hand specimen and backscatter image of the Este Porphyry	112
Figure 4.11	Amphibole Este Porphyry	113

Figure 4.12	Feldspar in the Este Porphyry	114
Figure 4.13	Backscatter image of perthitic texture, Ba-zonation in K-feldspar	116
Figure 4.14	Altered biotite in the Este Porphyry	117
Figure 4.15	Euhedral titanite with cleavage and compositional zoning	118
Figure 4.16	Banco Porphyry hand specimen	121
Figure 4.17	Plagioclase in the Banco Porphyry	122
Figure 4.18	K-feldspar in the Banco Porphyry	124
Figure 4.19	Backscatter image, perthitic texture, Ba zonation	125
Figure 4.20	Oeste Porphyry hand specimen	128
Figure 4.21	Whole-rock geochemistry	133
Figure 4.22	Classification of the rock types (Winchester and Floyd 1977)	135
Figure 4.23	Discrimination diagram (Pearce et al. 1984)	136
Figure 4.24	Discrimination diagram (Pearce et al. 1984)	137
Figure 4.25	Rare-earth element diagram	139
Figure 4.26	$^{40}\text{Ar}/^{39}\text{Ar}$ spectra for hornblende in the Fiesta Granodiorite	144
Figure 4.27	$^{40}\text{Ar}/^{39}\text{Ar}$ spectra of biotite in the Fiesta Granodiorite	145
Figure 4.28	$^{40}\text{Ar}/^{39}\text{Ar}$ spectra of K-feldspar in the Fiesta Granodiorite	147
Figure 4.29	Time versus temperature graph of the Fiesta Granodiorite	150
Figure 4.30	Stable isotope of the Este Porphyry	159
Figure 5.1	Potassic alteration zone in the Chuqui pit	163
Figure 5.2	Hand specimen showing typical texture (Cu1115)	164
Figure 5.3	Hand specimen with K-feldspar megacryst (Cu 1127)	165

Figure 5.4	Intersecting twins in plagioclase	167
Figure 5.5	Antiperthite in the potassic alteration zone	168
Figure 5.6	Backscatter image of antiperthite	169
Figure 5.7	Feldspar ternary diagram	170
Figure 5.8	Biotite in the potassic zone	171
Figure 5.9	Biotite composition diagram	173
Figure 5.10	Biotite analyses Mg/Fe vs. F	174
Figure 5.11	Na ₂ O vs TiO ₂ in biotite	175
Figure 5.12	Backscatter image of biotite and rutile	176
Figure 5.13	K-feldspar with inclusion of plagioclase	177
Figure 5.14	Perthite in the potassic zone displaying crosshatch twinning	179
Figure 5.15	Braided perthite in the potassic alteration zone	180
Figure 5.16	BaO vs K ₂ O in K-feldspar electron microprobe analyses	181
Figure 5.17	Recrystallized quartz in the potassic zone	182
Figure 5.18	Rutile pseudomorphing titanite	184
Figure 5.19	Rutile chemistry in the potassic zone compared to titanite in the fresh Este Porphyry	185
Figure 5.20	Whole-rock geochemistry	191
Figure 5.21	Trace-element correlation diagram	193
Figure 5.22	Rare-earth element plot	194
Figure 5.23	Range of measured δ ¹⁸ O values	200
Figure 5.24	Oxygen isotope geothermometry	205

Figure 5.25	Oxygen isotope of fluids in equilibrium with the potassic alteration mineral assemblage	207
Figure 6.1	Qser alteration zone in the Chuqui pit	213
Figure 6.2	Qser hand specimen (Cu 020)	215
Figure 6.3	Complete Qser alteration in thin section	216
Figure 6.4	Biotite in the Qser alteration zone	218
Figure 6.5	Radiating muscovite (note appearance of clay along mica cleavage planes)	220
Figure 6.6	X-ray diffraction of sericite	222
Figure 6.7	Chemical variations in sericite	225
Figure 6.8	Rutile in thin section	226
Figure 6.9	Anhydrite vein	228
Figure 6.10	Variation in Sr content of anhydrite	229
Figure 6.11	Activity diagram ($a_{\text{Na}^+}/a_{\text{H}^+}$) vs. $\log(a_{\text{K}^+}/a_{\text{H}^+})$ for the system Na-K-Al-Si-O-H at 350°C, 1kbar, quartz saturation	231
Figure 6.12	Activity diagram for the system $\text{K}_2\text{O}-\text{MgO}-\text{Al}_2\text{O}_3-\text{Si}_2\text{O}-\text{H}_2\text{O}$ at 300°C, H_2O saturation pressure, quartz saturation	234
Figure 6.13	Whole rock geochemistry comparison of the sericitic samples.	237
Figure 6.14	Al_2O_3 vs K_2O showing the correlation in the sericitic samples	239
Figure 6.15	Trace element diagram	241
Figure 6.16	Rare earth element plot of the Qser samples	243
Figure 6.17	Whole rock geochemistry comparison of the sericitic samples to the potassic alteration samples.	246
Figure 6.18	$^{40}\text{Ar}/^{39}\text{Ar}$ spectra for sample white mica in the Qser alteration zone . . .	249

Figure 6.19	$^{40}\text{Ar}/^{39}\text{Ar}$ spectra for white mica in the Qser alteration zone (Cu 070 and Cu 082)	251
Figure 6.20	$^{40}\text{Ar}/^{39}\text{Ar}$ spectra for sample white mica in the Qser alteration zone (Cu 203 and Cu 519)	252
Figure 6.21	$^{40}\text{Ar}/^{39}\text{Ar}$ spectra for sample Cu 494/ Cu 442, K-feldspar	254
Figure 6.22	$^{40}\text{Ar}/^{39}\text{Ar}$ spectra for sample Cu 1115, K-feldspar	256
Figure 6.23	$^{40}\text{Ar}/^{39}\text{Ar}$ spectra for sample Cu 1105, K-feldspar	257
Figure 6.24	$^{40}\text{Ar}/^{39}\text{Ar}$ spectra for sample Cu 494, Cu 442 and Cu 1115, biotite	259
Figure 6.25	Range of calculated oxygen isotope	265
Figure 6.26	Oxygen-deuterium isotope plot	267
Figure 7.1	Cooling curves	273
Figure 7.2	Porphyry tectonic model	275
Figure 7.3a	Chuquicamata porphyry intrusion model	281
Figure 7.3c	Chuquicamata porphyry intrusion model continued	285
Figure 7.3e	Chuquicamata porphyry intrusion model continued	286

List of Tables

Table 1.1	Summary of previous work done at Chuquicamata.	10
Table 2.1	Hard vs. soft metals and ligands	28
Table 2.2	Classification of alteration zone assemblages	35
Table 2.3	Estimated temperatures for different alteration zones	36
Table 2.4	Trioctahedral mica compositions	48
Table 2.5	Diocahedral mica compositions	58
Table 3.1	Previously published Fortuna Intrusive Complex ages	72
Table 3.2	Variation in terminology of the protoliths	76
Table 3.3	Previously published Chuquicamata Intrusive Complex ages	80
Table 3.4	Structural domains of Lindsay (1998)	85
Table 3.5	$^{40}\text{Ar}/^{39}\text{Ar}$ dates from the potassic zone.	89
Table 3.6	Qser dates	92
Table 4.1	Normalized whole rock geochemistry of the Fortuna and Chuquicamata Intrusive Complexes	132
Table 4.2	$^{40}\text{Ar}/^{39}\text{Ar}$ ages of the Fiesta Granodiorite	147
Table 4.3	Two-feldspar geothermometry	152
Table 4.4	Hornblende geobarometry	154
Table 4.5	Stable isotope data	157
Table 4.6	Calculated temperatures from stable isotope pairs	157
Table 4.7	Calculated $\delta^{18}\text{O}$ of the fluids in equilibrium with the minerals at 600°C.	158
Table 5.1	Stable isotope data for the potassic zone	204

Table 5.2	Temperatures calculated based on $\delta^{18}\text{O}$	205
Table 6.1	X-ray diffraction of white mica	221
Table 6.2	X-ray peaks of muscovite and illite	224
Table 6.3	$^{40}\text{Ar}/^{39}\text{Ar}$ muscovite ages (total gas vs. preferred)	248
Table 6.4	$^{40}\text{Ar}/^{39}\text{Ar}$ K-feldspar and biotite ages (total gas vs. preferred)	260

ABSTRACT

Chuquicamata, in northern Chile, is one of the world's greatest natural concentrations of copper. The Chuqui Intrusive Complex (CIC), developed during the Eocene-Oligocene, is composed of the heavily mineralized and hydrothermally altered Este, Oeste and Banco porphyries, and truncated by the West Fault. Juxtaposed across the West Fault lies the unaltered and unmineralized Fortuna Intrusive Complex (FIC).

The initial objective of this study was to unravel the evolution of hydrothermal alteration and its relation to intrusion of the various igneous phases. At the same time it was intended to answer some fundamental questions with practical implications, such as: 1) Is the FIC genetically related to the CIC or an extraneous body? 2) Was Chuquicamata formed by a protracted event or multiple phases of alteration? 3) What was the character of the fluids involved in the development of the main (potassic and quartz-sericitic) alteration zones? 4) What processes formed the conspicuous K-feldspar megacrysts, and important anhydrite veins of Chuquicamata? For this purpose a large sample set was studied using optical microscopy, electron probe microanalysis, lithochemistry and stable isotopes, and the study was developed in parallel to a geochronological study.

Petrographically and geochemically, the FIC is too felsic to be the source of the Este Porphyry magmas. High precision $^{40}\text{Ar}/^{39}\text{Ar}$ dating of hornblende, biotite and K-feldspar indicates the FIC is ~37.6-35.5 Ma, indicating it crystallized and cooled prior to the emplacement of the CIC (34-33 Ma).

The potassic alteration zone at Chuquicamata affects the Este Porphyry and is characterized by an assemblage of albite, K-feldspar, biotite, quartz and rutile. Similar textures and $^{40}\text{Ar}/^{39}\text{Ar}$ ages suggest that the potassic alteration zone did not result from an overprinting by a separate intrusion, but represents a more hydrous development phase of the *fresh* Este Porphyry. Stable isotope analyses suggest the potassic alteration zone was in equilibrium with magmatic fluids at 535°C, 60°C lower than the *fresh* Este Porphyry. The lack of Ca-bearing silicate minerals in the potassic zone resulted from high halogen-contents that preferentially partition Ca into the melt and fluid phase.

The Banco Porphyry was intruded into a cooled and potasically altered Este Porphyry, and has preserved igneous intermediate plagioclase (oligoclase-andesine), in contrast with the latter, which contains only albite, indicating that it was not affected by potassic alteration-mineralization. Therefore, the Banco Porphyry was not the source of the potassic alteration, as has been suggested by other workers.

The Quartz-sericite (Qser) alteration zone is characterized by an assemblage of muscovite, quartz, rutile and pyrite. The Qser alteration zone formed at ~31 Ma by reaction with a reducing and highly acidic fluid. Stable isotope studies indicate the fluids responsible for the alteration event were a magmatic-meteoritic mixture and yield temperatures of ~335° to 400°C. The magmatic component of the Qser alteration event is interpreted to reflect an intrusion at depth, not yet exposed nor recognized in drilling.

Anhydrite veining occurred late in the Qser alteration event. The anhydrite veins are the result of hot, CaCl^+ -rich magmatic fluids from depth mixing with meteoric water. The source of the Ca is interpreted to be magma at depth, and Sr isotope data suggest there was no contamination by relatively radiogenic upper crustal rocks.

Acknowledgements

First, let me express my appreciation to Marcos Zentilli and Milton Graves for the opportunity to work on this world class deposit. Thanks especially to Milton for singing my praises to Marcos in the beginning . . . before Marcos knew what he was getting into! A big thanks to Sandy Grist for all his support, both technical and personal.

Thank you also to Becky Jamieson and Peter Reynolds for all of their assistance in getting this thesis completed. My appreciation to Nick Culshaw and Barrie Clarke whose expertise in their respective fields was incredibly helpful. Thank you to Keith Taylor for his help with the radiometric dating. Dan Kontak's interest and knowledge of feldspars was very helpful and welcome.

I couldn't have finished without all the support of Norma Keeping and Darlene Van de Rijt. A big thanks to you both. Thank you to Gordon Brown and Bob MacKay who have provided me with some of the most valuable tools in this study. Thanks also to Debra Wheeler, whose patience and knowledge helped pulled it all together in the twelfth hour.

This work was made easier by those who worked with me on the Chuqui Project, namely, Darryl Lindsay, Meghan Lewis and Greg Pemberton. Thanks also to Anne-Marie Ryan, Sarah Carruzzo, Joyia Chakungal, Don Fox, Nick Wilson, and Ricardo Boric who were invaluable resources.

A special thanks to the students who made my stay at Dalhousie a special one, especially Anne Guimont, Adam Layman, and Warna Downey who aided me in my research and kept my office in some semblance of order. Bonnie, Melanie, Erin, and Annie and all those who let me work comfortably in the knowledge Cameron was in loving hands- my eternal gratitude. Thank you for all the support fellow grad students... I've been here too long to mention you all...

I am grateful for the opportunity the department gave me in its flexibility that allowed me to take time to teach... and also for the opportunity to meet such great babysitters!

Thank you to my husband, Don, for all his not so gentle pushes in the right general direction. To my son, Cameron, thank you for being such a good sleeper! Thanks to both my parents for all their support- they always seemed to know what I needed. Thank you Ginny and Dave for all the help you gave us over these years. And special thanks to all my friends who gave me the outlet I needed (and those precious hours of childcare!). Kristie, Eileen, Tracy, M, and Hannah- you guys are great!

I would also like to acknowledge the financial support of Cuesta Research Ltd and various research grants of Marcos Zentilli for making this research possible. Thank you to CODELCO- Chuquicamata Division for access to the mine and invaluable assistance.

Chapter 1

Introduction

1.1 General Statement

Evidence for the effects of hydrothermal systems are found everywhere on the Earth; however, comparatively few of these have produced economic ore deposits (Hedenquist and Lowenstern 1994). Therefore, exceptional conditions have to prevail in order to produce a mineral concentration of economic value. The hydrothermal alteration assemblages associated with larger than average ore deposits, a record of fluid-wallrock interactions at a grand scale, offer a unique basis for studying these processes and determining the source and geochemical properties of the hydrothermal fluids.

Chuquicamata is one of the largest known porphyry copper deposits in the world. The Chuquicamata Intrusive Complex, of Eocene-Oligocene age, accompanies a massive and complex system of hydrothermal alteration. During the early 1990s, Marcos Zentilli of Dalhousie University and Milton Graves of Cuesta Research Limited began a study of the structure and sulphide mineralogy at Chuquicamata that involved several students at Dalhousie. It became clear that a study of the hydrothermal alteration was an essential component of such an important mineralized system. This thesis focuses on the hydrothermal alteration at Chuquicamata with an emphasis on the two most important alteration zones, the potassic and quartz-sericite (Qser).

1.2 Introduction

The Chuquicamata porphyry copper deposit, often referred to as "Chuqui", is one of the largest porphyry copper deposits in the world in terms of size and grade, containing 10 billion tonnes of Cu-ore (Clark 1993). Mining at Chuquicamata began in pre-Hispanic times, and bulk scale open pit mining commenced in 1905.

At present, the pit is > 3 km wide by 4.5 km long and >900 m deep (Fig. 1.1). Over 2100 Mt of 1.52% Cu has already been removed with an estimated 11450 Mt of 0.76% Cu ore remaining (Ossandon and Zentilli 1997). This deposit is the result of an intense and protracted alteration process and a complex structural evolution. The immense size of this deposit required massive volumes of fluid to alter this mass of rock and to deposit such a large quantity of ore in a relatively small volume of the crust.

1.3 Location and geography

Chuquicamata is located in the Precordillera of the Chilean Andes, 240 km northeast of the port of Antofagasta (Fig. 1.2), at an elevation of 3000 m above sea level. Calama, the closest town to the deposit, is 16 km to the south. The Chuquicamata community (camp, concentrator, and smelter) has been located immediately to the south of the deposit, but is presently being relocated to Calama.

Chuquicamata is in the Atacama Desert, one of the driest places on Earth, where vegetation is found only in the vicinity of the Loa River System, which runs through Calama. Water is piped into the mine from the high Andes. Hyper-aridity has helped to preserve the original mineralogy, protecting the highly soluble minerals of supergene



Figure 1.1. The Chuquicamata pit is >3 km wide \times 4.5 km long and > 900 m deep. Dr. Nick Wilson for scale. The conveyor belt is visible in the background.

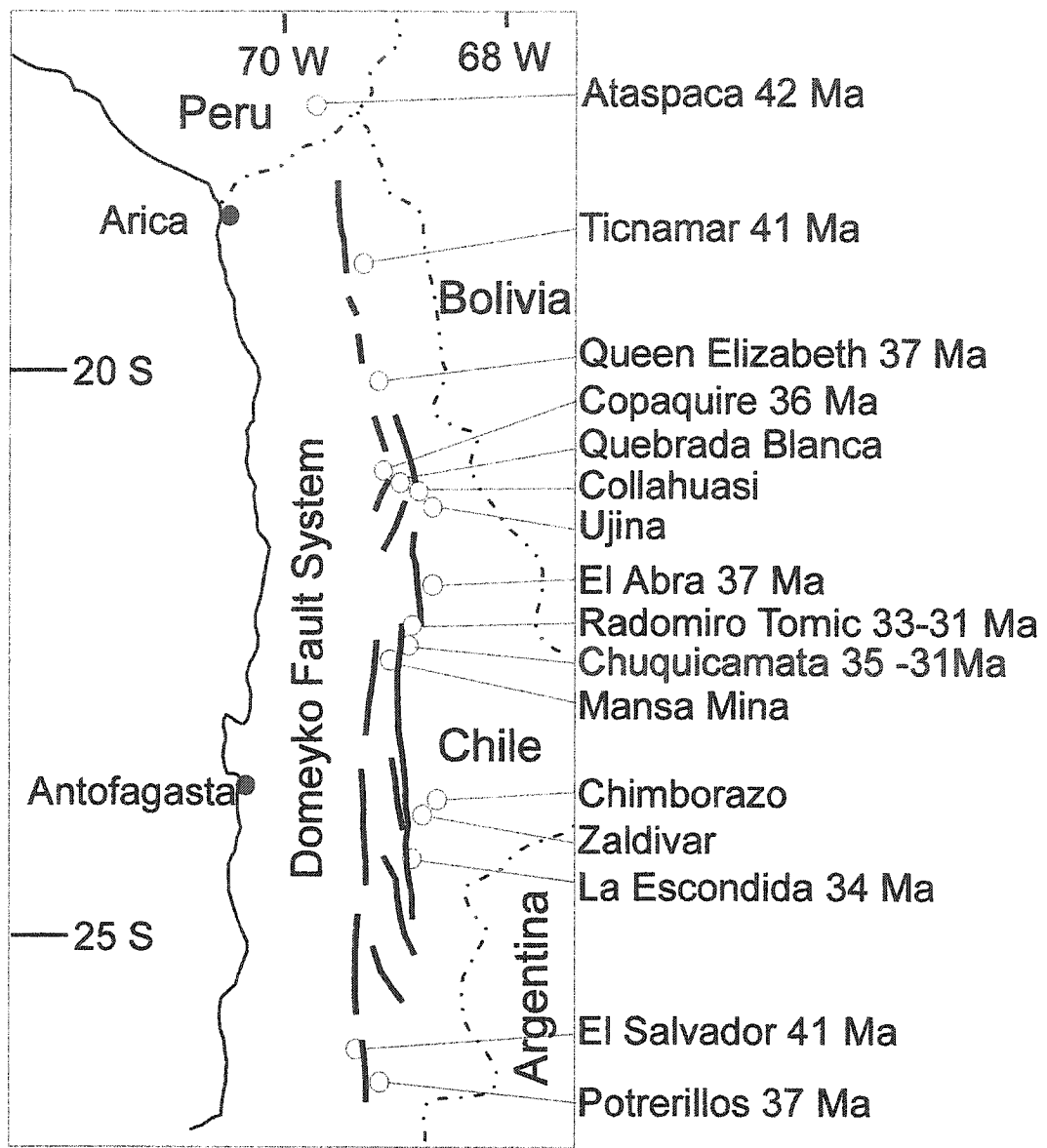


Figure 1.2. Chuquicamata is located on the Domeyko Fault System which hosts many other porphyry copper deposits such as Radomiro Tomic, El Abra and Quebrada Blanca. After Lindsay (1998).

blankets from dissolution. Waste rock surrounding the open pit dominates the landscape for kilometres and only the extreme aridity prevents acid rock drainage.

The Chuquicamata deposit lies adjacent to the Domeyko Fault System, a belt that hosts several other large porphyry copper deposits such as Collahausi, Quebrada Blanca, El Abra, Radiomiro Tomic, La Escondida, and El Salvador, all formed in the Eocene-Oligocene (Lindsay 1998) (Fig. 1.2).

1.4 Porphyry copper deposits

Although there are wide variations among porphyry copper deposits and they must be studied individually, there are also similarities in the major features of these deposits that have led to the development of generalized empirical models (e.g. Lowell and Guilbert 1970; Rose 1970; Sillitoe 1973).

Porphyry copper deposits are associated with subduction of oceanic crust in both island arcs (e.g. Phillippines) and at continental margins (e.g. west coasts of South and North America). Porphyry copper deposits are commonly of Tertiary age. There are, however, Mesozoic and Paleozoic porphyry deposits in North America, Australia and Asia (McMillan and Panteleyev 1988). There are some Precambrian porphyry-like deposits (Kirkham 1972; Gaál and Isohanni 1979); however, older porphyry deposits are often masked by metamorphism, post-mineralization alteration and erosion. The country rocks can be of any composition and the host is most often quartz diorite to quartz monzonite in composition (Lowell and Guilbert 1970).

Within porphyry copper systems, there are generally multiple phases of intrusion

with the earliest commonly hosting the mineralization (Hedenquist and Richards 1998). Some porphyry copper mineralization is deposited in the wall rock but the bulk of the mineralization is generally hosted by the intrusion itself (Lowell and Guilbert 1970). Porphyry copper deposits are centred on porphyry stocks from 100 m to several kilometres in diameter (Sillitoe 1996). They tend to be confined to the highly fractured upper parts of the felsic to intermediate porphyry stocks and the adjacent wallrocks (Burnham 1979).

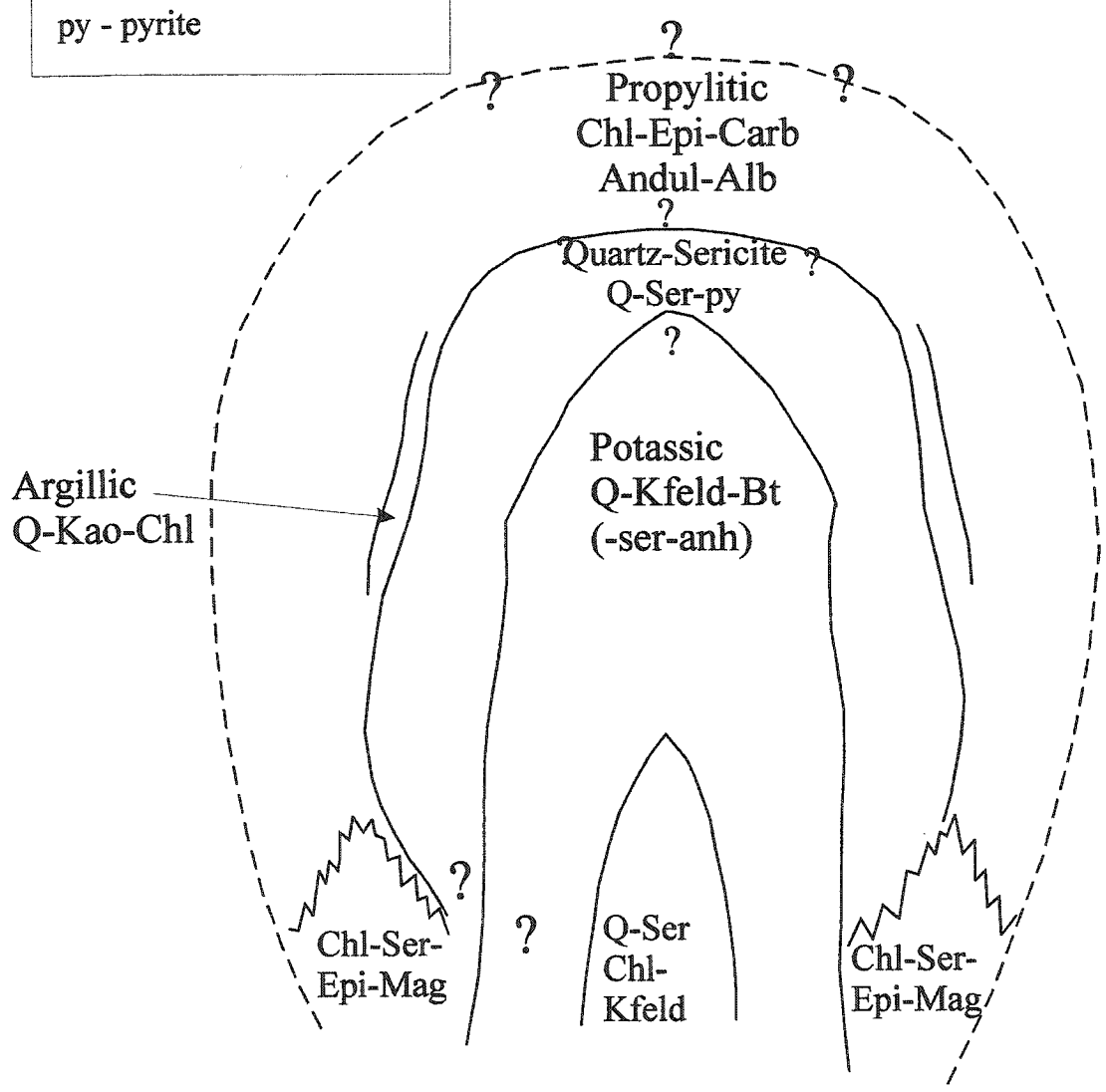
Porphyry copper deposits display 3-dimensional zoning of both alteration and mineralization. Although superseded by modern studies, the simplified 'onion skin' model of hydrothermal alteration in porphyry copper deposits shown in Figure 1.3 still provides a useful framework for discussion (Lowell and Guilbert 1970). The central potassic alteration zone is viewed as the hottest and paragenetically oldest. The potassic zone is characterized by quartz, K-feldspar, and biotite. The cooler Qser alteration surrounds the potassic zone and is characterized by quartz, white mica, and pyrite. The propylitic zone is the most peripheral. It is characterized by chlorite, epidote, carbonate, albite, and andalusite. An argillic zone may have developed between the Qser and propylitic zones, and some deposits include a peripheral magnetite zone at depth (Lowell and Guilbert 1970) (Fig. 1.3). A more detailed discussion of hydrothermal alteration is found in Chapter 2 of this study.

Most of the mineralization in porphyry copper systems is deposited in the quartz stockwork veins and disseminations associated with potassic alteration (Sillitoe 1996; Hedenquist and Richards 1998). There is much debate regarding role the Qser alteration

Mineral Abbreviations

- Q - quartz
- Kao - kaolinite
- Chl - chlorite
- Ser - sericite
- Epi - epidote
- Mag - magnetite
- Andul - andalusite
- Alb- albite
- Carb - carbonite
- Kfeld - Kfeldspar
- Bt - biotite
- anh - anhydrite
- py - pyrite

Figure 1.3. The “onion skin” model illustrates the simplified zonation of alteration in porphyry copper systems. After Lowell and Guilbert (1970).



plays in mineralization. One hypothesis is that the Qser contributes a portion of the ore in certain deposits (Hedenquist and Richards 1998) while others argue that the Qser alteration simply remobilizes earlier deposited metals (Brimhall 1980). Sillitoe (1996) suggested that where Qser alteration overprints potassic alteration mineralization may result in partial or complete removal of the metals.

1.5 Objectives of this study

The principal aim of this study was to develop a dynamic model for the history of intrusion and alteration of the Chuquicamata Intrusive Complex. In order to fulfill this goal, the following strategies were established:

1. Contrast the mineralogical and geochemical variations in the potassic and Qser alteration zones
2. Distinguish the effects of primary magmatic and external hydrothermal fluids in the deposit and their relative importance in the potassic and Qser zones, and
3. Develop a model for the chemistry of the hydrothermal fluids that resulted in the Qser and potassic assemblages.

Some of the questions that needed answers were:

- a. Is the Fortuna Intrusive Complex, which is in faulted contact in the west, genetically related to the Chuquicamata Intrusive Complex?
- b. Was the Chuquicamata porphyry deposit formed by a protracted event or multiple phases of alteration?

- c. What fluids were involved in the formation of the potassic and Qser alteration zones?
- d. What is the relative importance of magmatic melts versus fluid phases in the alteration?
- e. What was the source of the late anhydrite veins?

1.6 Previous work

Table 1.1 is a list of previous work done at the Chuquicamata porphyry copper deposit, starting with a first report by Waldemar Lindgren in 1917. The first comprehensive publications were by Lopez (1939, 1942) but then there was a gap of about 40 years, and most recently several theses (e.g. Lindsay 1998, Ballard 2001) and a current publication by Ossandón et al. (2001). Some of their research is summarized in Chapter 3.

1.7 Organization of the thesis

Following this introductory chapter, chapter 2 is a discussion of the governing processes of hydrothermal alteration including silicate stability and the nature of the hydrothermal fluids. This chapter is not specific to, but emphasizes, porphyry copper systems. A glossary of terms is given to help clarify the terminology used in this thesis.

Chapter 3 discusses the research previously done on the Chuquicamata porphyry copper deposit and summarizes what is already known about the alteration. This chapter also introduces the mineralization, structure and regional geology, which are not

Table 1.1 Previous work done on the Chuquicamata porphyry copper deposit (divided by subject).

Author, year	Subject	Summary or conclusion
Lindgren, 1917	general/regional	first detailed look at Chuqui as a whole
Ambrus, 1977, 1979		summary of porphyry petrography in northern Chile
Sillitoe, 1981	regional	dates for Chuqui
Maksaev, 1990		metallogeny, geologic evolution, thermochronology
Maksaev and Zentilli, 1999		thermochronology, metallogeny
Renzetti, 1957	general	described the regional and pit geology
Denison, 1969		description of Chuqui ore body exposed in 1960's (mainly supergene)
Guilbert and Park, 1986		summary of the geology
Zentilli et al., 1994		summary of geology (isotopes, mineralogy)
Mayne-Nicholls et al. 1995		recent but limited description of Chuqui
Ossandon et al. 2001		an up-to-date summary of research at Chuqui
Guilbert, 1963	petrology	described the petrology of the porphyries at Chuqui
Langerfeldt, 1964		described the petrology of the porphyries at Chuqui
Thompson, 1964		described porphyries
Tobey, 1971		super/hypogene zoning, alteration patterns
Turintvez et al., 1973		described porphyries, structure and alteration

Table 1.1 Previous work done on the Chuquicamata porphyry copper deposit (divided by subject).

Author, year	Subject	Summary or conclusion
Soto, 1979		summary of primary alteration and mineralization
Parada et al., 1987	petrology	petrology of Chuqui
Bandy, 1938	mineralogy	summary of sulphate mineral species found at Chuquicamata
Cook, 1978		summary of mineral species found at Chuquicamata
Lopez, 1939, 1942	ore minerals	structural relations, rock alteration and mineralization
Lewis, 1996		description/isotope hypogene/supergene covellite; temp of mineralization 300-375 °C
Sillitoe, 1973	Fortuna	Fortuna is protolith of Chuqui porphyry
Arnott et al., 1996		Fortuna is not the precursor of Chuqui porphyry
Dilles et al., 1997		Fortuna is the precursor of El Abra
Lindsay et al., 1994, 1995	structure	mineralization controlled by structure
Lindsay, 1998		structural domains and mineralization
McInnes et al. 1999		vertical displacement on the West Fault
Zentilli et al., 1995	geochronology	two hydrothermal pulses 35 and 31 Ma
Lindsay et al., 1996, 1997		dating recent movement on the West Fault
Reynolds et al., 1998		argon dating of alteration events
Ballard et al., 2001		U/Pb zircon laser ablation ICP-MS dating of Chuqui porphyries

discussed in any detail elsewhere in this thesis.

Chapters 4, 5 and 6 first present observations (e.g. petrographic descriptions, quantitative comparison of geochemistry, etc.) and then the author's interpretation (e.g. what does the petrography tell about the environment of formation, what processes could have yielded variations in the geochemistry). This approach allows the reader the opportunity to differentiate empirical evidence from discussion and interpretation, thus making the information more valuable for future research.

When investigating the effects of alteration, it is essential to have an idea of the composition of the 'unaltered' rocks or protolith. Chapter 4 introduces the least altered porphyries and describes their importance in the Chuquicamata Intrusive Complex as well as summarizing the mineralogy and geochemistry of the "fresh" rocks. This chapter also considers the Fortuna Intrusive Complex and its relationship to the Chuquicamata Intrusive Complex.

Chapter 5 addresses the genesis of the potassic alteration. Using petrography, geochemistry, and stable isotope analyses, the changes between the 'fresh' and potassic rocks, and the source and geochemical properties of the altering fluid are examined. In terms of exploration, it is essential to be able to differentiate between 'fresh' and potassically altered rocks.

Chapter 6 describes the Qser alteration and how it modifies the rocks it overprints. A description of how the degree of alteration affects the mineralogy, chemistry, and age of the overprinted rock leads to a genetic interpretation.

Chapter 7 provides answers to the questions posed in section 1.5, developing a

model for the evolution of the Chuquicamata porphyry system. The conclusions are presented in Chapter 8. Recommendations for future studies are also discussed in Chapter 8.

Eight appendices tabulate the sample information, petrology, electron microprobe analyses, X-ray diffractometry results, whole-rock and trace element geochemistry, stable isotopes data, $^{40}\text{Ar}/^{39}\text{Ar}$ ages, and geobarometry. Most appendices describe the methodology of the techniques used.

Chapter 2

Hydrothermal Alteration

2.1 Introduction

This chapter is a broad overview of hydrothermal alteration associated with ore deposits, emphasizing the alteration types associated with porphyry copper systems.

Chapter 2 addresses the factors favouring magma generation, the sources of hydrothermal fluids, and the alteration types seen in porphyry copper systems. To aid in the discussion of data reported in Chapters 4, 5, and 6, the changes in assemblages and mineral chemistry that can reveal the environment of deposition are addressed in section 2.7.

Hydrothermal alteration is commonly, but not exclusively, linked to igneous intrusions. Alteration is a form of 'metasomatism', where fluids add or subtract material from the original rocks (e.g. Mason and Moore 1982). The hydrothermal fluids that produce alteration may be of diverse origins. The changes in chemistry and mineral assemblages resulting from hydrothermal alteration are controlled by the original rock, the character of the fluids, and the pressure-temperature environment.

2.2 Source and nature of magmas in porphyry systems

Porphyry copper deposits are associated with subduction zones in both island arcs (e.g. Philippines) and continental margins (e.g. Chile, Peru). The generation of magma at subduction zones is the result of anatexis. A popular view of this process involves the addition of water to the overlying asthenosphere because of dehydration of the subducting slab, and increased pressure gradients due to crustal shortening and thickening cause

partial melting. Magmas at subduction zones can have a number of possible sources such as the mantle, subducted crust, and subducted sediments (Winter 2001).

A relatively new model proposed by Oyarzun et al. (2001) would have giant porphyry deposits result from adakitic magmatism derived from direct partial melting of the subducting slab. Previous work in northern Chile suggests that Sr and Nd are derived from the mantle wedge and that the relatively high large incompatible lithophile (LIL) and high field strength (HFS) element ratios in part reflect scavenging by hydrous fluids within the wedge (Rogers and Hawkesworth 1989). The authors conclude that the magma is principally generated in the mantle wedge and that there is little contribution from the subducted plate (Fig. 2.1) (Rogers and Hawkesworth 1989). Dehydration of the subducted slab and crustal thickening is suggested to have formed mantle-derived magmas at depths of 50 to 70 km (e.g. Hedenquist and Lowenstern 1994, Kay and Mpodozis 2001).

Granitic rocks are classified in many different ways. Many granitoid magmas are formed by the partial melting of previously existing rocks in the crust. Those formed by the partial melting of metabasalts ($\delta^{18}\text{O}$ values = 6 to 8 ‰; Ohmoto 1986 (Fig. 2.2)) are referred to as I-type granitoids (Chappell and White 1974) and are highly oxidizing (Burnham and Ohmoto 1980) (Fig. 2.3). Those formed by the melting of sedimentary rocks ($\delta^{18}\text{O}$ = 8 to 12‰; Ohmoto 1986 (Fig. 2.2)) are called S-type granitoids (Chappell and White 1974) and tend to be reducing in nature (Burnham and Ohmoto 1980) (Fig. 2.3).

Granitoid rocks are also classified based on their Fe-Ti-oxide contents: magnetite-

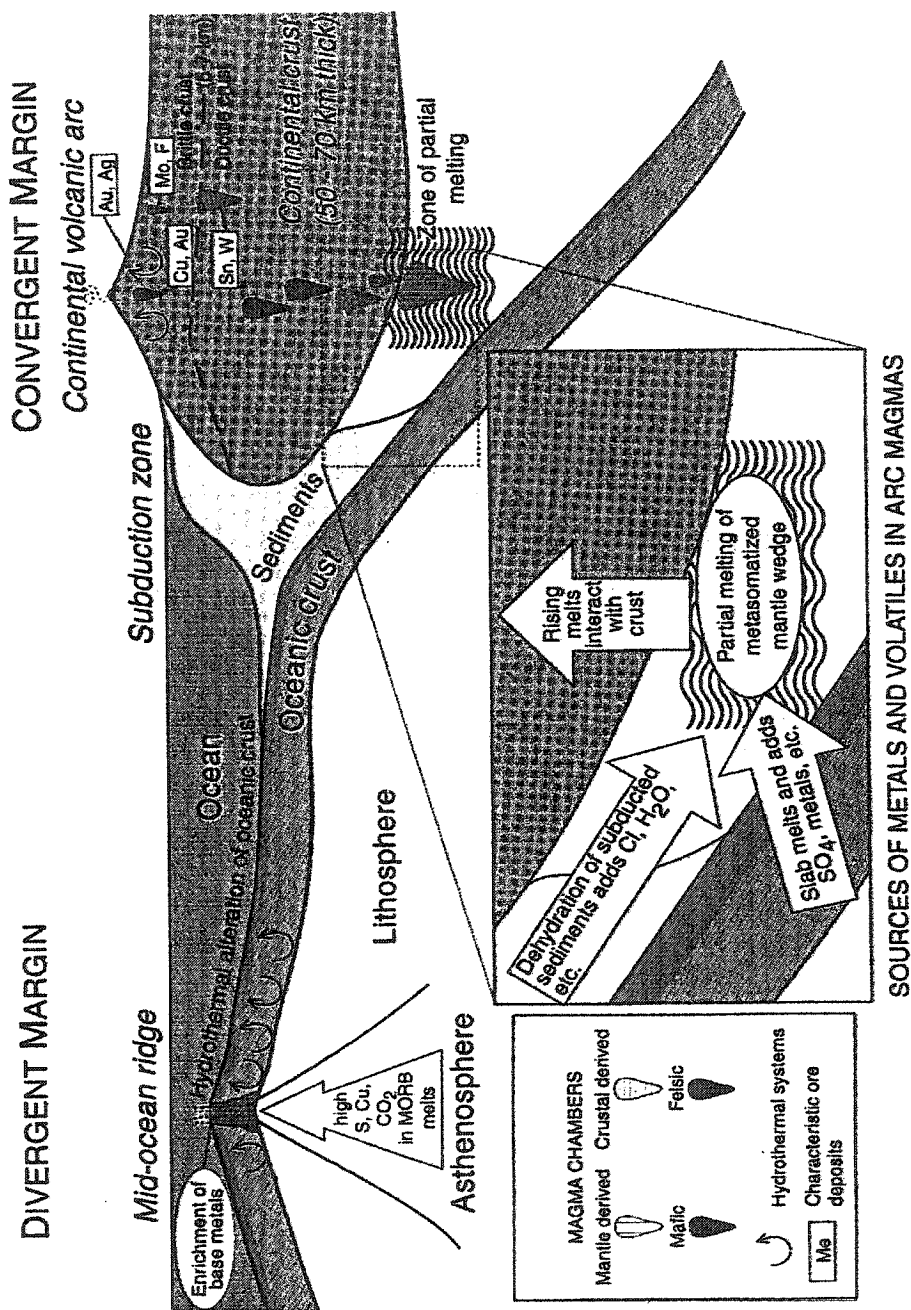


Figure 2.1. The tectonic setting of hydrothermal ore deposits. Fluids from the subducting, dehydrating slab and crustal shortening and thickening lead to partial melting of the mantle. From Hedenquist and Lowenstern (1994).

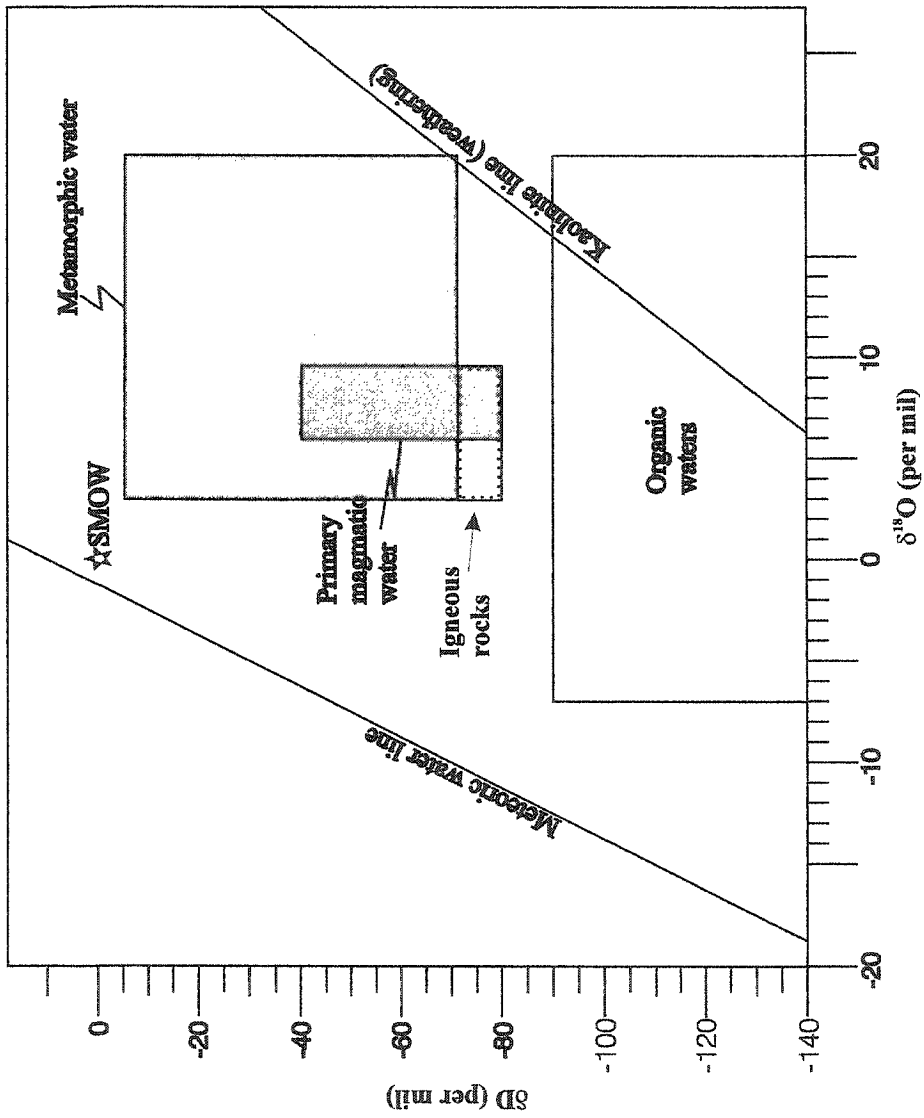


Figure 2.2. Compositional range of stable isotopes from natural waters. Hydrous minerals can be analyzed for oxygen-deuterium and plotted on the above diagram. After Taylor (1967) and Sheppard (1986) and references therein.

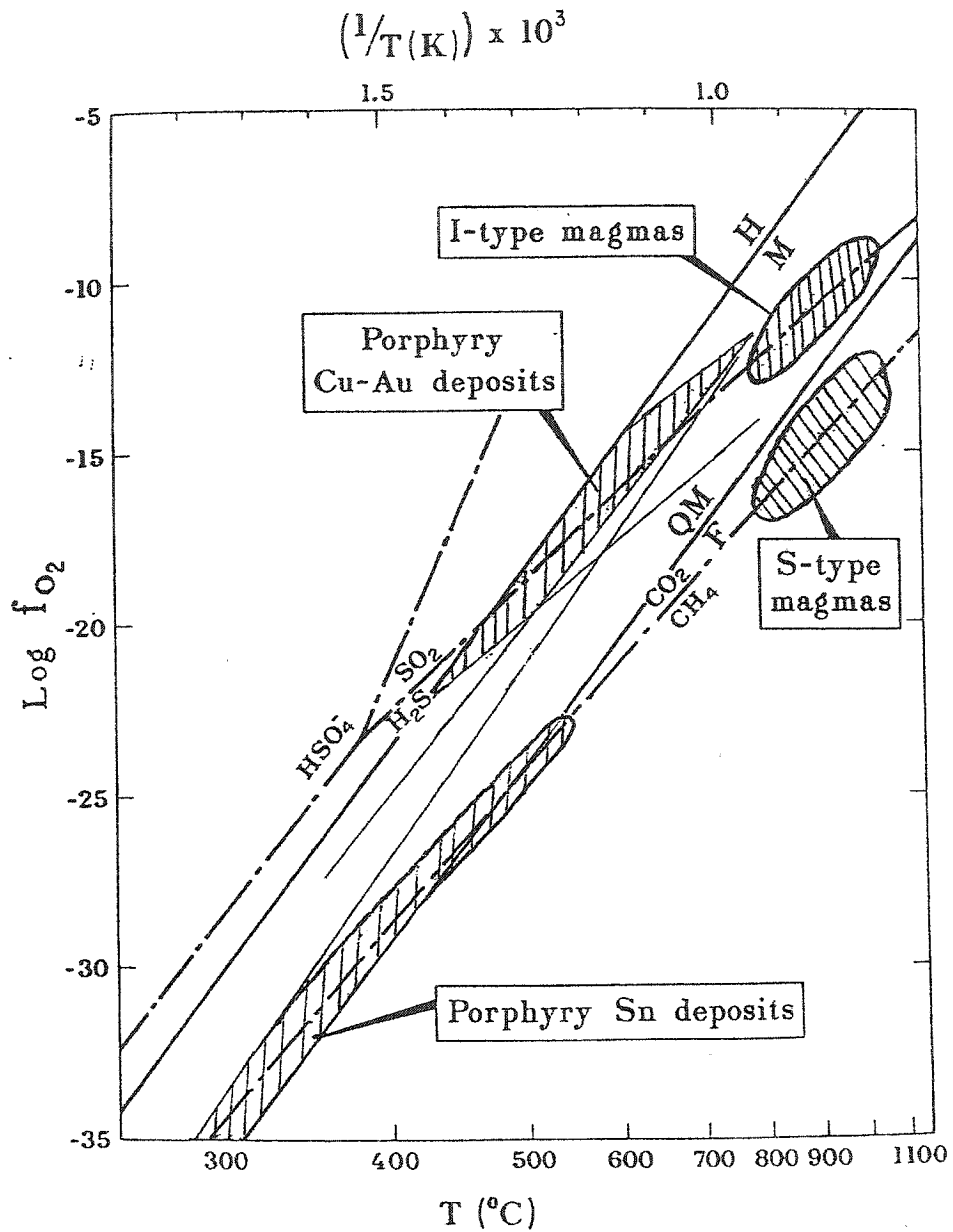


Figure 2.3. Oxygen fugacity versus temperature of magmas and porphyry deposits. Porphyry Cu-Au deposits are formed by oxidized magmas that crystallize at lower temperatures than I-type magmas. Porphyry tin deposits are considerably more reducing. After Burnham and Ohmoto (1980).

and ilmenite-series (Ishihara 1977). Magnetite-series granites host sulphide deposits of Cu, Zn, Pb, and Mo whereas ilmenite-series granites host W- and Sn-oxide deposits (Takagi and Tsukimura 1997). Magnetite-series granites have high oxygen fugacities which keep the base metals that form sulphides in solution (Fig. 2.3). In contrast, those metals that form oxides, such as tin, are kept in solution by reducing conditions.

According to Takagi and Tsukimura (1997), the most likely oxidizing agent is oxidized sulphur (SO_2). The genesis of magnetite- versus ilmenite-series granites is attributed to the SO_2 content and the $\text{SO}_2/\text{H}_2\text{S}$ ratios of the source magmas (Takagi and Tsukimura 1997). To produce an oxidizing (magnetite-series) granite there must be 250 to 1700 ppm of SO_2 as the dominant S-species (Takagi and Tsukimura 1997). When magmas contain H_2S as the dominant S-species and the SO_2 content is <250 ppm, only trace amounts of magnetite or none at all will crystallize, thus producing a reducing granite (ilmenite-series) (Takagi and Tsukimura 1997).

Porphyry copper deposits are generally hosted by magnetite-series, I-type granites produced by the partial melting of the mantle and lower crust (Fig. 2.1). Porphyry copper intrusions tend to crystallize at lower temperature ($\sim 600^\circ\text{C}$) than typical I-type granites and are subject to relatively higher degrees of subsolidus equilibration (e.g. Burnham and Ohmoto 1980).

2.3 Hydrothermal solutions

Alteration in hydrothermal systems can be rock or fluid dominated (Giggenbach 1997) (Fig. 2.4). In highly porous areas, the alteration is fluid dominated and may result

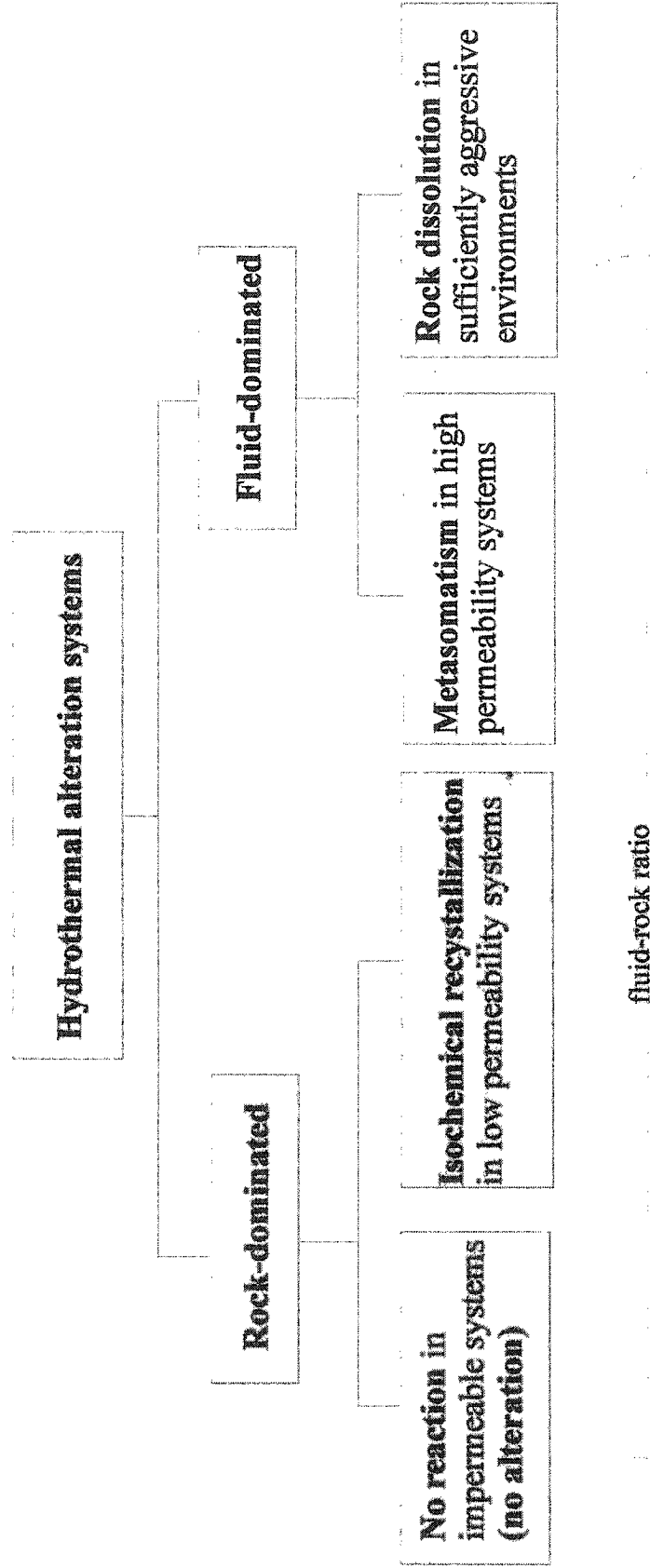


Figure 2.4. Water-rock (w/r) or fluid-rock ratio as a means of classifying hydrothermal alteration. After Giggenbach (1997). Propylitic alteration in porphyry copper systems is a rock dominated system characterized by isochemical recrystallization (Reed 1997). Qser alteration is fluid dominated and dissolution of the original rock is pervasive.

in metasomatism or rock dissolution (Giggenbach 1997) (Fig. 2.4). The resulting alteration is controlled in part by the nature of the hydrothermal solutions. It is also controlled by the transport pathway (Fig. 2.5) In porphyry copper deposits, the transportation path appears to be short enough that the primary fluids are changed minimally (Reed 1997) (Fig. 2.5). Deposition of the ore occurs in an ore trap where cooling, pressure reduction or other changes in the environment cause the precipitation of ore minerals and the genesis of alteration assemblages (Fig. 2.5).

2.3.1 Sources of solutions in hydrothermal alteration

Magmatic, meteoric, metamorphic, connate, and ocean waters may all contribute to hydrothermal fluids. The composition of the fluid is dependant on its primary source and its interaction with the wall rock along the transport path (Fig. 2.5). Studies of stable isotopes, fluid inclusions, and hydrothermal mineral assemblages can be used to help identify the source(s) of fluids in these deposits.

2.3.1.1 Hydrous magmas

The most abundant component of the volatile phase in felsic magmas is water, as evident from the common occurrence of hydrous minerals and the nature of fluid inclusions (Burnham 1997). The initial water contents of felsic magmas associated with porphyry hydrothermal systems range from 2.5 to 6.5 wt.% (Burnham 1997). In porphyry copper systems, the salinity may reach 60 wt.% equivalent NaCl based on fluid inclusion

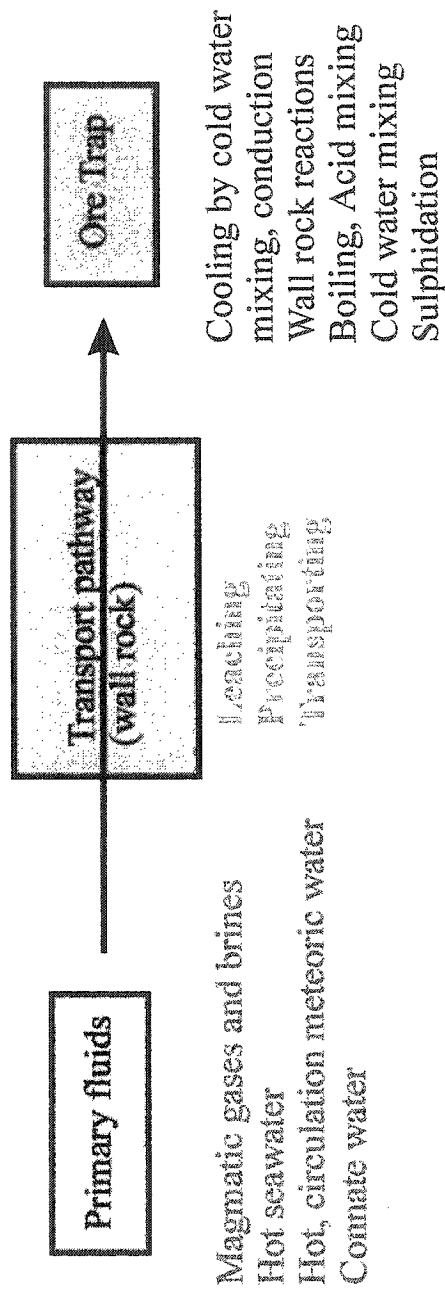


Figure 2.5. Primary fluids and transport pathways are both potential metal sources. After Reed (1997). The length of the transportation pathway determines the changes in the primary fluids. In porphyry copper deposits, it is believed the transportation path is relatively short (Reed 1997).

studies (Roedder 1984). Other common volatiles in felsic magmas are HCl, HF, H₂S, SO₂, H₂ and CO₂ (Burnham 1997).

The δ values of magmatic fluids may fall outside the magmatic range (Section 2.2) because the oxygen isotopic fractionation factors between minerals, silicate melts and hydrous fluids depends strongly on the composition of the minerals, melt and hydrous fluids (particularly the Cl and F contents) and on the pressure and temperature (Ohmoto and Oskvarek 1985). Also, the δD and $\delta^{18}O$ of magmatic fluids may vary depending on the metamorphic and diagenetic history of the source rocks (Ohmoto 1986). The δ values may change as magmatic fluids interact with wall rocks during cooling (Ohmoto 1986).

2.3.1.2 Meteoric fluids

Meteoric water circulates through the upper crust, carrying various solutes and altering the rocks it permeates. These meteoric fluids may mix with intruding magmatic fluids, especially where the magma has been emplaced at shallow depths (Fig. 2.6).

Meteoric fluids may continue to affect intrusive rocks after they have solidified (Hedenquist and Lowenstern 1994). Meteoric fluids locally permeate rocks at lower temperatures and can overprint or contribute to initial hydrothermal alteration. Meteoric fluids are important in high-sulphidation epithermal ore deposition and presumably in the upper levels of porphyry copper systems.

The isotopic signature of the meteoric water line has remained relatively unaffected over the last 250 Ma (Ohmoto 1986) (Fig. 2.2). Isotopic variations in meteoric water have three main characteristics in the present day (Ohmoto 1986):

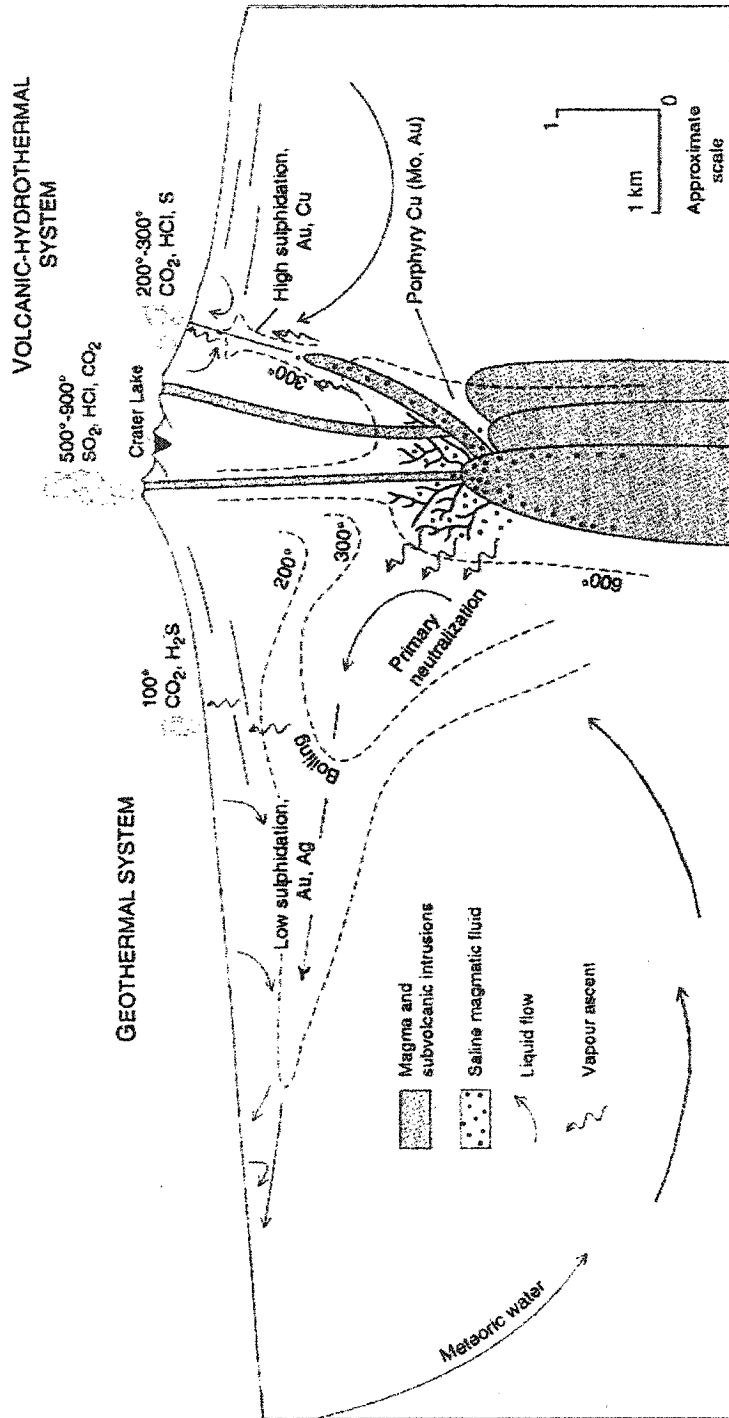


Figure 2.6. Multiple intrusions are responsible for the formation of hydrothermal systems. From Hedenquist and Lowenstern (1994).

1. δD and $\delta^{18}O$ vary linearly ($\delta D = 8 \delta^{18}O + 10\text{‰}$; Craig 1963)
2. δD and $\delta^{18}O$ values are negative in most places, and
3. δ values are dependent on geographic location (latitude and elevation).

2.3.1.3 Metamorphic fluids

There is an ambiguous distinction between pore or hydrothermal fluids and metamorphic fluids (Ohmoto 1986). In economic geology, metamorphic fluids are defined as those evolved by dehydration of hydrous minerals (Hoefs 1987, Ohmoto 1986). Metamorphic fluids may contribute components to mesothermal gold deposits.

Metamorphic fluids have wide variations in δ values ($\delta D = 0$ to -70‰ and $\delta^{18}O = 3$ to 20‰) (Fig 2.2). The isotopic composition varies with initial rock type and subsequent water-rock interaction (Hoefs 1987).

2.3.1.4 Connate waters

Connate fluids are those trapped in the interstices of sedimentary and extrusive igneous rocks at the time of deposition and burial. The salinity of connate waters increases with depth (Hanor 1979, Hoefs 1987). The isotopic composition of pore fluids depends on the initial type of fluid (e.g. seawater, magmatic), on the rocks or sediments the pore fluid occupy, and on the geochemical nature of the fluid (Hoefs 1987).

2.3.1.5 Seawaters

Seawater has a relatively constant deuterium and oxygen isotopic composition in present day ($\delta D = 0 \pm 10\text{‰}$; $\delta^{18}O = 0 \pm 1\text{‰}$) except in areas of high evaporation such as the Red Sea (Ohmoto 1986) (Fig. 2.2). The isotopic composition of ancient oceans is less certain (Ohmoto 1986). SMOW (standard mean ocean water) is used as a standard for oxygen-deuterium analyses. In submarine spreading centres, basaltic lavas react with seawater as they erupt and are buried. Seawater is an important factor in the formation of volcanogenic massive sulphide deposits but not of porphyry copper deposits, except where the latter form in island arcs.

2.3.1.6 Hydrothermal solutions in porphyry copper deposits

The different models proposed to explain the source of fluids and metals in porphyry copper deposits range from the orthomagmatic model of Burnham (1979), which suggests the fluids are magmatic in origin, to other models that propose the Cu and volatiles may be external to the magma (e.g. Norton 1982, Hedenquist and Lowenstern 1994).

It has been proposed that the water derived from the lower crust is secondary in importance to that derived from the subduction of oceanic crust in magmatic arc localities (Hedenquist and Lowenstern 1994, Lehmann et al. 2000). Dehydration of the oceanic crust may contribute recycled Cu and Zn (Hedenquist and Lowenstern 1994) (Fig. 2.1). Components such as H_2O , Cl, alkalis, and oxidized S may be transferred to the evolving magma as a fluid or to the melt when the altered oceanic crust is subducted (Hedenquist

and Lowenstern 1994 and references therein). The high Cl content of arc magmas supports this theory, as Cl is less abundant in strictly mantle-derived magmas (Hedenquist and Lowenstern 1994 and references therein). However, Cline and Bodnar (1991) conclude that typical calc-alkaline melts have sufficient Cu, Cl, and H₂O to form economic porphyry copper deposits (e.g. Burnham 1967).

2.3.2 Composition and precipitation of minerals from hydrothermal solutions

Factors such as salinity, pH, redox conditions, pressure, and temperature determine the solubility of components in hydrothermal solutions. The composition of hydrothermal solutions is an important factor controlling solubility, transportation, and deposition (Fig. 2.5). These variables also determine the method of precipitation (Fig. 2.5). The following sections examine components in the hydrothermal solutions and what may cause them to precipitate in the ore environment.

2.3.2.1 Base metals and ligands

Base metal cations are typically insoluble in fresh water. Since H₂O is the main component of most hydrothermal fluids (Burnham 1997), it must be modified in some way to increase its ability to transport metals. Metal cations form complex ions in saline fluids, making them more soluble (Helgeson 1964). The metal-carrying capacity of the fluids is partly dependant on their Cl⁻ content and the SO₂/H₂S fugacity ratio (Burnham and Ohmoto 1980).

Hydrogen chloride is strongly ionized below 350°C, but at higher temperatures it

becomes progressively more ion-paired (Chou and Frantz 1977, Barnes 1979). Chlorine complexes are the most efficient 'ligands' of base metals such as Cu (e.g. Hibbard 1995), because the Cu-Cl complexes are very stable (Seward and Barnes 1997) (Table 2.1).

Table 2.1. Class 'a' ligands tend to complex with Class 'a' metals and Class 'b' metals and ligands are more likely to complex with each other than with those of class 'a' when both are present (after Wood and Samson 1998; Seward and Barnes 1997)

Class "a" Metals (hard)	Borderline	Class "b" Metals (soft)
H ⁺ , Na ⁺ , K ⁺ , Ca ²⁺ , Mg ²⁺ , Sr ²⁺ , Al ³⁺ , Fe ³⁺	Zn ²⁺ , Pb ²⁺ , Fe ²⁺ , Cu ²⁺ , As ³⁺ , Sb ³⁺	Cu ⁺ , Au ⁺ , Sn ²⁺
Class "a" Ligands	Borderline	Class "b" Ligands
F ⁻ , H ₂ O, OH ⁻ , SO ₄ ²⁻ , HSO ₄ ⁻ , CO ₃ ²⁻	Cl ⁻ , Br ⁻	HS ⁻ , CN ⁻ , S ₂ O ₃ ²⁻ S ²⁻ , H ₂ S

Chlorine is also present in high concentrations in all hydrothermal ore-forming fluids (Seward and Barnes 1997). Experimental work indicates that an increase in the concentration of Cl partitions Cu into the aqueous fluid rather than the silicate melt phase of a magma (Keppler and Wyllie 1991, Bai and van Groos 1999). Conversely, Cl does not appear to complex with Mo (Webster 1997, Bai and van Groos 1999).

The cuprous chloride complex, CuCl⁰, is the dominant Cu-complex at all temperatures (Barnes 1979, Candela and Holland 1984). Since CuCl⁰ is more stable at higher temperatures (>250°C), the concentration of Cu in these hydrothermal fluids may be in the 1000's of ppm (Barnes 1979). The Cu solubility in fluids typical of porphyry

systems drops by 2 orders of magnitude between 350 and 250°C (Cline and Bodnar 1991). Copper remaining in solution below these temperature is assumed to be transported beyond the limit of the deposit where it would form a low-grade Cu halo around the ore zone (Cline and Bodnar 1991).

The precipitation of metal-chloride complexes is due to one or more of the following:

1. increase in H₂S (precipitating metal sulphides)
2. increase in pH (by reaction with carbonate or boiling off of acid)
3. decrease in chloride concentration (resulting from dilution with other fluids or addition of strong ion-pairing cations such as Ca²⁺), and
4. decrease in temperature (Barnes 1979).

Complexes other than Cl may be considered. However, bisulphide-copper complexes (Cu(HS)₃²⁻, Cu(HS)₂⁻, and Cu(HS)₂(H₂S)⁻) are important but not under those conditions found in porphyry copper systems (Barnes 1979). Fluorine is a 'hard ligand' (Table 2.1) and tends not to complex with Cu (Seward and Barnes 1997). Fluorine tends to partition into the melt and crystalline phases rather than the fluid phase (Webster and Holloway 1990). Fluorine has been proven experimentally to decrease the temperature of the liquidus in the Q-Ab-Or system, from 730° (F-free) to 630°C (4 wt% F) (Manning 1982). Fluorine also lowers the solidus (Dingwell 1985).

2.3.2.2 Silica

In hydrothermal solutions, silicon is present above 350°C largely as H₄SiO₄

(Fournier 1983), as depicted in the following equation (Rimstidt 1997):



The solubility of quartz increases with an increase in the salinity of the fluids (Fournier 1983) and is also affected by temperature and pressure (Jensen and Bateman 1979).

Quartz solubility increases with pH above 8 but changes in pH below 8 have little effect on quartz solubility (Rimstidt 1997). As hydrothermal solutions are rarely this basic this is obviously not the dominant mechanism for the dissolution of silica in these environments (Rimstidt 1997).

The solubility of silica is strongly controlled by pressure (Jensen and Bateman 1979). For example, a decrease in pressure from 1250 bars to 400 bars at a constant temperature (440°C) could result in the deposition of two-thirds of the silica dissolved in the fluid (Jensen and Bateman 1979).

The solubility of silica also decreases with a decrease in the salinity of the fluids (Fournier 1983); therefore, mixing a high-salinity, silica-rich fluid with a low salinity fluid at high temperatures may cause precipitation of quartz (Rimstidt 1997).

2.3.2.3 Alkalies

Hydrothermal solutions are essentially electrolyte solutions which are rich in alkali chlorides (Seward and Barnes 1997). The principal electrolyte is NaCl with lesser concentrations of KCl and CaCl₂ (Seward and Barnes 1997). Fluid inclusion work has indicated that hydrothermal solutions may be dilute to very saline. NaCl-equivalent

concentrations may be >50 wt.% in porphyry copper deposits (Roedder 1984).

Chlorides exist predominately as neutral complexes with alkalies, Fe, H, and Ca (Burnham and Ohmoto 1980). In order for Cu to deposit as an ore mineral, it must be concentrated in the fluid phase during second boiling (the exsolution of a hydrous phase from the silicate melt) rather than the melt (Cline and Bodnar). An increase in abundance of (Na,K)Cl increases the amount of Cu that partitions into the fluid phase rather than the melt (Cline and Bodnar 1991). Sodium chloride also increases the solubility of quartz. The ratio of Na:K remains the equal in the crystalline, melt and fluid phases when the system is in equilibrium (Cline and Bodnar 1991).

2.3.2.4 Sulphur

In hydrothermal fluids, S exists as both H_2S and SO_2 (Burnham and Ohmoto 1980). The fugacity ratio of these two components determines the solubility of base metals in the hydrothermal fluids (Burnham and Ohmoto 1980). The dominance of SO_2 in a system means it is oxidizing (Sasaki and Ishihara 1979).

Anhydrite may occur in the potassic alteration zone of porphyry copper deposits up to 10 to 15wt%. Gypsum may result from the hydration of anhydrite by circulating groundwater (Meyer and Hemley 1967).

2.3.2.5 Redox

High magmatic oxidation state is a key factor for the generation of porphyry copper deposits (Sasaki and Ishihara 1979, Burnham and Ohmoto 1980, Garrido et al.

2002). A measure of the oxidation state is the $\text{Fe}_2\text{O}_3/\text{FeO}$ ratio; if the ratio is between 1 and 3, the magma is considered to be highly oxidized (Garrido et al. 2002). This ratio, however, is susceptible to alteration and should only be used on fresh rocks (Garrido et al. 2002). In an oxidizing system, SO_2 is the dominant S species; the dominance of H_2S indicates a reducing environment (Sasaki and Ishihara 1979, Burnham and Ohmoto 1980).

As most magnetites in granites seem texturally to be the product of a late magmatic or subsolidus stage, it is evident that magnetite forms, not from melts, but from the alteration of Fe-bearing silicate minerals (Takagi and Tsukimura 1997). As the magnetite is a late stage, there must be an oxidizing agent in the porphyry system (Takagi and Tsukimura 1997).

High f_{O_2} of magmas may inhibit the separation and extraction of a S-rich phase, the main metal-capturing agent during magmatic fractionation (Tagaki and Tsukimura 1997). Fractional crystallization of an oxidizing magma without an early release of gases leads to the formation of S-rich mineralizing hydrothermal fluid (Matthews et al. 1995).

2.3.3 Reactive replacement and hydrolysis by hydrothermal solution

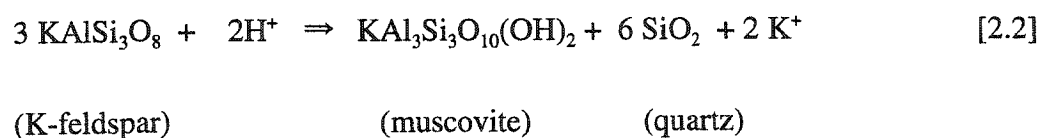
Chemical reactions can cause volume-for-volume exchange between the rock and fluid, modifying the original minerals. An example of this in a porphyry copper system is the chemical reaction that converts K-feldspar to muscovite in the Qser zone.

Hydrothermal systems tend to be open, and as a result, 'primary' rock chemistry may interact with additional elements causing disequilibrium reactions, leading to

changes in the mineralogy (Fig. 2.4). These changes are controlled by pressure and temperature, as well as by the composition of the original rock and the fluid (Fig. 2.5).

Fracture-controlled fluid flow is a common mechanism by which the fluids are granted access, resulting in the replacement of the original mineralogy. However, hydrothermal solutions may also infiltrate along grain boundaries causing changes in the mineralogy (e.g. Hibbard 1995). Changes in the chemistry of the original minerals may also occur, as described in Section 2.7.

Hydrolysis refers to the involvement of H^+ in alteration fluids and is linked to the solubility and association-dissociation relationships (Guilbert and Park 1986). Hydrolysis is the process that converts anhydrous minerals, such as feldspars, to hydrolyzed silicates, like micas and clays (Guilbert and Park 1986):



The presence of H^+ (i.e. acid solutions) allows the fluid to hydrate the tectosilicate, K-feldspar, to a phyllosilicate, muscovite. Hydrolysis is the most important reaction in hydrothermal alteration (Guilbert and Park 1986) as it controls the pH, an important factor in the solubility of metals.

2.4 Hydrothermal alteration in porphyry copper systems

Certain types of alteration are ubiquitous in hydrothermal deposits. In porphyry copper deposits, these include the formation of potassic, Qser, propylitic, and intermediate argillic alteration zones. Figure 1.3 shows a simplified zonation of porphyry

copper alteration. Sodic-calcic alteration has been described at the Yerington porphyry copper deposit (Dilles et al. 1995) but it is not widely recognized in other porphyry deposits, including Chuquicamata, and so is not discussed here.

Alteration zone names vary from deposit to deposit according to their characteristic assemblages. The terminology usually develops from the original mapping or primary development of the mine. In this thesis, the terms used are those applied by the Chuquicamata mine staff. Table 2.2 lists some definitions of alteration assemblages from the propylitic, potassic and Qser alteration zones, and the variations in defining the different alteration zone assemblages. Table 2.3 gives some estimates of the temperature conditions of alteration zones in various porphyry copper deposits.

2.4.1 Propylitic alteration

The propylitic alteration assemblage is characterized by the presence of albite, chlorite and epidote, with little change in the bulk chemical composition (Reed 1997). The resulting assemblage is rock-dominated, meaning the assemblage reflects the primary rock composition, not that of the fluid (Reed 1997) (Fig. 2.4). It is a low-temperature (200-350°C) alteration that forms under conditions similar to greenschist facies metamorphism (Reed 1997) (Table 2.3).

2.4.2 Potassic alteration

Potassic alteration is characterized by K-feldspar phenocrysts with or without biotite. It is also known as orthoclase-biotite alteration or K-silicate alteration. K-

feldspar replaces plagioclase and forms veinlets with quartz and sulphides (Rose and Burt 1979). Biotite, sericite, anhydrite, siderite, and sulphides are commonly associated with potassic alteration (Rose and Burt 1979). Potassic alteration is an example of fluid-dominated metasomatism (Fig. 2.4)

Table 2.2. Variation in characterization of alteration zones exist in the literature.

Author	Propylitic	Potassic	Quartz-Sericite
Meyer and Hemley 1967	epidote albite chlorite septechlorite carbonate sericite, pyrite Fe-oxides, zeolites montmorillonite	K-feldspar \pm Biotite Fe-oxide Fe-carbonates anhydrite no clay minerals	quartz sericite pyrite
Lowell and Guilbert 1970	chlorite epidote carbonate adularia albite	K-feldspar biotite \pm sericite \pm anhydrite	quartz sericite pyrite
Rose and Burt 1979	chlorite epidote	K-feldspar biotite green sericite anhydrite siderite	quartz sericite pyrite \pm kaolinite \pm carbonate \pm anhydrite \pm apatite \pm rutile
Reed 1997	albite chlorite epidote	K-feldspar and/ or biotite \pm sericite \pm chlorite \pm quartz	quartz sericite pyrite chlorite

Table 2.3. Tabulation of estimated temperature of alteration based on various techniques such as fluid inclusions and mineral associations.

Potassic

Deposit	Temperature	Reference
Chuquicamata, Chile	400-600°C	Lewis 1997
Santa Rita, NM	350-550°C	Beane 1974
Santa Rita, NM	390-580°C	Taylor et. al. 1971
Los Pelambres, Chile	550°C	Skewes and Atkinson 1985
El Salvador, Chile	525°C	Sheppard and Gustafson 1976
Sierrita, AZ	300-430°C	Preece and Beane 1982
Ray and Safford, AZ	350-410°C	Beane 1974
Bingham, UT and Galore Creek, BC	450-550°C	Beane 1974

Propylitic

Deposit	Temperature	Reference
general	200-350°C	Reed 1997
Sierrita, AZ	320-370°C	Preece and Beane 1982

Qser

Deposit	Temperature	Reference
Chuquicamata	300-435°C	Lewis 1997
Santa Rita, NM	285-390°C	Taylor et al. 1971
Sierrita, AZ	160-300°C	Preece and Beane 1982

Fluid inclusion studies and the presence of andalusite with K-feldspar at some porphyry copper deposits indicates the potassic alteration assemblages crystallized between 400 and 550°C (Table 2.3) (Taylor et al. 1971, Beane 1974). Because HCl is weakly ionized at these temperatures, the pH is probably higher than in the Qser.

The presence of chalcopyrite-pyrite with anhydrite and hematite and a scarcity of bornite-pyrite, magnetite, and pyrrhotite in the potassic zone suggests a high f_{O_2} and f_{S_2} (Rose and Burt 1979). At higher temperatures (500-600°C), there are large amounts of oxidized S in the fluid (Rose and Burt 1979).

Potassic alteration assemblages can be distinguished from their igneous counterparts by variations in the mineral compositions (see below).

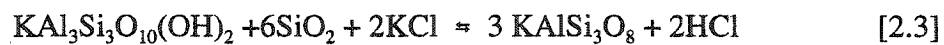
2.4.3 Quartz-Sericite (Qser) alteration

Qser alteration, also known as 'phyllitic' or 'sericitic' alteration, is characterized by the assemblage sericite, quartz and pyrite. According to Guilbert and Park (1986) Qser alteration involves the replacement of all major primary rock-forming minerals by sericite and quartz. Meyer and Hemley (1967) suggested that the Qser alteration zone grades into the potassic alteration zone. Veins and fractures with Qser alteration cut potassic and propylitic altered rocks in some deposits and, therefore, the delineation of the Qser alteration zone is very irregular (Rose and Burt 1979). These cross-cutting relations have been interpreted to show that the Qser alteration occurs after, or lasts longer than, the other alteration (Gustafson and Hunt 1975).

Qser alteration occurs at lower temperatures than potassic alteration (Table 2.3).

Acids, such as HCl, HSO_4^- , and H_2CO_3 dissociate at lower temperatures, and increase the acidity of the fluid. Qser is an example of fluid-dominated rock dissolution (Fig. 2.4).

It has been suggested that in porphyry copper deposits, a fluid that is in equilibrium with feldspar and muscovite at 500°C yields only muscovite at 250°C (Reed 1997). Additionally, a decrease in pressure (caused by the hydrostatic pressure reaching critical failure, ascension, etc.) favours the forward reaction below, with the production of HCl (Hemley et al. 1992):



Where such equilibria dominate in the potassic zone, pressure would decrease upon fracturing, precipitating K-feldspar and yielding HCl-enriched fluids into the cooler outer carapace of the porphyry system, producing $\text{H}^+ + \text{Cl}^-$ and hence Qser alteration via the reaction 2.2 (Reed 1997).

2.4.4 Intermediate argillic alteration

Intermediate argillic alteration is characterized by smectite and kaolinite replacing plagioclase (Reed 1997). The argillic alteration zone is depleted in Na and Ca.

Intermediate argillic alteration typically develops in a zone outside the sericitic zone (Reed 1997). At temperatures above 200 to 250°C , the argillic zone may not develop due to the instability of smectite at higher temperatures (Reed 1997).

2.5 Structural and tectonic constraints on hydrothermal alteration

Magmas can be generated by subduction of an oceanic plate. Using seismic

refraction, Wigger et al. (1994) interpret a weakened crust with reduced velocities which they suggest consists of partially melted zones in the lower crust under the Western Cordillera and Western Altiplano (Fig. 2.7). These partial melts rise along zones of lithospheric weakness and pond in the upper crust forming tabular magma chambers at depths of ≥ 6 km (Tosdal and Richards 2001). Below El Tatio/Laguna Colorado, the largest geothermal anomaly of South America, low velocities and scattered seismic waves indicate a partially melted zone or magma chambers at 10 to 30 km depth (Wigger et al. 1994).

Apophyses rise from these magma chambers and intrude to within 1 to 3 km of the surface (Tosdal and Richards 2001). At the reduced pressures at this depth, the magmas may undergo volatile exsolution and crystallize as porphyritic stocks (Tosdal and Richards 2001). Some of these intrusions may vent to the surface as volcanic equivalents (Burnham and Ohmoto 1980).

Fractures increase the permeability in the form of fractures or breccia networks through which hydrothermal fluids flow and alter the host rocks in the formation of porphyry copper deposit (Tosdal and Richards 2001). Fractures are produced by two main processes during the intrusion of porphyry stocks and dykes to near surface depths (1 to 3 km):

1. phase separation and volume expansion of hydrothermal fluids, and
2. tectonically induced failure (Tosdal and Richards 2001).

2.5.1 Phase separation and volume expansion of hydrothermal fluids

In porphyry copper deposits, parental magmas are fluid-rich, evident from the hydrous phenocrysts such as amphibole and biotite which require at least 3 wt.% H₂O in the initial melt (Burnham 1979). A minimum of 2 wt.% H₂O is required to provide the energy necessary to cause extensive fracturing during fluid exsolution and vaporization (Cline and Bodnar 1991). However, >5 wt.% H₂O would result in fluid exsolution and melt crystallization at depths greater than inferred for porphyry deposits (Cline and Bodnar 1991).

Fluid saturation of the magma may occur when anhydrous phases begin to crystallize, resulting in the exsolution of a volatile phase (second boiling) which necessitates a large increase in volume (Burnham 1979). The hydrothermal fluid exsolved at magmatic temperatures is in equilibrium with the coexisting magma and mineral phases (Tosdal and Richards 2001). The increase in volume may be accompanied by a pervasive brecciation of the volatile-saturated carapace of the intrusion (Fig. 2.8) (Burnham 1979).

Second boiling, or retrograde boiling, releases energy which may produce explosive volcanism ($P < 0.5$ kbar) or extensive fracturing ($P < 2$ kbar) (Burnham and Ohmoto 1980). Alternatively, the fluids may escape to surface along fault zones or breccia pipes (Tosdal and Richards 2001, Burnham 1979). As the high-temperature fluid migrates away from the parent magma, it cools. This cooling may result in the supercritical fluid intersecting its solvus and cause its separation into liquid and vapour phases, increasing the volume and resulting in additional fracturing (Burnham 1979).

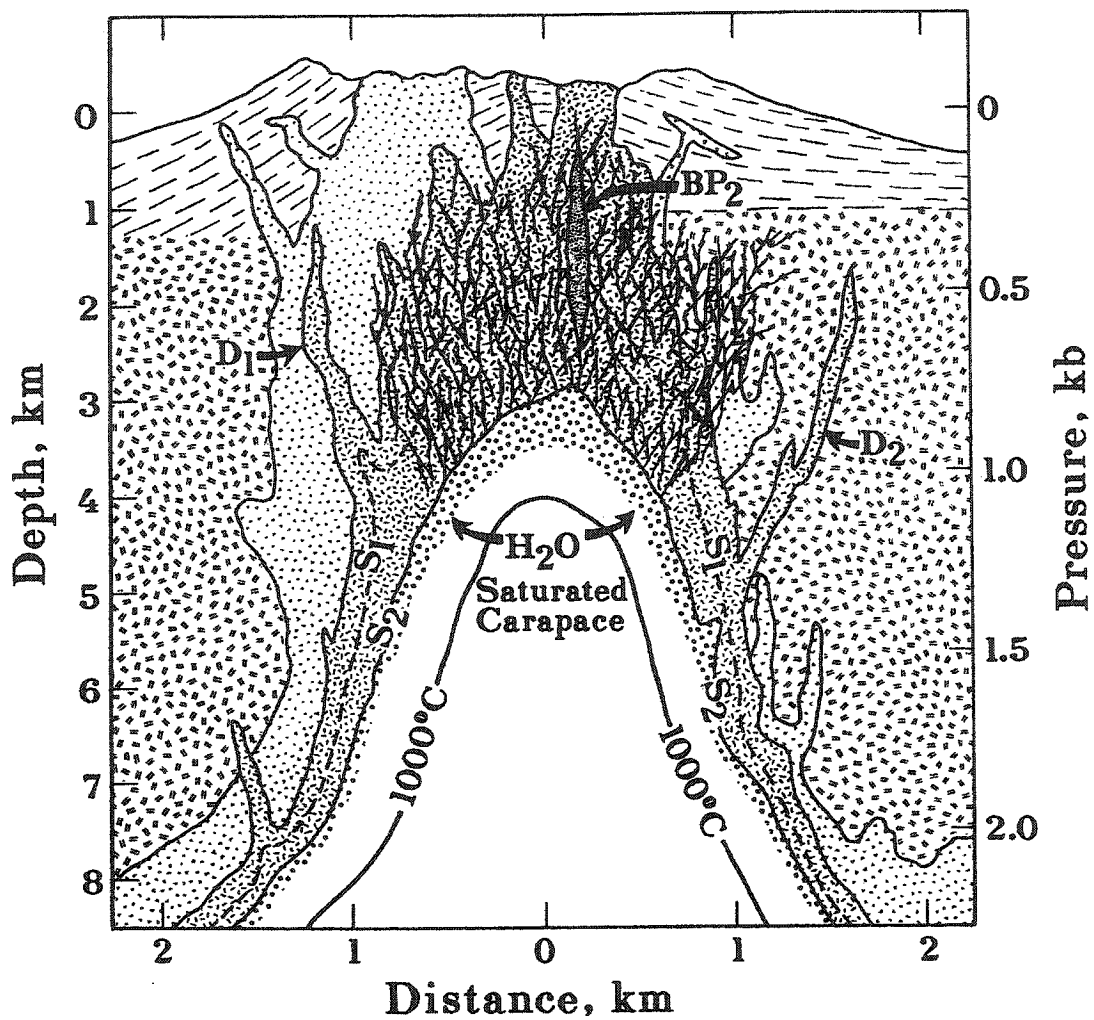


Figure 2.8. Schematic representation of the evolution of a fluid phase in a crystallizing porphyry pluton and the ensuing hydraulic fracturing of the rocks to form a mineralized and altered stockwork breccia. From Burnham (1979).

Sudden pressure drops related to hydrofracturing or sudden removal of the lithostatic load may also result in phase separation (Burnham 1979).

Rather than separating into a liquid and vapour phase, dissolved SO_2 at higher temperatures will react with the water to form H_2S and sulfuric acid (Burnham 1979). This results in low-temperature alteration assemblages that are stable at lower pH conditions (Tosdal and Richards 2001), resulting in alteration assemblages such as seen in the Qser.

The tendency of metals to partition into the fluid is important for the production of porphyry copper deposits (Cline and Bodnar 1991). A high alkali chloride content increases the tendency of base metals, such as Fe and Cu, to go into the fluid (Cline and Bodnar 1991). The fluids, also rich in SO_2 , precipitate metal sulphides during cooling or decompression. If the metals have not partitioned into the fluid during second boiling, they will not precipitate as ore minerals (Cline and Bodnar 1991).

2.5.2 Tectonically induced failure

In western South America, where the Nazca Plate is subducted under the South American Plate, oblique convergence has transmitted strain to the overriding plate which has resulted in deformation. The strain can be divided into arc-normal (convergent) and arc-parallel (strike-slip) components (Tosdal and Richards 2001). This tectonic stress may result in areas of reduced pressure or tensional zones creating pull-apart basins at fault intersections or jogs (Tosdal and Richards 2001). This extension may facilitate the ascent of magmas by lowering the lithostatic pressure.

2.6 Models for porphyry copper systems

Early models of alteration and mineralization zoning, introduced in the 1960's and 1970's (Meyer and Hemley 1967, Lowell and Guilbert 1970, Sillitoe 1973), were static and simplified (Fig. 1.3). The link between porphyry copper systems and subduction zones was recognized around this time but the complexity of timing and the importance of structure and of the composition of the fluids are still under investigation today. Once considered small, localized systems of mineralization, porphyry systems are now viewed as part of larger, regional systems (Hedenquist and Lowenstern 1994).

The first publication to depict the porphyry system as a part of a volcanic system was that of Sillitoe (1973) (Fig.2.9). Sillitoe envisioned the porphyry copper system as an intrusion, smaller than the magma chamber below, with alteration affecting the intrusion and the host rock (Fig. 2.9). This study also implied a relationship between porphyry intrusions and Pb-Zn skarn deposits where the granite contacted limestone hosts (Fig. 2.9). Recently, the link between epithermal systems and porphyry systems (Fig. 2.6) has been explored and interpreted through stable isotope and fluid inclusion studies (Hedenquist and Lowenstern 1994, Hedenquist et al. 1996).

The study of Sillitoe (1993) described the porphyry system as limited to one extended period of cooling (Fig. 2.10). Advances in radiometric dating techniques ($^{40}\text{Ar}/^{39}\text{Ar}$ and Re/Os) have furthered the hypothesis that hydrothermal systems are created in pulses of hydrothermal activity, not as a single protracted event (Hedenquist and Lowenstern 1994) (Fig. 2.6). In fact, to maintain hydrothermal activity for >100 ky, the

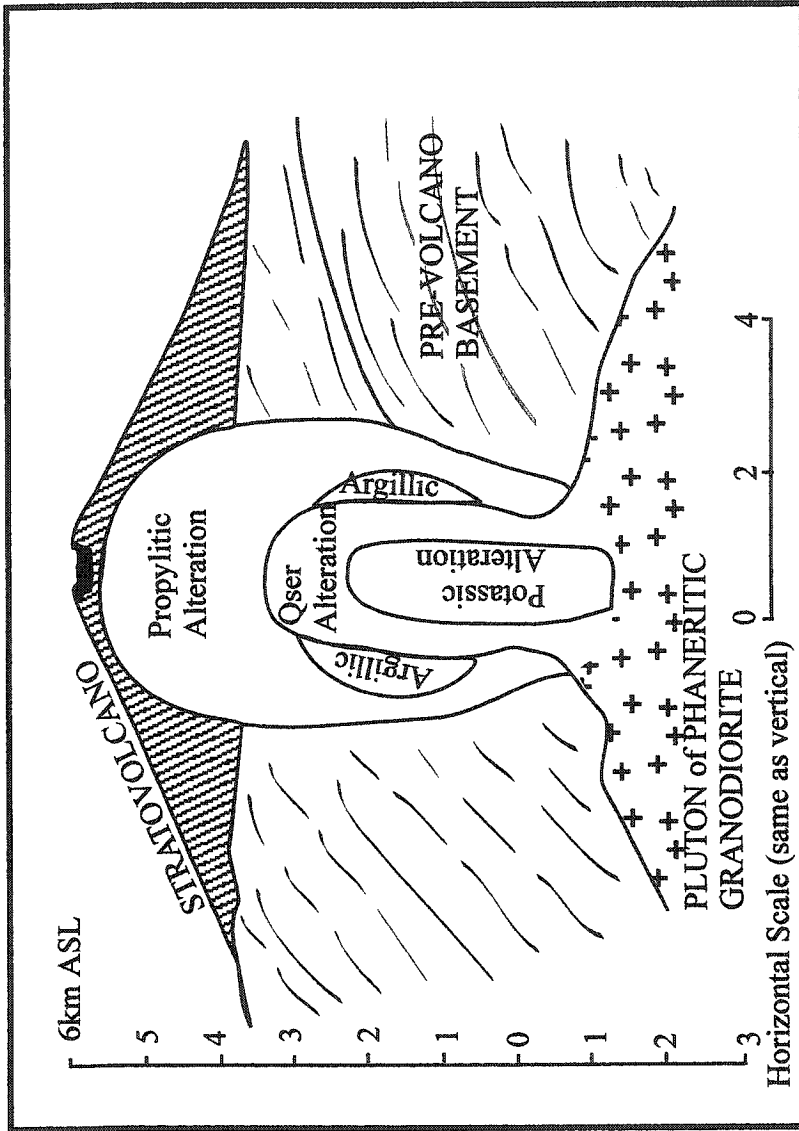


Figure 2.9. Porphyry copper deposit as a part of a volcanic system. After Sillitoe (1973).

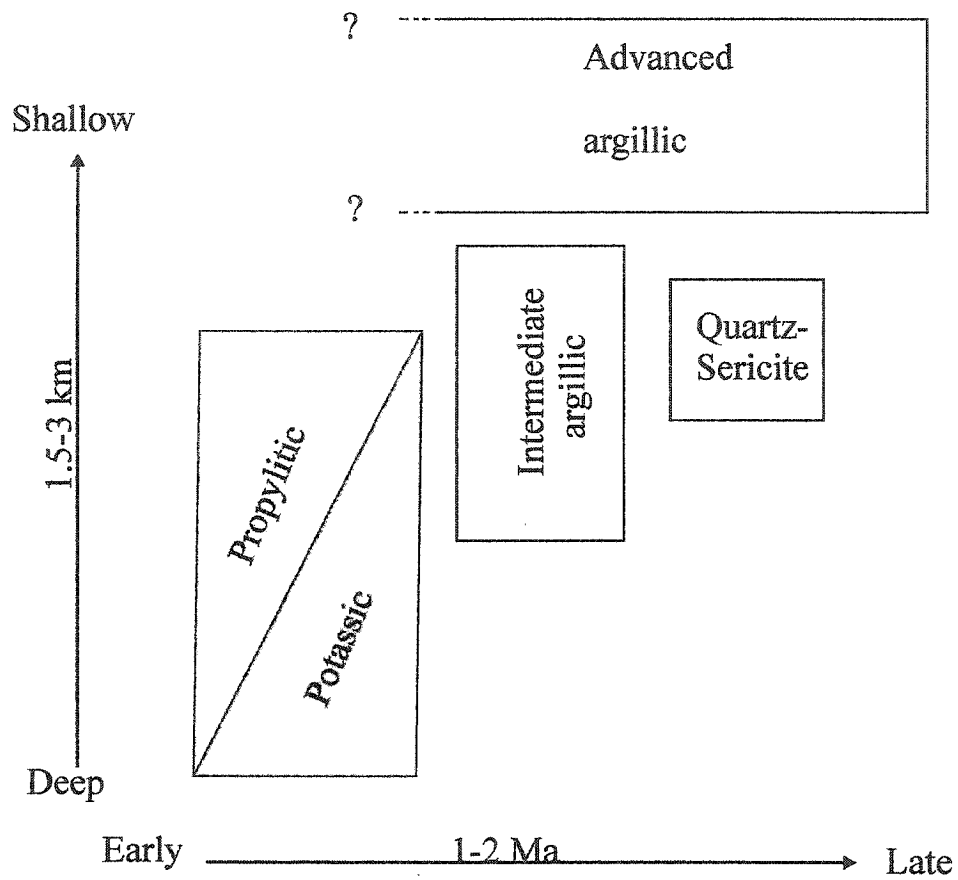


Figure 2.10. Alteration in porphyry copper systems as related to the level and timing of intrusion. After Sillitoe (1993).

lifetime of some hydrothermal systems, it is necessary to have multiple intrusions (Fig. 2.6) (Hedenquist and Lowenstern 1994).

Porphyry copper deposits are commonly localized in the highly fractured upper parts of felsic porphyry stocks (Burnham 1979). These fractures were produced by the action of aqueous fluids during and immediately following their separation from crystallizing magmas (Burnham 1979). Highly saline fluid inclusions coexist with vapour-rich inclusions, suggesting that boiling occurred in the potassic and Qser zones (Roedder 1979).

2.7 Distinguishing primary and secondary assemblages

Mineral assemblages and mineral chemistry can be used as tools to determine the environment of formation or subsequent changes in the environment. This section introduces some of the mineralogical tools that are used in this thesis, using examples mainly, but not exclusively, from porphyry copper conditions.

2.7.1 Biotite

Biotite is a ferromagnesian phyllosilicate commonly associated with porphyry copper deposits. The range of compositions can be defined by a quadrilateral of Deer et al. (1966) or by a ternary diagram of phlogopite, annite and proton-deficient (PD) oxyannite (Beane 1974, Jacobs and Parry 1979, Kusakabe et al. 1986). Substitutions of

Na, Ca, Ba, Rb and Cs are common for the X-site; Mn, Ti and Fe^{3+} for Y-site; Fe^{3+} and Ti for the Z-site; and F for OH^- (Deer et al. 1992).

Table 2.4. Typical compositions of biotite and phlogopite (Deer et al. 1992).

trioctahedral micas (200)	X	Y	Z
biotite	K_2	$(\text{Mg,Fe,Al})_6$	$\text{Si}_{6.5}\text{Al}_{2.3}$
phlogopite	K_2	$(\text{Mg,Fe}^{2+})_6$	Si_6Al_2

Models for porphyry copper deposits consider biotite, along with K-feldspar, an indicator mineral of potassic alteration (Meyer and Hemley 1967, Rose 1970). In the Qser alteration zone biotite can occur as inclusions in sericite, although chlorite is more often present in this zone (Meyer and Hemley 1967). Mafic minerals in the propylitic zone are often altered to chlorite (Beane 1982) but biotite may persist.

Distinguishing primary (i.e. igneous) from secondary (i.e. hydrothermal) biotite is an imprecise study. Work at various copper deposits have characterized some of the chemical and textural variations in biotite which may aid in the distinction of primary and secondary biotite, although these descriptions can vary by location.

A study of biotite at the Santa Rita Porphyry copper deposit, New Mexico, (Jacobs and Parry 1979) describes igneous biotite as phenocrystic to microphenocrystic. Hydrothermal biotite at Santa Rita occurs as secondary disseminated flakes, as aggregates of flakes resulting from recrystallization of igneous biotite or replacement of igneous hornblende, and as vein fillings (Jacobs and Parry 1979). An experiment by Brimhall et al. (1985) ran 0.10 m K_2SO_4 - H_2SO_4 aqueous solutions, buffered by a solid assemblage of

microcline, magnetite, quartz, and pyrite to fix the oxygen and sulphur fugacities at appropriate values for early stage porphyry-type potassic alteration of felsic intrusive rocks. In these experiments, hornblende was destroyed, producing biotite and anhydrite.

Hydrothermal biotite has a tendency to be enriched in Mg relative to primary biotite (Beane 1974, Jacobs and Parry 1979, Kusakabe et al. 1986). Beane (1974) studied hydrothermal deposits of North America and concluded that igneous biotites have molecular ratios of Mg/Fe <1.0 and hydrothermal biotites have ratios of Mg/Fe > 1.5. Kusakabe et al. (1986) suggest that the enrichment of the Mg in secondary biotite is due to the reaction of annite and PDoxyannite components with oxygen or water in the hydrothermal fluids to form K-feldspar and magnetite, creating a phlogopite-rich mineral.

In the Bingham mining district, Utah, biotite shows a systematic increase in Mg and F in hydrothermal biotite (Moore and Czamanske 1973, Parry et al. 1978). The alteration biotite also contains more Si, Al, and K and less Fe, Ti, Ba, and Cs than biotite in the unaltered rocks (Moore and Czamanske 1973, Parry et al. 1978). This result is probably due in part to the requirement of molecular neutrality and to differences in atomic radius. Titanium is precipitated as rutile during the alteration process (Moore and Czamanske 1973).

The substitution of F for OH in the crystal structure of biotite is controlled by the fugacity ratio of HF to H₂O in the fluid phase that last equilibrated with the mica, the cationic ratios in the biotite, and the temperature of the fluid-mica exchange (Munoz and Ludington 1974). Iron-rich biotite is much less efficient in removing fluorine from the fluid phase than phlogopite (Munoz and Ludington 1974).

Iron-fluorine avoidance occurs in naturally occurring ferromagnesian minerals. The antipathetic relationship of Fe and F was believed to be the result of the greater strength of the Mg-F bonds compared with Fe-F bonds (Ramberg 1952 in Mason 1992). Recent work has emphasized the importance of 'Fe-F avoidance' on cation distribution (Mason 1992). It is postulated that the kinetic of 'cluster formation', i.e., the development of groupings of the same atoms (e.g. Mg-Mg and F-F), may be a control on F-OH exchange between biotite and the associated fluid (Mason 1992).

The substitution of F for OH increases the thermal stability of the phlogopites (Munoz 1984). The substitution of F for OH in annite has a destabilizing influence on the annite crystal structure (Munoz 1984). This may be interpreted as further evidence of 'Fe-F avoidance'.

At the Henderson molybdenite deposit, Colorado, a Climax-type molybdenite deposit, anomalously high F-values have been found in biotite (up to 7.5wt%) (Gunow et al. 1980). It was also observed that the micas with the highest values of X_{Mg} have predominately higher values of F (Gunow et al. 1980).

There has been little published on chlorine substitution of the hydroxyl anions in biotite. Micas have relatively lower Cl than F-contents (Munoz 1984). The lower Cl contents may be due to a difference in ionic radius as the Cl has an ionic crystal radius of 1.81 Å, considerably larger than F- (1.31 Å) or OH- (1.38 Å) (Munoz 1984). There is a tendency for Cl to prefer Fe-end-member biotite. This tendency may be referred to as 'Mg-Cl avoidance'.

A study of granites and diorites from the Basin and Range structural province of

Utah and Nevada indicates that Cl is greater in biotite with higher Cu-content (Parry 1972). Although this study lacked statistical validity, it is evident that Cl content of biotite may be a useful exploration tool (Parry 1972). A study of Neogene granitic stocks and cupolas in Kyushu, Japan, compared biotite and apatite from barren and mineralized units (Nedachi 1980). This study found that bodies related to Pb-Zn deposits have high Cl:OH ratios, where those related to tin mineralization have low Cl:OH ratios (Nedachi 1980).

2.7.2 Feldspars

2.7.2.1 Albite

Albitization implies the replacement of calcium-rich plagioclase by albite and does not infer any textural relationships between the plagioclases (Moody et al. 1982). Albitization can occur in all rock types. Burial diagenesis (Ramseyer et al. 1992), greenschist facies metamorphism (Moody et al. 1982) and granitoids (Weidner and Martin 1987), may all be effected by albitization. However, it is unclear whether albite can form as the result of magmatic crystallization or if it only forms as the result of secondary replacement.

The alkali feldspar series is a pseudobinary system with solid solution (Fig. 2.11). With no water in the system, sanidine and albite will crystallize as a homogeneous unzoned alkali feldspar at a minimum temperature of 1063 °C (Hibbard 1995). However, this feldspar (e.g. anorthite) is not stable at temperatures below the solvus and the albite end-member exsolves from the K-feldspar to form perthite (Fig. 2.11) (see section

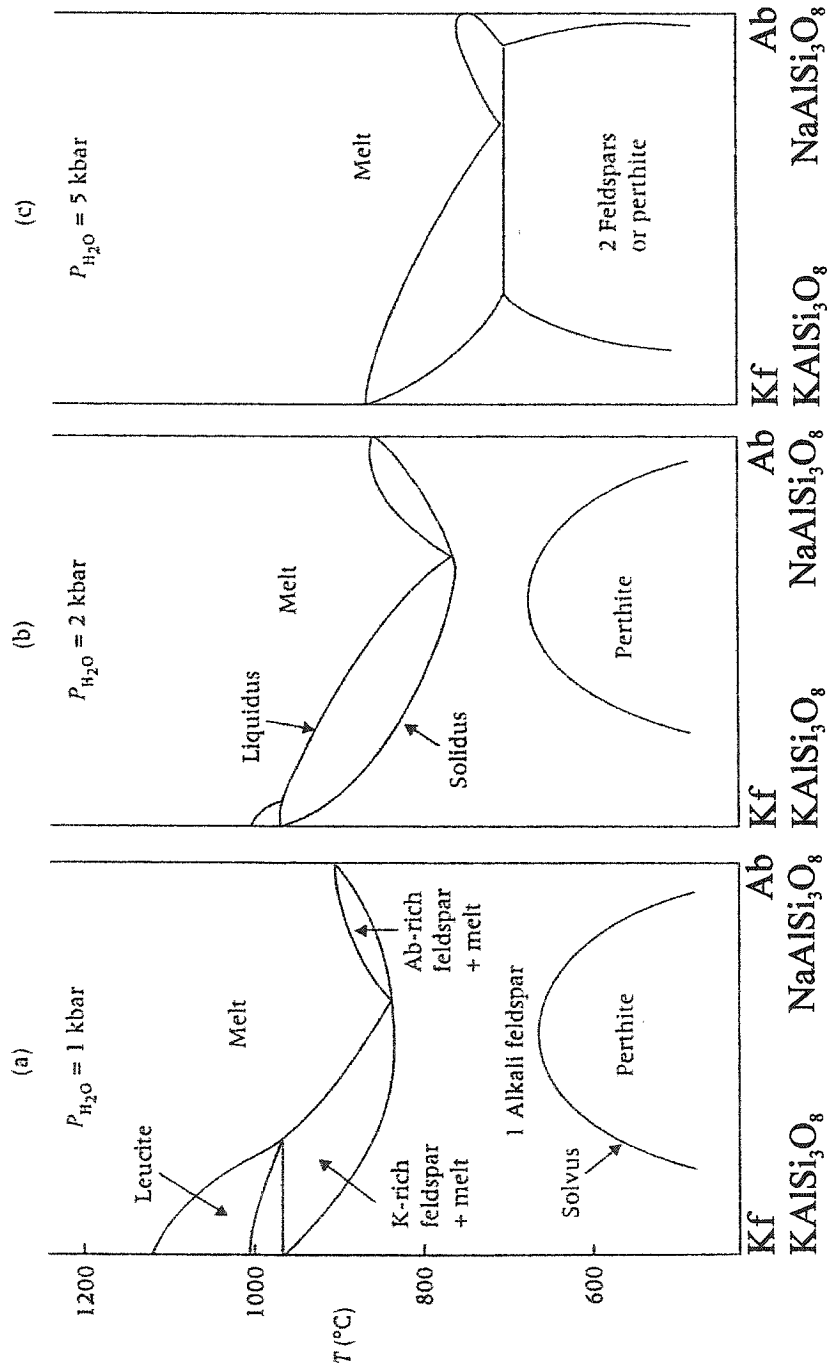


Figure 2.11. The alkali feldspar series is pseudobinary with solid solution. At low water pressure only one feldspar will crystallize which then unmix to form perthite. With higher water pressure the solidus intersects the solvus, allowing two albite and K-feldspar to crystallize directly from the melt. From Hibbard (1995) after Bowen and Tuttle (1950), Tuttle and Bowen (1958), Yoder et al. (1957), and Morse (1969).

2.4.2.4). However, the presence of water may depress the liquidus and solidus and raise the solvus (Fig. 2.11). At high P_{H_2O} the solidus may intersect the solvus, resulting in the crystallization of two feldspars: orthoclase and a Na-rich feldspar (Fig. 2.11) (Bowen and Tuttle 1950, Tuttle and Bowen 1958, Yoder et al. 1957, and Morse 1969 *in* Hibbard 1995).

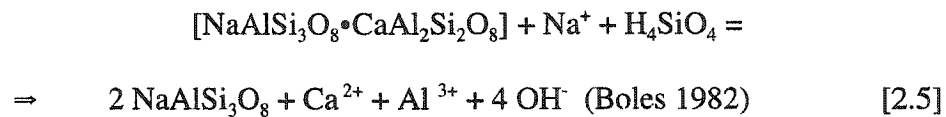
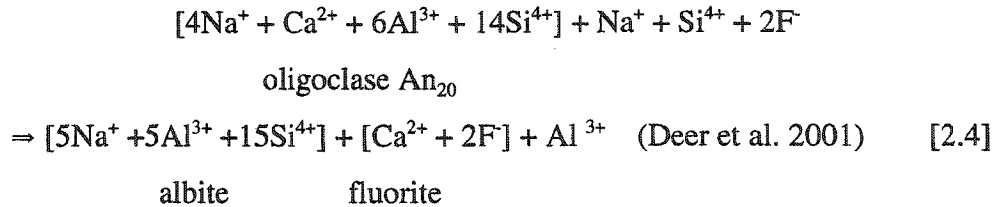
A study of a highly evolved leucogranite containing accessory muscovite, topaz and fluorite concluded that the bulk composition of the albite was close to primary because of a composition of An_1 (Weidner and Martin 1987). Work by Boles (1982) describes albitization of plagioclase in sandstones with compositions of Ab_{98} , contradicting the conclusion that low An-contents indicate a primary, magmatic albite.

Repeating albite and pericline twins are most common in Na- feldspars although most twins occur in albite (Deer et al. 2001). Albite may display albite and pericline twins simultaneously. A study by Callegari and De Pieri (1967) indicated that this 'chess board albite' only occurs in albite replacing K-feldspar; however, the authors concluded that it was not an inherited texture but rather the result of strain produced when the albite replaced the K-feldspar. Nevertheless, high albites are reported to form albite-pericline inversion twins when they invert from monalbite at the monoclinic-triclinic symmetry change (Smith and Brown 1988).

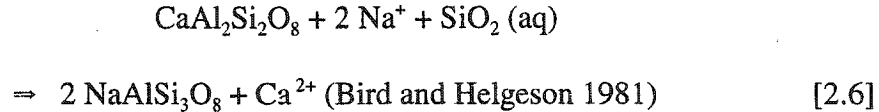
Study of the fluorine-rich leucogranite (Weidner and Martin 1987) also concluded that, in these subsolidus granite, albites and K-feldspars equilibrate at low temperatures (<200°C). The presence of albite over more calcic plagioclases is explained by fluorine linking with calcium that was stably incorporated into the melt's structure and was

thereby not available for incorporation in plagioclase (Weidner and Martin 1987).

The conversion of calcium-rich plagioclase to albite necessarily requires the release of Ca^{2+} and possibly Al^{3+} . The albitization of plagioclase may be the result of ionic exchange between a F-bearing hydrothermal fluid rich in Na and the plagioclase



or



2.7.2.2 Megacrysts

Megacrystic K-feldspar are generally euhedral and are common in granitoid plutons. They have been interpreted to be phenocrysts and porphyroblasts (e.g. Deer et al. 2001). The question of whether K-feldspar megacrysts crystallized from a melt or grew by replacement from a water-rich fluid phase under subsolidus conditions has been addressed by many authors (e.g. Vernon 1986, Long and Luth 1986). The evidence of phenocrystic origin in granitoid rocks includes twinning, zoning, and a distinct Ba-content (Deer et al. 2001).

In the Cathedral Peak Granodiorite, California, textural coarsening of K-feldspar may have promoted megacrystic growth (Higgins 1999). Nucleation occurred when the magma was undercooled and larger grains grew to megacrysts at the expense of small grains that were dissolved in the interstitial melt when intruded into warm host rocks (Higgins 1999). When cooling continued, the growth of the megacrysts was halted and K-feldspars began to nucleate again, forming part of the groundmass (Higgins 1999). Higgins (1999) suggests that chemically similar plutons that lack megacrysts may not have had the pause in cooling necessary for coarsening.

The partition coefficient for Ba between K-feldspar and silicate liquid or water-rich fluid phase is greater than 1. Calculated profiles of reverse concentric Ba-zoning observed in megacrysts favour an igneous origin (Long and Luth 1986). Furthermore, the presence or absence of reverse Ba-zoning is dependant on the temperature and relative timing of crystallization of K-feldspar with relation to plagioclase, quartz and mafic minerals; these factors are sensitive to the H₂O content of the magma (Long and Luth 1986). The reverse zoning is due to the crystallization of phases that reject Ba contemporaneously with the crystallization of K-feldspar (Long and Luth 1986). The crystallization of hornblende enhances the reversed zoning slightly because it increases Ba in the residual fluid phase early in the crystallization of K-feldspar (Long and Luth 1986).

2.7.2.3 Microcline versus orthoclase

With its monoclinic symmetry, the most common twinning law in orthoclase is

Carlsbad. Microcline is triclinic and is characterized by intersecting pericline and albite twins that produce crosshatch twins. During cooling of K-feldspar, the monoclinic orthoclase changes its symmetry from $C2/m$ to $C\bar{1}$, resulting in the crosshatched microcline crystals (Smith and Brown 1988). Therefore, the coexistence of the pericline and albite twins is taken as evidence that the triclinic microcline originally crystallized in the monoclinic system (Deer et al. 1992).

2.7.2.4 Perthite

Alkali feldspar below the solidus is not stable with a 25 to 90% albite composition (e.g. Hibbard 1995). This stability is due to the disparity in ionic radii of the larger K-ion when compared to the Na-ion. When an alkali feldspar is cooled slowly, lattice strain is alleviated by ion migration, resulting in the appearance of separate mineral phases. This exsolution produces perthite, which is characteristic of granitoids where slow cooling occurs in the plutonic environment.

Subsolvus granitoids often have coarse and irregular exsolution textures. In many igneous rocks, this coarse exsolution is the result of late-stage water concentrated during differentiation, not by the influx of hydrothermal fluids (Smith and Brown 1988). This 'deuteric coarsening' occurs at temperatures below 700°C and may be erroneously reported as albitization which often displays a chess-board texture (Smith and Brown 1988).

2.7.3 White Mica

The criteria for differentiating magmatic and secondary muscovite is mainly textural. Magmatic muscovites are characterized by sharp grain boundaries, grain sizes comparable to other magmatic minerals in the host rock, the absence of reaction with other minerals, the absence of other types of alteration in the host rock, and the mineral's relative abundance (Speer 1984).

If the mineral assemblage is relatively Al-poor, the muscovite is probably secondary (Deer et al. 1992). Muscovite crystallized from a melt is generally richer in Ti, Al and Na and poorer in Mg and Si than those formed by secondary processes (Miller et al. 1981, Deer et al. 1992). However, there is overlap in the compositional ranges of magmatic and secondary muscovite, limiting the usefulness of these generalizations (Speer 1984). Muscovite can only crystallize directly from a melt at pressures over 3.5 kbars (Speer 1984); below this pressure, it can form only in the solid state (Deer et al. 1992).

Common substitutions in the X-site of muscovite are Na, Rb, Cs, Ca and Ba (Deer et al. 1992). The substitution of Na for K decreases the thermal stability of muscovite (Speers 1984). Octahedral Al may be replaced by Mg, Fe³⁺, Mn, Li, Cr, Ti and V (Deer et al. 1992). In muscovite, the Z-site may vary in composition from Si₆Al₂ to Si₇Al (Deer et al. 1992).

Table 2.5. Typical compositions of illite and muscovite (based on 20O) (Deer et al. 1992).

Diocahedral (20O)	X	Y	Z
Muscovite	K_2	Al_4	Si_6Al_2
Illite	$K_{1.5-1.0}$	Al_4	$Si_{6.5-7.0}Al_{1.5-1.0}$

The name '*phengite*' is applied to muscovite where the Si:Al ratio is greater than 3 and the increase in Si is accompanied by substitution of Mg or Fe for Al in the octahedral site (Deer et al. 1992). The varying amounts of Fe^{2+} and Fe^{3+} in muscovite may result in a pale green, red or brown colour. *Hydromuscovites* are characterized by high OH-values and low K-values (Deer et al. 1992). A similar deficit in K is observed in *illite*, accompanied by an increase in the Si:Al ratio (Deer et al. 1992). Illite is a clay and so is distinguished from hydromica by grain size (illite $<4 \mu m$).

Fluorine may substitute for OH in muscovite (Deer et al. 1992). However, the F-values are significantly lower in dioctahedral micas than the trioctahedral micas (Gunow et al. 1980, Munoz 1984). Chlorine substitution for the hydroxyl anions is much less than F (Munoz 1984). The extent of hydroxyl replacement by halogens is controlled by the activity of the halogen ion during crystallization, the cation population of the octahedral sheet, the temperature of hydroxyl-halogen exchange, and the effects of post-crystallization leaching or enrichment due to hydrothermal fluids (Munoz 1984).

White mica in hydrothermal systems is often referred to as sericite, a phyllosilicate. The term was first introduced to designate fine-grained mica associated with ore deposits. It was described by Guilbert and Park (1986) as a fine-grained white mica that may be muscovite, hydromica, or phengite. Deer et al. (1992) describe sericite

as having a muscovite or paragonite composition. Therefore, care must be taken to identify the composition of the white mica where the term 'sericite' is applied.

2.7.4 Anhydrite

The solubilities of anhydrite and gypsum increase with increasing pressure and salinity and decreasing temperature (Blount and Dickson 1969, Blount and Dickson 1973). The amounts of calcium sulphates detected in most igneous rocks and hydrothermal deposits may be less than the amount that actually precipitated, as these minerals are very soluble at low temperatures and therefore easily dissolved by groundwater (Meyer and Hemley 1967, Luhr et al. 1984).

In order to precipitate anhydrite, the hydrothermal solution must be oxidizing and S-saturated. Sulphate minerals form as a result of decreasing the confining pressure (Rimstidt 1997) such as that which would accompany the retrograde boiling associated with porphyry copper intrusion (Burnham 1979). This boiling are associated with sulphide separation, mixing, and oxidation (Seward 1991) which are necessary for the precipitation of anhydrite. A decrease in the acidity of the solution would also convert the bisulphate to SO_4^{2-} and cause anhydrite to precipitate (Rimstidt 1997).

2.8 Glossary of terms

In economic geology, some nomenclature has evolved separately from those terms used in igneous and metamorphic petrology. To help alleviate the ambiguity, this section defines what is meant by some of these terms.

Primary vs Secondary: Primary minerals, textures and structures came into existence at the time the rock was formed. Secondary minerals, textures, and structures developed at the expense of the primary rocks and are the result of alteration.

Deuteric alteration: The alteration of primary magmatic minerals by water-rich solutions that separate from the magma at a late stage in its cooling history.

Ambiguity arises when trying to determine if deuterically altered granites, as most granites are, should be considered primary or secondary. If they have cooled slowly and are hydrous, they have undoubtedly undergone deuteric alteration while equilibrating with the water-rich fluid.

In this thesis, 'primary' is used to indicate a least-altered rock which may have experienced some deuteric alteration with mineralogy, textures, and structures that are original crystallization features. Here, deuteric alteration refers to the effects of the magma-derived fluid on the original compositions of the intrusion. However, only those minerals exhibiting secondary textures or chemistry are considered deuteric (e.g. change in the composition of a phase, or the replacement of one mineral for another).

Chapter 3

Geologic background and previous work

3.1 Introduction

Chuquicamata is arguably one of the largest porphyry copper deposits in the world. Many researchers have studied the Chuquicamata deposit as the workings have uncovered deeper and wider parts of this giant system. The immense size of the mine has made it difficult to characterize the entire deposit. The literature is characterized by individual and often internally inconsistent studies from almost a century of mining. The following chapter summarizes the previous work on alteration, and comments on some aspects of the deposit not directly addressed elsewhere in this study, such as mineralization and structure, which have been investigated by other authors (Table 1.1).

3.2 The Domeyko Cordillera

The Domeyko Cordillera (Fig. 3.1) has an elevation of 3500 m to 5000 m above sea level. It is underlain by Paleozoic to Triassic crystalline rocks, partially covered by folded Jurassic and Early Cretaceous marine strata (Maksaev 1990). The marine strata are unconformably overlain by Upper Cretaceous non-marine redbeds and mainly Paleogene volcanic rocks and various intrusives (Maksaev 1990).

The Domeyko Cordillera is the westernmost uplifted crustal block of the composite High Andes of northern Chile (Maksaev and Zentilli 1999) (Fig. 3.1). The Domeyko Cordillera hosts a narrow N-S trending belt of Late Eocene-Early Oligocene

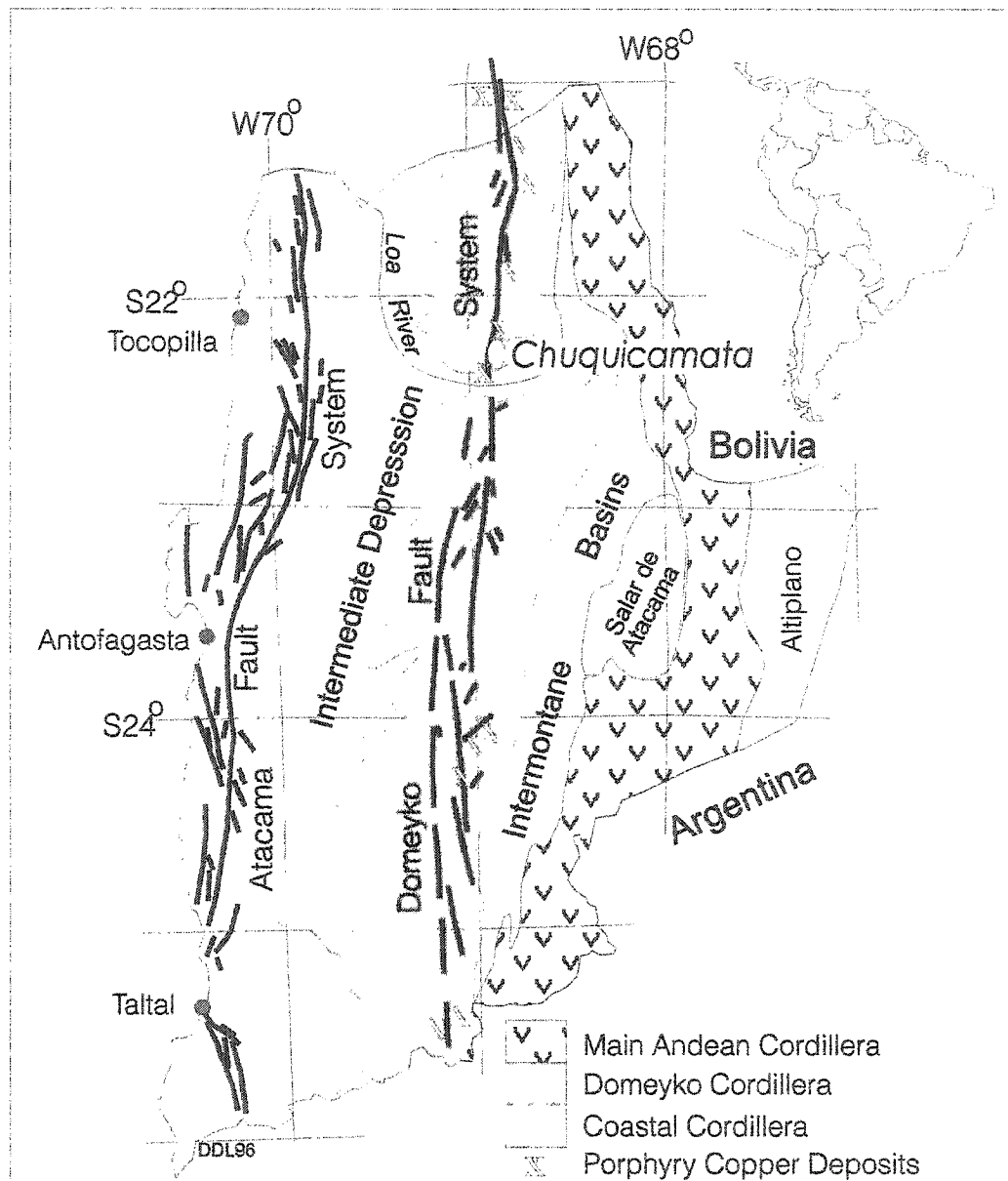


Figure 3.1. Geology of northern Chile. The Domeyko Cordillera are the westernmost uplifted crustal block of the composite High Andes of northern Chile (after Lindsay 1998, Makshev 1990). The Domeyko Fault System hosts many large porphyry deposits (see Figure 1.2).

giant porphyry copper deposits including Collahuasi, Chuquicamata, El Abra and La Escondida (Maksaev and Zentilli 1999) (Fig.1.2). These deposits are related spatially and genetically to the final igneous activity along this range, before the magmatic front jumped eastward 30 km in response to tectonic plate interaction (Maksaev and Zentilli 1999).

Using seismic refraction, Wigger et al. (1994) predict that the Nazca Plate is presently ~70 km below Chuquicamata and 10 km below the Moho discontinuity (Fig. 2.7). Their data also indicate a weakened crust with reduced velocities suggesting partially melted zones in the lower crust. These magma chambers are found under the Western Cordillera and Western Altiplano, the present magmatic front in the Andes.

High relative velocities and intermediate-angle oblique convergence between the Nazca and South American plates during the Eocene and early Oligocene resulted in crustal transpression and the initiation of the Domeyko Shear System localized along the magmatic front (Maksaev and Zentilli 1999). The Domeyko Fault System runs N10°E and is locally referred to as the West Fault or West Fissure. The West Fault (or Falla Oeste) is exposed along a 170 km zone extending from Calama to Quebrada Blanca (Fig. 1.2).

Crustal shortening and thickening led to uplift within the Domeyko Fault System and, according to apatite fission track data, to erosion of at least 4 to 5 km from the Paleozoic crystalline basement between 50 and 30 Ma (Maksaev and Zentilli 1999). Assuming that cooling was due to denudation alone, modelling of the fission track data

yields an exhumation of 200 to 100 m/My during this period (Maksaev and Zentilli 1999).

Crustal thickening deepened the zone of magma generation and magmas accumulated in the lower crust (Maksaev and Zentilli 1999). Neodymium and strontium isotopes indicate that the Chuquicamata and El Salvador porphyry copper systems were derived from mantle sources (Zentilli et al. 1988). Small volumes of melt rose rapidly to shallow levels along transtensional domains of the regional shear system (Maksaev and Zentilli 1999), resulted in the emplacement of the Eocene-Oligocene giant porphyry copper deposits.

The apatite fission track ages are marginally younger than the $^{40}\text{Ar}/^{39}\text{Ar}$ dates of the Chuquicamata porphyry copper deposit, implying fast cooling/exhumation of shallow mineralizing systems (ca. 2 to 3 km) (Maksaev and Zentilli 1999). After about 30 Ma, the fission track time-temperature history is compatible with extremely low rates of exhumation (ca. 50 m/My) (Maksaev and Zentilli 1999). This small amount of erosion has been due in part to the unusual aridity which has also led to the preservation of a rich supergene enrichment blanket at Chuquicamata (Maksaev and Zentilli 1999).

The Chuquicamata Porphyry System intruded mainly igneous rocks of Mesozoic and Paleozoic age (Fig. 3.1) (Lindsay 1998). The west part of the deposit is truncated by the West Fault, a branch of the Domeyko Fault System. In the east, the Chuquicamata Porphyry System intruded the Triassic Elena Granodiorite. This Mesozoic granodiorite has similar mineralogy and texture to the Este Porphyry, the main body in the

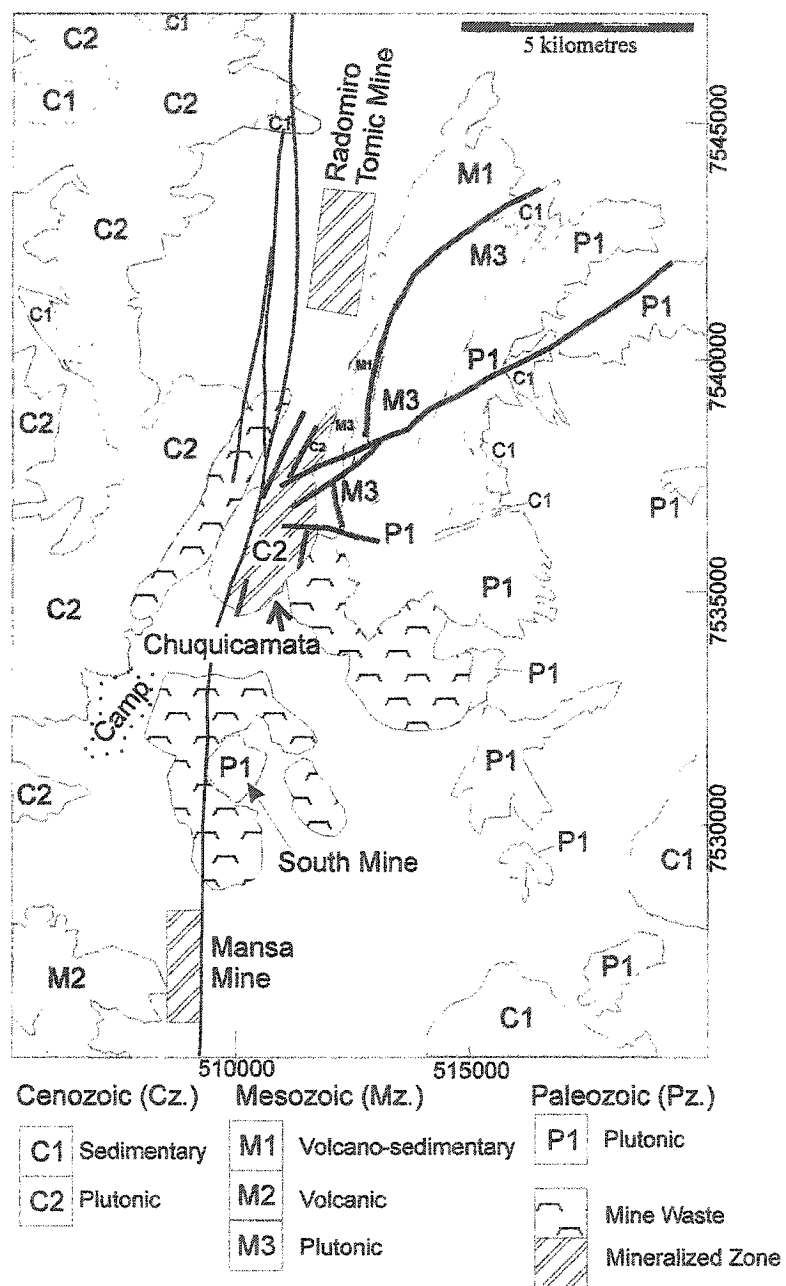


Figure 3.2. Regional geology of the Chuquicamata area. The M3 unit, east of the Chuquicamata mineralized zone, represents the Mesozoic Elena Granodiorite. From Lindsay 1998.

Chuquicamata Porphyry system (Ossandón et al. 2001). This similarity has led to difficulty in identifying the protolith of altered rocks in the east.

3.3 The Protoliths

Two intrusive systems are exposed in the Chuquicamata open-pit mine; the Chuquicamata and Fortuna Intrusive complexes. The Chuquicamata Intrusive Complex has been affected by hydrothermal alteration that abruptly ends at the West Fault, the contact with the Fortuna Intrusive Complex. The mineralization that makes the Chuquicamata deposit one of the richest copper deposits in the world, also ends at the West Fault.

The nature of the movement on the West Fault has been debated over the years, and two opposing theories have been proposed to explain the origin of the Fortuna Intrusive Complex: 1) it is the root or source of the Chuquicamata Intrusive Complex, or 2) it is a genetically unrelated intrusive complex.

3.3.1 Fortuna Intrusive Complex and the West Fault

The Fortuna Intrusive Complex comprises over a third of the exposed rock in the Chuqui pit and is mined as waste chiefly to maintain slope stability. Discernible units within the Fortuna Complex were first described in 1957 in a Ph.D. thesis by Renzetti. A detailed map of the complex was not published until Dilles et al. (1997) divided the Fortuna Complex into 3 units: the Antena Granodiorite which was intruded by the Fiesta Granodiorite, and the San Lorenzo porphyries which intruded the Fiesta Granodiorite. The San Lorenzo porphyry is further divided into the Tetera granite-aplite porphyry, the

San Lorenzo granodiorite porphyry, and the San Lorenzo mafic granodiorite porphyry (Dilles et al. 1997). The Fiesta Granodiorite comprises the majority of the Fortuna Complex exposed in the pit.

Sillitoe (1973) proposed that the Fortuna Intrusive Complex was the root of the Chuquicamata Porphyry Complex, uplifted along the near-vertical West Fault (Fig. 3.3). Sillitoe (1973) theorized that the other “half” of the Chuquicamata Intrusive Complex was subsequently eroded away. Parada et al. (1986) supported this theory and interpreted the Fortuna Intrusive Complex to be an unaltered precursor for the purpose of comparison with the altered Chuquicamata porphyries. Despite substantial evidence to the contrary, this view has supporters even in recent years (see below).

Ambrus (1979) suggested up to 40 km sinistral movement along the fault linking the El Abra Intrusive Complex and the Fortuna Intrusive Complex. This hypothesis was supported by extensive field work and $^{40}\text{Ar}/^{39}\text{Ar}$ dating by Makshev and Zentilli (1988) and Makshev (1990). Field work by Dilles et al. (1997) and Tomlinson and Blanco (1997) established that the amount of displacement was 35 ± 1 km based on various correlations of rock units on either side of the fault (Fig. 3.4). It is now generally accepted that pre-mineralization displacement on the West Fault System was dextral strike-slip under ductile conditions (Lindsay et al. 1995). Post-mineralization movement was sinistral strike-slip in a more brittle regime (Lindsay 1998).

McInnes et al. (1999) used apatite (U-Th)/He thermochronometry to estimate the amount of vertical fault displacement along the West Fault. They analyzed apatite on both sides of the West Fault, from the Fortuna Intrusive Complex and from the

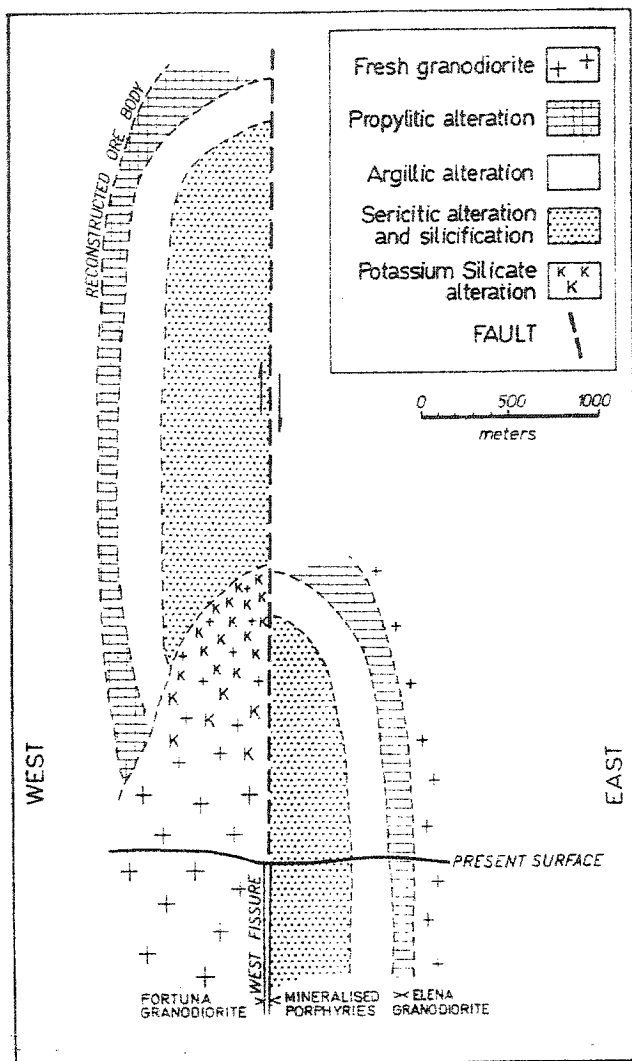


Figure 3.3. Depiction of possible vertical displacement on the West Fault. Sillitoe (1973) suggested that the Fortuna Intrusive Complex was the unaltered root of the Chuquicamata Porphyries. This hypothesis proposes that all of the movement on the West Fault has been vertical.

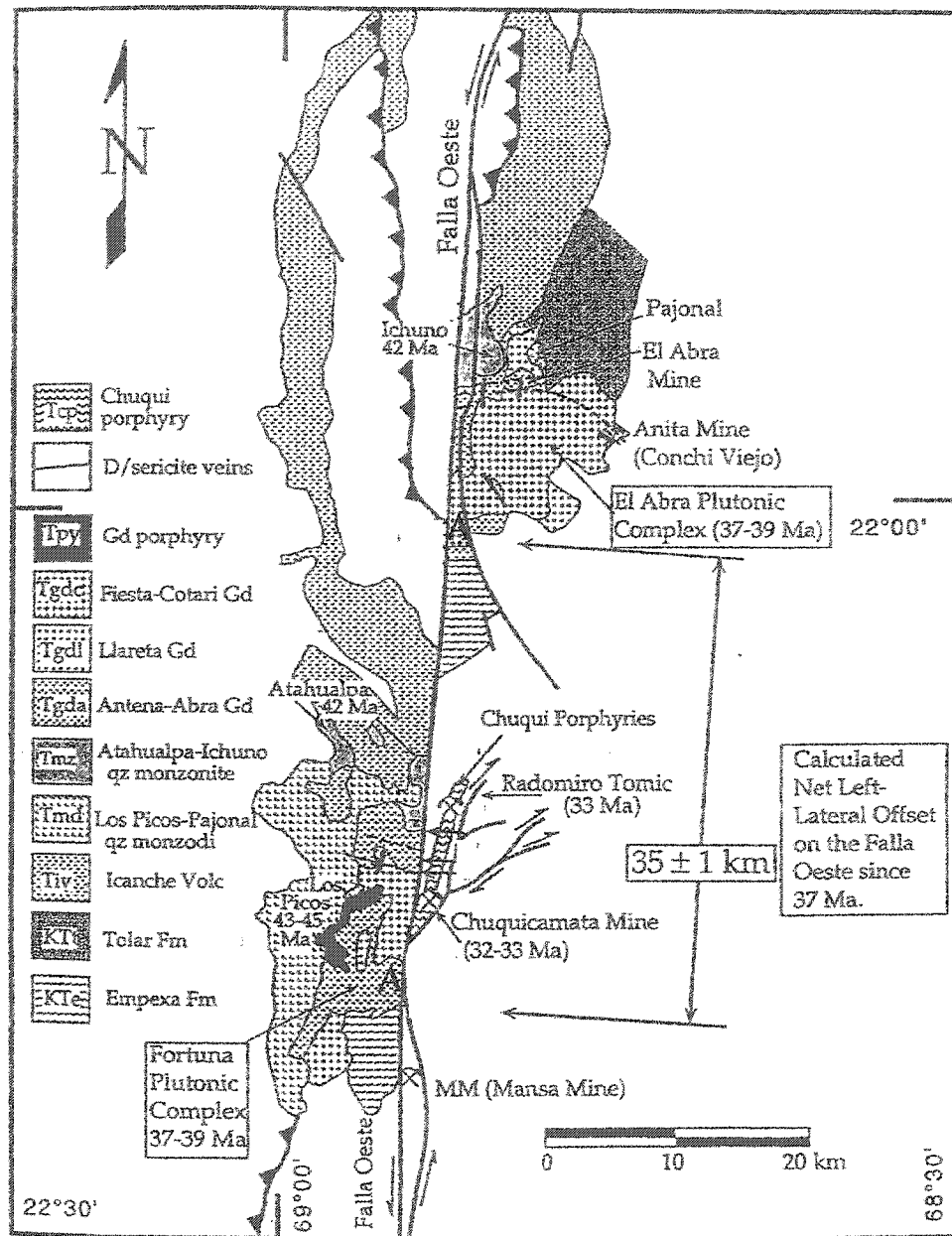


Figure 3.4. Regional geology of the Fortuna-El Abra region (from Dilles et al. 1997), showing the sinistral displacement of 35 ± 1 km along the West Fault (Falla Oeste). The Fiesta and Cotari granodiorites are shown in the same pattern (denoted by 'A').

Chuquicamata Intrusive Complex. Their work suggested that the post-mineralization exhumation was greater in the Fortuna block by $600 \pm 100\text{m}$ (Fig. 3.5).

Previously published ages are reported in Table 3.1. Early K-Ar biotite ages (Quirt 1972, Ambrus 1979) indicated that the age of the Fortuna Granodiorite is 35.9 to 39 Ma. More recently, the Antena Granodiorite yielded slightly discordant U/Pb zircon ages of 39.3 ± 0.4 Ma and 39.0-39.6 Ma K-Ar biotite ages (Dilles et al. 1997). A slightly discordant U/Pb zircon age of 37.6 ± 0.7 Ma and a 37.3-37.9 Ma K/Ar biotite age (Dilles et al. 1997) were reported for the Fiesta Granodiorite.

Structural and petrologic work have confirmed the similarities between the units of the El Abra Granodiorite Complex and those of the Fortuna Intrusive Complex (e.g. Dilles et al. 1997). The Antena Granodiorite is believed to be the equivalent of the Abra Granodiorite; the Cotari Granodiorite, which intruded the Abra Granodiorite, is believed to be equivalent to the Fiesta Granodiorite (Fig. 3.4) (Dilles et al. 1997). Dilles et al. (1997) suggest 35 ± 1 km left-lateral displacement along the West Fault.

Recently, there has been much debate regarding Os-isotope analytical work. Mathur et al. (2000) reported that among South American porphyry copper deposits, those with the highest Cu-concentrations have the least radiogenic (more mantle-like) Os isotopic composition, whereas highly radiogenic (more crust-like) Os isotopic compositions are evident in the smaller deposits (Fig. 3.6). Mathur et al. (2000) suggest that it may be possible to use this variation in Os isotopic compositions as an indicator of the amount of mineralization in a system. Chuquicamata has the lowest $^{187}\text{Os}/^{188}\text{Os}_i$ ratio

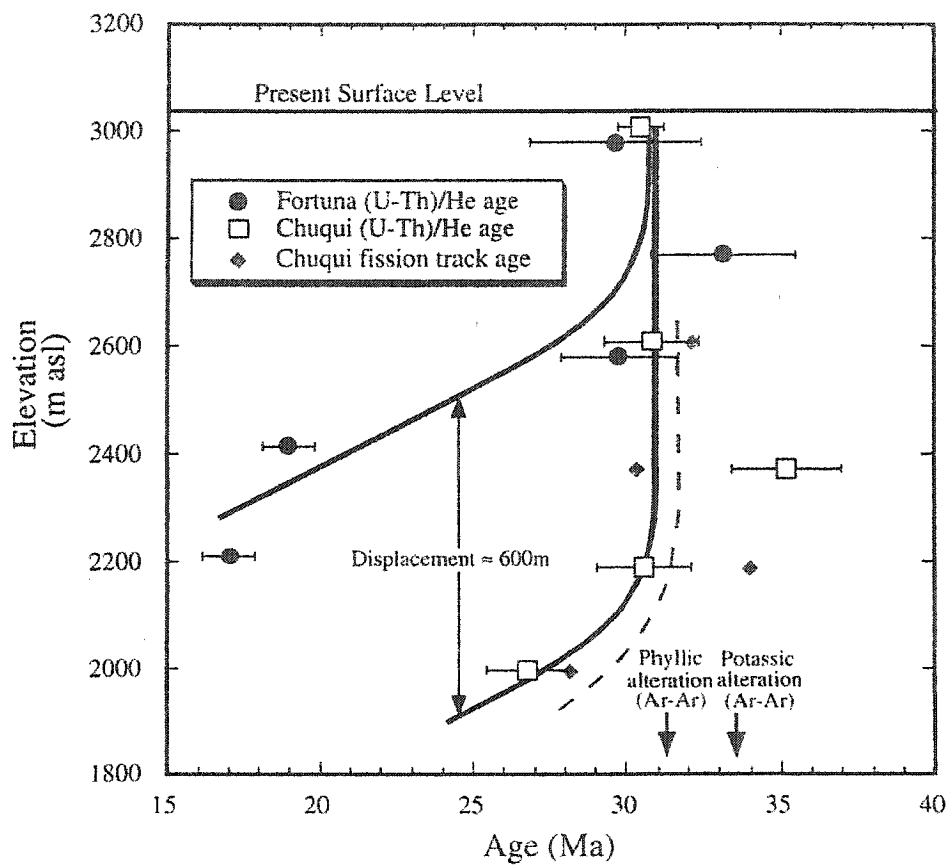


Figure 3.5. Age-elevation diagram constructed using apatite (U-Th)/He and fission track dating. Modelled cooling curves are shown as heavy lines. A geothermal gradient of $20^{\circ}\text{C}/\text{km}$ was calculated for both the Fortuna and Chuquicamata Intrusive Complexes. Ar-Ar dates are from Reynolds et al. (1998). Dashed line represents Chuquicamata fission track data. Figure from McInnes et al. (1999).

Table 3.1. Previously published dates from the Fortuna Intrusive Complex. Note the relatively large errors. The two U/Pb zircon ages are both from three slightly discordant samples (Tomlinson et al. 1997).

Lithology	Age \pm 2sigma (Ma)	Method	Reference
Antena Granodiorite	36.2 \pm 1.4	K/Ar Biotite	Ambrus 1979
	39.5 \pm 1.1	K/Ar Biotite	Maksaev et al. 1988b
	39.0 \pm 1.2	K/Ar Biotite	Maksaev et al. 1988b
	35.6 \pm 1.0	⁴⁰ Ar/ ³⁹ Ar TGA Biotite	Maksaev 1990
	40.6 \pm 1.2	K/Ar Biotite	Tomlinson et al.1997
	39.6 \pm 1.2	K/Ar Biotite	Tomlinson et al.1997
	36.3 \pm 1.1	K/Ar Biotite	Tomlinson et al.1997
	39.3 \pm 0.9	U/Pb Zircon	Dilles et al. 1997
Fiesta Granodiorite	37.8 \pm 1.2	K/Ar Biotite	Quirt 1972
	35.9 \pm 1.0	K/Ar Biotite	Ambrus 1979
	39.0 \pm 3.0	K/Ar Biotite	Ambrus 1979
	37.3 \pm 1.2	K/Ar Biotite	Tomlinson et al.1997
	37.6 \pm 0.7	U/Pb Zircon	Tomlinson et al.1997
	32.1	Fission track Apatite	Maksaev and Zentilli 1999
San Lorenzo Porph	38.5 \pm 1.1	K/Ar Biotite	Tomlinson et al.1997
	37.1 \pm 0.9	K/Ar Biotite	Tomlinson et al.1997

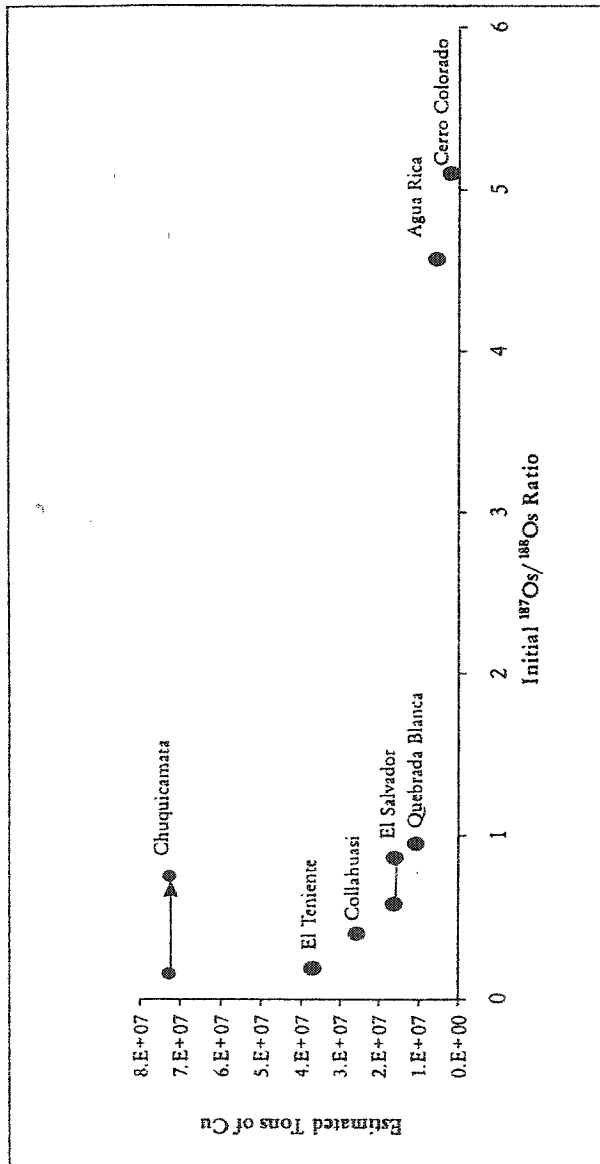


Figure 3.6. Cu-tonnage versus initial ¹⁸⁷Os/¹⁸⁸Os values of Chilean porphyry copper deposits. It was proposed that there is a correlation between Cu-tonnage and initial ¹⁸⁷Os/¹⁸⁸Os values (from Mathur et al. 2000). The more mantle-like, the higher the Cu-tonnage.

of 0.155 in Chilean porphyry deposits. However, there is a wide range in initial $^{187}\text{Os}/^{188}\text{Os}_i$ ratio at Chuquicamata. There also appears to be a connection between the age of the deposits and their initial Os signatures (Fig. 3.7).

McBride et al. (2001) contested the “size vs. Os ratio” hypothesis of Mathur et al. (2000) by analyzing samples from the Fiesta Granodiorite. Their research indicated that the relatively unmineralized Fiesta Granodiorite has an Os ratio similar to that of the Chuquicamata samples from Mathur’s (2000) study. Mathur et al. (2001) replied to this comment by suggesting that the results are compatible with either the Fortuna Intrusive Complex being the root of Chuquicamata or the Fortuna Intrusive Complex being related to the El Abra Porphyry copper deposit, as mentioned above. These hypotheses are discussed further in Chapter 7.

3.3.2 The "Chuqui" Porphyries

The “Chuqui Porphyries” are now referred to as the Chuquicamata Porphyry System or the Chuquicamata Intrusive Complex. The Chuquicamata Intrusive Complex was emplaced within a strike-slip fault system during the evolution of the Eocene-Oligocene magmatic arc (Lindsay 1998).

Several porphyries make up the Chuquicamata Intrusive Complex and they have been described by different researchers and the nomenclature has changed over time (Table 3.2). Renzetti (1957) recognized only one porphyry, where Langerfeldt (1964) and Guilbert (1963) recognized four; Turintvez et al. (1973) and Soto (1979) recognised three. Most recently, Ossandón et al. (2001) identified four porphyries. Differences in

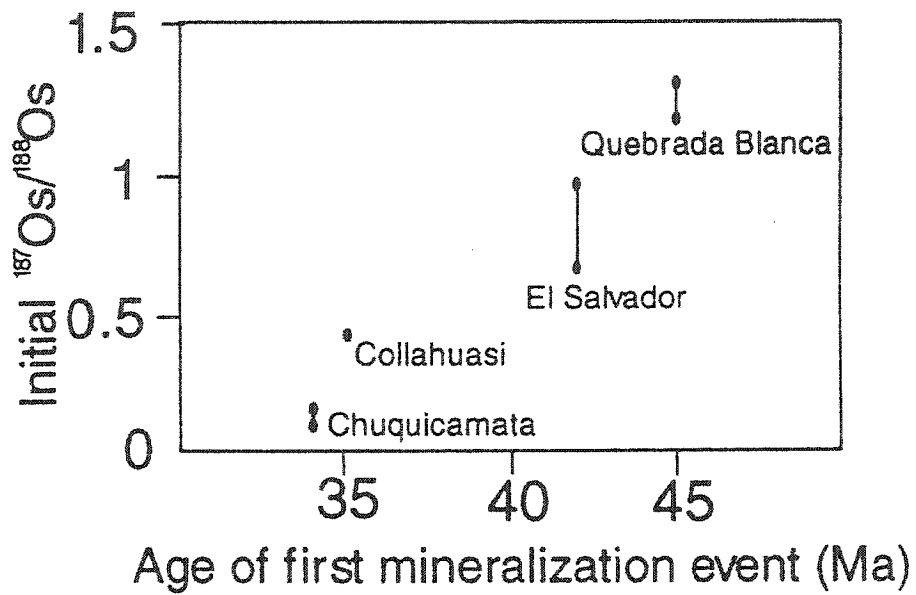


Figure 3.7. Age of mineralization versus initial $^{187}\text{Os}/^{188}\text{Os}$ (from Mathur et al. 2001). Younger deposits are more radiogenic.

Table 3.2. The nomenclature of the Chuquicamata porphyries has changed over the years because of difficulty in identifying the protoliths and the level of exposure. Note that the Banco Porphyry was identified and characterized earliest because of its distinct texture.

Author	Este Porphyry	Banco Porphyry	Oeste Porphyry	Other
Guilbert (1963)	"A" ?	Banco Porphyry	"B" ?	"C" (Este?)
Langerfeldt (1964)	Coarse interstitial?	Banco Porphyry	Aplitic ground mass ?	Ragged texture (Este?)
Thompson (1964)	East side Chuqui porphyry	Banco Porphyry		
Turintvez et al. (1973)	Porfido Este	Porfido Banco	Porfido Oeste	
Ambrus (1979)	Textura Este	Textura Banco	Textura Oeste	Textura "J"
Soto (1979)	Medium- to fine-grained phaneritic matrix	Fine-grained aphanitic matrix	Medium-grained aphanitic matrix	
Parada et al. (1987)	Porphyry I	Porphyry III	Porphyry II	
Mayne-Nicholls et al. (1995)	Porfido Este	Porfido Banco	Porfido Oeste	
Ossandon et al. (2001)	East Porphyry	Banco Porphyry	West Porphyry	Fine texture Porphyry

classification resulted from a combination of the level of exposure (i.e. depth of pit workings), changes in petrographic nomenclature, the development of new techniques available to discern rock types, differences in sampling techniques (due to the size of the deposit), and difficulties in finding unaltered rock in the pit.

The porphyries are distinct units, most easily recognised by the difference in their textures. Currently there is general acceptance at the mine of three distinctive porphyries: the Este Porphyry (also known as Porfido Este or the East Porphyry), the Oeste Porphyry (also known as Porfido Oeste or the West Porphyry) and the Banco Porphyry (also known as Porfido Banco). Table 3.2 summarizes the changes in the nomenclature over the years.

According to Parada et al. (1987), the Banco and Oeste porphyries intruded the Este Porphyry. However, only intrusive contacts between the Banco and Este porphyries have been observed (Ossandón et al. 2001). The crosscutting relationships between the Oeste Porphyry and Fine-grained Porphyry of Ossandón et al. (2001) remain unobserved and, therefore, are ambiguous; it is possible that they may simply represent textural variations of the Este and Banco porphyries.

3.3.2.1 Este Porphyry

The Este Porphyry is currently the most abundantly exposed mineralized rock in the Chuqui pit, however, during the early mining stages it was less widespread (Fig. 3.8). It now comprises over 80% of the exposed rock in the Chuquicamata Porphyry System (Lindsay 1998).

The Este Porphyry is characterized by abundant large orthoclase phenocrysts,

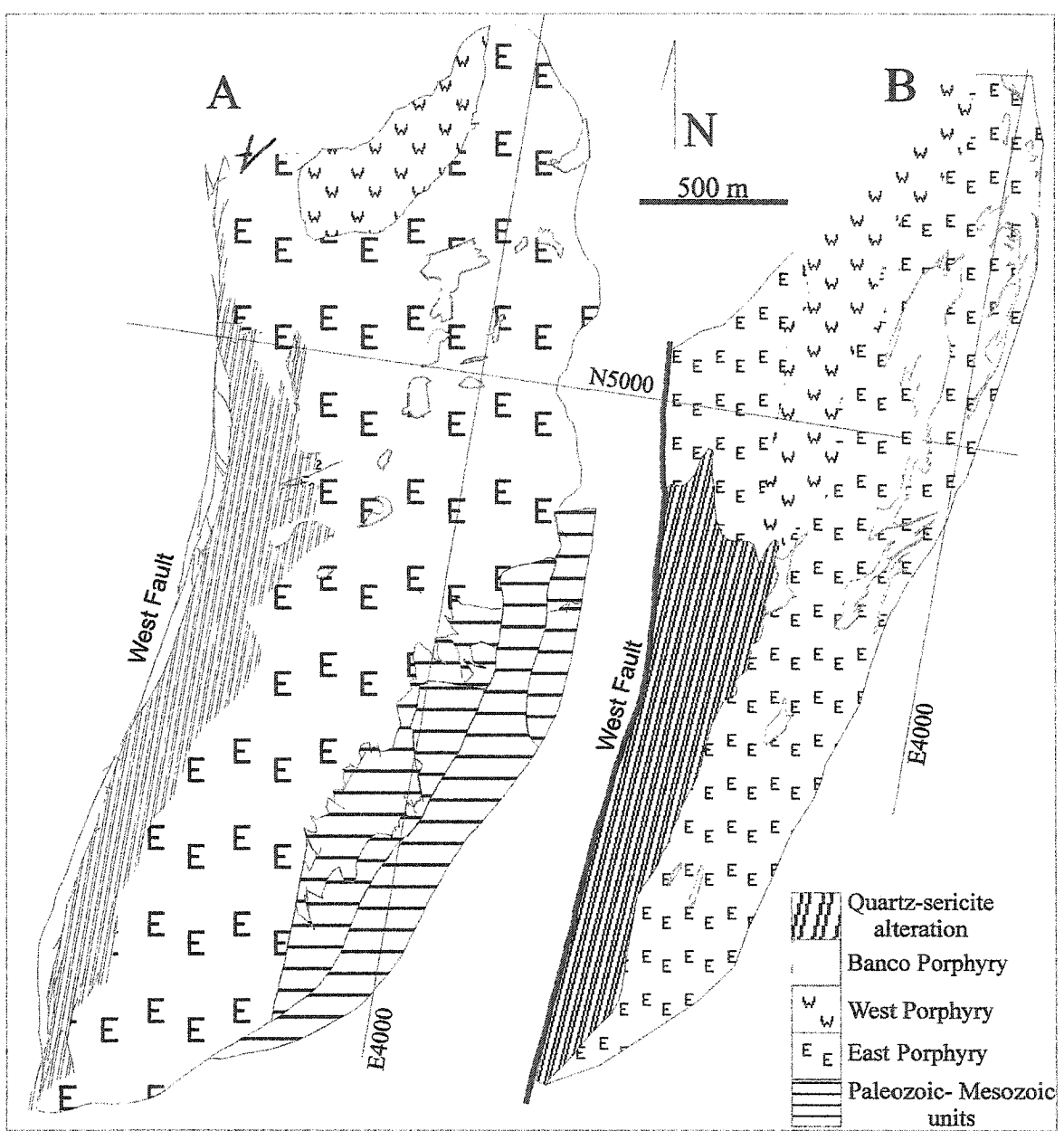


Figure 3.8. Comparison of the importance of the Banco and Oeste porphyries at different levels of exposure. A) The exposure in 1995; B) The level of exposure in 1966 (based on a report by Applegate 1966). After Lindsay (1998).

biotite 'books', quartz 'eyes', and euhedral plagioclase phenocrysts (An_{10-30}) (Ambrus 1979, Soto 1979, Turintvez et al. 1973). The potassium feldspar megacrysts have inclusions of quartz and plagioclase (Soto 1979) with a perthitic texture (Ambrus 1979). Soto (1979) described albite replacing the K-feldspar grains. The quartz eyes are elongate, polycrystalline aggregates, commonly with corroded edges (Soto 1979). Traces of amphibole and titanite are also recognized (Guilbert 1963). The Este Porphyry has "floating" phenocrysts in an intergranular ground mass of quartz and potassium feldspar (Thompson 1964, Langerfeldt 1964).

Parada et al. (1987) and Ambrus (1979) both reported the K-Ar biotite age for the Este Porphyry as 33.6 ± 0.9 Ma (Table 3.3). Ambrus (1979) also reported a K-Ar age of 34.8 ± 1.9 Ma. An $^{40}\text{Ar}/^{39}\text{Ar}$ K-feldspar age of 33.4 ± 0.4 Ma and $^{40}\text{Ar}/^{39}\text{Ar}$ biotite age of 33.9 ± 0.3 Ma were reported by Reynolds et al. (1998) (Table 3.3). An excimer laser ablation ICP-MS study reported a zircon U/Pb age of 34.6 ± 0.2 Ma (Ballard et al. 2001). Further discussion and interpretation of the age data of the Este Porphyry is presented in Chapters 5 and 7.

3.3.2.2 Banco Porphyry

The Banco Porphyry is most easily recognized because of its unique texture. The Banco Porphyry has a 'doubly porphyritic' texture distinguished by two populations of plagioclase lath sizes in an aphanitic quartz-feldspar-biotite groundmass (Langerfeldt 1964). It has been described as having a "porcelain" groundmass and fine-grained flow banding (Guilbert 1963). Soto (1979) reported quartz and tabular biotite in the Banco

Table 3.3. Previously published ages from the Chuquicamata Intrusive Complex.

Este Porphyry	Age	Mineral	Reference
K-Ar	34.8 ± 1.9 Ma.	Biotite	Ambrus (1979)
K-Ar	33.6 ± 0.9 Ma	Biotite	Parada et al. (1987)
⁴⁰ Ar/ ³⁹ Ar (preferred)	33.4 ± 0.4 Ma	K-feldspar	Reynolds et al. (1998)
⁴⁰ Ar/ ³⁹ Ar	33.9 ± 0.3 Ma	Biotite	Reynolds et al. (1998)
U-Pb LA ICP-MS	34.6 ± 0.2 Ma	Zircon	Ballard et al. (2001)
Banco Porphyry			
K-Ar	33.8 ± 1.3 Ma	Biotite	Parada et al. (1987)
⁴⁰ Ar/ ³⁹ Ar	33.1 ± 0.2 Ma	K-feldspar	Reynolds et al. (1998)
U-Pb LA ICP-MS	33.3 ± 0.3 Ma	Zircon	Ballard et al. (2001)
Oeste Porphyry			
K-Ar	31.8 ± 0.9 Ma.	Biotite	Ambrus (1979)
U-Pb LA ICP-MS	33.5 ± 0.2 Ma	Zircon	Ballard et al. (2001)

Porphyry. The K-feldspars are microperthitic, and are replaced locally by albite (Soto 1979). Trace amphibole and poikilitic potassium feldspars have been reported (Parada et al. 1987).

A 33.8 ± 1.3 Ma biotite K-Ar age for the Banco Porphyry was reported by Parada et al. (1987) (Table 3.3). K-feldspar yields an $^{40}\text{Ar}/^{39}\text{Ar}$ age of 33.1 ± 0.2 Ma (Reynolds et al. 1998) (Table 3.3). A U/Pb zircon ELA-ICP-MS age of 33.3 ± 0.3 Ma was reported by Ballard et al. (2001) (Table 3.3). Ossandón et al. (2001), based partly on the present thesis work, interpreted the Banco Porphyry to have intruded after the emplacement of the Este Porphyry but prior to potassic alteration. This interpretation on the relative age of the Banco Porphyry is not supported by the present study and is discussed further in Chapters 5 and 7.

3.3.2.3 Oeste Porphyry

When the pit mine was shallower, the Oeste Porphyry was a major component in the Chuqui porphyry (Fig. 3.8). It now comprises little (<5%) of the rock exposed in the pit and the rock exposed is typically altered by the Qser alteration phase.

The Oeste Porphyry is described as aphanitic with a fine-grained quartz-feldspar-biotite matrix. K-feldspar is perthitic, subhedral to anhedral, with size varying from 1 to 12 mm (Ambrus 1979, Soto 1979). The plagioclase phenocrysts are euhedral grains 1 to 3 mm long. Quartz eyes are predominantly allotriomorphic and monocrystalline with local bipyramids (Soto 1979). Biotite is found in small subhedral to euhedral books (Soto 1979).

Parada et al. (1987) and Ambrus (1979) have both reported a biotite K-Ar age of 31.8 ± 0.9 Ma (Table 3.3). Zircon U/Pb ELA-ICP-MS reveals a 33.5 ± 0.2 Ma age (Ballard et al. 2001; Table 3.3), making it practically indistinguishable in age from that of the Banco Porphyry.

3.4 Structural and mineralization evolution

The Chuquicamata Intrusive Complex was emplaced in a dextral strike-slip fault system that was active during the evolution of the Eocene-Oligocene magmatic arc (Lindsay 1998). Qser alteration is concentrated along deposit-scale fault systems and internally-fractured large-scale vein arrays (Lindsay 1998). These fault systems and vein arrays crosscut the potassic and propylitic alteration (Lindsay 1998).

Mineralization forms a stockwork or veinlet systems, with veinlets (<5 mm wide) and vein arrays (>>10 cm wide) (Lindsay 1998). The stockwork system is found in the potassic alteration zone and is composed of veinlets that have a definable emplacement sequence as follows:

- a. quartz \pm K-feldspar
- b. quartz
- c. quartz-molybdenite
- d. quartz-Cu-Fe sulphides
- e. Cu-Fe sulphides
- f. Cu-Fe sulphides and sericite alteration halo

The mineralized fractures formed as extensional (NE) and shear-extensional

(NNE and NNW) fractures that resulted from hydrofracturing influenced by the regional stress field (Lindsay 1998).

Larger scale mineralized vein arrays are spatially associated with Qser alteration. This mineralization sequence is dominated by quartz-molybdenite veins that are crosscut by enargite + pyrite \pm sphalerite veins and pyrite-dominated(+ chalcopyrite \pm chalcocite \pm covellite) veins (Lindsay 1998). A vertical relationship exists between the enargite-dominated and pyrite-dominated vein types but their relationship is unclear (Lindsay 1998). The orientations of these vein types coincide with dominant fault trends within structural domains (Lindsay 1998; Fig. 3.9; Table 3.4).

3.5 Alteration and mineralization

The first comprehensive, although simplified, description of the alteration at Chuquicamata was written by Guilbert and Park (1986) (Fig. 3.10). Earlier detailed descriptions of the alteration have been excluded as they are inconsistent and predate the late 20th century models for porphyry development. In 1993, Zentilli et al. were the first to propose the ‘multiple intrusion’ alteration model for Chuquicamata that led to this thesis.

In the 1990s, the mining company (CODELCO) carried out a comprehensive re-logging of all available drillcore (Mayne-Nichols et al. 1995). This study recommended the classification of two types of alteration: “fundamental” and “superposition”. “Fundamental” alteration includes potassic and Qser alteration. “Superposition” alteration refers to alteration zones that overprint the “fundamental” alteration as well as a

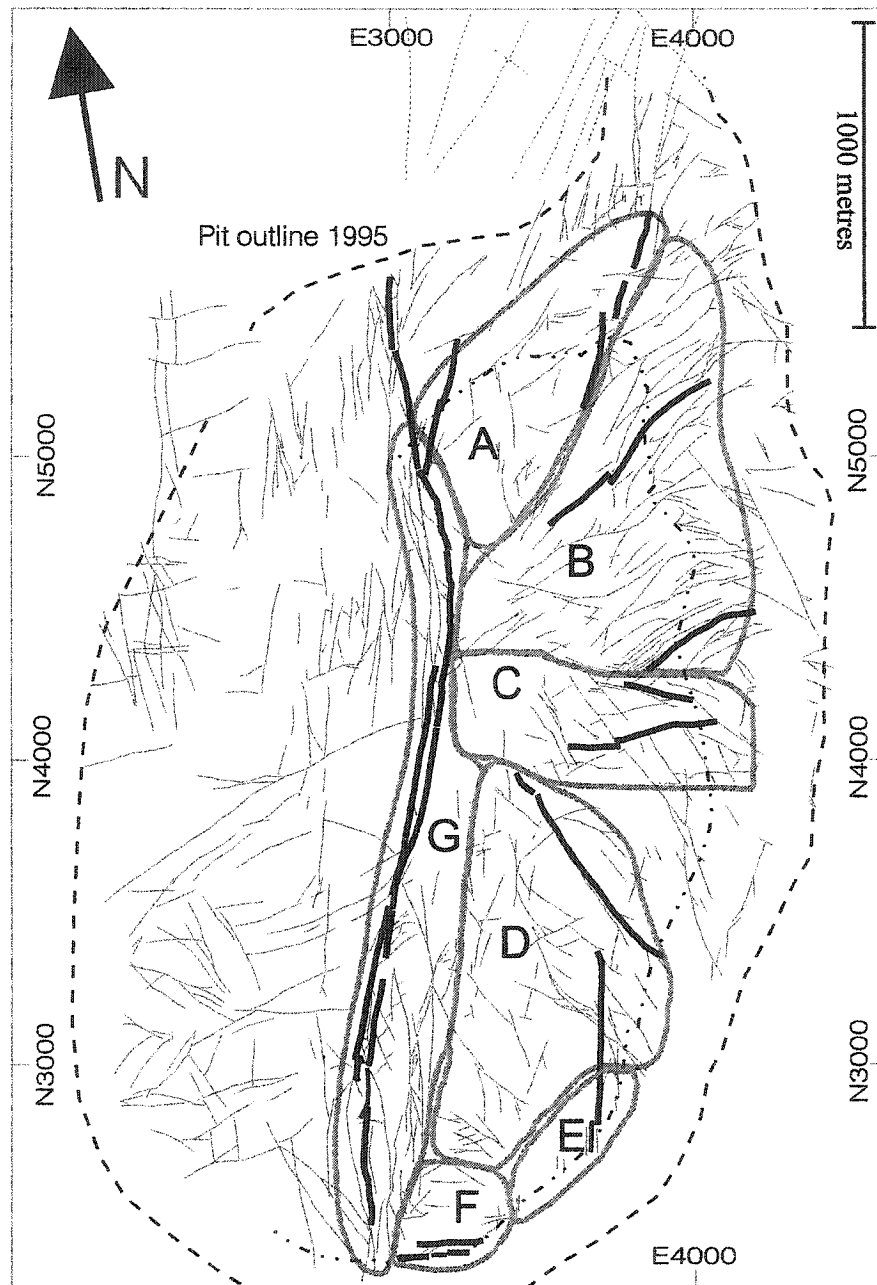


Figure 3.9. The structural domains of Lindsay (1998). The domains are based on timing, orientation and sense of movement. See Table 3.4 for details on these domains. From Lindsay (1998).

Table 3.4. The structural domains of Lindsay (1998) shown in Figure 3.9. The domains are defined based on the sense of motion, orientation and timing.

Domain	Initial Displacement	Latest Displacement	Orientation	Mineral Relation	Dilation
Messabi	Dextral	Sinistral	NNE-SSW	Dextral: pre-mineral sinistral: post-mineral	Low
A - Zaragoza-C2	Dextral Zaragoza 700m C2 400m	Zaragoza ? C2 sinistral	NNE-SSW and NE-SW	Dextral: pre-to syn-mineral	High
B - Estanques Blancos	Dextral	Dextral	prominent: NE-SW minor: WNW-ESE	Dextral: pre-,syn-, post-mineral?	High
C - Balmaceda	Sinistral	Dextral, sinistral (500 m, 300 m)	~E-W	Sinistral: pre-mineral dextral: syn post?	Mod-high
D - South Central	Sinistral	Sinistral (500 m)	~NW-SE	Sinistral: post	Low
E - South Eastern	Dextral??	Sinistral	NNE-SSW	Dextral: pre-mineral? sinistral: post-mineral?	Low-mod
F - Southern (Banco H1)		Dextral (<100 m)	ESE-WNW	Dextral: post	Low
G - West Fault Americana	Dextral?	Sinistral (35-37 km)	NNE-SSW	Dextral: syn-mineral? sinistral: post-mineral	Mod

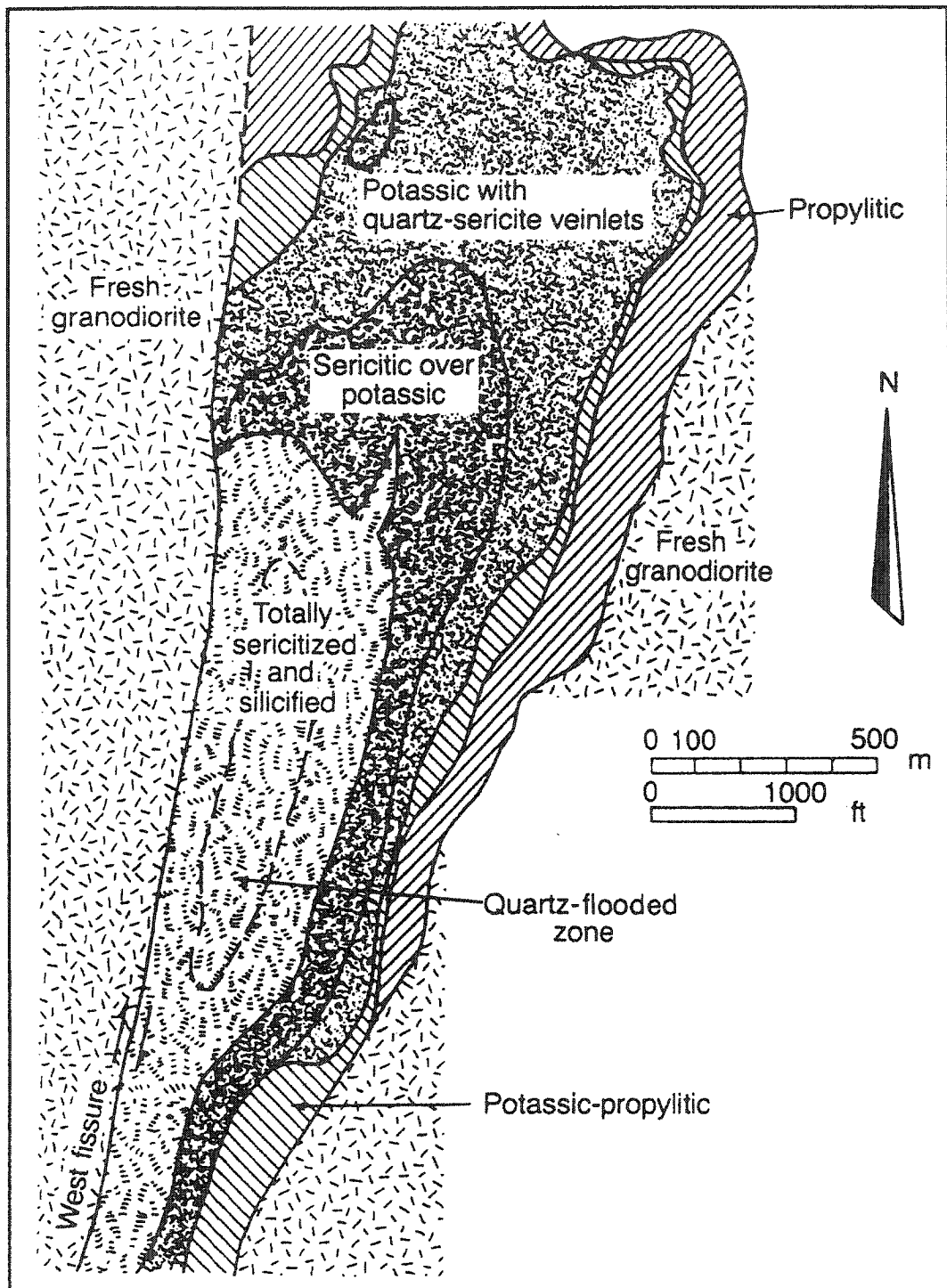


Figure 3.10. Simplified alteration zones within the Chuquicamata Porphyry System. From Guilbert and Park (1986).

zone known as the SK where the potassic alteration is overprinted by the Qser alteration. The “superposition” zones include chloritization, silicification, argillization, epidotization, and alunitization. The nomenclature of Mayne-Nicholls et al. (1995) is empirical and field-based and was evolving when this project started; therefore, it was not used during sampling for this thesis.

Work on geochronological, isotope, and geochemical studies by Cuesta Research Ltd. in the mid- to late-1990s led to several unpublished confidential reports. These research contracts resulted in several research theses at Dalhousie University (e.g. Lewis 1997, Lindsay 1998), including the present study.

Ossandón et al. (2001) classified the deposit components based on the principal stages of mineralization and are described briefly in the following section. The studies and findings of other workers have been incorporated to augment the descriptions of Ossandon et al. (2001). The stages described are the early (potassic), quartz-molybdenite, main (Qser) and late stages.

3.5.1 Early stage

According to the model of Ossandón et al. (2001), early-stage alteration includes potassic, quartz-K-feldspar, silicification and propylitic alteration (described in Figure 3.1 as propylitic and potassic-propylitic).

Potassic alteration is characterized by an assemblage of secondary biotite, with local quartz and secondary K-feldspar inclusions (Ossandón et al. 2001). Megacrysts of K-feldspar were earlier considered magmatic but the presence of resorbed inclusions of

plagioclase indicate that they may also be potassic alteration features (Ossandón et al. 2001). Quartz was reported as recrystallized (Ossandón et al. 2001). Intermediate plagioclase has been completely replaced by albite. Ossandón et al (2001) also reported the presence of anhydrite in the potassic alteration zone. Ossandón et al. (2001) claim that all of the porphyries of the Chuquicamata Porphyry system have been affected by potassic alteration. This claim is discussed by the present author in Chapter 5.

Mayne-Nicholls et al. (1995) described the potassic alteration as the early phase based on the following criteria:

- a) the preservation of the rock texture,
- b) the stability of feldspars and biotite,
- c) the addition of potassium feldspar veinlets, and
- d) the replacement of mafic minerals by biotite.

Late veins of sericite with sericitic halos are present in minor amounts and the halos do not strongly affect the texture of the rock (Mayne-Nicholls et al. 1995).

K-feldspar ages from the potassic alteration zone range from 32.9 to 33.8 Ma, with a mean of 33.4 ± 0.3 Ma (Reynolds et al. 1998) (Table 3.5). The biotite ages yield a wider range of ages, as discussed in Chapters 5 and 7. Potassic alteration was coeval with the cooling and deformation of the host porphyries in a ductile to brittle regime, related to the dextral strike-slip system (Lindsay 1998).

Veins of quartz and K-feldspar are associated with the potassic alteration (Ossandón et al. 2001). The potassic alteration zone is associated with chalcopyrite-bornite mineralization without pyrite (Ossandón et al. 2001). Temperatures of

mineralization for the potassic zone are 400 to 600°C, based on sulphide phase equilibria (Lewis 1997).

Table 3.5. Previously published potassic ages.

Sample #	Mineral	Age	Reference
Cu 406	K-feldspar	33.7 ± 0.2 Ma	Reynolds et al.(1998)
	Biotite	34.0 ± 0.4 Ma	Reynolds et al.(1998)
	Biotite	35.2 ± 0.2 Ma	Reynolds et al.(1998)
Cu 408	K-feldspar	33.6 ± 0.2 Ma	Reynolds et al.(1998)
	Biotite	32.8 ± 0.2 Ma	Reynolds et al.(1998)

Quartz-K-feldspar ('Ksil' of Mayne-Nichols et al. 1995) alteration forms a band of hard white rock across the potassic zone (Ossandón et al. 2001). The quartz-K-feldspar alteration resulted in the obliteration of the original texture and the biotite is completely replaced by quartz and K-feldspar (Ossandón et al. 2001). Residual intermediate plagioclase is replaced by albite (Ossandón et al. 2001). Ksil is apparently related to zones of cataclastic deformation (Mayne-Nichols et al. 1995).

The zone of **silicification** also lacks biotite but has less intense cataclastic deformation than the main quartz-K-feldspar alteration (Ossandón et al. 2001). Some of the original texture may be preserved locally in the zone of silicification.

The **propylitic** alteration zone occurs on the east side of the pit (Fig. 3.10). Ossandón et al. (2001) described the propylitic alteration as having chlorite and epidote with specular hematite veinlets. According to Mayne-Nichols et al. (1995), the propylitic zone (referred to as the chloritic alteration zone in that report) is identified by the

presence of veins and veinlets of chlorite, as well as veinlets of magnetite or hematite. Langerfeldt (1964) described this zone as fresh, except for the chloritization of all mafic minerals. The propylitic alteration zone is associated with low-grade chalcopyrite-pyrite mineralization (Ossandón et al. 2001).

3.5.2 Quartz-molybdenite stage

Almost all molybdenite at Chuquicamata is present in quartz veins. A set of small (<1 cm) quartz-molybdenite veins is younger than early stage quartz and quartz-K-feldspar veins (Ossandón et al. 2001). Larger “blue” quartz veins (0.5 to 1 m), with abundant molybdenite appear to be later than smaller veins, and are clearly cut by main-stage Qser veins (Ossandón et al. 2001). Lindsay (1998) showed that quartz-molybdenite veins have a strong preferred orientation consistent with a discrete event within a brittle dextral strike-slip shear system. In some locations quartz-molybdenite veins are strongly recrystallized and show stylolites, evidence of pressure solution (Lindsay 1998).

3.5.3 Main stage

The Qser zone typifies main-stage alteration. It was channelled through late faults (Lindsay 1998) and obliterated much of the original texture of the affected rocks (Fig. 3.10). Pyrite-enargite veins are also characteristic of this stage (Lindsay 1998). Only in areas of weak main-stage alteration is the original rock texture discernible. Langerfeldt (1964) described plagioclase and orthoclase that are mainly converted to sericite and noted that mafic minerals are absent and biotite is ‘bleached’. Mayne-

Nichols et al. (1995) divided the Qser alteration into 'strong' or 'minor' intensities based on the degree of alteration of the original protolith.

Mayne-Nichols et al. (1995) recognized two transition zones (SK and KS), each characterized by the style and abundance of sericitization of the potassically altered rocks. These zones are not useful in a study of alteration; however, they are important to mining geologists because of the Cu enrichment related to the sericitic alteration event.

The SK (sericitic over potassic in Figure 3.10) is characterized by extreme sericitization. The original texture of the rock has been partly obliterated. Potassium feldspar is metastable and mafic minerals have been discoloured and corroded; in this sub-unit the sericitization is pervasive (Mayne-Nichols et al. 1995).

The KS (potassic with quartz-sericite veinlets in Figure 3.10) is characterized by potassic alteration. The rock texture can be easily reconstructed and potassium feldspar and mafic minerals are stable (Mayne-Nichols et al. 1995). In this sub-unit the sericite is restricted to halos around veinlets and quartz veins (Mayne-Nichols et al. 1995).

Typically mineralized vein assemblages in the main stage are pyrite-chalcopyrite-bornite, pyrite-bornite-digenite \pm enargite, and pyrite-digenite-covellite \pm enargite (Ossandón et al. 2001). It has been proposed by some consultants that the Cu sulphides in the Qser zone are recycled from the potassic zone. However, the Qser zone at Chuqui tends to have double the Cu grade of the potassic, suggesting that, in addition to remobilization, there has been an addition of Cu.

Radiometric dating of the Qser zone has consistently given ages of ~31.0 Ma (Table 3.6). Ambrus (1977) reported K-Ar sericite ages of 31.0 ± 1.2 Ma. $^{40}\text{Ar}/^{39}\text{Ar}$

dating of sericite indicates that the Qser alteration event occurred at 31.0 ± 0.3 Ma (Reynolds et al. 1998). Further $^{39}\text{Ar}/^{40}\text{Ar}$ dating is discussed in Chapter 6. Re-Os dates on related pyrite mineralization gave an age of 31 ± 2 Ma (Mathur et al. 2000).

Table 3.6. Previously published Qser ages.

Method	Age	Mineral	Reference
K-Ar	31.0 ± 1.2 Ma.	sericite	Ambrus (1977)
$^{40}\text{Ar}/^{39}\text{Ar}$	31.0 ± 0.3 Ma	sericite	Reynolds et al. (1998)
Re-Os	31 ± 2 Ma	pyrite	Mathur et al. (2000)

To determine the temperature, chemistry, and source of hydrothermal fluids that caused the Qser alteration zone a S-isotope study was done by Lewis (1997). This S-isotope study of sulphide-sulphate pairs indicated the range of equilibration temperatures of mineralization to be 300 to 375°C (Lewis 1997) (Fig. 3.11). Lewis (1997) also suggested a temperature of 300 to 435°C for the Qser alteration, based on sulphide phase equilibria. The low temperatures are interpreted as representing meteoric-magmatic fluid mixing (Lewis 1997). Based on the sulphate to sulphide ratio (4:5), the oxygen fugacity equilibria. The low temperatures are interpreted as representing meteoric-magmatic fluid mixing (Lewis 1997). Based on the sulphate to sulphide ratio (4:5), the oxygen fugacity was interpreted to be moderate to high for an acidic environment (Lewis 1997).

Two unpublished fluid inclusion studies at Chuquicamata (Collao 1987; Vega 1989) yielded a wide range of homogenization temperatures (210-470°C) and salinities (1-40 wt,% NaCl-equivalent) (Fig. 3.12). It is probable that secondary inclusions were analyzed and thus the mean T_H obtained, $347 \pm 4^\circ\text{C}$ (Vega 1989) and $338 \pm 5^\circ\text{C}$ (Collao

1987), probably represent an average of the Qser alteration event. These temperatures are consistent with the S-isotope studies mentioned above (Lewis 1997).

3.5.4 Late stage

Covellite-dominant veins characterize the late-stage primary mineralization (Ossandón et al. 2001). Covellite associated with digenite, and conspicuously without quartz, pyrite or other sulphides, constitutes a distinct late-stage mineralization (Ossandón et al. 2001). These late-stage veins may contain red hematite and anhydrite (Ossandón et al. 2001).

3.5.5 Supergene enrichment

Mining of the supergene deposit at Chuqui commenced in pre-historic times and the supergene zone was mainly mined out by the middle of this century; little has been recorded as to the alteration associated with the supergene enrichment (Ossandón et al. 2001). However, a low-grade supergene deposit remains in the north of the pit area (Ossandón et al. 2001). The main ore minerals found in the supergene blanket are antlerite ($\text{CuSO}_4 \cdot \text{Cu}(\text{OH})_2$), brochantite ($4\text{CuO} \cdot \text{SO}_3 \cdot 3\text{H}_2\text{O}$), atacamite ($\text{CuCl}_2 \cdot 3\text{Cu}(\text{OH})_2$), chrysocolla ($\text{CuO} \cdot \text{SiO}_2 \cdot 2\text{H}_2\text{O}$), and copper pitch ($\text{CuMn} \cdot 8\text{Fe}$). The supergene alteration appears to have been mainly quartz and sericite accompanied by kaolinitic clay (Ossandón et al. 2001).

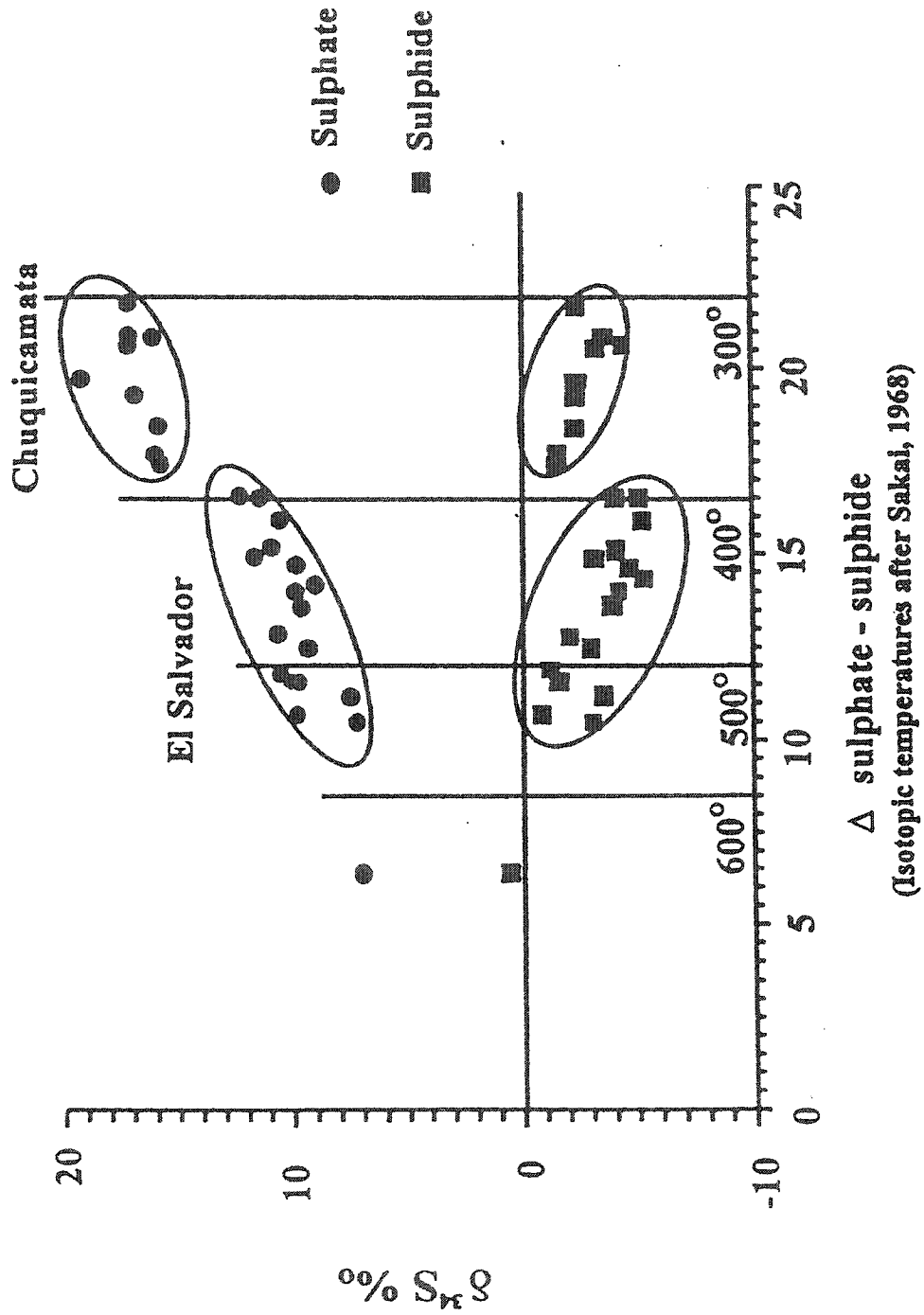


Figure 3.11. S-isotope data showing the range of temperatures for sulphide-sulphate equilibration. From Lewis (1997).

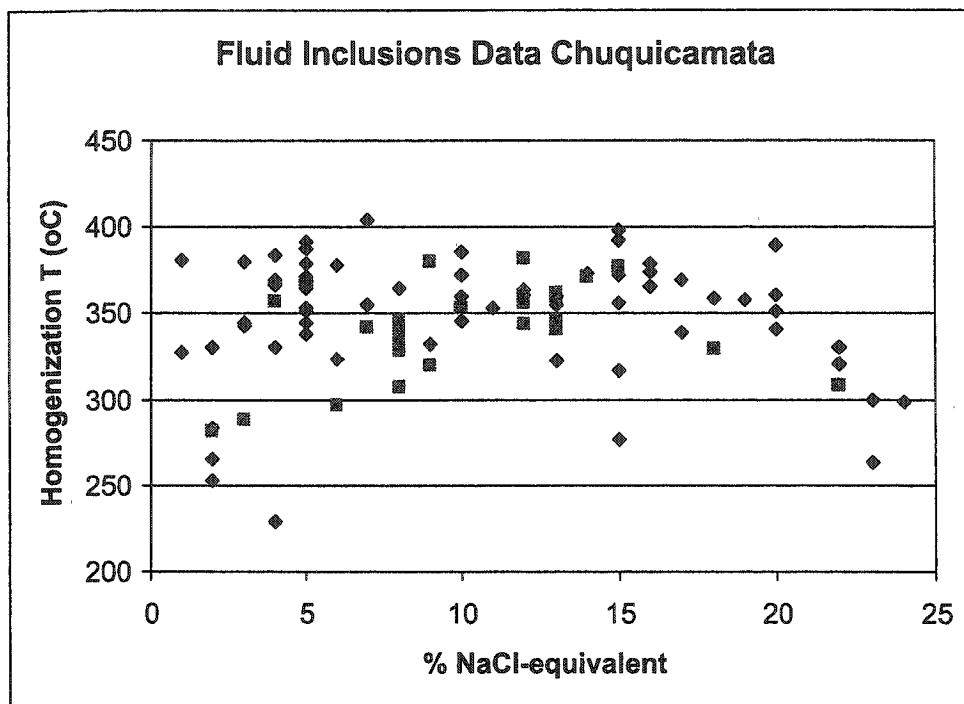


Figure 3.12. Fluid inclusion data of Vega (1989- diamonds) and Collao (1987- squares). It is likely that these are secondary fluid inclusions and the salinity and homogenization temperature data represent an average of the Qser alteration event

Chapter 4

The Fortuna and Chuquicamata Intrusive Complexes

4.1 Introduction

As explained in Chapter 3, two separate intrusive complexes are exposed in the Chuqui pit. The Fortuna and Chuquicamata Intrusive Complexes are in faulted contact along the West Fault, a branch of the Domeyko Fault System (Fig. 4.1). To the east of the fault, the Chuquicamata Intrusive Complex hosts the largest porphyry copper deposit in the world; to the west, the Fortuna Intrusive Complex is essentially unmineralized but is mined to maintain slope stability. The relationship of the Fortuna Intrusive Complex to the Chuquicamata porphyry deposit has been in question for decades.

Although available as part of the mine archives, a detailed map of the Fortuna Intrusive Complex was not published until Dilles et al. (1997). In that report the Fortuna Complex is divided into 3 units: the Antena Granodiorite, the Fiesta Granodiorite which intruded the Antena Granodiorite, and the San Lorenzo porphyries which intruded the Fiesta Granodiorite (Fig. 4.2). The San Lorenzo porphyry is further divided into the Tetera granite-aplite porphyry, the San Lorenzo granodiorite porphyry, and the San Lorenzo mafic granodiorite porphyry (Dilles et al. 1997). The Fiesta Granodiorite comprises the majority of the Fortuna Complex exposed in the Chuqui pit and is the main unit described here.

The Chuquicamata Intrusive Complex, also known as the Chuqui Porphyry Complex, is primarily composed of three porphyries: the Este Porphyry, the Banco

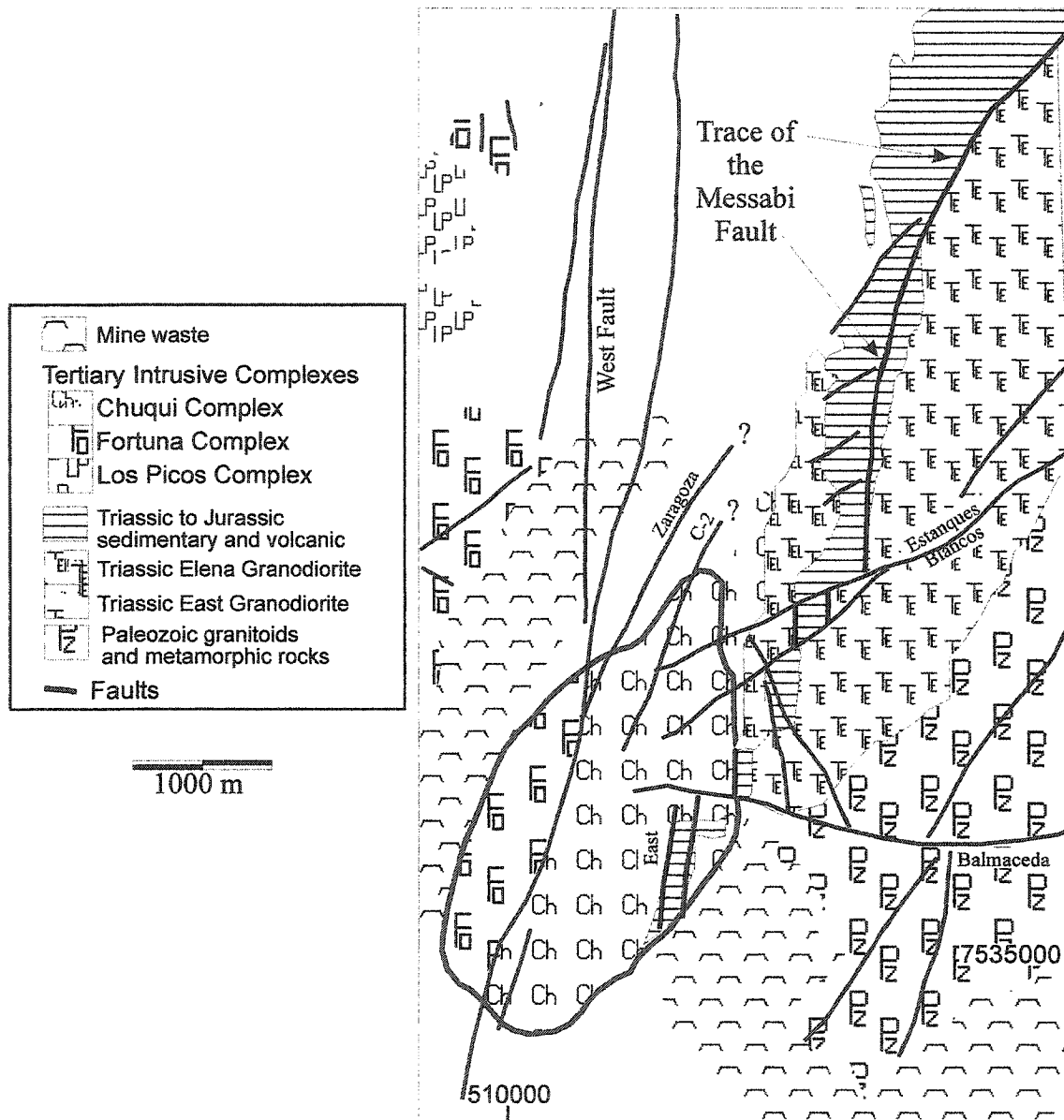


Figure 4.1. Both the Chuquicamata and Fortuna Intrusive complexes outcrop in the Chuqui pit, outlined in red. The Fortuna Intrusive Complex outcrops west of the West Fault. The Chuquicamata Intrusive Complex, in the east of the pit, is composed of the Este, Banco and Oeste porphyries (after Lindsay 1998).

Porphyry, and the Oeste Porphyry (Fig 4.3). The three porphyries are distinct units but are most easily identified by their textural differences. The Banco Porphyry is the most easily recognized by its doubly porphyritic texture and aphanitic groundmass. The Este Porphyry is recognized by its 'crowded' texture characterized by minor amount of groundmass and abundant phenocrysts. The Oeste Porphyry has the most abundant groundmass and fewest phenocrysts. A fourth porphyry has been described by some authors (e.g. Guilbert 1963, Ambrus 1979), although it is debated whether it is a different unit or merely a textural variation of the Este Porphyry. Most recently, Ossandón et al.(2001) describe a 'fine texture porphyry'; this porphyry was not identified during sampling for this project and, therefore, it is not included in the study. The development of the nomenclature of the porphyries was discussed in Chapter 3.

The Este Porphyry (also called the 'East Porphyry') is the most abundant of the Chuqui porphyries in terms of volume and pit exposure. It composes about 80% of the rock volume of the Chuquicamata Intrusive Complex (Lindsay 1998); (Fig. 4.3) and is altered throughout the pit. The Este Porphyry intrudes the Paleozoic-Mesozoic rocks in the east (Fig. 3.1). It extends 5 km north to host the Radomiro Tomic (RT) porphyry copper deposit (Fig 1.2) (Lindsay 1998).

The Banco and Oeste porphyries each comprise about 5% of the rock volume (Lindsay 1998). The Banco Porphyry intrudes the Este Porphyry as dyke-like bodies in the northern part of the mine (Fig. 4.3). This is the only cross-cutting relationship among the Chuqui porphyries documented in core or outcrop. The Oeste Porphyry is limited to the northern region of the Chuqui pit. It is not observed in contact with the Banco

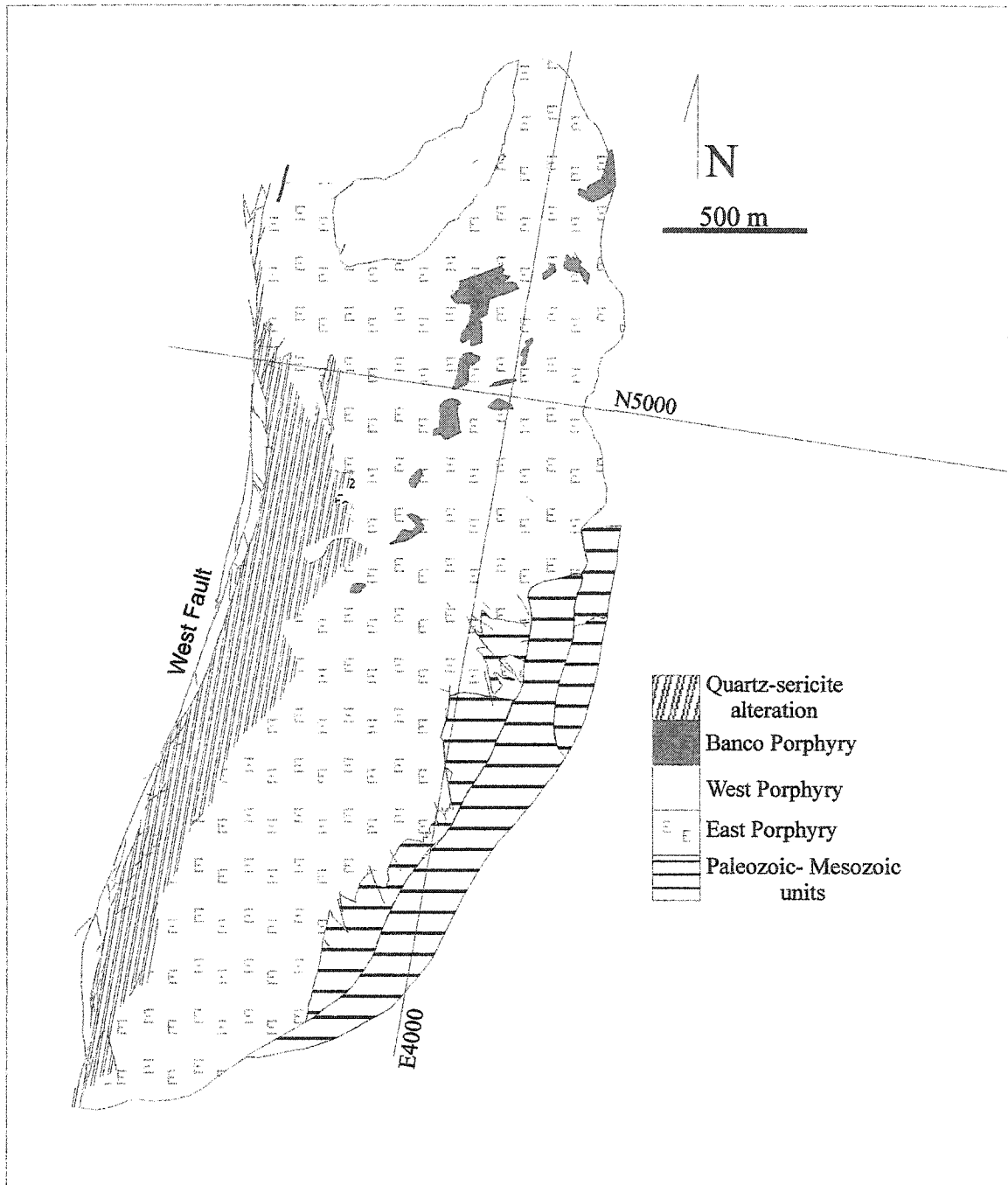


Figure 4.3. Distribution of the porphyries of the Chuquicamata Intrusive Complex. The Este, Banco and Oeste porphyries are identified based on textural differences (after Lindsay 1998, based on open pit mapping 1995). Note: the area identified as quartz-sericite alteration has been too altered to identify the host rock.

Porphyry and appears to have a gradational or faulted contact with the Este Porphyry (Lindsay 1998).

The remaining 10% of the Chuquicamata Intrusive Complex exposed in the pit has been extensively altered and the primary mineralogy and texture are not discernible. These rocks are dominated by Qser alteration. The Qser and argillic alteration completely obliterate the original texture and mineralogy but it is generally believed to represent mainly altered Este Porphyry.

With the assistance of the mine staff, samples were selected that best represented the 'freshest' and most representative Fiesta Granodiorite and Este, Oeste, and Banco porphyries. These samples were used as representative of the protoliths and compared to the alteration zones in Chapters 5 and 6.

The Este Porphyry hosts most of the mineralization. It is largely affected by alteration in the pit. For this reason, the "freshest" Este Porphyry was sampled outside the pit, between Chuqui and the Radimiro Tomic pit excavated to the north (Appendix A). The sample (Cu 769) was collected from what has been mapped as an offshoot of the main porphyry body that would have cooled more quickly than the main intrusive body and, therefore, was less susceptible to the effects of subsolidus replacement and deuteric fluids associated with the cooling pluton. Although a ~0.5 mm vein of sericite is visible in hand specimen, there is no evidence that it has affected the rest of the sample or the primary mineralogy. However, this entire region has been affected by some degree of ductile deformation (Lindsay 1998).

The Oeste Porphyry is located in an area of predominant Qser alteration. For this

study, a 'least-altered' sample (Cu 516) of Oeste was collected from the pit. It is greatly affected by the Qser alteration; however, less altered samples are unlikely to be found.

Two samples (Cu 514 and Cu 1333) of the Banco Porphyry were selected from the pit. They are easily identified by their texture and have also been overprinted by Qser alteration, although less pervasively than the Oeste Porphyry sample.

4.2 Petrology and mineralogy

4.2.1 The Fiesta Granodiorite of the Fortuna Intrusive Complex

4.2.1.1 Observations

The Fiesta Granodiorite is typically leucocratic, with anhedral mafic minerals comprising ~15-30% of the rock (Fig. 4.4). Although mostly anhedral, a few mafic grains show euhedral forms. White plagioclase is euhedral to subhedral and <1 cm long. Megascopic K-feldspar appears interstitial in hand specimen. The Fiesta Granodiorite typically has a medium-grained (1-5 mm) hypidiomorphic texture. For this study, sample Cu 046 has been selected as petrographically typical Fiesta Granodiorite.

The **amphiboles** are pleochroic green to yellow green. One good cleavage is typical and a second poor cleavage is observed locally. Twinning may be seen in the basal sections of some grains. In all other samples from the Fiesta Granodiorite, the amphiboles are partially altered to biotite (Fig. 4.5). In sample Cu 789, the amphiboles are intimately intergrown with biotite and chlorite. The amphiboles in the Fiesta

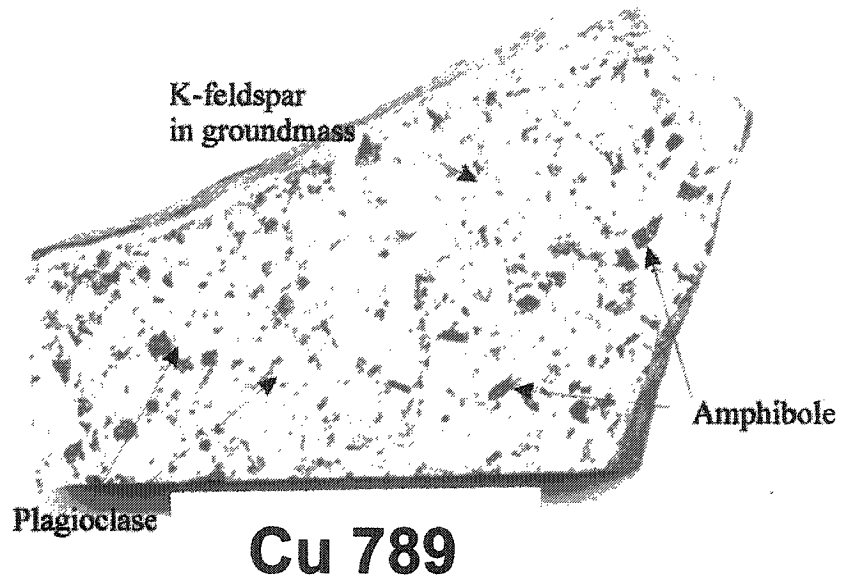
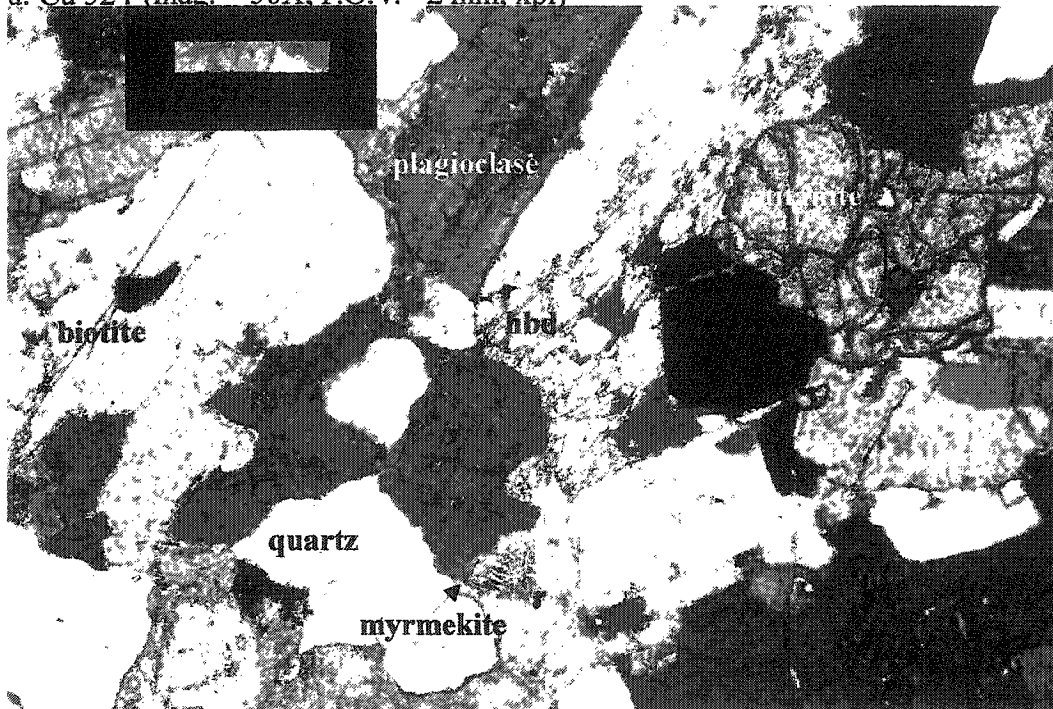


Figure 4.4. Hand specimen of the Fiesta Granodiorite (Cu 789).
White label is 5 cm long for scale.

a. Cu 524 (mag. = 50X; F.O.V.= 2 mm, xpl)



b. Cu 046 (mag. = 50X, F.O.V. = 2 mm, xpl)

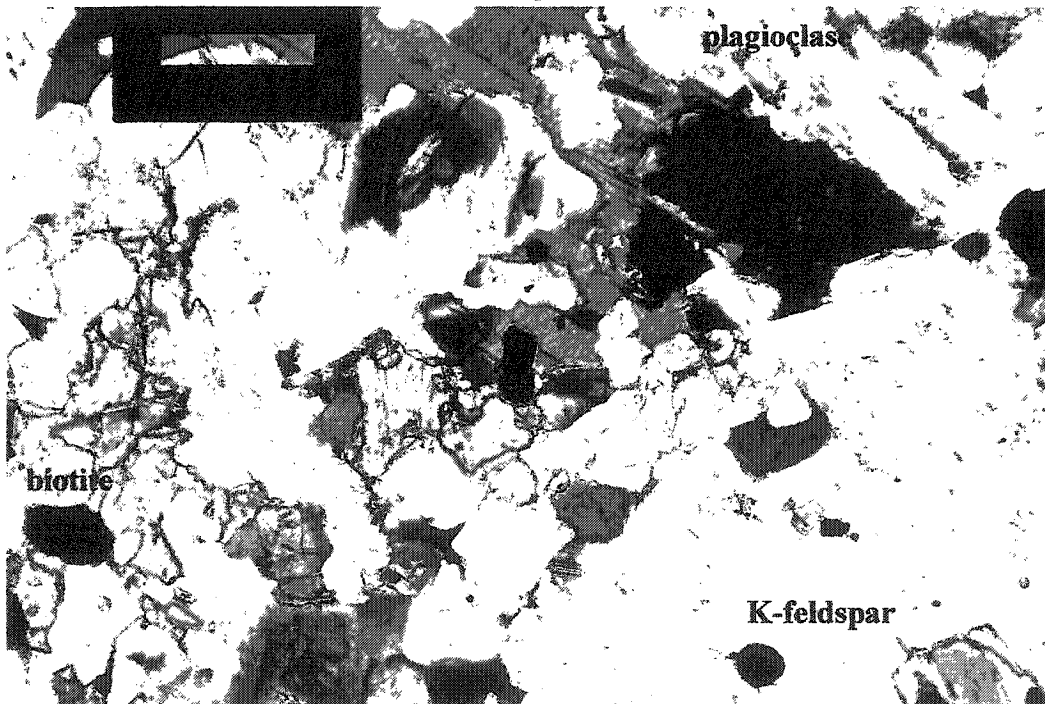


Figure 4.5. Typical mineral assemblages in the Fiesta Granodiorite. a) Large titanite, metastable hornblende, biotite, plagioclase and quartz. Myrmekite is found locally. b) Poikilitic K-feldspar, biotite, hornblende, plagioclase and quartz (hbd= hornblende). (mag.= magnification, F.O.V. = field of view, xpl = cross polarized light)

Granodiorite are calcic with actinolite to magnesio-hornblende compositions (Fig. 4.6).

Plagioclase in the Fiesta Granodiorite has oscillatory zoning and is variably altered to sericite and clays (Fig. 4.5). Plagioclase is <1 cm in length and euhedral to subhedral. Plagioclase laths may be included in K-feldspar. Plagioclase in the Fiesta Granodiorite has a composition of An₃₀₋₅₅ (Fig. 4.7). A fine-grained myrmekitic texture occurs locally (Fig. 4.5).

Biotite occurs as intergrowths with chlorite and amphibole and as individual grains (Fig. 4.5). Biotite has partially replaced hornblende and is altered by chlorite. Biotite in the Fiesta Granodiorite is locally associated with titanite. Fresh biotite is pleochroic brown to yellow and is highly birefringent with one very good cleavage (Fig. 4.5).

In the Fiesta Granodiorite, the **K-feldspar** locally displays micropertthitic texture and may be poikilitic with inclusions mainly of plagioclase but also of hornblende and quartz (Fig. 4.5). In some cases, it is difficult to discern where the K-feldspar grain boundaries are in the poikiolitic granodiorite. K-feldspar appears unaffected by micaceous alteration but inclusions of plagioclase in the K-feldspar grains are locally affected. Electron microprobe analyses indicate that BaO is enriched in the K-feldspar in concentric zones near the edge of the grain and around inclusions (Fig 4.8).

Titanite is anhedral to subhedral and some crystals display a good cleavage in one direction (Fig. 4.5). The grains are up to 1 mm in length. They are enriched in FeO and Al₂O₃ and in various trace elements such as Nb, Sb, Nd, Ce, Th and La (Fig. 4.9). Electron microprobe analysis has also confirmed the presence of **magnetite** in the Fiesta

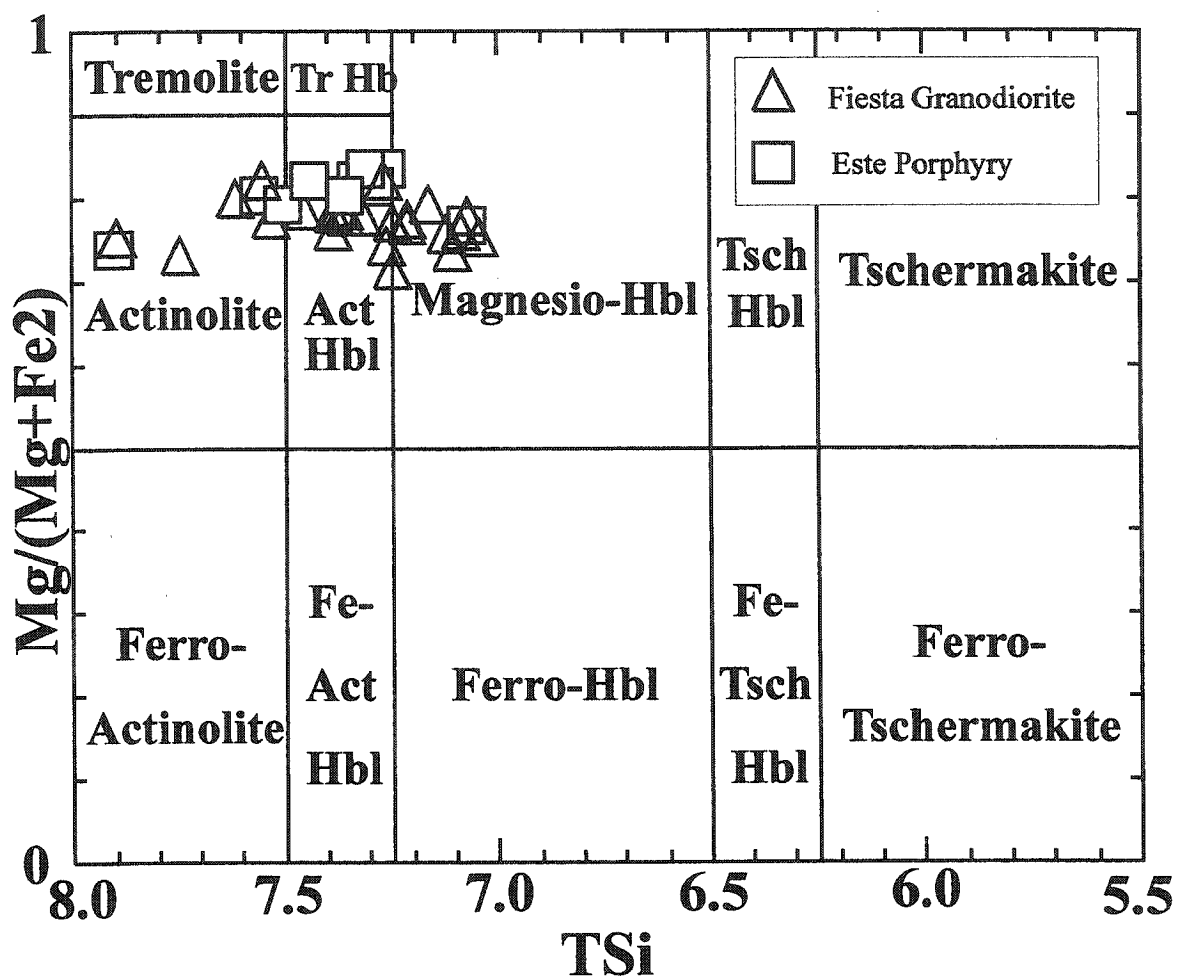


Figure 4.6. Amphibole composition diagram (Leake 1978) comparing the Este Porphyry and Fiesta Granodiorite. The Este and Fiesta amphibole microprobe analyses plot mainly in the actinolitic-hornblende to magnesio-hornblende fields with some analyses plotting in the actinolite field. The Fiesta Granodiorite and Este Porphyry plot in a similar range. Mg, Fe^{2+} and Si in the T-site are calculated from electron microprobe analyses using Minpet. Terminology after Leake (1978).

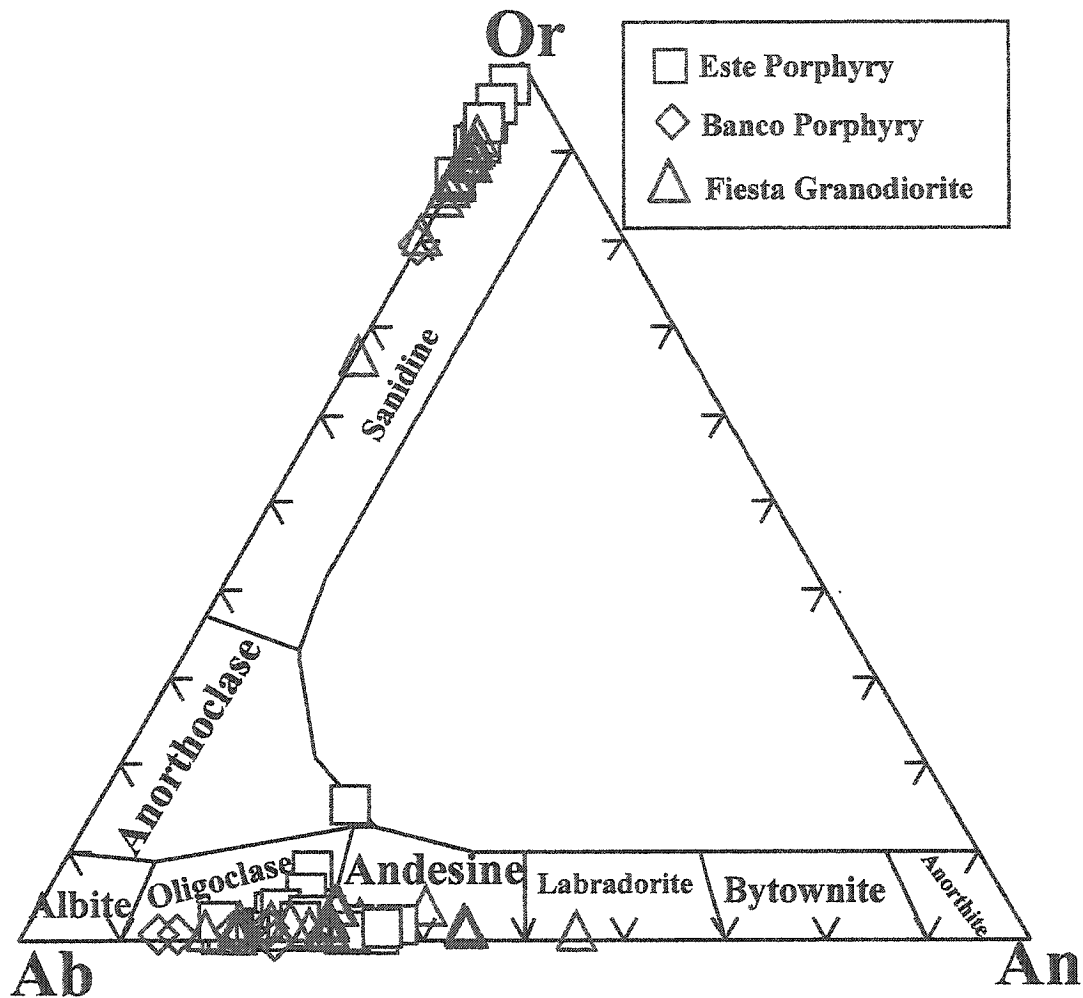


Figure 4.7. Albite-anorthite-orthoclase plot for feldspars of the Fortuna and Chuquicamata Intrusive complexes. The feldspar of the Banco Porphyry have an oligoclase composition. The Este Porphyry plagioclase range from oligoclase to andesine in composition. The Fiesta Granodiorite plagioclase are oligoclase to labradorite. All three units have Na in the K-feldspar.

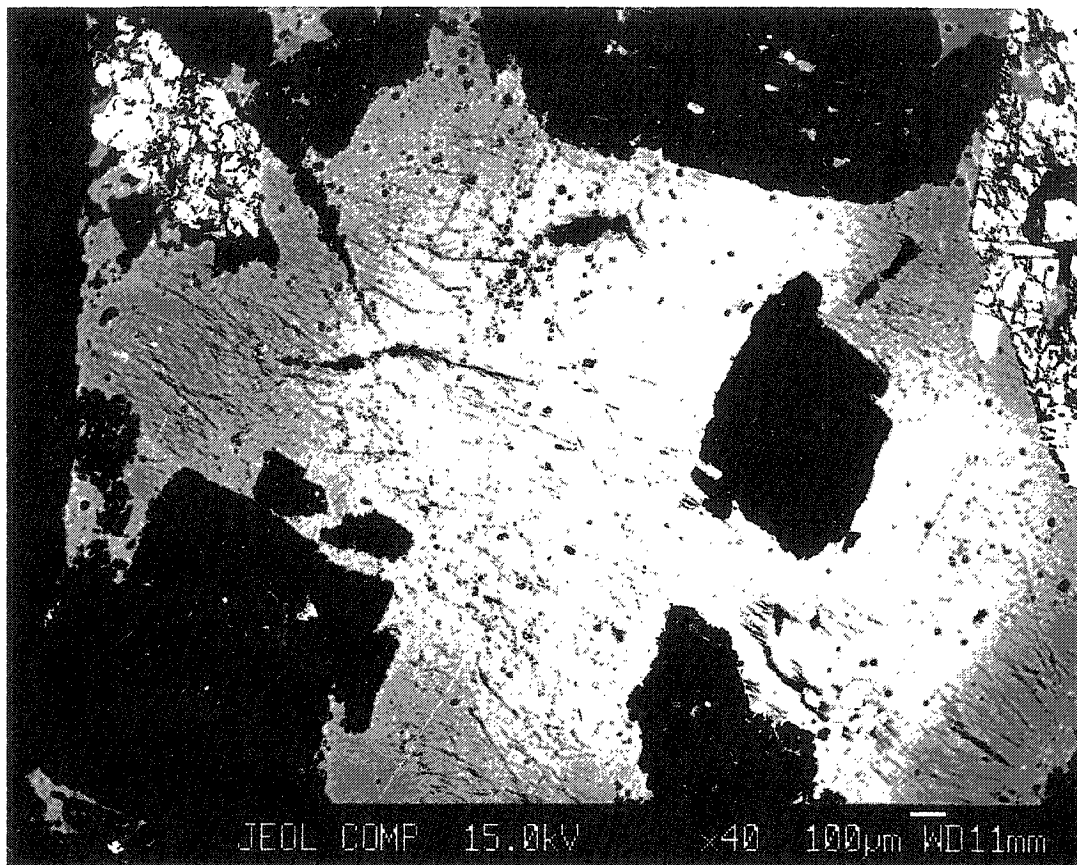


Figure 4.8. Electron microprobe backscatter image of K-feldspar from the Fiesta Granodiorite. Barium is enriched in zones in the K-feldspar (the brightest areas).

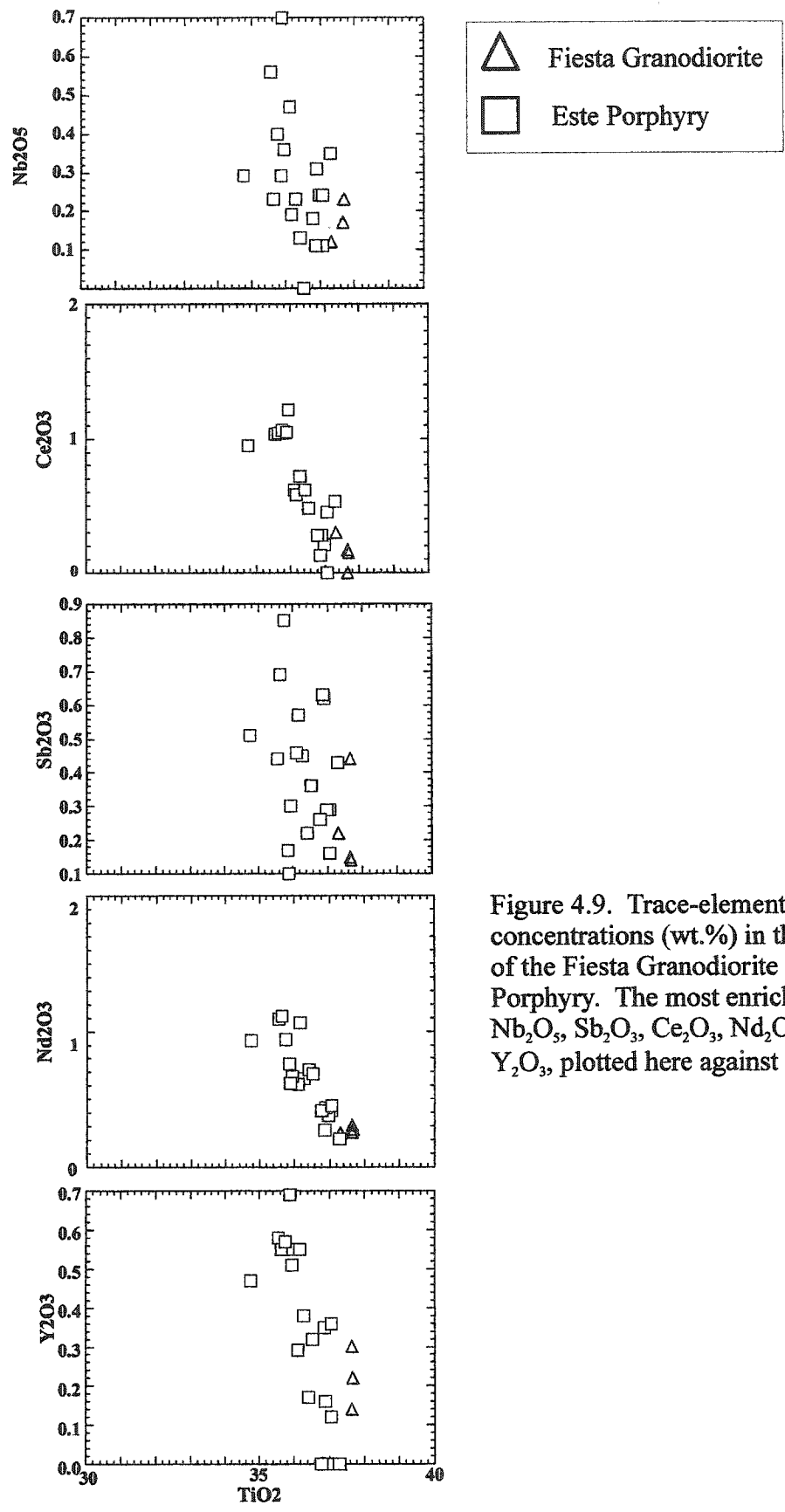


Figure 4.9. Trace-element concentrations (wt.%) in the titanites of the Fiesta Granodiorite and the Este Porphyry. The most enriched are Nb_2O_5 , Sb_2O_3 , Ce_2O_3 , Nd_2O_3 and Y_2O_3 , plotted here against TiO_2 .

Electron microprobe analysis has also confirmed the presence of **magnetite** in the Fiesta Granodiorite.

4.2.1.2 Discussion

The Fiesta Granodiorite is characterized by calcic amphibole, plagioclase, biotite, K-feldspar, recrystallized quartz, titanite and magnetite (Figs. 4.4 and 4.5). The texture is mainly medium-grained hypidiomorphic granular (Fig. 4.4).

Biotite and chlorite have partially altered the hornblende along cleavages and grain boundaries demonstrating that **amphibole** in the Fiesta Granodiorite are metastable. The amphiboles are actinolite to magnesio-hornblende in composition (Fig. 4.6).

Plagioclase is oligoclase to labradorite (Fig. 4.7). **K-feldspar** is perthitic with Ba-enriched zones around inclusions; the Ba-enrichment is the result of the inclusions inability to accommodate the Ba-ion. The Ba-zonation and perthitic texture indicate the K-feldspar are of magmatic origin as described in Sections 2.7.2.2 and 2.7.2.4. Inclusions of plagioclase in the K-feldspar indicate that some of the K-feldspar is late. A myrmekitic texture is rare and is interpreted to be of magmatic origin.

The Fiesta granodiorite has abundant **titanite** which is enriched in Fe and trace elements. The presence of magnetite indicates the magma was oxidizing.

4.2.2 Este Porphyry (*Porfido Este*) of the Chuquicamata Intrusive Complex

The 'freshest' Este Porphyry sample was collected ~2 km north (N6853, E4397)

of the Chuqui pit in order to avoid the effects of alteration in the pit. The sample is not mineralized and has few veins.

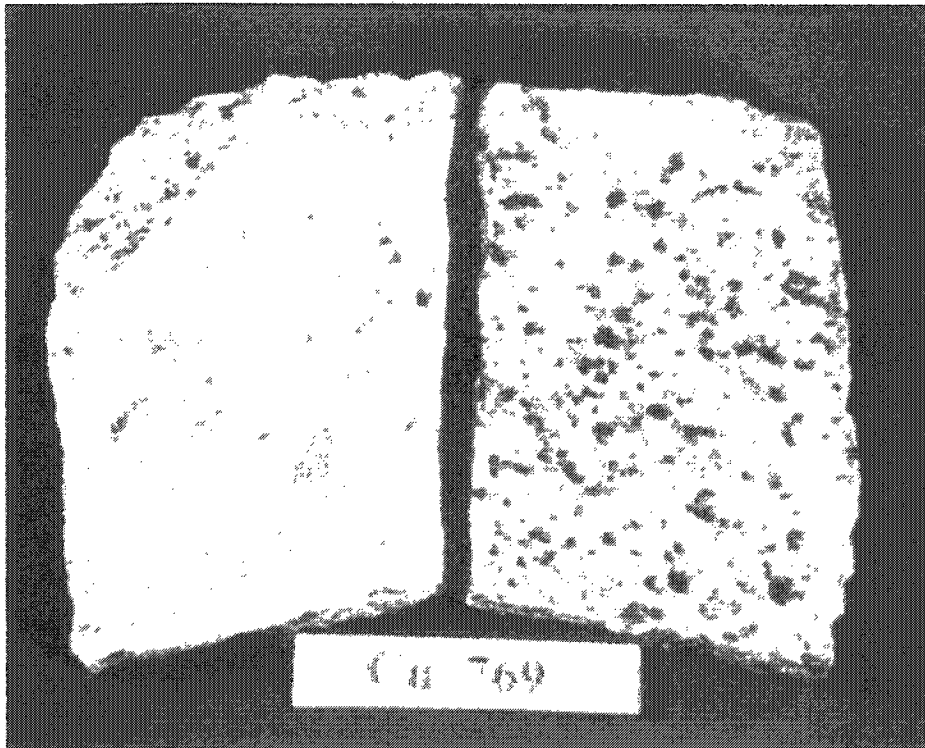
4.2.2.1 Observations

The Este Porphyry is medium-grained and appears hypidiomorphic granular in hand specimen (Fig. 4.10). In thin section, and especially when stained using sodium cobaltinitrate, the fine-grained groundmass reveals a more porphyritic texture (Fig 4.10). The minor groundmass in the Este Porphyry is fine-grained quartz and K-feldspar. There are 10-15% mafic minerals in these samples.

Amphibole grains up to 3 mm long have been affected by varying degrees of alteration to biotite and chlorite (Fig. 4.11). Locally, amphibole may be unaltered. In thin section the amphiboles show one good cleavage and a second fair cleavage, and exhibit twinning and a green to yellow pleochroism (Fig. 4.11). The amphibole is primarily actinolitic hornblende to magnesio-hornblende in composition, according to the terminology of Leake (1978) (Fig. 4.6).

Plagioclase phenocrysts comprise the bulk of the unaltered Este Porphyry. The grains average 2 to 6 mm in length and are euhedral to subhedral (Fig. 4.10). Plagioclase phenocrysts display oscillatory compositional zoning and twinning in cross-polarized light (Fig. 4.12). Albite twins or intersecting pericline-albite twins (Fig. 4.12) may be bent. Plagioclase is andesine-oligoclase (An_{18-37}) (Fig. 4.7).

Potassium feldspar is a relatively minor phase in the Este Porphyry. K-feldspar occurs as rare phenocrysts and in the fine-grained groundmass. Phenocrysts of K-feldspar



a.

b,

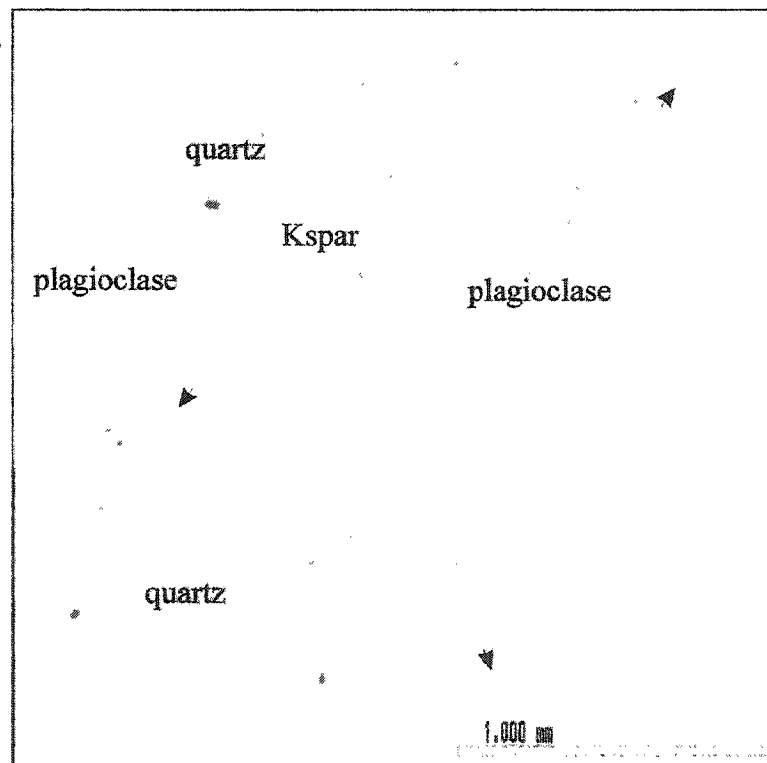
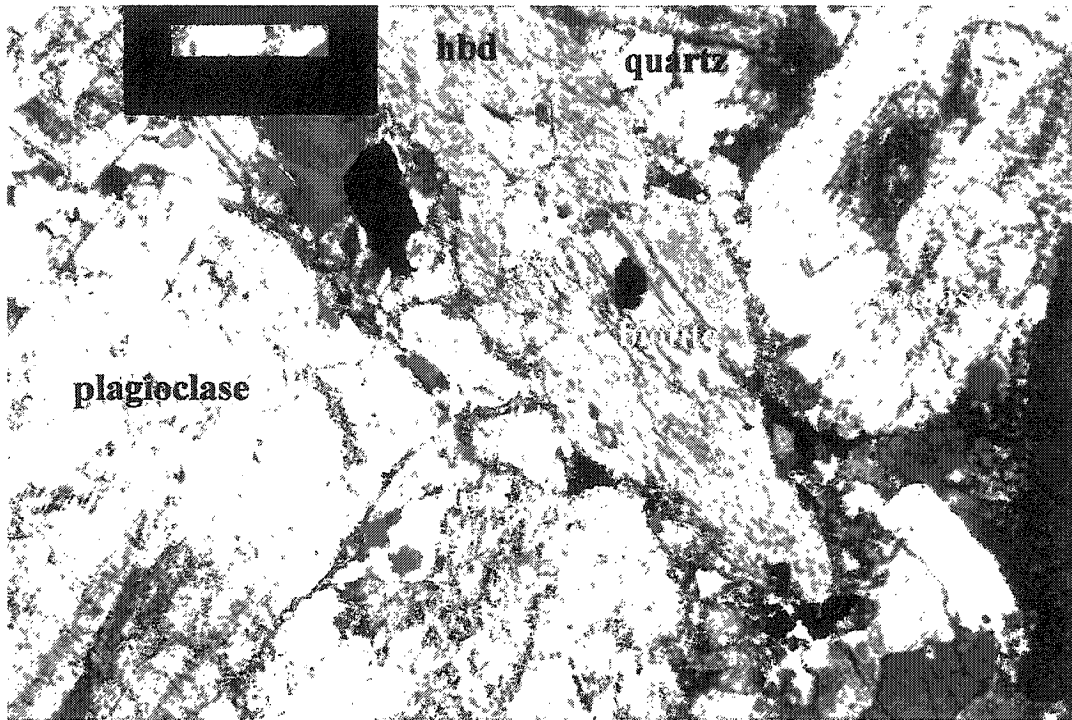


Figure 4.10. The Este porphyry. It is medium-grained and appears hypidiomorphic in hand specimen. a) When stained using sodium cobaltinitrite, the fine-grained groundmass reveals a more porphyritic texture. The label is 5 cm long. (sodium cobaltinitrite has stained K-bearing minerals yellow). b) A backscatter image shows the interstitial nature of K-feldspar.



b. Cu 769 (mag. = 50X, F.O.V. = 2 mm, ppl)

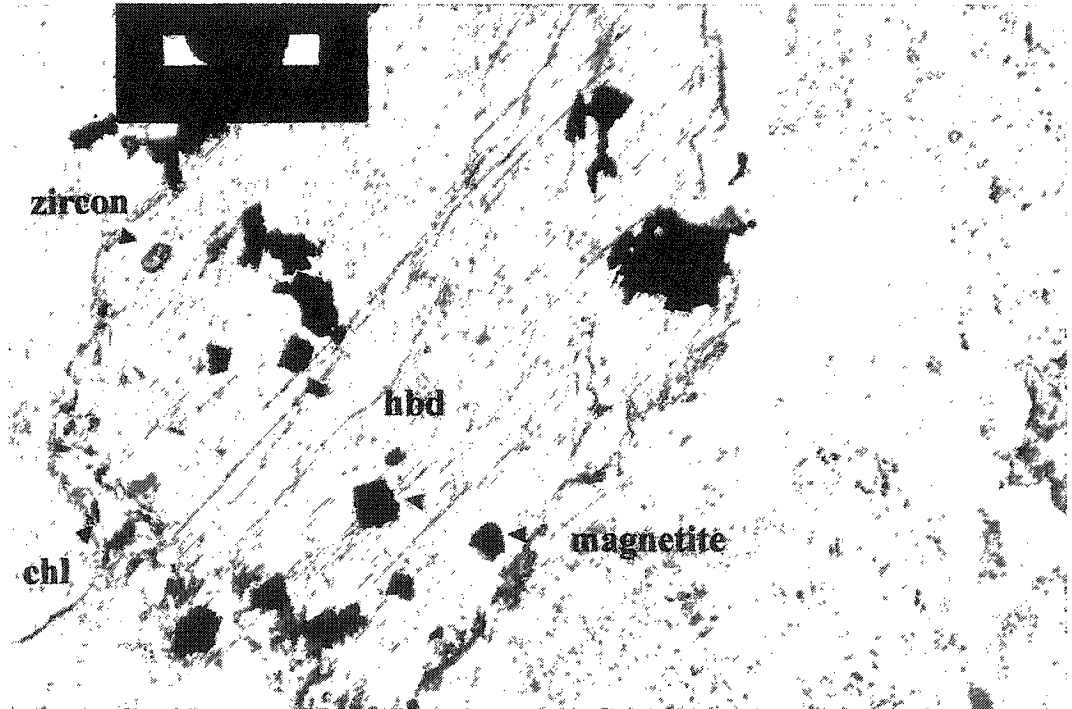
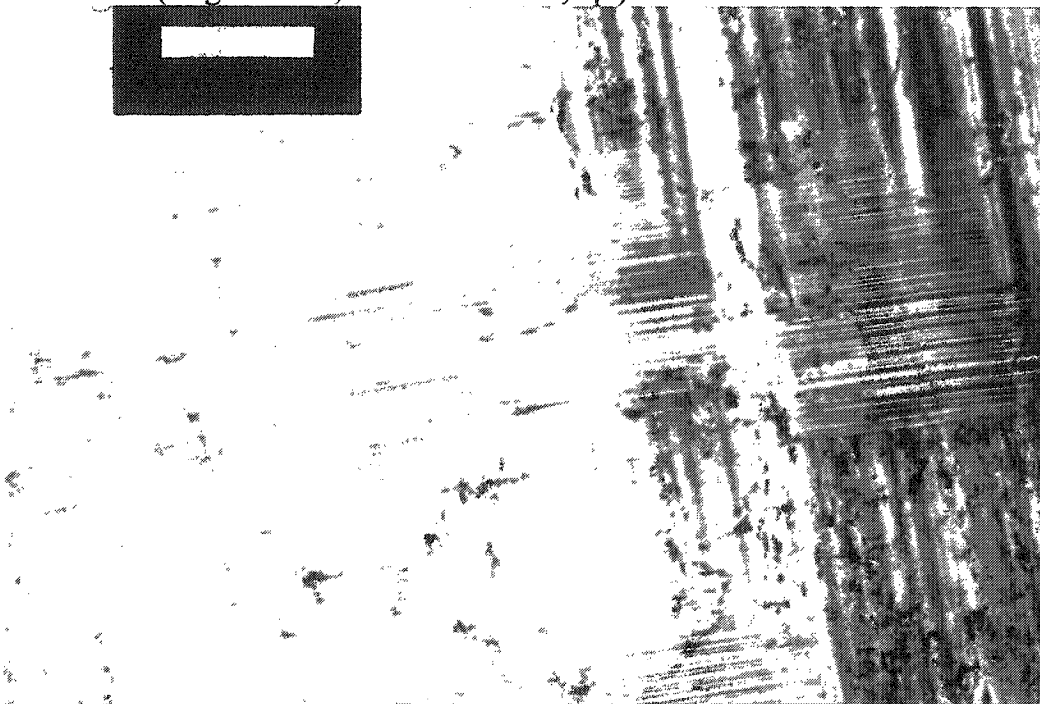


Figure 4.11. Amphibole in the Este Porphyry. a) A basal section of amphibole (hbd) altering to biotite. b) An amphibole is altered to chlorite along the crystal edges. Note the yellow colour of the amphibole in plane-polarized light (ppl). The opaque grains are magnetite.

a. Cu 769 (mag. = 200X, F.O.V. = 0.5 mm, xpl)



b. Cu 769 (mag. = 50X, F.O.V.= 2 mm, xpl)

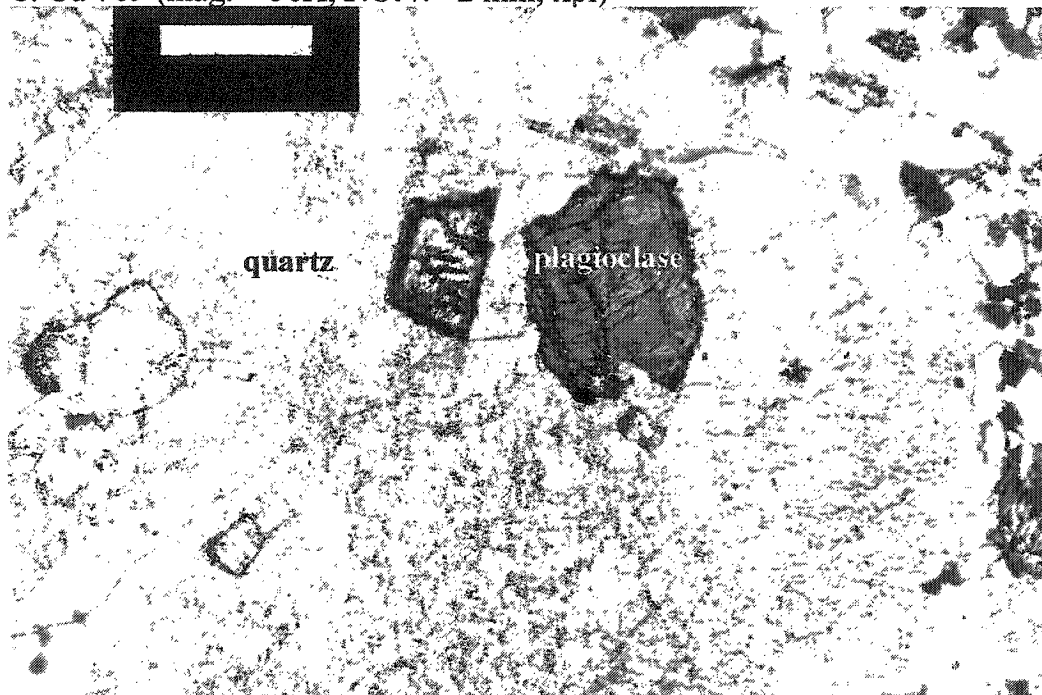


Figure 4.12. Feldspar in the Este Porphyry a) Intersecting pericline and albite twins in albite. Note the secondary fluid inclusions. b) Inclusions of plagioclase and quartz in K-feldspar.

have inclusions of quartz, plagioclase and biotite (Fig. 4.12). Plagioclase inclusions have the same compositions as plagioclase phenocrysts in the rest of the sample (i.e. andesine-oligoclase).

Rare K-feldspar megacrysts are visible in hand specimen, and embayments of the crystals occur locally. Perthitic grains have microscopic lamellae (Fig. 4.13). Barium is present in all analysed grains and is enriched in concentric zones (Fig. 4.13). X-ray diffraction confirmed that the K-feldspar in the Este Porphyry is monoclinic orthoclase (Appendix D).

Quartz occurs as grey mesoscopic phenocrysts (Fig. 4.10). In thin section, quartz forms polycrystalline 'eyes' averaging 2 mm in diameter. Quartz has been recrystallized with local undulose extinction. It is also the main constituent of the groundmass (Fig. 4.10).

Some **biotite** grains appear to be primary (i.e. occur independent of amphibole but may be affected by chloritization) (Fig. 4.14a) whereas other grains are possibly replacements of amphibole (whereas amphibole and biotite \pm chlorite are intimately intergrown) (Figs. 4.11a and 4.14b). In both cases, biotite displays chloritization or irregular grain boundaries). Inclusions of apatite and zircon are associated with biotite.

Titanite is associated with magnetite, biotite/chlorite and amphibole (Fig.4.15). Most grains exhibit euhedral diamond-shaped crystals. Some grains show cleavage (Fig. 4.15). The titanite is up to 3 mm in length. Titanite in the Este Porphyry is zoned with enriched areas of trace elements (Fig. 4.15) such as Nd, Nb, La, Sb, Y and Ce (Fig. 4.9).

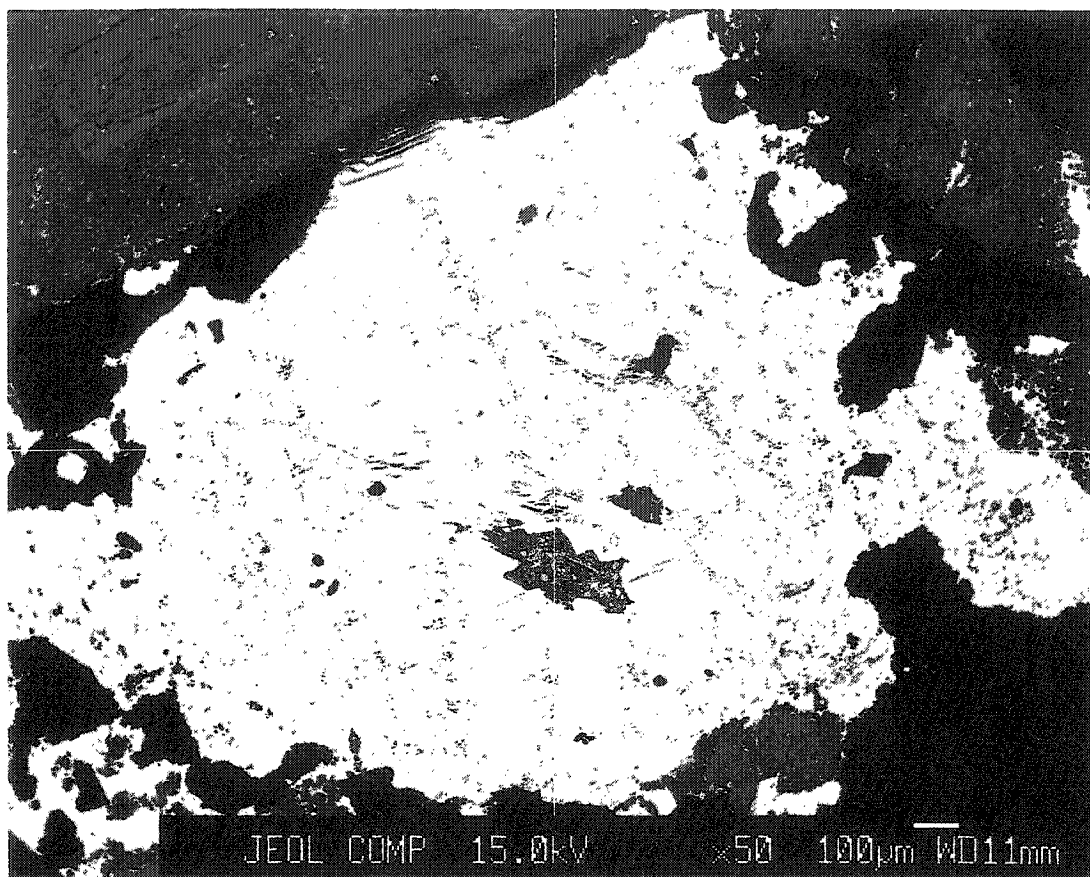
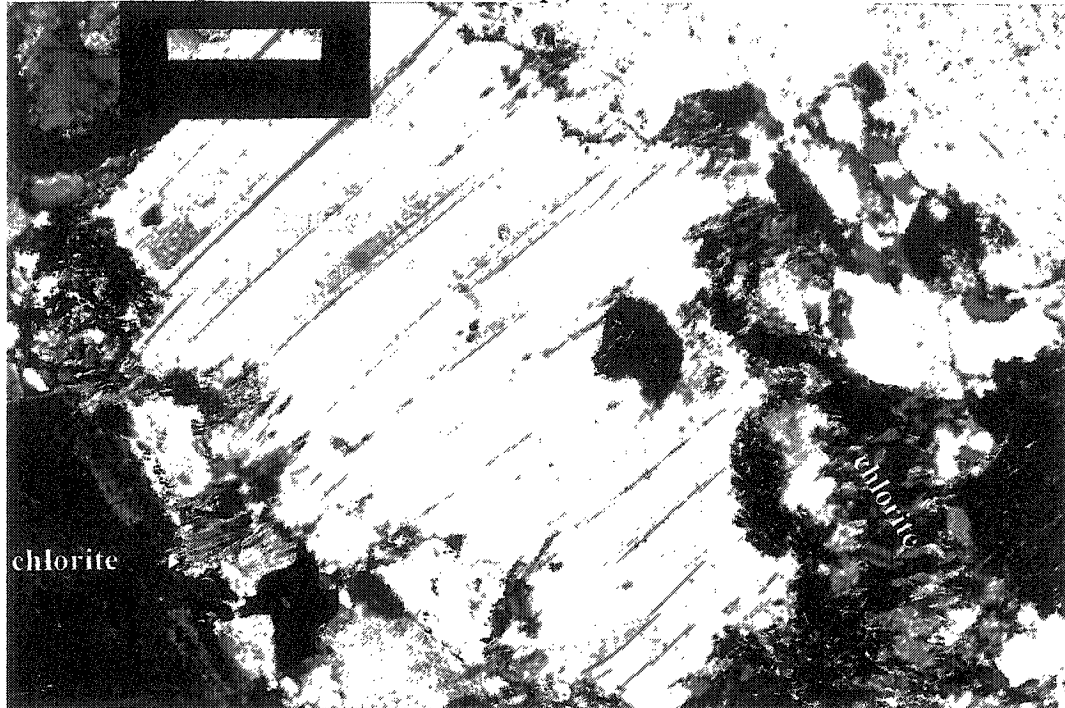


Figure 4.13. A backscatter image of compositional zoning of BaO in K-feldspar. It is common in the 'unaltered' Este Porphyry. The lightest band represents an enrichment of BaO.

a. Cu 769 (mag. = 50X, F.O.V. = 2 mm, xpl)



b. Cu 769 (mag = 50X, F.O.V. = 2 mm, xpl)

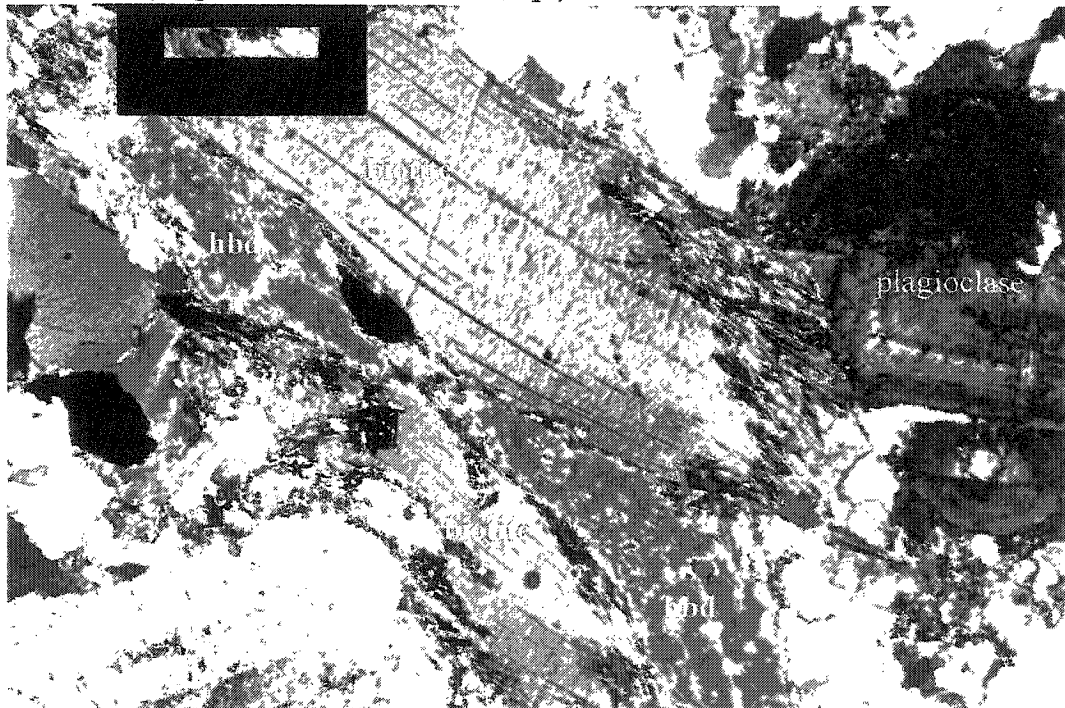
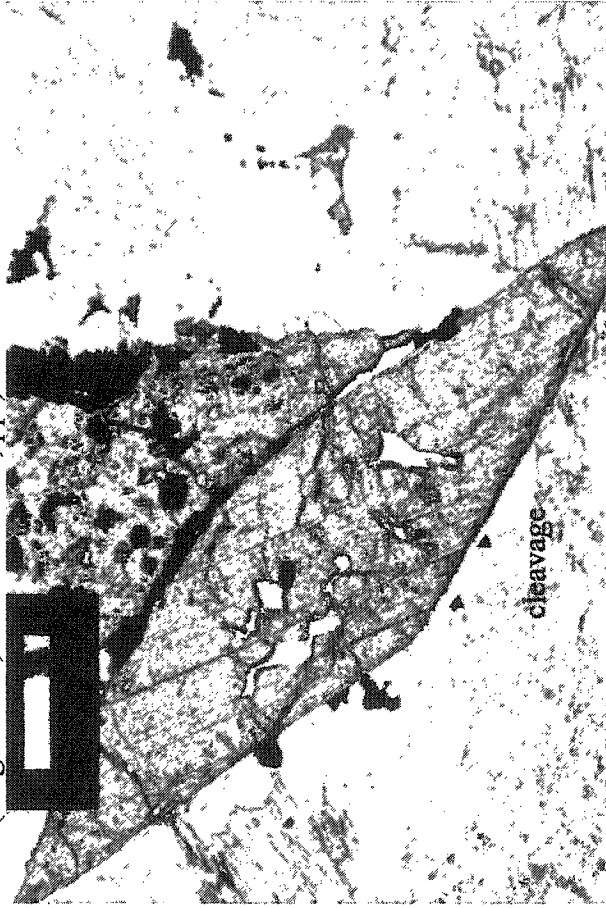


Figure 4.14. Biotite in the Este Porphyry. It is metastable throughout the 'unaltered' Este Porphyry. a) Biotite is altered to chlorite along the grain boundaries. b) Biotite as a replacement of amphibole.

a. Cu769 (mag. = 50X, F.O.V. = 2 mm, ppl)



b. Electron microprobe backscatter image (Cu 769).

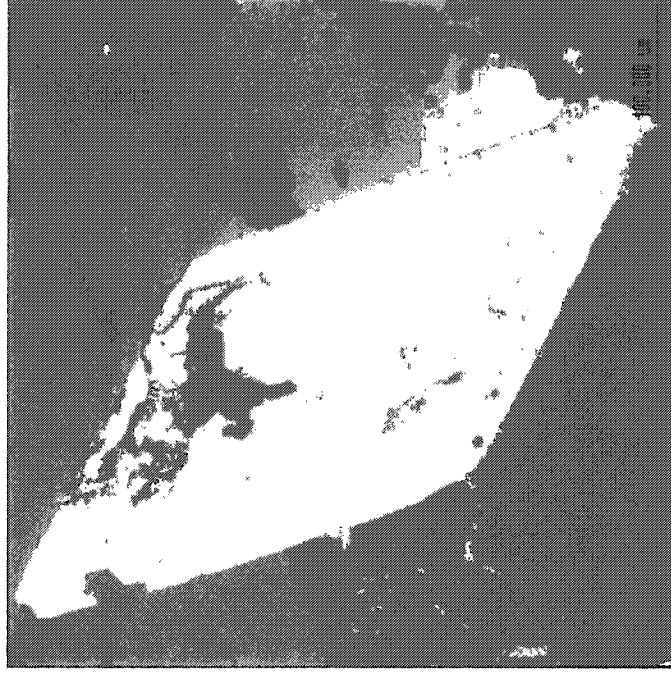


Figure 4.15. Large, euhedral titanite in the least-altered Este Porphyry.
a) Some grains display cleavage. b) Backscatter imaging on the electron microprobe displays concentric compositional zoning in the titanite. This zonation is related to the presence of trace elements and Fe.

Magnetite is spatially associated with biotite and amphibole (Fig. 4.11) and has <0.5 wt.% TiO₂ (Appendix C).

4.2.2.2 Discussion

The Este Porphyry is hypidiomorphic granular to porphyritic with a groundmass of quartz and K-feldspar.

Actinolitic-**hornblende** to magnesio-hornblende is interpreted to be metastable because it is seen to be altered to biotite and chlorite. Euhedral to subhedral **plagioclase** phenocrysts of andesine to oligoclase composition are the most abundant mineral phase. They display oscillatory compositional zoning.

The inclusions of plagioclase and quartz in **K-feldspar** phenocrysts, as well as the interstitial nature of fine-grained K-feldspar, distinguish K-feldspar as a late phase. The exsolution lamellae in K-feldspar suggest a magmatic origin (Section 2.7.2.4). Regular reverse Ba zonation in K-feldspar supports magmatic crystallization (e.g., Long and Luth 1979) (Fig. 4.12). The extreme regularity of the Ba-zonation indicates that this Ba-enriched zone crystallized contemporaneously with minerals that do not preferentially partition Ba, such as plagioclase and hornblende (Long and Luth 1979).

Polycrystalline pods of recrystallized **quartz** represent primary quartz phenocrysts that have been affected by strain. This strain has affected the rocks throughout the study area (Lindsay 1998). Large chemically zoned **titanite** represents a sink for trace elements such as Nd, Nb, La, Y and Ce in the cooling magma.

4.2.3 Banco Porphyry (*Porfido Banco*) of the Chuquicamata Intrusive Complex

The samples of 'fresh' Banco Porphyry studied here (Cu 514 and Cu 1333) have been affected by Qser alteration. The original texture and mineralogy of the Banco Porphyry have been preserved and are easily discerned. These samples are from dyke-like bodies that were intruded into areas of potassically altered Este Porphyry (Fig. 4.3). The reason these samples are considered to be 'fresh' and not 'potassic' is discussed more thoroughly in Chapter 5.

4.2.3.1 Observations

The Banco Porphyry has a bimodal population of plagioclase phenocrysts and hence has been termed "doubly porphyritic". The smaller phenocrysts average ~0.5 mm long and are most abundant; the larger phenocrysts are typically >2 mm long. K-feldspar grains are pink and visibly poikilitic in hand specimen. Mafic minerals comprise less than 5% of the rock discernible in hand specimen. Sodium cobaltinitrite staining confirms that the aphanitic matrix is primarily K-feldspar (Fig. 4.16).

The **plagioclase** phenocrysts are euhedral to subhedral and range from weakly to moderately altered to sericite (Fig. 4.17). The smaller population of plagioclase is more intensely sericitized than the larger grains (Fig. 4.17). Locally, grains display bent and fractured twins (Fig. 4.17). Electron microprobe analyses indicate the plagioclase is oligoclase (An_{13-26}) (Fig. 4.7).

Phenocrysts of **quartz** are grey and measure up to 1 cm in diameter in hand specimen (Fig. 4.16). In thin section, they are found as polycrystalline quartz 'eyes' and

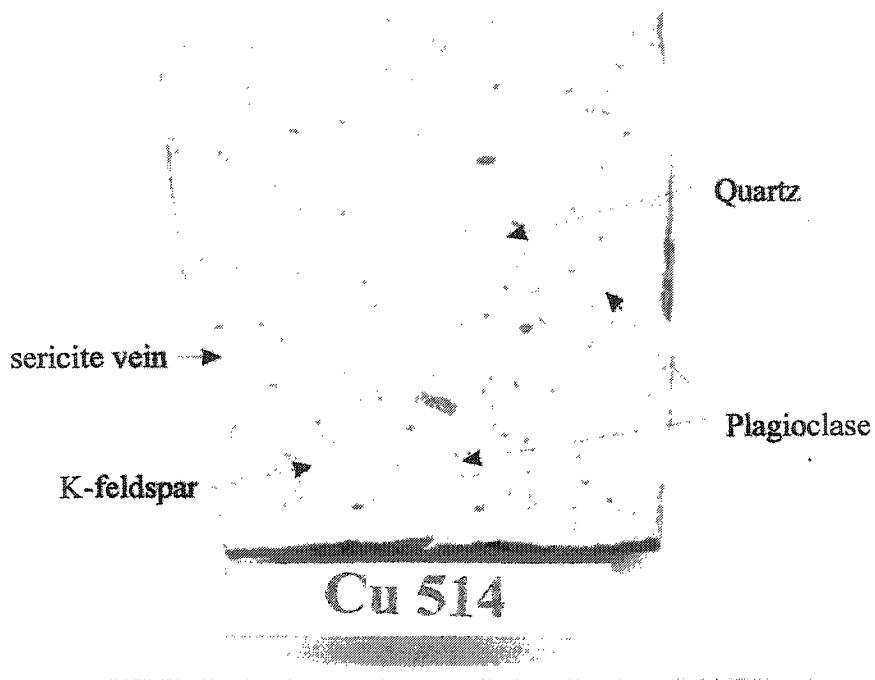
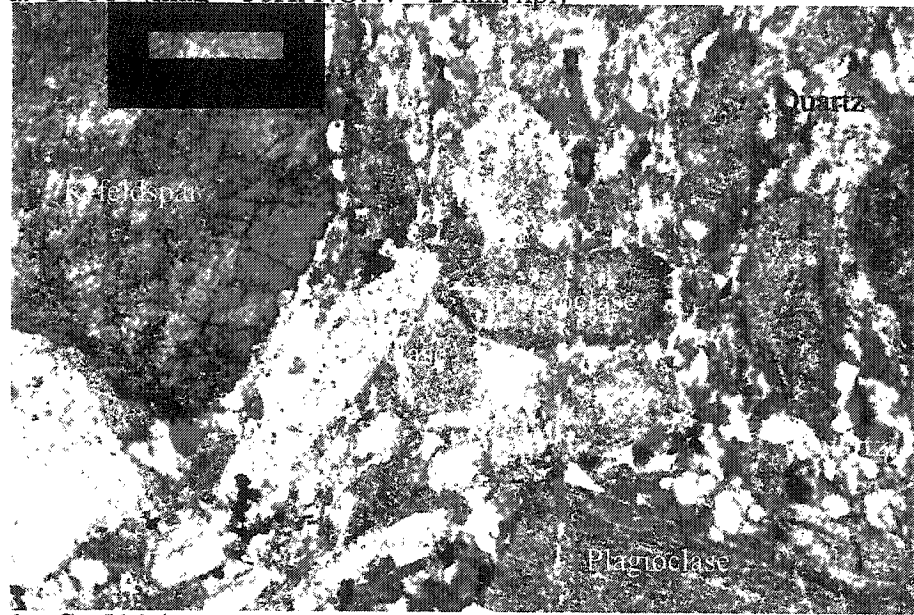


Figure 4.16. Hand specimen of the Banco Porphyry. It has a very-fine groundmass with phenocrysts of quartz (grey), plagioclase (white) and K-feldspar (yellow). Slab stained using sodium cobaltinitrite which stains the K-bearing minerals yellow. The bright yellow line across the slab represents a sericite vein. The label is 5 cm long.

a. Cu 514 (mag = 50X, F.O.V. = 2 mm, xpl)



b. Cu 514 (mag. = 50X, F.O.V. = 2 mm, xpl)

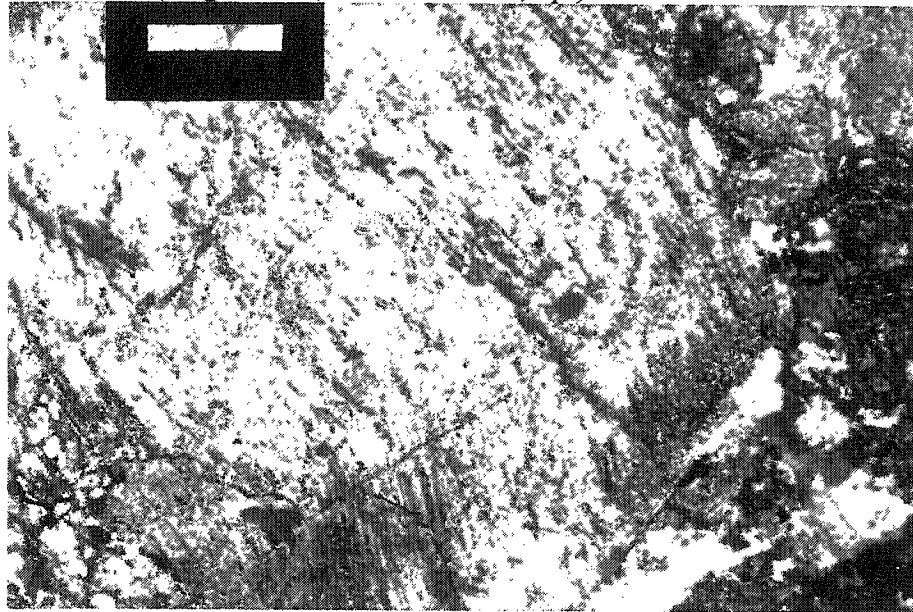


Figure 4.17. The Banco Porphyry with a doubly porphyritic texture.
 a) Phenocrysts of plagioclase with a large K-feldspar phenocryst on the left. Note the small quartz grains in the groundmass. b) Plagioclase grains with bent twins.

display undulose extinction. Quartz is also found in the matrix (Fig. 4.17).

Large **potassium feldspar** phenocrysts up to 1 cm across display minor alteration. Microperthitic textures were observed. Inclusions of plagioclase are common, as are quartz inclusions near the edges of K-feldspar grains (Fig. 4. 18). Inclusions of plagioclase in K-feldspar are locally altered to sericite. BaO is present in patches within the K-feldspar, with a particularly enriched zone near the rim (Fig. 4.19). Megacrysts of K-feldspar occur locally.

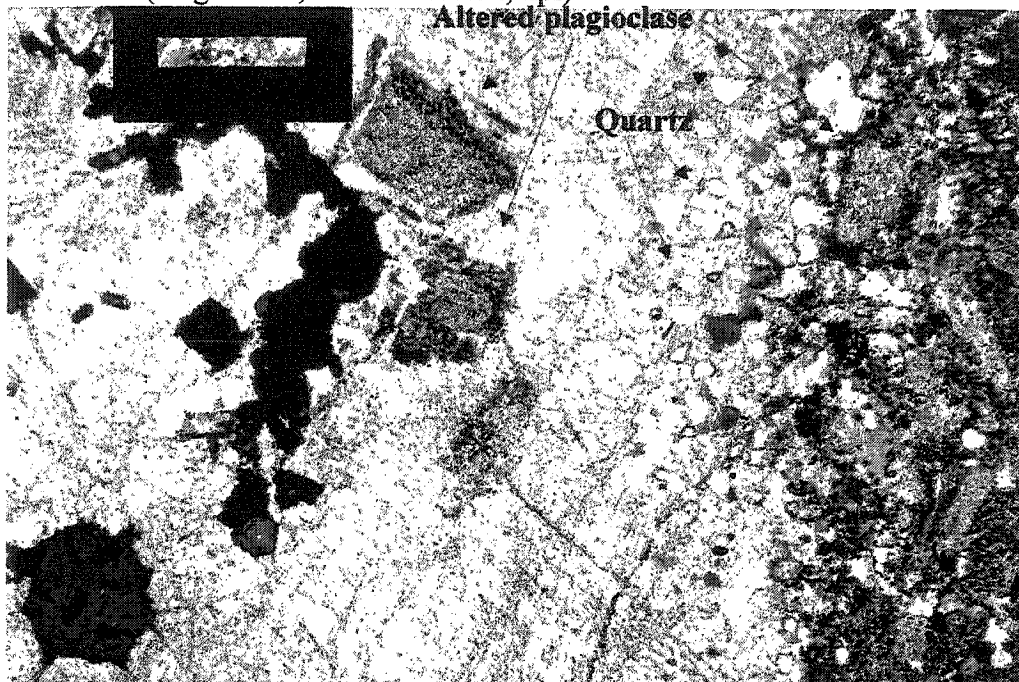
Biotite has kinked cleavage and may be chloritized. Biotite is pleochroic brown-yellow and is consistently <1 mm, in size, although they may occur in clusters up to 3 mm in size. **Chlorite** displays an anomalous inky blue birefringence and occurs as an alteration product of biotite. Minor opaques are scattered throughout the samples.

Rutile occurs as needles; it is either found along the cleavage planes of biotite, or as a diamond-shaped pseudomorph. Reconnaissance microprobe work indicates that the rutile contains FeO but no trace elements were analyzed.

4.2.3.2 Discussion

The different sizes between the phenocrysts and the groundmass is interpreted to represent two-stages of cooling. An initial period of slow cooling led to nucleation and the growth of plagioclase, quartz, and K-feldspar phenocrysts in the magma chamber. Later, rapid cooling occurred during the intrusion of the Banco Porphyry dykes into the already solidified Este Porphyry, forming the aphanitic groundmass and enclosing the fine-grained quartz inclusions in the K-feldspar phenocrysts (Fig. 4.18).

a. Cu 514 (mag = 50X, F.O.V. = 2 mm, xpl)



b. Cu 514 (mag = 50X, F.O.V. = 2 mm, xpl)

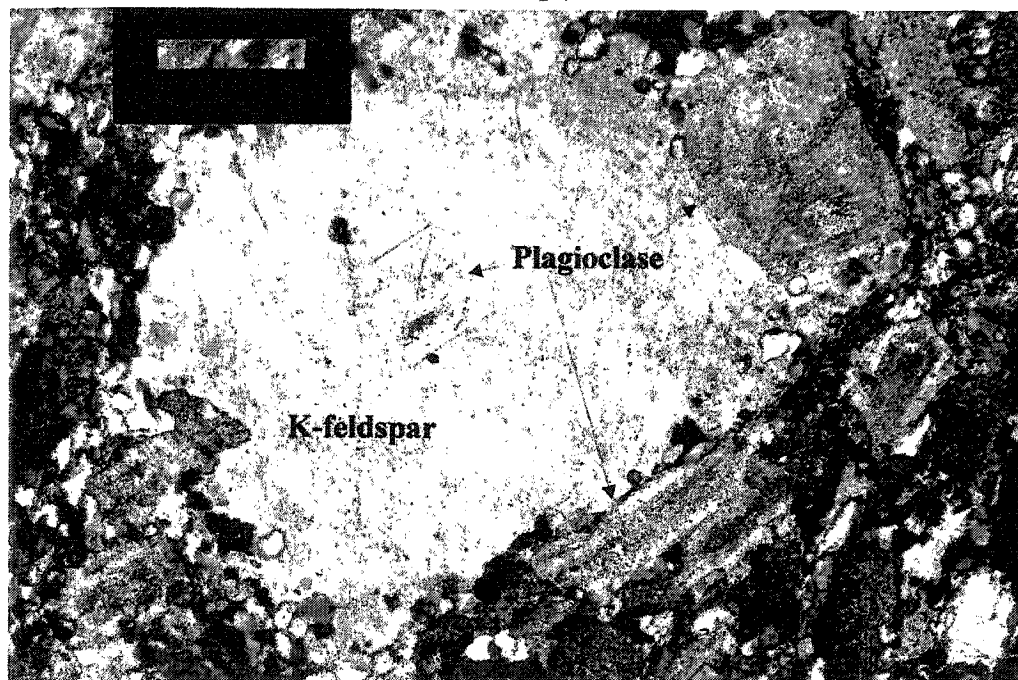


Figure 4.18. a) K-feldspar phenocryst with quartz inclusions at the rim and altered plagioclase inclusions toward the core. b) Another K-feldspar grain with irregular edges and a plagioclase inclusion.

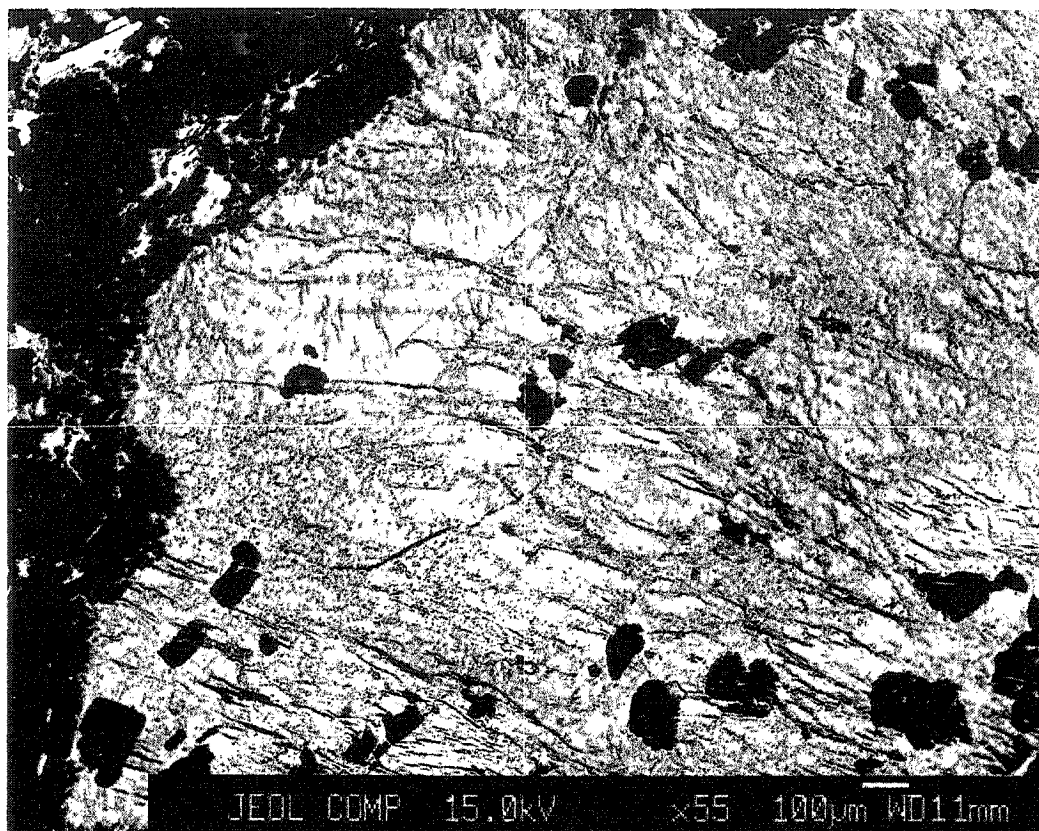


Figure 4.19. Zoned K-feldspar in the Banco Porphyry. The brightest areas are Ba-enriched; they appear brighter because the BaO increases the relative density.

The oligoclase composition of the plagioclase suggests they are more sodic than those of the Este Porphyry. The inclusions of plagioclase and quartz in the K-feldspar and the perthitic texture suggest a magmatic origin for the potassium feldspar (Section 2.7.2.4). The reverse Ba zonation in the K-feldspar is (Fig. 4.19) also interpreted to be of magmatic origin as, described in Section 2.7.2.2. The irregular edges of the K-feldspar phenocrysts (Fig. 4.18), which envelop the small quartz grains, represent very late growth. During the final cooling stage, the K-feldspar continued to grow, enclosing the latest nucleated quartz, which otherwise would have remained in the groundmass.

The pseudomorphing of a diamond-shaped mineral (interpreted to be titanite) by rutile needles is believed to be a secondary alteration, possibly occurring during the Qser alteration.

4.2.4 Oeste Porphyry (*Porfido Oeste*) of the Chuquicamata Intrusive Complex

A sample of Oeste Porphyry was selected with the aid of mine geologists. Although it is pervasively altered by Qser alteration, this sample (Cu 516) is believed to be the best sample to be found at the present level of mining, because the Oeste Porphyry outcrops only in the west, coinciding with the pervasive Qser and argillic alteration zones (Fig. 4.3). The Oeste Porphyry was not sampled to compare alteration effects, for it is a relatively minor phase in the Chuqui pit.

4.2.4.1 Observation

The Oeste Porphyry has an open texture, with phenocrysts 'floating' in the groundmass (Lindsay 1998) (Fig. 4.20). The groundmass is very fine-grained quartz and is more abundant than in either the Este Porphyry or Banco Porphyry.

No **amphiboles** were observed in the Oeste Porphyry in this study. **Plagioclase** is totally altered to clay or white mica, but the original euhedral crystal forms are still easily discernible. The laths of plagioclase average less than 5 mm in length. Relict laths of **biotite** (~2 mm long) were observed with rutile along the relict cleavage. **Zircon** was associated with this relict biotite grain. **Potassium feldspar** occurs as fine-grained phenocrysts with minor to moderate micaceous alteration. The Oeste Porphyry has rounded pods of polycrystalline, recrystallized **quartz** phenocrysts less than 1 cm long. **Rutile** is also present as needles arranged in a diamond-shape, and associated with relict biotite.

4.2.4.2 Discussion

The Oeste Porphyry has more matrix and fewer phenocrysts than the Este Porphyry. The Oeste Porphyry has only one size population of plagioclase phenocrysts, differentiating it from the Banco Porphyry. From thin section studies, it is apparent that the Oeste Porphyry originally had phenocrysts of plagioclase, K-feldspar, quartz, and biotite. All of these phenocrysts are <5 mm in length. The groundmass is primarily quartz and K-feldspar. The rutile appears to be replacing titanite and/or amphibole as the needles are arranged in a diamond-shape.

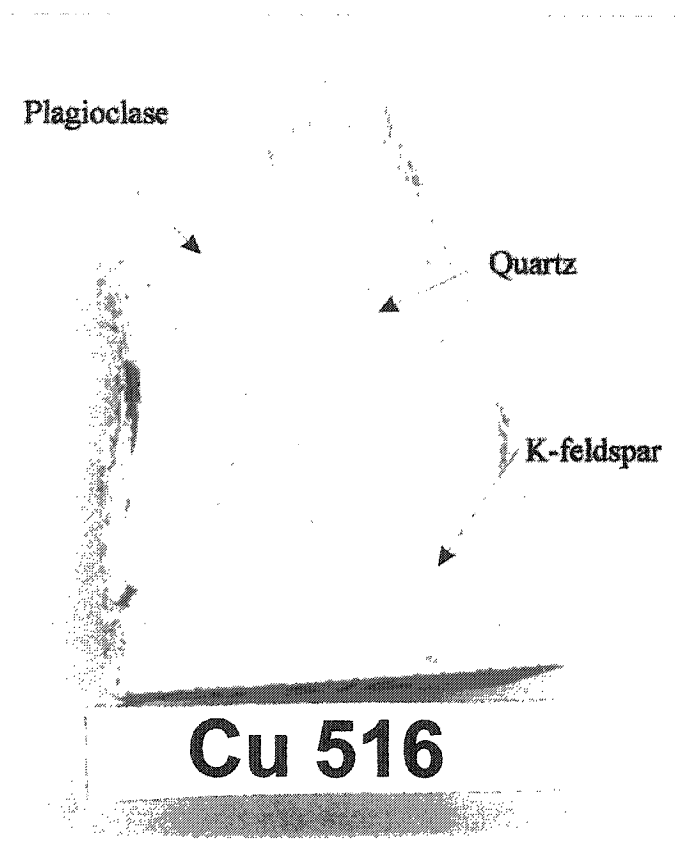


Figure 4.20. Hand specimen of Oeste Porphyry. It has been strongly affected by fracturing and alteration. The white label is 5 cm.

4.2.5 Interpretation

The **Fiesta Granodiorite** has a higher mafic index than the **Este Porphyry**; however, the mineral compositions overlap. The amphiboles of both units fall within the same compositional range (actinolitic- to magnesio-hornblende) (Fig. 4.6). Although the **Fiesta Granodiorite** has more calcic plagioclase than the **Este Porphyry**, the plagioclase compositions overlap (Fig. 4.7). Abundant titanite in the **Fiesta Granodiorite** and the **Este Porphyry** has a similar enrichment in trace elements (Fig. 4.9); however, the compositional zoning observed in the **Este Porphyry** titanites is not observed in the **Fiesta Granodiorite** (Fig 4.15). Ba-zonation of the K-feldspar is found in both the **Este Porphyry** and the **Fiesta Granodiorite** and the Ba-values fall within the same range (Appendix C).

Mineralogically, the **Fiesta Granodiorite** could represent a deeper equivalent of the **Este Porphyry**. The grain sizes are equivalent; however, the **Fiesta Granodiorite** lacks megacrystic K-feldspars.

Mineralogically, the **Banco Porphyry** is more felsic than the **Este Porphyry**. The plagioclase in the **Banco Porphyry** consistently falls in the oligocene compositional range, within the range of the more sodic **Este Porphyry** plagioclase compositions (Fig. 4.7). The **Banco Porphyry** lacks amphibole and contains only minor biotite. The groundmass is primarily K-feldspar and quartz.

The **Banco Porphyry** has two size populations of plagioclase. Quartz and K-feldspar phenocrysts are approximately the same size as the larger plagioclase grains, suggesting that they nucleated and grew during a period of slow cooling prior to intrusion of the **Banco Porphyry** dykes. The smaller population of plagioclase phenocrysts likely

nucleated at the same time as the larger grains, supported by their similar compositions. Their smaller size is due to low local Ca- and Na-activities. K-feldspar phenocrysts, and locally megacrysts, include rims of fine-grained quartz and the small population of plagioclase, indicating that K-feldspar is one of the last phases to crystallize. Final crystallization occurred as the Banco Porphyry dykes intruded into the Este Porphyry, forming the aphanitic groundmass of K-feldspar and quartz. Field relations support the interpretation that the Banco Porphyry intruded into a completely cooled Este Porphyry.

The groundmass of the **Oeste Porphyry** is very fine-grained quartz and is more abundant than in either the Este or Banco porphyries. The groundmass of the Oeste Porphyry is coarser than that of the Banco Porphyry, but finer than that of the Este Porphyry. The Oeste Porphyry has only one size population of plagioclase phenocrysts. The plagioclase in the Oeste Porphyry is of undetermined composition. The Oeste Porphyry is interpreted to have cooled slowly; slow cooling resulted in the nucleation and growth of the plagioclase phenocrysts before magma ascension. This ascent resulted in a moderate rate of cooling that formed the fine-grained groundmass.

4.3 Geochemistry of the Fortuna and Chuquicamata Intrusive Complexes

Whole-rock and trace element analyses of characteristic samples from the Fiesta Granodiorite, and Este, Banco, and Oeste porphyries were done at the Chemex Ltd. lab in Vancouver, BC. The raw data (un-normalized) are reported in Appendix E. Details of the analytical procedure and reported detection limits are also given in Appendix E.

The normalized, LOI-free whole-rock geochemistries of the Fiesta Granodiorite

and the Este, Banco, and Oeste porphyries are reported in Table 4.1. These data are plotted as bar graphs in Figure 4.21 to compare the variations in the major elements between the units. Samples from the Banco and Oeste porphyries have been affected by varying degrees of Qser alteration. The chemical effects of this alteration are discussed in Section 4.3.3.

4.3.1 Whole-rock geochemistry

The SiO_2 values are slightly higher in the Chuqui porphyries than in the Fiesta Granodiorite (Fig. 4.21). The SiO_2 values of the Este Porphyry (70.55 wt.%) fall within the range of SiO_2 values for the Banco Porphyry (69.5-70.66 wt.%). One sample from each of the Fiesta Granodiorite, the Este and Banco porphyries have identical Al_2O_3 values (16.97 wt.%). The other Banco Porphyry sample has a higher Al_2O_3 content (18.02 wt.%) and the Fiesta Granodiorite has a lower value (15.54 wt.%).

The TiO_2 , $\text{Fe}_2\text{O}_{3\text{tot}}$, MgO and CaO values are consistently highest in the Fiesta Granodiorite compared to the Chuqui porphyries. The Este Porphyry has more CaO relative to the Banco Porphyry but has similar TiO_2 , $\text{Fe}_2\text{O}_{3\text{tot}}$ and MgO values.

The Este Porphyry has relatively less K_2O (1.73 wt.%) than the other units. There is a wide range in the K_2O values of the Banco Porphyry (3.18-4.21 wt.%). The Fiesta Granodiorite has consistent K_2O values (4.04-4.51 wt.%), higher than those of the Banco Porphyry. The Fiesta Granodiorite has the lowest values of Na_2O (2.53-3.7 wt.%). The Na_2O values for the Banco Porphyry vary widely (3.85-5.31 wt.%). The Este Porphyry falls between the two Banco samples (4.12 wt.%).

Table 4.1 Whole-rock geochemistry from the 'unaltered' rocks of the Chuquicamata district, normalized to 100%.

	Fiesta Granodiorite	Fiesta Granodiorite	Este Porphyry	Banco Porphyry	Banco Porphyry	Oeste Porphyry
SiO ₂	67.17	66.02	70.55	69.5	70.66	73.08
TiO ₂	0.58	0.44	0.32	0.29	0.31	0.21
Al ₂ O ₃	15.54	16.97	16.96	16.97	18.02	15.95
Fe ₂ O ₃ tot	3.32	3.69	2.44	2.27	1.41	0.76
MnO	0.07	0.08	0.04	0.04	0.01	0.02
MgO	1.59	1.34	0.7	0.63	0.38	0.12
CaO	3.85	4.22	3.05	1.82	1.05	0.32
Na ₂ O	3.7	2.53	4.12	5.31	3.85	5.32
K ₂ O	4.04	4.51	1.73	3.18	4.21	4.15
P ₂ O ₅	0.17	0.21	0.11	0.04	0.08	0.06
Total	100.03	100.01	100.02	100.05	99.98	99.99

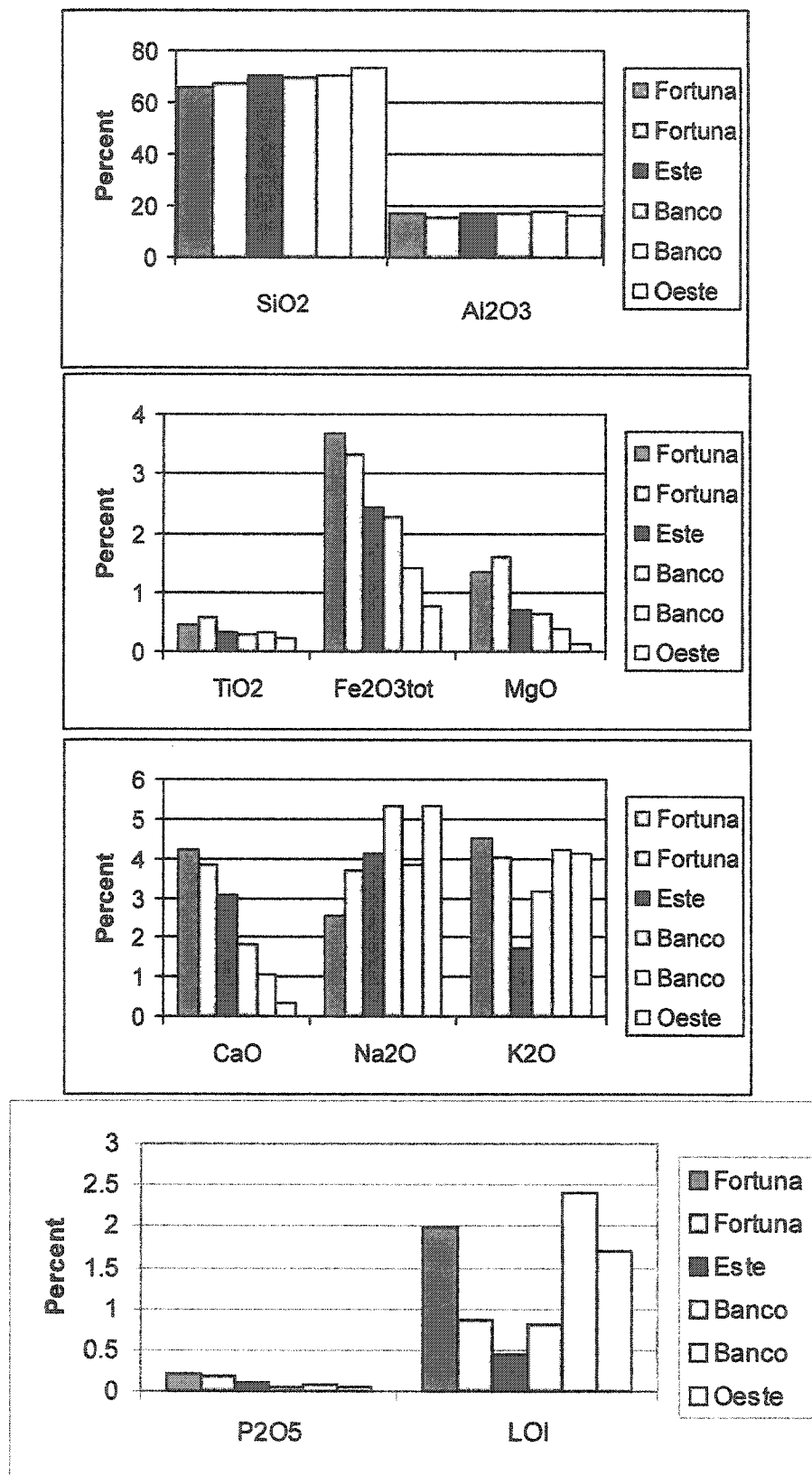


Figure 4.21. Whole-rock geochemistries of the Chuquicamata and Fortuna Intrusive complexes (normalized to 100%, LOI-free).

The Este Porphyry has the lowest LOI value (0.44 wt.%). There is a wide variation in the loss-on-ignition (LOI) values for both the Banco Porphyry (0.80-2.41 wt.%) and the Fiesta Granodiorite (0.85-1.97 wt.%).

The Oeste Porphyry has been extensively altered and, therefore, the whole-rock geochemistry has undoubtedly been affected. The Oeste Porphyry sample has slightly higher silica values and lower alumina values than the other Chuqui porphyries. It has consistently lower TiO_2 , $\text{Fe}_2\text{O}_{3\text{tot}}$, MgO , and CaO values than the other samples. It has Na_2O and K_2O values similar to the Banco Porphyry. The LOI values in the Oeste Porphyry (1.7%) fall between those of the Banco Porphyry samples but is considerably higher than the Este Porphyry.

4.3.2 Trace and rare earth element geochemistries

Whole-rock and trace element geochemistries of the Fiesta Granodiorite samples (Cu 524 and Cu 526) indicate the Fiesta Granodiorite of the Fortuna Intrusive Complex is rhyodacitic (volcanic equivalent of granodiorite) (Fig. 4.22). Figure 4.22 indicates the three Chuqui porphyries are also the intrusive equivalent of rhyodacite (granodiorite).

The Fiesta Granodiorite and Banco and Este Porphyries plot in the volcanic arc or syn-collisional granitoid field of the diagram of Pearce et al. (1984) (Fig. 4.23). A plot of Rb vs. Y+Nb classifies the Fiesta Granodiorite, Este and Banco porphyries as the volcanic arc granite field (Pearce et al. 1984) (Fig. 4.24). The Este Porphyry plots in the same position as one of the Fiesta Granodiorite samples (Fig. 4.24).

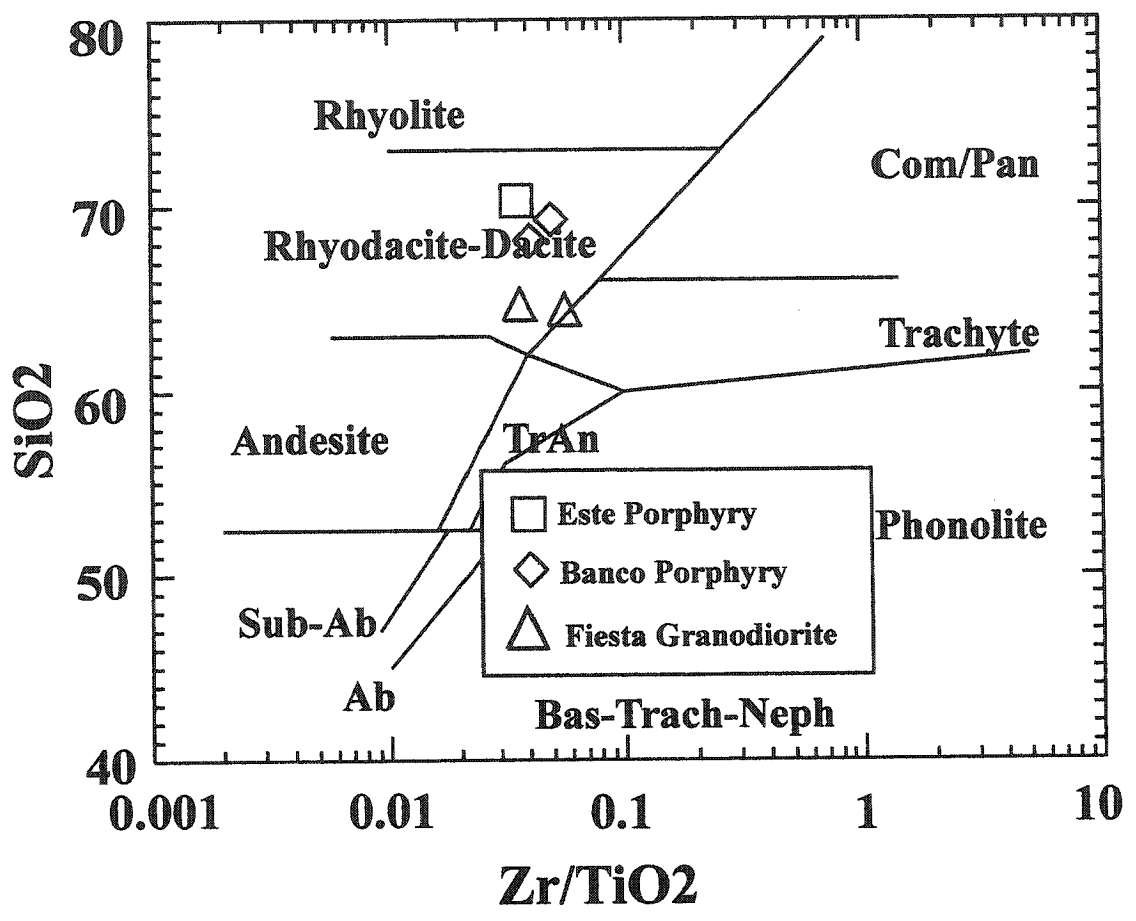


Figure 4.22. The Banco and Este porphyries and Fiesta Granodiorite plot as rhyodacite (the magmatic equivalent to a granodiorite). The Banco Porphyry is a subvolcanic rock and may even be classified as a rhyodacite. Fields after Winchester and Floyd (1977).

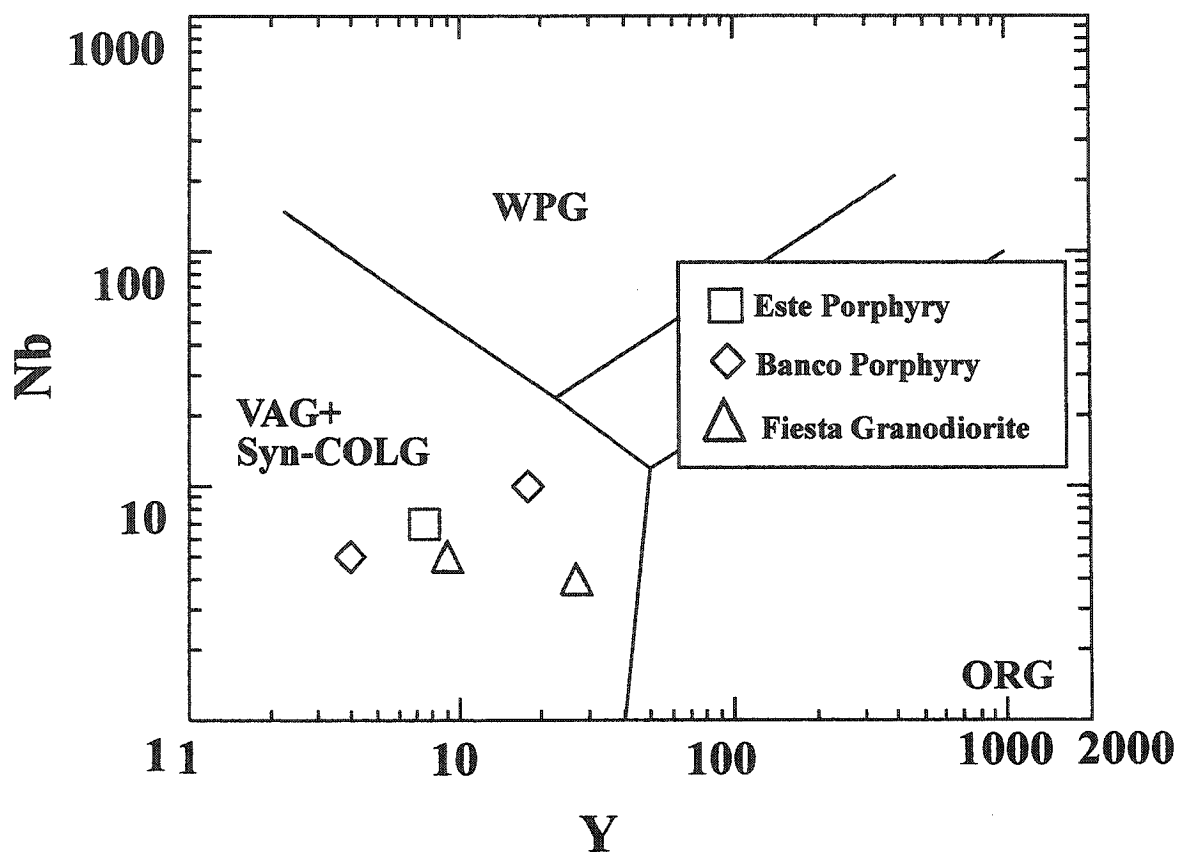


Figure 4.23. The Este and Banco Porphyries and the Fiesta Granodiorite are volcanic arc to syn-collisional granitoids. Diagram of Pearce et al.(1984).

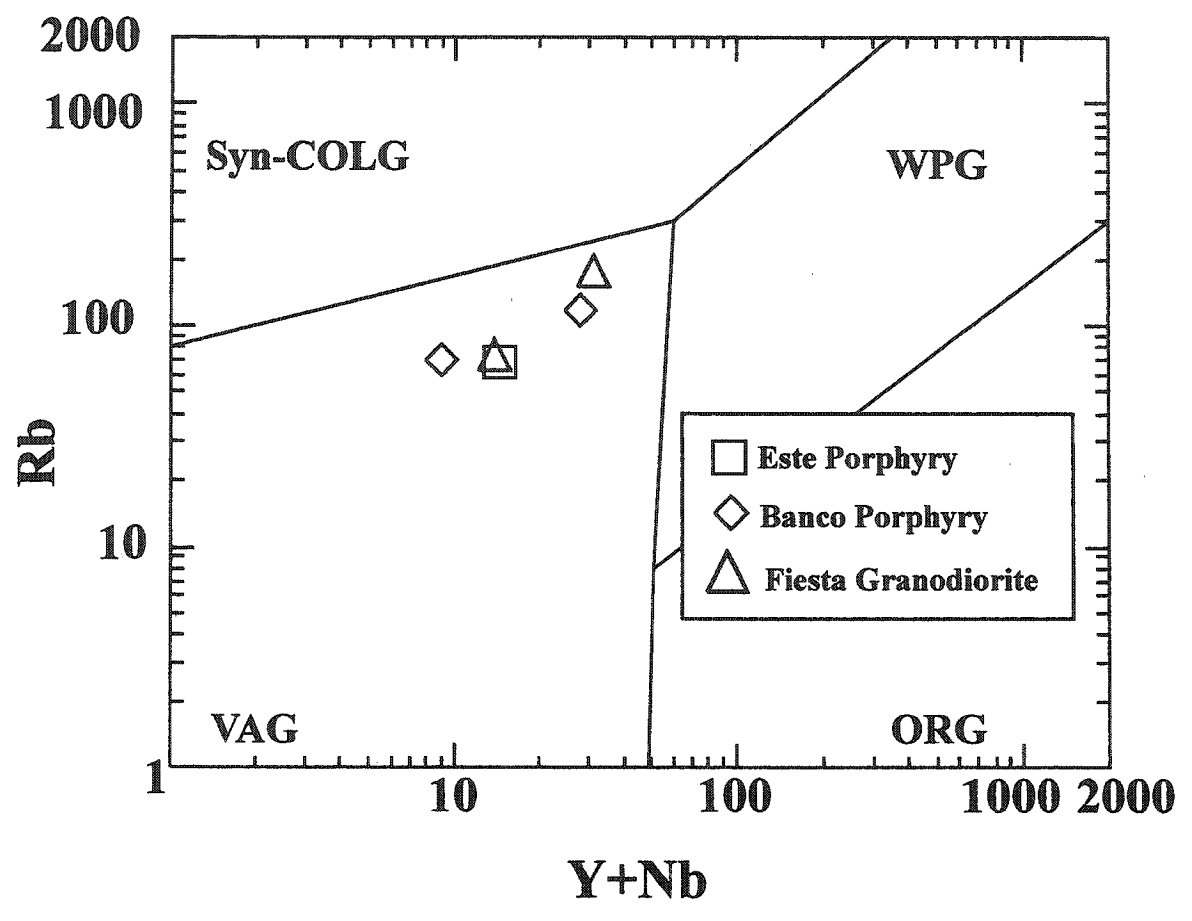


Figure 4.24. The Este and Banco porphyries and the Fiesta Granodiorite are of volcanic arc affinity. Diagram after Pearce et al. (1984).

Rare-earth element analyses for all units are enriched in light rare-earth elements (LREEs) compared to heavy rare-earth elements (HREEs) (Fig. 4.25). The Fiesta Granodiorite appears to be enriched relative to the Chuqui porphyries; however, it has some overlap with the Este Porphyry. The Banco Porphyry is more REE-depleted than the Este Porphyry, particularly in the LREEs, but is more enriched than the Oeste Porphyry. It is unclear whether the relative depletion of the Banco and Oeste porphyries may reflect the degree of Qser alteration or a more depleted source. Regardless of the relative abundance of the REEs, the trend is the same for all units, with a decrease in abundance with increase in atomic number in the LREEs. The HREEs give a flatter and irregular trend. Note the absence of a negative Eu-anomaly in all units.

4.3.3 Discussion of geochemistry

The Chuqui porphyries have slightly elevated SiO_2 values compared to the Fiesta Granodiorite. A quartz-rich groundmass is the reason for the highest silica value in the Oeste Porphyry. The Al_2O_3 values are consistent for all units. This reflects the relative abundance of feldspars and the distribution of Al in the alkali and plagioclase feldspars.

There are higher values for all basic elements (i.e. TiO_2 , $\text{Fe}_2\text{O}_{3\text{tot}}$, MgO and CaO) in the Fiesta Granodiorite compared to the Chuqui porphyries. These higher values confirms the more mafic geochemical nature of the Fiesta Granodiorite seen in the lower SiO_2 content and reflects the relatively higher abundance of mafic minerals and more calcic nature of the plagioclase than in the Chuqui porphyries.

The Este Porphyry is slightly more enriched in TiO_2 , $\text{Fe}_2\text{O}_{3\text{tot}}$, and MgO than the

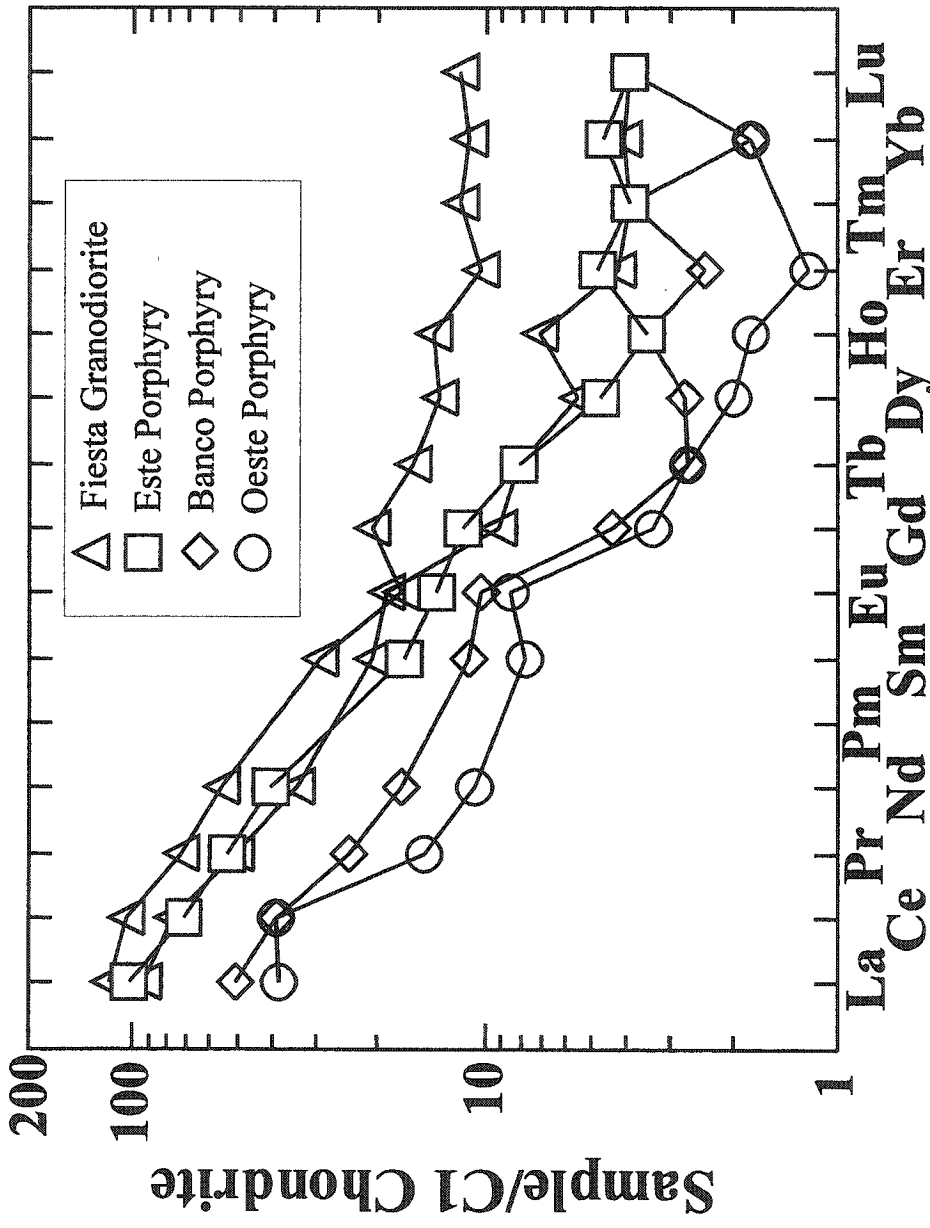


Figure 4.25. Rare-earth element plot for the Fiesta Granodiorite and the Chuquicamata Porphyries.

Banco Porphyry and has much higher CaO content ($\Delta_{\text{CaO}} \geq 1.23$ wt.%) because the Este Porphyry has more abundant basic minerals (amphibole, biotite, and titanite). Some of the plagioclase is more calcic in the Este Porphyry than the Banco Porphyry also reflected in the higher CaO value (Fig 4.7). Also, the plagioclase has been altered to sericite in the Banco Porphyry, replacing some of the Ca with K-rich mica. The Oeste Porphyry has the lowest CaO, FeO and MgO values of all the porphyries, reflecting the replacement of mafic minerals (biotite and An-end-member plagioclase) by sericite and clays.

Variations in Na₂O and K₂O mainly reflect the abundance and composition of feldspars and the degree of sericite alteration. Na₂O is lowest in the Fiesta Granodiorite, reflecting the more calcic plagioclase. The plagioclases in these two samples (Cu 524 and 526) show only minor sericite alteration and, therefore, the K₂O values reflect the abundance of K-feldspar, biotite and amphibole.

Na₂O is higher in Este Porphyry than Fiesta Granodiorite because of the more sodic nature of the plagioclase. The K₂O is lowest in the Este Porphyry because K-bearing minerals (i.e. K-feldspar and biotite) are less abundant than in the Fiesta Granodiorite and Banco Porphyry. In the Este Porphyry, K-feldspar occurs primarily as interstitial groundmass; biotite and amphibole are metastable and not as abundant as in the Fiesta Granodiorite and there is no sericite alteration of the plagioclase in the Este Porphyry, in contrast to the Banco Porphyry.

The high Na₂O values in the Banco Porphyry reflect the more sodic nature of the plagioclase than in the Fiesta Granodiorite. K₂O is high in the Banco Porphyry due to the abundance of K-feldspar and the K-mica alteration of the plagioclase. There is only

minor biotite in the Banco Porphyry and, therefore, it contributes only a small amount of K_2O . K_2O is highest in the Banco Porphyry sample characterized by large megacrystic K-feldspar (Cu 1333) although these megacrysts were intentionally avoided in the geochemical sample analyzed.

Although no microprobe data are available for the feldspar of the Oeste Porphyry feldspars, it is apparent that the plagioclase is very sodic as the Na_2O content is very high. This value likely reflects the remnant plagioclase in the sample but may also indicate the presence of paragonite-composition sericite. The high Na_2O and K_2O reflect the abundance of alkali feldspars and sericite alteration.

The high LOI in the Fiesta Granodiorite sample Cu 526 is due to the abundance of hydrous minerals, such as biotite and amphibole, as well as minor sericite alteration of the plagioclase. There are few hydrous minerals in the Este Porphyry which has the lowest LOI. High LOI-values in the Banco and Oeste porphyries reflect the degree of sericitic alteration.

Trace-element discrimination diagrams show that the Fiesta Granodiorite and Este and Banco Porphyries are granodioritic in composition (Fig. 4.22). The Fiesta Granodiorite and Chuqui Porphyries formed in a volcanic arc tectonic setting (Figs. 4.23 and 4.24).

Rare-earth element analyses indicate a possible garnet- or hornblende-rich source indicated by the steep slope of the LREEs (Fig. 4.25). However, the flatter HREE trend is less meaningful. As there are so few samples from each unit, a definite source is not discernible.

The depletion of REEs in the Banco and Oeste Porphyries may be the result of Qser alteration, a trend observed and discussed further in Chapters 5 and 6.

The absence of a Eu-anomaly may be indicative of high oxygen fugacities. Europium preferentially partitions into the melt with a 3+ charge and into plagioclase with a 2+ charge (Rollinson 1993). Therefore, Eu^{3+} is the referred ion at high f_{O_2} and, therefore, partitions into the melt (Rollinson 1993). In this way, Eu avoids being removed from the melt in plagioclase. The estimated high oxygen fugacity is supported by the presence of magnetite and titanite.

4.4 Geochronology

Radiometric dates previously published for the Fortuna and Chuquicamata Intrusive complexes are reported in Chapter 3 (Tables 3.1 and 3.3). High-precision $^{40}\text{Ar}/^{39}\text{Ar}$ ages were obtained for the Chuquicamata Intrusive Complex during this project (Reynolds et al. 1998) and, therefore, no further dates were obtained during this study (Table 3.3). The Fortuna Intrusive Complex has been dated using only the K-Ar and discordant U-Pb (Table 3.1). Poor precision in the published ages led to further dating of the Fiesta Granodiorite using the $^{40}\text{Ar}/^{39}\text{Ar}$ method.

4.4.1 $^{40}\text{Ar}/^{39}\text{Ar}$ of the Fiesta Granodiorite

Data for the $^{40}\text{Ar}/^{39}\text{Ar}$ dates are given in Appendix G. Appendix G also describes the methodology of this method. Samples were separated and analyzed at Dalhousie University.

4.4.1.1 Hornblende

Spectra obtained from hornblende separates from samples Cu-046 and Cu-524 are concordant within error over the final ~80% of gas release (Fig. 4.26). Best estimates of age are 37.2 ± 1.2 and 37.9 ± 2 Ma, respectively. These ages correspond to observed $^{37}\text{Ar}/^{39}\text{Ar}$ ratios of ~7 to 12 and 9 to 11, respectively (Fig. 4.26). In each case, these measurements are at the lower limit of values inferred from electron microprobe determinations of Ca/K ratios (Appendix G) (Fig. 4.26). Hence, some contamination from biotite is suspected, a conclusion consistent with the observed petrography and with the very low $^{37}\text{Ar}/^{39}\text{Ar}$ ratios apparent over the initial ~20% of gas release.

Data obtained from hornblende separates of sample Cu-789 are characterized by abundant gas at relatively low extraction temperatures, discordant age spectra, and low $^{37}\text{Ar}/^{39}\text{Ar}$ ratios (Fig. 4.26). Hence, the total gas age of 36 ± 0.3 Ma is interpreted as a biotite age.

4.4.1.2 Biotite

Spectra obtained from biotite separates from samples Cu-046 and Cu-524 are concordant over ~95% of the gas release at ages of 36.4 ± 0.4 and 36.4 ± 0.6 Ma, respectively (Fig. 4.27). The moderately discordant spectrum obtained for Cu-407 biotite has an average age of 36.9 ± 0.4 Ma over the bulk of the gas release.

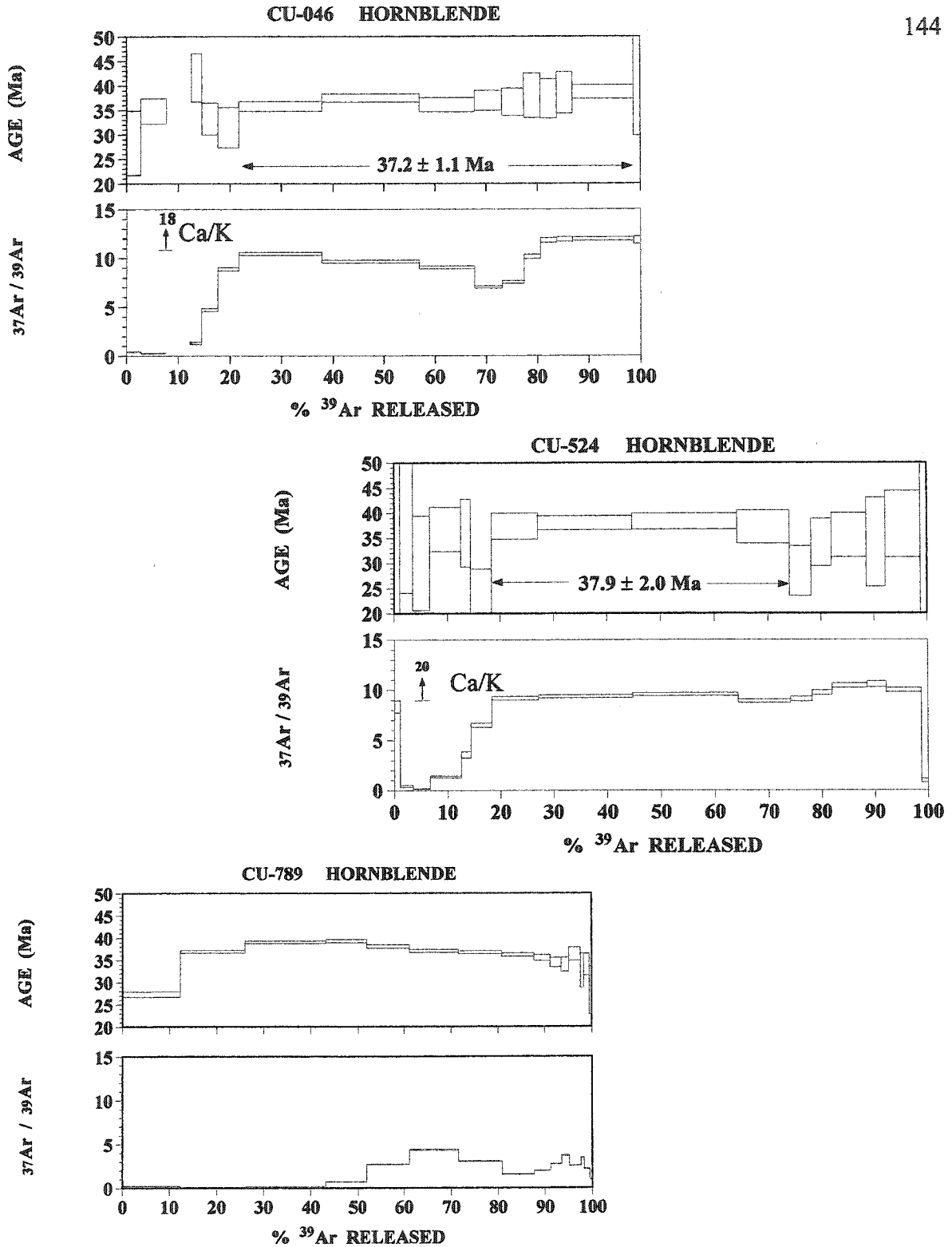


Figure 4.26. Hornblende age spectra and ³⁷Ar/³⁹Ar spectra. The ratio of ³⁷Ar to ³⁹Ar indicates the amount of calcium present. The lack of ³⁷Ar/³⁹Ar in sample Cu 789 supports the conclusion that this is a biotite spectrum.

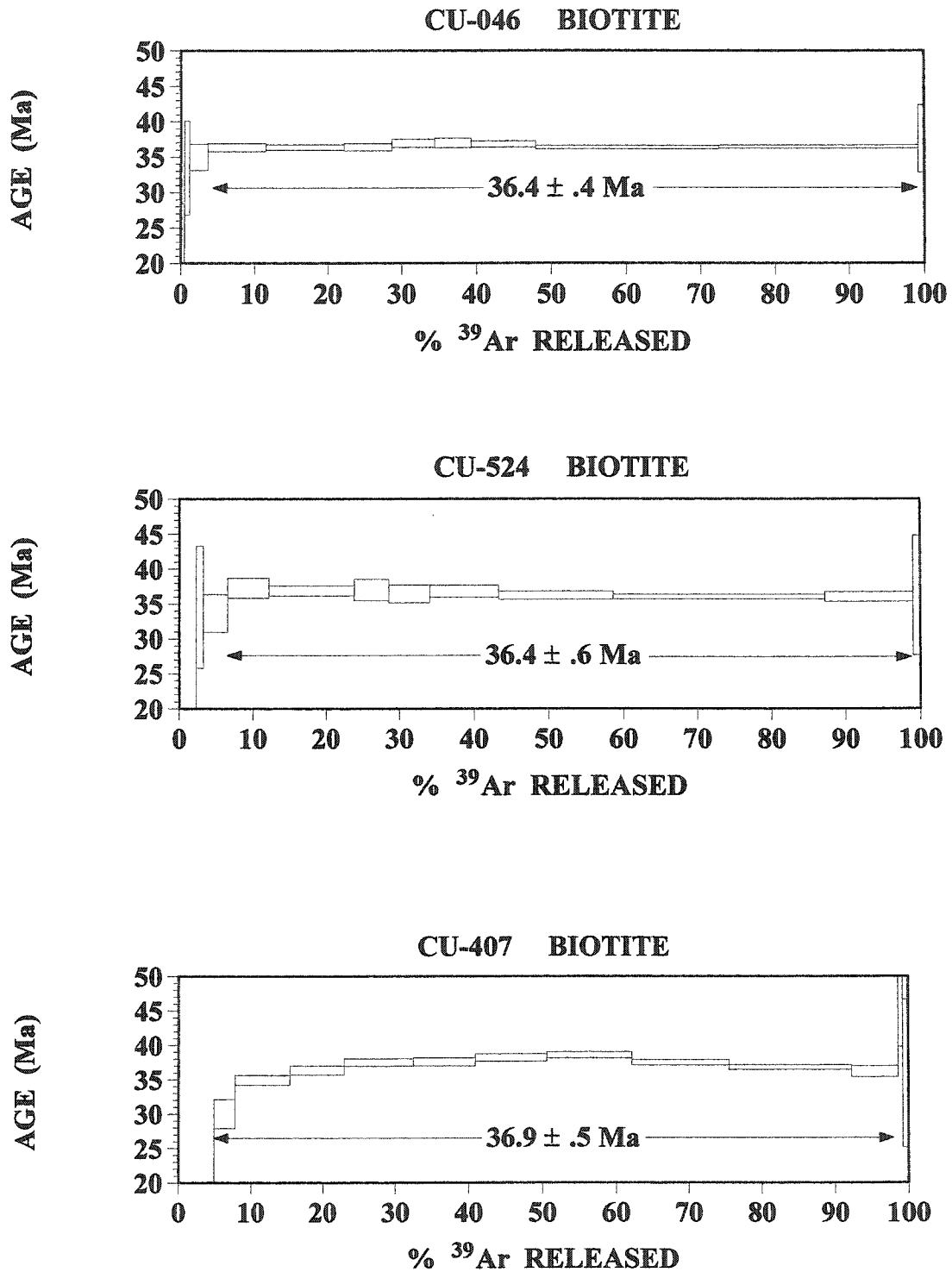


Figure 4.27. $^{40}\text{Ar}/^{39}\text{Ar}$ spectra for biotite in the Fiesta Granodiorite are well-constrained.

4.4.1.3 K-feldspar

This mineral yielded the most consistent data in the present study. All four Fiesta samples (Cu-789, Cu-407, Cu-046, Cu-1061) had age plateaus comprising ~65 to 80% of the total gas release over the latter portions of the age spectra (Fig. 4.28). Plateau ages range from 35.0 ± 0.3 Ma to 35.8 ± 0.5 Ma; the mean is 35.5 ± 0.2 Ma.

Sample Cu 790 from the Tetera Porphyry yielded a K-feldspar plateau age of 35.5 ± 0.4 Ma over 80% of the total gas released. This age is consistent with the mean of the Fiesta Granodiorite samples.

4.4.1.4 Discussion of $^{40}\text{Ar}/^{39}\text{Ar}$ ages

The results of the $^{40}\text{Ar}/^{39}\text{Ar}$ study are presented in Table 4.2. The mean age of hornblende in the Fiesta Grandiorite is 37.6 ± 0.7 Ma (samples Cu 046 and Cu 524). The mean age of Fiesta Granodiorite biotite is 36.4 Ma (omitting sample Cu 407 because of its discordance) and the K-feldspar mean age is 35.5 ± 0.2 Ma (all samples).

The error ranges on the amphibole ages are significant, but the ages are invariably older than the biotite and K-feldspar ages (Figure 4.29). This difference in ages is consistent with the higher closure temperature of amphiboles ($\sim 500^\circ\text{C}$) and the lower closure temperatures of biotite ($\sim 300^\circ\text{C}$) and K-feldspar ($170\text{-}300^\circ\text{C}$). The small difference between the amphibole and K-feldspar (<2 Ma) ages indicates rapid cooling ($\sim 150^\circ\text{C}/\text{My}$).

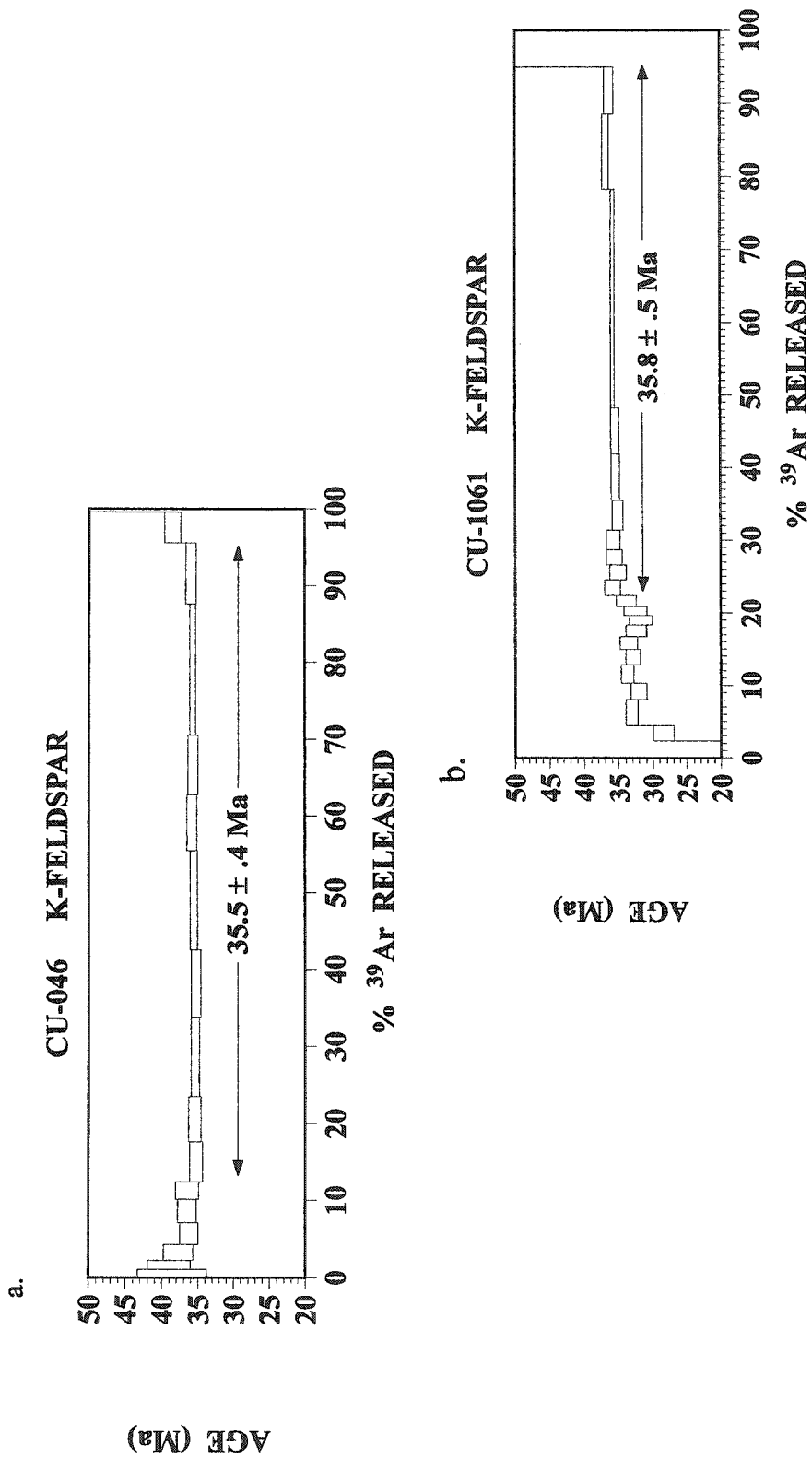


Figure 4.28. a and b) K-feldspar $^{40}\text{Ar}/^{39}\text{Ar}$ spectra from the Fiesta Granodiorite.

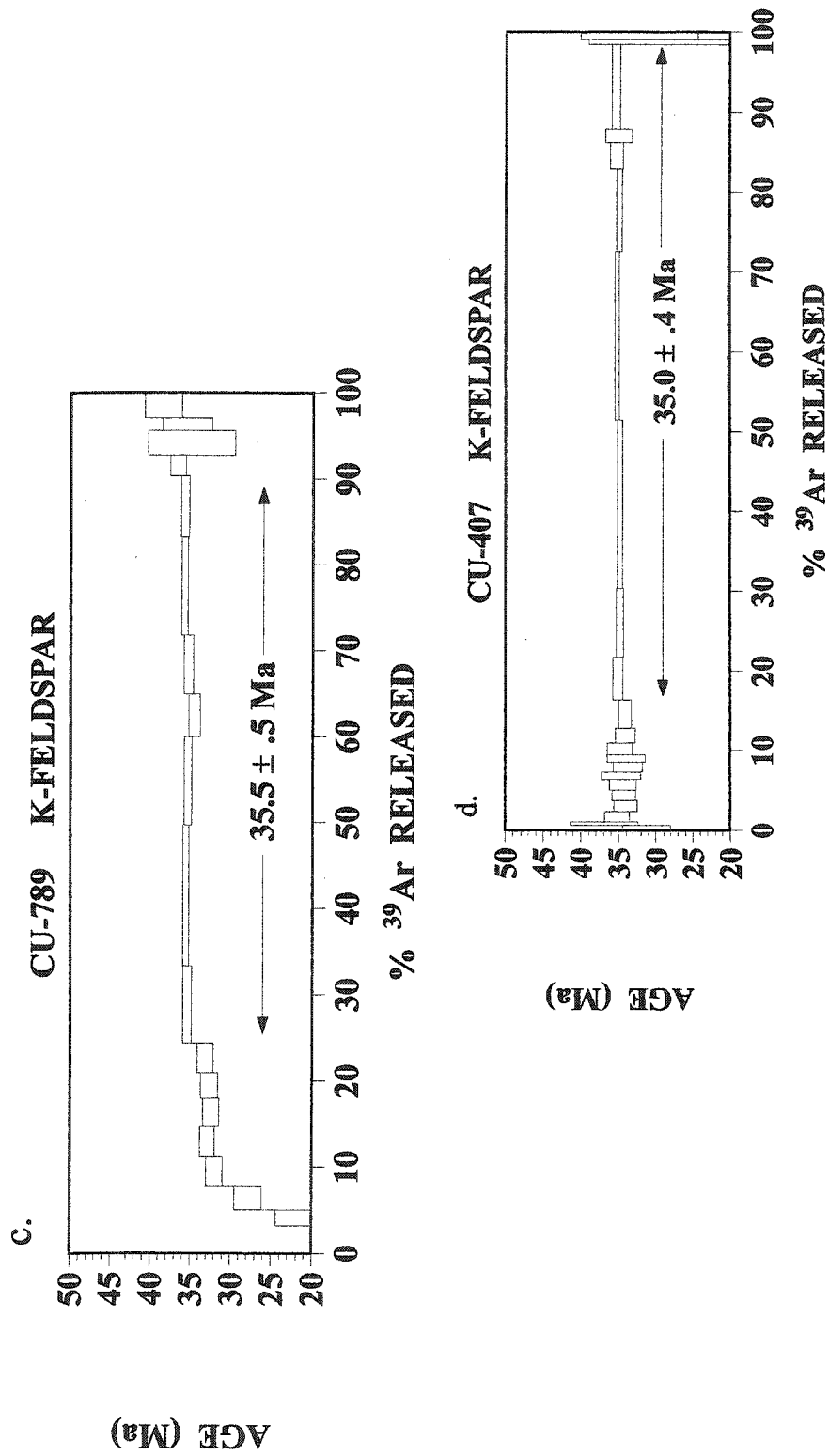


Figure 4.28. c and d) K-feldspar $^{40}\text{Ar}/^{39}\text{Ar}$ spectra from the Fiesta Granodiorite.

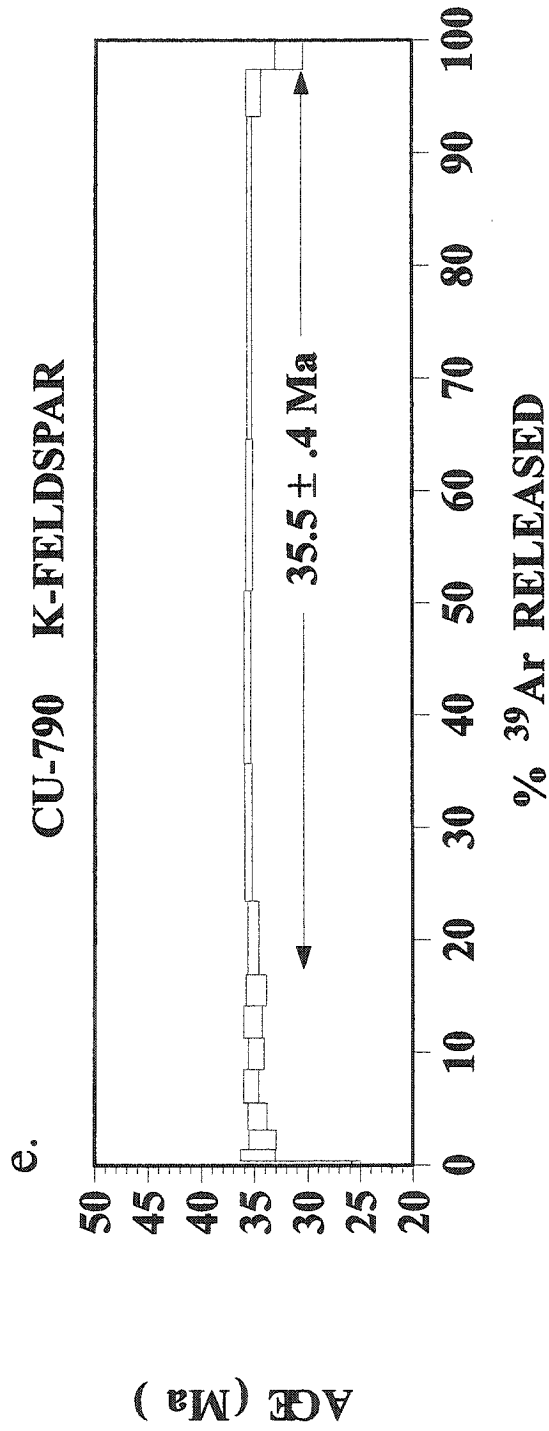


Figure 4.28. e) K-feldspar ⁴⁰Ar/³⁹Ar spectra from the Tetera Porphyry.

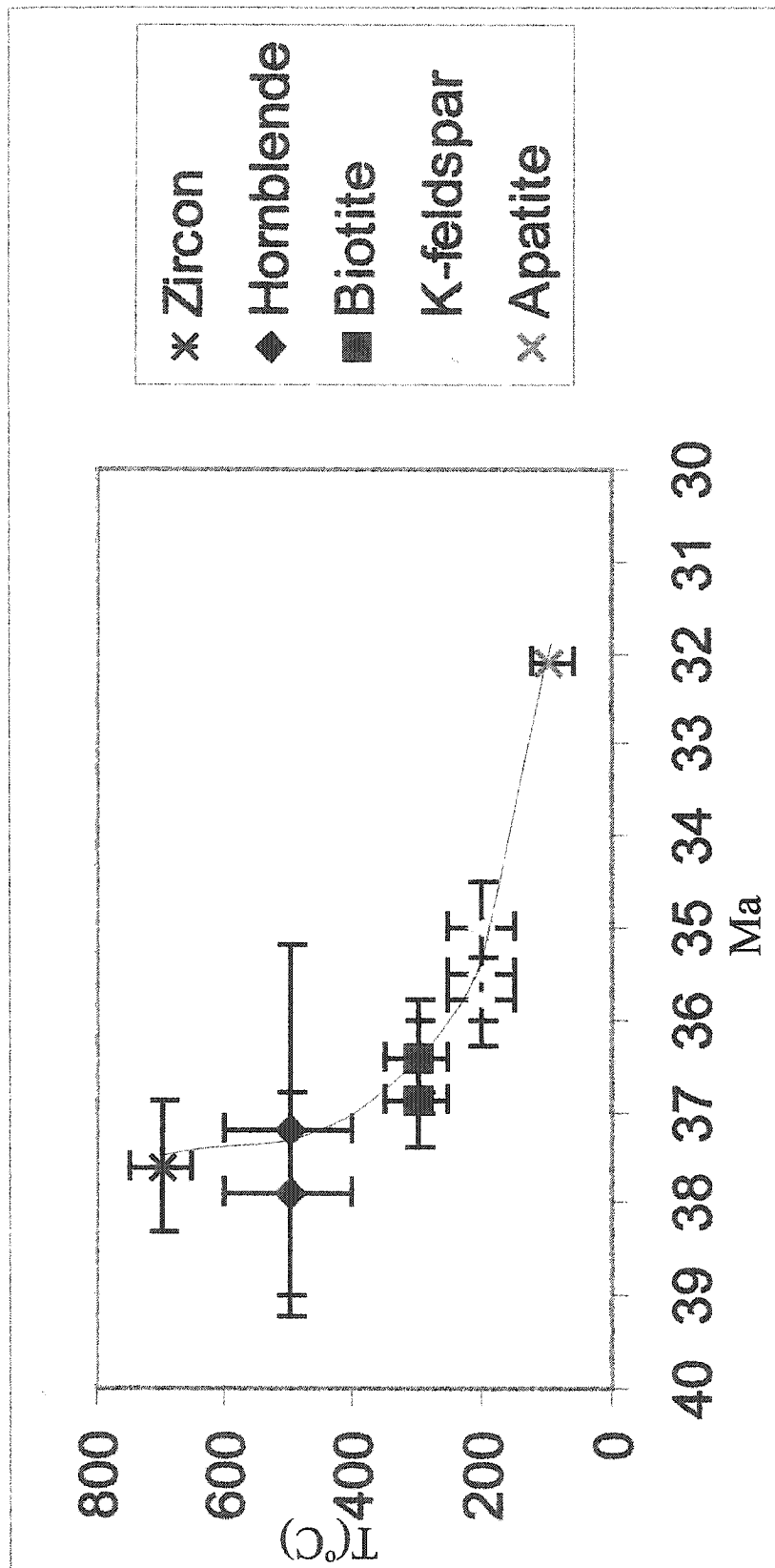


Figure 4.29. Cooling curve for the Fiesta Granodiorite. The Fiesta Granodiorite cooled quickly from 800 to 300° (from data in Dilles et al. 1997; Tomlinson et al. 1997; Maksiyev and Zentilli 1999; and this study).

Table 4.2 $^{40}\text{Ar}/^{39}\text{Ar}$ ages of the Fiesta Granodiorite from this study. The calculated mean (± 2 standard deviations) for each mineral is reported in bold font (*- not calculated in the mean).

Sample #	Hornblende	Biotite	K-feldspar
Cu 046	37.2 ± 1.1 Ma	36.4 ± 0.4 Ma	35.5 ± 0.4 Ma
Cu 407		36.9 ± 0.5 Ma*	35.0 ± 0.4 Ma
Cu 524	37.9 ± 2.0 Ma	36.4 ± 0.6 Ma	
Cu 789	36.0 ± 0.3 Ma*		35.5 ± 0.5 Ma
Cu 1061			35.8 ± 0.5 Ma
mean	37.6 ± 1.0 Ma	36.4 ± 0.0 Ma	35.5 ± 0.2 Ma

Figure 4.29 shows a possible cooling curve for the Fiesta Granodiorite based on the $^{40}\text{Ar}/^{39}\text{Ar}$ data in this study and the U/Pb zircon and apatite fission track data reported in Table 3.1. Cooling was very rapid between 700° and 500°C . Between 500°C and 300°C , the cooling slowed to $200^\circ\text{C}/\text{My}$ and continue to slow significantly to at least $\sim 200^\circ\text{C}$.

4.5 Two-feldspar geothermometry

The following equation is a two-feldspar thermometer refined by Haselton et al. (1983):

$$T_K = \frac{(X_{\text{Or}}^{\text{AF}})^2 (18810 + 17030 X_{\text{Ab}}^{\text{AF}} + 0.364 P) - (X_{\text{Ab}}^{\text{PL}})^2 (28230 - 39520 X_{\text{Ab}}^{\text{PL}})}{10.3 (X_{\text{Or}}^{\text{AF}})^2 + 8.3143 \ln \left\{ \frac{(X_{\text{Ab}}^{\text{PL}})^2 (2 - X_{\text{Ab}}^{\text{PL}})}{X_{\text{Ab}}^{\text{AF}}} \right\}}$$

where T is temperature in degrees Kelvin, X = the mole fractions, and P is pressure in bars.

The two-feldspar geothermometry gives a temperature of 534 to 565°C for the Fiesta Granodiorite over pressures of 1 to 3 kbars (Table 4.3). This constrains the temperature at which the feldspar compositions equilibrated.

Table 4.3. Temperatures calculated using two-feldspar geothermometry (Haselton et al. 1983).

Pressure	Fiesta An ₄₆ Or ₈₈	Este An ₃₉ Or ₉₅	Banco An ₃₇ Or ₈₀
1000 bars	534°C	322°C	678°C
2000 bars	550°C	333°C	694°C
3000 bars	565°C	344°C	710°C

The Banco Porphyry has a considerably higher temperature range (678 to 710°C) over the pressure range of 1 to 3 kbars (Table 4.3), likely due to equilibration in feldspar compositions during rapid cooling.

The Este Porphyry temperatures are considerably lower (322 to 344°C) (Table 4.3). These lower temperatures may be due to slow cooling, allowing re-equilibration of feldspar compositions. It is unlikely the Este Porphyry crystallized at pressures higher than 3 kbars, so higher temperatures are not likely to have been achieved using this process. The two-feldspar geothermometer of Haselton et al. (1983) is untested below 500°C and, therefore, the temperature determined for the Este Porphyry is tenuous. Still, it seems reasonable to assume that subsolidus re-equilibration of feldspar compositions occurred below 500°C in the Este Porphyry.

4.6 Hornblende geobarometry

There are enough thermodynamic constraints on the composition of hornblende that the total aluminum values in the rims of hornblende of calc-alkaline rocks may be used to calculate the pressure of solidification (Hammarstrom and Zen 1986, Hollister et al. 1987, and Schmidt 1991). The requirements to constrain the degrees of freedom and make the Al-content of hornblende a valid geobarometer are the following (Hammarstrom and Zen 1986; Hollister et al. 1987):

- 1) the rocks should be calc-alkaline;
- 2) an assemblage of plagioclase-quartz-hornblende-biotite-orthoclase-magnetite-titanite must have crystallized together;
- 3) to constrain temperature, only the compositions of the rims of the hornblende should be determined (the rims were the only part of the grains that could have crystallized with the other phases in the final melt);
- 4) the plagioclase rim compositions should be between An_{25} and An_{35} ; and
- 5) the pressure has to have been >2 kbars (the limit of the experimentation).

Using these conditions, the Al_{total} contents of hornblende in two samples of the Fiesta Granodiorite (Cu 046 and Cu 524) and one sample of the Este Porphyry (Cu 769) were calculated and the pressures determined using the equations of the aforementioned authors. The results are presented in Table 4.4.

Pressures of < 2 kbars were derived for all samples, except for the Este Porphyry. However, it is unclear whether the calculated pressures >2 kbars are values from rim

analyses of the amphibole. All values <2 kbar are below the limit of validity for this technique.

It would be reasonable to assume that the Fiesta Granodiorite solidified at <2 kbars. Alternatively, the hornblendes may be metastable in the Fiesta Granodiorite which

Table 4.4. Calculated pressures from the Este Granodiorite and Este Porphyry using hornblende geobarometry. Hornblende geobarometer uses the total cation amount of aluminum. $P = -4.76 + 5.64Al_{total}$ (Hollister et al. 1987), $P = -3.92 + 5.03Al_{total}$ (Hammarstrom and Zen 1986), $P = -3.01 + 4.76Al_{total}$ (Schmidt 1991). The electron microprobe data for hornblende are reported in Appendix C.

Sample #	Range of Al_{total}	Equation	Calculated pressure
Cu 046 (Fiesta)	0.668-0.905	Hollister et al. (1987)	-0.992-0.344 (kbars)
		Hammarstrom and Zen(1986)	-0.560-0.632 (kbars)
		Schmidt (1991)	0.170-1.30 (kbars)
Cu 524 (Fiesta)	0.684-0.918	Hollister et al. (1987)	-0.902-0.417 (kbars)
		Hammarstrom and Zen(1986)	-0.479-0.698 (kbars)
		Schmidt (1991)	0.246-1.360 (kbars)
Cu 789 (Fiesta)	0.629-0.978	Hollister et al. (1987)	-1.21-0.756 (kbars)
		Hammarstrom and Zen(1986)	0.756-0.999 (kbars)
		Schmidt (1991)	-0.016-1.645 (kbars)
Cu 769 (Este)	0.640-1.08 (not all rims)	Hollister et al. (1987)	-1.15-1.33 (kbars)
		Hammarstrom and Zen(1986)	-0.701-1.51 (kbars)
		Schmidt (1991)	0.0364-2.131 (kbars)

affected the Al-content in the hornblende. Metastability seems a likely alternative as

some of the pressures have negative values. Regardless, in the Fiesta Granodiorite, the results are not within the experimental limits of the technique, perhaps due to subsolidus effects which also affected the two-feldspar geothermometry in Section 4.5.

In the Este Porphyry, the plagioclase compositions fall within the error range for this analytical technique, however, the rim compositions were only locally calcic enough to satisfy the analytical requirements. The composition of plagioclase rims is required to constrain the degrees of freedom and, therefore, this unit is unsuitable for this technique. The hornblende in the Este Porphyry is interpreted to be metastable, which may also affect the reliability of this technique. Temperatures calculated using two-feldspar thermometry indicates the temperature of crystallization necessary to confine the degrees of freedom using hornblende barometry may not reflect the actual temperature at which the hornblende compositions were fixed.

4.7 Stable Isotopes of the Este Porphyry

Mineral separates from the Este Porphyry were analyzed at the laboratory of Dr. Kurt Keyser at Queen's University in Kingston, Ontario, for oxygen and hydrogen stable isotopes. The results are presented in Table 4.4 and Appendix F, reported as $\delta^{18}\text{O}$ in ‰,

$$\text{where } \delta^{18}\text{O } \text{‰} = \left(\frac{{}^{18}\text{O}/{}^{16}\text{O}_{(\text{sample})} - {}^{18}\text{O}/{}^{16}\text{O}_{(\text{standard})}}{{}^{18}\text{O}/{}^{16}\text{O}_{(\text{standard})}} \right) \times 1000$$

with SMOW as the standard.

The measured values of $\delta^{18}\text{O}$ can be used to determine the temperature of equilibrium and the $\delta^{18}\text{O}$ and δD of the fluid in equilibrium with the minerals gives an

indication of the source of the fluid (e.g. Rollinson 1993). For the temperatures and calculated $\delta_{\text{H}_2\text{O}}$ values to be valid, the minerals must be in isotopic equilibrium. Three features may indicate whether isotopic equilibrium was achieved. The first is the presence of isotopic reversals (O'Neil 1986). For example, the order of $\delta^{18}\text{O}$ enrichment should be quartz>K-feldspar>biotite; if this order is different for the measured values, the minerals may not be in isotopic equilibrium. The second requirement is unusually large isotopic fractionations. If the $\Delta_{\text{quartz-feldspar}}$ is very high (1.3 to 1.8 is the normal range), then isotopic equilibrium has been affected (O'Neil 1986). Finally, the temperatures calculated for multiple pairs of minerals must be concordant (O'Neil 1986) and reasonable.

Non-altered I-type plutonic rocks have “normal” igneous values which are $\delta\text{D} \sim -50$ to -90‰ and $\delta^{18}\text{O} \sim +5.5$ to $+10\text{‰}$ (Sheppard et al. 1969). All Este Porphyry values fall within this range (Table 4.5); there are no isotopic reversals (Table 4.5); and there are no significantly large isotopic fractionations ($\Delta_{\text{quartz-feldspar}} = 1.2\text{‰}$). All of these conditions indicated that there was isotopic equilibrium.

4.7.1 Isotope thermometry

Temperatures were determined using oxygen isotopes from quartz-K-feldspar, quartz-biotite and K-feldspar-biotite pairs applying the equation:

$$1000 \ln \alpha^1_2 \approx \delta^{18}\text{O}_1 - \delta^{18}\text{O}_2 \approx A(10^6\text{T}^{-2}) + B$$

where α is the isotopic fractionation factor, T is temperature in degrees Kelvin, and A and B are experimentally determined constants. The constants used in these calculations are

from Bottinga and Javoy (1973 and 1975) and are tabulated in Appendix F.

The results of the temperature calculations are given in Table 4.6. These temperatures are somewhat concordant with a mean temperature of $595^{\circ} \pm 25^{\circ}\text{C}$. The concordance of temperatures supports the equilibration of isotopes.

Table 4.5. Stable isotope δ -values for the Este Porphyry.

Mineral	measured $\delta^{18}\text{O}$	measured δD
Quartz	9.4	n/a
K-feldspar	8.2	n/a
Plagioclase (An ₃₀)	8.2	n/a
Biotite	5	-85

Table 4.6 Calculated temperatures from stable isotope pairs from the Este Porphyry (using constants of Bottinga and Javoy 1973).

Mineral pair	Bottinga and Javoy 1973, 1975
Quartz-K-feldspar	626°C
Quartz-Biotite	586°C
K-feldspar-Biotite	575°C

The mean temperature (595°C) is low for magmatic environments. However, low temperatures can be expected in plutonic rocks where the temperature of equilibration may represent subsolidus temperatures and not the temperature of crystallization (Faure 1977). This temperature is much higher than that acquired using two-feldspar geothermometry (Section 4.5). The isotopic age is more reasonable for an intrusive granitoid.

4.7.2 Isotopic composition of crystallizing fluids

Oxygen and deuterium values for the fluids in equilibrium with the minerals were calculated assuming a temperature of 600°C. This value is within the error of the calculated temperature (Table 4.7).

The water in equilibrium with “normal” igneous values should have values of $\delta D \sim -40$ to -80‰ and $\delta^{18}O \sim 5.5$ to 9.5‰ (Sheppard et al. 1969). These values are considered to represent “primary” magmatic water, implying the water was transported with the magma. The water in equilibrium with the minerals of the Este Porphyry ranges in $\delta^{18}O$ from 7.58 to 7.99 ‰, well within this primary range. The narrow range of calculated values is consistent with isotopic equilibrium.

The fluid in equilibrium with the biotite has a δD value of -54.26‰ , which is within the range of “normal” igneous values. A plot of the biotite oxygen-deuterium values in Figure 4.30 shows that biotite equilibrated with fluids of magmatic origin.

Table 4.7 Calculated $\delta^{18}O$ of the fluids in equilibrium with the minerals at 600°C.

Mineral	calculated $\delta^{18}O$	reference
quartz	7.720	Bottinga and Javoy 1973
K-feldspar	7.793	O'Neil and Taylor 1967 Bottinga and Javoy 1973
plagioclase	7.968	Bottinga and Javoy 1973
biotite	7.575	Bottinga and Javoy 1973, 1975

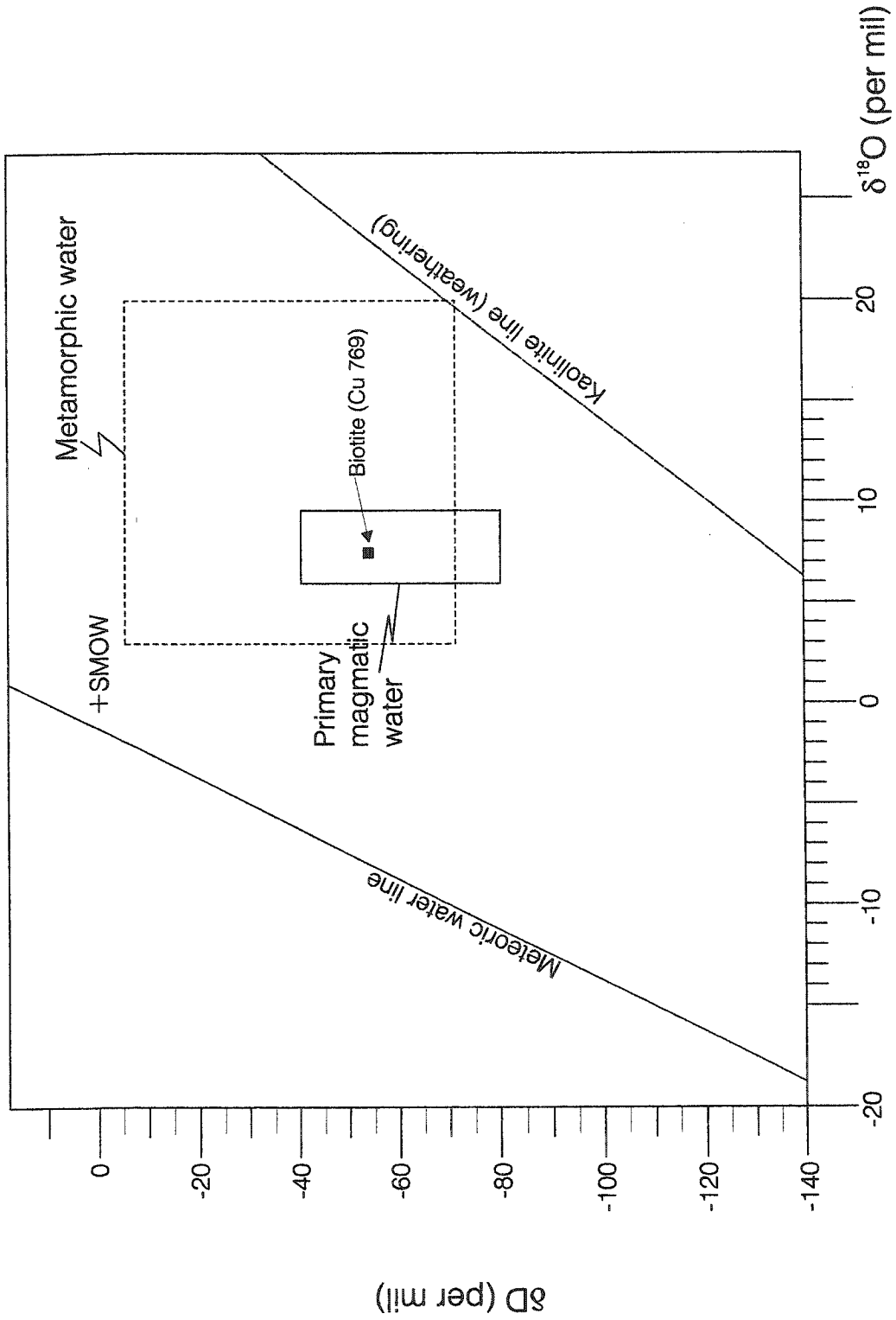


Figure 4.30. Biotite in the Este Porphyry plots as magmatic biotite. The calculations are made assuming a temperature of equilibration of 600°C. Diagram after Sheppard (1986) and references therein.

4.8 Summary

The Fiesta Granodiorite and Este Porphyry have amphiboles and plagioclases with similar compositions, and similar trace-element enrichment in the titanites (Figs. 4.6, 4.7 and 4.9). The K-feldspar in both units is poikilitic with Ba-enriched zones, indicative of a magmatic origin. Magnetite, zircon, and apatite are present in both units. The Fiesta Granodiorite has a higher mafic index and, a slightly more calcic plagioclase, indicating it is more mafic than the Este Porphyry.

The Fiesta Granodiorite has a higher percentage of basic elements than the Chuqui porphyries. These elements are found in the more mafic minerals (i.e. amphibole, biotite, and calcic plagioclase). The lowest K_2O value in the Este Porphyry supports the observation of lesser amounts of K-feldspar. The lowest CaO values in the Banco and Oeste Porphyries is due to the more sodic plagioclase and the absence of titanite and amphibole.

Trace-element discrimination diagrams show the Fiesta Granodiorite and Este and Banco porphyries are granodioritic in composition (Fig. 4.22). According to trace elements, all three units formed in a volcanic arc tectonic setting (Figs. 4.23 and 4.24).

The Banco Porphyry has a 'doubly porphyritic' texture and was intruded into the Este Porphyry as a subvolcanic dyke. The BaO zonation, euhedral plagioclase inclusions, and perthitic texture supports a magmatic origin for the K-feldspar (Figs. 4.18 and 4.19).

The determination of a source magma using rare-earth element data was inconclusive (Fig. 4.25). The absence of a negative Eu-anomaly is interpreted to represent a high oxygen fugacity in the magmas (Candela 1990) (Fig. 4.25).

$^{40}\text{Ar}/^{39}\text{Ar}$ ages for the Fiesta Granodiorite indicate that an intrusion age of 37.6 ± 0.7 Ma. A cooling rate of $200^\circ\text{C}/\text{My}$ during intrusion (until 35.5 Ma) is interpreted to have been followed by significantly slow cooling (Fig. 4.29).

The Fiesta Granodiorite is significantly older than the Este Porphyry (~ 34 Ma). The Banco Porphyry, which intruded the Este Porphyry, is estimated to have an age of ~ 33 Ma from previous $^{40}\text{Ar}/^{39}\text{Ar}$ and U/Pb analyses (Reynolds et al. 1998; Ballard et al. 2001), significantly younger than the Este Porphyry.

Although inconclusive, hornblende geobarometry indicates that the Fiesta Granodiorite and Este Porphyry likely crystallized at pressures below 2 kbars. Assuming a pressure of formation of < 2 kbars, the range of temperatures determined using two-feldspar geothermometry can be narrowed to values determined for pressures between 1 to 2 kbars. The Fiesta Granodiorite can be concluded to have crystallized at 534 to 550°C .

The two-feldspar geothermometer was inconclusive in the Este Porphyry but the Banco Porphyry intruded the Este Porphyry after the Este Porphyry had cooled and been emplaced, it can be assumed that the Banco Porphyry intruded at a higher crustal level (i.e. lower pressure) than the Este Porphyry. Therefore, assuming a pressure of intrusion ~ 1 kbar, a temperature of $\sim 678^\circ\text{C}$ is concluded for crystallization of the Banco Porphyry.

Stable isotope data indicate the Este Porphyry crystallized in equilibrium with primary magmatic fluids (Fig. 4.30). The calculated temperature, $\sim 595^\circ\text{C}$, is consistent with slowly cooled granitoid rocks.

Chapter 5

Petrology and Geochemistry of the Potassic Alteration Zone

5.1 Introduction

As defined in Chapter 2, the potassic alteration is characterized by K-feldspar, usually with biotite. K-feldspar occurs as a replacement of plagioclase and in veinlets (Rose and Burt 1979). Guilbert and Park (1986; Fig. 11.12) suggested that the potassic alteration zone *sensu stricto* at Chuquicamata occurs only in areas cut by Qser veinlets. In Figure 3.5, the potassic alteration zone is displayed as telescoped with other alteration zones (Guilbert and Park 1986): overprinted by Qser, cut by Qser veins and transitional with the propylitic zone. Detailed mapping by mine geologists indicates that the potassic alteration zone occurs near the centre of the Chuquicamata pit (Fig. 5.1): in the east, the potassic alteration zone has a transitional contact with the propylitic alteration zone (Chapter 3); in the west, the potassic alteration zone is overprinted by Qser alteration (Chapter 6). The potassic alteration zone, *sensu stricto*, occurs as patches between the Qser and propylitic zones.

5.2 Petrology of the potassic alteration zone of the Este Porphyry

The potassic mineral assemblage of the Este Porphyry is characterized by quartz, plagioclase, K-feldspar and biotite with accessory rutile, apatite, and zircon (Figs. 5.2 and 5.3). The potassically altered rocks of the Este porphyry are medium-grained to

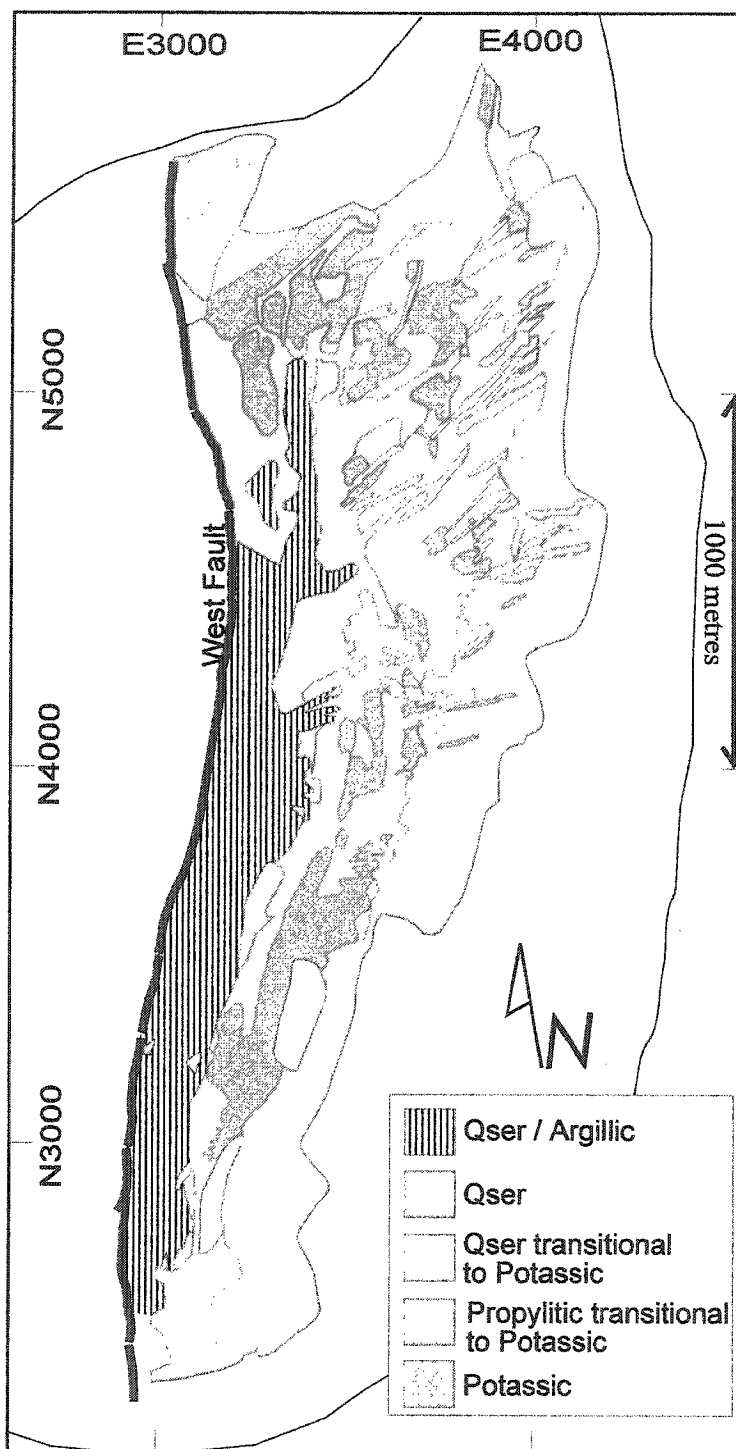


Figure 5.1. Distribution of the potassic alteration zone (shown in shades of pink). It is transitional with the propylitic alteration in the west and overprinted by the Qser alteration in the east.

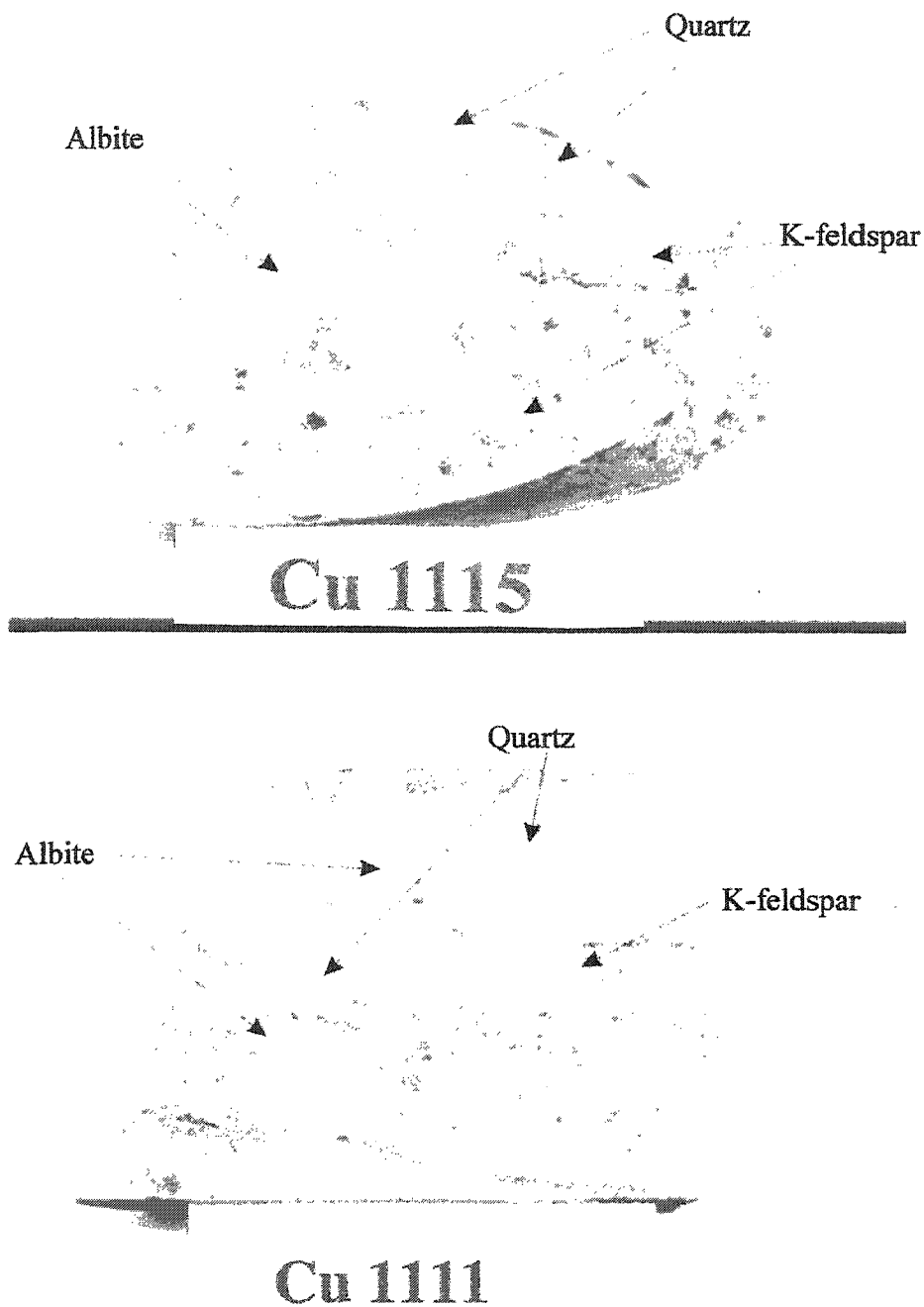


Figure 5.2. Hand specimen showing typical texture in the potassic alteration zone. K-feldspar forms phenocrysts, as well as interstitial groundmass (yellow colour is sodium cobaltinitrite which stains K-rich minerals). White label is 5 cm long for scale.

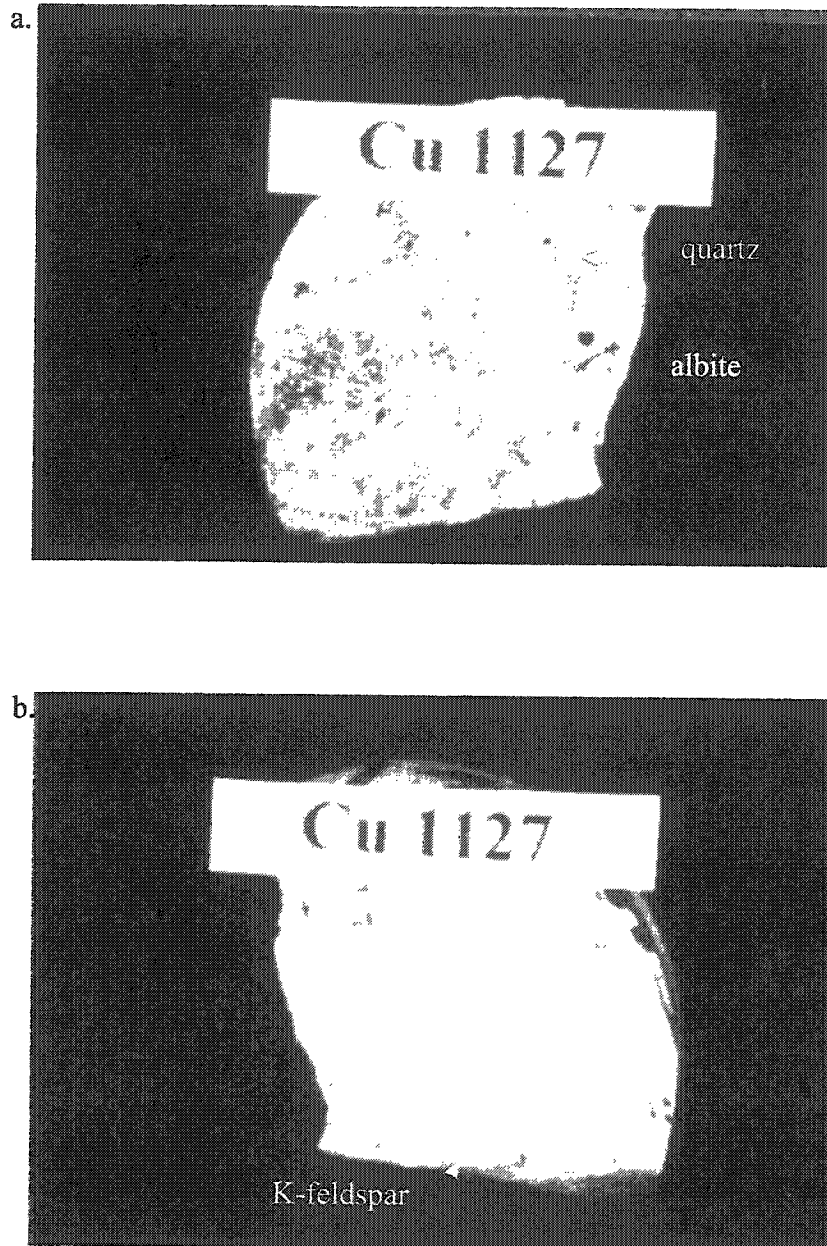


Figure 5.3. Typical K-feldspar megacryst with concentrically zoned albite inclusions (Cu 1127). The white minerals are albite, the grey are quartz. b) Stained using sodium cobaltinitrate which stains the K-bearing minerals yellow. The white labels are 5 cm across.

porphyritic (Figs. 5.2 and 5.3). Euhedral poikilitic potassium feldspar megacrysts are present locally (Fig. 5.3).

5.2.1 Mineralogy

5.2.1.1 Plagioclase

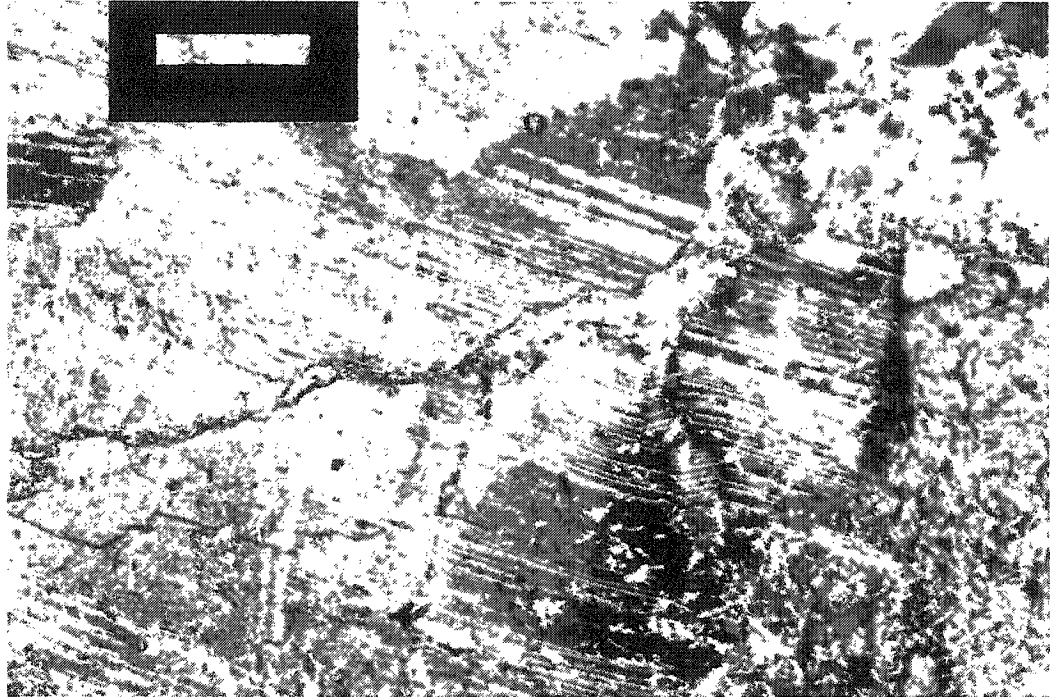
Plagioclase is the most abundant mineral in the potassic alteration zone (Fig. 5.2). In hand specimen, the plagioclase grains appear white and medium-grained (Fig. 5.2). In thin section, the plagioclase is euhedral to subhedral with albite twinning (Fig. 5.4). Intersecting albite and pericline twins are found locally and may be bent, reflecting strain (Fig. 5.4). Patches of K-feldspar are found in plagioclase phenocrysts, forming antiperthite; however, the plagioclase twins are continuous on either side of the patches (Figs. 5.5 and 5.6).

Plagioclase in the potassic alteration zone is sodic ($An_{<6}$). It falls in the albite compositional field (Fig. 5.7) with consistently <1.5 wt.% CaO. Sodic feldspar also occurs as exsolution lamellae in string, braided and flame perthites within host K-feldspar (see Section 5.2.1.4).

5.2.1.2 Biotite

Biotite is present locally in the potassic alteration zone of the Chuquicamata deposit. It is typically pleochroic brown to yellow with a high birefringence and good cleavage (Fig. 5.8). “Shreddy” biotite, with its eroded edges, relict cleavage and high

a. Cu1106 (mag. = 50X, F.O.V = 2 mm, xpl)



b. Cu1109 (mag. = 100X, F.O.V.= 1 mm, xpl)

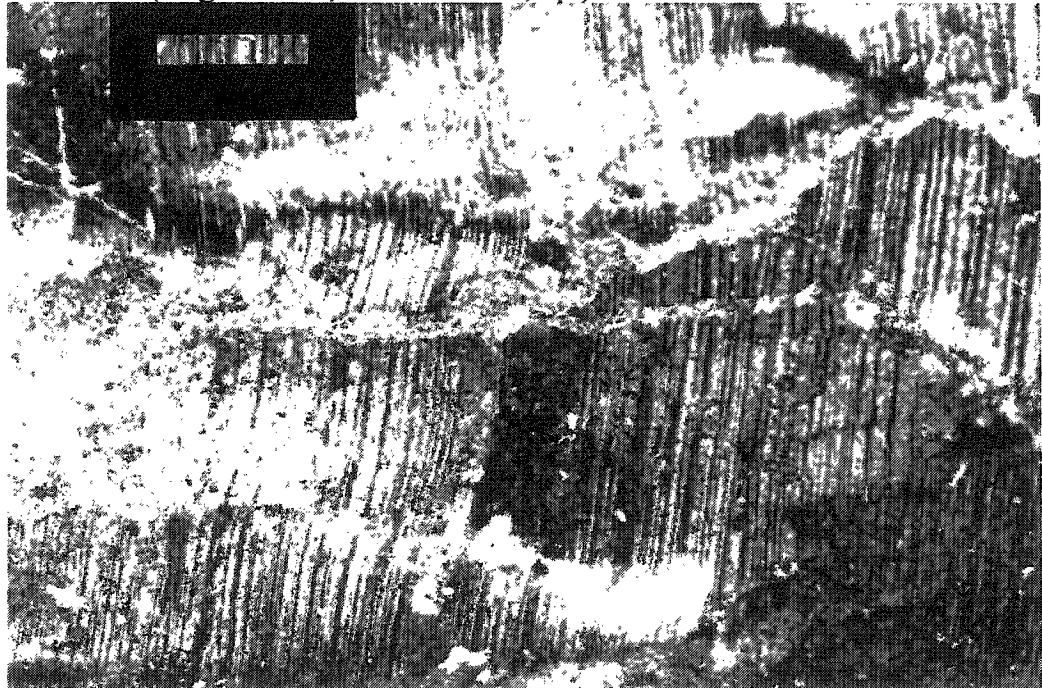
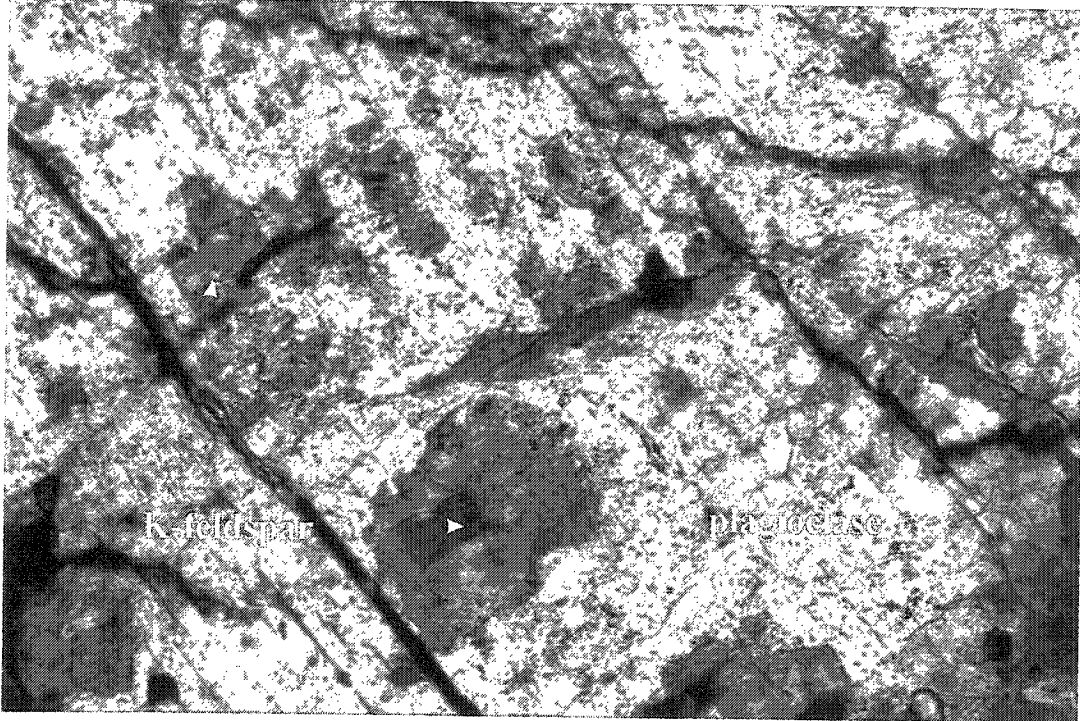


Figure 5.4. Feldspar in the potassic alteration zone. a) Intersecting pericline and albite twins. b) Bent twins. Both samples have been affected by Qser alteration. Note the Qser veins running through both plagioclase grains.



b. Cu 1101 (mag. = 100X, F.O.V.= 1.5 mm, xpl)



Figure 5.5. Antiperthite in the potassic alteration zone. Irregular blebs of K-feldspar occur throughout the large plagioclase grains.

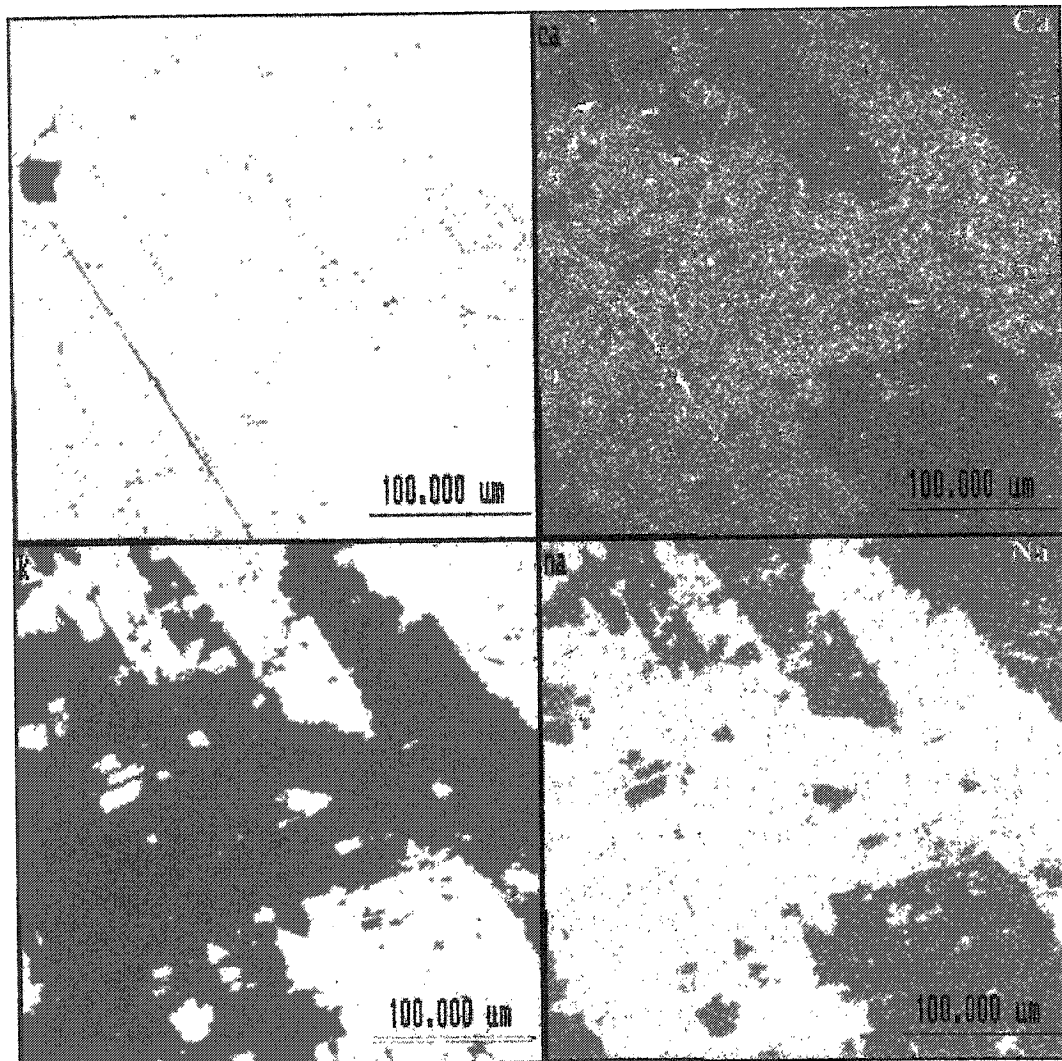


Figure 5.6. Electron microprobe images of antiperthite. Upper left: back scatter image Remaining: elemental X-ray maps measuring Ca, Na and K. The brighter the spot, the more of the element there is present. (Cu 1146)

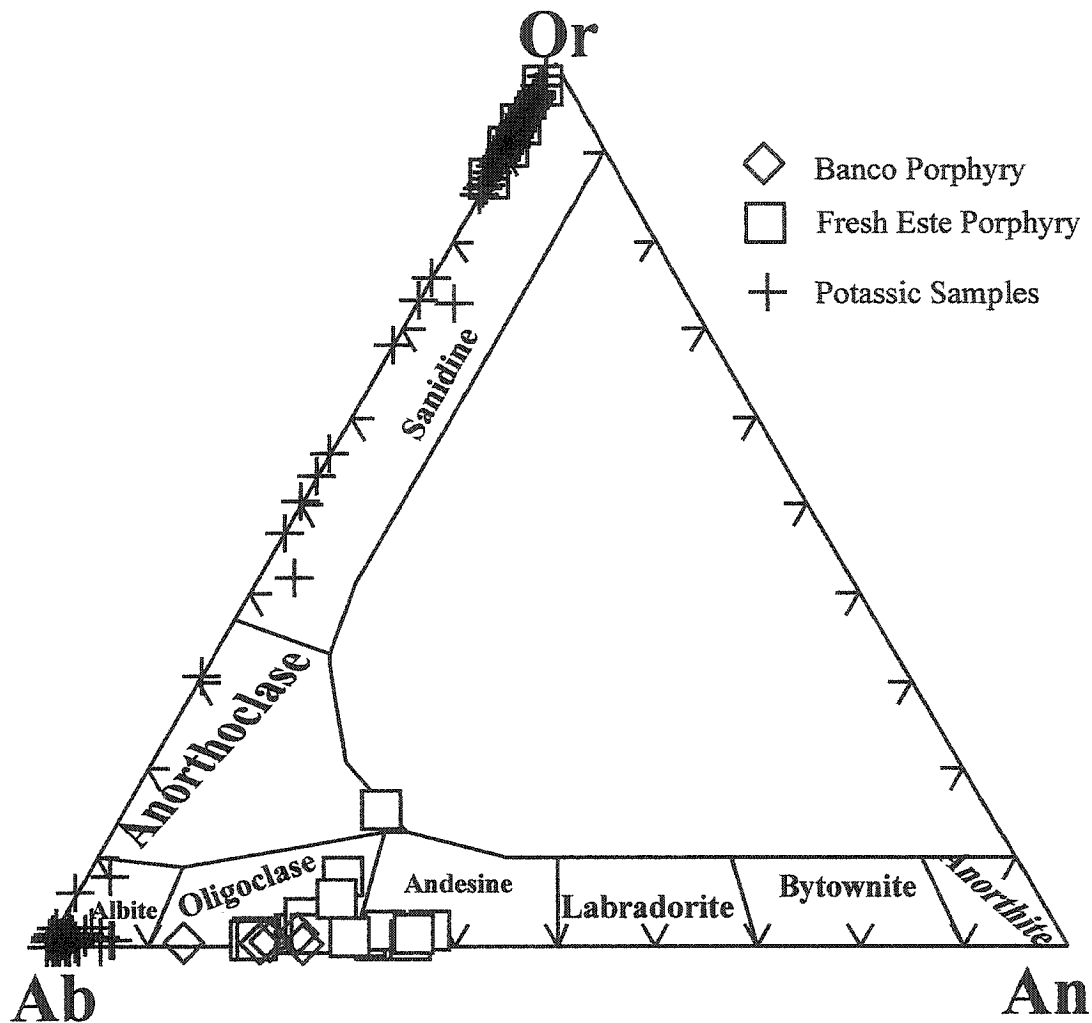
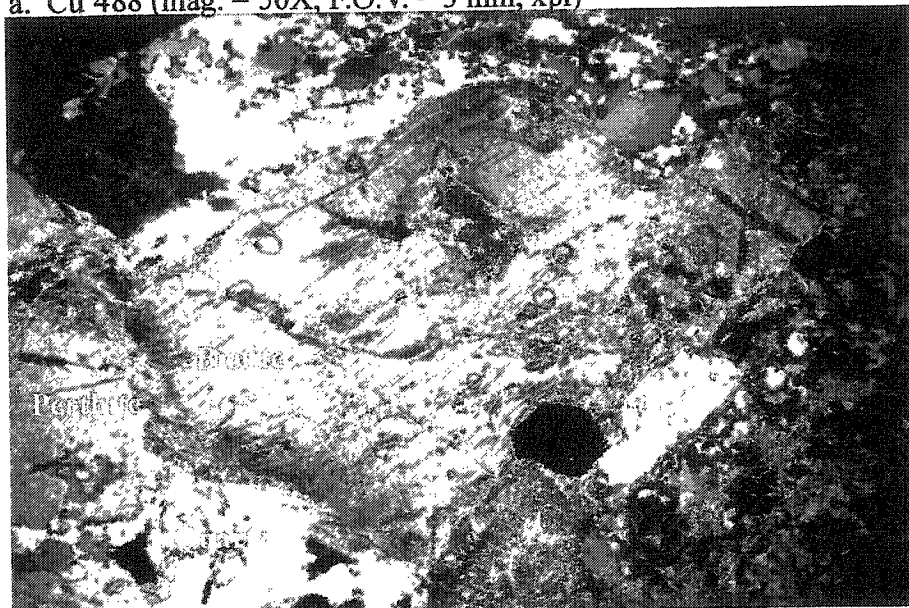


Figure 5.7. Ternary feldspar diagram. All plagioclase in the potassic zone is albitic in composition. This is more sodic than the andesine-oligoclase of the fresh Este Porphyry.

a. Cu 488 (mag. = 50X, F.O.V. = 3 mm, xpl)



b. Cu 494 (mag. = 100X, F.O.V. = 1.5 mm, xpl)

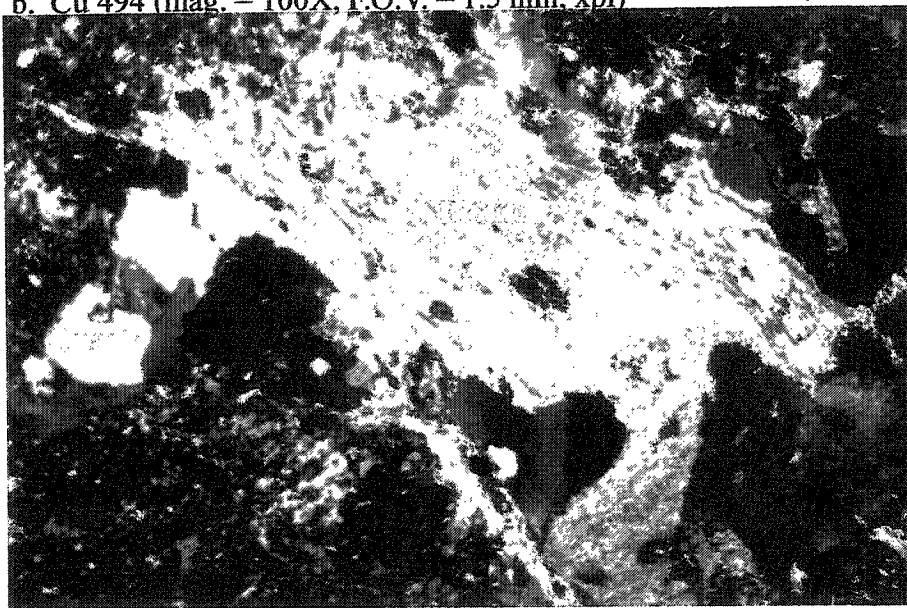


Figure 5.8. Biotite in the potassic zone at Chuquicamata. It is commonly corroded along cleavage and grain boundaries.

birefringence is less abundant. Rare examples of biotite that appear green in plane-polarized light (Cu 1169).

Electron microprobe analyses show that the biotite is Mg-rich. According to the classification of Deer et al. (1992), the biotite has a phlogopitic composition but there are no firm boundaries separating the annite and phlogopite fields (Fig. 5.9). In another classification scheme, the arbitrary ratio of 2:1 for Mg:Fe (Deer et al. 1966) is used to differentiate phlogopite and biotite (Fig. 5.10). In this case, more than half of the samples of biotite analysed are phlogopite *sensu stricto* (Fig 5.10) and those that plot in the biotite range are Mg-rich annite. Biotite-phlogopite in the potassic alteration zone is fluorine-rich (1.63- 6.24 wt%F) (Fig. 5.10).

A plot of Na₂O vs TiO₂ (Fig. 5.11) shows that biotite from the fresh sample plot in the same field as the biotite in the potassic samples, however, the potassic biotite vary more and have typically lower TiO₂ and higher Na₂O than the those in the fresh sample. Rutile is found along cleavage planes and grain boundaries of biotite in the potassic alteration zone (Fig. 5.12).

5.2.1.3 K-feldspar

In hand specimens, anhedral K-feldspar appears to fill mainly the interstices as a late phase (Fig. 5.2). There are also large, euhedral megacrysts of K-feldspar which locally display concentric zones of inclusions (Fig. 5.3). In thin section, the K-feldspar forms medium- to coarse-grained poikilitic grains with inclusions of mainly albite and locally quartz and biotite grains (Fig 5.13).

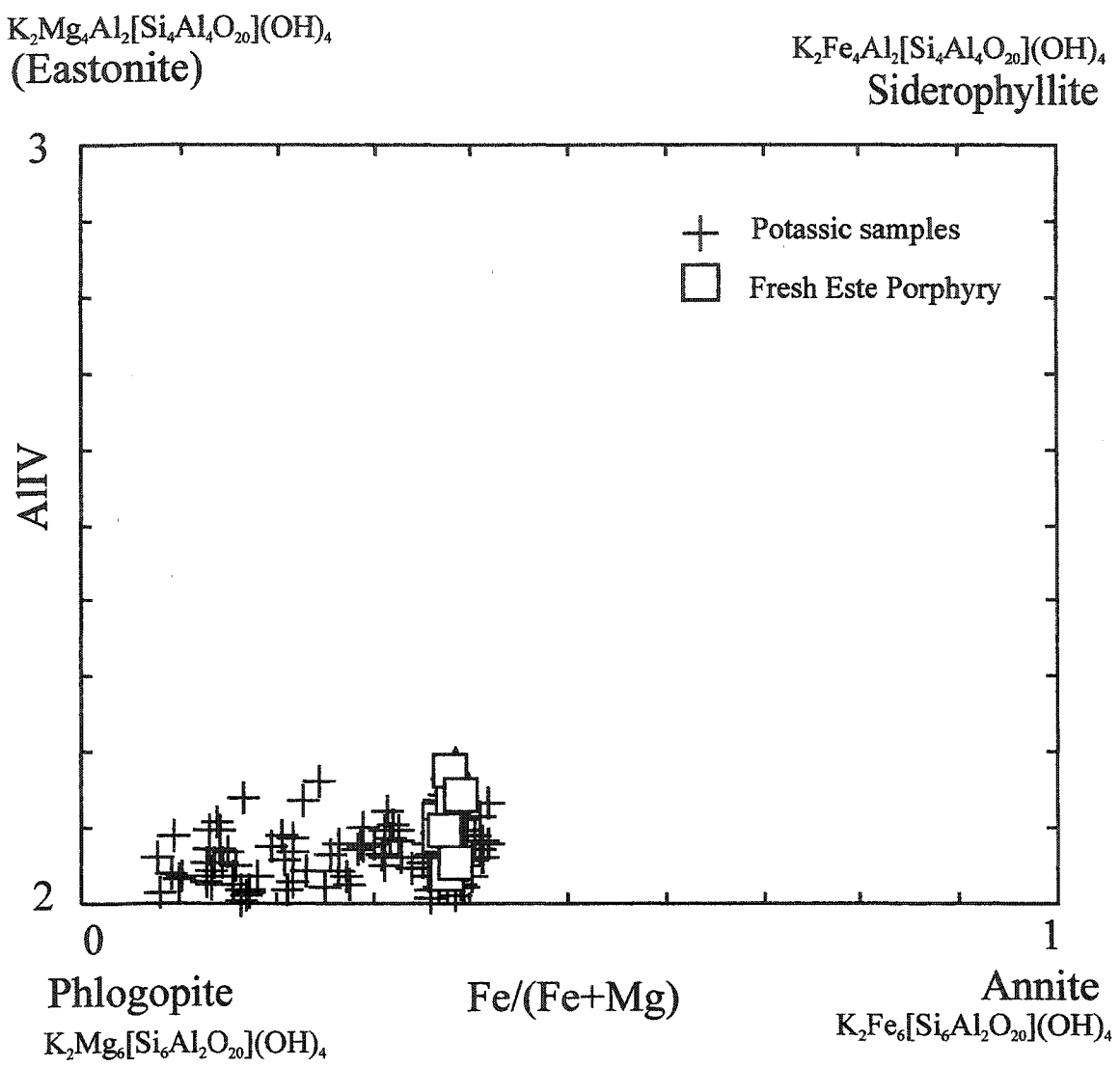


Figure 5.9. Biotites in the fresh and potassic samples are phlogopitic (after Deer et al. 1992).

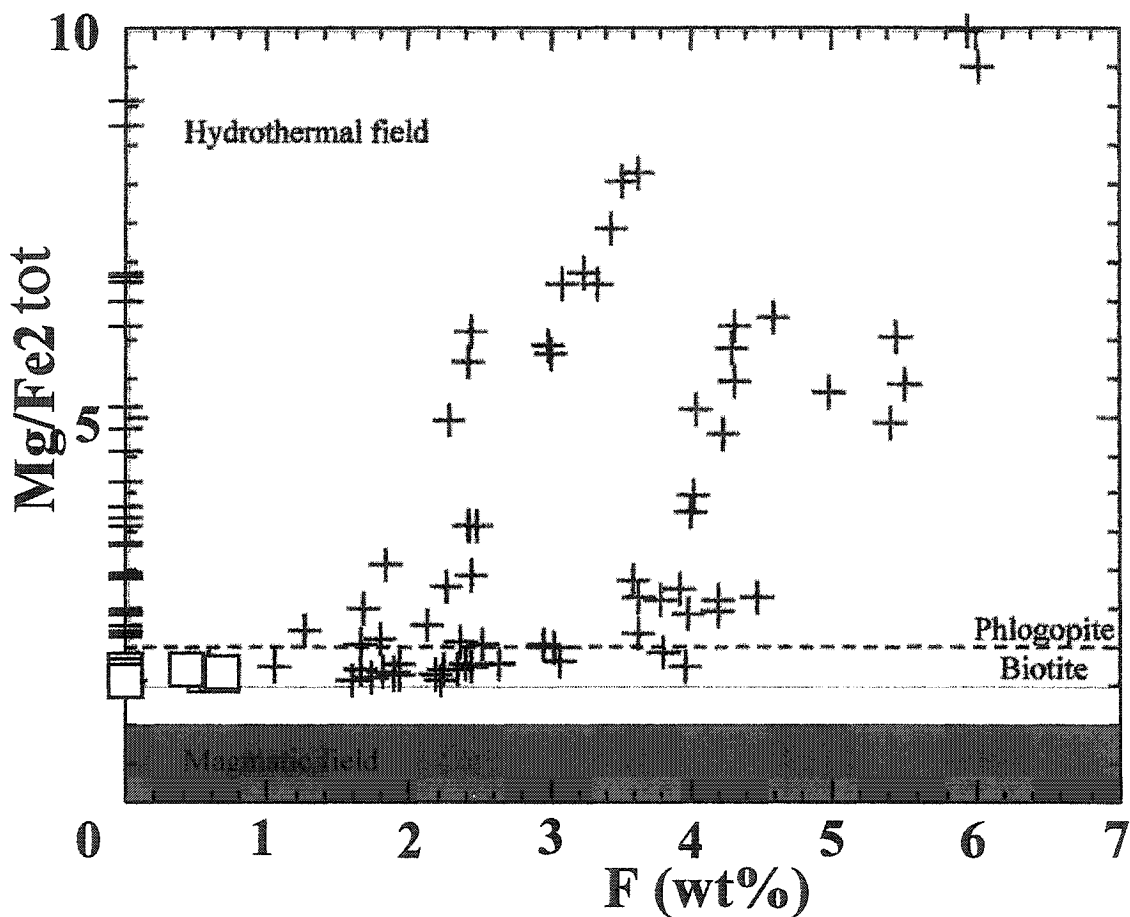


Figure 5.10. Biotite from the potassically altered and fresh Este Porphyry plot in the hydrothermal field. Deer et al. (1966) chose an arbitrary value to define the boundary between biotite ($Mg/Fe < 2$) and phlogopite ($Mg/Fe > 2$). This arbitrary boundary is shown here as a dashed line. Beane (1974) noted that igneous biotite had $Mg/Fe < 1.0$ and altered biotite had $Mg/Fe > 1.5$. These fields are illustrated in red and blue. All biotite in the fresh and altered Este Porphyry plots as alteration biotite and is mainly phlogopitic in composition. Those biotites that appear to have 0% F were not analysed for F and are assumed to have F-contents comparable to those showing a range of values.

- Fresh Este Porphyry
- + Potassic samples

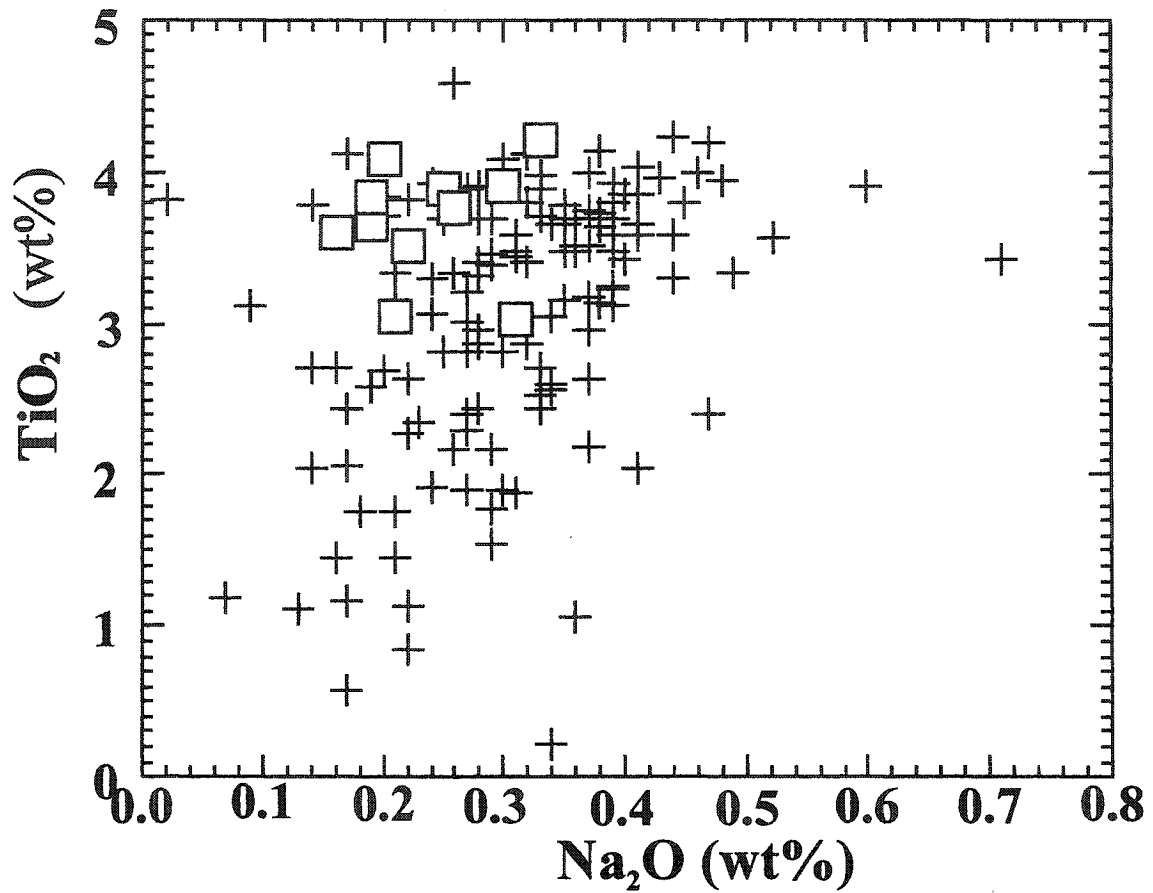


Figure 5.11. Biotite in the 'fresh' Este Porphyry and the potassic alteration zone have < 1 wt% Na₂O. 'Fresh' Este biotite are relatively enriched in TiO₂.

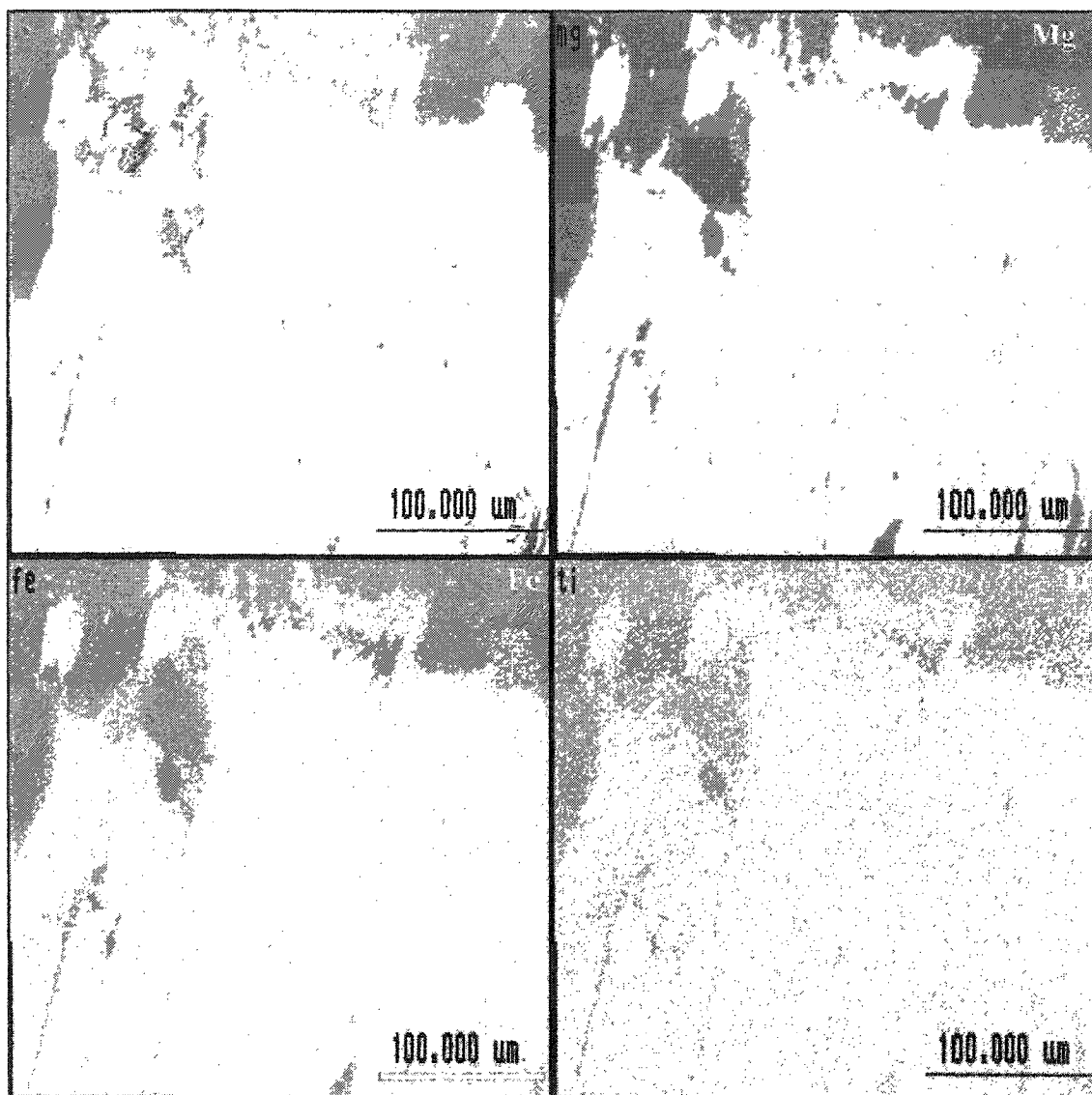
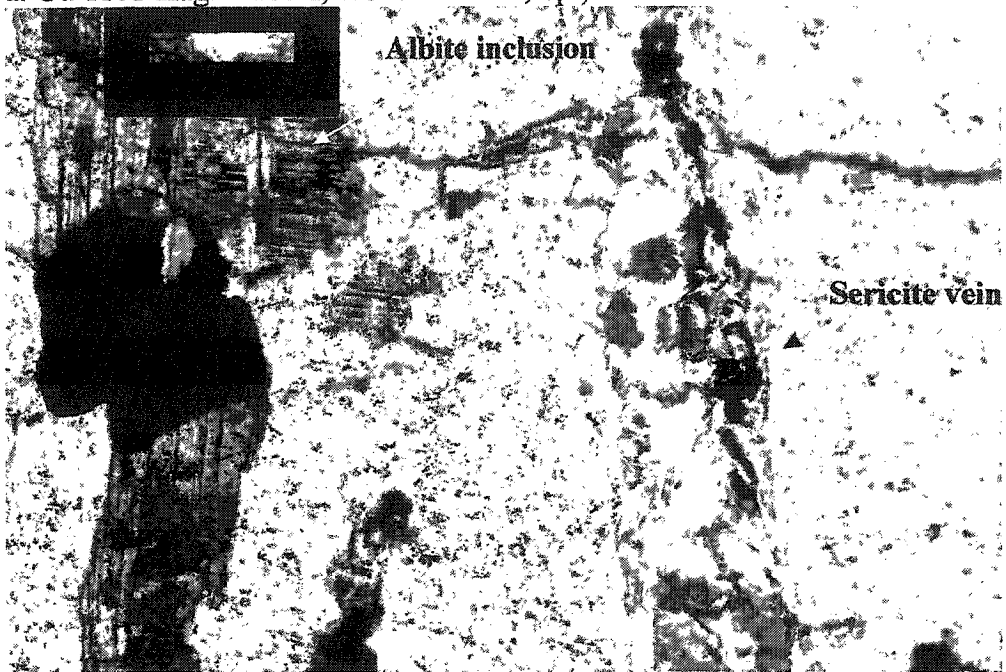


Figure 5.12. Electron microprobe images of biotite from a Qser-overprinted-potassic sample (Cu 1115). Top left: back scatter image. Remaining: elemental X-ray maps measuring Mg, Fe, and Ti. The bright grains in the bottom right image are rutile, forming along the cleavage planes of a biotite that is altering to a more phlogopitic mica .

a. Cu 1101 mag. = 100X, F.O.V. = 1 mm; xpl)



b. Cu 1105 (mag. = 50X, F.O.V. = 2 mm, xpl)

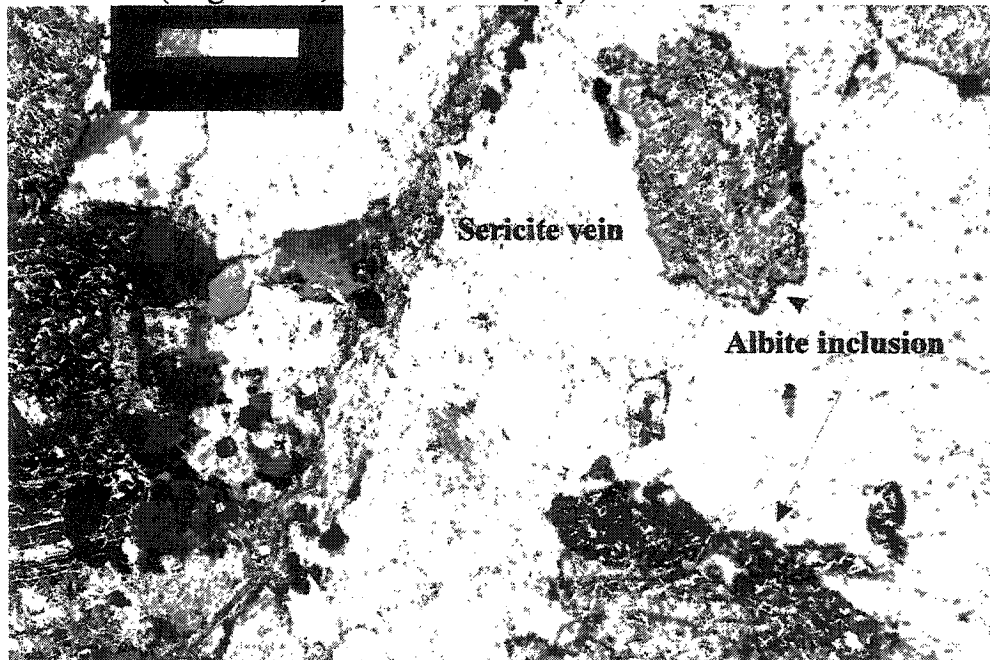


Figure 5.13. K-feldspar in the potassic zone. a) K-feldspar grain with an inclusion of albite, both relatively fresh, cut by a sericite vein. b) K-feldspar phenocryst with inclusions of altered albite.

Most of the K-feldspar is microperthitic. 'String' perthite is the most common form of perthite (Fig. 5.14a). Locally, braided and flame perthites occur in relatively smaller grains and around inclusions and grain boundaries (Fig. 5.14-5.16). The perthitic lamellae are mainly discontinuous throughout the grains (Figs. 5.14 and 5.15).

Locally, K-feldspar grains may exhibit cross-hatch twinning (Fig. 5.14). This twinning is not visible at certain angles of rotation under cross-polarized light. Perthitic lamellae are also apparent in the grains exhibiting cross-hatch twinning (Fig. 5.14). K-feldspar grains exhibit undulose extinction.

The K-feldspar of the potassic alteration zone has Ba contents similar to those of the fresh Este Porphyry (Fig. 5.16). The Ba-enrichment is visible in the backscatter images of K-feldspar, but the zones are not as regular as those in the fresh Este Porphyry (Fig. 5.16).

5.2.1.4 Quartz

Quartz occurs in the potassic alteration zone as polycrystalline lenses up to one centimetre in length (5.2). In hand specimen, quartz appears grey, irregular, and locally elongate (Fig. 5.2). Quartz has been ubiquitously recrystallized in the potassic alteration zone (Fig. 5.17). It invariably displays an undulose extinction (Fig. 5.17) and locally, quartz has been ribbonized.

a. Cu 1112 (mag. = 100X, F.O.V. = 1 mm, xpl)



b. Cu 1112 (mag. = 200X, F.O.V. = 0.5 mm; xpl)

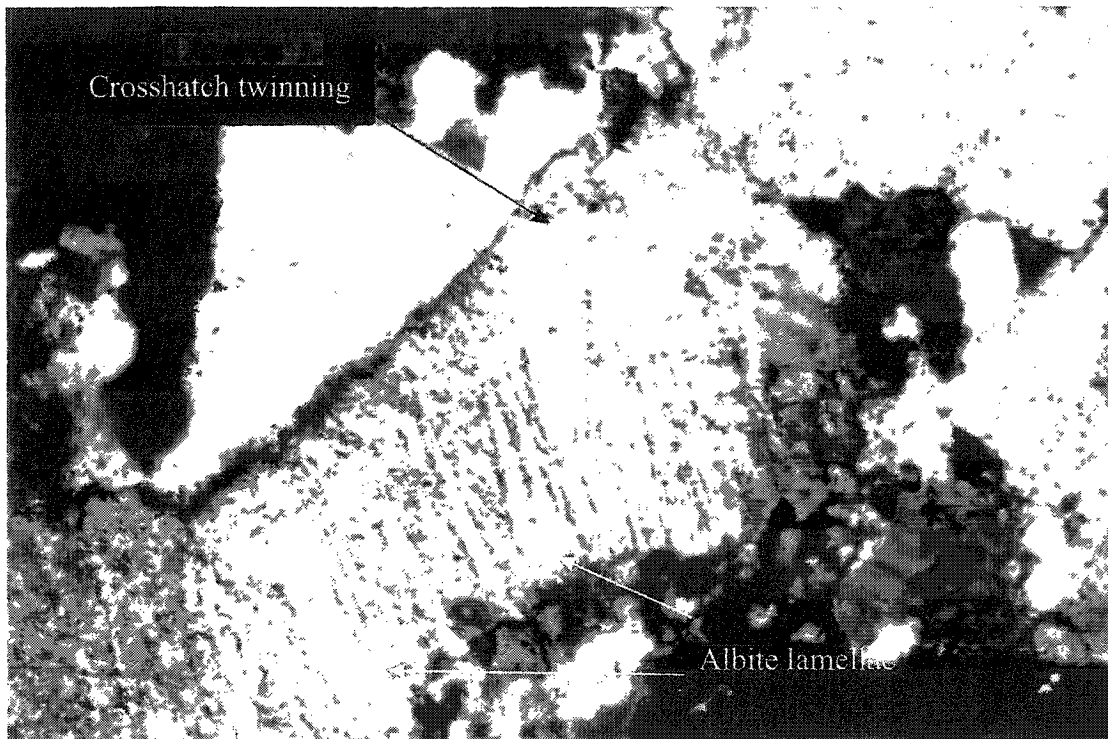
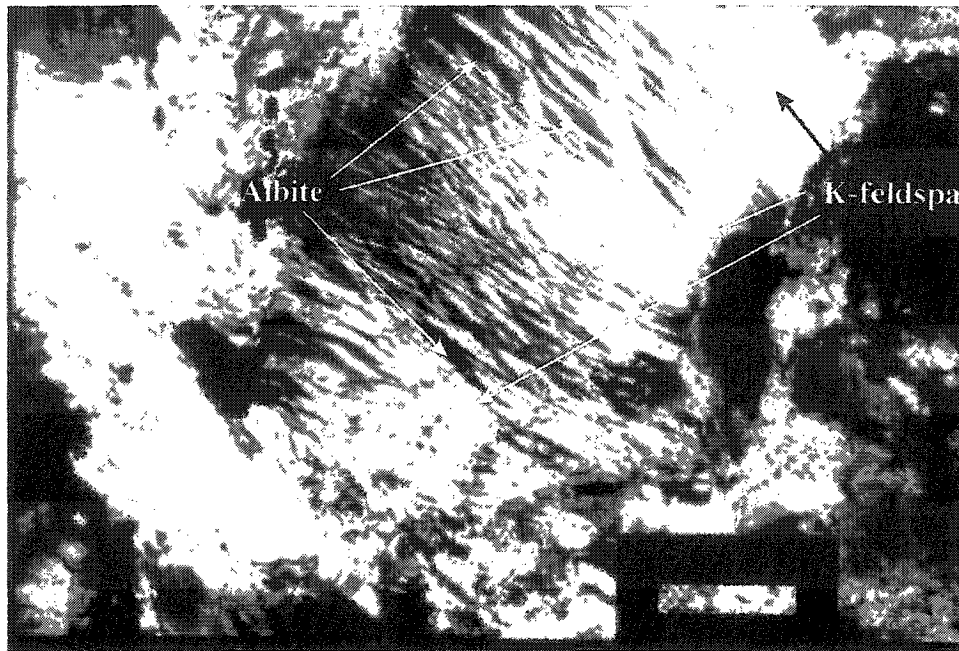


Figure 5.14. Photomicrographs of perthite in the potassic zone (Cu 1112). a) String perthite with cross-hatch twinning. b) Flame perthite with faint cross-hatch twinning.

a. Cu1114 (mag. = 200X, F.O.V. = 0.5 mm, xpl)



b. Cu1141 (mag.= 200X, F.O.V. = 0.5 mm, xpl)

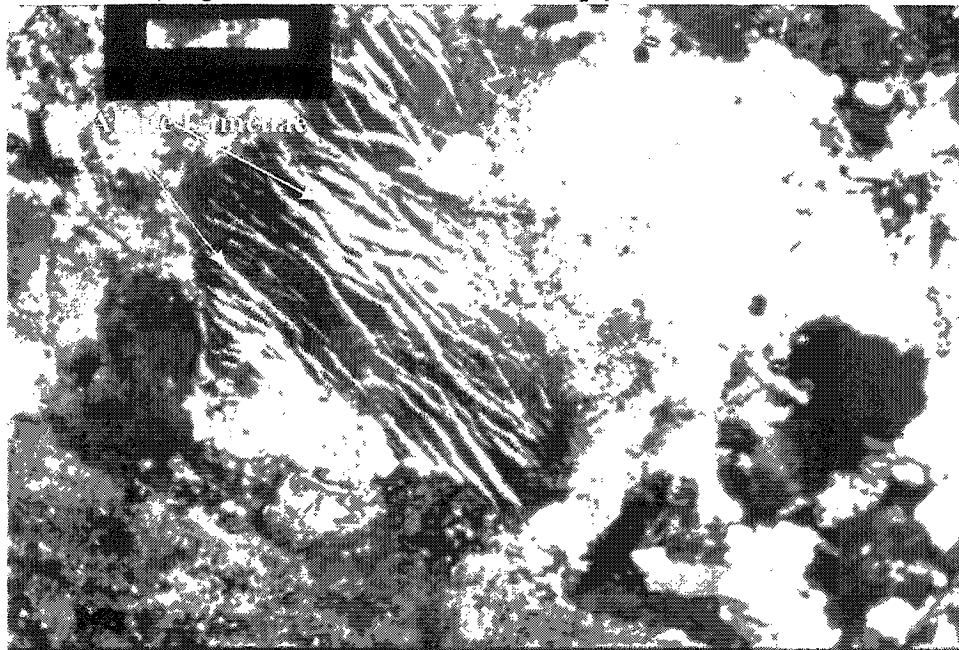


Figure 5.15. Braided perthite grains in the potassic zone. They are finer-grained than string perthite grains. a) K-feldspar is pale grey with dark ribbons of albite b) K-feldspar hosts the braided lamellae.

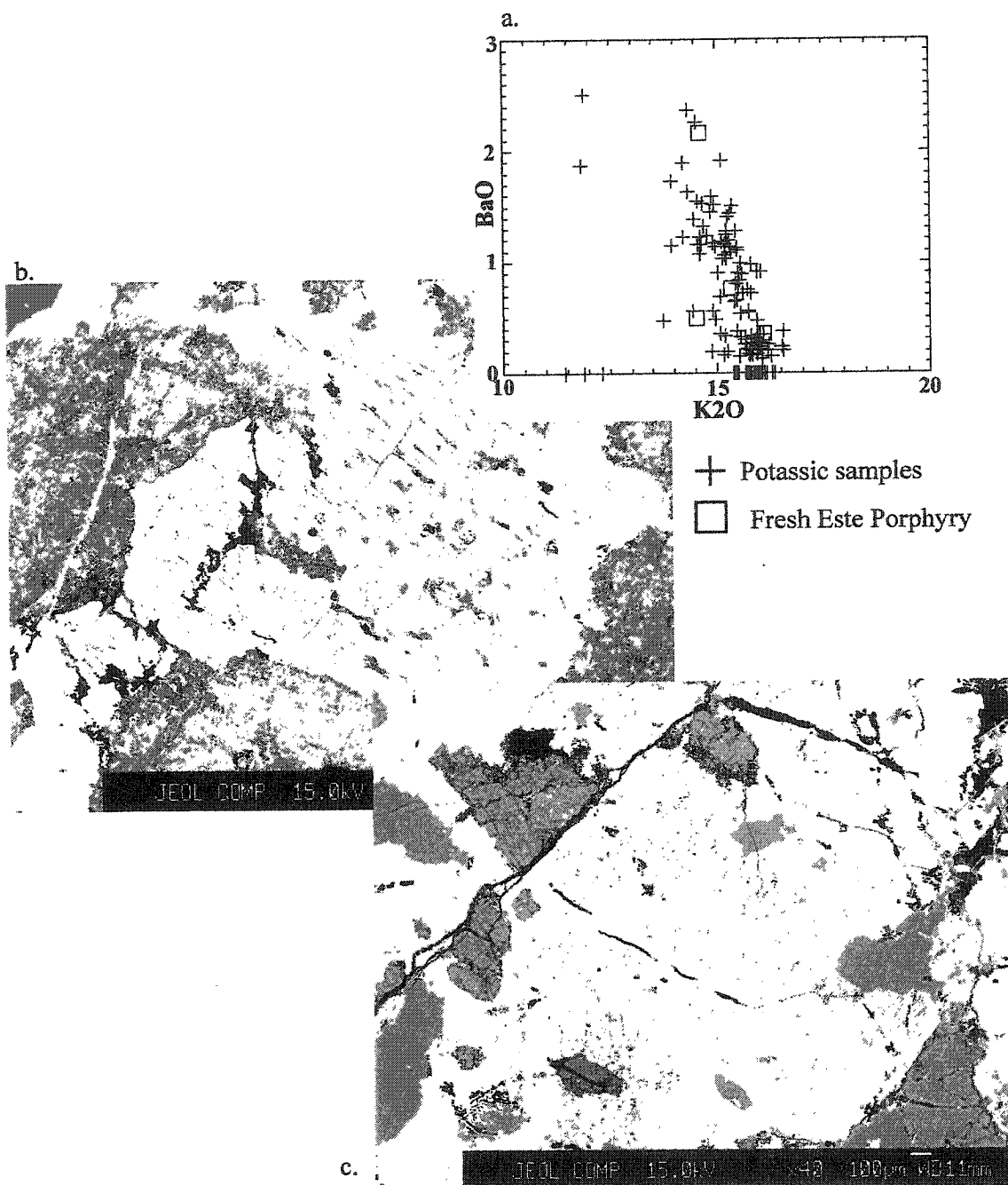
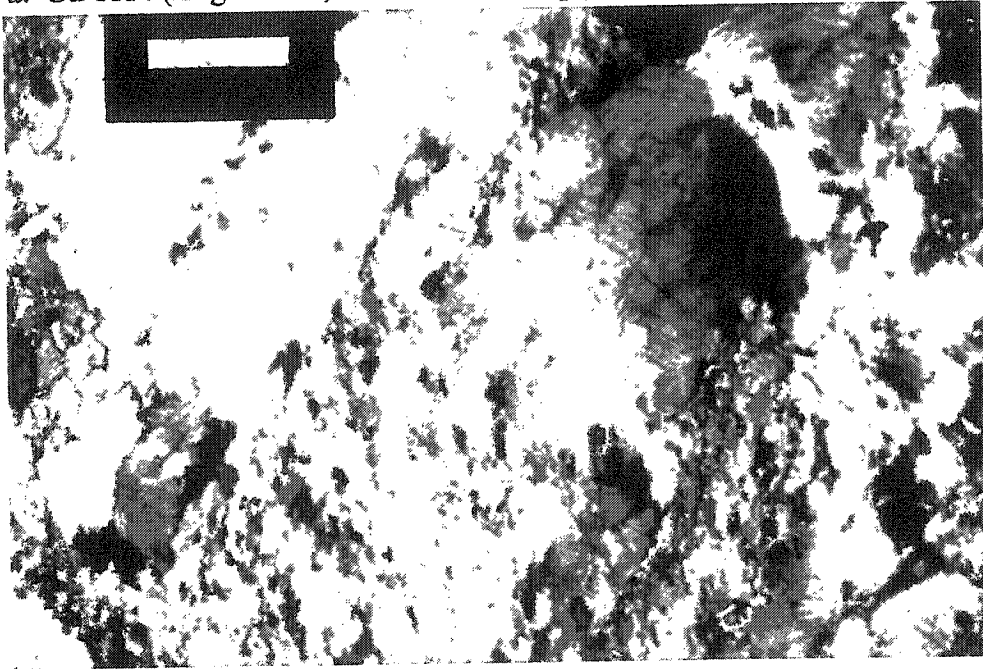


Figure 5.16. a) A wide variation in the BaO content of the K-feldspar of the potassic zone. This variation is similar to that of the Fresh Este Porphyry, however, the potassic samples lack the magmatic zonation. b and c) Backscatter images of K-feldspar. Lighter areas are Ba-enriched.

a. Cu 1114 (mag. = 50X, F.O.V. = 2 mm, xpl)



b. Cu1127 (mag. = 50X, F.O.V. = 2 mm, xpl)

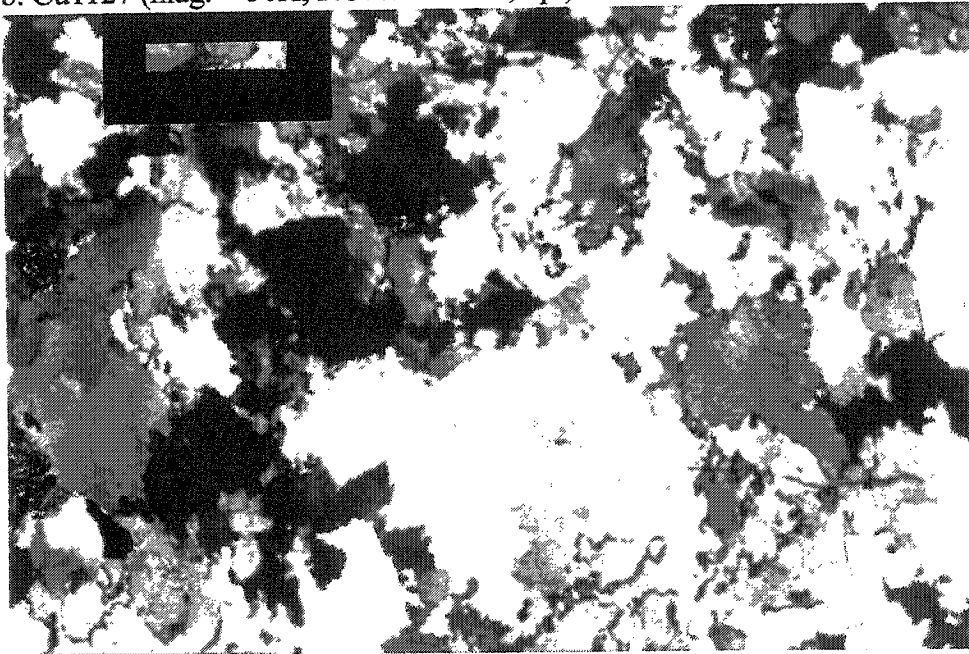


Figure 5.17. Quartz in the potassic zone. It has been extensively recrystallized. Undulose extinction in quartz is present throughout the potassic alteration zone.

5.2.1.5 Chlorite

Chlorite occurs locally in the potassic alteration zone along crystal faces and cleavage planes of biotite.

5.2.1.6 Ti-minerals

Titanite has not been observed in the samples of the potassic alteration zone. Instead, rutile is common in this zone and occurs as needles, sometimes pseudomorphing a diamond-shaped mineral (Fig. 5.18). Rutile is associated with biotite, as irregular grains along grain boundaries and cleavage planes (Fig. 5.12 and 5.18).

Rutile in the potassic alteration zone may have significant amounts of Fe, Nd, Nb, La, V, Sb, and locally, Ce and Zn (Fig 5.19). However, some rutile grains within this zone do not appear to be enriched in any of these elements (Fig 5.19). Grains with and without trace-element enrichments may occur in the same sample. CaO values are consistently <0.1 wt.%.

5.2.1.7 Accessory minerals

Fluoro-apatite is commonly associated with phlogopite in the potassic alteration zone. Apatite is generally euhedral and consistently F-rich with minor Cl. Zircon is also present as an accessory mineral in the potassic alteration zone. Magnetite and pyrite were identified in the potassic assemblage.

In this study, sulphate minerals were not observed with the potassic alteration assemblages; however, anhydrite veins associated with Qser alteration were observed

a. Cu 442 (mag. = 100X, F.O.V. = 1.5 mm, ppl)



b. Cu 1112 (mag. = 50X, F.O.V. = 3 mm, ppl)

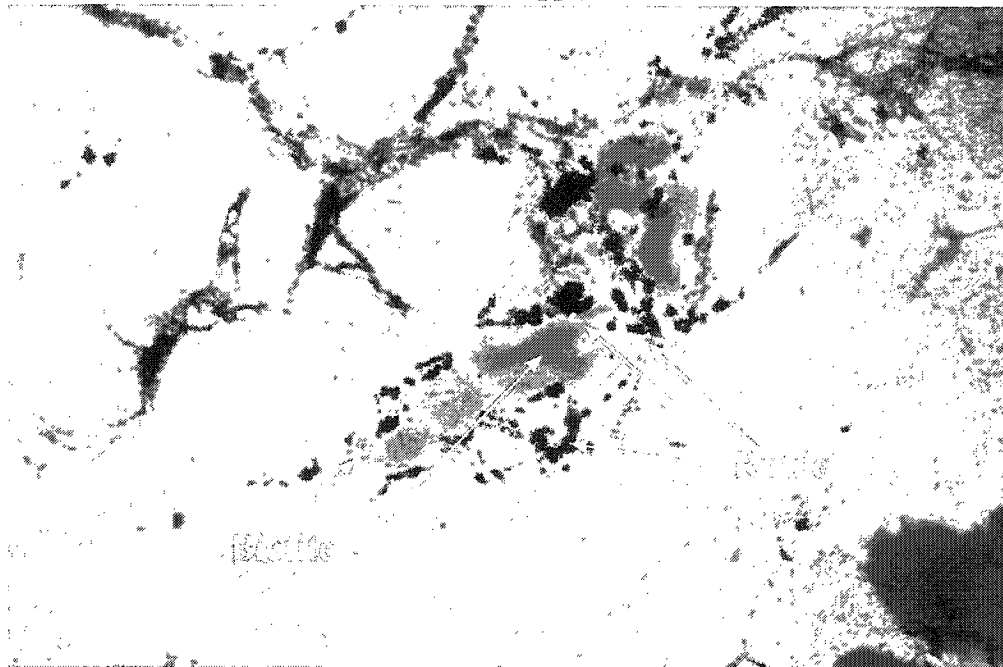


Figure 5.18. Rutile in the potassic zone. a) Rutile pseudomorphs primary titanite. b) Rutile along grain and cleavage boundaries of biotite.

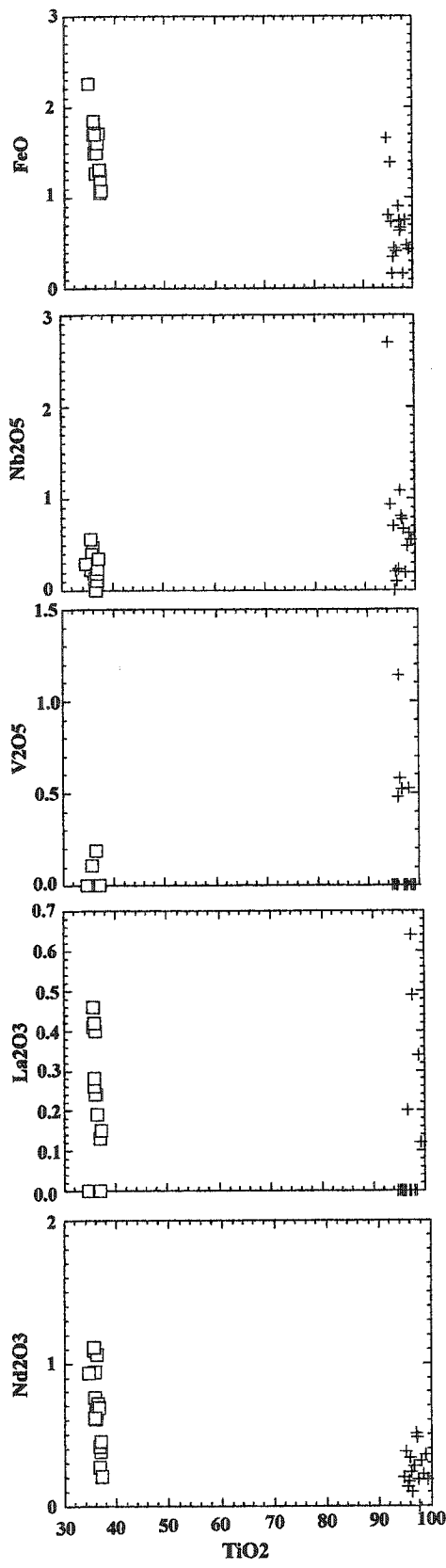


Figure 5.19. Variations in trace-element geochemistry of rutile in the potassic alteration zone compared to the titanite of the fresh Este Porphyry.

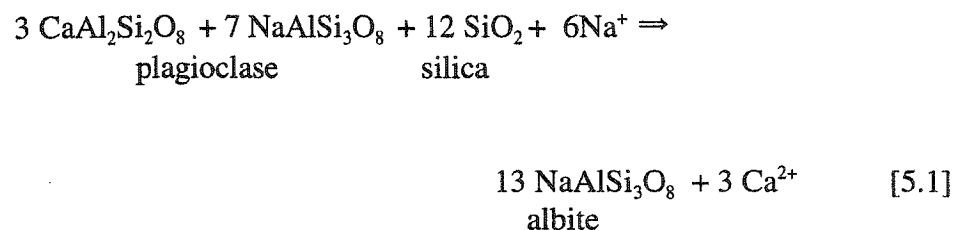
□ titanite in the Este Porphyry
+ rutile in the Potassic alteration zone

cross-cutting the potassic assemblages. Anhydrite was reported in the potassic alteration zone by Ossandón et al. (2001), but the author suspects that all the anhydrite in the potassic alteration zone is in Qser veins (see below).

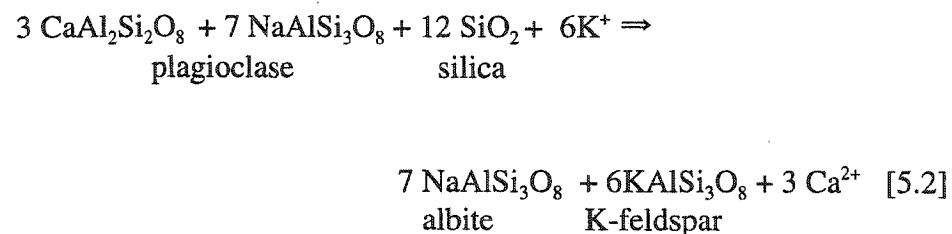
5.2.2 Interpretation

At first glance, the fresh and potassically altered Este Porphyry appear similar. Upon closer examination, the author has determined that they are most easily distinguished by their plagioclase compositions.

Plagioclase is as abundant in the fresh Este Porphyry as it is in the potassic alteration zone, indicating that there was a one-to-one volumetric replacement of andesine-oligoclase by albite,

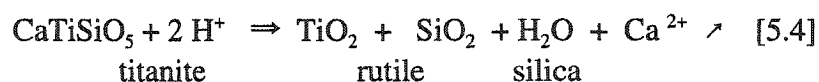


Some of the plagioclase has patches of K-feldspar forming antiperthites which are interpreted to have been the result of replacement of andesine-oligoclase by K-feldspar and albite,



twinning, the perthitic texture, and euhedral inclusions of albite. The coarseness of the perthitic lamellae indicates that there was a deuteritic fluid (Section 2.7.2.4; Smith and Brown 1988). Also, the inconsistent Ba distribution that is observed locally in the K-feldspars indicates there was remobilization of Ba following crystallization.

Rutile needles after titanite occur as diamond-shaped aggregates:



The presence of magnetite in the potassic alteration zone indicates that the environment was initially oxidizing. The presence of pyrite is attributed to the sulphidation of magnetite during the subsequent Qser overprint (Chapter 6).

Anhydrite in the potassic alteration zone at Chuquicamata, was observed only in veins, which are interpreted to belong to the same generation of veins as those that cut the Qser zone. Some authors report to have found anhydrite in the groundmass of the potassic alteration zone at Chuquicamata (Ossandón et al. 2001). It is possible that anhydrite was precipitated in the magmatic environment, as anhydrite is insoluble at high temperatures; however, anhydrite is highly soluble at lower temperatures and in high salinity fluids (Blount and Dickson 1969, 1973). The potassic Este Porphyry is a medium-grained granodiorite with megacrysts, an indication that it cooled relatively slowly. Therefore, even if the anhydrite had crystallized at high (e.g. magmatic) temperatures, the potassically altered rocks would have had to cool through the range of temperatures at which anhydrite is highly soluble. Although it is possible that the Ca^{2+} (liberated by the destruction of Ca-silicates during potassic alteration) precipitated as Ca-

sulphate, it is more likely that deposition occurred later and at higher crustal levels and lower pressures. In other porphyry copper deposits, where the groundmass is finer and subvolcanic (i.e. with rapid cooling), anhydrite could conceivably have been preserved in the potassic alteration zone (e.g. Meyer and Hemley 1967, Lowell and Guilbert 1970).

5.3 The Banco Porphyry

The 'fresh' Banco Porphyry described in Chapter 4 was intruded as dykes into the potassically altered Este Porphyry (Fig. 4.3). The Banco Porphyry samples have oligoclase (Fig. 4.7). The lack of albite, which is essential to the definition of the potassic alteration zone in the Este Porphyry, indicates that the Banco Porphyry was not affected by the potassic alteration.

5.4 Geochemistry

The potassic alteration zone is mainly overprinted by the Qser and/or cut by Qser veins. Therefore, a careful petrographic study, combined with electron microprobe analyses, was conducted before selecting a sample that represented the "most" potassic assemblage and the "least" affected by Qser. Sample Cu 1112 was selected as the best potassic sample because the plagioclase grains have only a dusting of sericite and the biotite and K-feldspar grains have been unaffected by the Qser alteration.

5.4.1 Whole-rock geochemistry

To determine the effect of the altering fluid on the geochemistry of the potassic alteration zone, the whole-rock geochemistry of the fresh Este Porphyry was compared to that of the potassic alteration zone (normalized to 100%, LOI-free) (Fig. 5.20). The raw data are reported in Appendix E.

SiO₂ values for the fresh and potassic samples are similar (70.2 and 70.64 wt.%, respectively) (Fig. 5.20); TiO₂ is identical in the two samples (0.32 wt.%) (Fig. 5.20). The potassic sample has slightly less Al₂O₃ than the fresh sample ($\Delta_{\text{Al}_2\text{O}_3}=1.14$ wt.%). There is a significant decrease in the Fe₂O_{3 total} (> 3x) and the MgO (1.5x) values in the potassic alteration zone (Fig. 5.20). MnO values are low in both the fresh and the potassic alteration zone (0.04 and 0.01 wt.%, respectively). CaO is depleted by a factor of nearly 10 in the potassic alteration zone (Fig. 5.20). Na₂O is higher in the potassic alteration zone (1.67 wt.%) (Fig. 5.20). K₂O in the potassic alteration zone is enriched by 2.37 wt.% (Fig. 5.20). P₂O₅ is nearly halved in the potassic alteration zone relative to the fresh sample (Fig. 5.20).

The density difference between the potassic and fresh rock is negligible (Appendix E). The equal abundance of plagioclase from the fresh to the potassic samples supports a 1 to 1 volumetric substitution.

5.4.2 Trace and rare-earth element geochemistries

The trace element correlation diagram compares the abundance of elements in the fresh and potassic samples (Fig. 5.21). The line for $r=1$ indicates a constant value. If the

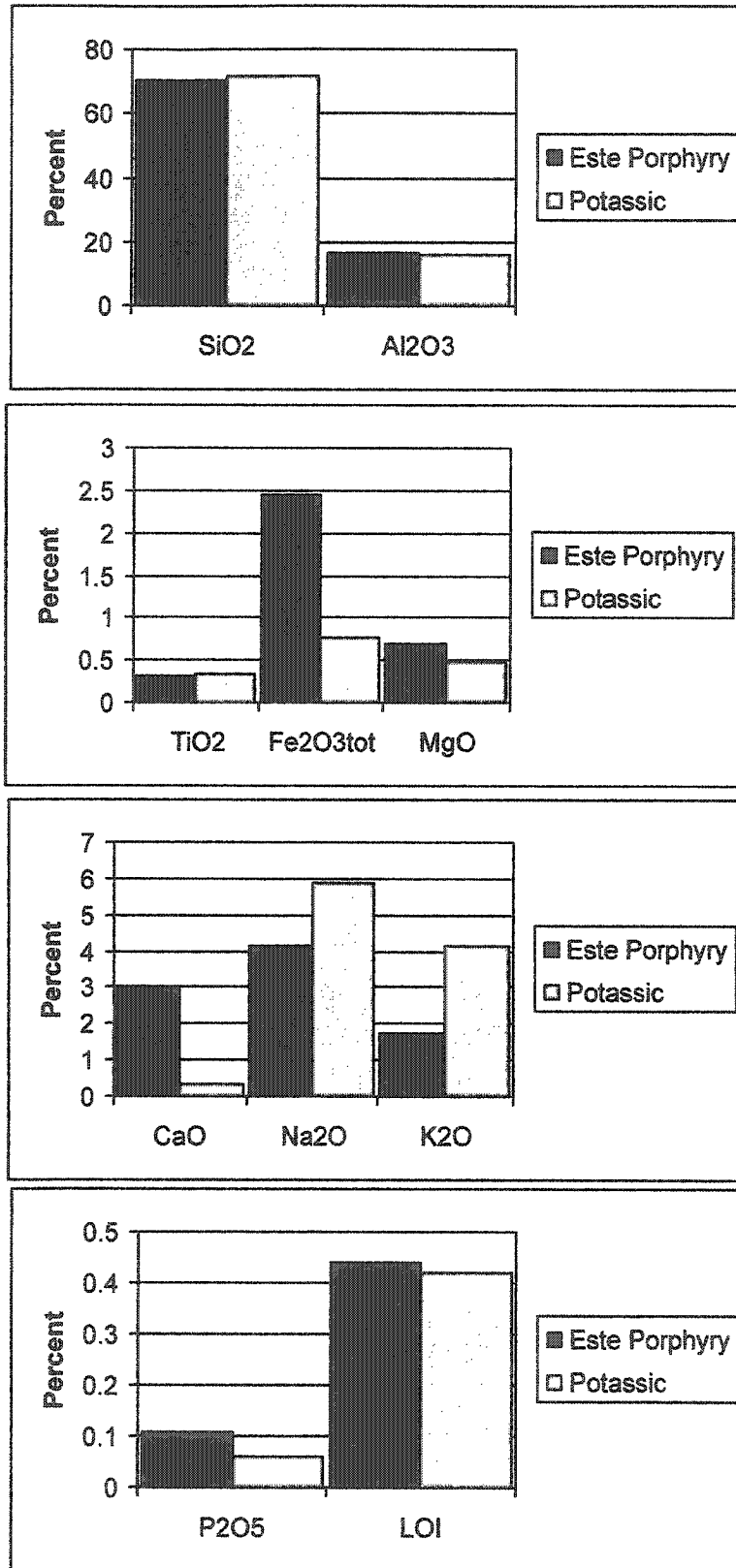


Figure 5.20. Whole-rock geochemistries of the fresh and potassic Este Porphyry. Geochemical changes from the 'fresh' Este Porphyry to the potassic alteration zone are reflected in the mineralogy.

sample plots above the line, then the potassically altered sample is enriched in that element and, if it plots below, the altered sample is depleted relative to the fresh sample (Fig. 5.21). Barium and Sr are significantly depleted (440 ppm and 551 ppm, respectively) in the potassic samples relative to the fresh Este Porphyry (Fig. 5.21).

The *fresh* Este Porphyry (125 ppm) is only 17 ppm more enriched in Zr than the sample from the potassic alteration zone (108 ppm), indicating the Zr is relatively immobile during potassic alteration event. Also, there is little change in the Rb values with alteration. However, the Nb or Y values in the potassic alteration zone are enriched relative to the fresh Este Porphyry ($\Delta_{\text{Nb}} = 11$ ppm; $\Delta_{\text{Y}} = 5$ ppm)(Fig. 5.21). Although the difference in values are not great, the potassic alteration zone has a ~60% increase in Nb and a ~40% increase in Y relative to the fresh Este Porphyry.

The rare-earth element pattern in the potassic alteration zone is similar in shape to that of the fresh Este Porphyry (Fig. 5.22). The values are slightly depressed, but the relative trend remains the same. The steep slope of the LREEs indicates a strongly differentiated magma (Fig. 5.22). The HREEs have values close to the detection limit, making the resulting trend questionable. The Eu-value in the potassic alteration zone is depressed compared to the Banco and Este porphyries, but there is no distinctly negative Eu-anomaly (Fig. 5.22).

5.4.3 Interpretation

Silica, TiO_2 , Al_2O_3 and Zr appear to have been relatively immobile (Fig. 5.20 and 5.21). This immobility supports the hypothesis that Ti-bearing minerals were altered to

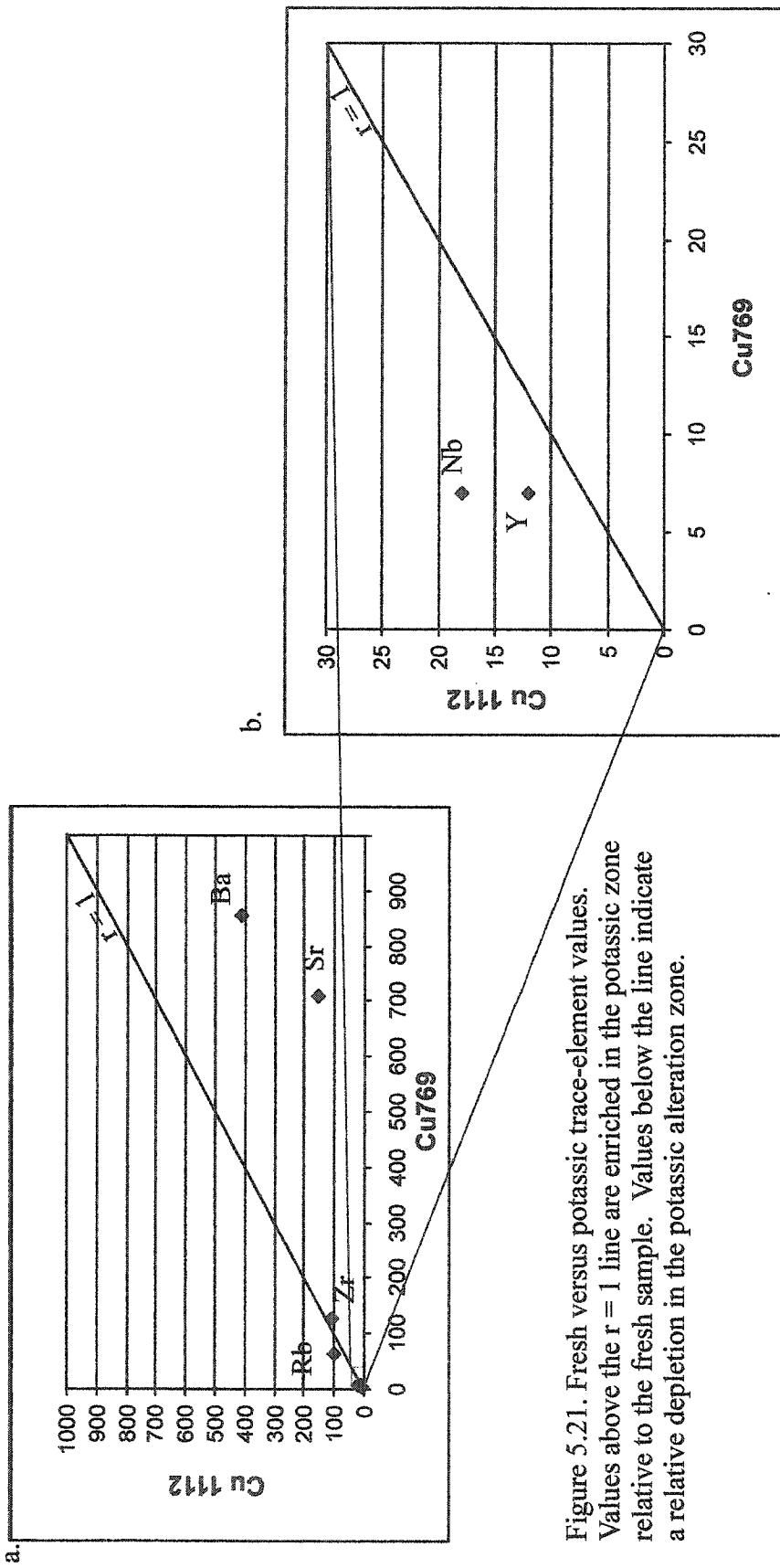


Figure 5.21. Fresh versus potassic trace-element values. Values above the $r = 1$ line are enriched in the potassic zone relative to the fresh sample. Values below the line indicate a relative depletion in the potassic alteration zone.

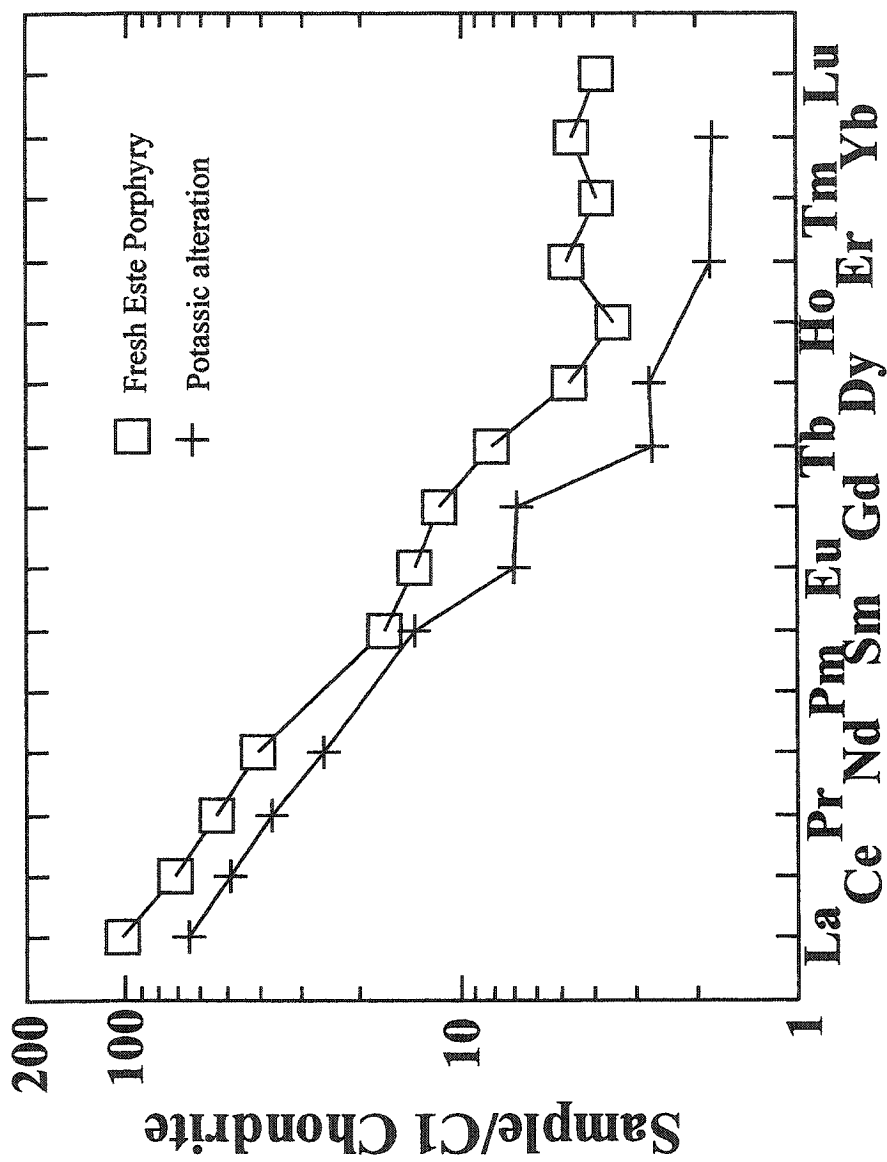


Figure 5.22. Rare earth elements in the potassic alteration zone relative to the fresh Este Porphyry.

other Ti-bearing minerals. The Ti-immobility is seen in the pseudomorphing of titanite by rutile (equation [5.4]) and the formation of rutile along the cleavage planes of biotite as Ti^{4+} is expelled from the biotite structure (Figs. 5.12 and 5.18). The most aluminous minerals (e.g. the feldspars) have had their volumes and alumina contents preserved, even if their compositions changed (equations [5.1] and [5.2]).

The depletion in Fe_2O_3 total, MnO, and MgO reflects the destruction of amphibole and titanite and of less abundant biotite. Further, the depletion of Fe_2O_3 total is due to the conversion of more Fe-rich igneous biotite to Mg-rich hydrothermal biotite (Fig. 5.11).

The large depletion of CaO reflects the destruction of all Ca-silicate minerals found in the fresh rock (i.e. andesine-oligoclase, titanite, and amphibole). The replacement of these minerals by sodic and potassic minerals results in an increase in the Na_2O and K_2O contents.

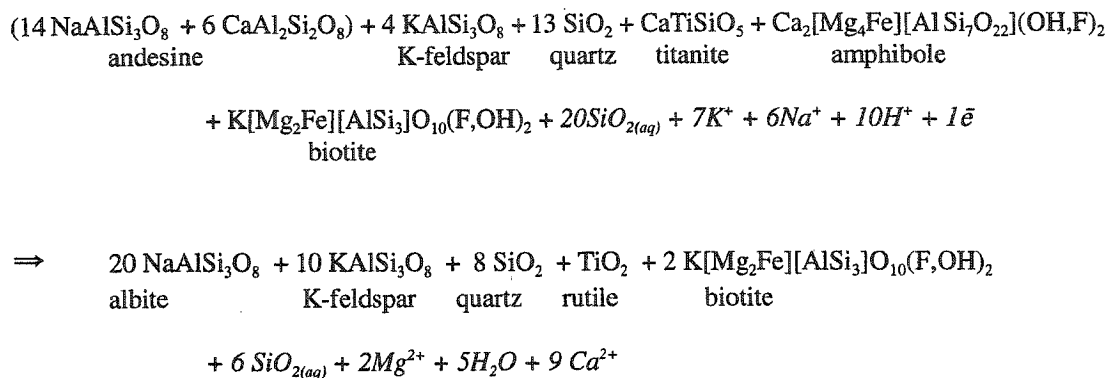
The enrichment of Na_2O and K_2O is the result of K^+ and Na^+ added to the system by chloride-rich melt and/or deuteritic fluids. The silicate melt and/or hydrous fluid deposited K-feldspar and albite after andesine-oligoclase and abundant megacrystic perthitic K-feldspar. Slow cooling allowed more time for K-feldspar megacrysts to crystallize from the last melt.

The depletion of Ba may reflect a lower abundance of mafic minerals such as biotite and amphibole which can accommodate Ba in their structures. Also, the deuteritic fluid interpreted to have caused the coarsening of perthitic lamellae and remobilized Ba in K-feldspar may have also removed Ba from K-feldspar locally. The relatively unchanged LOI indicates there was little hydrolysis during this alteration event.

The depletion of Sr coincides with the depletion of Ca for which Sr substitutes. The relative increase of Nb in the potassic alteration zone is reflected in the increase of Nb in the potassic rutile compared to the fresh titanite (Fig. 5.19.). The increase in Y in the potassic alteration zone is more problematic, as Y is measured in the titanite of the fresh sample but not detected in the rutile. This relative enrichment may be the result of sample bias.

The relative depletion of LREEs in the potassic alteration zone may be the result of the destruction of mafic minerals. Lanthanum, Ce, Nd, Sm, and Gd partition strongly into biotite and hornblende. The depletion of europium may be the result of destruction of calcic end-member plagioclase, hornblende and biotite which accommodate Eu in their structures (Rollinson 1993).

Based on whole rock geochemistry, CIPW norms were calculated for the fresh Este Porphyry and the potassic alteration zone (Appendix E). The ratio of quartz : K-feldspar : plagioclase was calculated and the plagioclase value was determined to be invariable from the fresh to potassic samples. Plagioclase was assigned a value of 20, and quartz and K-feldspar values were calculated based on the calculated ratios. Minor mineral phases were assigned a value of 1, although these values don't necessarily reflect their relative abundances.



Species in italics represent those elements assumed to have been taken into solution (i.e. mobile elements). A more detailed explanation of the calculations used for determining this equation is found in Appendix E.

5.5 Geochronology and timing

Argon ages determined during this study and published by Reynolds et al. (1998) are reported in Chapter 3 (Table 3.4). Reynolds et al. (1998) determined the age of the potassic event was $\sim 33.4 \pm 0.3$ Ma based on the ages of samples Cu 406, Cu 408, Cu 514 and Cu 769 (Table 3.3; Table 3.4). Sample Cu 769 is a sample of fresh Este Porphyry and Cu 514 is representative of the Banco Porphyry and so were removed from this mean. A recalculated mean yields a potassic K-feldspar age of 33.7 ± 0.1 Ma. This age is the same as that of fresh Este Porphyry, within the calculated error (33.4 ± 0.4 Ma; K-feldspar argon age). These similar ages indicate that the K-feldspar in the fresh Este Porphyry samples was either reset by the potassic event or the potassic alteration is the same age as the intrusion of porphyry.

The recalculated mean of biotite ages from the potassic alteration zone (removing Este and Banco Porphyry ages) is 34.0 ± 0.7 Ma. This is the same age as the biotite from the Este Porphyry (33.9 ± 0.3 Ma).

The Banco Porphyry (33.1 ± 0.2 Ma) is significantly younger than the mean age of K-feldspar in the potassic alteration zone (33.7 ± 0.1 Ma). The younger age of the Banco Porphyry is consistent with the mineralogical evidence that the Banco Porphyry was unaffected by the potassic alteration (Section 5.3).

5.6 Stable isotopes

Mineral separates from the potassic alteration zone were analyzed for oxygen and hydrogen isotopes. K-feldspar, quartz, and biotite were separated from three samples (Cu 442, Cu 494, and Cu 1115). These samples were selected based on three criteria:

- a) the minerals analyzed were free from Qser alteration,
- b) there was sufficient biotite in the sample (biotite is relatively rare in the potassic alteration zone), and
- c) there was sufficient sample to separate adequately quantities of minerals for analysis.

K-feldspar was separated from a fourth sample (Cu 1105). $\delta^{18}\text{O}$ values are based on the SMOW standard.

5.6.1 Oxygen isotopes

The tendency of minerals to concentrate ^{18}O varies from quartz (the highest) to K-feldspar to biotite (lowest) (O'Neil 1986). The absolute values of $\delta^{18}\text{O}$ of igneous rocks and their minerals are determined by several factors:

- 1) the temperature of crystallization;
- 2) the $\delta^{18}\text{O}$ of magma;
- 3) the effects of fractional crystallization;
- 4) the retrograde effects resulting from reequilibration at subsolidus temperatures;
and
- 5) the interaction with aqueous fluids (O'Neil 1986).

Taylor (1968) suggested that the $\delta^{18}\text{O}$ values of igneous plutons may be changed after crystallization by interaction with meteoric water and by exchange with magmatic water derived from the parent magma.

5.6.1.1 Data from the potassic alteration zone

The quartz in these samples have a narrow $\delta^{18}\text{O}$ range of 10.4 to 11.1 ‰ (Fig. 5.23). Biotite values range from 6.6 to 7.9 ‰ (Fig. 5.23). K-feldspar $\delta^{18}\text{O}$ values have the widest range from 8.9 to 11.0 ‰ (Fig. 5.23). One K-feldspar sample (Cu 1105) with $\delta^{18}\text{O}$ value = 11.0 ‰ represents a megacrystic grain.

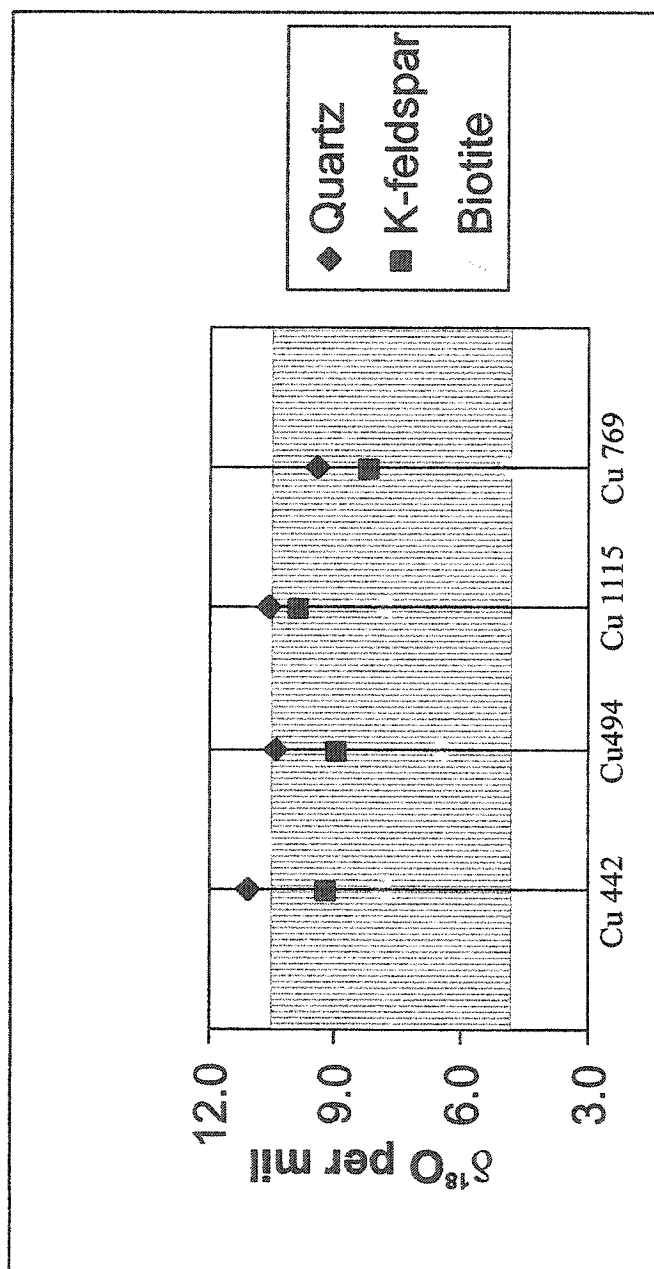


Figure 5.23. Measured $\delta^{18}\text{O}$ values from the potassic and fresh Este Porphyry (Cu 769). There are no reversals in the measured $\delta^{18}\text{O}$ values. All values plot in the magmatic range (shown as shading) except the quartz of Cu 442 (Taylor 1968, Sheppard 1969).

5.6.1.2 Isotopic Equilibrium

The isotopic contents of the three minerals fall in the predicted order, supporting the idea that these minerals reached isotopic equilibrium (Fig. 5.23). According to Taylor (1968), $\delta^{18}\text{O}$ of quartz in all plutonic rocks normally falls within the range +8.5 to +10.6 ‰. Sample Cu 442 is the only sample not to fulfil this particular criterion.

There is a significant variation in the $\Delta_{\text{quartz-K-feldspar}}$. The typical magmatic range is 1.3 to 1.8 (O'Neil 1986). Samples Cu 442 and Cu 494 give values of 1.9 and 1.5, respectively, which are close to or within this range. However, sample Cu 1115, has a much lower $\Delta_{\text{quartz-K-feldspar}}$ value (0.8), perhaps indicating a lack of equilibrium in this sample. This low $\Delta_{\text{quartz-K-feldspar}}$ value may indicate reequilibration.

Mineralogically, cloudiness in alkali feldspars, and veins filled with quartz, alkali feldspar, or sulphide minerals suggests later fluid-rock interaction that may have re-equilibrated ^{18}O isotope values in igneous intrusions (Taylor et al. 1971). These mineralogical characteristics are all present in the potassic alteration zone, indicating that O-isotopic data should be applied with caution in this zone.

Concordance of isotopic thermometers is also a good test of isotopic equilibrium. If three or more mineral pairs give concordant temperatures, they should be in equilibrium. The problem with this test is that if one of the minerals is not in equilibrium, then two of the three pairs give poor estimates of temperature. The results of isotopic thermometry are discussed in Section 5.6.1.3.

In biotite, replacement of OH^- by F^- is an important factor. This factor is important because the hydroxyl site ^{18}O values can be much different from silicate ^{18}O

values (Taylor 1967, Zheng 1993b). The hydroxyl oxygen is held in the structure by weaker bonds than silicate-oxygen and may have a relatively lower ^{18}O value (Zheng 1993b). This variation may affect biotite-quartz and biotite-K-feldspar temperature calculations. This affect on temperature calcualteions is of concern in the potassic alteration zone because the F-contents are so high in the biotites (Fig. 5.10).

5.6.1.3 Temperature of equilibration

The temperatures of isotopic equilibrium were determined using the equation $\{1000 \ln \alpha^1_2 \approx \delta_1 - \delta_2 = A(10^6 T^{-2}) + B\}$ for measured $\delta^{18}\text{O}$ mineral pairs. The calculated temperatures span a wide range (Table 5.2; Fig. 5.24).

The widest range (445 to 926°C) of temperatures occurs in sample Cu 442. The biotite-K-feldspar temperatures are unreasonably high for this system and the quartz $\delta^{18}\text{O}$ value is outside the magmatic range. These wide range in temperatures indicate that the three minerals were not in isotopic equilibrium and, therefore, these temperatures are unreliable.

Sample Cu 1115 has the narrowest range of values which would seem to support isotopic equilibrium; however, the temperatures (771 to 833°C) are too high for a pluton which has undergone slow cooling. The temperatures are considered unreliable as they are obviously the result of subsolidus effects. The high temperatures combined with the anomalously low $\Delta_{\text{quartz-K-feldspar}}$ indicate that this samples has been re-equilibrated.

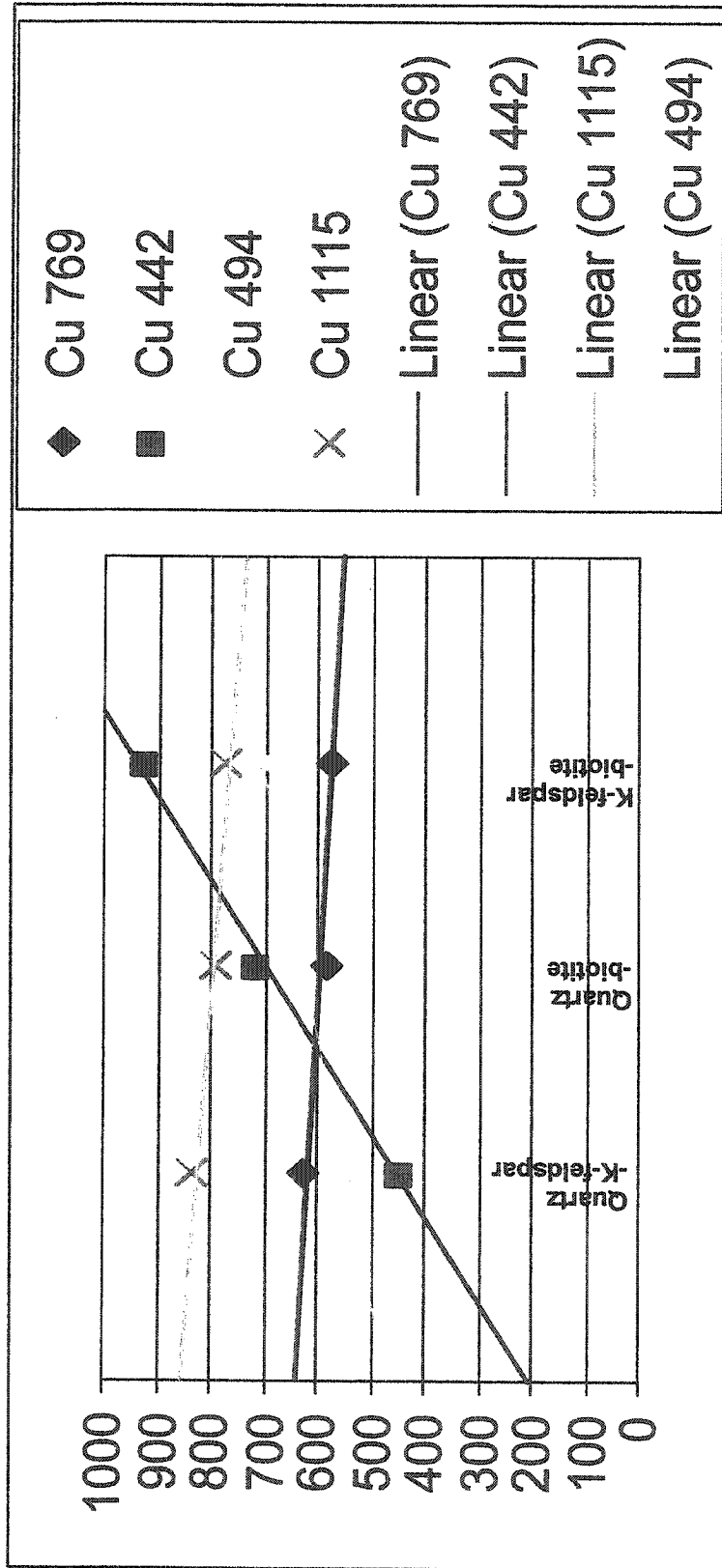


Figure 5.24. Oxygen-isotope thermometry. The temperature ranges for the fresh Este Porphyry (Cu 769) are the best constrained. Although sample Cu 1115 has a narrow range of temperatures, it is evident these temperatures are too high for a slowly cooled pluton. Sample Cu 494 has a wider range of temperatures but the quartz-K-feldspar temperature is within the accepted age for potassic alteration. Biotite less reliably attains isotopic equilibrium, particularly in F-rich, slowly cooled varieties and therefore, in the potassic samples, these temperatures are disregarded. Sample Cu 442 has obviously not achieved isotopic equilibrium.

Table 5.1 Measured $\delta^{18}\text{O}$ isotopes from the potassic zone.

Sample #	Mineral	$\delta^{18}\text{O}$ (‰)
Cu 442	quartz	11.1
	k-feldspar	9.2
	biotite	7.9
Cu 494	quartz	10.4
	k-feldspar	8.9
	biotite	6.6
Cu 1115	quartz	10.6
	k-feldspar	9.8
	biotite	7.9
Cu 1105	k-feldspar	11.0

Table 5.2 Temperatures calculated based on $\delta^{18}\text{O}$. Calculations are based on the experimental work of Bottinga and Javoy (1973, 1975).

Sample	Qtz-Kspar	Kspar-Bt	Qtz-Bt
Cu 442	445°C	926°C	716°C
Cu 494	535°C	697°C	646°C
Cu 1115	833°C	771°C	788°C

Sample Cu 494, which has the only $\Delta_{\text{quartz-K-feldspar}}$ value in the magmatic range, gives a wide range of values (535 to 697°C) which suggests disequilibrium. However, the quartz-K-feldspar temperature is within the range of potassic alteration (Table 2.3) and this temperature may represent the temperature of isotopic equilibration. The calculated biotite temperatures may have been affected by the F substitution in the hydroxyl site as mentioned in Section 5.6.1.2.

5.6.1.4 Isotopic composition of fluids

Sulphide phase equilibria calculated by Lewis (1997) gave an estimated temperature of 400 to 600°C for the mineralization temperature. To calculate the ^{18}O values of the fluids, a temperature of 550°C is assumed. This temperature was chosen to represent a more slowly cooled version of the fresh Este Porphyry which was calculated to have equilibrated at ~600°C (Table 4.5). It is also close to the calculated temperature for the quartz-K-feldspar pair of sample Cu 494 (535°C), which may represent a subsolidus isotopic equilibrium temperature.

Using the constants of Bottinga and Javoy (1973, 1975), and based on a temperature of 550°C, the oxygen isotope ratio was calculated for the fluid in equilibrium with the minerals using the equation:

$$1000 \ln \alpha^1_2 \approx \delta_1 - \delta_2 \approx A(10^6 T^{-2}) + B.$$

The calculated $\delta^{18}\text{O}$ values mainly plot within the range of the magmatic waters (Fig. 5.25).

5.6.1.5 Interpretation

The potassic samples are enriched in $\delta^{18}\text{O}$ relative to their fresh magmatic counterparts (Fig. 5.23). The range of $\delta^{18}\text{O}$ in magmatic minerals is +5.5 to +10.0‰ (Sheppard et al. 1969) but, according to Taylor (1968), $\delta^{18}\text{O}$ of quartz in all plutonic rocks should fall within the range, +8.5 to +10.6 ‰. Quartz in sample Cu 442 is higher than this range as is the K-feldspar of Cu 1105 which supports the conclusion that temperatures determined for Cu 442 are unreliable.

Based on what has been determined to be the most reliable data, a temperature of ~535°C has been determined for the potassic alteration zone. It is obvious, from the temperatures calculated for biotite pairs (Table 5.2) and the calculated values of ^{18}O (Fig. 5.25), that biotite did not achieve equilibrium with the crystallizing fluid with the K-feldspar and quartz samples.

The $\delta^{18}\text{O}$ values of igneous plutons may be changed after crystallization by exchange, not only with meteoric water, but also with magmatic water derived from the parent magma (Faure 1977). Sample Cu 1105, the megacrystic K-feldspar, has a $\delta^{18}\text{O}$

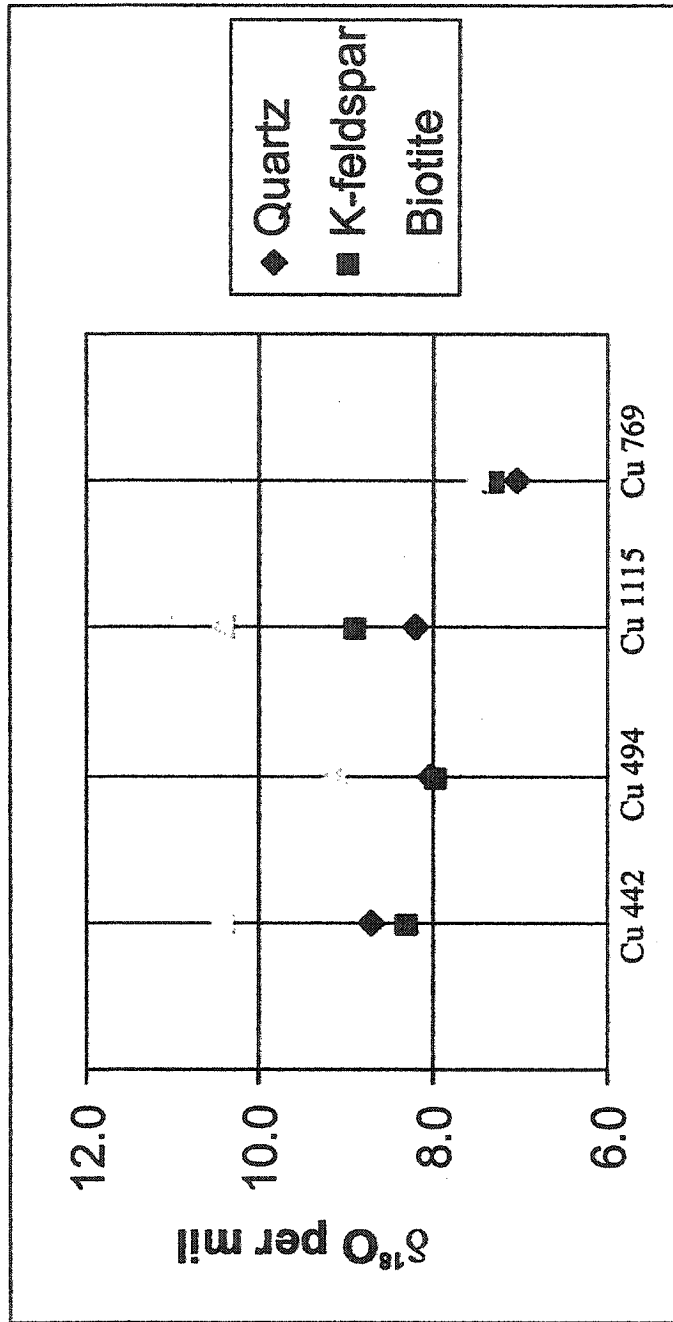


Figure 5.25. The calculated values $\delta^{18}\text{O}$ in the potassic zone at 550°C . The fresh sample (Cu 769) has been calculated at 600°C . That the values of the fresh sample plot so close together is evidence of equilibrium achieved at that temperature. Note that the biotite in each of the potassic samples plots away from the quartz and feldspar values.

value above the magmatic range. This high $\delta^{18}\text{O}$ value is interpreted to represent a more slowly cooled feldspar that was equilibrated with late magmatic-early hydrothermal fluids, resulting in an elevated value. This K-feldspar is therefore considered a magmatic phase that has been affected by deuteritic fluids.

5.6.2 Hydrogen isotopes

Oxygen-hydrogen isotopic analyses were conducted on three biotite samples from the potassic alteration zone (Cu 442, Cu 494, and Cu 1115). There was insufficient sample for a δD measurement which may in part be due to the high F-values (Fig. 5.10). Fluorine in the hydroxyl site would replace OH, decreasing the measurable hydrogen for isotopic analyses.

5.7 Summary

The potassic alteration zone is overprinted by the Qser in most of the Chuquicamata deposit (Fig. 5.1). In analyzing samples from the potassic alteration zone using geochemical techniques, it is important to do a thorough petrographic study first as moderate Qser alteration is not necessarily observable in hand specimen.

The potassic alteration zone is characterized by a lack of Ca-silicate minerals. More important than the presence of K-feldspar megacrysts, which are also observed in the fresh Este Porphyry, the albitic composition of the plagioclase feldspar is the most diagnostic feature of the potassic alteration zone.

Biotite in the potassic alteration zone is variably more Mg- and F-rich than the biotite in the fresh Este Porphyry. It is also relatively Fe- and Ti-poor. The depletion of Fe in biotite during potassic alteration leads to the expulsion of Ti which, as well, leads to the deposition of rutile along the cleavages of the biotite grains. Those biotite in the potassic zone with compositions similar to those in the fresh Este Porphyry are interpreted to have been affected less by the deuteric fluids.

K-feldspars in the potassic alteration zone are orthoclase or orthoclase inverting to microcline. The presence of cross-hatch twinning and perthitic textures support a magmatic origin for the K-feldspars (Sections 2.7.2.3 and 2.7.2.4).

Anhydrite in the potassic alteration zone, described by other authors (e.g. Ossandon et al. 2001), is interpreted to be related to Qser veining (Chapter 6).

Silica, TiO_2 , Al_2O_3 , and Zr remain immobilized in the potassic alteration zone. CaO is depleted as is observed in the absence of Ca-bearing silicates in the potassic alteration zone. Potassium and Na_2O are enriched in the potassic alteration zone relative to the fresh rock which is seen in an increase in the abundance of K-feldspar and the albitic composition of plagioclase.

The REEs have a similar pattern in the potassic alteration zone as in the fresh sample, although the values are slightly depressed. This depression is likely due to the mobilization of some elements during the destruction of hornblende and the removal of Fe and Ca from the system. Regardless, the potassic and fresh rocks appear to have the same source. The lack of an Eu-anomaly is interpreted to indicate a highly oxidizing

magma, as is typical of porphyry copper systems (Burnham and Ohmoto 1980; Candela 1990) (Fig. 2.1).

The interpretation of the O-isotopes indicates that the potassic alteration zone equilibrated at a temperature of about 535°C. This is cooler than that determined for the fresh Este Porphyry (~595°C).

$^{40}\text{Ar}/^{39}\text{Ar}$ ages indicate the potassic alteration zone reached argon closure temperatures at the same time as the fresh Este Porphyry. The similar ages indicate one of two possibilities: either the fresh mineral assemblage has had its argon reset by the potassic alteration or the potassically altered rocks are a more hydrous equivalent of the fresh intrusion. The author favours the latter explanation because stable isotopes indicate the minerals in the potassic alteration zone are magmatic in origin.

It is proposed here that the destruction of Ca-silicate minerals is due to high fluorine and/or chlorine contents. The hydration of the Este magma following early anhydrous crystallization would also lead to concentrations of incompatible elements (e.g. Cl, F, and Cu) in the melt. The work of Weidner and Martin (1987) proposed that the presence of albite over more calcic plagioclases in a F-rich leucogranite was the result of F linking with the Ca, leaving the Ca not available for plagioclase formation. At Chuquicamata, the antiperthitic texture of the plagioclase in the potassic alteration zone indicates that the plagioclase first crystallized from a melt (likely as andesine) and was then replaced albite. This replacement is interpreted to have occurred by stripping of Ca from the Ca-bearing silicate minerals by highly reactive anions.

K-feldspar in the potassic zone display typically magmatic features such as perthitic lamellae, crosshatch twinning and euhedral inclusions, however, the Ba-zonation that is concentric in the fresh Este Porphyry is irregular in the potassic alteration zone. This irregular zonation is interpreted to be the result of remobilization of Ba during cooling by deuteritic fluids. Deuteritic fluids are also interpreted to be the cause of coarsened perthitic lamellae in the potassic alteration zone

The Banco Porphyry is ~0.6 Ma younger than the potassic alteration zone. The younger age is supported by the absence of potassic alteration observed in the Banco Porphyry.

Chapter 6

Petrology and Geochemistry of the Quartz-Sericite (Qser) Alteration Zone

6.1 Introduction

The quartz-sericite (Qser) alteration zone is characterized by an assemblage of quartz, white mica, and pyrite. The Qser overprints all other rock units in the Chuquicamata porphyry deposit and is truncated to the west by the West Fault which juxtaposes it against the Fortuna Intrusive Complex (Chapter 4) (Fig. 6.1). Immediately east of the West Fault, the Qser zone is pervasive and obliterates the mineralogy and texture of the host rock it has replaced. Further to the east, the Qser overprints the potassic and propylitic alteration zones to varying degrees, strongly controlled by local faults (Fig. 6.1). Adjacent to the West Fault, the Qser is difficult to distinguish from the argillic alteration zone (not discussed in this study) and therefore, has not been differentiated from it in Figure 6.1.

Pervasive Qser alteration was rock-destructive, replacing the original assemblages with white mica and quartz. Veins of sericite follow planes of brittle fracture and are found locally in the potassic, propylitic and fresh rocks. Late veins of Ca-sulphate and sulphides are also associated with the Qser event and cross-cut the potassic and propylitic assemblages.

The Qser alteration event is associated with an episode of sulphide deposition characterized by abundant pyrite and enargite. Associated Cu mineralization is characterized by chalcopyrite and hypogene covellite.

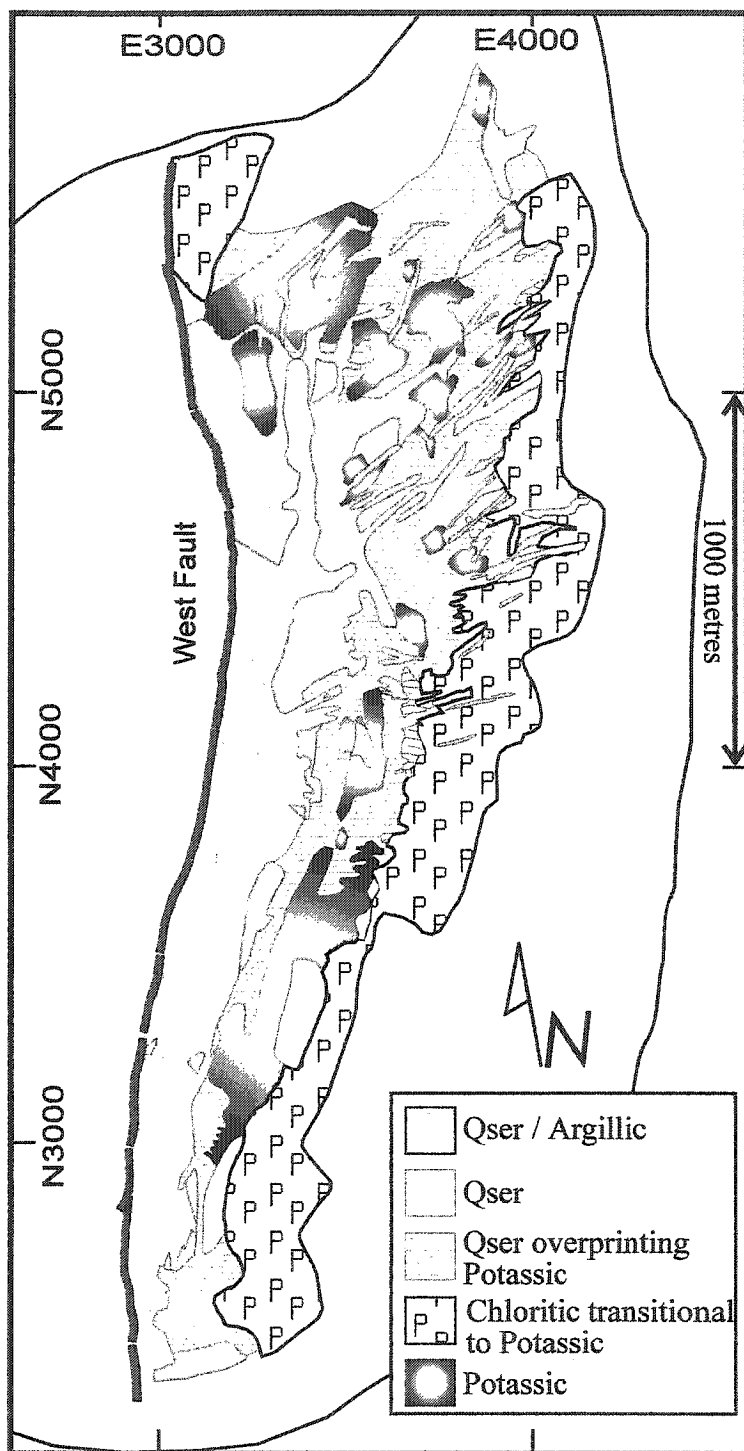


Figure 6.1. Distribution of the Qser alteration zone in the Chuqui pit. The Qser alteration zone is truncated by the West Fault. Immediately east of the fault the Qser is not differentiated from the argillic alteration. The Qser overprints the potassic zone (shown in paler yellow than the Qser sensu stricto).

6.2 Petrology

The Qser alteration is characterized by quartz and white mica with accessory rutile. Veins of quartz, sericite, and anhydrite associated with Qser alteration may crosscut other alteration zones leaving the host rocks relatively unaffected, or the Qser may preferentially replace certain minerals.

In hand specimen, the Qser altered rocks vary from white and friable to grey and silicified (Fig. 6.2). “Sericite” ranges from cryptoscopic grains to large macroscopic flakes and from white to pale green in colour. Veins of sulphate may be white to pink (Fig. 6.2).

6.2.1 Textures

In rocks that have been completely replaced by the Qser alteration, the original texture is no longer observed (Fig. 6.3). White mica grows as microscopic radiating flakes or in clotted masses with fine- to medium-grained quartz lenses and stringers, replacing the original mineralogy.

Where complete replacement has not occurred, as in the zone of ‘Qser transitional to potassic’ (Fig. 6.1), the original textures of the rock may be completely or partially preserved (Fig. 6.3). In these cases, white mica preferentially replaces minerals, such as albite, which may maintain its original euhedral shape (see Section 6.2.2.1).

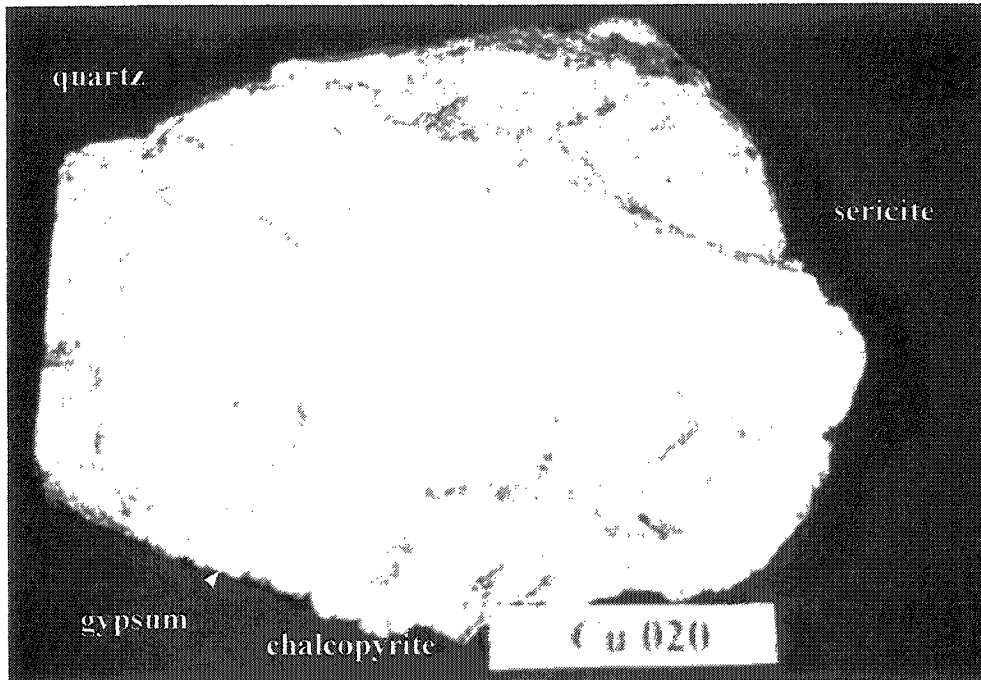
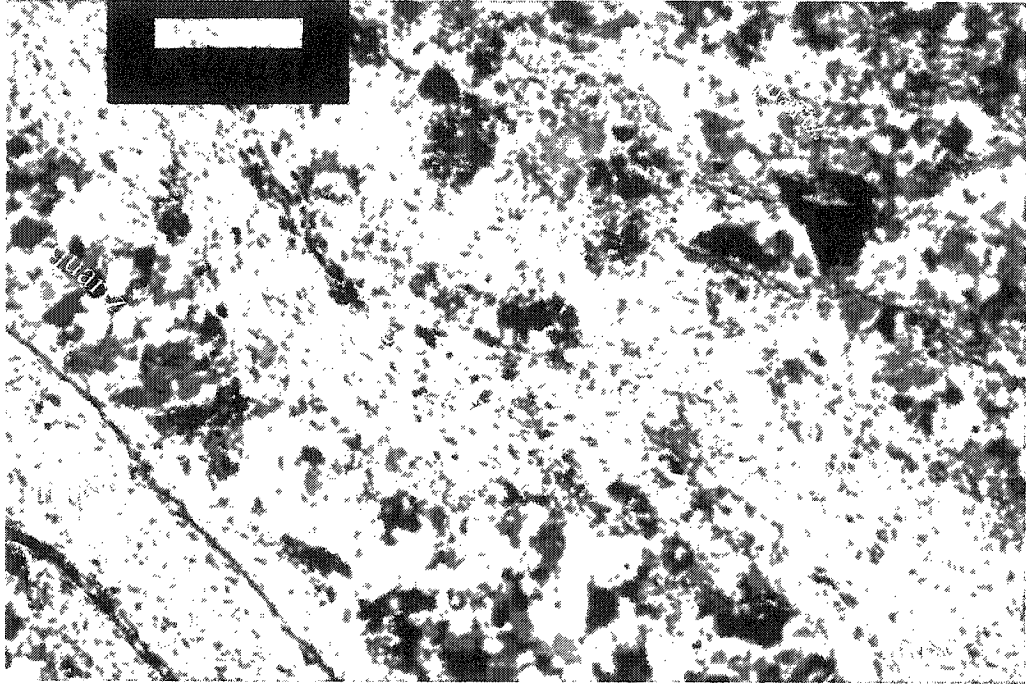


Figure 6.2. Sample Cu 020 is characterized by quartz (grey) cut by white veins of sericite. The large pink vein is gypsum. The brassy veinlet is chalcopyrite. White label is 5cm across.



b. Cu 140 (mag. = 50X; F.O.V. = 2 mm, xpl)

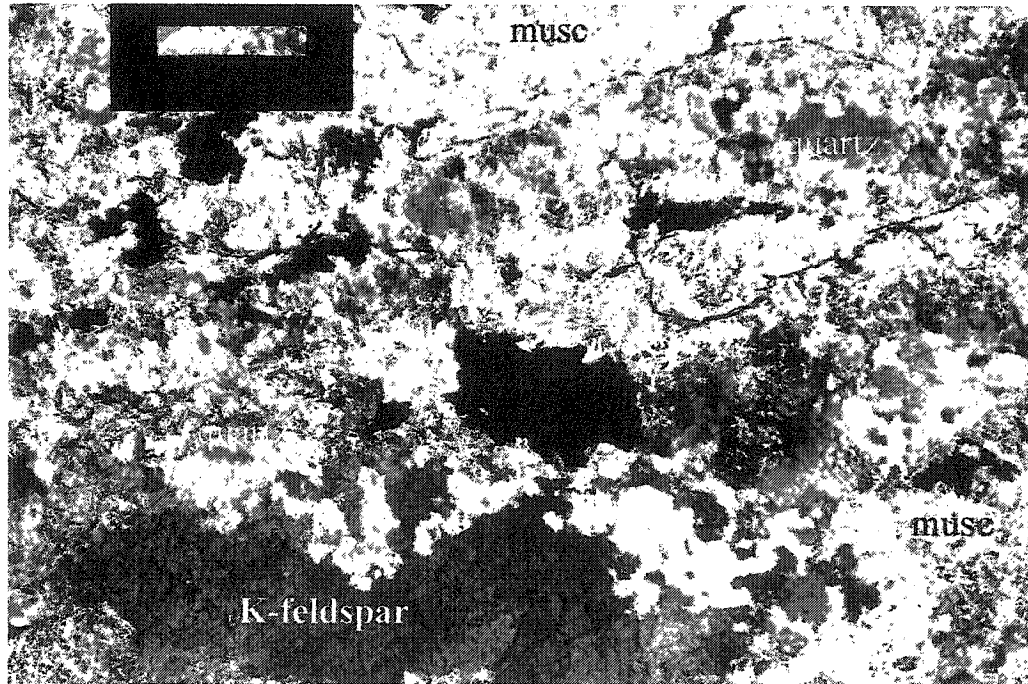


Figure 6.3. a) Complete Qser alteration. Quartz and sericite are the only silicate minerals present. b) K-feldspar has been preserved.

6.2.2 Mineralogy

6.2.2.1 Plagioclase

In areas of extreme Qser alteration, plagioclase is completely replaced by white mica (Fig. 6.3). In areas only moderately affected by Qser alteration or Qser veins, plagioclase is altered to white mica to varying degrees (Fig. 6.4). Plagioclase is highly susceptible to the effects of the Qser event. Where other minerals in the potassic assemblage are unaffected, plagioclase may be extensively altered to white mica (Fig. 6.3). Plagioclase inclusions in K-feldspar may be completely altered to white mica where the K-feldspar appears unaffected (Fig. 5.13).

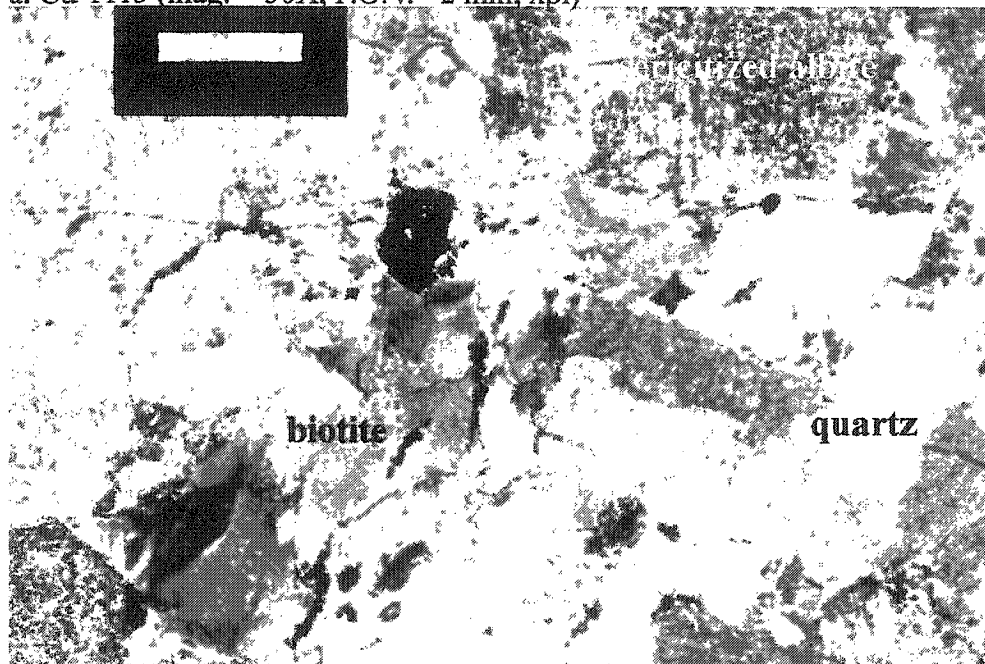
6.2.2.2 Mafic Minerals

Biotite and amphibole are not present in the Qser alteration zone. Biotite has been pseudomorphed by coarse muscovite grains with rutile growing along the relict cleavage planes (Fig. 6.4). Where Qser overprints potassic alteration, biotite may be preserved where the albite is replaced (Fig. 6.4).

6.2.2.3 K-feldspar

Where the Qser alteration is intense, K-feldspar is completely replaced by white mica (Fig. 6.3). Where the alteration is weak, K-feldspar may remain relatively unaltered (Fig. 6.3), even though all other minerals may be completely altered, including plagioclase inclusions within the K-feldspar (Figs. 5.13 and 6.4). In some thin sections of

a. Cu 1115 (mag. = 50X, F.O.V. = 2 mm, xpl)



b. Cu 140 (mag. = 50X, F.O.V. = 2 mm, xpl)



Figure 6.4. a) Biotite is present where albite is altered to sericite. Note the K-feldspar is relatively unaltered. b) Biotite has been replaced by coarse sericite, whereas the rest of the minerals have been altered to a fine-grained sericite. Note the rutile along the cleavage planes of the former biotite.

moderate Qser alteration, the K-feldspar appears cloudy in plane-polarized light, but looks relatively less altered in crossed-nichols.

6.2.2.4 Quartz

Quartz occurs in the Qser zone as polycrystalline lenses of recrystallized grains and in veins. In hand specimen quartz is grey (Fig. 6.2). Quartz displays undulose extinction in crossed-nichols (Figs. 6.3 and 6.4).

6.2.2.5 Sericite

In hand specimen, sericite is fine-grained and generally white, although green sericite occurs locally (Fig. 6.2). Individual grains are not readily discernable without a microscope and, in some cases, the grains are even cryptoscopic. In the Qser alteration zone, sericite replaces the original mineral assemblages. Where Qser is intense, sericite with quartz dominates the mineralogy (Fig. 6.5).

In Qser-overprinted potassic rocks, white mica and minor clay preferentially replace minerals in a particular order (Fig. 6.3 and 6.4): albite may be 'sericitized' where all other minerals appear relatively fresh; and biotite pseudomorphed by white mica, with rutile growing along cleavage planes, is present where K-feldspar remains relatively unaffected (Fig. 6.4).

Clay mineral(s) are observed petrographically along cleavage planes of radiating mica grains in the coarsely sericitized samples and as a fine-grained alteration of feldspars in the less intensely Qser-altered rocks (Fig. 6.5).



b. Cu 443 (mag. = 100X, F.O.V. = 1 mm, ppl)



Figure 6.5. White mica has a radiating morphology with clay minerals along cleavage planes and grain boundaries. Both figures are of the same area. The clay is interpreted to be illite. Clay appears dark in both: a) Cross-polarized light. b) Plane-polarized light.

X-ray diffraction was used to confirm the mineralogy of those samples used for $^{40}\text{Ar}/^{39}\text{Ar}$ age dating and stable isotope analyses (Appendix D). The large number of peaks in phyllosilicates makes positive X-ray diffraction identification difficult. Identification is particularly difficult if the mica or clay is a mixture of two or more phyllosilicates; X-ray diffractometry of different white micas can yield coinciding peaks with similar intensities (Table 6.1).

Table 6.1 Results of X-ray diffraction Qser samples.

Sample #	X-ray diffraction results
Cu 020	Illite/muscovite (?)
Cu 070	Muscovite-2M1
Cu 082	Illite-2M1
Cu 093	Illite-2M1
Cu 203	Gypsum, Illite (?)
Cu 519	Muscovite-2M1
Cu 090	Illite/muscovite (?)
Cu 807	Illite-2M1
Cu 128	Illite-2M1

This difficulty in identifying micas is complicated by sample contamination by other minor fine-grained phases; for example, quartz and gypsum are commonly intimately intergrown with the sericite in the Qser zone. The presence of quartz is indicated by an enhanced 2θ peak at 26° and a 2θ peak at 11° indicates the presence of gypsum (Fig. 6.6). From the X-ray diffraction analysis, it can be concluded that the sericite is a dioctahedral phyllosilicate, or a mixture of more than one phyllosilicate. Sericite from the Qser has

'SERICITE' DIFFRACTOGRAMS

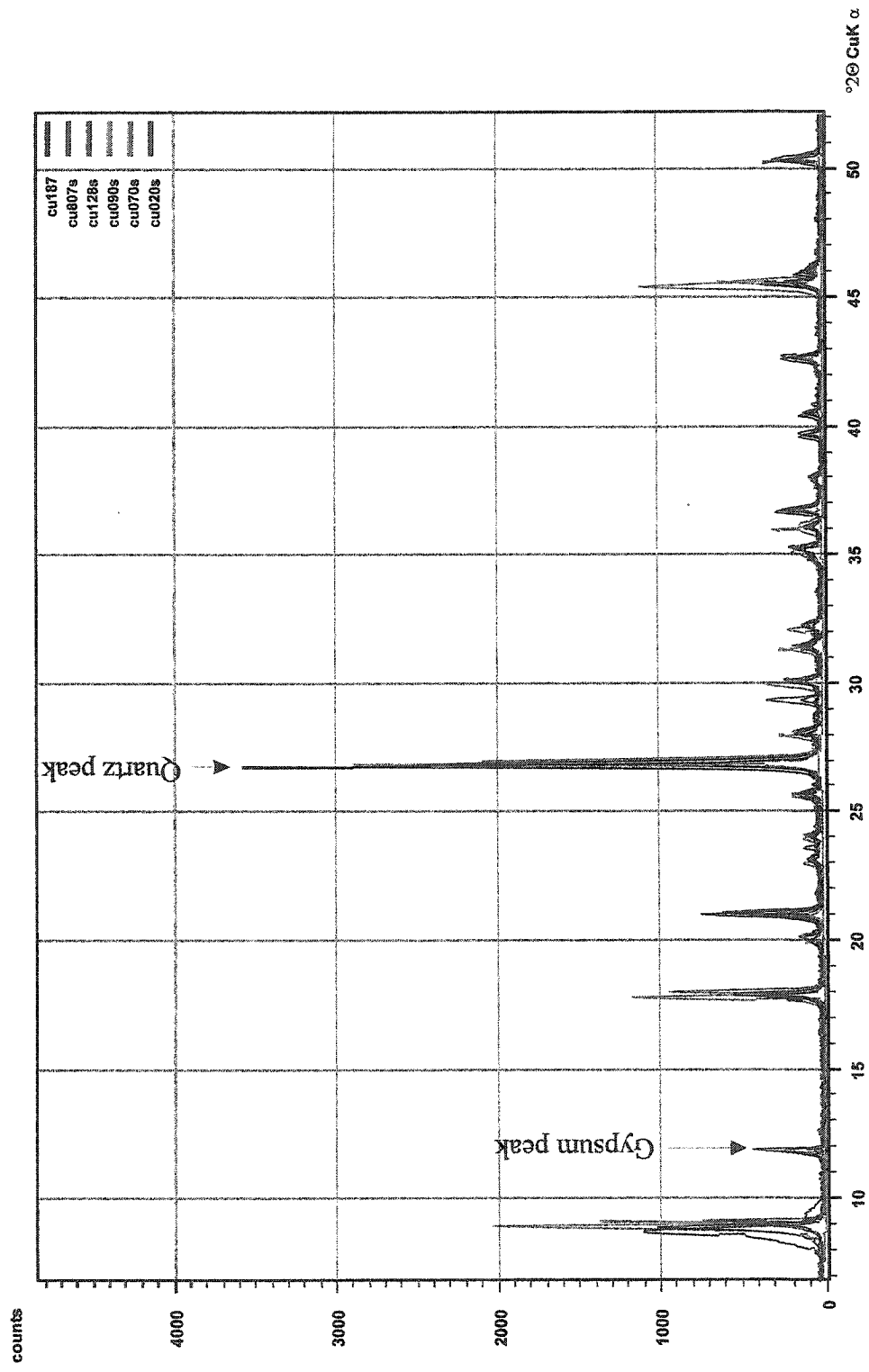


Figure 6.6. X-ray diffractograms of selected micaceous minerals.

produced patterns that could be from either muscovite or illite (Table 6.2; Appendix D).

Illite and muscovite also have similar chemical compositions; the formula for illite is $K_{2-x}Al_{6-x}Si_{6+x}O_{20}(OH)_4$; if $x = 0$, the mineral is muscovite (Deer et al. 1992). This similarity makes it difficult to distinguish them using electron microprobe analyses. Electron microprobe analyses did not confirm the presence of clay minerals, as the total values and K_2O values for the white mica analyses were too high for clay (Fig. 6.7).

Electron microprobe analyses indicate no chemical variation between the white mica in veins, in pervasive masses or in replacements of plagioclase (Appendix C). There is a strong correlation between Al_2O_3 and $FeO+MgO$, indicating Mg and Fe may have substituted for Al (Fig. 6.7); the abundance of Mg and Fe shows the muscovite is phengitic in composition. All of the white micas analyzed are F-rich (up to 1.8%); (Fig. 6.7).

6.2.2.6 Ti-minerals

Rutile is the only Ti-mineral found in the Qser alteration zone. The rutile needles are red under strong plane polarized light and typically form pseudomorphs after diamond-shaped minerals (Fig.6.8). White mica replacing biotite has small grains of rutile along cleavage planes (Fig. 6.4). Rutile found along biotite cleavages tends to be finer grained than that found in the pseudomorphs and occurs as anhedral crystals.

Electron microprobe analyses from one pervasively altered Qser sample (Cu 093) indicate that the pseudomorphing rutile of the Qser zone falls within the compositional range of the rutile in the potassic zone, in both FeO and trace element contents.

Table 6.2 Difficulty in determining mica-clay nomenclature by X-ray diffraction is demonstrated in these tables which show the five most intense peaks for three minerals, illite and 2 muscovite. Peaks in micas and clays are often similar and even if there is no mixture with other mineral identification is difficult. Specifically, quartz has a primary peak at 3.34 Å and is intimately related to the mica and clay. Note that the primary peak (intensity =100) is within 0.04Å in the three examples given and the secondary peak is separated by only 0.04Å. The dÅ indicates the d-spacing in angstroms and intensity is given in percent.

Illite-2M1	dÅ	Intensity
	10.0	90
	5.02	50
	3.34	100
	2.988	18
	2.005	50

Muscovite-1M, syn	dÅ	Intensity
	10.1	100
	4.49	90
	3.66	60
	3.36	100
	2.582	90

Muscovite-2M1	dÅ	Intensity
	9.95	95
	4.97	30
	3.32	100
	2.987	35
	2.566	55
	1.993	45

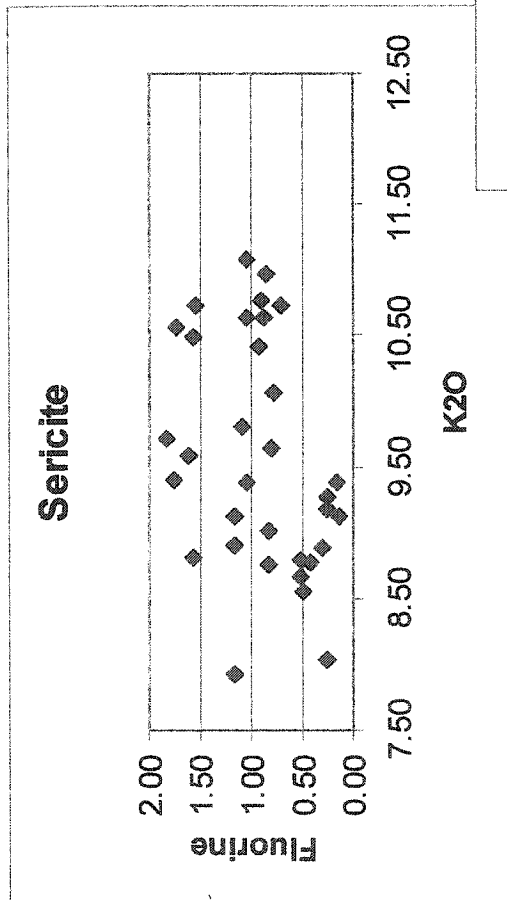
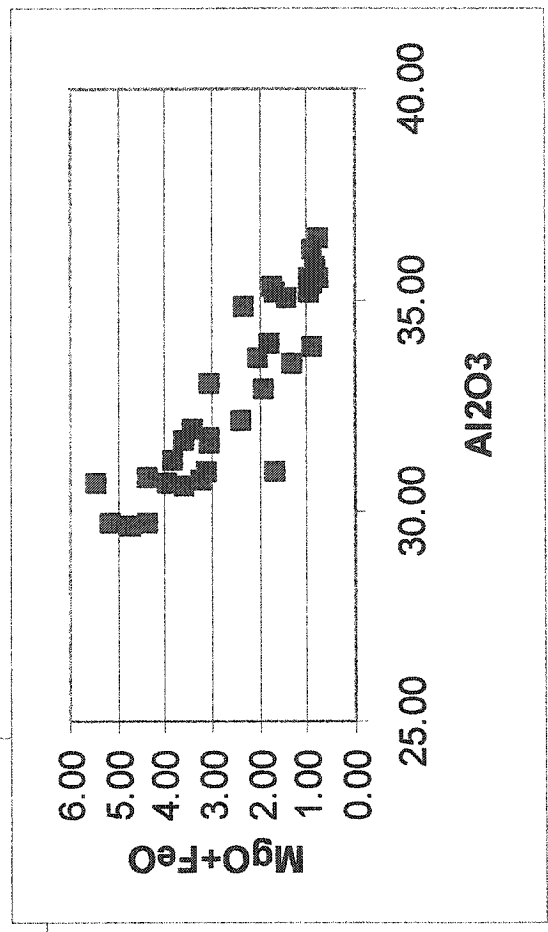
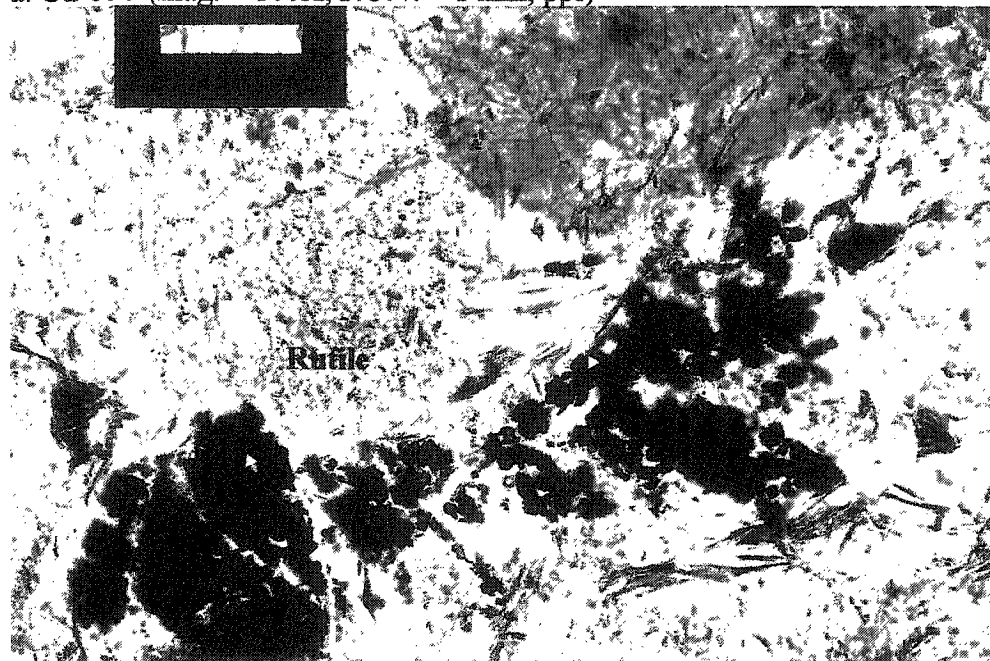


Figure 6.7. a) F- values vary in the muscovite of the Qser alteration zone. Values are reported here in weight percentages.

Figure 6.7. b) High FeO and MgO values in the muscovite. These values indicate the muscovite in the Q-ser alteration zone is phengitic in composition.



a. Cu 093 (mag. = 100X, F.O.V. = 1 mm, ppl)



b. Cu 443 (mag. = 50X, F.O.V. = 2 mm, ppl)

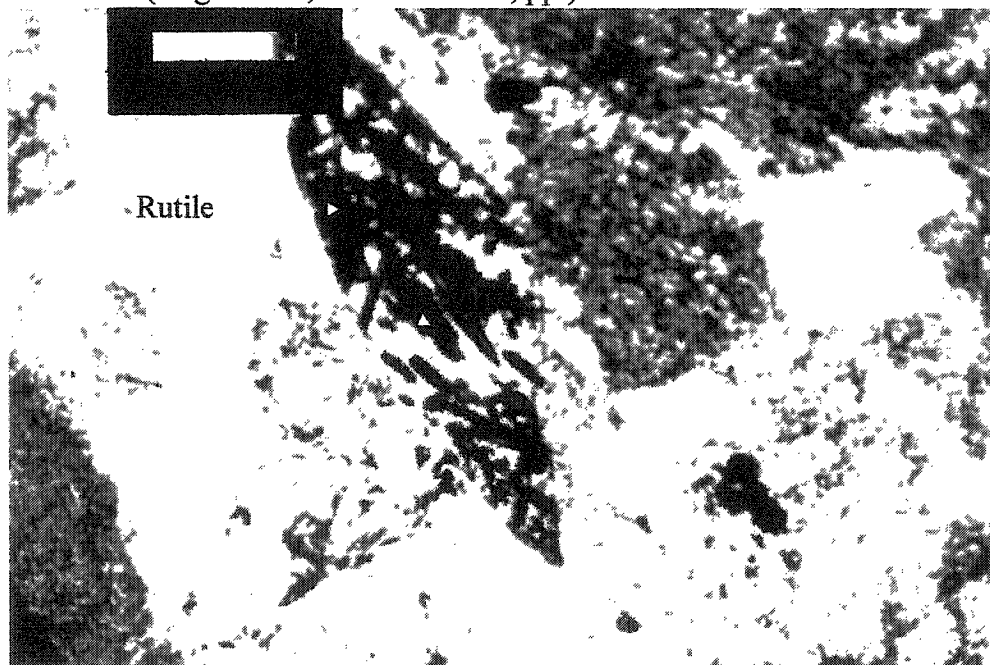


Figure 6.8. a) Rutile in a pervasively sericitized sample. b) Mainly sericitized sample with needle-like rutile forming a diamond-shaped pseudomorph after titanite.

6.2.2.7 Accessory minerals

There was no apatite observed in the Qser alteration zone.

6.2.2.8 Sulphate

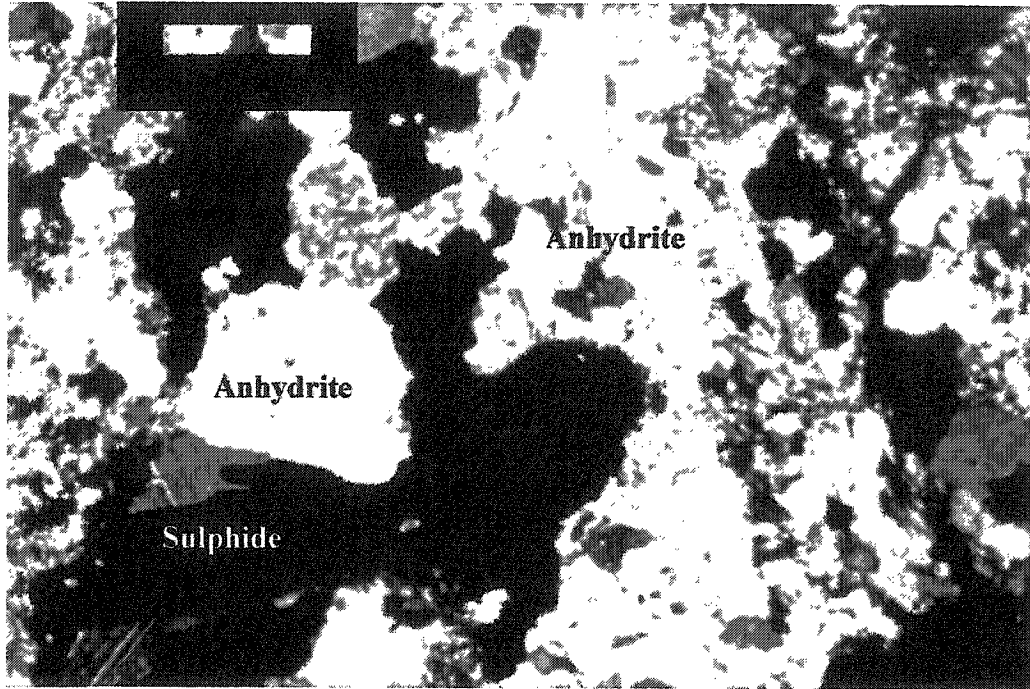
Both anhydrite and gypsum occur in veins cutting the Qser zone as well as other zones. Anhydrite and gypsum are associated with quartz, sericite, and sulphides. In hand specimen, anhydrite is colourless and displays good crystal form with good cleavage in up to three directions. Gypsum forms large, colourless grains or white or pink veins in hand specimen (Fig. 6.2). Satinspar gypsum is rare.

In thin section, anhydrite has a high birefringence, with twins visible in both crossed-nichols and reflected light (Fig. 6.9). It is colourless in plane-polarized light, and exhibit a moderate to high positive relief which may change as the stage is rotated (due to variable refractive indexes). Anhydrite is commonly associated with quartz, sericite, and sulphides such as hypogene covellite, digenite, and chalcopyrite (Fig. 6.9).

Gypsum is colourless in thin section. with (Fig. 6.9); under reflected light, it appears dark brown. It shows a low birefringence and has moderately high positive relief. Gypsum occurs with supergene covellite, chalcocite, and Cu oxides. Gypsum may occur in veins with anhydrite, sericite, and quartz (Fig. 6.9).

X-ray diffraction has confirmed the existence of gypsum and anhydrite (Appendix D). Electron microprobe analyses of anhydrite indicate a variation in Sr content (0 to 2%) (Fig. 6.10). Anhydrite with no detectable Sr is optically identical to anhydrite with Sr.

a. Cu 106 (mag. = 50X, F.O.V. = 2 mm, xpl)



b. Cu 1142 (mag. = 100X, F.O.V. = 1 mm, xpl)

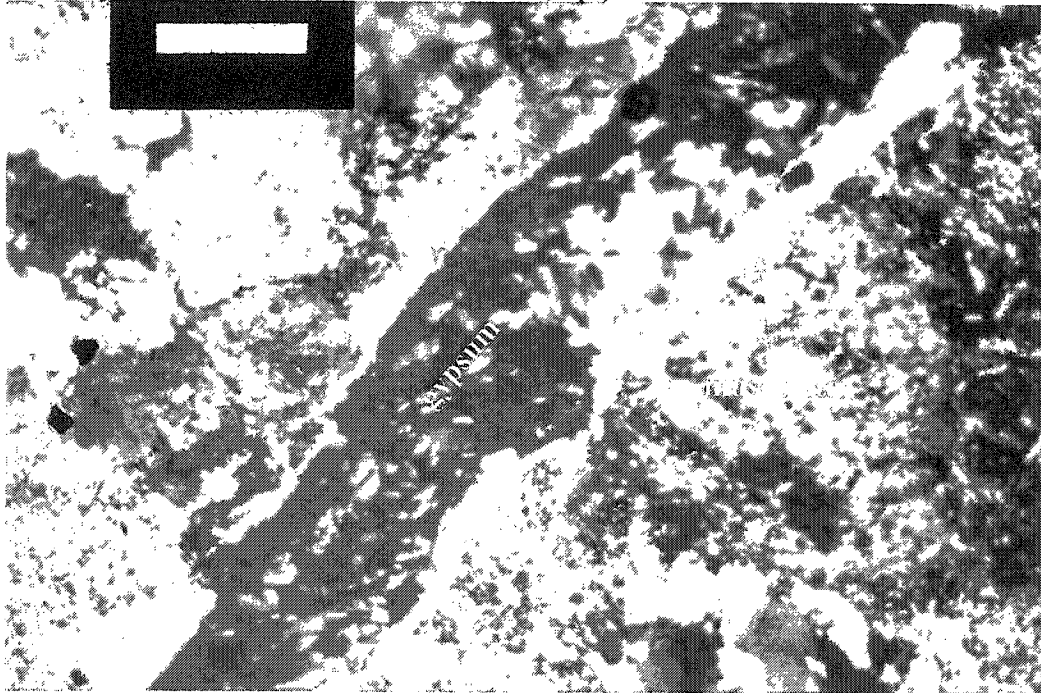


Figure 6.9. a) A vein of highly birefringent anhydrite associated with sulphides (opaque in transmitted light). b) Gypsum in a vein with sericite selvages.

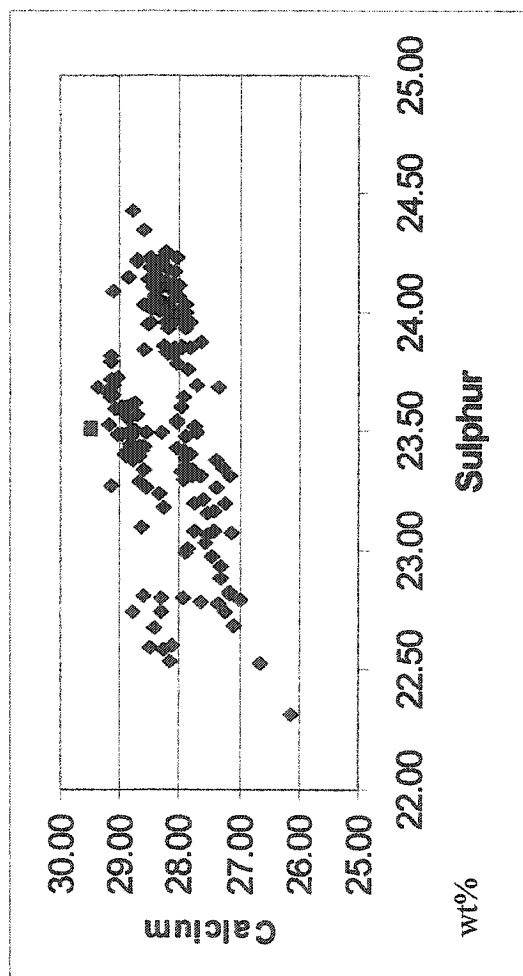
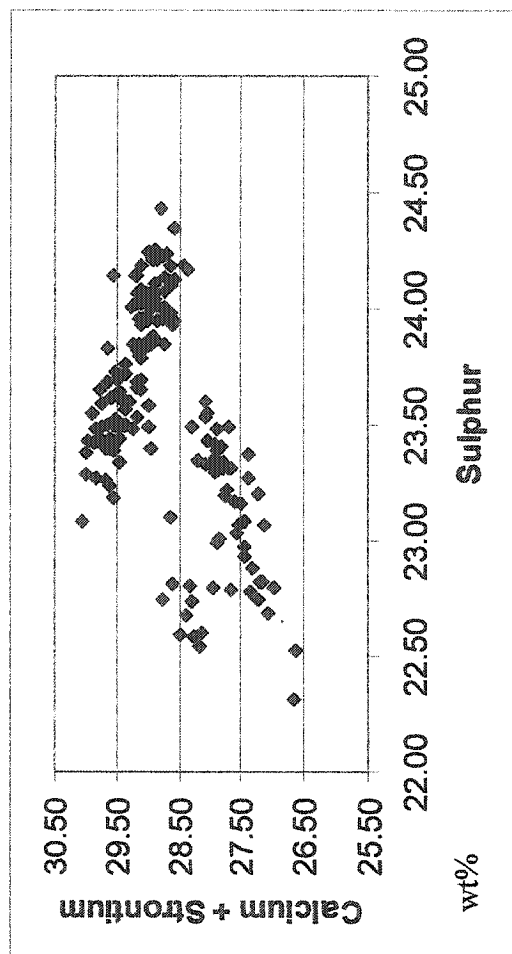


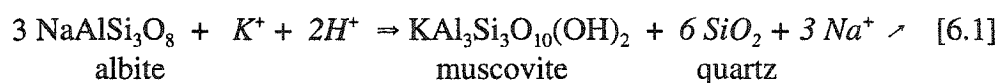
Figure 6.10. Electron microprobe analyses of anhydrite. Stoichiometrically, anhydrite should have 23.5wt.% S and 29.4wt.% Ca (red square). At Chuquicamata, the S-values are within 1wt% this value, however, the Ca-values are consistently lower. The anhydrite is locally enriched in Sr. The addition of Sr and Ca, moves the chemistry of the Chuqui anhydrites to a more ideal stoichiometry. (The stoichiometry of gypsum would have S=18.6wt.% and Ca=23.2wt.%, confirming none of the samples analyzed are gypsum).



6.2.3 Interpretation

Any original mineral assemblages are completely replaced in the regions intensely affected by Qser alteration. An assemblage of sericite, quartz, and pyrite is characteristic of this zone, with some remnant K-feldspar where alteration has been incomplete. Based on electron microprobe analyses and X-ray diffraction, it is concluded that sericite at Chuquicamata is mainly phengitic muscovite with minor amounts of illite. Throughout the rest of this thesis, muscovite and sericite will be used interchangeably.

The alteration of **plagioclase** occurs early in Qser alteration (Fig. 6.4). Replacement of albite by muscovite involves K^+ replacement of Na^+ and hydrolysis, as represented in equation 6.1.



Species predicted to be in solution are shown in italics. The arrow indicates the species that are removed in solution. SiO_2 is a byproduct of the alteration of albite to muscovite and may deposit as crystalline quartz or it may remain in aqueous solution. There are no new Na-bearing minerals in the Qser zone (e.g. paragonite), indicating that Na^+ is completely removed from the system, probably in solution.

An activity diagram for the system Na-K-Al-Si-O-H at 350°C and 1 kbar illustrates the breakdown of albite (equation 6.1) to muscovite with an increase in acidic conditions (Fig. 6.11). Location A in Figure 6.11 marks where the potassic assemblage (K-feldspar-albite) was initially stable in the K-feldspar. An increase in acidity shifts the stability to a triple point where albite alters to muscovite (Fig. 6.11, location B, where K-

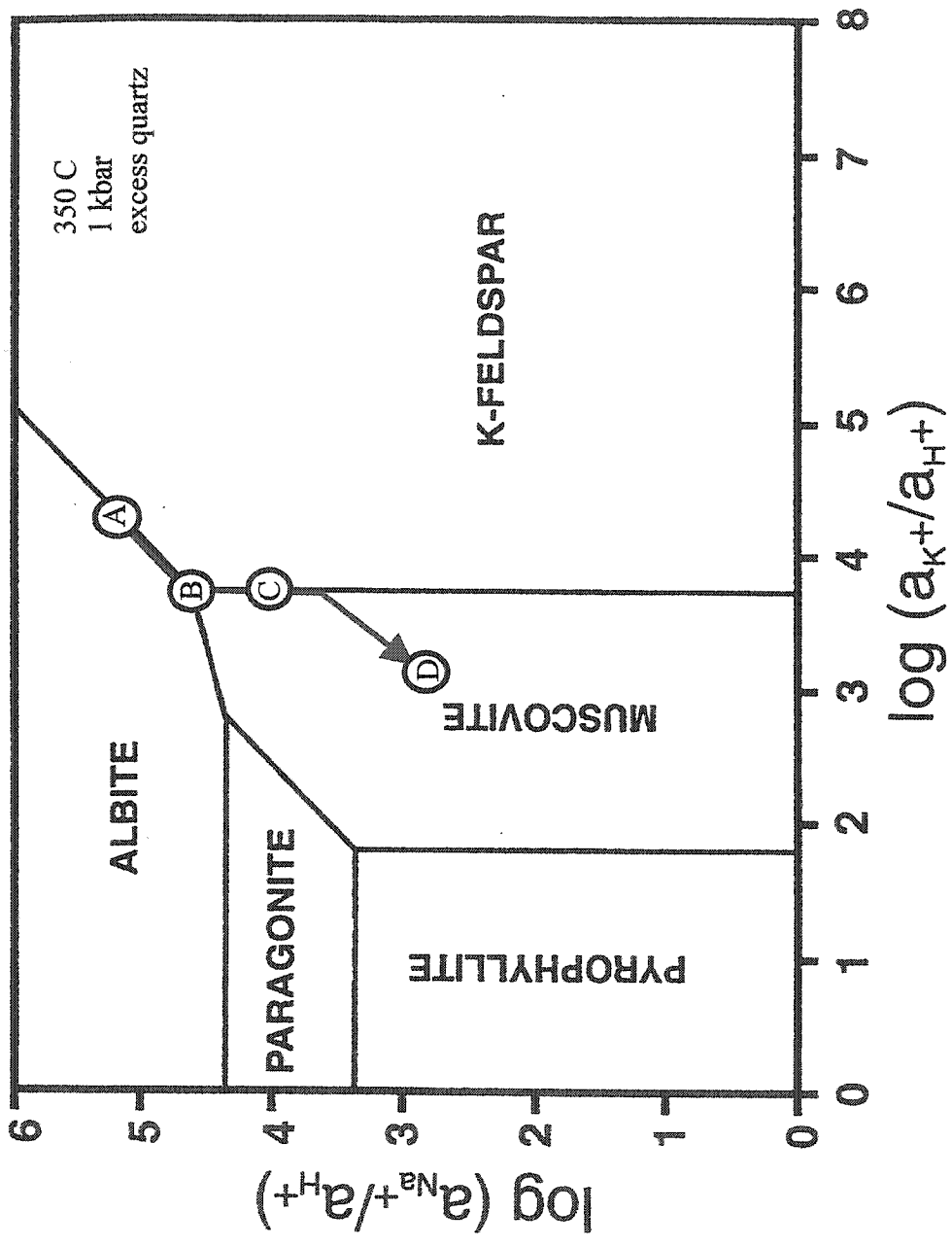
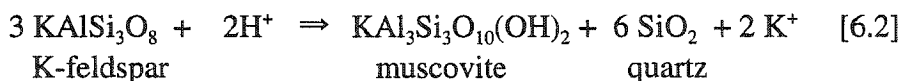


Figure 6.11. Activity diagram showing the sericitization of albite and K-feldspar at 350°C and 1 kbar. The red arrow represents the path of alteration. Following the alteration of the albite, the alteration would have proceeded down the muscovite-K-feldspar line until the K-feldspar was completely altered. The actual point (i.e. activities) at which this would have happened is arbitrary (diagram after Wood, 1998).

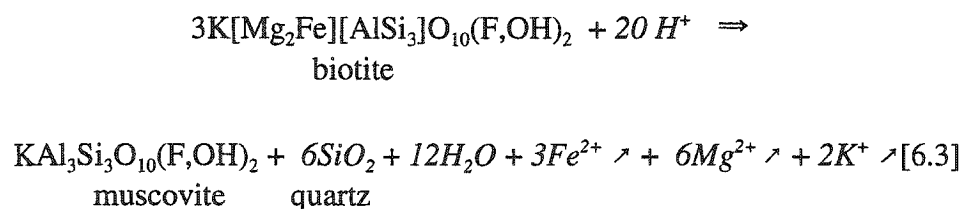
feldspar remains stable), as implied by the petrography. In order to keep K-feldspar stable, there must have been an addition of K^+ , that is an increase in K-activity, to keep the ratio of $K^+ : H^+$ activities constant (Fig. 6.11). If the K-activity were to become too high, albite would alter to K-feldspar rather than muscovite. The removal of Na^+ would have no effect on the K-feldspar stability (Fig. 6.11, location B to C). An increase in H^+ or a decrease in K^+ would move the line from the K-feldspar to the muscovite stability field (Fig. 6.11, location D).

SiO_2 is a product of hydrolysis of K-feldspar to muscovite and may remain in an aqueous solution or deposit as a quartz.



Figures 6.11 and 6.12 shows how a decrease in pH could drive the fluid composition from the K-feldspar to muscovite stability field without any change in a_{K^+} .

In some thin sections muscovite after **biotite**, where K-feldspar remains unaltered, indicates that biotite altered before K-feldspar but following the replacement of albite.



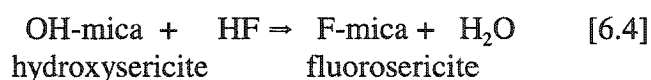
In this reaction, SiO_2 is a mineral product. The activity diagram in Figure 6.12 displays how an increase in acidity can lead to the alteration of phlogopite to muscovite without affecting the stability of K-feldspar. At location E (Fig. 6.12), phlogopite and K-

feldspar are in equilibrium. An increase in H^+ or a decrease in K^+ would move the assemblage to the right where it intersects a triple point (Fig. 6.12, location F). At location F, phlogopite alters to muscovite while K-feldspar remains stable as observed in thin section (Fig. 6.4) suggesting that K^+ and H^+ are both increasing. A decrease in Mg^{2+} may occur as it is removed from the system but this will not affect the stability of K-feldspar. In order to alter K-feldspar to muscovite there must again be an increase in H^+ or a decrease in K^+ (Fig. 6.12, locations G to H).

As shown in the activity diagrams discussed above (Figs. 6.11 and 6.12), an increase in H^+ or decrease in K^+ is necessary to alter K-feldspar to muscovite (at constant pressure and temperature). If K^+ is consumed, and the K-activity decreases, during the alteration of albite, the K-feldspar would have become unstable and alter to muscovite (Fig. 6.11). Therefore, K^+ must be added to the system locally to preserve the K-feldspar during albite alteration.

The alteration of biotite to muscovite liberates K^+ , increasing a_{K^+} , which would help to stabilize the K-feldspar. However, in our case, there is too little biotite to have stabilized the more abundant K-feldspar. Therefore, a decrease in pH or the a_{K^+} would be responsible for the alteration of K-feldspar. Changes in the $a_{Mg^{2+}}$ and a_{Na^+} do not affect the K-feldspar-muscovite stability relationship.

As the white mica is F-rich, it is possible that some of the H^+ could be substituted by F (equations 6.1, 6.2 and 6.3).



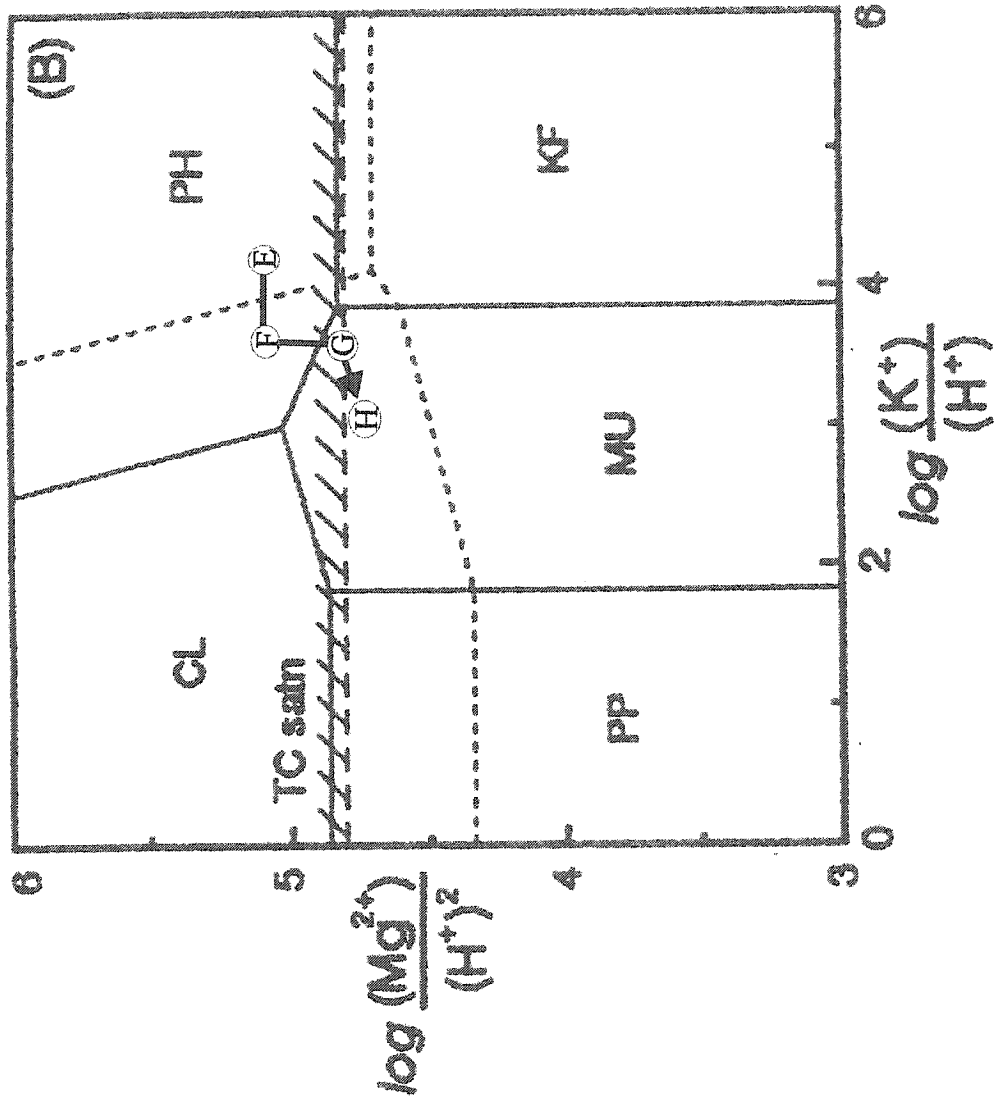


Figure 6.12. The system $K_2O-MgO-Al_2O_3-SiO_2-H_2O$ at quartz saturation and $300^\circ C$ (diagram after Beane (1994)). Diagonal lines indicate limit imposed on $(Mg^{2+})/(H^+)^2$ by talc saturation. Dashed lines indicate shift in biotite stability field to account for Mg-Fe solid solution (Beane 1974). PP- pyrophyllite, CL-clinocllore, MU- muscovite, KF- K-feldspar, PH- phlogopite, and TC satn- talc saturation.

This reaction would increase the activity of H^+ , thereby lowering the pH and increasing the effectiveness of the fluid to alter the original assemblage.

Rutile appears to be stable in the Qser zone and shows the same enrichment of FeO and trace elements as the rutile in the potassic zone (Chapter 5). Therefore, the rutile must have been preserved during the Qser alteration, and not mobilized and redeposited.

The consumption of H^+ during the hydrolysis of K-feldspar and albite during the Qser alteration would result in a decrease in acidity (Fig. 6.11). A decrease in the acidity of the solution would convert the bisulphate to SO_4^{2-} and cause anhydrite to precipitate (Rimstidt 1997).

The anhydrite is locally enriched in Sr (Fig. 6.10). It is unclear why there is a variation in the Sr-content. It may be the result of the anhydrite hydrating to gypsum (which can accommodate very few impurities in its chemical structure); however, there is no evidence in the electron microprobe analyses to suggest that any of those grains analyzed were gypsum (i.e. the ratios of Ca:S:O are close to ideal anhydrite values) or that there is a correlation between the Sr-content and the degree of hydration (Fig. 6.10). The Sr is substituting for Ca (Fig. 6.10) because the values are closer to stoichiometric anhydrite if Sr²⁺ values are added to Ca²⁺. The variation in Sr-content may be related to the time of crystallization. If anhydrite crystallized rapidly at the end of the Qser alteration event, Sr would have been incorporated into the last of the minerals to crystallize.

The association of anhydrite with hypogene sulphides and gypsum with supergene sulphides supports the hypothesis that gypsum formed by hydration of anhydrite (Lewis 1997).

6.3 Geochemistry

Four samples of Qser alteration were analyzed for whole-rock, trace-element and rare-earth element geochemistry during this study. They were selected based on typical Qser assemblages. One sample, Cu 020, was obviously contaminated with veins of sulphate and sulphide; however, because S-bearing minerals are typical of the Qser zone, Cu 020 was analyzed precisely for this reason (Fig. 6.2).

6.3.1 Whole-rock geochemistry of the Qser zone

In the Qser alteration zone, the relative abundance of major elements is variable (see Appendix E for detailed analyses). As only two phases characterize the Qser zone (quartz and sericite), the whole-rock geochemistry depends largely on the relative abundance of each.

Four Qser samples were analyzed for major elements using XRF. The values displayed in Figure 6.13 are normalized to 100%, LOI-free. The abundance of SiO₂ ranges from 76.22 to 90.5 wt.% (Fig. 6.13). There is also a wide variation in the alumina values, from 5.06 to 12.4 wt.% (Fig. 6.13). TiO₂ values range from 0.07 to 0.26 wt.% (Fig. 6.13). Sample Cu 020 has twice as much Fe₂O₃ as the other Qser samples (Fig. 6.13). On the other hand, there is very little variation in the Fe₂O₃ contents of the rest of

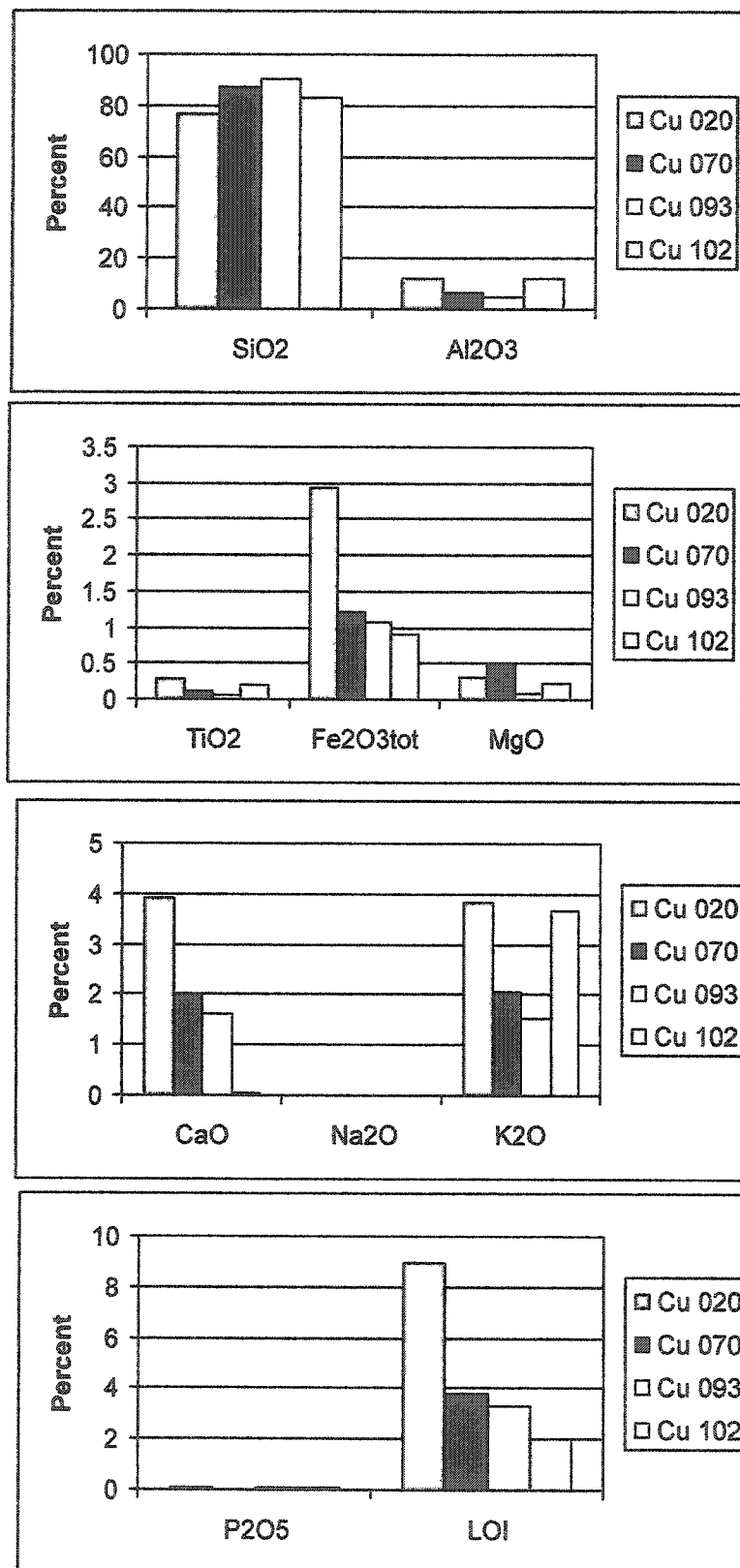


Figure 6.13. Whole-rock geochemistries of the Qser samples. The values are normalized to 100%, LOI-free.

the samples. MgO values ranges from 0.08 to 0.49 wt.% (Fig. 6.13). However, there is only one sample that has detectable MnO at 0.01 wt.% and there is no detectable Na₂O in any of the Qser samples (Fig. 6.13). CaO has a wide range of values, from 0.05 to 3.92 wt.% (Fig. 6.13). K₂O varies from 1.53 to 3.83 wt.% (Fig. 6.13). P₂O₅ has a relatively narrow range of 0.03 to 0.09 wt.%. LOI varies over a very broad range from 1.99 to 8.97 wt.% (Fig. 6.13).

6.3.2 Interpretation of whole-rock geochemistry

The broad range in SiO₂, Al₂O₃, and K₂O values reflects the relative abundances of quartz and K-mica in the samples analyzed (Fig. 6.13), i.e., the higher the SiO₂, the more quartz in the sample. Al₂O₃ and K₂O are directly proportional, indicating that their whole rock abundances are linked to the mineral chemistry of the mica (Fig. 6.14). The electron microprobe analyses of micas are more variable than the whole-rock analyses (Fig. 6.14). The Al:K ratio has a narrow range of 2.96 to 3.05 in the whole rock samples, but in mica, the ratio ranges from 2.74 to 4.05 (mean = 3.24). These values are consistent with the 3:1 ratio of Al:K in muscovite, the only Al- and K- bearing mineral in the pervasive Qser zone. The variation in the electron microprobe analyses may be the result of analytical error.

Mafic elements occur in minor amounts in the Qser zone because of the destruction of the mafic minerals (biotite and hornblende). MnO values are below detection in all Qser samples except one (Cu 070). TiO₂ and MgO values are consistently low (< 0.3wt% and < 0.5wt%, respectively). Fe₂O₃tot is enriched in Cu 020, a sample cut

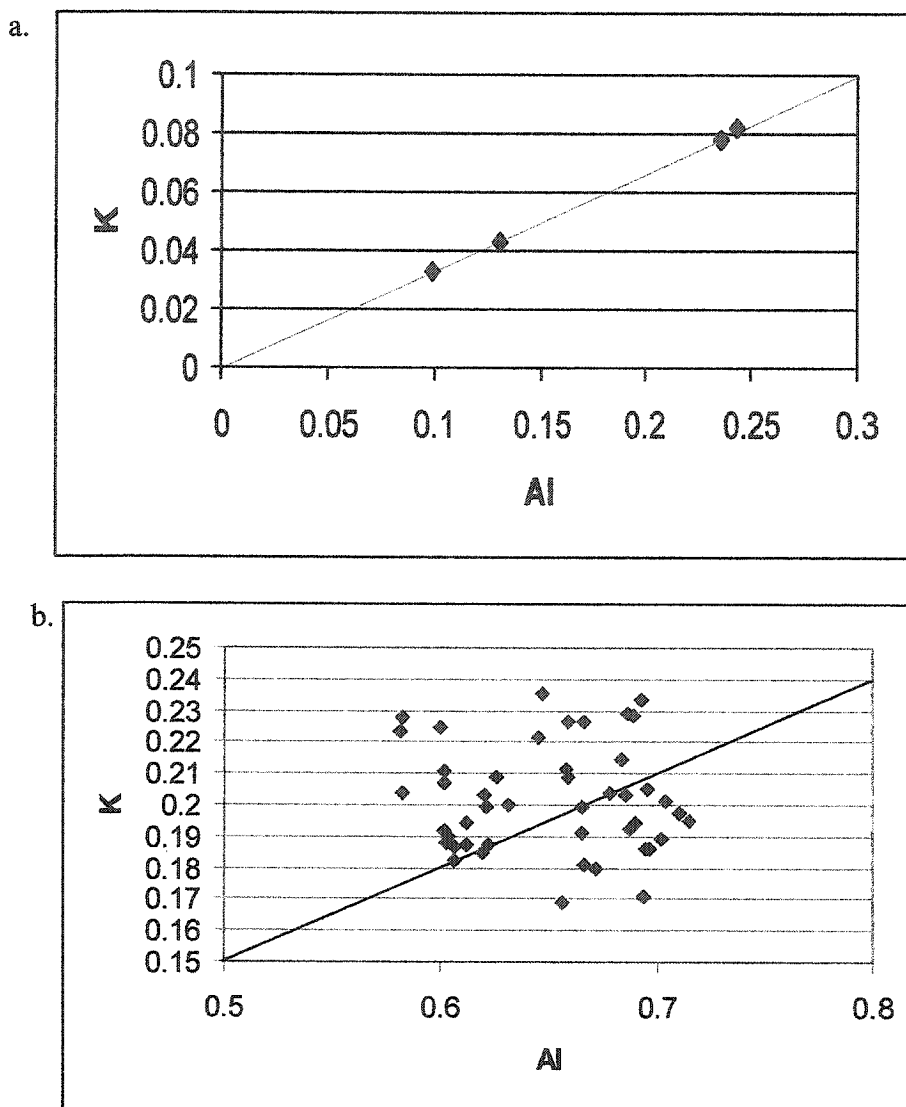


Figure 6.14. Whole-rock geochemistry of the Qser alteration zone and electron microprobe data of muscovite. The cationic ratio of Al:K is 3:1 in the whole-rock analyses. There is more variation in the microprobe data but the values cluster around a 3:1 ratio (mean 3.24). The formula of muscovite is $\text{KAl}_3\text{Si}_3\text{O}_{10}(\text{OH})_2$.

by veins of sulphide and sulphate (Fig. 6.2). The $\text{Fe}_2\text{O}_3_{\text{total}}$ enrichment in Cu 020 is due to the abundance of pyrite and chalcopyrite veins in this sample. The $\text{Fe}_2\text{O}_3_{\text{total}}$ values for the other three samples are consistently low (~1 wt%) which is present mainly in sulphides.

The large variability in CaO values is the result of relative abundance of Ca-sulphate in the samples. In the Qser zone, Ca-sulphates are the only Ca-bearing minerals present. Cu 020 has abundant gypsum and also the highest CaO value. Sample Cu 102 has only 0.05wt% CaO, indicating the absence of anhydrite or gypsum.

The absence of Na_2O in Qser samples demonstrates the complete removal of Na from the system. This absence is consistent with the lack of Na-bearing minerals in the Qser alteration zone. The high values of LOI are the result of hydrolysis. Feldspars and biotites have been hydrated to sericite. The LOI values also reflect the presence of gypsum (sample Cu 020; Fig. 6.2).

6.3.3 Trace-element and rare-earth element geochemistries

The Qser samples are consistently depleted in Ba, Rb, Nb, and Y relative to the potassic sample (Fig. 6.15). The depletion of Ba in the Qser zone is consistent with the destruction of K-feldspar, in which Ba is enriched in the fresh and potassic zones (Figs. 4.13 and 5.16). The depletion of Rb likely also reflects the destruction of the K-feldspar, which preferentially partitions Rb (e.g. Rollinson 1993).

The variable relative concentrations of Zr and Sr is ascribed to the heterogeneity of the samples (Fig. 6.15). Zr is typically considered immobile and its variation can be

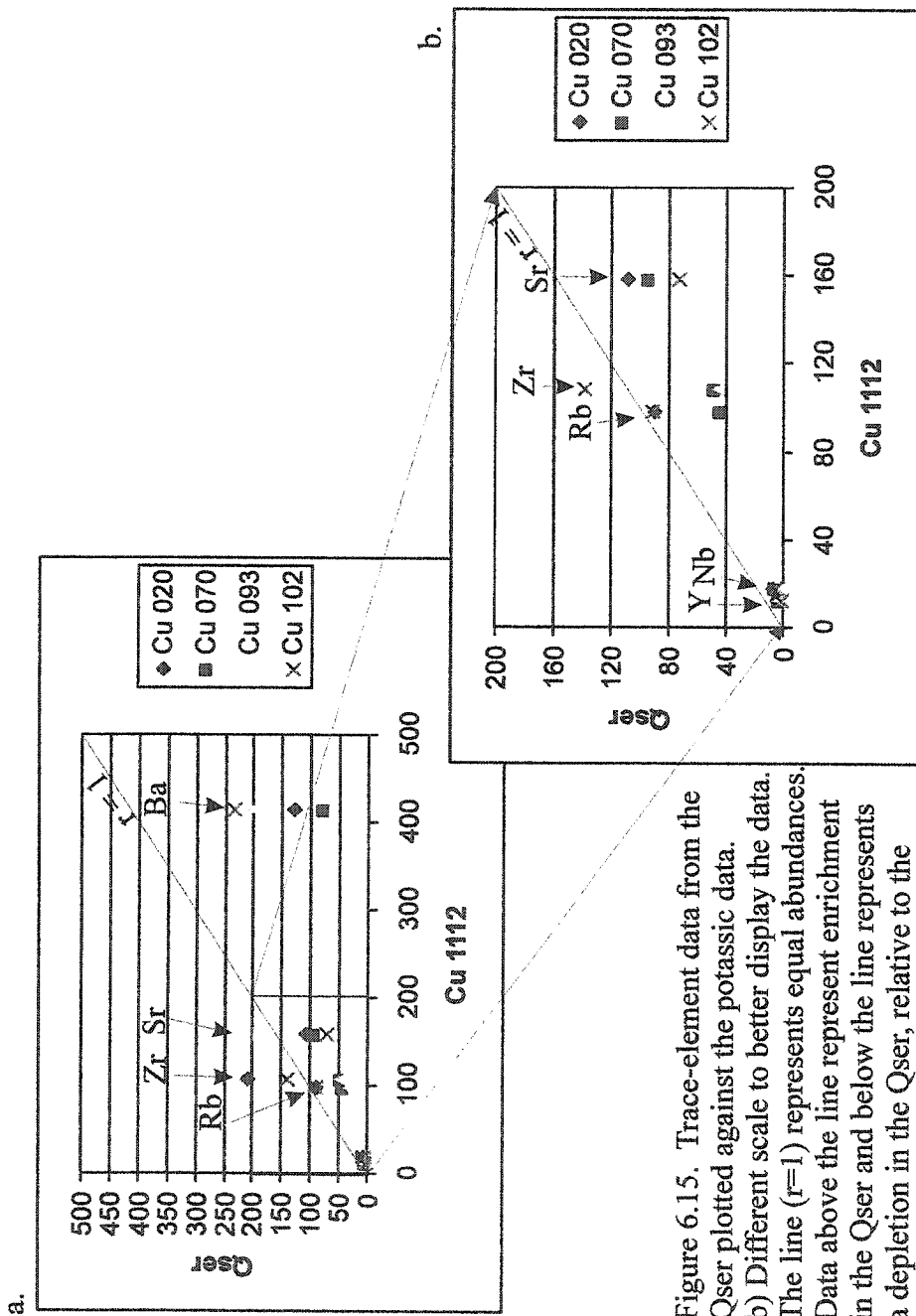


Figure 6.15. Trace-element data from the Qser plotted against the potassic data.
 b) Different scale to better display the data.
 The line ($r=1$) represents equal abundances.
 Data above the line represent enrichment in the Qser and below the line represents a depletion in the Qser, relative to the potassic alteration.

attributed to local concentrations of Zr-bearing phases (i.e. zircon).

Strontium, which has a charge of 2+, typically substitutes for Ca. In the case of the Qser, the Sr concentrates in anhydrite, the only Ca-bearing phase. The lowest Sr value is in Cu 102, a sample without CaO (i.e. no anhydrite). Where the anhydrite has been hydrated to gypsum, the Sr has been removed such as in sample Cu 020 which is also depleted in Sr. Sample Cu 093 has CaO but a lower LOI indicating the Ca is present as anhydrite and is also enriched in Sr.

In the Qser zone, Y has been depleted by over three times, and Nb by over half, relative to the potassic sample. This depletion may reflect the relative abundance of rutile which concentrates Nb. In the fresh/potassic rocks Y would have been partitioned into the magnetite and apatite. Both of these phases are destroyed in the Qser zone, likely resulting in the depletion of Y seen here.

The rare-earth element patterns of the Qser samples are similar to those of the potassic and fresh samples (Fig. 6.16). The behaviour is consistent with the hydration of minerals, such as K-feldspar, resulting in an increased volume but the same abundance of elements. Europium is depleted in all of Qser samples but two samples have a negative Eu- anomaly. These samples also have the lowest Sr values as well, indicating that the Eu may have been partitioned into the anhydrite following the destruction of the feldspars. The samples with higher Sr and Ca values have depressed Eu values relative to the potassic sample, but display a similar trend. REEs are very soluble under low pH conditions, resulting in the leaching of the lightest REEs and Eu^{2+} (Taylor and Fryer 1982). This may also account for the negative Eu-anomaly in the two Qser samples.

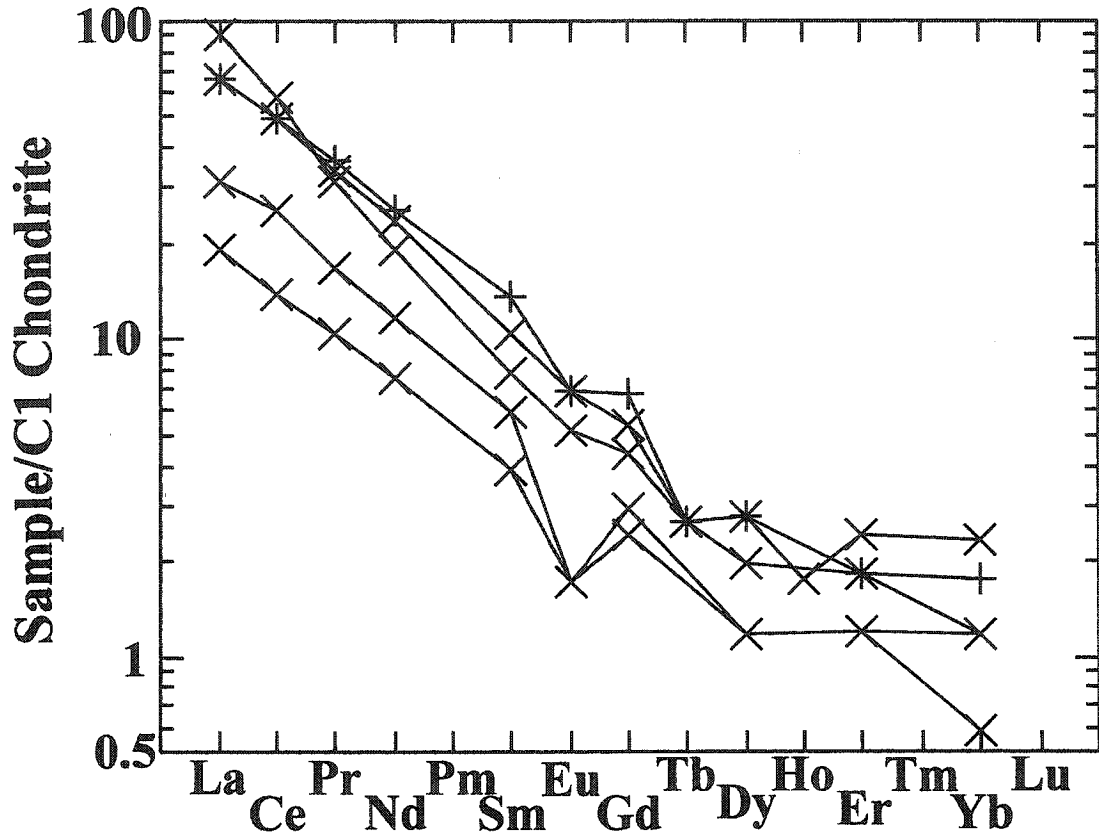


Figure 6.16. Rare-earth element data from the Qser (X) and potassic (+) zones normalized to C1 chondrite.

6.3.4 Comparison of the whole-rock geochemistries in the potassic and Qser zones

Figure 6.17 compares the whole-rock chemistry of the Qser samples to that of a potassic alteration sample (Cu 1112) and a potassic alteration sample that has been only partially overprinted by Qser alteration (i.e. where albite has been sericitized but other minerals remain unaffected (Cu 1115)), henceforth referred to as Kser.

Silica content is considerably lower in the potassic alteration sample than in those affected by Qser alteration (Fig 6.17). The increase in SiO_2 in the Qser zone indicates that the SiO_2 produced in the reactions 6.1, 6.2, and 6.3, must be precipitated rather than leaving the system in aqueous solution. Although quartz is increased volumetrically, the overall SiO_2 content would remain the same since no silica has been added in these equations. Therefore, the increase in SiO_2 values also suggest that the hydrothermal fluids responsible for the Qser alteration event may have been silica-rich and resulted in quartz deposition and thus a relative increase in SiO_2 content (Fig. 6.17).

The potassic alteration and Kser samples have higher values of Al_2O_3 . As the Al_2O_3 values are highly variable in the Qser zone, a correlation with the potassic zone is somewhat ambiguous. The only Al-bearing mineral in the Qser zone is sericite; in the potassic zone, there are several Al-bearing minerals, such as the feldspars and biotite. Aluminum is considered to be a relatively immobile element, therefore variations are interpreted to be the result of sample heterogeneity.

The TiO_2 values are slightly lower in the Qser zone than in the potassic sample (Fig. 6.17). These lower values may represent sample heterogeneity as rutile appears to be preserved in the Qser alteration zone. Rutile in the Qser zone has a similar trace-

element enrichment compared to the potassic zone and is therefore considered to have been unaffected by the Qser alteration event.

The higher Fe_2O_3 value in the Kser sample than in the potassic sample reflects the greater abundance of biotite (Fig. 6.17). The range in values of Fe_2O_3 in the Qser samples reflects the abundance of pyrite.

MgO is highly variable in the Qser zone and thus, a correlation with the potassic zone is not conclusive (Fig. 6.17). The relative enrichment of MgO in the Kser sample (Cu 1115) reflects the greater abundance of biotite.

The relatively low CaO values in the potassic alteration and Kser samples (Cu 1115 and Cu1112) compared to the Qser samples are consistent with the absence of Ca-bearing silicate and sulphate minerals in the potassic (Fig. 6.17). CaO in the Qser zone samples is probably due to the presence of Ca-sulphate veins in the Qser.

The Kser sample (Cu 1115) has less Na_2O than the potassic sample because of the alteration of Na-feldspar to sericite (Fig. 6.16). The complete depletion of Na_2O in the Qser samples represents the complete alteration of Na-feldspar.

The Kser sample has more K_2O relative than both the potassic and Qser samples (Fig. 6.17). This relative enrichment is due to the sericite replacement of the Na-feldspar, resulting in a relative increase of K. The alteration of K-feldspar and biotite results in a relative depletion of K (equations [6.2], [6.3]), as is seen in the Qser whole-rock analyses (Fig. 6.17).

P_2O_5 values are similar in the potassic and Qser alteration zones (Fig. 6.17). Although apatite was not observed in the Qser zone, the P may be the result of remnant,

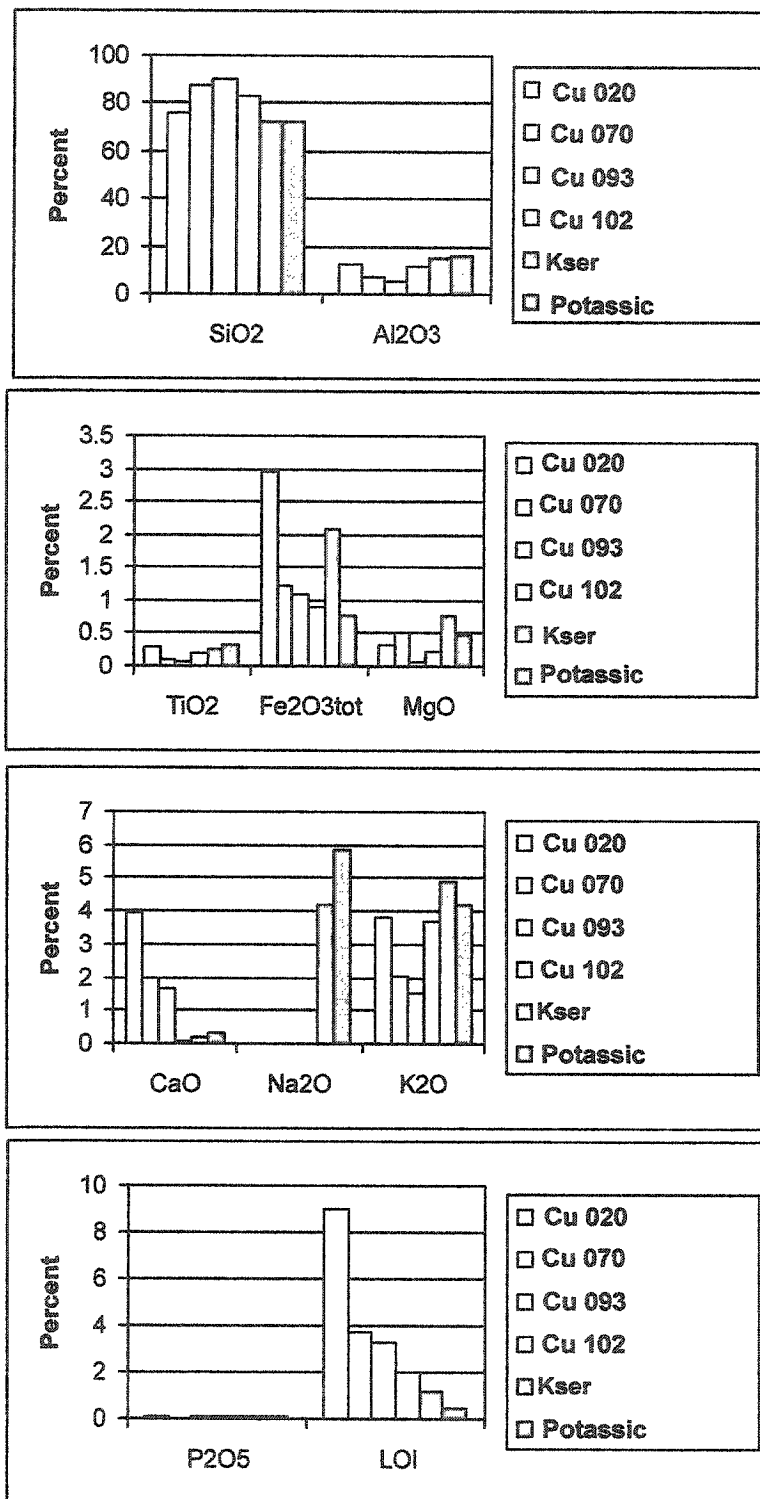


Figure 6.17. Comparison of the whole-rock geochemistries of the Qser and potassic alteration samples. Kser (Cu1115) represents Qser-partially-overprinting-potassically-altered sample.

fine-grained apatite. It may also represent another phosphorous mineral or the substitution of P for S in sulphate minerals such as alunite which has been reported in the Qser zone. There is significant turquoise associated with supergene zone which could account for the P, but no turquoise was observed in our samples.

LOI values increase from the potassic alteration zone to the Kser to Qser (Fig. 6.16). This increase in LOI reflects the increase in hydrous phases (Fig. 6.17). Hydration of albite and K-feldspar to muscovite, as well as hydration of anhydrite to gypsum accounts for this increase in LOI.

6.4 Geochronology

Reynolds et al. (1998) concluded that the Qser alteration event occurred at 31.0 ± 0.3 Ma based on the analysis of four samples (Table 3.5). Subsequent dating of sericite was done for this study in the same laboratory (Dalhousie University) to corroborate the age of the Qser alteration event.

Potassic samples partially overprinted by Qser alteration were also dated and were determined to be affected by the Qser alteration. In each potassic sample (Cu 494, Cu 442, Cu 1115 and Cu 1105), the albite has been replaced by white mica or clay, leaving the K-feldspar and biotite apparently unaffected.

6.4.1 White mica

Five samples were selected for dating from the Qser sample suite, based on typical Qser mineralogy and textures and the presence of adequate sample material for analyses.

Results and isotope correlation plots are reported in Appendix G. Dating sericite is difficult because the fine-grain size and the potential for recoil in stepwise heating.

Samples Cu 093, Cu 082, and Cu 070 were obtained from drill core 3472 at the 3200N section (602.60 m, 332.20 m, 224.33 m depth, respectively). They were sampled at varying depths to determine the possible effect of elevation on age (Appendix A).

Cu 093

Sample Cu 093 yielded a concordant spectrum with a total gas age of 31.1 ± 0.2 Ma (Table 6.3). The preferred age over the final 75% of the ^{39}Ar released is 31.1 ± 0.3 Ma (Fig. 6.18). At a step around 85%, the argon was lost due to a system error (Fig. 6.18). The absence of argon eliminates the importance of this step in the age calculation and thus did not contribute to the age calculation.

Table 6.3 $^{40}\text{Ar}/^{39}\text{Ar}$ ages for the Qser zone.
The mean preferred age of the muscovite is 31.1 ± 0.2 Ma.
*- not used to calculate the mean.

Sample #	Total gas age	Preferred age
Cu 070	31.0 ± 0.5 Ma	31.0 ± 0.6 Ma
Cu 082	31.4 ± 0.2 Ma	30.9 ± 0.3 Ma
Cu 093	31.1 ± 0.2 Ma	31.1 ± 0.3 Ma
Cu 203	31.2 ± 0.2 Ma	30.6 ± 0.3 Ma*
Cu 519	31.5 ± 0.2 Ma	32.1 ± 0.3 Ma*

An isotope correlation plot of Cu 093 confirms the preferred age of 31.1 Ma, with an error of ± 0.4 Ma (Fig. 6.18). The correlation is well constrained by the data.

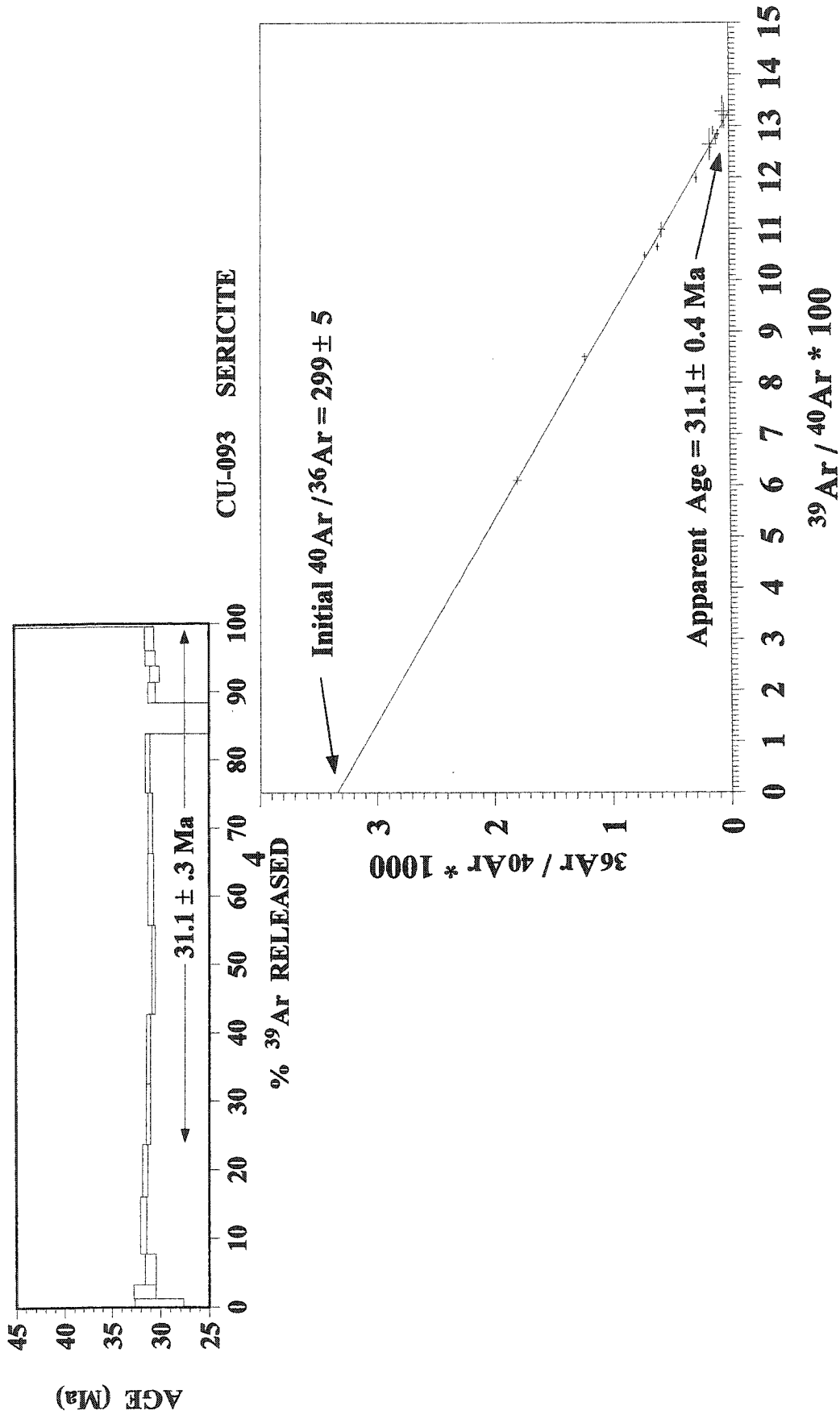


Figure 6.18. a) $^{40}\text{Ar}/^{39}\text{Ar}$ age spectrum of sericite in sample Cu 093. b) Isotope correlation diagram for sample Cu 093 displaying a line well-constrained by the data.

Cu 082

Sample Cu 082 has a narrow range of ages (31.4 to 30.6 Ma) over 40% of gas released (Fig. 6.19). The preferred age is 30.9 ± 0.3 Ma.

The range in ages (i.e., 0.8 My) does not fulfil the requirements of Fleck et al. (1977) for an acceptable plateau. According to Fleck et al. (1977), the allowable spread for this particular sample, based on errors, is 0.63 My. However, since 1977, there has been an increase in precision of the $^{39}\text{Ar}/^{40}\text{Ar}$ method and a decrease in the size of error bars, so it is possible that this sample represents a reasonable plateau.

Cu 070

Sample Cu 070 gives a poorly defined plateau age of 31.0 ± 0.6 Ma over 50% of gas, but has relatively large error ranges (Fig. 6.19). This age is within the range of the previous two samples and the reported age of the Qser alteration event (Reynolds et al. 1998).

Cu 203

This spectrum is U-shaped, with a large range in ages (Fig. 6.20). The shape of the spectrum may be due to incomplete resetting of the argon during the Qser event and, therefore, the older age steps may represent the ages of the potassic minerals being reset. However, it is more likely that some of the steps in Cu 203 have been affected by recoil. The preferred age is 30.6 ± 0.3 Ma, an average over the final 60% of gas released. This age has not been used in the calculation of the mean age of the Qser due to complications with the spectra.

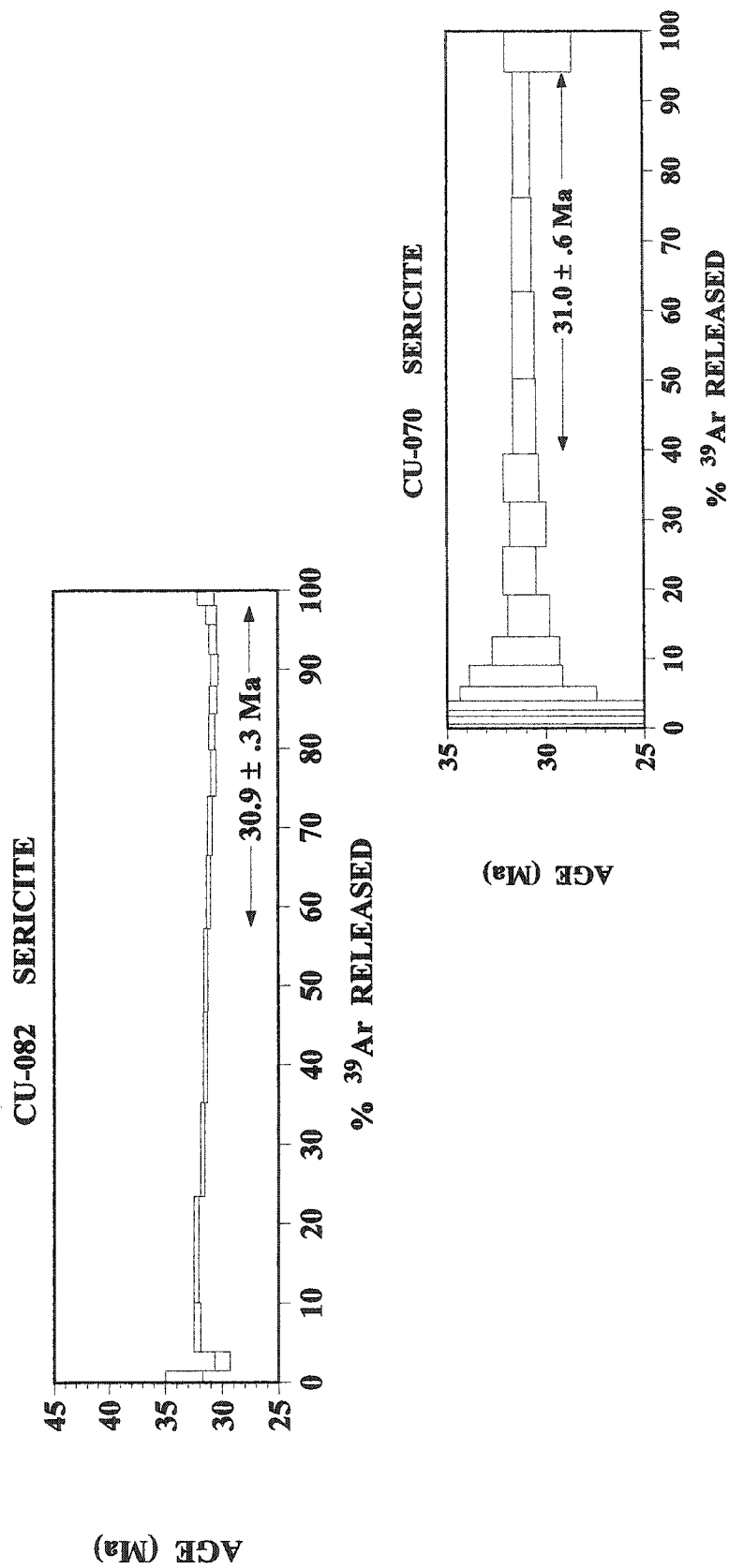


Figure 6.19. ⁴⁰Ar/³⁹Ar ages of sericite in the Qser alteration zone (Cu 070 and Cu 082).

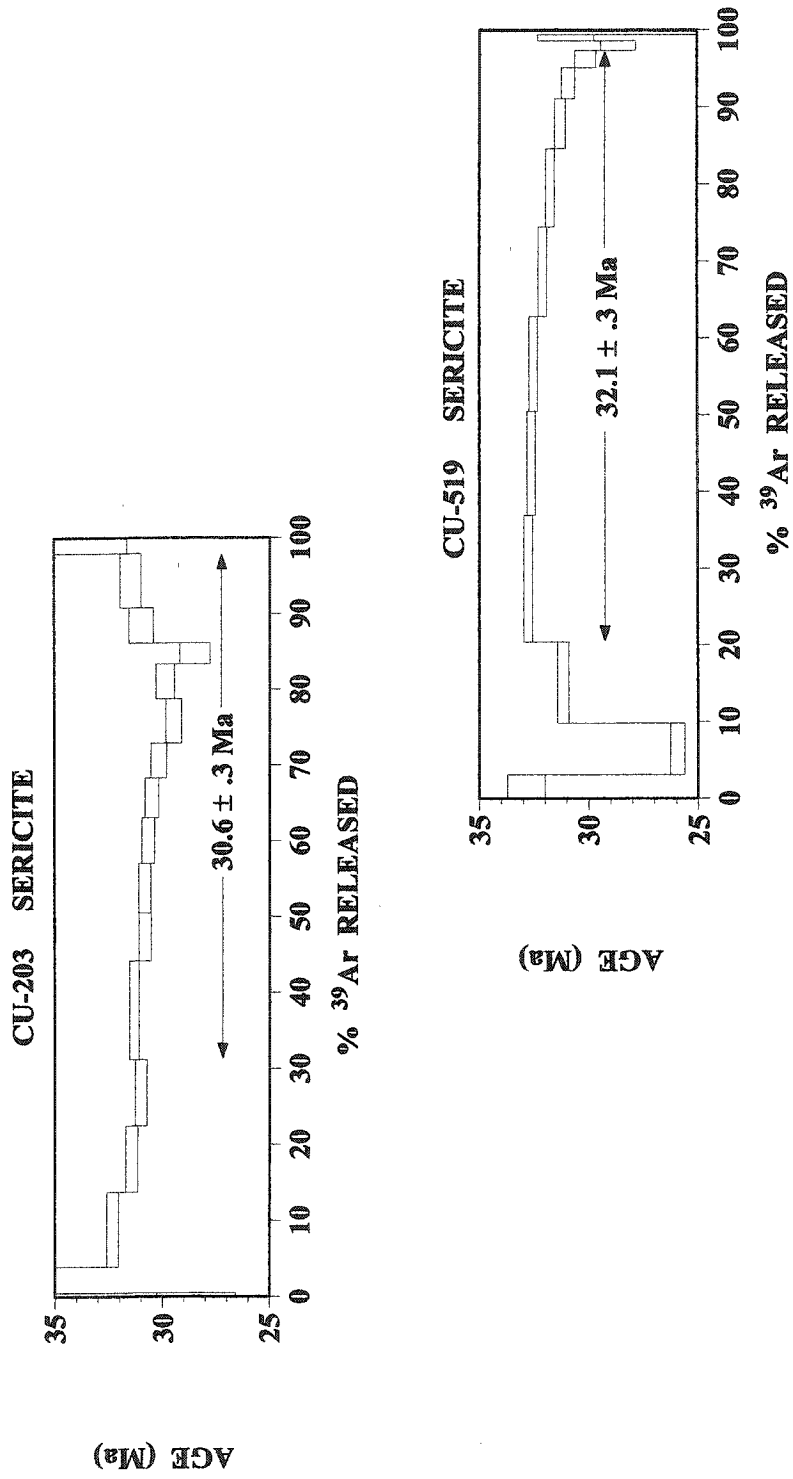


Figure 6.20. $^{40}\text{Ar}/^{39}\text{Ar}$ ages of sericite in the Qser alteration zone (Cu 203 and Cu 519).

Cu 519

Cu 519 has a saddle-shaped spectrum, with a large range of ages (Fig. 6.20). The preferred age is 32.1 ± 0.3 Ma, an average over 70% of the gas released. The sample does not give a plateau age and is not considered reliable. Therefore, it has not been used to determine the mean age of the Qser zone.

6.4.2 Potassic alteration overprinted by Qser

In an attempt to better constrain the age of the potassic event, four samples were analyzed using $^{40}\text{Ar}/^{39}\text{Ar}$. However, as will be shown, these samples have been overprinted by Qser alteration, which has affected the final ages.

6.4.2.1 K-feldspar

As it was impossible to ensure that sericitized albite inclusions were not contained in the K-feldspar separates, it was important to look at the temperature of argon release, to ensure the ages determined were K-feldspar ages. The K-feldspar ages from samples Cu 442/Cu 494 (see below), Cu 1105 and Cu 1115 were dated to determine if their ages had been affected by the Qser event. In all cases, preferred ages were determined using gas that was released above 1150°C . The sericite should have released all its argon by this temperature and the only mineral being dated then should be the K-feldspar.

Cu 442 and Cu 494

K-feldspars from samples Cu 442 and Cu 494 were inadvertently analyzed together in the furnace. Both samples are from similar elevations at the same latitude.

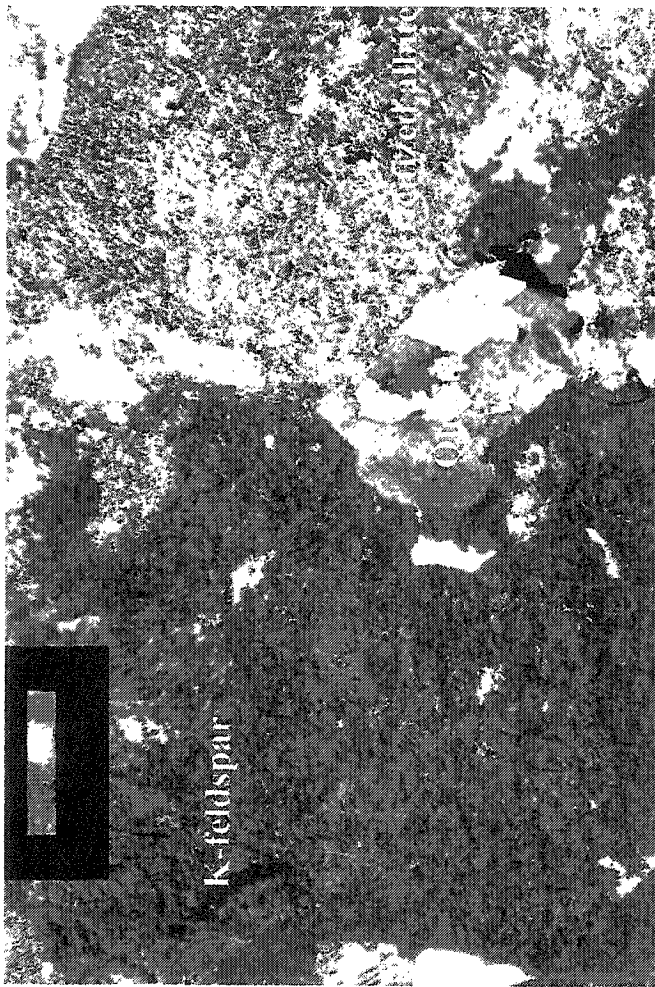
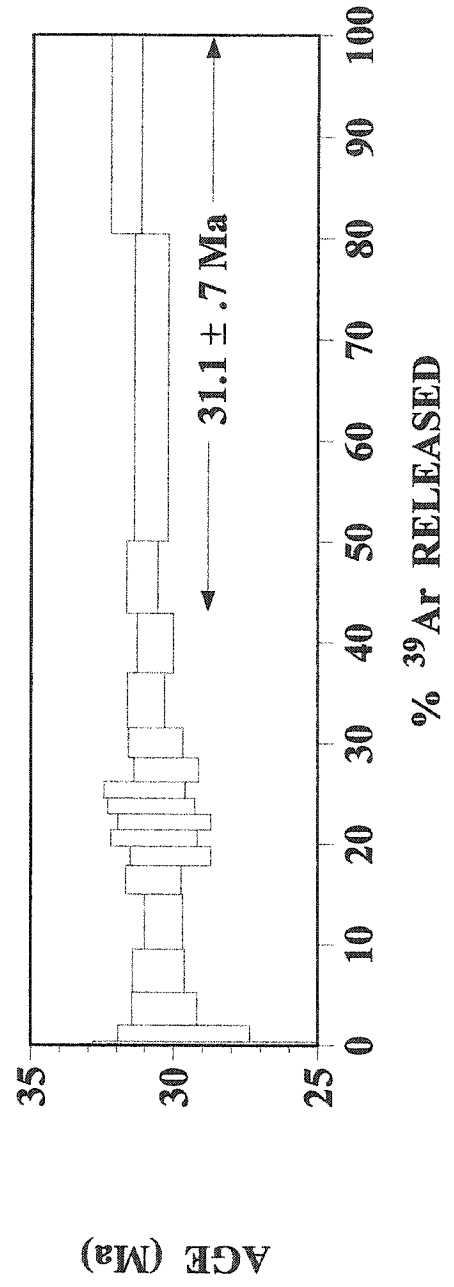


Figure 6.21. Albite in Cu 494 and Cu 442 are sericitized, leaving the K-feldspar relatively unaffected.

Cu 494 (mag. = 50X, F.O.V. = 2 mm, xpl)

CU-494/442 K-FELDSPAR



Both samples also represent potassic alteration with a Qser overprint. K-feldspar in both samples have inclusions of sericitized albite (Fig. 6.21).

The ages are somewhat concordant but with large errors. The final 55% of ^{39}Ar was released above 1150°C , well above the temperature at which ^{39}Ar should have been released from muscovite. These final three steps give an age of 31.1 ± 0.7 Ma which should represent the composite K-feldspar age.

The calculated error is relatively large, but the age is identical to the age of the Qser alteration event (Section 6.4.1), distinct from the time of the potassic event (Section 5.5), and 2.6 Ma lower than the reported age of the potassic alteration event (Reynolds et al. 1998).

Cu 1115

Cu 1115 is characterized by perthitic phenocrysts of K-feldspar with sericitized albite inclusions (Fig. 6.22). This sample Cu 1115 has a poorly defined spectrum (Fig. 6.22). The last 50% of ^{39}Ar was released above 1150°C and gives a preferred age of 31.5 ± 0.6 Ma (Table 6.4). The last two steps have large errors and are interpreted to be the result of recoil. The calculated error is relatively large but the calculated age is consistent with the Qser event (Section 6.4.1) and well below the age of the potassic alteration (Section 5.5).

Cu 1105

K-feldspar in Cu 1105 has inclusions of sericitized albite (Fig. 6.23). The final three degassing steps ($>1250^\circ\text{C}$) in sample Cu 1105 account for 55% of the ^{39}Ar release and give a preferred age of 31.8 ± 0.3 Ma. This age is slightly older than the other



Cu 1115 (mag. = 50X, F.O.V. = 2 mm, xpl)

Figure 6.22. Sample Cu 1115 has been partially overprinted by Qser alteration. b) Only steps over 1150°C were used to determine the age of the K-feldspar to eliminate the argon contributed by the sericite.

CU-1115 K-FELDSPAR

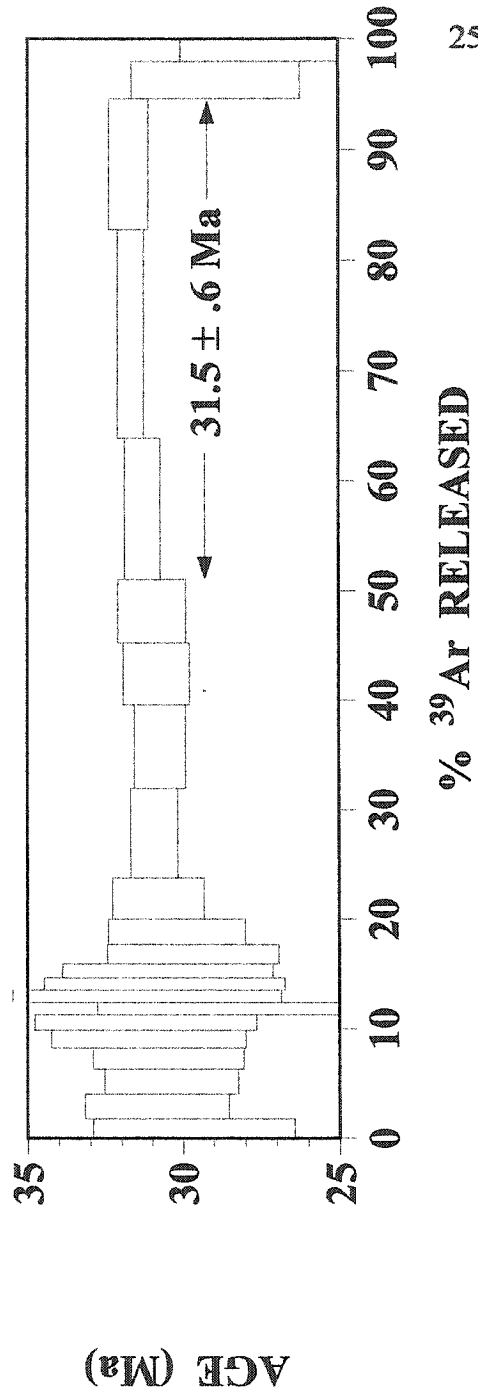
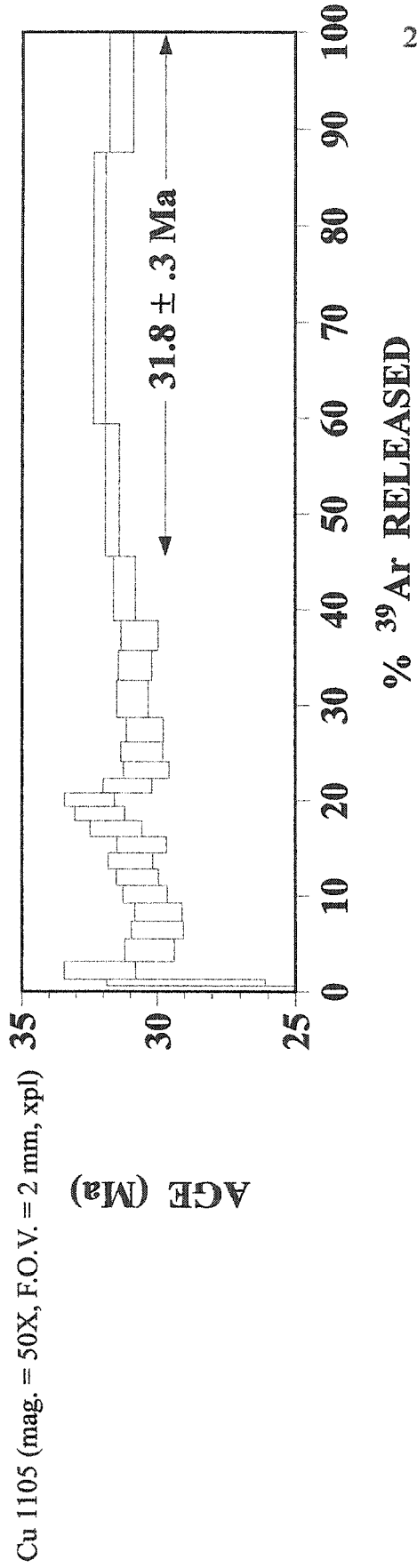




Figure 6.23. Sample Cu 1105 has been partially overprinted by Qser alteration, apparently resetting the K-feldspar argon age.

CU-1105 K-FELDSPAR



samples but certainly reflects a Qser alteration age, even though the K-feldspar is petrographically unaltered (Fig. 6.23).

6.4.2.2 Biotite

Samples of biotite from Cu 442, Cu 494 and Cu 1115 were dated initially to determine the age of the potassic zone. However, the ages apparently do not reflect that event; instead, they were assessed to determine the effect of the Qser alteration on the potassic alteration.

Cu 442

The total gas age of biotite in sample Cu 442 is 31.0 ± 0.3 Ma (Fig. 6.24). Leaving out three end steps which are interpreted to represent K-feldspar contamination, the preferred age is 31.1 ± 0.2 Ma.

Cu 494

The total gas age of sample Cu 494 is 30.9 ± 0.4 (Fig. 6.24). If reassessed to remove the end steps, the preferred age is 31.3 ± 0.3 Ma.

Cu 1115

Fine-grained pleochroic brown-yellow biotite in Cu 1115 is corroded along grain boundaries and is associated with rutile. This sample yielded a total gas age of 31.7 ± 0.2 Ma. The preferred age is 31.7 ± 0.4 Ma (Fig. 6.24).

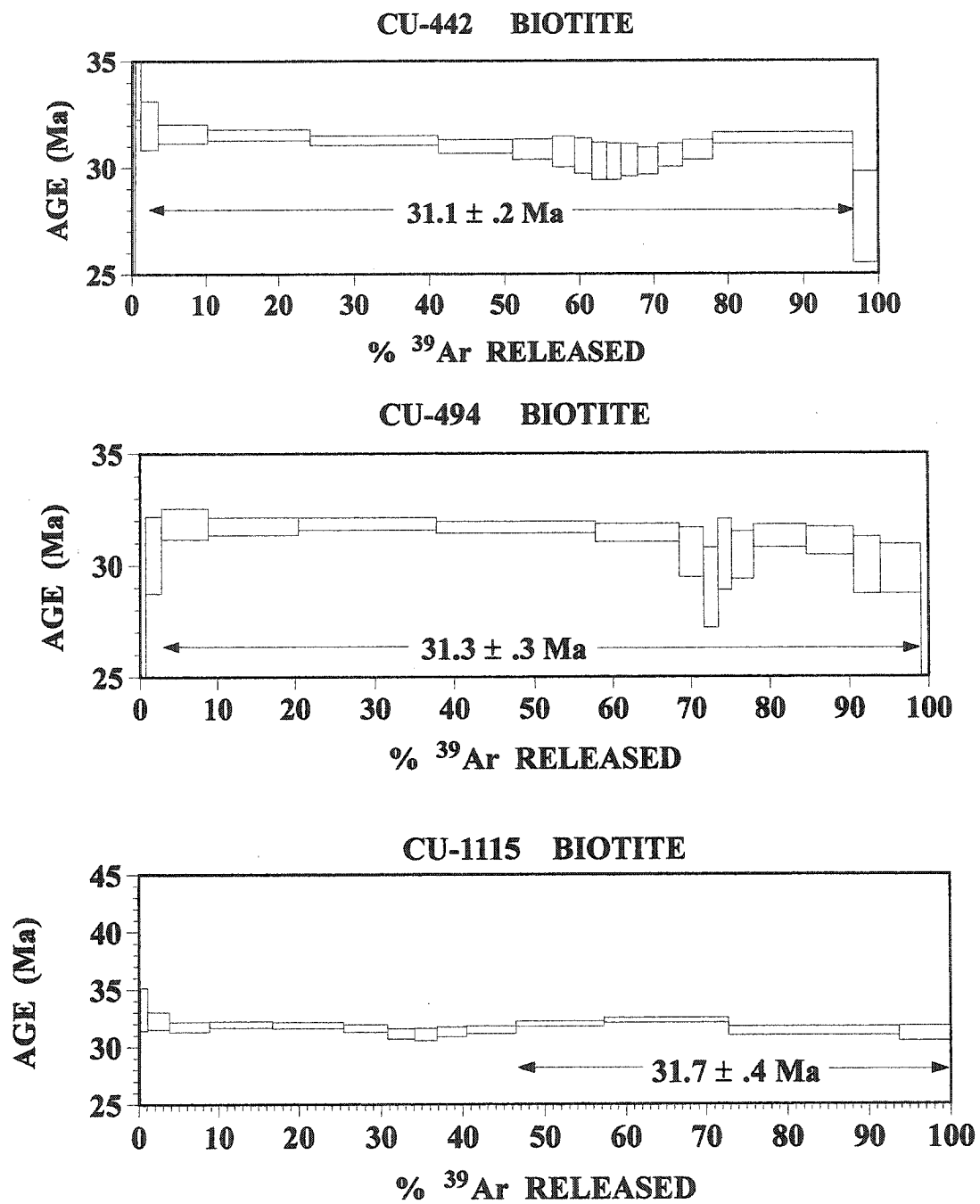


Figure 6.24. $^{40}\text{Ar}/^{39}\text{Ar}$ spectra from biotite in potassic samples overprinted by Qser alteration

6.4.3 Interpretation

Muscovite ages are given in Table 6.4. A comparison of total gas to preferred ages shows a minimal difference, supporting the reliability of the dates obtained.

Table 6.4 $^{40}\text{Ar}/^{39}\text{Ar}$ ages for potassic alteration minerals where the samples have been overprinted by the Qser zone. The mean biotite age is 31.4 ± 0.6 Ma. The mean K-feldspar age is 31.5 ± 0.7 Ma.

Sample #	Mineral	Total gas age	Preferred age
Cu 494/442	K-feldspar	30.8 ± 0.5 Ma	31.1 ± 0.7 Ma
Cu 494	Biotite	30.9 ± 0.4 Ma	31.3 ± 0.3 Ma
Cu 442	Biotite	31.0 ± 0.3 Ma	31.1 ± 0.2 Ma
Cu 1105	K-feldspar	31.3 ± 0.2 Ma	31.8 ± 0.3 Ma
Cu 1115	K-feldspar	30.8 ± 0.6 Ma	31.5 ± 0.6 Ma
	Biotite	31.7 ± 0.2 Ma	31.7 ± 0.4 Ma

Samples Cu 203 and Cu 519 have total gas ages close to the calculated mean age, supporting the hypothesis that their preferred ages were unreliable due to recoil effects.

Sample Cu 093 has the best spectrum and the isotope correlation plot is well defined by the data. Cu 093 has a preferred age of 31.1 ± 0.3 Ma which is nearly identical to the mean age of the three Qser white mica samples (31.0 ± 0.2 Ma).

Therefore, it is concluded that the Qser alteration event occurred at 31.0 ± 0.2 Ma.

Samples Cu 070, Cu 082 and Cu 093 are all located in drill core 3472. They are separated by a maximum of 388 m in elevation. The ages are nearly identical, suggesting that Qser alteration occurred at the same time over this range of elevations.

Total gas ages have been reported to illustrate how similar they are to the preferred ages (Tables 6.3 and 6.4). In the Qser samples, Cu 519 and Cu 203, the total

gas ages are more reasonable than the preferred ages, indicating that recoil was likely responsible for the unreliable spectra.

K-feldspar and biotite samples give mean ages slightly higher than those determined for the Qser alteration event (31.5 ± 0.7 Ma and 31.4 ± 0.6 Ma, respectively), but are consistently lower than those determined for the potassic zone (Section 5.5). These mean ages are coincident with the muscovite ages within their calculated errors. This consistency between ages is interpreted to have resulted from nearly complete resetting of the potassic ages by the Qser event.

Fine planes of alteration in the K-feldspar indicate microscopic and cryptoscopic pathways that have been healed by hydrothermal fluids. The temperatures of the Qser alteration are estimated to be 300 to 435 °C (Lewis 1997); these temperatures are higher than the closure temperatures of biotite and K-feldspar. The $^{40}\text{Ar}/^{39}\text{Ar}$ data indicates the potassic zone has been reheated, resetting the potassic ages.

6.5 Stable Isotopes

Separation of muscovite and quartz in the fine-grained, pervasively altered Qser samples was impossible, given the microscopic grain size and the size of the samples collected. Sample Cu 070 was the only sample with sericite flakes large enough to be separated from the quartz. The other five samples were a mixture of muscovite and quartz.

Qser alteration is a low temperature alteration (Table 2.3). Sulphur isotopic temperature calculations for sulphide-sulphate pairs indicate a temperature of 300-375 °C

for mineralization at Chuquicamata (Lewis 1997). The problem with using $\delta^{18}\text{O}$ to determine isotopic fractionation in this zone is that most $\delta^{18}\text{O}$ -fractionation studies have been developed for temperatures over 500°C .

6.5.1 Isotope geothermometry

Using the fractionation constants of Eslinger et al. (1979), a temperature of 421°C was calculated for the quartz-muscovite $\delta^{18}\text{O}$ pair (Cu 070). The Eslinger et al. (1979) fractionation constants are calculated for $350\text{-}500^\circ\text{C}$. Although the fractionation constants of O'Neil and Taylor (1969) were calculated for a temperature range of 400 to 600°C , here they give a temperature of 334°C for the quartz-sericite pair of Cu 070. Both calculated temperatures are consistent with the estimated temperature of Qser alteration in other porphyry copper deposits (Table 2.3) and at Chuquicamata (Section 3.5.2).

Hydrogen isotopes are not used as geothermometers because the isotopic fractionation factors among hydrous minerals are relatively insensitive to temperature (e.g. kaolinite-sericite pair), too sensitive to the chemical composition of the minerals (e.g. biotite), and not well calibrated for most minerals (Ohmoto 1986). Another major problem with a hydrogen isotope thermometer is that exchange between fluids and minerals occurs even at relatively low temperatures (Ohmoto 1986).

6.5.2 Isotopic equilibrium

As only one muscovite-quartz pair was analyzed, it is difficult to establish whether isotopic equilibrium was achieved. Taylor et al. (1971) suggested that, for temperatures $< 600^{\circ}\text{C}$, $\Delta_{\text{quartz-sericite}} < 2.5$ indicates disequilibrium. Sample Cu 070 has $\Delta_{\text{quartz-sericite}} = 2.6\text{‰}$ which is therefore consistent with isotopic equilibrium according to this criterion.

Quartz appears to be resistant to isotopic exchange with hydrothermal solutions even up to temperatures in excess of 500°C (Taylor et al. 1971). Therefore, unless there is specific evidence (e.g. petrographic) that the quartz recrystallized in a new environment, then the isotopic composition of quartz cannot be used as an indicator of the fluid phase associated with alteration (Taylor et al. 1971).

Taylor (1968) explains that the $\delta^{18}\text{O}$ of all plutonic igneous quartz lies in the range of 8.5 to 10.6‰. The $\delta^{18}\text{O}$ value of the quartz in Cu 070 is 11.2‰, indicating it is not magmatic. If the quartz from Cu 070 was precipitated during the Qser alteration, then it may have equilibrated with the muscovite. This would be consistent with the precipitation of quartz during the hydrolysis of K-feldspar, biotite and albite (equations 6.1, 6.2, and 6.3).

Petrographically, sample Cu 070 is massive quartz, mica and sulphides. The massive habit of the quartz suggests that the quartz could have precipitated and achieved isotopic equilibrium during the Qser event.

6.5.3 Isotopic fractionation

The $\delta^{18}\text{O}$ and δD values of the fluids that formed in equilibrium with the quartz and sericite were determined assuming a temperature of 350°C , based on oxygen and sulphur isotope geothermometry from this study and Lewis (1997). As the samples were a mixture of quartz and muscovite in most of the samples, end-member values were calculated using quartz and muscovite fractionation constants so that a range of the $\delta^{18}\text{O}$ values could be estimated (Fig. 6.25).

6.5.4 Interpretation of quartz-mica isotopic data

The temperature of isotopic equilibration in the Qser zone is estimated to be $\sim 334\text{--}421^\circ\text{C}$. Unfortunately, this range does not refine the constraint on the previously estimated temperature range for the Qser. However, the range of mineralization temperatures, $300\text{--}375^\circ\text{C}$, is consistent with the lower temperature determined (Lewis 1997).

The high value for the quartz in Cu 070 ($\delta^{18}\text{O} = 11.2\text{‰}$) is similar to that for sample Cu 442 ($\delta^{18}\text{O} = 11.1\text{‰}$) in the potassic alteration zone, indicating that the alteration of albite in the partially overprinted potassic zone may have been deposited a second generation of quartz.

Sericites are fine-grained and post-depositional isotopic exchange is a concern (Taylor et al. 1971). If sericite has undergone extensive O and H isotopic exchange in local groundwater, under near-surface conditions, the $\delta^{18}\text{O}$ and δD may lie near the

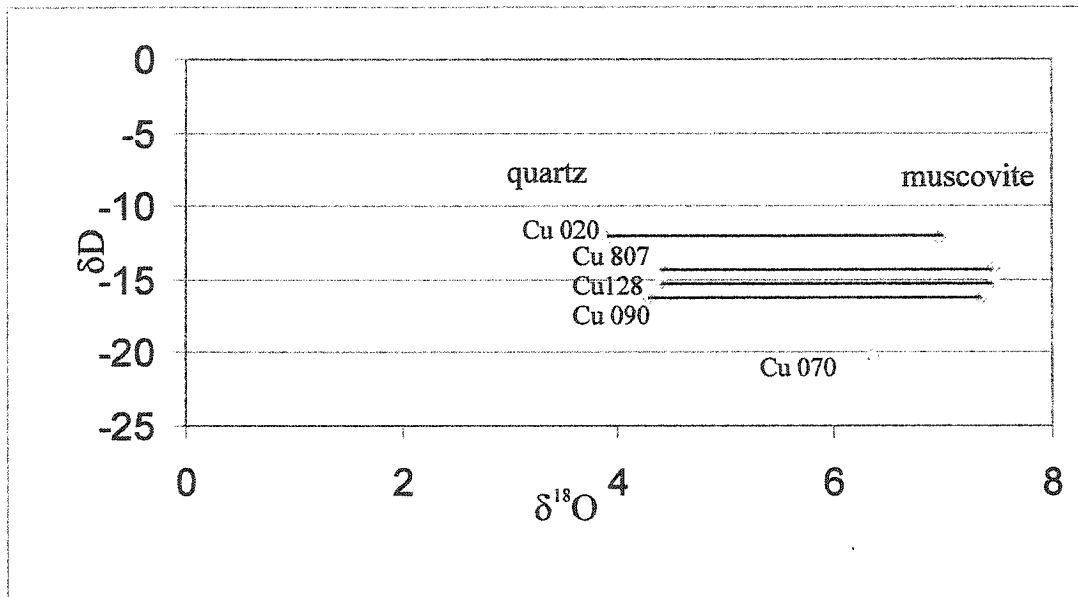


Figure 6.25. Samples 020,090, 128, and 807 are mixtures of quartz and muscovite and are plotted here to show the range of possible isotopic compositions. Cu 070 was a pure muscovite sample and thus plots as a single point.

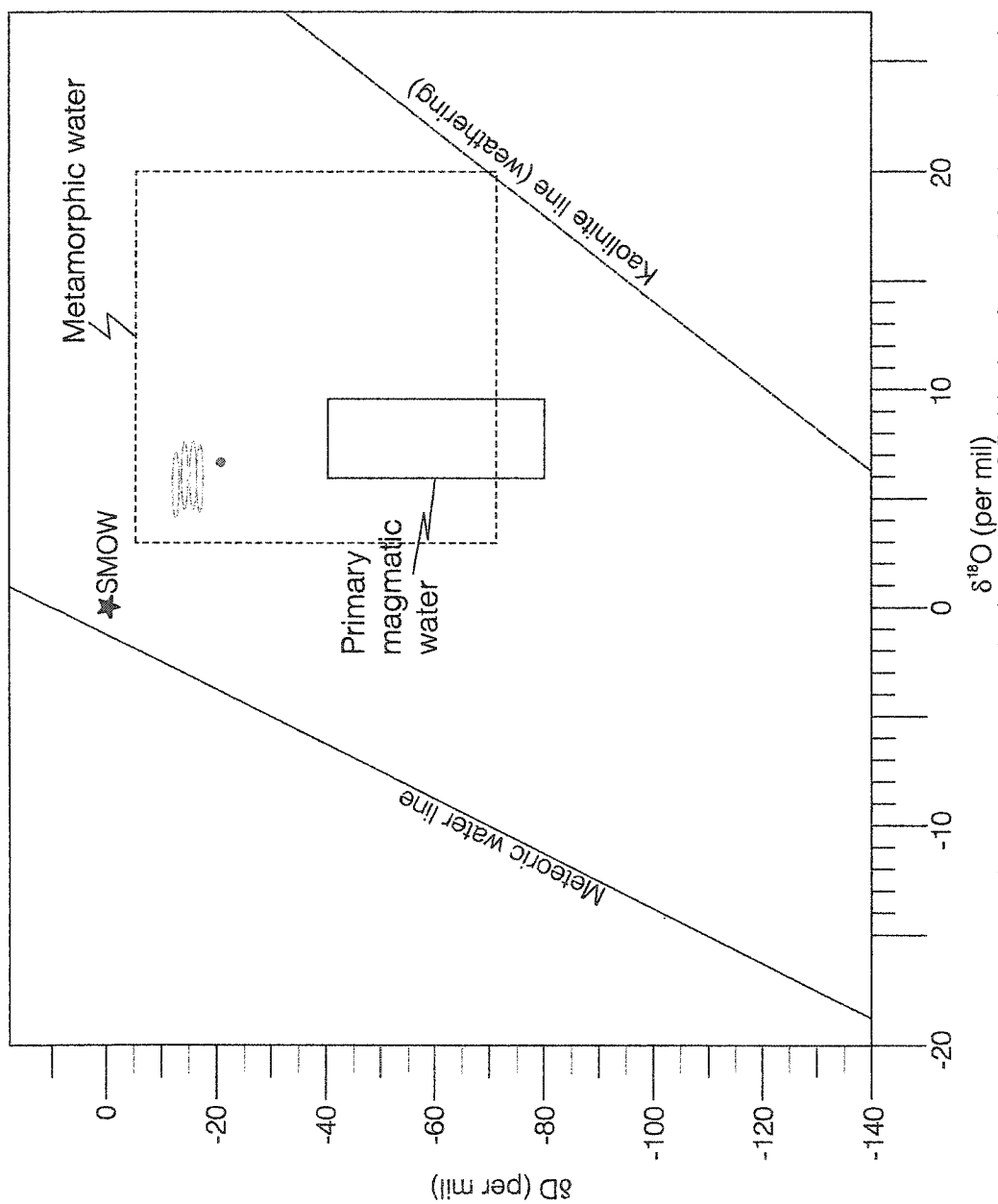


Figure 6.26. Oxygen-deuterium plot to ascertain the source of fluids that formed the Qser alteration zone (after Sheppard 1986 and references therein). The calculations are based on equilibrium achieved at 350°C. See Figure 6.25 for an explanation of the range of values .

confining pressure, or a decrease in the salinity (Rimstidt 1997). Such a decrease in confining pressure would accompany the second boiling associated with the Qser stage of porphyry copper intrusion (Burnham 1979).

The Qser zone is concluded to have an age of 31.0 Ma. This event has reset the potassic alteration ages and therefore care must be taken when sampling to further constrain the age of the potassic alteration event.

Stable isotopes indicate the Qser alteration event equilibrated at temperatures of 334 to 421 °C. The fluids were a mixture of meteoric and magmatic with low pHs.

Chapter 7

Discussion

7.1 The relationship between the Fortuna and Chuquicamata Intrusive Complexes

As explained earlier, the Fortuna Intrusive Complex, exposed west of the West Fault in the Chuqui pit, was initially thought to be an integral part of the Chuqui mineralized system (Lindgren 1917). In the 1970's, it was suggested that the Fortuna Granodiorite could be the 'unaltered' equigranular root of the Chuqui Porphyry, faulted vertically to abut the giant porphyry copper deposit (e.g. Sillitoe 1973). Henceforth, the Fortuna Intrusive Complex was interpreted in chemical and petrographic comparisons as an unaltered, deep, equigranular equivalent of the Chuquicamata Intrusive Complex (e.g. Parada et al. 1987).

As regional field mapping advanced (e.g. Ambrus 1979, Dilles et al. 1997), it was hypothesized that the Fortuna Intrusive Complex could be part of the El Abra porphyry system, located ~35 km to the north. These authors proposed that the El Abra System was displaced by ca. 35 to 40 km with sinistral movement along the West Fault to dock by the Chuquicamata Intrusive Complex (Ambrus 1977, Makshev 1990, Dilles et al. 1997). The significance of the Fortuna Intrusive Complex and the nature of the movement along the West Fault remain matters of heated controversy, made evident from the recent literature disputing the amount of vertical and horizontal movement on the West Fault (McInnes et al. 2000, Mathur et al. 2001, McBride et al. 2001). This debate is important to the mining community, because if, as hypothesized, the Chuquicamata

porphyry deposit was divided by a strike slip fault, where is the other 'half' of the ore body? Many millions of dollars have been spent in trying to locate it in the last decade.

Although many authors have studied the movement on the West Fault (e.g. Ambrus 1979, Lindsay 1998, McInnes et al. 2001) and have petrochemically compared the Fortuna to the El Abra Intrusive Complex (e.g. Makshev 1990, Dilles et al. 1997, Tomlinson et al. 1997), the only studies that compare the Fortuna and Chuquicamata Intrusive Complexes are those that assume the Fortuna was the *root* of the Chuquicamata system (e.g. Parada et al. 1987). The Fiesta Granodiorite, the main body of the Fortuna Intrusive Complex, and the Este Porphyry, the principal unit of the Chuquicamata Intrusive Complex, were described in Chapter 4 of this thesis. They are contrasted and compared here in the context of this discussion. The reader is referred to Figures 4.4 to 4.14 and Figs. 4.21 to 4.25 for clarity.

Petrologically and chemically, the Fiesta Granodiorite is more mafic than the Este Porphyry (66.02 vs. 70.55 wt.% SiO₂). The Fiesta Granodiorite has relatively more amphibole and biotite, and the plagioclase is more calcic (Figs. 4.6, 4.7, and 4.9). This more mafic mineralogy is reflected in the whole-rock geochemistry where the Fiesta Granodiorite is consistently enriched in mafic elements (i.e. TiO₂, Fe₂O₃, MgO, and CaO) compared to the Este Porphyry (Fig. 4.21). Although mafic minerals are more abundant in the Fiesta Granodiorite, the mineral compositions are similar to those in the Este Porphyry (i.e. actinolite to magnesio-hornblende; oligoclase to andesine feldspar) (Figs. 4.6 and 4.7).

The similar mineral compositions and SiO₂ contents of these two units would

appear to support the hypothesis that the Fiesta Granodiorite is the root of the Este Porphyry (Fig. 4.21). The similar Ba-enrichment in the K-feldspar (Fig. 4.8 and 4.13) and trace-element enrichment (Fig. 4.9) in the titanite of the Fiesta Granodiorite and Este Porphyry also support a common genesis. Still, the Fiesta Granodiorite appears to be too felsic to have been the *source magma* of the Este Porphyry.

Although inconclusive, hornblende geobarometry indicates that the Fiesta Granodiorite probably crystallized at pressures below 2 kbars. This pressure is too shallow to have been the *root* of the Este Porphyry, which probably crystallized at similar pressures. Dating by McInnes et al. (2001) suggests only 600m \pm 100m vertical displacement along the West Fault. The open pit is over 800m deep and no “Fiesta-like” root has been observed. It is obvious that the alteration extends much deeper, indicating that the Fiesta Granodiorite cannot possibly represent the unaltered root of the Chuquicamata Intrusive Complex.

Using the $^{40}\text{Ar}/^{39}\text{Ar}$ dating method, mean ages of 37.6 ± 0.7 Ma to 35.5 ± 0.2 Ma for amphibole and K-feldspar, respectively, were determined for the Fiesta Granodiorite (Chapter 4). Using these ages and those reported in Table 3.1 and Table 3.3, cooling curves were determined for the Fiesta Granodiorite and the Este Porphyry (Fig. 7.1). It is clear from Figure 7.1 that the Fiesta Granodiorite is considerably older than the Este Porphyry. Intrusion ages of 37.6 ± 0.7 Ma for the Fiesta Granodiorite and 34.6 ± 0.2 Ma for the Este Porphyry (U/Pb zircon ages of Tomlinson et al. 1997 and Ballard et al. 2001, respectively) indicate a difference of more than 3 My. If the Fiesta Granodiorite cooled at 35.5 Ma ($^{40}\text{Ar}/^{39}\text{Ar}$ K-feldspar cooling), it could not have been the *source* of the 34.6 Ma

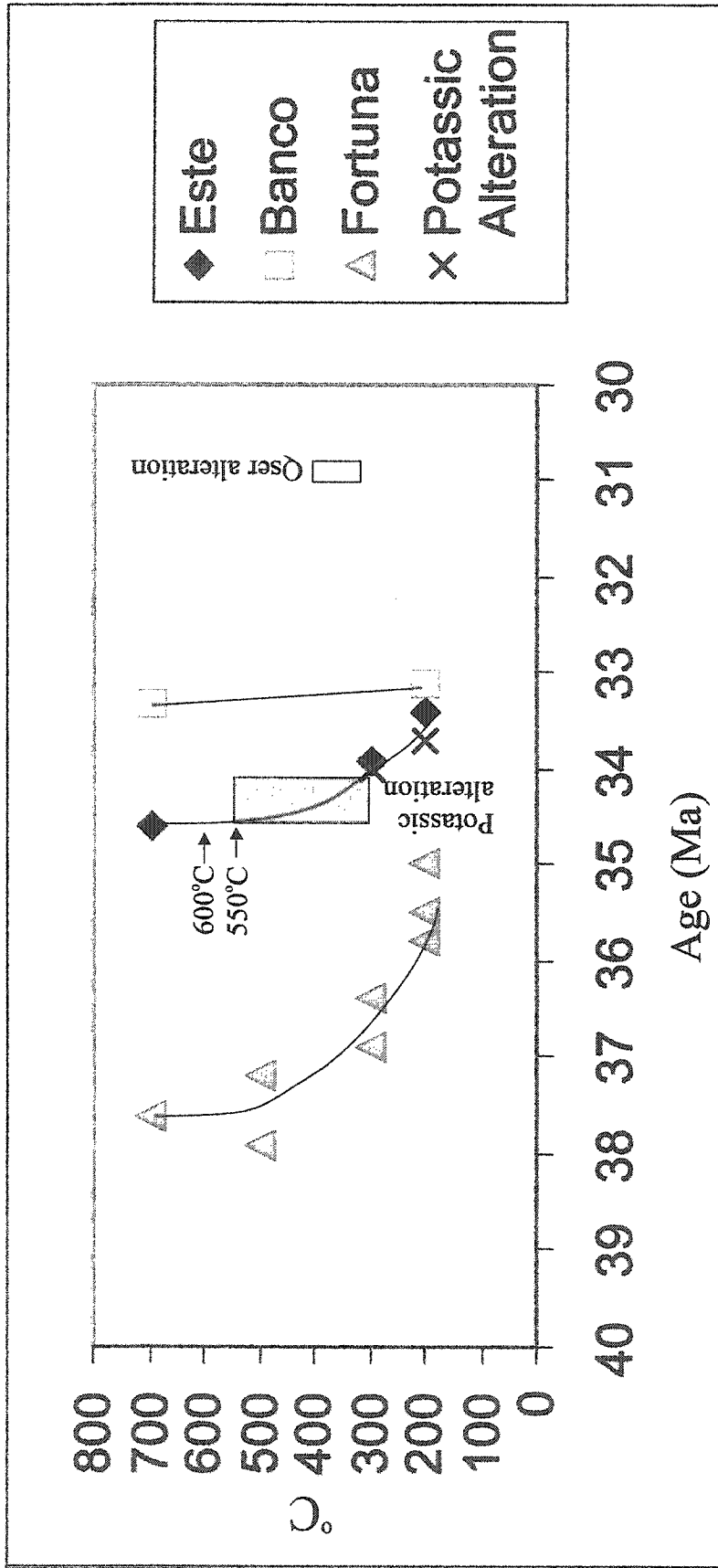


Figure 7.1. Cooling curve of the Fortuna and Chuquicamata Intrusive complexes. Age-temperature plot of alteration events in the Chuquicamata deposit. The Este and Banco porphyries have steep cooling curves based on the $^{40}\text{Ar}/^{39}\text{Ar}$ data from Reynolds et al. (1998) and the U/Pb data of Ballard et al. (2001). They are considerable younger than the Fortuna Intrusive Complex (based on U/Pb ages of Dilles et al. 1997, apatite of Maksiav and Zentilli 1999 and this study). The potassic alteration is approximately the same age as the Este Porphyry. As the potassic alteration and the fresh Este Porphyry are considered the same unit, a single cooling curve was calculated for them. Calculation of the range of temperatures is constrained by closure temperatures of the dating techniques as well as S- and O-isotopes from this thesis and Lewis (1997); these suggest an age range of 34.1 to 34.6 Ma for the potassic alteration/fresh Este Porphyry. The Qser is assumed to have formed at 300-400°C at ~31.0 Ma.

intrusion of the Este Porphyry. Cooling ages ($^{40}\text{Ar}/^{39}\text{Ar}$ of biotite and K-feldspar) of the Este Porphyry are 2.1 to 2.5 My younger than those from the Fiesta Granodiorite (Fig. 7.1). This broad difference in ages totally eliminates the possibility that the Fiesta Granodiorite is the root or the source of the Este Porphyry.

So, how is it that the Este Porphyry and the Fiesta Granodiorite are so similar in petrography and geochemistry and yet are not genetically related? It is evident from the REE data (Fig. 4.25) that the Fiesta Granodiorite and Este Porphyry share a similar source and were both highly oxidized magmas with no negative Eu-anomaly.

Figure 7.2 shows a model for the production of similar intrusions from a common magma chamber. Partial melting above the subducted slab occurred during the dehydration of the subducted slab and the overlying sediments, and the crustal thickening and shortening related to the strain of plate convergence (Chapter 2) (e.g. Maksaeu and Zentilli 1999, Kay and Mpodozis 2001). It has been proposed that the Eocene-Oligocene porphyry deposits are merely apophyses from a larger magma chamber (Fig. 7.2) (e.g. Sillitoe 1973, Tosdal and Richards 2001). Given the present tectonic situation (e.g. Wigger et al. 1994) (Chapter 2) this magma chamber (Fig. 7.2), formed along the magmatic front during the Eocene-Oligocene by ponding of magma that rose through lithospheric weaknesses above the subducting oceanic slab (Wigger et al. 1994, Maksaeu and Zentilli 1999). Apophyses rose from this magma chamber through transtensional domains along the Domeyko Fault System (Lindsay 1998) as differentiated, volatile-rich magmas (e.g. Burnham 1979, Hedenquist and Lowenstern 1994) (Fig. 7.2). These apophyses rose to within 1-3 km of the surface (Burnham 1979, Cloos 2001), exsolving

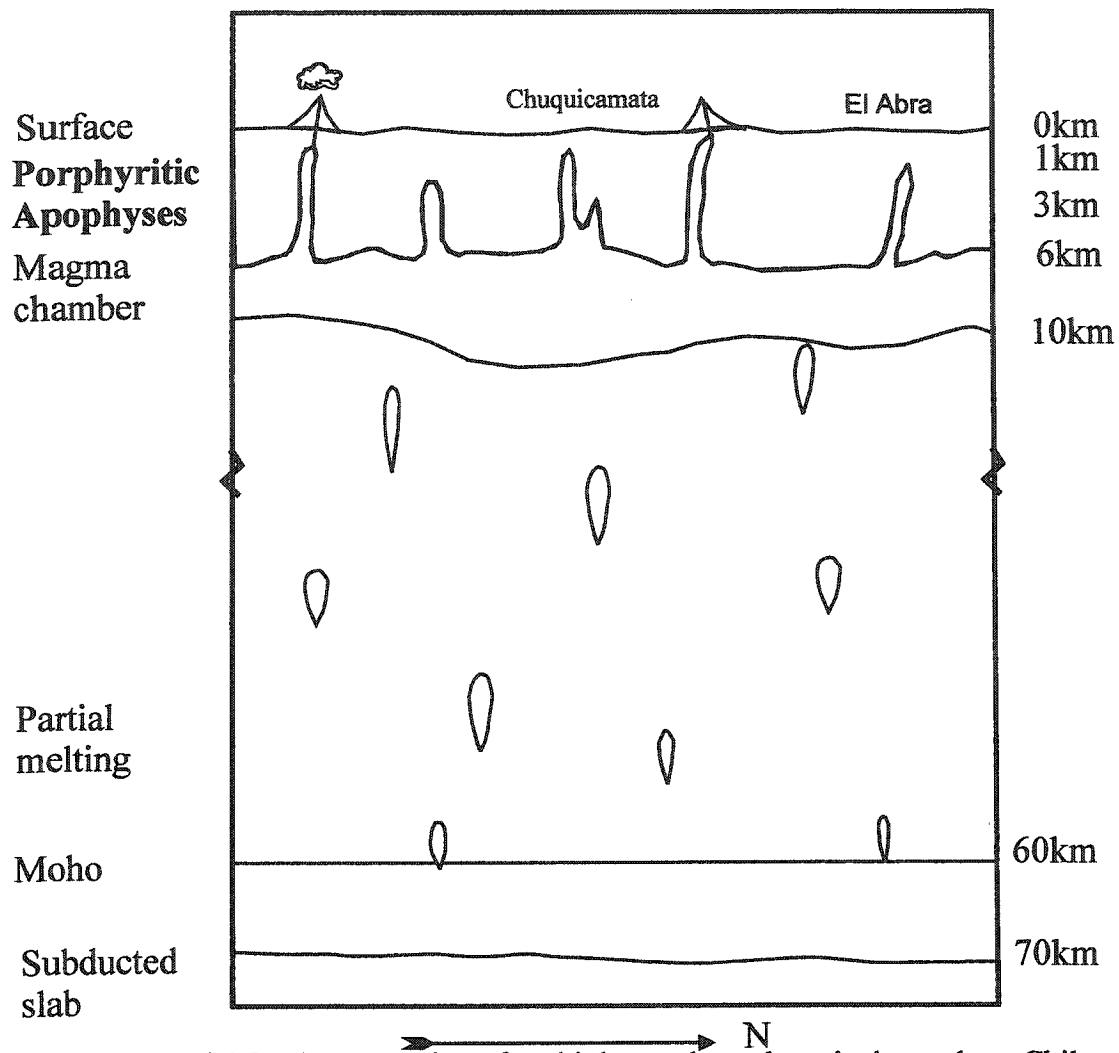


Figure 7.2. Model for the generation of multiple porphyry deposits in northern Chile. Partial melting above the subducted slab was triggered by crustal shortening and thickening, and the dehydration of the subducted slab and sediments (Maksaev and Zentilli 1999, Kay and Mpodozis 2001). A magma chamber formed at 6 to 10km depth (Sillitoe 1973, Wigger et al. 1994, Tosdal and Richards 2001) where the magmatic front was located during the Eocene-Oligocene 30 km west of where it is today (Maksaev 1988). The depth of the subducted slab that generated the Eocene-Oligocene porphyry deposits is still unresolved; however, radiometric isotope studies by Zentilli et al. (1988) and Maksaev (1990) suggest that the melts were mantle-derived (Chapters 2 and 3). Porphyritic apophyses rise, from the 6 to 10 km deep magma chamber along transtensional domains of the Domeyko Fault System (Lindsay 1998), to depths of 1 to 3 km (Sillitoe 1973, Burnham 1979). This model borrows from Sillitoe (1973), Hedenquist and Lowenstern (1994), Lindsay (1998), Maksaev and Zentilli (1999), Kay and Mpodozis (2001), and Tosdal and Richards (2001).

volatiles and crystallizing as porphyritic dykes (Burnham 1979, Hedenquist and Lowenstern 1994, Cloos 2001) (Fig. 7.2).

The modern day seismic refraction and geomagnetic deep sounding work of Wigger et al. (1994) and Schwarz et al. (1994) shows that a low resistivity zone as large as 50 to 200 km lies today under the Central Andes at depths as shallow as 20 km; this zone is interpreted to be a pocket of magma. The residence time of these magma chambers is more than 10 My. From this modern history, it is hypothesized that hot magmatic bodies of this magnitude existed along the Eocene-Oligocene magmatic front (Fig. 2.7).

Therefore, the El Abra-Fortuna Intrusive Complex and the Chuquicamata Intrusive Complex may have shared a common *source*, thus explaining their similar petrographies and geochemistries. Nevertheless, radiometric dating indicates that the Fortuna Intrusive Complex intruded prior to the Chuquicamata Intrusive Complex.

7.2 The age of the Banco Porphyry

A cooling curve for the Este and Banco Porphyries was constructed using the ages in Table 3.3. Figure 7.1 shows the Banco Porphyry is consistently younger than the Este Porphyry, even considering the different analytical techniques and the different blocking temperatures.

The relative timing of the Banco Porphyry intrusion is supported by the lack of albite. The presence of oligoclase indicates that the Banco Porphyry was unaffected by potassic alteration and, therefore, it must have been intruded following the potassic

alteration of the Este Porphyry, as displayed in Figure 7.3c. This relationship is supported by the consistently older radiometric ages of the potassic alteration (33.7-33.9 Ma) than the Banco Porphyry (~33 Ma). The above facts refute the claim by Ballard et al. (2001), that the Banco Porphyry is the *source* of fluids for the potassic alteration.

As shown schematically in Figure 7.2, Banco Porphyry was probably another apophysis from the magma chamber at depth. Rare-earth element data (Fig.4.25) suggest that the Este and Banco Porphyries probably shared a parent magma, as described above. The subvolcanic Banco Porphyry, whose aphanitic groundmass has led to it being called 'porcelain', obviously cooled very quickly, chilled on already cool altered rocks of the Este Porphyry.

7.3 The nature of the potassic alteration

The origin of the potassic alteration assemblage is a major focus of this project. Is the potassic alteration a more slowly cooled version of the fresh Este Porphyry or was the Este Porphyry affected by a later potassic hydrothermal event, as proposed by Ballard et al. (2001)? Are the megacrystic K-feldspars found in the potassically altered Este Porphyry magmatic or hydrothermal in origin? Indeed, how does one tell the potassically altered from fresh host rock? These questions were central to this study on alteration and fundamental for the geological staff of the mine. After all, how can one characterize the changes that affect the host rock if one can't recognize the *primary* mineralogy?

Megascopically, the *fresh* versus *potassically altered* Este Porphyry appear very similar. The presence of amphibole and titanite in the fresh sample are not discernable in

hand specimen, nor is the composition of the plagioclase. The most important distinguishing feature of the potassic zone is the absence of Ca-bearing silicates. The presence of albite is a more diagnostic feature than the megacrystic K-feldspars (which are also present in the fresh Este Porphyry) or the biotite (present only locally and the compositional ranges overlap).

The distinction between the potassic and fresh rocks is very important but the question as to the origin of the potassic alteration zone has not yet been answered. Is the potassic assemblage *magmatic* or *hydrothermal* in origin?

The **K-feldspars** of the potassic alteration zone are primarily perthitic. Perthitic textures form in slowly cooled granitic rocks (e.g. Hibbard 1995) and, therefore, the potassic K-feldspars, including the megacrysts, are interpreted here to have crystallized from a magma (Chapter 2).

The **perthitic lamellae** in the potassic alteration zone are coarser than those of the fresh Este Porphyry (Fig. 4.13, 5.14, and 5.15), interpreted here to be the result of a more hydrous magma. As mentioned in Chapter 2, this 'deuteric coarsening' has resulted from late-stage water concentrated by fractionation and not from the influx of hydrothermal fluids (e.g. Smith and Brown 1988). The euhedral plagioclase inclusions and crosshatch twinning in the K-feldspars are also interpreted to be of magmatic origin.

The magmatic **Ba zoning** in K-feldspar of the fresh Este Porphyry is not as regular in the K-feldspar of the potassically altered Este Porphyry. Although there are areas of K-feldspar Ba enrichment, reverse zoning occurs only locally (Fig. 5.16). This lack of reverse zoning is interpreted to be the result of late deuteric fluid migration

following feldspar crystallization (Chapter 5). The perthitic texture supports the magmatic origin of the K-feldspar, but this texture does not rule out remobilization of elements. The Ba content of the potassic alteration K-feldspars is within the same range as those in the fresh Este Porphyry (Fig. 5.16). In some grains, there appears to be Ba enrichment around the albite inclusions (Fig. 5.16). Zones of enrichment are interpreted here to result from the inability of the inclusions to accommodate Ba during crystallization or subsequent remobilization.

The **biotites** in the fresh Este Porphyry have compositions that overlap with the potassic alteration biotite. However, there are some fairly consistent trends in the biotite composition that help to identify the potassically altered biotite. The potassic biotites tend to be more phlogopitic, with lower Ti and higher F-values, than the fresh biotite (Figs. 5.9, 5.10, and 5.11). Those biotites in the potassic zone that compositionally overlap with the fresh Este Porphyry are interpreted here to be less affected by late magmatic (deuteric) fluids than those that are more phlogopitic. As discussed in Chapter 2, potassically altered biotite grains have rutile along their cleavage planes, the result of Ti being released from the trioctahedral structure at the same time as Fe (Figs. 5.12 and 5.18). The high F-values in the potassic biotites reflect the F-content of the deuteric fluid (Chapter 2).

The **albitic plagioclase** in the potassic alteration zone is not the primary magmatic composition. The P_{H_2O} would have to have been too high ($P_{H_2O} \approx 5$ kbars) at such low lithostatic pressures ($P_L < 1.5$ kbar) to crystallize two alkali feldspars in such a high level intrusion (Fig. 2.10). The secondary nature of the feldspar composition is supported by

the patch antiperthites which are interpreted to result from alkali feldspar replacement of primary andesine-oligoclase (chapter 5).

$^{40}\text{Ar}/^{39}\text{Ar}$ dating (Reynolds et al. 1998) indicates the potassic alteration has the same age as the Este Porphyry, within error (Fig. 7.1). These ages are interpreted to represent cooling ages as the minerals display magmatic features (e.g. perthitic texture, crosshatch twinning). Therefore, the potassic alteration zone is interpreted to represent a more hydrous version of the Este Porphyry, which depressed the temperature of the solidus. It is possible that the high-F content of the magma, evident in the F-content of the biotite of the potassic zone, was increased during crystal fractionation of the melt. This increase in F-activity may have 'stripped' the Ca from the plagioclase, forming albite. Depressurization during hydraulic fracturing (e.g. Philipps 1986, Cloos 2001) (Fig. 7.3) was probably responsible for the final rapid cooling.

Oxygen isotopic data indicate that the potassic zone equilibrated at a lower temperature ($\sim 535^\circ\text{C}$) than the fresh Este Porphyry (595°C) (Tables 4.5 and 5.2). The $\delta^{18}\text{O}$ values are consistent with a magmatic fluid (Fig. 4.30). The only exception to this trend is the megacrystic K-feldspar $\delta^{18}\text{O}$, which falls outside the magmatic range. This characteristic is interpreted here to represent re-equilibration during cooling. This reequilibration would have been the result of the same deuteric effect that remobilized the Ba and coarsened the perthitic lamellae in the K-feldspars.

In this case, potassic alteration can be considered transitional between the effects of late magmatic and deuteric alteration (Fig. 7.3a). There is no evidence (petrographic, geochemical, or isotopic) to suggest that fluids external to the magma were involved.

~34.0 Ma

281

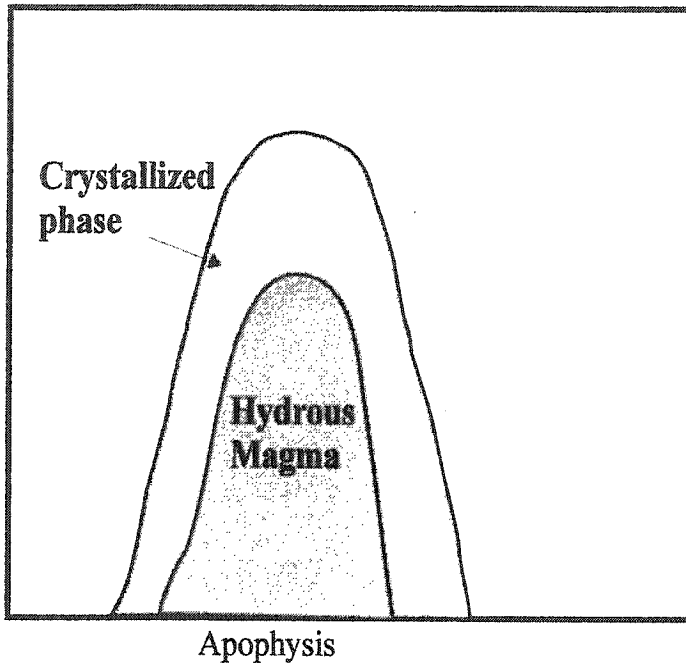


Figure 7.3a. Following the intrusion of Este Porphyry, crystallization of mainly anhydrous phases resulted in a more hydrous magma. This magma was also rich in Cl, F, and Cu. A fluid-rich phase concentrates at the top of the carapace. (after Burnham 1979)

~33.9 Ma

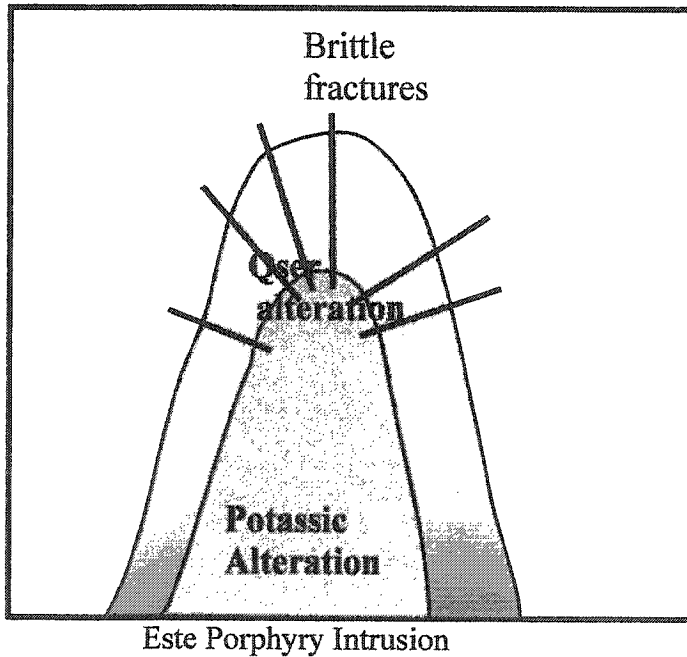


Figure 7.3b. When the hydrous phase separated from the magma (second boiling), $P_{H_2O} > P_{lithostatic}$, it results in hydraulic fracturing. These brittle fractures created pathways used by highly acid fluids that formed the Qser alteration. (after Burnham 1979)

plagioclases in an F-rich leucogranite was the result of F linking with the Ca, leaving the Ca unavailable for plagioclase formation. It is suggested here that the concentration of a hydrous phase by crystal fractionation not only hydrated the remaining melt, but saturated it in F and Cl. This enrichment of ligands essentially stripped the crystallized andesine-oligoclase of Ca, replacing it with alkali feldspars, and replacing the hornblende and titanite with biotite and rutile, respectively. The concentration F is also interpreted to have contributed to the lowering of the solidus temperature (Dingwell 1985). K-feldspar and quartz that had already crystallized would have remained relatively unaffected because these minerals would not react with an already K-rich fluid.

Figure 7.1 shows cooling curves for the Este and Banco porphyries. From this diagram, it can be deduced that the Este Porphyry had completely cooled before the Banco Porphyry was intruded. The absence of albitized plagioclase in the Banco Porphyry indicates it was also intruded following the potassic alteration. Potassic ages reported in Chapter 3 indicate that the alteration must have occurred contemporaneously with the intrusion of the Este Porphyry. It is therefore concluded that the potassic alteration resulted from a more hydrous phase of the Este Porphyry that had a depressed solidus temperature.

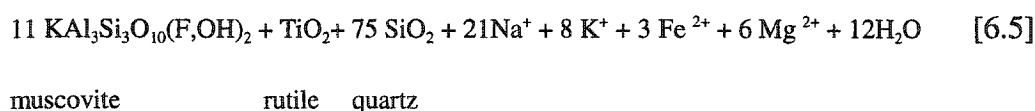
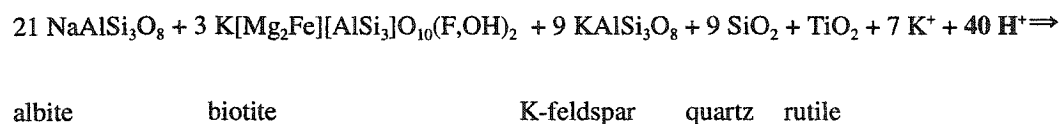
Based on the assumption that the potassic alteration zone had reached isotopic equilibrium at 550°C and that the potassic alteration event ceased to affect the biotite composition prior to the $^{40}\text{Ar}/^{39}\text{Ar}$ closure temperature of the biotite, an age of 34.1-34.6 Ma is proposed for the potassic alteration event (Fig. 7.1).

Stable isotope data of potassic alteration samples in this study have been

interpreted to give equilibrium temperatures of $\sim 535^{\circ}\text{C}$, only 60°C lower than those determined for the fresh Este Porphyry. It was also determined that the fluids in equilibrium with the potassic alteration minerals were of magmatic origin.

7.4 The nature of the Qser alteration

The assemblage of quartz, sericite and pyrite characterizes the Qser alteration zone (Chapter 6). The crystallization of pyrite attests to the reducing conditions of the altering fluid (H_2S). The hydration of all original minerals indicates a highly acidic environment (Chapter 6). This acidity is supported by equation 6.5, which indicates the high H^+ content necessary to hydrate the potassic assemblage. The reducing environment is interpreted to be represented by the presence of H_2S .



The Qser alteration zone was formed by a mixture of magmatic and meteoric waters (Fig. 6.26). The brittle fractures of the Qser (Lindsay 1998) increased the surface area available for reactions and aided circulation, which likely facilitated the strongly pervasive nature of the Qser.

The Qser was formed at $\sim 31 \text{ Ma}$ (Fig. 7.1), significantly later than the Este and Banco porphyries (Fig. 7.3d). Therefore, another pulse of magma is predicted to have

~33 Ma

285

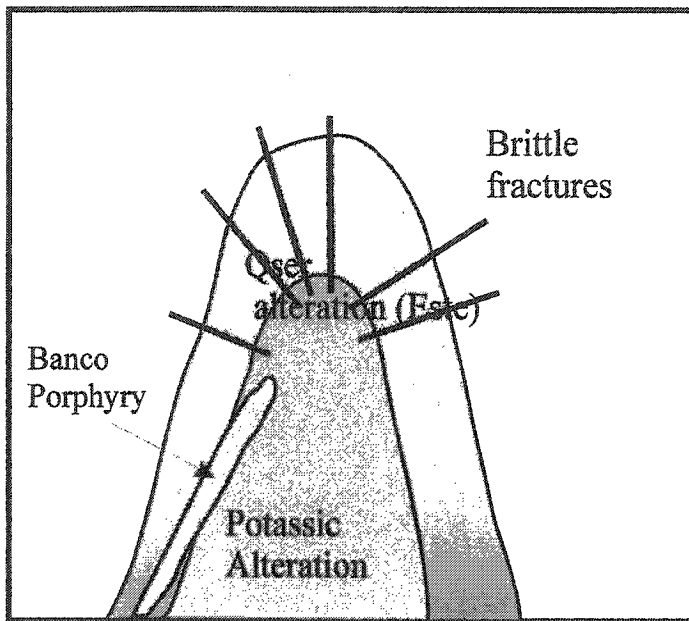


Figure 7.3c. The Banco Porphyry intruded the Este Porphyry at ~33 Ma. The Banco Porphyry was less hydrous than the Este Porphyry. After Burnham (1979).

~31 Ma

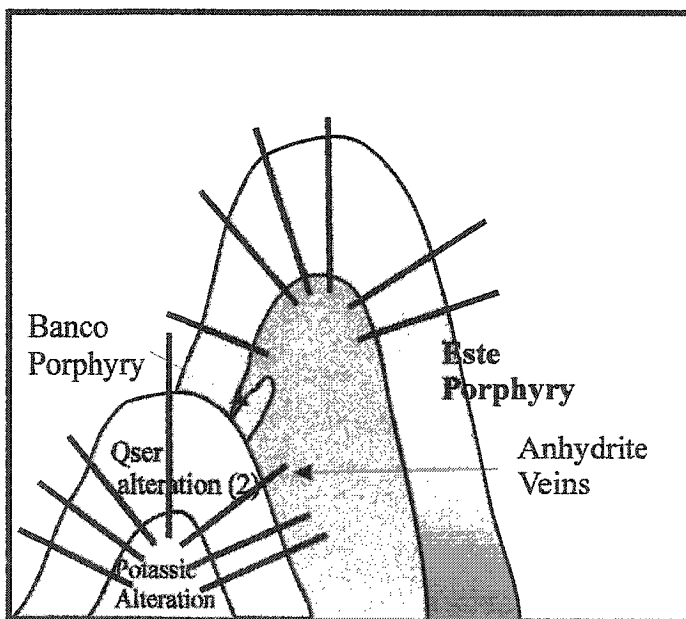


Figure 7.3d. A third intrusion, not yet exposed, supplied the heat and some fluid for the 31 Ma Qser alteration event which overprinted the potassic alteration and the Banco Porphyry. Late anhydrite veins are interpreted to have formed from Ca liberated during a later potassic alteration event associated with this third intrusion. After Burnham (1979).

Third intrusion at depth.
Not yet at surface.

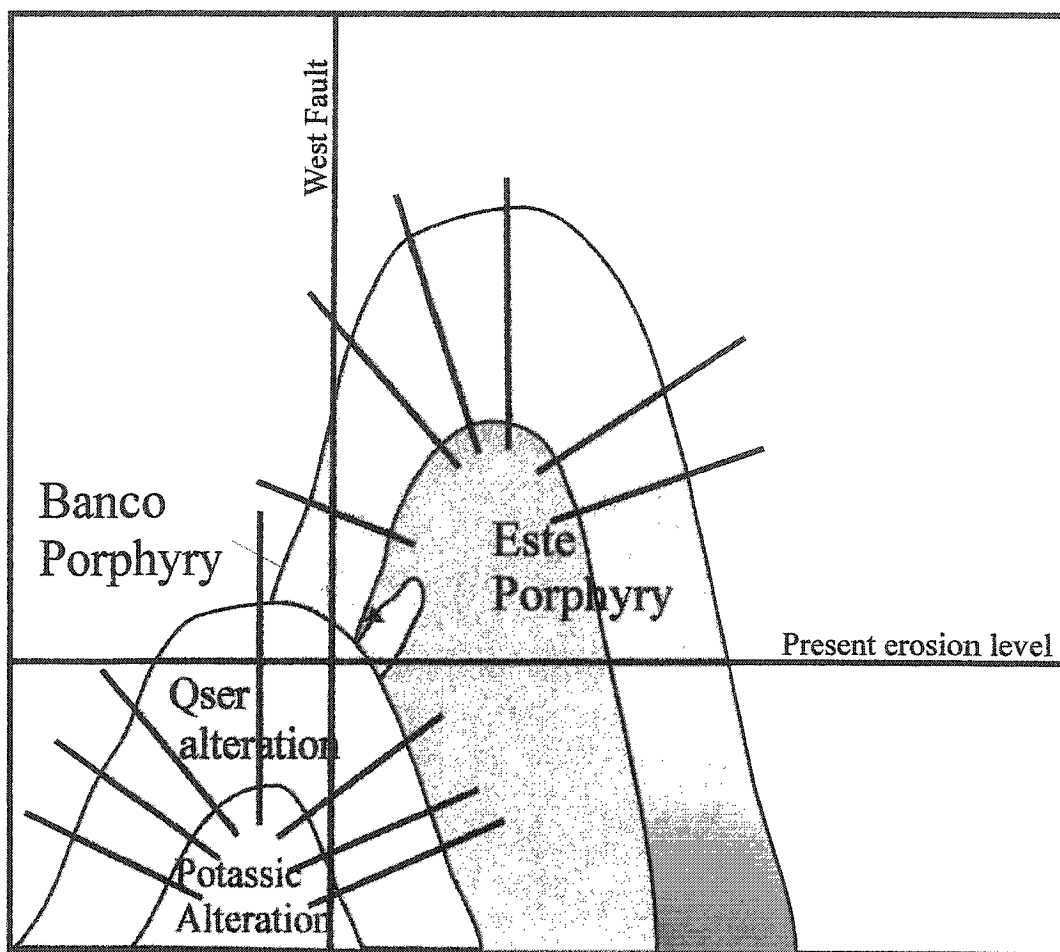


Figure 7.3e. Present erosion level and the West Fault produces the alteration pattern seen today. The potassic alteration zone in the third intrusion is not yet exposed. (after Burnham 1979)

supplied the heat and considerable fluid for this event (Fig. 7.3d) (Zentilli et al. 1995). This pulse of magma is interpreted to have been another apophysis from the postulated magma chamber, as illustrated in Figure 7.2.

7.5 The formation of anhydrite

Although it has been reported by some authors (e.g. Ossandón et al. 2001), the presence of anhydrite as a phase in the potassic alteration zone of Chuquicamata is refuted here. Not only was anhydrite not observed in the potassic zone *sensu stricto* during this study, but an investigation into the solubility of CaSO_4 confirms that, even if it had been precipitated at the temperatures of potassic alteration, in a slowly cooled (i.e. coarse-grained) pluton, anhydrite would have been dissolved as it cooled through the low temperature solubility of anhydrite (Blount and Dickinson 1969, 1973). Therefore, the anhydrite reported in the potassic zone must represent superimposed Qser veinlets.

As the Qser alteration mainly overprints the potassic zone, which is Ca-depleted, where did the Ca in the anhydrite come from? The source of Ca is interpreted here to be the intrusion at depth that supplied heat and fluids to the Qser alteration event (Fig. 7.3d). It is interpreted that a potassic alteration event occurred at a depth not yet revealed by mining or drilling. The fluids evolved from this intrusion would be rich in Ca, based on the observation that the second potassic alteration zone is leached of Ca as described in equation 5.5 (Fig. 7.3).

Anhydrite was precipitated where CaCl^+ from the deep potassic alteration zone mingled with the fluids of the late Qser, which would have been NaSO_4 -rich due to the

destruction of albite. As these veins are also rich in cupriferous sulphides, it is interpreted that these deep fluids were the probable source for Qser-related mineralization.

Chapter 8

Conclusions

After the previous discussion in Chapter 7 the following conclusions can be reached:

- 1) **The Fiesta Granodiorite is not co-genetic with the Este Porphyry.** That is, the Fiesta Granodiorite is not the *root* or *source*, yet may have shared a common deep batholithic source (Fig. 7.2; 'magma chamber').

- 2) **The potassic alteration zone at Chuquicamata is not a superimposed effect on the Este Porphyry by some extraneous magma, but represents a more evolved hydrous stage in the evolution of the Este Porphyry.** The potassic alteration zone is essentially the same age as the Este Porphyry but the solidus temperature was depressed by the abundant volatiles.

- 3) **Following the above conclusion, it can be postulated that minerals in the potassic alteration assemblage formed by primary magmatic crystallization, but their compositions were modified by deuteritic fluids of the Este Porphyry during cooling.** The most conspicuous effect of this evolution is the albitization of the plagioclase, which in the *fresh* Este Porphyry is oligoclase-andesine. K-feldspar in the potassic alteration zone exhibit magmatic features such as perthitic lamellae and crosshatch twinning but

only locally displays the regular Ba zonation observed in the K-feldspar of the *fresh* Este Porphyry. The lack of concentric reverse Ba zonation is concluded to be the result of deuteritic remobilization of elements. Potassically altered biotite has higher Mg:Fe ratio, higher F values and lower Ti than biotite in the *fresh* Este Porphyry. The removal of Ca during from the potassic alteration zone resulted in the replacement of amphibole by biotite and titanite by rutile.

4) The lack of Ca in the potassic alteration zone resulted from deuteritic fluids enriched in Cl and F which leached the Ca from the already crystallized Ca-bearing silicates. Calcium was replaced by K and Na in the feldspars and biotites when a Cl- and F-rich fluid preferentially complexed with the calcium.

5) The Banco Porphyry intruded after the cooling and potassic alteration of the Este Porphyry. Its younger radiometric ages and unaltered plagioclase indicate that it cannot be the *source* of the potassic alteration, as suggested by Ballard et al. (2001).

6) The second Qser alteration event, not related to the Este Porphyry, was probably caused by a third intrusion. As suggested by Zentilli et al. (1995), a porphyry intrusion, not yet exposed, supplied the heat, fluids, and metals that formed the Qser alteration zone. The Qser alteration formed in a reducing, highly acidic environment at ~31.1 Ma.

7) **Potassic alteration of the porphyry intrusion at depth supplied the Ca for the formation of the anhydrite veins.** Qser alteration event generated an oxidizing fluid that crystallized anhydrite when it mixed with CaCl_2 from an unexposed intrusion at depth. This third intrusion brought in other elements besides Ca, such as a net input of Cu, As, and Zn (eg. Lewis 1997, Graves et al. 1997).

Some important questions remain unresolved:

- 1) What is the nature of the proposed third intrusion at depth that supplied the heat and fluids for the second Qser alteration event? Only deep drilling, well below the bottom of the pit, could answer this question.

- 2) Where is the mineralization associated with the two mineralizing events (the potassic and the Qser alteration/mineralization events) that was faulted away by the West Fault? It is possible, but not proven, that part of the Qser (~31 Ma) alteration and mineralization is located in the Mansa Mina deposit west of the West Fault, 14 km south of the Chuquicamata pit

- 3) How many magmatic pulses were involved in the formation of the Chuquicamata Intrusive Complex? Do the quartz-molybdenum veins represent another magmatic pulse? It appears likely that the post-potassic alteration, pre-Qser alteration, blue veins were formed by a felsic intrusion at depth; but this hypothesis remains speculative.

There is a great deal of research to be done at Chuquicamata. I would recommend the following projects:

- 1) To understand the Chuquicamata system more fully, a study of the quartz-molybdenite veins using fluid inclusions and Re/Os, in particular. A study of poorly investigated alteration zones (such as the silicification and propylitic) would also be advantageous.
- 2) Now that criteria exist for the identification of the potassic zone, and the influence of the Qser overprint on the potassic alteration dates are known, a more rigorous argon dating program should be undertaken to establish a larger data base on the cooling ages of the K-feldspar and biotite. Also, U/Pb dating of zircon and titanite from the fresh and potassic alteration should be done to confirm the interpreted common intrusion age.
- 3) A strontium isotope analyses of anhydrite would give insight into the origin of sulphate veins, possible confirming the existence of an unseen porphyry at depth, and ruling out the involvement of extraneous Ca (and Sr) from the country rocks which should be relatively more radiogenic.

Appendix A
Sample Locations

CU #	Field #	X	Y	depth
66	Z-93-701	3200N	DDH 3472	268m
67	Z-93-702	3200N	DDH 3472	275.6m
68	Z-93-703	3200N	DDH 3472	276.6m
69	Z-93-704	3200N	DDH 3472	278.32m
70	Z-93-705	3200N	DDH 3472	224.33m
71	Z-93-706	3200N	DDH 3472	286.76m
72	Z-93-707	3200N	DDH 3472	292.18m
73	Z-93-708	3200N	DDH 3472	295.66m
74	Z-93-709	3200N	DDH 3472	295.79m
75	Z-93-710	3200N	DDH 3472	304.0m
76	Z-93-711	3200N	DDH 3472	306.4m
77	Z-93-712	3200N	DDH 3472	306.84m
78	Z-93-713	3200N	DDH 3472	309.47m
79	Z-93-714	3200N	DDH 3472	310.42m
80	Z-93-715	3200N	DDH 3472	313.34m
81	Z-93-716	3200N	DDH 3472	316.23m
82	Z-93-717	3200N	DDH 3472	322.2m
83	Z-93-718	3200N	DDH 3472	327.53m
84	Z-93-719	3200N	DDH 3472	311.32m
85	Z-93-720	3200N	DDH 3472	556.2m
86	Z-93-721	3200N	DDH 3472	557.4m
87	Z-93-722	3200N	DDH 3472	557.92m
88	Z-93-723	3200N	DDH 3472	558.64m
89	Z-93-724	3200N	DDH 3472	559.13m
90	Z-93-725	3200N	DDH 3472	566.53m
91	Z-93-726	3200N	DDH 3472	601.03m
92	Z-93-727	3200N	DDH 3472	601.83m
93	Z-93-728	3200N	DDH 3472	602.60m
94	Z-93-729	3200N	DDH 3472	470.05m
95	Z-93-730	3200N	DDH 3472	471.12m
96	Z-93-731	3200N	DDH 3472	473.82m
97	Z-93-732	3200N	DDH 3472	475.65m
98	Z-93-733	3200N	DDH 3472	479.42m
99	Z-93-734	3200N	DDH 3472	481.95m
100	Z-93-735	3200N	DDH 3472	133.46m
101	Z-93-736	3200N	DDH 3472	134.32m
102	Z-93-737	3200N	DDH 3472	137.72m
103	Z-93-738	3200N	DDH 3472	139.72m
104	Z-93-739	3200N	DDH 3472	142.05m
105	Z-93-740	3200N	DDH 3472	143.77m
106	Z-93-741	3200N	DDH 3472	446.50m

Appendix A: Sample Locations

CU #	Field #	X	Y	depth
107	Z-93-742	3200N	DDH 3472	446.93m
108	Z-93-743	3200N	DDH 3472	449.24m
109	Z-93-744	3200N	DDH 3472	453.35m
110	Z-93-745	3200N	DDH 3472	453.56m
111	Z-93-746	3200N	DDH 3472	698.20m
112	Z-93-747	3200N	DDH 3472	700.30m
113	Z-93-748	3200N	DDH 3472	703.36m
114	Z-93-749	3200N	DDH 3472	703.97m
115	Z-93-750	3200N	DDH 3472	722.56m
116	Z-93-751	3200N	DDH 3472	723.91m
117	Z-93-752	3200N	DDH 3472	727.75m
118	Z-93-753	3200N	DDH 3472	727.96m
119	Z-93-754	3200N	DDH 3472	635.08m
120	Z-93-755	3200N	DDH 3472	636.86m
121	Z-93-756	3200N	DDH 3472	637.52m
122	Z-93-757	3200N	DDH 3472	656.71m
123	Z-93-758	3200N	DDH 3472	658.80m
124	Z-93-759	3200N	DDH 3472	659.14m
125	Z-93-760	3200N	DDH 3472	659.28m
126	Z-93-761	3200N	DDH 3472	512.28m
127	Z-93-762	3200N	DDH 3472	513.58m
128	Z-93-763	3200N	DDH 3472	517.42m
129	Z-93-764	3200N	DDH 3472	519.22m
130	Z-93-765	3200N	DDH 3472	521.21m
131	Z-93-766	3200N	DDH 3472	523.87m
132	Z-93-767	3200N	DDH 3472	530.35m
133	Z-93-768	3200N	DDH 3472	530.61m
134	Z-93-769	3200N	DDH 3472	536.86m
135	Z-93-770	3200N	DDH 3472	538.29m
136	Z-93-771	3200N	DDH 3472	408.13m
137	Z-93-772	3200N	DDH 3472	409.56m
138	Z-93-773	3200N	DDH 3472	410.72m
139	Z-93-774	3200N	DDH 3472	411.36m
140	Z-93-775	3200N	DDH 3472	415.12m
141	Z-93-776	3200N	DDH 3472	435..20m
142	Z-93-777	3200N	DDH 3472	436.48m
143	Z-93-778	3200N	DDH 3472	441.01m
144	Z-93-779	3200N	DDH 3472	441.40m
145	Z-93-780	3200N	DDH 3472	441.67m
146	Z-93-781	3200N	DDH 3472	445.36m

DDH 2620 CU #	3200N Field #	X	Y	Z
147	Z-93-782	3200N	DDH 2620	10.93m
148	Z-93-783	3200N	DDH 2620	17.40m
149	Z-93-784	3200N	DDH 2620	21.32m
150	Z-93-785	3200N	DDH 2620	22.24m
151	Z-93-786	3200N	DDH 2620	29.66m
152	Z-93-787	3200N	DDH 2620	30.62m
153	Z-93-788	3200N	DDH 2620	31.04m
154	Z-93-789	3200N	DDH 2620	31.44m
155	Z-93-790	3200N	DDH 2620	32.05m
156	Z-93-790A	3200N	DDH 2620	35.82m
157	Z-93-791	3200N	DDH 2620	36.27m
158	Z-93-792	3200N	DDH 2620	39.55m
159	Z-93-793	3200N	DDH 2620	62.96m
160	Z-93-794	3200N	DDH 2620	63.46m
161	Z-93-795	3200N	DDH 2620	64.07m
162	Z-93-796	3200N	DDH 2620	67.99m
163	Z-93-797	3200N	DDH 2620	69.08m
164	Z-93-798	3200N	DDH 2620	109.76m
165	Z-93-799	3200N	DDH 2620	112.61m
166	Z-93-800	3200N	DDH 2620	114.62m
167	Z-93-801	3200N	DDH 2620	116.82m
168	Z-93-802	3200N	DDH 2620	118.64m
169	Z-93-803	3200N	DDH 2620	210.35m
170	Z-93-804	3200N	DDH 2620	210.66m
171	Z-93-805	3200N	DDH 2620	212.46m
172	Z-93-806	3200N	DDH 2620	212.80m
173	Z-93-807	3200N	DDH 2620	213.00m
174	Z-93-808	3200N	DDH 2620	217.32m
175	Z-93-809	3200N	DDH 2620	221.15m
176	Z-93-810	3200N	DDH 2620	221.75m
177	Z-93-811	3200N	DDH 2620	226.13m
178	Z-93-812	3200N	DDH 2620	228.45m
179	Z-93-813	3200N	DDH 2620	233.54m
180	Z-93-814	3200N	DDH 2620	233.85m

DDH 2967 CU #	4500N Field #	X	Y	depth	elevation (m)
181	Z-93-815	4500N	DDH 2967	671.5m	
182	Z-93-816	4500N	DDH 2967	224.76m	2234
183	Z-93-817	4500N	DDH 2967	225.10m	2233
184	Z-93-818	4500N	DDH 2967	233.04m	2226
185	Z-93-819	4500N	DDH 2967	234.45m	2224
186	Z-93-820	4500N	DDH 2967	314.74m	2150
187	Z-93-821	4500N	DDH 2967	316.26m	2151
188	Z-93-822	4500N	DDH 2967	319.59m	2147.5
189	Z-93-823	4500N	DDH 2967	324.69m	2144
190	Z-93-824	4500N	DDH 2967	325.20m	2142.5
191	Z-93-825	4500N	DDH 2967	325.49m	2142
192	Z-93-826	4500N	DDH 2967	325.93m	2142
193	Z-93-827	4500N	DDH 2967	408.00m	2067
194	Z-93-828	4500N	DDH 2967	411.38m	2064
195	Z-93-829	4500N	DDH 2967	413.77m	2062
196	Z-93-830	4500N	DDH 2967	415.40m	2060
197	Z-93-831	4500N	DDH 2967	566.23m	1924
198	Z-93-832	4500N	DDH 2967	567.48m	1923
199	Z-93-833	4500N	DDH 2967	569.42m	1921
200	Z-93-834	4500N	DDH 2967	574.23m	1916
201	Z-93-835	4500N	DDH 2967	574.87m	1915.5
202	Z-93-836	4500N	DDH 2967	575.14m	1915
203	Z-93-837	4500N	DDH 2967	576.98m	1913
204	Z-93-838	4500N	DDH 2967	513.05m	1972
205	Z-93-839	4500N	DDH 2967	514.90m	1970
206	Z-93-840	4500N	DDH 2967	518.65m	1968
207	Z-93-841	4500N	DDH 2967	605.70m	1888
208	Z-93-842	4500N	DDH 2967	607.97m	1886
209	Z-93-843	4500N	DDH 2967	619.86m	1875
210	Z-93-844	4500N	DDH 2967	455.90m	2023.5
211	Z-93-845	4500N	DDH 2967	456.40m	2022
212	Z-93-846	4500N	DDH 2967	461.20m	2018
213	Z-93-847	4500N	DDH 2967	209.10m	2248
214	Z-93-848	4500N	DDH 2967	211.60m	2247

CU #	Field #	X	Y	depth	elevation (m)
431	Z93-852	4500N	DDH 2242	38.55m	2478
432	Z93-853	4500N	DDH 2242	40.91m	2476
433	Z93-854	4500N	DDH 2242	56.45m	2462
434	Z93-855	4500N	DDH 2242	95.86m	2436
435	Z93-856	4500N	DDH 2242	103.07m	2421
436	Z93-857	4500N	DDH 2242	103.83m	2420
437	Z93-858	4500N	DDH 2242	138.24m	2392
438	Z93-859	4500N	DDH 2242	139.15m	2392
439	Z93-860	4500N	DDH 2242	141.28m	2390
440	Z93-861	4500N	DDH 2242	142.13m	2390
441	Z93-862	4500N	DDH 2242	145.32m	2387
442	Z93-863	4500N	DDH 2242	149.60m	2384
443	Z93-864	4500N	DDH 2242	151.38m	2382
444	Z93-865	4500N	DDH 2242	154.42m	2381
445	Z93-866	4500N	DDH 2242	153.63m	2380
446	Z93-867	4500N	DDH 2242	156.77m	2378
447	Z93-868	4500N	DDH 2242	160.76m	2375
448	Z93-869	4500N	DDH 2242	161.04m	2375
449	Z93-870	4500N	DDH 2242	161.41m	2374
450	Z93-871	4500N	DDH 2242	161.98m	2374
451	Z93-872	4500N	DDH 2242	164.98m	2372
452	Z93-873	4500N	DDH 2242	189.86m	2351
453	Z93-874	4500N	DDH 2242	193.10m	2248
454	Z93-875	4500N	DDH 2242	193.78m	2248
455	Z93-876	4500N	DDH 2242	193.86m	2248
456	Z93-877	4500N	DDH 2242	194.2m	2247
457	Z93-878	4500N	DDH 2242	195.76m	2246
458	Z93-879	4500N	DDH 2242	196.55m	2246
459	Z93-880	4500N	DDH 2242	200.04m	2244
460	Z93-881	4500N	DDH 2242	200.75m	2244
461	Z93-882	4500N	DDH 2242	202.52m	2242
462	Z93-883	4500N	DDH 2242	252.55m	2204
463	Z93-884	4500N	DDH 2242	257.63m	2200
464	Z93-885	4500N	DDH 2242	258.45m	2198
465	Z93-886	4500N	DDH 2242	260.14m	2196
466	Z93-887	4500N	DDH 2242	261.02m	2195
467	Z93-888	4500N	DDH 2242	261.27m	2195
468	Z93-889	4500N	DDH 2242	263.23m	2194
469	Z93-890	4500N	DDH 2242	263.66m	2194
470	Z93-891	4500N	DDH 2242	264.53m	2193
471	Z93-892	4500N	DDH 2242	264.98m	2192

CU #	Field #	X	Y	depth	elevation (m)
472	Z93-893	4500N	DDH 2242	265.60m	2191
473	Z93-894	4500N	DDH 2242	284.39m	2179
474	Z93-895	4500N	DDH 2242	286.74m	2176
475	Z93-896	4500N	DDH 2242	282.04m	2178
476	Z93-897	4500N	DDH 2242	288.10m	2175
477	Z93-898	4500N	DDH 2242	288.65m	2174
478	Z93-899	4500N	DDH 2242	288.95m	2174

DDH 2234 CU#	4500N Field #	X	Y	depth	elevation (m)
479	Z93-900	4500N	DDH 2234	294.20m	2290
480	Z93-901	4500N	DDH 2234	295.55m	2288
481	Z93-902	4500N	DDH 2234	295.98m	2288
482	Z93-903	4500N	DDH 2234	297.53m	2286
483	Z93-904	4500N	DDH 2234	297.89m	2286
484	Z93-905	4500N	DDH 2234	298.65m	2286
485	Z93-906	4500N	DDH 2234	299.82m	2285
486	Z93-907	4500N	DDH 2234	301.37m	2284
487	Z93-908	4500N	DDH 2234	301.95m	2284
488	Z93-909	4500N	DDH 2234	302.69m	2282
489	Z93-910	4500N	DDH 2234	305.73m	2280
490	Z93-911	4500N	DDH 2234	307.95m	2276
491	Z93-912	4500N	DDH 2234	306.79m	2280
492	Z93-913	4500N	DDH 2234	308.20m	2276
493	Z93-914	4500N	DDH 2234	216.30m	2364
494	Z93-915	4500N	DDH 2234	219.84m	2360
495	Z93-916	4500N	DDH 2234	221.49m	2360
496	Z93-917	4500N	DDH 2234	244.40m	2338
497	Z93-918	4500N	DDH 2234	245.49m	2336
498	Z93-919	4500N	DDH 2234	245.68m	2336
499	Z93-920	4500N	DDH 2234	249.15m	2335
500	Z93-921	4500N	DDH 2234	250.00m	2334
501	Z93-922	4500N	DDH 2234	250.70m	2334
502	Z93-923	4500N	DDH 2234	252.15m	2332
503	Z93-924	4500N	DDH 2234	253.27m	2330
504	Z93-925	4500N	DDH 2234	107.86m	2470
505	Z93-926	4500N	DDH 2234	108.32m	2468
506	Z93-927	4500N	DDH 2234	111.09m	2465
507	Z93-928	4500N	DDH 2234	113.65m	2462
508	Z93-929	4500N	DDH 2234	114.71m	2462
509	Z93-930	4500N	DDH 2234	115.80m	2660

DDH 1843 CU #	3600N Field #	X	Y	depth (m)
1101	AMA-01	3600N	DDH1843	14.77-14.85
1102	AMA-02	3600N	DDH1843	15.15-15.25
1103	AMA-03	3600N	DDH1843	32.75-32.82
1104	AMA-04	3600N	DDH1843	24.70-24.79
1105	AMA-05	3600N	DDH1843	37.03-37.10
1106	AMA-06	3600N	DDH1843	44.60-44.66
1107	AMA-07	3600N	DDH1843	62.90-63.00
1108	AMA-08	3600N	DDH1843	66.71-66.81
1109	AMA-09	3600N	DDH1843	86.12-86.23
1110	AMA-10	3600N	DDH1843	103.04-103.10
1111	AMA-11	3600N	DDH1843	103.98-104.17
1112	AMA-12	3600N	DDH1843	116.22-116.40
1113	AMA-13	3600N	DDH1843	138.48-138.62
1114	AMA-14	3600N	DDH1843	152.80-152.90
1115	AMA-15	3600N	DDH1843	157.30-157.50
1116	AMA-16	3600N	DDH1843	154.30-154.65
1117	AMA-17	3600N	DDH1843	185.85-186.00
1118	AMA-18	3600N	DDH1843	193.90-194.00
1119	AMA-19	3600N	DDH1843	207.58-207.70
1120	AMA-20	3600N	DDH1843	223.75-223.85
1121	AMA-21	3600N	DDH1843	228.50-228.57
1122	AMA-22	3600N	DDH1843	253.50-253.85
1123	AMA-23	3600N	DDH1843	354.75-354.85
1124	AMA-24	3600N	DDH1843	400.95-401.10
1125	AMA-25	3600N	DDH1843	449.85-450.00
1126	AMA-26	3600N	DDH1843	462.00-462.10

DDH 2839 CU #	3600N Field #	X	Y	depth (m)
1127	AMA-27	3600N	DDH2839	7.45-7.55
1128	AMA-28	3600N	DDH2839	8.70-8.85
1129	AMA-29	3600N	DDH2839	17.50-17.65
1130	AMA-30	3600N	DDH2839	42.40-42.50
1131	AMA-31	3600N	DDH2839	42.80-42.90
1132	AMA-32	3600N	DDH2839	58.75-59.00
1133	AMA-33	3600N	DDH2839	72.85-73.08
1134	AMA-34	3600N	DDH2839	79.00-79.10
1135	AMA-35	3600N	DDH2839	84.95-85.05
1136	AMA-36	3600N	DDH2839	85.20-85.30
1137	AMA-37	3600N	DDH2839	92.00-92.20
1138	AMA-38	3600N	DDH2839	95.00-95.10
1139	AMA-39	3600N	DDH2839	96.20-96.30
1140	AMA-40	3600N	DDH2839	134.30-134.40
1141	AMA-41	3600N	DDH2839	137.95-138.10
1142	AMA-42	3600N	DDH2839	159.50-159.65
1143	AMA-43	3600N	DDH2839	165.05-165.30
1144	AMA-44	3600N	DDH2839	167.30-167.45
1145	AMA-45	3600N	DDH2839	173.80-174.00
1146	AMA-46	3600N	DDH2839	189.70-189.90
1147	AMA-47	3600N	DDH2839	192.80-193.00
1148	AMA-48	3600N	DDH2839	199.15-199.25
1149	AMA-49	3600N	DDH2839	209.95-210.05
1150	AMA-50	3600N	DDH2839	228.75-228.90
1151	AMA-51	3600N	DDH2839	231.20-231.50

DDH 1752 CU #	3600N Field #	X	Y	depth (m)
1152	AMA-52	3600N	DDH1752	233.1-233.25
1153	AMA-53	3600N	DDH1752	245.00-245.10
1154	AMA-54	3600N	DDH1752	248.00-248.15
1155	AMA-55	3600N	DDH1752	197.77-197.92
1156	AMA-56	3600N	DDH1752	256.60-256.75
1157	AMA-57	3600N	DDH1752	279.00-279.30
1158	AMA-58	3600N	DDH1752	290.10-290.30
1159	AMA-59	3600N	DDH1752	299.87-300.17
1160	AMA-60	3600N	DDH1752	310.00-310.30
1161	AMA-61	3600N	DDH1752	329.85-330.00
1162	AMA-62	3600N	DDH1752	333.95-334.15
1163	AMA-63	3600N	DDH1752	61.80-61.95
1164	AMA-64	3600N	DDH1752	19.40-19.50
1165	AMA-65	3600N	DDH1752	93.30-93.45
1166	AMA-66	3600N	DDH1752	119.60-119.80
1167	AMA-67	3600N	DDH1752	137.30-137.40
1168	AMA-68	3600N	DDH1752	161.85-161.95
1169	AMA-69	3600N	DDH1752	198.90-199.00
1170	AMA-70	3600N	DDH1752	184.40-184.45
1171	AMA-71	3600N	DDH1752	385.50-385.70
1172	AMA-72	3600N	DDH1752	281.55-281.70
1173	AMA-73	3600N	DDH1752	262.30-262.50

Other Samples

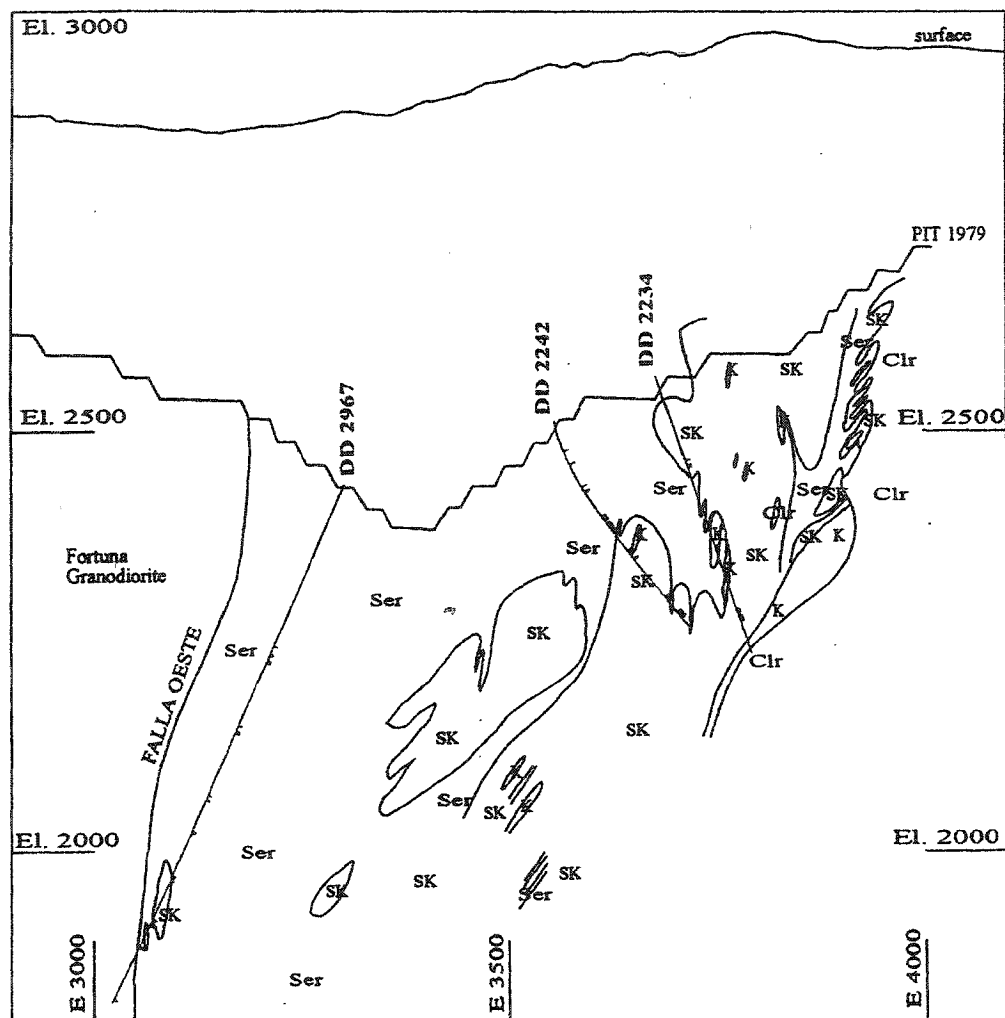
304

Cu#	field #	x	y	z
406		N4527	E4110	2770m
408		N4930	E3750	banco I3
510	Z93-931	N3650	E3750	banco H1
511	Z93-932	N3650	E3750	banco H1
512	Z93-933	N3100	E3180	banco L3
513	Z93-934	N4000	E3450	banco M3
514	Z93-935	N4900	E3950	banco F4
516	Z93-937	N5640	E3700	banco F4
524	Z93-940	N2450	E3000	banco I1
526	Z93-942	N4300	E2770	banco I3
746	DL93-059		metre 18	banco F4
769	MZ-32-94	N6853	E4397	
801/833	DL94-19	N5675	E3795	2770m
803/855	DL94-67	N4747	E4025	2724m
850	DL94-65	N5100	E3590	2620m
877	DL94-122A	N5978	E4620	3030m
877	DL94-122B	N6000	E4632	3030m
925	DL95-57	N2839	E3697	2657m
1039	DL95-140	N3878	E3420	2365m
1046	DL95-127	N3030	E3600	2593m
1073	DL95-83	N4001	E3896	2621m
1074	DL95-92	N5445	E3878	2748m
1174	AMA-74			
1175	AMA-75			
1198	VM-1	N3086	E2930	2412m
1199	VM-2	N4620	E3268	2443m
	VM-3	N4720	E3319	2441m
	VM-4	N4759	E3455	2444m
1204	VM-5	N4689	E3471	2441m
1333		N5300	E3950	2722m, G3
1334		N3399	E3169	c.2411
1335		N4863	E3361	banco M3

Fortuna samples

305

Cu#	field #	x	y	z
46	Z-209-93	N 7 533 750	E 507 680	
407	grabsample	N4800	E2400	banco C2
524	Z93-937	N5640	E3700	banco F4
526	Z93-940	N2450	E3000	banco I1
181	Z-93-815	4500N	DDH 2967	671.5m
789	DL-94-55	N3894	E2767	J1-2592m
790	DL-94-54	N3670	E2475	2671m
791	DL-94-56	N3970	E2590	I3-2619m
1061		N4263	E2873	2543m

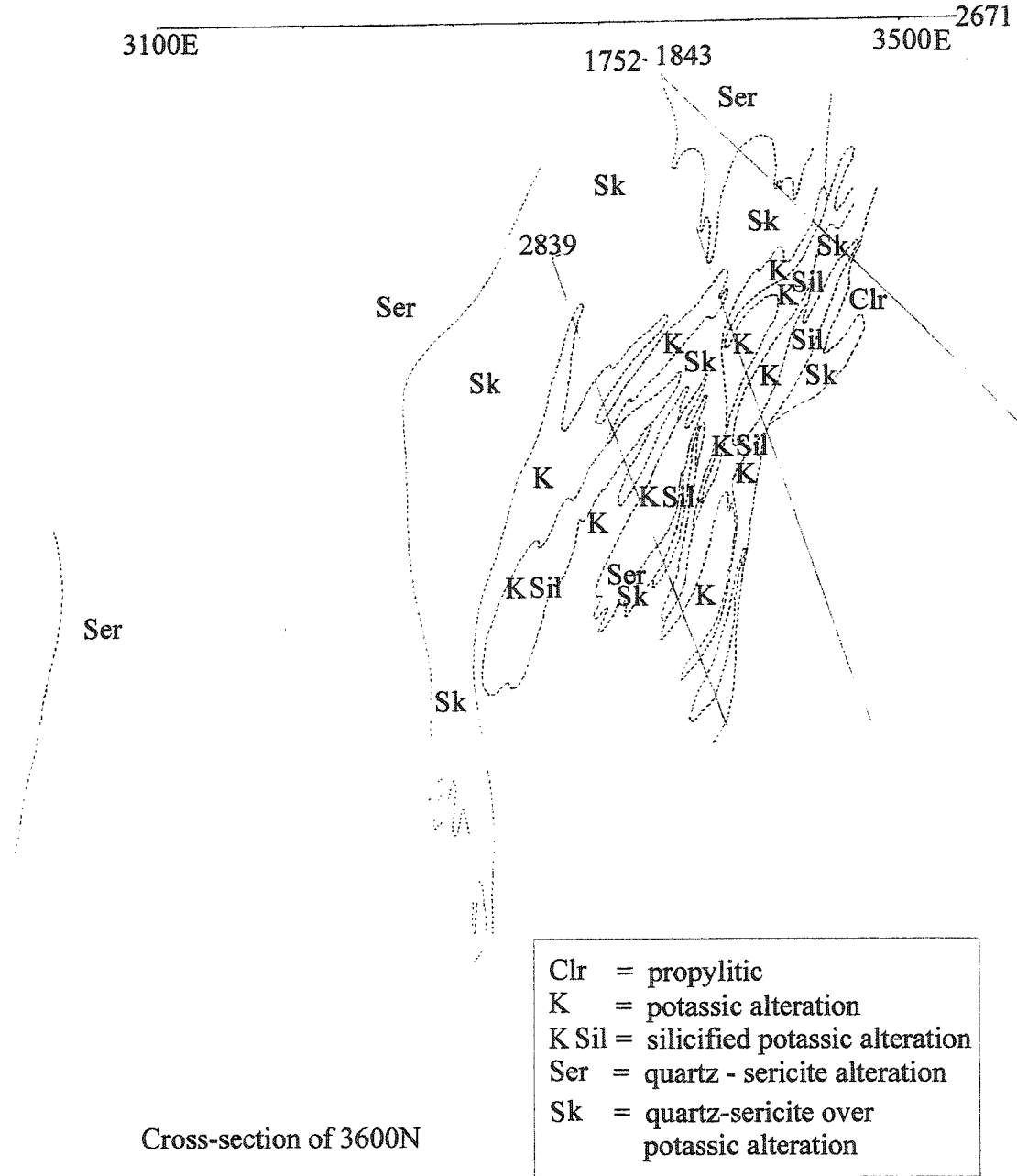


Clr = propylitic
 K = potassic alteration
 K Sil = silicified potassic alteration
 Ser = quartz - sericite alteration
 Sk = quartz-sericite over
 potassic alteration

Cross-section of 4500N

Appendix A: Sample Location

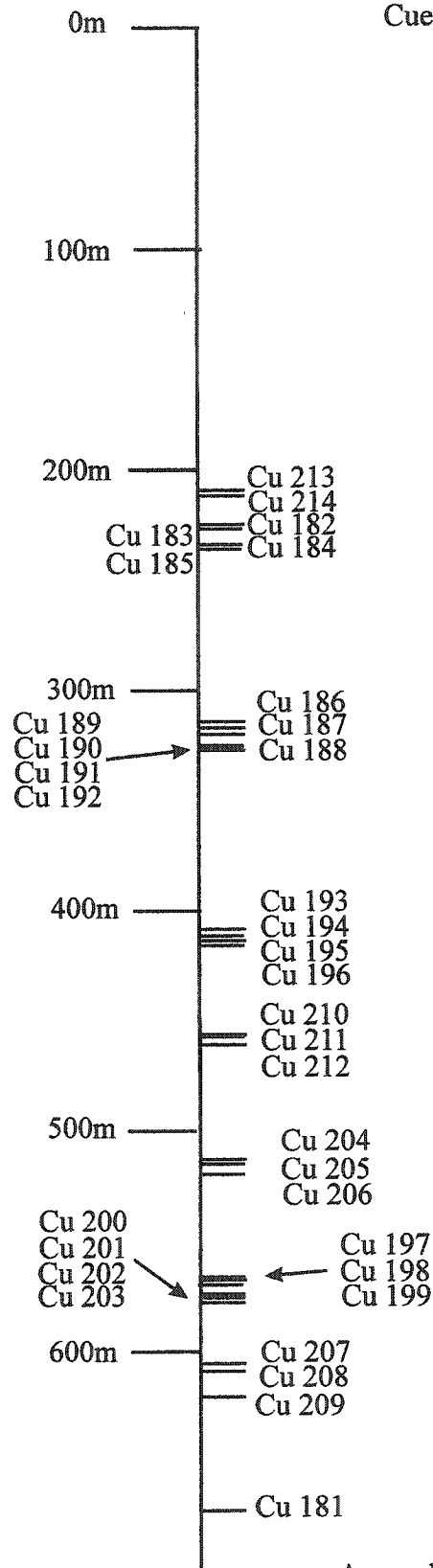
3600 section



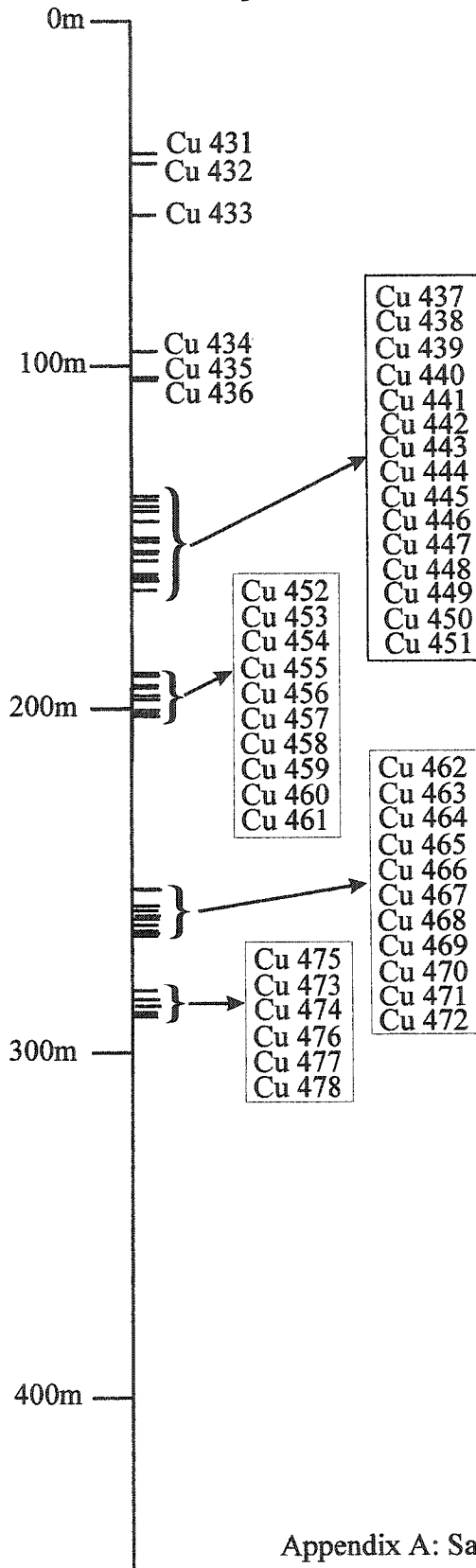
Appendix A: Sample Location

DDH 2967

Cuesta Samples

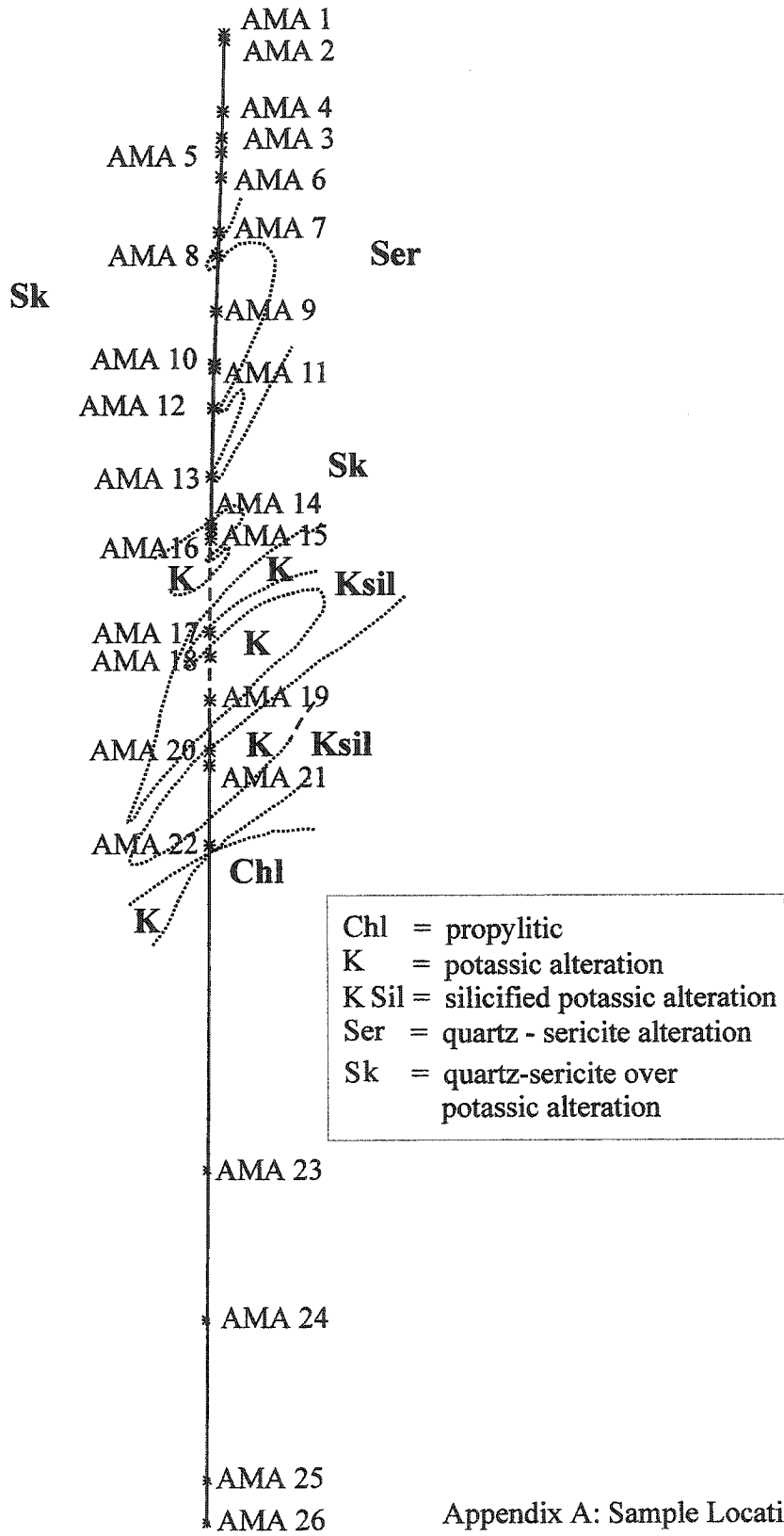


Appendix A: Sample Location

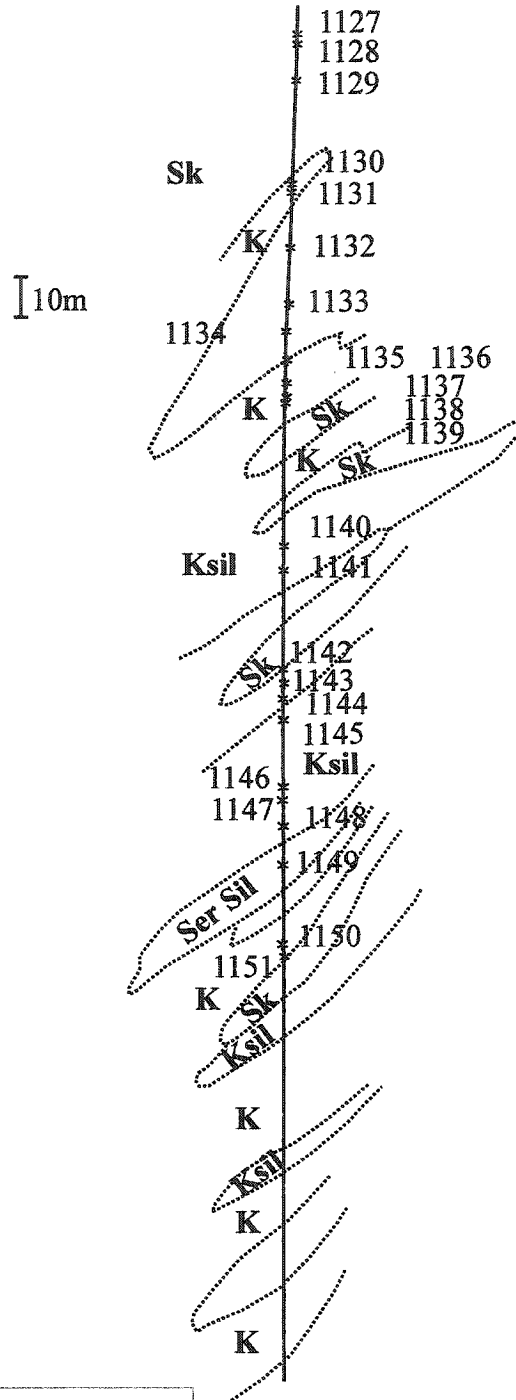


Appendix A: Sample Location

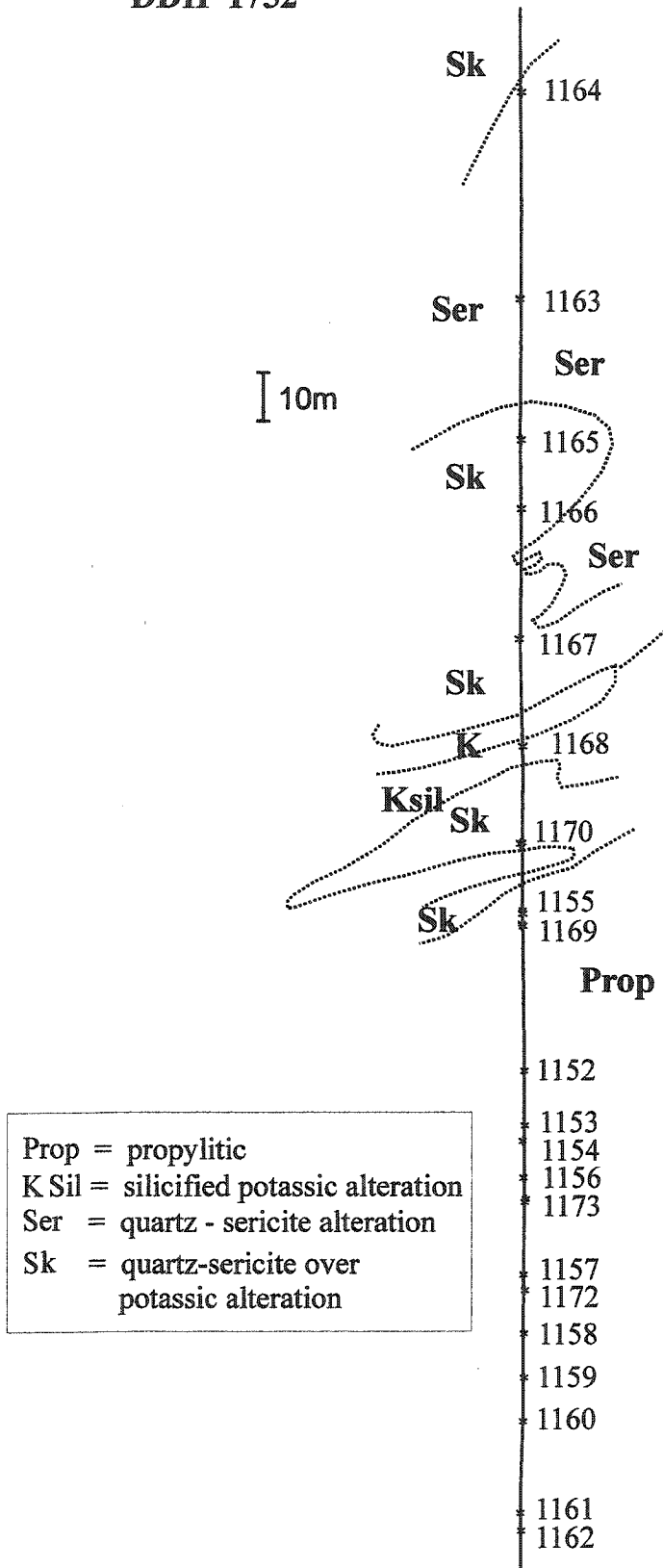
Chuquicamata



Appendix A: Sample Location



K = potassic alteration
K Sil = silicified potassic alteration
Ser = quartz - sericite alteration
Sk = quartz-sericite over potassic alteration



Appendix A: Sample Location

Appendix B

Petrography

Diamond drill hole 3472

Sample #	K-feldspar	Quartz	Plagioclase	Micas	Other
Cu070		very fine grained (50%)		sericite (50%)	vein of anhydrite/gypsum
Cu076		very fine grained groundmass to medium grained in veins, recrystallized		sericite also veins in a very fine quartz matrix	anhydrite vein (1cm across)
Cu080		very fine grained (30-40%)		sericite (60-70%) more grungy	anhydrite in vein zoned grain-looks like quartz
Cu086		very fine grained (20-30%)		sericite (70-80%)	anhydrite in vein with quartz
Cu088		fine grained (20-25%) recrystallized		sericite (75-80%)	sulphate?
Cu090		very fine grained (50%+)		sericite (50%)	small anhydrite veins
Cu091		recrystallized (50%)		sericite (50%)	grains of anhydrite in vein
Cu095	possible K-feldspar grain	mainly, recrystallized, undulose extinction		sericite	gypsum vein

Cu097					anhydrite veins surrounded by opaques gypsum vein
Cu101				fine to medium grained, recrystallized	mainly sericite, radiating
Cu105				very fine grained recrystallized	sericite
Cu106				mainly very fine quartz (90%)	lots of sulphides likely a vein
Cu110				very fine grained (40-50%)	anhydrite covellite
Cu113				very fine to fine, recrystallized, (50-60%) veins of coarser quartz	many veins of mainly quartz and opaques sulphate? covellite
Cu114				recrystallized (40-50%)	vein of quartz with 1 grain of anhydrite
Cu115				recrystallized (50%)	anhydrite in vein
Cu120				recrystallized coarser quartz in vein	anhydrite in vein with quartz
				fine grained, recrystallized, coarser in veins	anhydrite (vein)

Cu121			very fine to fine recrystallized, (25-35%)			sericite (>quartz)	anhydrite in vein with sulphides
Cu122			recrystallized (50%)			sericite (coarse) (50%)	anhydrite surrounded by gypsum in vein fluid inclusions in quartz
Cu124			mainly very fine, coarser in veins				dark vein
Cu129			fine (~50%)			sericite (~50%)	a couple grains of anhydrite in quartz vein
Cu131			fine grained recrystallized (40%)			sericite (60%)	anhydrite in quartz vein
Cu134			undulose most associated with vein			mainly sericite, very fine	anhydrite in quartz veins
Cu135			fine grained (~40%) recrystallized			sericite, some radiating	mafic mineral? anhydrite in veins
Cu140			very fine to fine (50%), recrystallized			sericite (50%)	anhydrite in veins
Cu144			very fine to medium grained (90%)			(little) sericite in veins	anhydrite in veins rutile?

Diamond Drill Hole 2620

Appendix B: Petrography

#	K-feldspar	Quartz	Plagioclase	Micas	Other
Cu148	large grains	hard to distinguish form K-feldspar	no plagioclase left	sericite or saussurite	
Cu149	moderate alteration	fine grained	no plagioclase left	sericite	
Cu152		fine grained (35-40%)		sericite (60-65%)	
Cu156		(50%)		sericite (50%)	claim ser- mainly sulphate
Cu157	mod alteration, fine to coarse grained (30%)	dissolved (20%)	<5% left	sericite (10%)	40% dark alteration
Cu160		undulose extinction	relict twins?	sericitic replacement of feldspar	
Cu161	strained extinction mod. alteration (20%)	(20%)	altered to ser, kinked twins (60%- altered)		
Cu162	fractured, inclusions of fresh plagioclase, fine to med. grained, little to mod alteration	very fine grained (20-25%)		biotite not fresh, no cleavage	vein mineral similar to 144
Cu164	coarse grained, few grains, altered	undulose extinction		sericite	

Cu187		10-30%, undulose extinction, slightly altered ? recrystallized	some twinning	most of thin section is sericite	anhydrite hexagonal mineral- quartz or apatite very fine grained
Cu192		<10%	antiperthite???	mostly sericite	anhydrite
Cu193		quartz in vein and matrix		mostly sericite	anhydrite
Cu195		serrate edges		lots of sericite	anhydrite?
Cu201		serrate edges		mostly sericite	anhydrite?
Cu203		undulose extinction, serrated edges, some med. grained size		mainly sericite	anhydrite?
Cu204		present		sericite	gypsum?
Cu206		present	grungy alteration	sericite	
Cu207	possibly relict?	undulose extinction irregular edges	can see twinning in altered feldspar	mainly sericite and other alteration minerals	
Cu208		undulose extinction		mainly sericite	anhydrite?
Cu211		40%		60% sericite	massive anhydrite? associated with opaques

Cu214		undulose extinction (not all grains), serrate edges		mainly sericite	
--------------	--	---	--	-----------------	--

Diamond Drill Hole 2242

#	K-feldspar	Quartz	Plagioclase	Micas	Other
Cu431		undulose extinction recrystallized (<1/2 mm), coarser in veins		mainly sericite	sulphate?
Cu433		undulose extinction (95%), very fine- to medium-grained			sulphate?
Cu434		undulose extinction (95%+)			sulphate?
Cu436	minor to moderate alteration (5%) difficult to tell but apparently perthitic	very fine grained recrystallized (20%)	very little left (was main mineral before alteration)	feldspars altered to dark grunge sericite dusts slide	rutile in vein
Cu438	large grain, moderate alteration or strain extinction or perthitic texture?	fine grained, little alteration (25-30%) recrystallized	mainly altered to sericite	mainly sericite	

Cu443	<5%		serrate edges (~50%)	euhedral grains altered to sericite	sericite in veins (~50%) does appear to affect surrounding	rutile
Cu445			60%		sericite 40%	
Cu447	<5% minor, small grains left	serrate edges, undulose extinction recrystallized (30-40%) v.v. fine mainly <1/4mm			sericite (60-70%) grades into darker grunge	brown nearly opaque alteration sulphate?
Cu448	some remaining?	very fine grained, undulose extinction, recrystallized		none remaining	sericite? brown grungy alteration	
Cu453	no twins, perthitic? biaxial, little to moderate alteration	serrate edges, very fine grained, recrystallized		nearly completely altered to sericite	sericite	sulphate?
Cu457	feathery extinction large grain cut by vein?	present			coarser grained than usual	gypsum veins cut through sericite and feldspar
Cu468	little to moderate alteration twinned K-feldspar? (25%)	very fine grained, serrate edges, recrystallized (25%)			very little biotite, dark brown, pleochroic sericite (50%)	
Cu473	present	serrate edges, very fine grained		zoned and twinned grains	biotite altered, dark brown, pleochroic	

Cu475	30%	30%	moderate alteration, relict plagioclase (5%)	sericite 30%	sulphate?
--------------	-----	-----	--	--------------	-----------

Diamond Drill Hole 2234

#	K-feldspar	Quartz	Plagioclase	Micas	Other
Cu487	plagioclase inclusions (10%)	15-20% undulose extinction serrate edges	replaced by sericite; fresh as inclusions in K-feldspar	mostly sericite	quartz sericite vein
Cu488	fresh plagioclase inclusion in K-feldspar, possible perthitic texture	(20%) undulose extinction, serrate edges	very altered, zoning and twinning	sericite mainly replacing feldspar; some cleaved biotite pale to dark brown inclusion of apatite, kinked	anhydrite
Cu494	moderate to extensive alteration	undulose extinction (30-40%)	relict twinning, none left	pleochroic brown, mainly altered biotite (<5%) 60% sericite-altered feldspar	sulphate ?
Cu495		10% quartz		mainly sericite	sulphate ?

Cu496	moderate alteration, feathery extinction	little alteration, serrate edges	twinning, extensive to complete alteration to sericite	biotite- pleochroic yellow/brown, cleavage, high birefringence	sulphate ?
Cu499		quartz		sericite	sulphate?
Cu504		serrate edges, undulose extinction	can see relict twinning	sericite altering felspars; brown pleochroic biotite with some cleavage	
Cu508		serrate edges, recrystallized	sericitized, elongate and twinned	biotite red-brown to green pleochroism, kinked	rutile amphibole? look for K-feldspar

#	K-feldspar	Quartz	Plagioclase	Mica	Other
Cu 1101	large phenocryst w/ strained extinction and inclusion plagioclase+quartz braided perthite (?)	undulose extinction polycrystalline, recrystallized	minor sericite; mainly plagioclase.; some display twins and zoning; average 2mm; many patch antiperthite; some grains with intersecting twins	no biotite sericite veins	v. fractured, no ser outside veins small veinlets quartz/ser vein opaques with ser zircon gypsum vein
Cu 1102	strained extinction large grain (1.5cm) inclusions of quartz, plagioclase stringers run through minor perthite	undulose extinction elongate, polycrystalline pods, recrystallized	mainly plagioclase fresh and twinned kinked twins intersecting twins patch antiperthite large grain (6mm long)	no biotite sericite veins	veinlets cut inclusions in K- feldspar very fractured- devitrified glass groundmass veinlets of opaques, quartz, ser

Cu 1103	fresh with quartz inclusion other fresh, strained extinction no or cryptocrystalline perthite	fine grained ratty elongate (almost ribbons)	extensively sericitized some twinning seen 1-4mm mainly plagioclase	no biotite sericite in plagioclase	coarse white mica unknown minerals in veins apatite or rutile
Cu 1104	K-feldspar >2mm long very fractured	undulose extinction ratty groups as well as in groundmass	some grains >2mm mainly fine and fractured with albite twinning relatively fresh	no biotite sericite in veins	very fine grained, ser in veinlets through minerals and rimming them epidote? very fractured, less glassy than Cu1102
Cu 1105	strained extinction; blebs of quartz at edges of grains; inclusions of plagioclase, rutile and quartz; large grains <2cm; albite inclusion- minor to extreme sericitization; minor perthite near edges	polycrystalline pods, recrystallized; groundmass	some very altered 2-3.5mm average a few with v.little ser	biotite pleochroic, some cleaved; is it in a vein? at edge of K megacryst-pushed out of way sericite in plagioclase	large white micas, epidote (?) unknown vein mineral (blue-green) veinlets of ops and gyp apatite (?)

<p>Cu 1106 *</p>	<p>strained extinction inclusions of sericitized plagioclase, fresh plagioclase and quartz ser x-cut veinlets microcline (?), perthitic</p>	<p>polycrystalline, recrystallized</p>	<p>extreme to moderate alteration to ser kinked twins intersecting twins</p>	<p>no biotite sericite in the plagioclase</p>	<p>veinlets of quartz and ser zircon</p>
<p>Cu 1107 *</p>	<p>quartz inclusions along edges of K-feldspars one string perthite microcline? ser along x-cut veinlets</p>	<p>very fine grained between altered plagioclase</p>	<p>moderate to strong sericitization; some altered to saussurite or clay; patch antiperthite</p>	<p>some red-yell strong pleochroic; other weak pleochroic brown-green-colourless all less than 2mm, all in gm; dark</p>	<p>zircon assoc w biot</p>
<p>Cu 1108</p>	<p>fairly fresh, cut by veins of ser, strained extinction</p>	<p>undulose extinction, fractured, polycrystalline recrystallized</p>	<p>patch antiperthite very little plagioclase intersecting twins very fine grained</p>	<p>no biotite sericite veins</p>	<p>sericitic veins throughout, very fractured</p>

<p>Cu 1109</p>	<p>strained extinction inclusions of quartz, plagioclase- kinked and fractured large elongate grain (<3cm) large string perthite small braided grain microcline</p>	<p>undulose extinction recrystallized, polycrystalline</p>	<p>some very fresh very fractured some grains with intersecting twins some replacement perthites inclusions in K-feldspar with minor sericite</p>	<p>v. small vein of brown-possible v.v. fine biotite; veins sericite</p>	<p>-very fractured and veined -veinlets of sericite do not appear to affect surrounding minerals -appears groundmass might be partly glass -unknown altered, high relief mineral</p>
<p>Cu 1111</p>	<p>braided perthite inclusions of quartz, plagioclase (altered), white mica, op strained extinction perthitic-string</p>	<p>undulose extinction polycrystalline elongate patches</p>	<p>sericitized- some nearly completely; can see twins on edge of some grains; few grains minor affected by sericite; patch antiperthite inclusion altered to sericite</p>	<p>no biotite</p>	<p>rutile and zircon opaques assoc with veins</p>
<p>Cu 1112</p>	<p>string perthite strained extinction inclusions of plagioclase and quartz</p>	<p>polycrystalline, undulose extinction recrystallized</p>	<p>patch antiperthite intersecting twins minor to moderate sericite alteration kinked twins</p>	<p>very little, pale and cleaved assoc with opaque small grains some intergrown with muscovite</p>	

<p>Cu 1114</p>	<p>strained extinction string perthite braided perthite some relatively small and difficult to identify; larger grain with inclusions of quartz, plagioclase</p>	<p>undulose extinction ratty, polycrystalline (almost ribbonized in places) recrystallized</p>	<p>patch antiperthite intersecting twins kinked twinning cores often sericitized</p>	<p>very little biotite, ragged edges cleaved and pleochroic, kinked possibly associated with veining; sericite in plagioclase</p>	<p>very fractured sericitic veins zircon (?) some sections of slide extensively sericitized</p>
<p>Cu 1115</p>	<p>large megacryst w/ inclusion of altered plagioclase, biotite- perthitic, fractured, veined braided perthite</p>	<p>polycrystalline, irregular edges some appear elongate</p>	<p>moderate to strong sericitization 1-3mm some altered to clay?</p>	<p>biotite nice cleavage, high birefringence. some dark w/o cleavage assoc. w/ diamond shaped opaque. all kinked, patchy</p>	<p>anhydrite or calcite vein unknown green mineral rutile and biotite apatite</p>
<p>Cu 1116</p>	<p>perthites w/ inclusion of quartz, plagioclase very fractured</p>	<p>v. fine, recrystallized, polycrystalline</p>	<p>minor to strong sericitization patch perthite (K?) kinked twins</p>	<p>biotite intergrown w/muscovite (.5mm) other biotite, not assoc w/muscovite <.5mm</p>	<p>very fractured/sheared diamond shaped grunge sericitic veins phenocryst brittle fracture</p>

Cu 1117	perthitic K-feldspar w/ inclusions of altered plagioclase, quartz minor microcline braided perthite	recrystallized, undulose extinction, polycrystalline	plagioclase with double twins very sericitized, some kinked twins	small grain with cleavage, high birefringence	sericitic veins (surrounding opaques) zircon in plagioclase grain, in quartz
Cu 1118	large K-feldspar with small inclusions and perthitic lamellae, strained extinction, minor microcline flame perthite inclusion in K-feldspar, braided perthite	ratty edges, also some straight undulose extinction not all recrystallized	brown, high relief alteration in ppl-clay and biotite perthitic included in albite? rims remain	biotite kinked, pleochroic, birds eye extinction	clay alteration of feldspar (brown grungy); large zircon assoc. with biotite and op.; usual radiating mineral from 1103 (variscite?)
Cu 1119	unaltered, quartz incln, 1-2mm some string perthite braided and flame at edge of large phenocryst minor microcline like twins in interior	undulose, .1-.2mm grains ratty edges, polycrystalline eyes-elongate 2mm groundmass	minor sericitic, clay alteration some have no twins; kinking, some intersecting twins, 2-3mm, inclusion of plagioclase	green-brown pleochroism, v. altered at grain boundaries, assoc. w/ granular opaques; some uncleaved and nonpleochroic (~2mm)	anhydrite vein vein of opaque minerals zircon in biotite gm- quartz, minor biotite and feldspar possible calcite and clay

Cu 1120	strained extinction string perthite, slightly altered inclusion of plagioclase (one small biotite grain) braided perthite	strained, undulose extinction, not all recrystallized	minor to moderate alteration, kinked twins patch perthite some clay alteration intersecting twins	pleochroic, pale ratty f.g. biotite associated with opaques patch 7mm long	pseudomorphed diamonds of rutile (?)
Cu 1121	strained extinction inclusion of fresh plagioclase (kinked and fractured) string perthite string perthite (~1cm) with inclusion plagioclase, quartz	polycrystalline, undulose extinction recrystallized	strained extinction doubly twinned replacement	dark, uncleaved and pleochroic and cleaved small grain included in K-feldspar	altered glass ? large ser and quartz vein cuts thin section zircon
Cu 1122	small grains, strained extinction		very fractured sericitized to varying degrees	minor biotite, assoc with opaques patch of chlorite also assoc with veins (w anhydrite) green high birefringence. mica	very fractured veins of gypsum chlorite and calcite veins

Cu 1123	difficult to tell from quartz	grains look like K-feldspar	it is here	chlorite and biotite in veinlets	very fractured and altered matrix is sericite and quartz
Cu 1125	strained, exsolution fractured with inclusions slightly sericitized	recrystallized	sericitized moderately	biotite associated with veining	anhydrite or gypsum veins
Cu 1126	grain at edge ~1cm perthite w inclusion plagioclase uneven grain boundary	recrystallized	possible replacement some plagioclase w little alteration broken and kinked twins	chlorite vein and incl of feldspar; pleochroic high birefringence green mica; all assoc w opaques	zircon apatite
Cu 1127	some grains with plagioclase, quartz, biotite inclusions strained extinction zoned inclusions in perthitic phenocryst cross hatch twinning	recrystallized, polycrystalline not elongate found in groundmass	some twins and zoning, altered in zones, little to moderate alteration to sericite intersecting twins some clay?	biotite pleochroic, shows some cleavage ragged edges very fine to >2mm	zircon some very altered feldspar lots of fracturing rutile with diamond shape K-spar veins

Cu 1128	strained extinction large grain with inclusions of plagioclase (altered) possible x-hatch twins in smaller grain	polycrystalline grains some are elongate but it is unclear if they are associated with veins	some extensively sericitized; showing relict euhedral shape very altered	some cleaved some not, slight to highly pleochroic; only small, unhappy grains	fractured, many veins
Cu 1129	small, strained extinction inclusions of plagioclase large grain with ser stringers (<1cm)	recrystallized, polycrystalline, not elongate vein with sericite selvages	patch antiperthite, extinguishing cores, some strongly sericitized euhedral grains near vein	patchy assoc. with opaques some fresh	veins op surrounded by quartz, surrounded by sericite zircon
Cu 1130	moderately altered, sericitization large grain with perthitic text. inclusions of biotite, quartz, plagioclase	undulose extinction recrystallized, eyes 2-4 mm makes up most of groundmass	some grains very altered; possible antiperthitic grains approx. 2mm some grains with intersecting twins "pinched" twins	small, cleaved and pleochroic grains- brown-colourless, ratty edges, assoc. w/ op.; one large kinked cleaved grain; some uncleaved, nonpleochroic grains	fractured, veins of sericite pervasive sericitization one of the very euhedral grains apatite

<p>Cu 1132</p>	<p>v. large grain with inclusion of plagioclase, (twinned, kinked), quartz, biotite; biotite inclusion not pleochroic strained extinction large fracture (glass?) dissects grain</p>	<p>undulose extinction recrystallized, not elongate, polycrystalline</p>	<p>sericitized (minor-very) mainly along twins, sometimes cores; euhedral, patch antiperthite (seen in a plagioclase inclusion, too!)</p>	<p>pleochroic, ratty, cleavage two small, intergrown with muscovite some low birefringence., no cleavage</p>	<p>lots of sericite fine grained, is there glass? opaques in veins zircon (Unknown min-vein related? +relief, biaxial +ve, colourless, square)</p>
<p>Cu 1134</p>	<p>small strained extinction inclusion of quartz perthitic</p>	<p>undulose extinction very little elongate very fine grained</p>	<p>sericitized, almost completely no twins seen</p>	<p>brown pleochroic with high birefringence show some cleavage up to 2mm</p>	<p>zircon veins opaques and colorless near isotropic mineral</p>
<p>Cu 1135</p>				<p>biotite inclusion in K-feldspar; cleaved and uncleaved biotite; pleochroic, high birefringence.</p>	

Cu 1136	inclusions of plagioclase, quartz, biotite minerals displaced at rim of grain unusual extinction, exsolution	undulose extinction	minor alteration	pleochroic, high birefringence, partly cleaved biotite, all <2mm	zircon unknown mineral
Cu 1137	large grain with inclusion quartz, biotite, altered feldspar; partially altered	v. little undulose extinction ratty, granular edges	extensive alteration can see remnant twinning	beautiful, assoc. w/ op and ap some nonpleochroic, no cleavage	apatite
Cu 1138	strained extinction, quartz inclusions with flincks, some microcline	ratty edges, little undulose extinction	some unaltered with twins v. alter feldspar (sericite)	pleochroic, high birefringence some cleavage, assoc w/ op.	very altered feldspar
Cu 1140	strained extinction fractured or perthitic inclusions of sericitized plagioclase	fine-grained quartz matrix ragged, fractured	sericitized		lots of sericite here

Cu 1141	small perthitic grain	ratty and fractured	show twinning, nearly fresh, others extensively altered	high birefringence, no app. cleavage two here do display cleavage	
Cu 1142	strained extinction perthitic cores in some grains inclusions of quartz fine braided perthites	undulose extinction ratty edges, elongate	plagioclase altered almost completely to sericite/clay	ragged, very fine no pleochroism, low birefringence. some biotite, pleochroic, high birefringence, cleaved	vein of very low birefringence, low relief, colourless min... sounds like glass what a mess of alteration
Cu 1144	inclusions of quartz, op strained extinction, microcline, flame perthite, 1.5mm grains	undulose extinction recrystallized	very altered-clay?	stringers of sericite	zircon, sulphate in vein sericite veinlets dark patchy grains-change relief when rotate
Cu 1145	perthites string and braided a non-textured grain with inclusion, perthite growing from flames	beautiful ribbonized, squished around other grains recrystallized	mainly sericitized plagioclase, replacement feldspar	dark and shreddy biotite	

Cu 1146	small braided perthite	undulose extinction	bent and broken twins look fresh! replacement feldspar	ratty pleochroic biotite assoc w/ op slightly pleochroic, high birefringence. strings of sericite a dark biotite	veinlets of sericite, plagioclase, K-feldspar and quartz fractured and ground up v.f.g, gm chewed up strained extinction, uneven edges
Cu 1147		ribbon quartz		clay alteration	calcite vein and replacing plagioclase
Cu 1150	strained extinction, feathery 2 small braided perthites microcline	recrystallized, strained large crystals, undulose; elongate; inclusions of rounded biotite/anhydrite+feldspar ribbonized	moderate alteration replacement feldspar some are less altered, double twins	pleochroic, high birefringence cleavage, ratty w/ opaque	stringers of sericite vein of gypsum diamond shaped rutile square, colourless high rel, high birefringence. grain zircon in gm

<p>Cu 1151</p>	<p>strained extinction minor alteration fine braided perthite</p>	<p>undulose extinction slightly elongate recrystallized</p>	<p>sericitized, euhedral grains some fresh rims on replacement feldspar</p>	<p>kinked, very little "primary" some high birefringence, pleochroic others low birefringence, not pleochroic, no cleavage ser alteration 1/2 of slide some K left with Q</p>	<p>(half of slide) large amount of ser appears to be in vein and alteration of plagioclase fractured diamond shaped rutile</p>
<p>Cu 1152</p>	<p>strained extinction inclusions perthitic grains braided perthite relict microcline?</p>	<p>undulose extinction, recrystallized some very fine grains polycrystalline</p>	<p>twinned, relatively fresh twins kinked replacement feldspar</p>	<p>sericite in groundmass sericite veins</p>	<p>pretty chewed up most grains dusty alteration matrix is microcrystalline a lot of little veinlets and fractures gypsum veining, possible anhydrite vein</p>
<p>Cu 1153</p>	<p>microcline/ braided perthite replacement K- feldspar, albite/quartz inclusions is the K-feldspar sericitized?</p>	<p>recrystallized, undulose extinction</p>	<p>twinned, some doubly one doubly twinned being replaced</p>	<p>sericitization of K- feldspar? and albite</p>	<p>very fractured zircon</p>

<p>Cu 1158</p>	<p>feathery braided perthite K-feldspar with inclusions, minor strained extinction, v.f. perthite</p>	<p>recrystallized, undulose extinction myrmekite</p>	<p>alteration in zoning (not rim) of plagioclase, neat euhedral shapes plagioclase twinned, ser alteration, 6wt%Ca in cores possibly some anhydrite</p>	<p>cleaved and uncleaned fresh grains and chloritization?</p>	<p>apatite vein of chl/rutile? anhydrite vein unusual opaque</p>
<p>Cu 1159</p>	<p>strained extinction inclusion of plagioclase</p>	<p>recrystallized</p>	<p>twinned plagioclase, K-feldspar replacing albite?</p>		
<p>Cu 1160</p>	<p>exsolution(thin lamellae), myrmekite strained extinction</p>	<p>recrystallized</p>	<p>strained extinction fine twins, little alteration</p>	<p>rimmed by muscovite? biotite is very pale sericite in groundmass</p>	<p>anhydrite veins? sericite in gm rutile</p>

<p>Cu 1161</p>	<p>inclusions of altered plagioclase (twinned and zoned), biotite, large inclusion, show strained extinction very fine perthitic texture flame/braid perthite not altered dusty like plagioclase very little texture here</p>	<p>fractured, undulose extinction, recrystallized, ribbonized</p>	<p>moderate to totally sericitized, some twinning visible possible calcite replacement</p>	<p>pleochroic brown-yellow, high birefringence, some cleavage dark and fresh</p>	<p>sulphate in altered feldspar grain? anhydrite? --> changes relief</p>
<p>Cu 1162</p>	<p>shows strained extinction dusty alteration, inclusion of plagioclase, recrystallization of deposition along vein looks like delta</p>	<p>quartz is ratty, undulose extinction, strained. recrystallized and ribbonized</p>	<p>plagioclase mod. alteration, twins visible doubly twinned</p>	<p>biotite in a vein, high birefringence. brown-yellow, some cleavage, other biotite localized around vein (in contact)</p>	<p>gypsum vein</p>

Cu 1165	strained extinction braided larger grain with inclusions and perthitic text appears unaffected by the pervasive alteration	undulose extinction ratty edged grains, elongate polycrystalline	edges of grains altered by sericite appear to be unaffected but display no twins kinked twins in moderately altered grains	really pale, high birefringence, cleaved, assoc. with opaques	very fractured, chewed up sericite localized around the twins
Cu 1167	strained extinction inclusions of quartz, plagioclase perthite, fractured	undulose extinction polycrystalline	kinked twins some with twins in two directions altered	dark fine grained biotite	sericitization in veins very fractured
Cu 1169	inclusions of green biotite, sericitized feldspar, strained extinction	recrystallized, shattered grains, undulose extinction,	sericitized feldspar grains, dusty plagioclase some twinning visible	green biotite in groundmass, cleaved, high birefringence; green biotite in veins- same morphology don't see any chlorite	
Cu 1174	some perthitic, strained extinction			cleaved pleochroic biotite	

Sample	K-feldspar	Quartz	Plagioclase	Mafics	Other
Cu 769	fine-grained; string perthite occurs locally; very little K-feldspar relative to plagioclase and rare phenocrysts	mainly in the groundmass; also as clusters of recrystallized grains that might be considered phenocrystic	sample is mainly plagioclase, some grains show zoning with/without twinning, patch antiperthite; intersecting twins up to 6mm	amphibole- green-yellow pleochroic, hornblende (1-2mm); biotite is pleochroic brown-yellow as distinct grains and altering amphibole	Titanite- euhedral and cleavage locally, mg; minor groundmass of mainly quartz with K-feldspar
Cu 746	perthite with some sericitized lamellae, K-feldspar with albite inclusions, perthite very fine	partly recrystallized	partly altered	biotite is partly chloritized	
Cu 510	braided perthite	fractured, recrystallized	small twinned grains, dusted by sericite	sericite in veins and alteration of feldspar	very fractured many ser veins calcite veins, bits of rock floating in calcite
Cu 512	subhedral perthite with quartz inclusions at rim (biaxial negative	recrystallized, polycrystalline	small phenocrysts- altered cores, twinned rims; larger phenocrysts- not as altered core, dusty throughout; patch antiperthite	biotite-high δ , pleochroic brown-yellow	gm-mainly quartz doubly porphyritic mainly plagioclase phenocrysts

Cu 513						
Cu 514	Quartz inclusion rims Inclusions of chl, plag	polycrystalline, recrystallized	plag serd or clay altd, kinked twins, some cores missing; patch antiperthite	biotite-pleochroic yellow-brown, high δ partly chloritized veins of biotite-chl	double porphyritic groundmass- quartz mainly plagioclase phenocrysts	
Cu 524	25%	25% graphic texture	twinned and zoned, most abundant, fresh to slightly altered (cores altered)	biotite-pleochroic brown/yellow with chl intergrowths and apatite inclusions, good cleavage; little amphibole, pleochroic, green- yellow, cleavage	lots of titanite abundant apatite	
Cu 046	strained extinction low 2V, optically neg some plagioclase inclusion	5-10% graphic texture	twinned, zoned fresh to slightly altd	bt-fresh, good cleavage, pleo bwn- yll; amph pleo yll- gm, high δ , some cleavage	titanite	

Cu 407	more K-feldspar than quartz, fresh, plagioclase inclusion		most abundant, twinned and zoned, kinked and moderate to extreme sericite/saussurite alteration	little biotite-chloritized, biotite-pleochroic yellow-brown amphibole-yellow/green pale, good cleavage-rare	titanite
--------	---	--	---	---	----------

Cu 1154	no twins, rounded, minor ser.	recrystallized, undulose extinction many FLINCS	twinned, some doubly little sericitization	lots of v.f. gm ground up
Cu 1155	some f.g., small microcline strained extinction in large K small quartz inclusion, no apparent perthite		no apparent plagioclase/albite twinning	mainly v.f. grained-broken up gm looks like a lot of stress but feldspar don't demonstrate this?
Cu 1156	strained ext., inclusion of quartz, biotite, altered plagioclase w. thin perthitic texture, 1 kspars has braids and flames perthitic microcline	recrystallized, ribbonized	albite being replaced by K-feldspar thinly twinned plagioclase ser. altered a feldspar completely replaced by ser or clay and anhydrite	v.f.g rock
Cu 1157	small K-feldspar with strained extinction, small quartz inclusion	recrystallized, almost ribbonized	fractured and twinned plagioclase (1.5mm)	v.f.g

Appendix C
Electron Microprobe Data

Electron microprobe analyses were done in Robert MacKay's laboratory at Dalhousie University to confirm identification of phases for petrography, as well as to study variations in the mineral chemistry. A JEOL 733 electron microprobe with four wavelength dispersive spectrometers and an Oxford Link eXL energy dispersive system was used. The resolution of the energy dispersive detector was 137 eV at 5.9 KeV. Each spectrum was acquired for 40 seconds, with an acceleration voltage of 15 Kv and a beam current of 15 nA. Probe spot size was approximately 1 micron. Link's ZAF matrix correction program was used to correct the raw data. Cobalt metal was used to calibrate the instrument. The precision of the instrument on cobalt metal (n=10) was $\pm 0.5\%$ at 1 standard deviation. The relative accuracy for major elements was ± 1.5 to 2.0% . Geological standards were used as controls. Detection limits for most elements using the energy dispersive system range from approximately 0.1 to 0.3%.

X-ray back-scatter images were also done on the JOEL 733 electron microprobe to clearly display differences in the density of minerals.

Sample	SiO ₂	Al ₂ O ₃	CaO	Na ₂ O	K ₂ O	BaO	Total
Cu1102-8	69.21	19.61	0.07	10.05	0.18	0.00	99.12
Cu1102-13	69.35	19.76	0.26	9.70	0.15	0.12	99.34
Cu1102-14	68.77	19.65	0.00	10.73	0.10	0.06	99.31
Cu1102-22	66.79	18.57	0.03	5.42	8.35	0.09	99.25
Cu1102-23	66.33	18.68	0.24	10.89	0.35	0.00	96.49
Cu1115-05	67.83	19.19	0.15	10.25	0.09	0.00	97.51
Cu1115-11	65.94	19.45	0.56	9.23	0.20	0.24	95.62
Cu1119-03	71.12	19.94	0.05	9.42	0.32	0.05	100.90
Cu1119-04	70.40	19.93	0.00	9.57	0.10	0.06	100.06
Cu1119-05	69.79	20.47	0.39	8.23	1.09	0.13	100.10
Cu1116-02	68.69	20.14	0.27	10.70	0.10	0.00	99.90
Cu1122-02	68.06	20.73	0.64	10.20	0.34	0.11	100.07
Cu1136-3-7	68.55	20.22	0.55	11.13	0.10	0.00	100.56
Cu1136-6-7	68.08	20.08	0.64	11.21	0.04	0.05	100.10
Cu1136-7-7	67.29	20.43	1.23	10.48	0.10	0.00	99.53
Cu1136-8-7	68.26	19.86	0.43	11.23	0.08	0.06	99.93
Cu1136-11-1	68.72	19.83	0.29	10.59	0.16	0.12	99.72
Cu1136-13-2	69.13	19.64	0.01	9.06	0.88	0.13	98.86
Cu1136-14-7	68.93	20.18	0.42	11.06	0.10	0.00	100.69
Cu1117-1-9	68.62	19.75	0.06	10.98	0.10	0.06	99.56
Cu1117-3-9	68.04	20.15	0.38	11.42	0.09	0.00	100.09
Cu1117-4-3	69.12	19.86	0.05	10.96	0.10	0.01	100.11
Cu1117-5-3	68.99	19.73	0.20	10.41	0.01	0.15	99.49
Cu1141-3-3	68.79	19.80	0.05	11.33	0.07	0.11	100.15
Cu1141-4-3	68.51	19.64	0.04	10.25	0.09	0.10	98.63
Cu1141-5-3	68.81	19.88	0.19	11.43	0.16	0.00	100.47
Cu1129-1-7	69.21	19.84	0.15	10.95	0.16	0.00	100.31
Cu1129-7-3	68.71	19.92	0.14	11.44	0.13	0.00	100.33
Cu1129-8-3	68.14	19.63	0.17	11.08	0.03	0.06	99.11
Cu1138-1-7	68.46	19.97	0.42	10.49	0.08	0.07	99.49
Cu1138-3-7	67.87	20.14	0.65	10.24	0.18	0.00	99.08
Cu1138-6-3	68.33	19.67	0.18	10.94	0.17	0.00	99.30
Cu1101-1-3	69.29	19.75	0.05	10.93	0.16	0.00	100.18
Cu1106-1-i	68.33	19.59	0.00	10.38	0.00	0.00	98.29
Cu1106-2-i	69.66	20.03	0.22	11.08	0.00	0.00	100.98
Cu1106-5-d	68.33	19.98	0.28	10.91	0.12	0.00	99.63
Cu1106-6-3	69.34	19.96	0.00	10.68	0.00	0.00	99.98
Cu1106-7-3	69.26	20.02	0.17	10.41	0.12	0.00	99.98
Cu487-04	67.79	19.77	0.34	9.17	0.19	0.16	97.42
Cu487-05	67.73	20.05	0.51	10.08	0.06	0.00	98.43
Cu1146-02pl	68.24	19.98	0.48	10.34	0.11	0.13	99.27
Cu1146-03	68.69	20.07	0.40	11.12	0.06	0.06	100.39

Appendix C: Albite

Sample	SiO2	Al2O3	CaO	Na2O	K2O	BaO	Total
Cu1146-04	67.49	20.46	0.97	10.24	0.14	0.00	99.30
Cu176	67.44	20.92	1.24	10.34	0.11	0.00	100.06
Cu176-02	69.21	19.95	0.08	10.55	0.07	0.17	100.03
Cu176-03	69.07	19.89	0.09	9.51	0.08	0.00	98.64
Cu176-04	68.00	20.59	0.97	9.34	0.10	0.19	99.18
Cu176-08	69.55	20.15	0.20	9.29	0.14	0.18	99.52
Cu157-03	66.87	20.03	0.66	5.57	6.54	0.38	100.06

Anhydrite		CaK	S K	O K	SrL	Total	
Cu204a-1		28.10	23.85	45.92	0.86	98.73	28.96
3		28.15	23.97	46.58	0.88	99.58	29.03
	4	28.51	24.01	46.73	0.73	99.99	29.24
	5	27.74	23.52	46.47	1.80	99.53	29.54
	6	28.48	23.96	46.00	0.59	99.03	29.07
	7	28.05	24.23	46.72	0.73	99.74	28.78
	8	28.24	24.26	46.45	0.66	99.61	28.90
	9	28.17	23.95	46.60	0.87	99.58	29.03
10a		26.15	22.31	47.70	0.50	96.66	26.65
10b		28.20	24.04	46.96	0.81	100.01	29.01
10c		28.25	24.02	47.66	0.88	100.81	29.13
10d		28.09	24.01	46.73	0.84	99.66	28.92
10e		27.18	23.32	48.86	0.48	99.83	27.65
	12	27.98	23.85	46.65	1.17	99.65	29.15
	13	27.64	23.88	46.56	1.28	99.36	28.92
	14	27.95	23.64	46.37	1.52	99.48	29.46
	16	28.32	24.10	46.59	0.33	99.34	28.65
	17	27.37	23.69	46.53	1.81	99.39	29.18
	18	28.13	23.83	46.21	0.96	99.13	29.09
	19	28.01	24.07	46.02	0.90	99.00	28.91
Cu204b-1		28.37	24.15	45.95	0.80	99.27	29.17
	2	27.71	23.70	46.07	1.79	99.26	29.50
	3	27.29	23.35	46.76	0.90	98.30	28.19
	8	28.23	23.96	45.77	0.94	98.89	29.16
	9	27.83	23.96	45.41	0.95	98.15	28.78
	10	28.34	24.01	46.15	0.94	99.44	29.28
	11	28.39	24.19	46.03	0.73	99.34	29.12
	12	28.06	23.79	45.59	1.07	98.50	29.12
	14	28.22	23.83	45.85	1.42	99.33	29.64
	15	28.06	24.07	46.27	0.95	99.36	29.02
	17	27.87	23.76	45.73	1.50	98.86	29.37
	18	27.84	23.85	46.11	0.89	98.68	28.73
Cu193-2		28.00	24.12	46.40	0.66	99.17	28.65
	3	27.90	24.03	45.76	1.21	98.90	29.12
	4	28.18	23.97	45.24	0.54	97.92	28.72
	5	28.09	24.17	45.81	0.27	98.34	28.36
	6	28.01	23.98	45.66	0.68	98.34	28.69
	7	27.92	23.93	46.13	0.69	98.67	28.61
Cu195-1		28.24	24.00	46.73	0.73	99.70	28.97
	4	28.21	23.95	46.10	0.36	98.61	28.57
	5	28.42	24.07	46.41	0.33	99.24	28.75
	7	28.18	24.19	46.37	0.25	98.98	28.43
	8	28.54	23.95	46.69	0.32	99.50	28.86
	9	28.41	24.02	46.94	0.47	99.83	28.88
	10	27.99	23.60	46.72	0.10	98.41	28.09
	12	28.11	24.12	46.77	0.47	99.47	28.58
	13	28.50	24.23	46.36	0.22	99.31	28.72
	14	28.18	23.82	45.76	1.01	98.77	29.19

Cu454-1	27.23	23.20	50.99	0.00	101.43	27.23
2	27.24	22.74	48.05	0.00	98.04	27.24
3	27.70	23.32	49.20	0.00	100.22	27.70
5	27.31	22.93	47.58	0.13	97.95	27.44
6	27.86	23.01	48.71	0.00	99.57	27.86
7	27.17	22.82	51.11	0.00	101.10	27.17
9	27.38	23.38	48.34	0.00	99.10	27.38
10	27.66	23.32	49.45	0.00	100.42	27.66
14	27.60	23.22	49.44	0.13	100.39	27.73
15	27.14	23.07	50.83	0.00	101.04	27.14
17	27.70	23.49	49.85	0.00	101.05	27.70
18	27.46	22.98	47.30	0.00	97.74	27.46
Cu490-1	28.17	24.01	45.98	0.58	98.73	28.75
2	28.60	23.84	46.40	0.64	99.48	29.24
3	29.16	23.65	44.95	0.63	98.38	29.79
4	28.31	24.03	45.88	0.59	98.80	28.90
5	28.33	24.22	46.62	0.61	99.77	28.93
6	28.43	24.07	46.85	0.54	99.89	28.97
7	27.82	23.41	50.94	0.00	102.17	27.82
11	27.40	23.27	49.14	0.00	99.81	27.40
12	27.43	23.17	49.57	0.17	100.34	27.60
13	27.92	23.31	47.87	0.00	99.11	27.92
14	28.80	24.43	47.00	0.00	100.23	28.80
16	27.99	23.33	49.30	0.10	100.71	28.09
17	28.17	23.98	46.83	0.46	99.44	28.63
18	28.31	24.21	45.97	0.61	99.10	28.92
19	28.48	24.04	46.57	0.61	99.70	29.09
20	28.27	23.86	46.30	0.61	99.05	28.89
21	28.59	24.03	46.34	0.58	99.54	29.17
22	28.11	24.09	46.13	0.56	98.90	28.67
23	28.01	24.07	46.13	1.18	99.39	29.19
24	28.54	24.14	46.33	0.67	99.69	29.21
Cu440-8	27.44	23.08	48.60	0.00	99.12	27.44
10	27.76	23.20	48.27	0.00	99.22	27.76
12	26.65	22.53	53.33	0.00	102.50	26.65
15	27.08	22.69	48.91	0.00	98.68	27.08
17	27.92	23.42	48.35	0.00	99.70	27.92
20	28.07	23.54	47.04	0.00	98.64	28.07
21	27.80	23.31	49.10	0.00	100.21	27.80
22	27.80	23.34	49.82	0.00	100.95	27.80
24	27.53	23.07	51.15	0.00	101.75	27.53
Cu493-2	27.91	23.36	50.96	0.00	102.23	27.91
3	27.52	23.16	49.05	0.00	99.73	27.52
4	27.90	23.48	50.31	0.00	101.69	27.90
5	27.90	22.99	48.26	0.00	99.15	27.90
6	27.95	22.80	49.61	0.00	100.35	27.95
7	27.66	22.79	46.98	0.00	97.42	27.66
8	28.30	23.49	49.09	0.00	100.88	28.30
10	27.35	22.78	48.99	0.00	99.11	27.35
Cu182a-1	27.19	22.82	49.74	0.00	99.75	27.19

Appendix C: Anhydrite

Cu182a-2	27.90	23.39	50.65	0.00	101.94	27.90
3	27.95	23.34	49.34	0.00	100.63	27.95
4	28.06	23.43	51.52	0.00	103.01	28.06
7	27.58	23.03	49.25	0.00	99.87	27.58
Cu078-1	28.59	24.35	47.42	0.00	100.35	28.59
2	28.71	24.22	46.55	0.18	99.66	28.89
3	28.72	24.23	46.26	0.14	99.35	28.86
4	29.13	24.09	46.53	0.00	99.75	29.13
5	28.22	24.25	46.64	0.78	99.88	28.99
9	28.23	24.14	47.07	0.51	99.94	28.74
Cu504-2	27.93	23.30	51.21	0.00	102.44	27.93
3	28.04	23.55	47.94	0.00	99.53	28.04
4	28.46	24.21	46.38	0.41	99.46	28.87
5	28.50	24.19	46.67	0.14	99.50	28.64
6	28.47	24.11	46.43	0.44	99.44	28.91
7	27.95	23.96	46.53	1.14	99.58	29.09
8	28.19	23.93	46.02	0.92	99.06	29.11
9	28.26	24.04	46.60	0.63	99.54	28.89
10	26.99	22.79	49.50	0.00	99.28	26.99
11	27.33	22.88	50.96	0.00	101.18	27.33
12	27.99	23.86	46.03	0.99	98.88	28.99
13	27.90	24.00	45.78	0.87	98.55	28.77
Cu187-2	28.67	23.39	45.83	1.01	98.91	29.68
3	28.74	23.62	45.43	0.83	98.63	29.57
4	28.60	23.34	45.32	0.87	98.13	29.47
5	28.55	23.26	44.92	1.12	97.85	29.67
6	28.35	23.24	45.23	1.29	98.11	29.63
7	28.87	24.15	45.64	0.69	99.34	29.56
Cu208-1	28.64	23.10	46.18	0.00	97.92	28.64
2	28.66	23.42	46.10	1.22	99.40	29.88
3	28.69	23.29	45.63	1.30	98.91	30.00
4	28.83	23.44	44.92	0.94	98.13	29.77
5	28.27	23.18	45.45	1.28	98.20	29.56
6	29.03	23.49	45.84	0.21	98.56	29.24
7	28.78	23.38	45.13	1.23	98.52	30.01
8	28.17	22.54	45.48	0.00	96.19	28.17
9	28.13	22.61	44.09	0.00	94.83	28.13
10	29.18	23.53	45.56	0.00	98.27	29.18
11	29.17	23.82	45.72	0.00	98.71	29.17
12	28.77	23.43	45.30	1.03	98.53	29.80
13	29.13	23.70	45.54	0.00	98.36	29.13
14	29.15	23.72	45.39	0.22	98.49	29.37
15	28.98	23.49	45.19	0.00	97.66	28.98
Cu211-1	28.73	23.51	45.05	0.80	98.09	29.54
2	28.67	23.44	44.89	1.31	98.30	29.97
3	28.96	23.60	45.71	0.35	98.63	29.31
4	28.72	23.57	44.85	0.64	97.78	29.36
6	28.83	23.48	44.96	1.00	98.27	29.83
7	28.80	23.50	45.83	0.59	98.72	29.38
8	27.77	23.09	45.18	2.28	98.32	30.05

Cu211-9	28.90	23.60	44.81	0.46	97.78	29.36
10	29.08	23.60	44.37	0.65	97.70	29.73
Cu203b-1	28.75	23.41	46.73	0.81	99.70	29.56
2	28.62	23.44	46.39	1.00	99.44	29.61
3	28.83	23.50	46.26	0.82	99.42	29.65
4	28.98	23.59	47.11	0.00	99.68	28.98
5	29.18	23.66	46.81	0.00	99.66	29.18
6	29.16	23.79	46.57	0.00	99.52	29.16
7	28.95	23.40	46.38	0.00	98.73	28.95
8	29.12	23.65	46.73	0.00	99.51	29.12
Cu082-1	28.75	23.39	45.36	0.80	98.30	29.55
2	29.36	23.69	45.52	0.30	98.87	29.66
3	28.84	23.44	45.24	0.62	98.15	29.46
4	28.87	23.55	45.88	1.05	99.35	29.92
6	28.58	23.50	45.31	1.17	98.55	29.74
7	29.03	23.73	45.44	0.51	98.71	29.54
8	28.68	23.43	44.78	0.84	97.73	29.52
10	28.92	23.40	45.20	0.70	98.21	29.61
11	29.15	23.27	44.82	0.69	97.93	29.85
12	28.82	23.61	45.80	0.62	98.84	29.43
Cu185-1	28.41	22.68	46.30	0.00	97.39	28.41
2	28.78	22.74	47.61	0.00	99.14	28.78
4	28.60	22.81	48.16	0.00	99.58	28.60
5	28.26	22.58	46.60	0.00	97.45	28.26
6	28.50	22.59	48.24	0.00	99.33	28.50
7	28.32	22.81	44.32	0.00	95.45	28.32
8	28.30	22.74	48.85	0.00	99.89	28.30

	SiO2	TiO2	Al2O3	FeO	MnO	MgO	CaO	Na2O	K2O	Cr2O3	NiO	Cl	BaO	ZrO2	La2O3	P2O5	F	sum
Cu478-1	38.59	2.17	15.62	14.65	0.20	13.76	0.04	0.29	9.54	0.00	0.20	0.06	0.02	0.00	0.00	0.19	n/a	95.32
Cu478-2	38.32	2.70	14.99	15.59	0.16	13.89	0.00	0.33	9.06	0.02	0.00	0.04	0.00	0.00	0.00	0.00	n/a	95.09
Cu478-3	40.83	1.75	19.11	12.78	0.05	10.43	0.00	0.18	9.27	0.13	0.00	0.07	0.10	0.00	0.13	0.00	n/a	94.84
Cu478-4	38.75	2.44	15.22	14.72	0.12	14.31	0.08	0.28	9.50	0.03	0.00	0.04	0.04	0.00	0.00	0.00	n/a	95.52
Cu478-5	37.93	2.34	15.43	14.86	0.15	13.73	0.04	0.23	9.39	0.00	0.00	0.08	0.00	0.00	0.00	0.00	n/a	94.18
Cu478-6	37.95	2.69	15.51	15.23	0.15	13.23	0.09	0.20	9.23	0.00	0.00	0.08	0.00	0.00	0.00	0.00	n/a	94.36
Cu478-7	37.69	2.96	15.10	15.18	0.15	13.51	0.01	0.28	9.68	0.06	0.00	0.09	0.00	0.00	0.00	0.00	n/a	94.72
Cu478-8	38.18	2.63	15.66	15.70	0.05	13.37	0.01	0.22	9.86	0.04	0.13	0.11	0.00	0.00	0.18	0.00	n/a	96.15
Cu478-9	37.97	1.92	15.81	14.46	0.18	13.28	0.15	0.24	8.92	0.08	0.00	0.02	0.00	0.00	0.00	0.00	n/a	93.04
Cu478-10	38.83	2.06	16.03	14.69	0.08	13.79	0.00	0.17	9.44	0.00	0.00	0.06	0.00	0.00	0.00	0.00	n/a	95.14
Cu478-12	37.40	2.04	15.88	14.81	0.16	13.19	0.05	0.41	8.61	0.10	0.17	0.09	0.05	0.00	0.00	0.00	n/a	92.96
Cu478-13	38.19	2.17	16.79	14.71	0.08	12.90	0.08	0.26	9.08	0.07	0.00	0.07	0.26	0.00	0.00	0.00	n/a	94.65
Cu478-14	37.05	3.18	14.92	15.73	0.14	12.49	0.03	0.37	9.31	0.07	0.02	0.05	0.32	0.00	0.00	0.00	n/a	93.70
Cu478-15	37.33	2.59	15.45	15.95	0.24	12.89	0.05	0.19	9.51	0.00	0.00	0.06	0.00	0.00	0.14	0.00	n/a	94.39
Cu478-16	37.61	2.71	15.90	15.75	0.16	12.99	0.04	0.16	9.34	0.05	0.00	0.05	0.07	0.00	0.12	0.00	n/a	94.94
Cu478-17	36.90	3.20	15.10	15.75	0.15	12.33	0.00	0.27	9.58	0.12	0.05	0.10	0.41	0.00	0.00	0.00	n/a	93.94
Cu478-18	37.82	2.95	15.66	15.80	0.25	13.05	0.00	0.37	9.64	0.00	0.01	0.05	0.00	0.00	0.00	0.00	n/a	95.61
Cu478-19	37.08	2.60	15.43	15.36	0.18	12.81	0.00	0.34	9.21	0.00	0.00	0.08	0.15	0.00	0.00	0.00	n/a	93.25
Cu478-20	38.27	3.70	14.82	12.31	0.18	15.43	0.07	0.25	9.91	0.05	0.10	0.09	0.13	0.00	0.00	0.00	n/a	95.32
Cu478-21	38.60	3.24	15.29	12.46	0.23	15.30	0.00	0.39	9.96	0.00	0.00	0.07	0.23	0.00	0.00	0.11	n/a	95.88
Cu494-1	38.16	4.23	15.13	12.46	0.17	15.24	0.00	0.44	9.72	0.00	0.00	0.06	0.59	0.00	0.12	0.00	n/a	96.32
Cu494-2	39.62	2.41	16.19	6.63	0.28	19.01	0.03	0.27	9.58	0.00	0.00	0.05	0.00	0.00	0.00	0.00	n/a	94.07
Cu494-4	37.55	3.95	13.73	13.01	0.14	15.73	0.06	0.30	9.33	0.00	0.00	0.14	0.23	0.00	0.18	0.00	n/a	94.34
Cu494-5	37.07	2.40	14.49	9.83	0.19	16.15	0.08	0.47	8.46	0.01	0.05	0.04	0.16	0.00	0.00	0.00	n/a	89.40
Cu494-6	38.19	3.80	14.52	11.69	0.21	16.06	0.00	0.25	10.01	0.03	0.00	0.11	0.23	0.00	0.00	0.00	n/a	95.10
Cu494-7	40.07	2.43	15.70	7.27	0.25	19.69	0.00	0.33	10.16	0.03	0.07	0.12	0.07	0.00	0.12	0.00	n/a	96.30

	SiO2	TiO2	Al2O3	FeO	MnO	MgO	CaO	Na2O	K2O	Cr2O3	NiO	Cl	BaO	ZrO2	La2O3	P2O5	F	sum
Cu465-1	39.81	3.04	15.44	5.58	0.23	20.28	0.00	0.34	10.01	0.00	0.00	0.02	0.06	0.00	0.00	0.00	n/a	94.81
Cu465-2	39.57	3.32	14.96	5.64	0.28	20.53	0.01	0.28	10.05	0.06	0.05	0.02	0.00	0.00	0.00	0.00	n/a	94.76
Cu465-3	39.67	1.77	15.93	4.40	0.08	21.60	0.00	0.29	10.39	0.00	0.00	0.02	0.22	0.00	0.24	0.00	n/a	94.59
Cu465-4	39.56	3.93	15.56	5.46	0.03	20.30	0.01	0.39	9.99	0.01	0.05	0.00	0.00	0.00	0.00	0.00	n/a	95.29
Cu465-5	39.50	2.43	15.99	8.71	0.09	18.14	0.01	0.17	10.05	0.07	0.10	0.08	0.00	0.00	0.00	0.00	n/a	95.33
Cu465-7	38.90	2.27	16.09	9.40	0.09	17.54	0.05	0.22	9.71	0.00	0.00	0.03	0.52	0.00	0.13	0.00	n/a	94.95
Cu465-8	39.21	2.87	16.47	9.75	0.20	16.33	0.04	0.32	9.46	0.00	0.00	0.04	0.15	0.00	0.00	0.00	n/a	94.83
Cu465-9	38.67	4.58	15.35	9.18	0.10	17.32	0.00	0.26	10.14	0.00	0.03	0.06	0.03	0.00	0.00	0.00	n/a	95.73
Cu465-10	38.78	3.90	15.14	7.82	0.07	18.22	0.07	0.28	9.93	0.00	0.00	0.05	0.47	0.00	0.00	0.00	n/a	94.74
Cu162-1	39.50	2.53	15.34	5.48	0.02	20.99	0.01	0.33	10.50	0.02	0.01	0.01	0.27	0.00	0.36	0.00	n/a	95.37
Cu162-2	39.81	2.64	15.16	7.84	0.02	20.03	0.06	0.37	10.03	0.00	0.00	0.09	0.00	0.00	0.00	0.00	n/a	96.06
Cu162-4	38.89	4.09	15.55	5.69	0.09	19.70	0.00	0.30	9.24	0.00	0.11	0.24	0.37	0.00	0.19	0.00	n/a	94.47
Cu162-5	39.72	3.86	15.15	5.27	0.08	20.19	0.00	0.41	9.66	0.01	0.00	0.18	0.04	0.00	0.00	0.00	n/a	94.56
Cu162-6	38.37	3.81	14.81	8.40	0.06	18.16	0.00	0.22	9.91	0.07	0.00	0.07	0.04	0.00	0.00	0.00	n/a	93.93
Cu162-7	39.18	3.47	15.66	8.82	0.00	17.75	0.06	0.31	10.18	0.08	0.00	0.06	0.43	0.00	0.18	0.13	n/a	96.31
Cu162-8	39.99	2.81	15.60	4.27	0.00	21.74	0.00	0.25	9.65	0.07	0.11	0.18	0.00	0.00	0.00	0.00	n/a	94.68
Cu162-09	40.05	2.87	16.05	3.31	0.09	21.90	0.00	0.28	10.26	0.05	0.00	0.01	0.04	0.00	0.12	0.00	n/a	95.02
Cu162-10	39.69	3.29	15.65	5.29	0.00	20.06	0.01	0.24	9.91	0.00	0.00	0.09	0.00	0.00	0.00	0.00	n/a	94.22
Cu162-11	40.22	2.70	14.56	3.81	0.01	22.25	0.00	0.17	10.11	0.00	0.18	0.04	0.09	0.00	0.00	0.00	n/a	94.13
Cu162-12	40.93	3.14	14.79	3.76	0.07	21.79	0.00	0.21	10.03	0.02	0.00	0.02	0.07	0.00	0.17	0.00	n/a	94.99
Cu181-06	36.16	4.57	13.90	15.24	0.72	14.60	0.05	0.32	8.44	0.00	0.09	0.03	0.00	0.00	0.00	0.00	n/a	94.13
Cu181-07	36.30	4.33	13.43	15.91	0.51	14.20	0.00	0.19	8.74	0.00	0.00	0.06	0.64	0.00	0.00	0.00	n/a	94.31
Cu508-01	37.89	3.06	14.88	15.11	0.00	14.00	0.00	0.24	9.41	0.00	0.00	0.12	0.39	0.00	0.20	0.10	n/a	95.40
Cu508-02	38.04	2.82	15.10	14.26	0.16	14.14	0.12	0.30	9.07	0.00	0.00	0.08	0.14	0.00	0.23	0.00	n/a	94.46
Cu508-03	37.94	3.11	15.28	14.95	0.09	13.83	0.00	0.21	9.98	0.00	0.07	0.03	0.00	0.00	0.00	0.00	n/a	95.50
Cu508-04	37.82	3.88	14.43	15.27	0.07	14.47	0.03	0.33	9.81	0.05	0.00	0.10	0.40	0.00	0.22	0.00	n/a	96.89

	SiO2	TiO2	Al2O3	FeO	MnO	MgO	CaO	Na2O	K2O	Cr2O3	NiO	Cl	BaO	ZrO2	La2O3	P2O5	F	sum
Cu508-05	37.45	3.70	14.62	15.22	0.12	14.09	0.01	0.35	9.65	0.02	0.00	0.08	0.12	0.00	0.00	0.00	n/a	95.42
Cu508-09	37.98	3.70	14.40	12.00	0.11	16.58	0.00	0.29	9.33	0.04	0.05	0.08	0.09	0.00	0.00	0.00	n/a	94.67
Cu508-10	38.30	3.22	15.00	10.53	0.11	17.13	0.07	0.39	8.81	0.00	0.06	0.06	0.04	0.00	0.00	0.00	n/a	93.71
Cu508-11	38.29	4.20	14.50	12.24	0.08	15.89	0.02	0.47	9.00	0.03	0.24	0.04	0.34	0.00	0.00	0.00	n/a	95.34
Cu508-13	37.61	4.00	14.25	16.39	0.08	13.81	0.00	0.46	9.68	0.02	0.01	0.10	0.42	0.00	0.21	0.00	n/a	97.04
Cu508-14	37.17	3.91	14.35	15.90	0.09	13.84	0.07	0.60	9.61	0.08	0.14	0.09	0.73	0.00	0.20	0.00	n/a	96.78
Cu508-15	37.69	3.71	14.11	15.94	0.04	13.37	0.00	0.33	9.17	0.10	0.08	0.10	0.11	0.00	0.00	0.00	n/a	94.75
Cu508-16	37.20	3.92	14.31	15.58	0.11	13.05	0.03	0.24	8.79	0.05	0.00	0.08	0.34	0.00	0.00	0.00	n/a	93.69
Cu508-17	37.72	3.96	14.55	16.17	0.00	12.95	0.00	0.43	9.79	0.15	0.00	0.10	0.11	0.00	0.00	0.00	n/a	95.92
Cu508-18	37.42	3.71	15.19	16.47	0.00	12.88	0.00	0.20	9.81	0.00	0.10	0.03	0.21	0.00	0.17	0.00	n/a	96.19
Cu508-19	37.31	3.83	14.56	16.28	0.11	13.19	0.00	0.25	9.56	0.04	0.00	0.09	0.18	0.00	0.14	0.13	n/a	95.69
Cu508-20	37.63	3.11	14.91	15.89	0.13	13.59	0.00	0.39	9.88	0.00	0.00	0.09	0.51	0.00	0.00	0.00	n/a	96.13
Cu508-21	39.77	2.04	17.88	12.79	0.14	12.33	0.00	0.14	8.72	0.10	0.00	0.05	0.25	0.00	0.00	0.00	n/a	94.21
Cu1115-01	37.16	3.80	13.91	15.72	0.03	14.06	0.00	0.45	9.44	0.10	n/a	0.04	0.12	n/a	n/a	n/a	2.23	94.83
Cu1115-02	37.77	3.13	13.53	14.94	0.05	15.16	0.00	0.38	9.42	0.01	n/a	0.12	0.26	n/a	n/a	n/a	2.41	94.80
Cu1115-03	36.83	3.57	13.17	12.89	0.39	14.95	0.00	0.24	9.50	0.00	n/a	0.12	0.16	n/a	n/a	n/a	2.37	91.83
Cu1115-04	37.62	3.01	14.24	13.64	0.30	15.76	0.00	0.27	9.31	0.00	n/a	0.08	0.21	n/a	n/a	n/a	2.52	94.43
Cu1115-06	37.38	3.85	13.69	14.99	0.10	14.66	0.00	0.40	9.34	0.00	n/a	0.07	0.35	n/a	n/a	n/a	2.24	94.83
Cu1115-07	38.19	3.44	13.43	15.00	0.16	14.62	0.00	0.31	9.55	0.00	n/a	0.10	0.25	n/a	n/a	n/a	2.34	95.05
Cu1115-08	39.75	1.55	16.30	9.52	0.90	15.80	0.00	0.29	9.03	0.06	n/a	0.07	0.00	n/a	n/a	n/a	2.45	93.27
Cu1115-09	37.11	4.12	14.14	15.50	0.13	14.33	0.00	0.17	9.82	0.01	n/a	0.09	0.51	n/a	n/a	n/a	2.19	95.92
Cu1115-10	36.95	3.83	13.81	15.61	0.05	14.21	0.00	0.20	9.67	0.05	n/a	0.10	0.40	n/a	n/a	n/a	1.74	94.87
Cu1115-11	38.98	3.41	15.94	13.70	0.32	12.91	0.00	0.28	8.97	0.00	n/a	0.07	0.00	n/a	n/a	n/a	1.82	94.58
Cu1115-12	37.29	3.78	13.71	16.17	0.20	14.33	0.00	0.35	9.64	0.05	n/a	0.03	0.34	n/a	n/a	n/a	1.61	95.89
Cu1115-13	37.15	3.96	13.94	15.42	0.10	14.45	0.00	0.30	9.65	0.07	n/a	0.07	0.15	n/a	n/a	n/a	1.94	95.25
Cu1115-14	37.35	3.34	13.72	15.67	0.00	14.59	0.00	0.26	9.62	0.02	n/a	0.11	0.28	n/a	n/a	n/a	1.89	94.96

	SiO2	TiO2	Al2O3	FeO	MnO	MgO	CaO	Na2O	K2O	Cr2O3	NiO	Cl	BaO	ZrO2	La2O3	P2O5	F	sum
Cu115-15	37.31	3.42	13.89	15.57	0.10	14.80	0.00	0.40	9.60	0.01	n/a	0.13	0.62	n/a	n/a	n/a	1.90	95.86
Cu1120-01	40.21	1.46	13.90	5.63	0.16	21.65	0.00	0.16	9.90	0.00	n/a	0.07	0.05	n/a	n/a	n/a	3.24	93.21
Cu1120-02	42.04	0.57	13.03	4.06	0.09	23.99	0.00	0.18	10.15	0.00	n/a	0.01	0.00	n/a	n/a	n/a	4.31	94.12
Cu1120-04	40.14	1.76	14.09	5.71	0.30	21.52	0.00	0.21	10.25	0.00	n/a	0.04	0.04	n/a	n/a	n/a	3.35	94.08
Cu1120-05	38.63	1.88	15.13	12.02	0.40	15.43	0.00	0.31	9.34	0.00	n/a	0.06	0.00	n/a	n/a	n/a	2.12	93.21
Cu1120-06	40.29	1.91	14.30	6.43	0.33	21.00	0.00	0.27	9.73	0.00	n/a	0.05	0.07	n/a	n/a	n/a	3.01	94.39
Cu1120-07	40.25	1.19	14.30	4.93	0.32	22.48	0.00	0.07	10.20	0.07	n/a	0.03	0.18	n/a	n/a	n/a	3.64	94.00
Cu1120-08	40.56	1.12	14.16	5.04	0.26	22.70	0.00	0.13	10.18	0.00	n/a	0.02	0.00	n/a	n/a	n/a	3.52	94.17
Cu1120-09	40.40	1.16	14.47	5.36	0.26	22.31	0.00	0.19	10.28	0.10	n/a	0.02	0.00	n/a	n/a	n/a	3.45	94.55
Cu1142-1	41.05	2.81	15.95	9.62	0.00	15.45	0.12	0.27	9.13	0.15	n/a	0.05	0.18	n/a	n/a	0.08	3.59	94.86
Cu1142-2	39.40	3.34	14.96	9.97	0.00	17.64	0.11	0.49	9.97	0.08	n/a	0.10	0.02	n/a	n/a	0.00	4.21	96.06
Cu1142-3	38.73	3.82	14.20	13.07	0.14	16.04	0.00	0.20	10.21	0.01	n/a	0.08	0.31	n/a	n/a	0.03	3.63	96.84
Cu1142-4	38.41	3.97	14.69	11.63	0.10	15.99	0.02	0.33	9.96	0.03	n/a	0.10	0.05	n/a	n/a	0.00	3.99	95.29
Cu1142-5	39.52	3.75	14.71	6.64	0.04	19.83	0.00	0.37	10.35	0.00	n/a	0.10	0.27	n/a	n/a	0.00	4.99	95.58
Cu1128-1	38.45	2.30	14.86	11.35	0.13	16.88	0.00	0.27	10.43	0.10	n/a	0.17	0.15	n/a	n/a	0.03	4.47	95.13
Cu1128-2	38.72	4.14	14.19	13.82	0.16	15.03	0.02	0.38	10.01	0.00	n/a	0.07	0.21	n/a	n/a	0.00	3.82	96.76
Cu1128-3	38.06	3.59	14.22	14.78	0.17	14.52	0.00	0.41	9.83	0.20	n/a	0.13	0.17	n/a	n/a	0.00	3.96	96.08
Cu1107-1	37.89	3.43	14.04	11.17	0.03	16.36	0.07	0.71	8.86	0.00	n/a	0.13	0.00	n/a	n/a	0.05	3.79	92.74
Cu1107-2	39.27	3.30	14.48	11.24	0.00	17.44	0.00	0.44	10.43	0.01	n/a	0.06	0.00	n/a	n/a	0.00	3.93	96.65
Cu1107-3	40.14	1.13	16.89	4.19	0.37	22.34	0.00	0.22	11.03	0.00	n/a	0.07	0.00	n/a	n/a	0.00	6.02	96.39
Cu1107-4	41.82	0.21	20.28	4.16	0.10	14.38	0.19	0.34	9.68	0.14	n/a	0.39	0.17	n/a	n/a	0.03	4.32	91.87
Cu1107-5	38.30	4.12	14.26	11.69	0.07	16.26	0.00	0.32	9.91	0.08	n/a	0.14	0.38	n/a	n/a	0.00	4.20	95.54
Cu1138-1	39.24	3.45	14.25	7.07	0.12	19.47	0.03	0.29	10.30	0.00	n/a	0.10	0.16	n/a	n/a	0.03	5.41	94.50
Cu1138-2	39.60	3.58	14.58	6.58	0.10	19.98	0.00	0.39	10.43	0.00	n/a	0.14	0.35	n/a	n/a	0.00	5.51	95.74
Cu1112-1	39.72	3.94	14.04	6.62	0.00	20.25	0.00	0.48	10.23	0.05	n/a	0.18	0.05	n/a	n/a	0.00	4.33	95.56
Cu1112-2	39.78	4.00	14.09	5.97	0.09	21.02	0.02	0.37	10.42	0.00	n/a	0.13	0.14	n/a	n/a	0.00	4.59	96.01

	SiO2	TiO2	Al2O3	FeO	MnO	MgO	CaO	Na2O	K2O	Cr2O3	NiO	Cl	BaO	ZrO2	La2O3	P2O5	F	sum
Cu1112-3	39.29	4.03	14.22	8.89	0.00	18.76	0.01	0.41	10.13	0.03	n/a	0.07	0.13	n/a	n/a	0.00	4.01	95.98
Cu1112-4	39.25	3.79	14.41	6.77	0.00	19.29	0.00	0.39	10.10	0.11	n/a	0.14	0.31	n/a	n/a	0.15	4.04	94.70
Cu1119-1	39.66	3.89	13.54	11.76	0.05	17.42	0.00	0.27	10.08	0.09	n/a	0.06	0.00	n/a	n/a	0.03	3.63	96.85
Cu1119-2	39.67	1.90	14.90	8.64	0.26	19.33	0.00	0.30	10.31	0.00	n/a	0.04	0.04	n/a	n/a	0.07	4.02	95.45
Cu1119-3	39.99	1.06	15.60	6.26	0.33	20.70	0.06	0.36	9.39	0.05	n/a	0.06	0.00	n/a	n/a	0.08	4.31	93.95
Cu1119-4	39.61	1.46	15.32	7.61	0.16	20.29	0.00	0.21	10.68	0.12	n/a	0.04	0.00	n/a	n/a	0.00	4.25	95.50
Cu769-1	37.59	3.90	13.69	15.36	0.54	14.33	0.02	0.30	9.64	0.00	n/a	0.19	0.54	n/a	n/a	0.03	0.57	96.12
Cu769-2	37.82	3.52	13.33	15.67	0.37	14.54	0.00	0.22	9.64	0.07	n/a	0.14	0.33	n/a	n/a	0.02	0.65	95.69
769incl	38.26	3.61	14.04	15.78	0.40	14.52	0.02	0.16	10.07	0.00	n/a	0.16	0.15	n/a	n/a	0.00	0.68	97.16
Cu769-4	38.07	4.21	14.02	14.98	0.34	14.40	0.00	0.33	9.91	0.06	n/a	0.15	0.36	n/a	n/a	0.00	0.43	96.81
cu769-5	37.79	4.08	13.79	15.32	0.43	14.46	0.00	0.20	9.69	0.09	n/a	0.11	0.35	n/a	n/a	0.02	0.68	96.32
Cu1158-1	39.63	0.85	13.86	12.78	0.38	17.62	0.07	0.22	10.13	0.00	n/a	0.10	0.00	n/a	n/a	0.10	2.96	95.73
Cu1158-2	38.38	3.69	13.38	15.40	0.23	14.80	0.00	0.28	9.83	0.00	n/a	0.08	0.32	n/a	n/a	0.00	1.65	96.38
Cu1158-4	37.96	3.80	13.82	14.85	0.14	14.92	0.01	0.32	9.94	0.00	n/a	0.05	0.38	n/a	n/a	0.06	1.93	96.25
Cu1162-3	37.56	3.82	13.65	14.75	0.16	14.61	0.09	0.02	9.67	0.10	n/a	0.06	0.28	n/a	n/a	0.00	0.58	94.74
Cu1130-1	40.40	3.65	14.68	3.97	0.07	22.20	0.00	0.34	10.78	0.02	n/a	0.06	0.00	n/a	n/a	0.00	5.95	96.17
Cu1130-2	40.22	3.33	14.33	3.57	0.07	22.65	0.00	0.21	10.56	0.07	n/a	0.11	0.00	n/a	n/a	0.10	6.24	95.23
Cu1130-3	39.54	3.69	14.73	6.06	0.04	20.49	0.01	0.36	10.53	0.02	n/a	0.09	0.39	n/a	n/a	0.00	5.45	95.95
cu746-10	39.20	4.34	13.64	12.40	0.17	17.10	0.00	0.32	10.53	0.00	n/a	0.14	0.00	n/a	n/a	0.00	0.94	98.79
cu1115-1	38.46	3.47	13.26	15.87	0.10	15.57	0.00	0.35	10.24	0.00	n/a	0.08	0.44	n/a	n/a	0.00	2.44	100.28
cu1115-2	38.23	3.59	13.39	14.78	0.03	14.82	0.00	0.44	9.91	0.00	n/a	0.09	0.37	n/a	n/a	0.00	2.64	98.29
cu1115-3	39.74	2.57	13.91	13.62	0.24	15.44	0.00	0.34	9.92	0.00	n/a	0.16	0.18	n/a	n/a	0.00	3.03	99.15
cu1115-5	38.56	3.64	13.17	15.25	0.03	15.81	0.06	0.38	10.26	0.06	n/a	0.09	0.01	n/a	n/a	0.00	3.06	100.36
cu1146-1	38.78	3.52	13.55	9.28	0.01	18.69	0.00	0.36	10.28	n/a	n/a	0.14	0.16	n/a	n/a	0.03	2.42	97.23
cu1146-2r	39.37	3.38	13.69	6.43	0.05	21.37	0.00	0.29	10.51	n/a	n/a	0.17	0.02	n/a	n/a	0.00	2.99	98.27
cu1146-3	39.50	3.69	14.12	5.70	0.03	21.39	0.00	0.39	10.57	n/a	n/a	0.13	0.38	n/a	n/a	0.01	3.08	98.98

	SiO2	TiO2	Al2O3	FeO	MnO	MgO	CaO	Na2O	K2O	Cr2O3	NiO	Cl	BaO	ZrO2	La2O3	P2O5	F	sum
cu1146-4	38.44	3.47	13.71	9.43	0.10	19.01	0.00	0.39	10.23	n/a	n/a	0.14	0.05	n/a	n/a	0.03	2.48	97.46
cu1135-1	38.31	3.58	14.73	7.11	0.17	19.72	0.02	0.31	10.22	n/a	n/a	0.08	0.33	n/a	n/a	0.08	2.28	96.94
cu1135-2	37.79	3.85	14.26	10.34	0.05	17.93	0.00	0.40	10.13	n/a	n/a	0.01	0.00	n/a	n/a	0.00	1.83	96.59
cu1135-4	39.12	3.69	14.18	6.13	0.14	21.02	0.04	0.38	10.34	n/a	n/a	0.18	0.33	n/a	n/a	0.05	2.44	98.03
cu1135-5	39.00	3.15	14.32	6.46	0.00	20.66	0.00	0.35	10.31	n/a	n/a	0.10	0.38	n/a	n/a	0.07	2.43	97.25
cu1127-1	36.68	3.40	13.42	16.10	0.17	14.41	0.01	0.32	9.88	n/a	n/a	0.16	0.08	n/a	n/a	0.03	0.04	94.69
cu1127-2	37.06	3.78	13.31	16.35	0.21	14.18	0.03	0.14	9.84	n/a	n/a	0.11	0.08	n/a	n/a	0.00	0.00	95.10
cu1147-1	36.90	3.42	13.82	14.87	0.13	13.14	0.11	0.26	8.86	n/a	n/a	0.11	0.03	n/a	n/a	0.02	0.90	92.56
cu1147-2	38.00	3.31	14.39	13.48	0.08	13.10	0.11	0.43	9.11	n/a	n/a	0.05	0.04	n/a	n/a	0.11	0.84	93.05
cu1146-1	38.29	3.52	13.64	11.25	0.15	17.61	0.00	0.37	10.24	n/a	n/a	0.12	0.22	n/a	n/a	0.03	2.27	97.72
cu494-1a	37.15	3.73	13.41	13.19	0.24	15.11	0.09	0.38	9.57	n/a	n/a	0.04	0.05	n/a	n/a	0.03	1.66	94.62
Cu494-3a	39.55	2.84	17.80	10.09	0.00	11.89	0.07	0.31	9.57	n/a	n/a	0.04	0.05	n/a	n/a	0.05	1.12	93.38
cu494-4b	37.82	3.65	13.95	13.37	0.10	15.96	0.02	0.41	9.90	n/a	n/a	0.09	0.21	n/a	n/a	0.05	1.80	97.34
cu494-5b	37.94	3.48	14.01	11.68	0.19	16.56	0.08	0.36	10.00	n/a	n/a	0.19	0.00	n/a	n/a	0.00	1.68	96.18
cu769-1a	36.94	3.66	12.86	15.63	0.27	14.77	0.01	0.19	9.47	n/a	n/a	0.13	0.20	n/a	n/a	0.00	0.00	94.12
cu769-3a	36.74	3.04	13.33	15.58	0.36	14.97	0.04	0.21	9.37	n/a	n/a	0.10	0.22	n/a	n/a	0.00	0.00	93.95
cu769-4a	36.87	3.83	13.29	16.05	0.32	14.59	0.01	0.19	9.55	n/a	n/a	0.13	0.21	n/a	n/a	0.00	0.00	95.05
cu769-5a	36.75	3.88	13.47	15.97	0.36	14.67	0.01	0.25	9.71	n/a	n/a	0.12	0.25	n/a	n/a	0.07	0.00	95.52
cu769-6a	36.56	3.03	13.22	15.77	0.34	14.12	0.03	0.31	8.63	n/a	n/a	0.16	0.04	n/a	n/a	0.00	0.00	92.19
cu769-7a	36.70	3.76	13.08	16.43	0.32	14.45	0.00	0.26	9.70	n/a	n/a	0.21	0.24	n/a	n/a	0.06	0.00	95.21
cu508-1a	37.25	2.18	14.54	14.78	0.05	14.65	0.02	0.37	9.87	n/a	n/a	0.07	0.24	n/a	n/a	0.00	1.05	95.06
cu508-2a	37.42	3.65	13.97	12.72	0.05	15.77	0.00	0.35	9.81	n/a	n/a	0.09	0.38	n/a	n/a	0.00	1.27	95.48
cu181-3a	35.13	4.05	13.40	16.21	0.77	15.65	0.18	0.29	6.93	n/a	n/a	0.11	0.06	n/a	n/a	0.02	0.00	92.79
cu181-4a	34.26	4.02	13.85	16.58	0.69	15.07	0.07	0.23	6.46	n/a	n/a	0.07	0.44	n/a	n/a	0.01	0.00	91.78
cu181-5a	35.80	3.66	13.09	15.21	0.65	14.57	0.05	0.24	8.61	n/a	n/a	0.04	0.55	n/a	n/a	0.04	0.00	92.50

	SiO ₂	Al ₂ O ₃	Na ₂ O	K ₂ O	Cl	BaO	La ₂ O ₃	P ₂ O ₅	Total
Cu1102-1	64.56	18.34	0.69	15.92	0.00	0.00	0.00	0.00	99.50
Cu1102-2	63.53	18.10	0.53	15.52	0.00	0.60	0.00	0.12	98.40
Cu1102-3	64.36	18.89	0.78	15.29	0.00	1.19	0.28	0.06	100.84
Cu1102-4	64.31	18.60	0.56	15.71	0.00	0.76	0.00	0.05	99.98
Cu1102-5	64.21	18.70	0.78	15.47	0.00	1.13	0.00	0.00	100.28
Cu1102-6	64.98	18.63	0.45	15.81	0.00	0.30	0.00	0.09	100.27
Cu1102-9	63.51	18.52	0.74	15.16	0.00	1.17	0.00	0.22	99.31
Cu1102-10	64.36	18.57	0.65	15.33	0.00	1.09	0.19	0.00	100.18
Cu1102-11	63.84	18.55	0.68	14.97	0.00	1.14	0.13	0.03	99.35
Cu1102-15	63.32	18.49	1.21	14.21	0.10	1.23	0.00	0.11	98.66
Cu1102-16	64.14	18.52	0.40	15.43	0.00	0.81	0.00	0.02	99.32
Cu1102-17	64.04	18.61	0.54	15.58	0.00	0.89	0.00	0.00	99.66
Cu1102-18	64.76	18.67	0.73	15.54	0.00	0.84	0.00	0.00	100.55
Cu1102-19	63.63	18.31	0.56	15.54	0.00	0.54	0.00	0.00	98.58
Cu1102-20	64.69	18.75	0.66	15.80	0.00	0.07	0.11	0.37	100.46
Cu1102-21	64.56	18.41	0.61	15.77	0.00	0.17	0.00	0.21	99.73
Cu1115-1	64.25	18.65	0.63	15.95	0.00	0.49	0.00	0.00	99.97
Cu1115-2	64.28	18.92	1.52	14.23	0.00	1.89	0.18	0.02	101.02
Cu1115-3	64.50	18.88	0.76	14.95	0.00	1.52	0.00	0.00	100.62
Cu1115-45	64.09	18.41	0.58	15.50	0.00	0.91	0.00	0.07	99.56
Cu1115-6	63.33	18.88	1.31	14.34	0.00	2.36	0.25	0.00	100.47
Cu1115-8	64.59	18.79	0.67	15.36	0.00	1.51	0.00	0.15	101.07
Cu1115-9	64.06	19.03	2.50	11.84	0.00	1.87	0.00	0.05	99.35
Cu1115-10	63.98	18.71	0.90	14.56	0.00	1.55	0.00	0.07	99.75
Cu1115-13	64.32	18.74	0.59	15.44	0.00	1.28	0.00	0.06	100.44
Cu1115-14	64.56	18.82	0.44	15.96	0.00	0.91	0.00	0.07	100.75
Cu1115-16	63.79	18.83	0.87	14.85	0.00	1.45	0.00	0.00	99.80
Cu1115-20	62.99	18.72	0.79	14.48	0.00	1.39	0.00	0.09	98.45
Cu1115-21	64.06	18.72	1.12	14.68	0.00	1.33	0.00	0.11	100.02
Cu1115-22	64.34	18.74	0.57	15.80	0.00	0.73	0.00	0.08	100.26
Cu1105-2	62.71	18.91	1.26	11.88	0.66	2.51	0.00	0.00	97.93
Cu1105-3	63.44	18.93	0.93	14.53	0.00	2.26	0.19	0.00	100.27
Cu1105-4	64.90	18.24	1.10	15.09	0.00	0.35	0.22	0.04	99.94
Cu1105-5	64.31	18.42	0.53	15.98	0.00	0.28	0.00	0.00	99.53
Cu1105-8	64.09	18.57	0.49	15.47	0.00	1.10	0.30	0.00	100.03
Cu1105-9	64.41	18.60	0.68	15.41	0.00	0.65	0.00	0.01	99.77
Cu1105-10	64.57	18.60	0.59	15.30	0.00	1.14	0.10	0.10	100.40
Cu1105-11	64.52	18.49	0.56	16.03	0.00	0.92	0.00	0.09	100.61
Cu1105-14	64.02	18.52	0.88	15.24	0.00	1.25	0.25	0.07	100.22
Cu1105-15	64.09	18.45	0.78	15.26	0.00	1.41	0.12	0.02	100.12
Cu1105-16	63.99	18.56	0.83	15.21	0.00	1.28	0.17	0.00	100.06
Cu1105-17	63.60	18.61	0.60	15.10	0.00	1.91	0.11	0.00	99.93

Appendix C: K feldspar

	SiO2	Al2O3	Na2O	K2O	Cl	BaO	La2O3	P2O5	Total
Cu1106-4-1	64.47	18.73	0.34	15.48	n/a	1.13	n/a	n/a	100.15
Cu487-01k	64.59	18.37	0.27	15.52	0.02	0.15	n/a	0.08	98.91
Cu487-02k	63.31	19.06	0.67	14.32	0.70	1.64	n/a	0.00	99.70
Cu1146-01k	64.68	18.38	0.51	15.74	0.00	0.17	n/a	0.01	99.48
Cu1146-05	65.06	18.59	0.84	15.45	0.02	0.00	n/a	0.00	99.96
Cu1150-02	65.37	18.73	0.68	15.81	0.01	0.34	n/a	0.05	100.95
Cu1150-03	64.75	19.14	0.97	15.12	0.03	1.18	n/a	0.01	101.19
Cu1150-04	65.46	18.87	1.59	13.74	0.01	0.47	n/a	0.00	100.14
Cu457-01	63.99	19.24	1.36	13.94	0.00	1.73	n/a	0.00	100.26
Cu457-02	63.92	18.92	0.92	14.92	0.00	1.17	n/a	0.00	99.85
Cu457-03	64.56	18.91	1.34	14.54	0.01	1.16	n/a	0.05	100.52
Cu457-04	64.62	18.94	0.70	15.31	0.00	1.44	n/a	0.14	101.02
Cu457-05	65.04	18.72	0.53	15.93	0.02	0.30	n/a	0.07	100.54
Cu457-06	64.74	18.97	1.14	14.61	0.01	1.23	n/a	0.09	100.70
Cu457-08	64.93	18.74	0.82	15.19	0.03	0.33	n/a	0.00	100.05
Cu436-01	65.21	18.62	0.56	15.68	0.00	0.26	n/a	0.03	100.34
Cu436-03	64.46	18.49	0.62	15.50	0.00	0.09	n/a	0.00	99.16
Cu436-04	63.73	18.13	0.63	14.68	0.16	0.00	n/a	0.00	97.33
Cu157-01	64.28	18.74	1.04	14.77	0.00	1.24	n/a	0.00	100.07
Cu157-02	64.49	18.96	1.21	14.61	0.00	1.08	n/a	0.00	100.35
Cu176-05	64.10	18.58	0.54	15.21	0.00	1.03	n/a	0.01	99.45
Cu176-06	65.33	18.75	0.69	14.96	0.14	0.49	n/a	0.11	100.36
Cu176-07	65.47	18.88	1.17	14.44	0.02	0.56	n/a	0.03	100.54
Cu164-01	63.99	18.83	0.68	14.67	0.14	1.53	n/a	0.00	99.84
Cu164-02	65.06	19.00	0.93	13.94	0.07	1.15	n/a	0.06	100.15
Cu164-03	63.52	18.66	0.33	13.64	0.06	1.52	n/a	0.00	97.73
Cu164-04	64.40	18.82	0.53	15.04	0.03	0.90	n/a	0.18	99.71
Cu746-1	64.82	18.75	1.56	14.41	0.01	1.16	0.09	0.00	100.79
Cu746-3	64.53	18.67	1.48	14.69	0.02	1.23	0.07	0.06	100.76
Cu746-5	63.87	18.22	1.14	15.41	0.02	0.54	0.23	0.03	99.47
Cu746-6	63.14	18.36	0.67	15.23	0.00	1.16	0.05	0.05	98.65
Cu769-z1	64.00	18.20	0.94	15.15	0.03	0.53	0.02	0.00	98.86
Cu769-z5	65.20	18.51	0.49	15.48	0.00	0.50	0.05	0.00	100.23
Cu769-z6	64.30	18.32	0.74	15.24	0.01	0.35	0.04	0.21	99.22

	SiO2	Al2O3	Na2O	K2O	Cl	BaO	La2O3	P2O5	Total
Cu1105-18	64.50	18.76	0.76	15.14	0.00	1.03	0.10	0.00	100.29
Cu1124-4	65.14	18.49	0.44	16.03	0.00	0.23	0.14	0.03	100.51
Cu1120-2	65.94	18.80	0.53	15.68	0.00	0.32	0.13	0.17	101.56
Cu1120-3	64.79	18.43	0.78	15.48	0.00	0.38	0.00	0.00	99.86
Cu1119-01	66.15	18.77	0.42	15.97	0.00	0.00	0.00	0.00	101.32
Cu1119-06	65.68	18.95	0.77	15.20	n/a	1.07	n/a	n/a	101.67
Cu1116-03	65.06	18.65	0.69	15.46	n/a	0.66	n/a	n/a	100.52
Cu1122-01	65.84	19.04	1.14	15.09	n/a	0.69	n/a	n/a	101.81
Cu1122-03	66.07	18.77	0.74	15.74	n/a	0.55	n/a	n/a	101.88
Cu1136-1-7	65.41	18.25	0.47	15.90	0.02	0.07	n/a	0.11	100.24
Cu1136-2-7	65.70	18.35	0.39	16.05	0.00	0.13	n/a	0.10	100.72
Cu1136-4-7	65.42	18.38	0.71	15.72	0.00	0.00	n/a	0.08	100.32
Cu1136-5-7	65.06	18.49	0.51	15.89	0.00	0.27	n/a	0.17	100.39
Cu1136-9-7	64.64	18.55	0.66	15.57	0.02	0.32	n/a	0.00	99.76
Cu1136-15-7	64.66	18.65	0.61	15.96	0.07	0.04	n/a	0.00	99.98
Cu1136-16-1	64.90	18.48	0.77	15.66	0.00	0.30	n/a	0.09	100.22
Cu1136-17-1	65.06	18.63	0.61	16.00	0.06	0.35	n/a	0.12	100.83
Cu1136-18-1	64.27	18.99	0.97	14.93	0.00	1.52	n/a	0.09	100.78
Cu1136-19-1	64.34	19.04	1.12	14.64	0.00	1.16	n/a	0.00	100.29
Cu1117-7-1	64.78	18.55	0.58	15.42	0.13	0.01	n/a	0.01	99.48
Cu1117-8-1	64.65	18.94	0.55	15.80	0.02	0.98	n/a	0.00	100.95
Cu1117-9-1	64.90	18.55	0.64	15.68	0.03	0.08	n/a	0.03	99.91
Cu1117-10-1	64.28	18.93	0.68	15.55	0.00	0.99	n/a	0.00	100.44
Cu1117-11-2	66.10	18.72	5.14	8.93	0.02	0.05	n/a	0.02	98.99
Cu1117-12-2	65.35	18.66	0.97	14.89	0.01	0.20	n/a	0.10	100.18
Cu1117-13-2	65.19	18.67	0.85	15.48	0.05	0.04	n/a	0.00	100.28
Cu1141-1-1	65.19	18.48	0.50	16.00	0.04	0.15	n/a	0.01	100.38
Cu1141-2-1	64.72	18.34	0.84	15.75	0.00	0.00	n/a	0.29	99.93
Cu1129-2-7	64.28	18.14	0.37	15.71	0.07	0.05	n/a	0.17	98.78
Cu1129-3-7	64.50	18.63	0.58	15.99	0.04	0.27	n/a	0.13	100.14
Cu1129-4-7	65.03	18.45	3.51	11.46	0.52	0.13	n/a	0.05	99.16
Cu1129-5-1	65.03	18.43	0.37	15.72	0.00	0.06	n/a	0.09	99.71
Cu1129-6-1	65.19	18.70	0.45	15.76	0.04	0.56	n/a	0.12	100.82
Cu1129-9-1	64.56	18.44	0.55	15.86	0.02	0.06	n/a	0.10	99.59
Cu1129-10-1	65.00	18.52	0.26	16.06	0.02	0.04	n/a	0.07	99.97
Cu1138-2-7	64.89	18.66	0.44	15.98	0.04	0.13	n/a	0.38	100.53
Cu1138-4-7	64.92	18.61	0.76	15.69	0.00	0.22	n/a	0.36	100.55
Cu1138-5-1	65.01	18.55	0.51	15.83	0.06	0.27	n/a	0.00	100.23
Cu1138-7	64.89	18.72	0.57	15.94	0.00	0.24	n/a	0.14	100.49
Cu1101-2	64.72	18.79	0.67	15.74	0.02	0.08	n/a	0.12	100.15
Cu1101-4-1	65.28	18.68	0.50	16.04	0.02	0.06	n/a	0.03	100.60
Cu1106-3-1	63.78	18.93	0.74	14.90	n/a	1.59	n/a	n/a	99.93

Appendix C: K feldspar

	SiO2	TiO2	Al2O3	FeO	MnO	MgO	CaO	V2O5	Cr2O3	NiO	Nb2O5	Ta2O5	ZnO	SO4
Cu514-c	0.62	94.58	0.00	0.70	0.00	0.00	0.00	n/a	n/a	n/a	n/a	n/a	n/a	n/a
Cu514-i	0.31	94.23	0.00	0.93	0.00	0.00	0.00	n/a	n/a	n/a	n/a	n/a	n/a	n/a
cu1147-g	0.39	96.12	0.00	0.77	0.00	0.00	0.00	n/a	n/a	n/a	n/a	n/a	n/a	n/a
cu1147-I	0.41	93.14	0.00	1.21	0.00	0.00	0.00	n/a	n/a	n/a	n/a	n/a	n/a	n/a
cu1126-o	0.45	92.44	0.00	0.65	0.00	0.00	0.00	n/a	n/a	n/a	n/a	n/a	n/a	n/a
cu1126-bz	0.32	94.34	0.00	1.04	0.00	0.00	0.00	n/a	n/a	n/a	n/a	n/a	n/a	n/a
cu1126-zd	0.27	95.44	0.00	1.11	0.00	0.00	0.00	n/a	n/a	n/a	n/a	n/a	n/a	n/a
cu746-h	0.00	96.24	0.57	0.00	0.00	0.00	0.00	n/a	n/a	n/a	n/a	n/a	n/a	n/a
Cu1101-1	2.00	96.18	0.00	0.35	0.06	0.00	0.03	1.14	0.06	0.18	0.21	0.00	0.00	0.05
Cu1101-2	1.07	98.15	0.07	0.16	0.00	0.05	0.00	0.53	0.27	0.07	0.20	0.00	0.00	0.00
Cu1101-3	1.70	96.34	0.00	0.44	0.09	0.00	0.00	0.58	0.11	0.13	0.10	0.00	0.00	0.02
Cu1101-4	1.67	95.87	0.00	0.16	0.15	0.00	0.00	0.48	0.11	0.00	0.00	0.00	0.00	0.10
Cu1101-5	1.32	96.72	0.03	0.41	0.03	0.00	0.09	0.52	0.00	0.00	0.23	0.00	0.00	0.07
Cu1115-4	0.43	98.36	0.04	0.75	0.03	0.06	0.05	0.00	0.20	0.02	0.49	0.00	0.00	0.02
Cu1115-5	0.29	98.91	0.00	0.48	0.08	0.05	0.07	0.00	0.22	0.02	0.62	0.00	0.00	0.08
Cu1115-6	0.30	97.04	0.07	0.90	0.10	0.00	0.08	0.00	0.14	0.00	1.09	0.00	0.03	0.00
Cu1115-7	0.33	99.23	0.07	0.43	0.00	0.05	0.00	0.00	0.20	0.00	0.55	0.00	0.04	0.06
Cu1115-8	0.45	94.67	0.07	1.66	0.11	0.00	0.10	0.00	0.08	0.05	2.70	0.21	0.25	0.00
Cu1115-9	0.80	97.26	0.13	0.74	0.00	0.00	0.00	0.00	0.20	0.12	0.81	0.00	0.03	0.09
Cu1115-10	0.34	97.54	0.08	0.64	0.00	0.05	0.01	0.00	0.11	0.00	0.78	0.00	0.27	0.05
CU1115-11	0.45	95.57	0.19	1.39	0.05	0.00	0.06	0.00	0.05	0.12	2.25	0.17	0.17	0.08
Cu1115-12	3.03	95.62	1.00	0.73	0.00	0.03	0.17	0.00	0.07	0.00	0.70	0.00	0.35	0.12
Cu1115-13	0.73	95.03	0.07	0.81	0.00	0.00	0.04	0.00	0.05	0.00	0.94	0.00	0.04	0.04
Cu1115-17	0.43	97.71	0.00	0.67	0.16	0.00	0.03	0.00	0.00	0.00	0.67	0.00	0.19	0.06
Cu746-12t	0.17	98.81	0.00	1.46	0.00	0.00	0.01	0.00	0.05	0.00	0.45	0.00	0.00	0.00
Cu746-14t	0.26	100.69	0.01	0.83	0.00	0.00	0.05	0.00	0.12	0.00	0.21	0.00	0.10	0.00

Appendix C: Rutile

	PbO	Sb2O3	UO3	ThO2	La2O3	Ce2O3	Nd2O3	Y2O3	P2O5	Co2O	SnO2	Total
Cu514-c	n/a	n/a	n/a	n/a	n/a	n/a	n/a	n/a	0.00	n/a	n/a	95.90
Cu514-i	n/a	n/a	n/a	n/a	n/a	n/a	n/a	n/a	0.00	n/a	n/a	95.47
cu1147-g	n/a	n/a	n/a	n/a	n/a	n/a	n/a	n/a	0.00	n/a	n/a	97.44
cu1147-l	n/a	n/a	n/a	n/a	n/a	n/a	n/a	n/a	0.00	n/a	n/a	94.76
cu1126-o	n/a	n/a	n/a	n/a	n/a	n/a	n/a	n/a	0.00	n/a	n/a	93.86
cu1126-bz	n/a	n/a	n/a	n/a	n/a	n/a	n/a	n/a	0.00	n/a	n/a	95.70
cu1126-zd	n/a	n/a	n/a	n/a	n/a	n/a	n/a	n/a	0.00	n/a	n/a	96.83
cu746-h	n/a	n/a	n/a	n/a	n/a	n/a	n/a	n/a	0.00	n/a	n/a	96.81
Cu1101-1	0.00	0.04	0.00	0.00	0.00	0.00	0.24	0.00	0.00	0.00	n/a	100.54
Cu1101-2	0.08	0.00	0.00	0.00	0.00	0.00	0.32	0.00	0.00	0.00	n/a	100.95
Cu1101-3	0.00	0.05	0.00	0.00	0.00	0.01	0.10	0.00	0.00	0.00	n/a	99.66
Cu1101-4	0.00	0.22	0.00	0.00	0.00	0.00	0.34	0.00	0.00	0.09	n/a	99.17
Cu1101-5	0.01	0.11	0.00	0.00	0.20	0.00	0.28	0.00	0.00	0.00	n/a	100.02
Cu1115-4	0.02	0.01	0.00	0.00	0.08	0.00	0.22	0.00	0.00	0.00	n/a	100.78
Cu1115-5	0.00	0.01	0.06	0.00	0.34	0.30	0.36	0.00	0.00	0.00	n/a	101.91
Cu1115-6	0.07	0.04	0.00	0.00	0.00	0.00	0.51	0.00	0.00	0.00	n/a	100.39
Cu1115-7	0.04	0.04	0.09	0.00	0.12	0.03	0.19	0.00	0.01	0.00	n/a	101.47
Cu1115-8	0.26	0.06	0.00	0.26	0.00	0.00	0.20	0.00	0.10	0.04	n/a	101.26
Cu1115-9	0.09	0.00	0.00	0.00	0.00	0.00	0.48	0.00	0.00	0.02	n/a	100.77
Cu1115-10	0.00	0.16	0.00	0.00	0.64	0.34	0.19	0.00	0.00	0.08	n/a	101.27
Cu1115-11	0.00	0.00	0.02	0.00	0.00	0.00	0.14	0.00	0.00	0.00	n/a	100.70
Cu1115-12	0.00	0.49	0.00	0.00	0.03	0.01	0.17	0.00	0.06	0.05	n/a	102.64
Cu1115-13	0.00	0.20	0.00	0.00	0.00	0.00	0.38	0.00	0.07	0.00	n/a	98.39
Cu1115-17	0.00	0.12	0.00	0.00	0.49	0.03	0.00	0.00	0.03	0.00	n/a	100.59
Cu746-12t	0.16	n/a	0.05	0.05	0.16	0.07	0.39	0.00	0.07	0.00	0.02	101.94
Cu746-14t	0.00	n/a	0.00	0.01	0.24	0.00	0.21	0.00	0.00	0.11	0.01	102.85

Appendix C: Rutile

	SiO2	TiO2	Al2O3	FeO	MnO	MgO	CaO	V2O5	Cr2O3	NiO	Nb2O5	Ta2O5	ZnO	SO4
Cu091-6	1.13	97.12	0.02	0.72	0.04	0.00	0.13	0.00	0.05	0.00	0.49	0.00	0.10	0.03
Cu091-7	1.82	95.67	0.00	1.03	0.08	0.00	0.07	0.28	0.00	0.00	0.53	0.00	0.00	0.13
Cu512-1t	0.01	98.21	0.00	0.76	0.00	0.00	0.00	0.00	0.10	0.02	0.34	0.19	0.11	0.00
Cu512-2t	1.68	91.07	0.00	2.42	0.13	0.00	0.03	0.41	0.03	0.08	3.42	0.00	0.00	0.12
Cu512-3t	0.80	95.73	0.08	0.91	0.09	0.00	0.10	0.00	0.00	0.00	1.37	0.03	0.00	0.12
Cu512-6t	0.47	97.17	0.00	0.83	0.13	0.06	0.03	0.00	0.00	0.14	0.82	0.00	0.00	0.08

	PbO	Sb2O3	UO3	ThO2	La2O3	Ce2O3	Nd2O3	Y2O3	P2O5	Co2O	SnO2	Total
Cu091-6	0.01	n/a	0.02	0.00	0.13	0.08	0.14	0.00	0.02	0.00	0.00	100.23
Cu091-7	0.00	n/a	0.04	0.00	0.00	0.00	0.27	0.00	0.00	0.00	0.02	99.92
Cu512-1t	0.00	n/a	0.01	0.13	0.26	0.09	0.35	0.00	0.00	0.02	0.00	100.60
Cu512-2t	0.07	n/a	0.03	0.00	0.22	0.18	0.19	0.00	0.00	0.00	0.00	100.08
Cu512-3t	0.00	n/a	0.00	0.00	0.04	0.00	0.16	0.00	0.01	0.02	0.00	99.46
Cu512-6t	0.00	n/a	0.07	0.08	0.78	0.31	0.39	0.00	0.00	0.09	0.00	101.45

spot	SiO2	TiO2	Al2O3	FeO	MnO	MgO	CaO	Na2O	K2O	Cl	F	Cr2O3	BaO	SUM
Cu185-01	46.75	0.00	35.83	0.35	0.00	0.50	0.00	0.19	8.88	0.00	0.30	0.03	0.20	93.03
Cu185-02	43.59	0.23	33.94	0.27	0.14	0.62	0.06	0.12	9.38	0.00	0.16	0.00	0.00	88.51
Cu185-03	45.82	0.17	35.42	0.38	0.00	0.49	0.09	0.20	8.03	0.02	0.26	0.00	0.00	90.88
Cu185-04	45.14	0.19	35.22	0.43	0.00	0.50	0.00	0.17	9.13	0.02	0.15	0.00	0.00	90.95
Cu185-05	47.01	0.03	36.48	0.23	0.03	0.53	0.03	0.01	9.17	0.00	0.26	0.05	0.02	93.86
Cu195-01	49.88	0.26	30.80	1.85	0.06	2.56	0.00	0.20	8.91	0.03	1.16	0.00	0.00	95.70
Cu195-02	48.34	0.46	30.71	3.26	0.00	2.19	0.05	0.12	9.01	0.00	0.84	0.06	0.00	95.05
Cu195-03	49.26	0.27	31.71	1.13	0.00	2.45	0.00	0.14	9.38	0.03	1.04	0.01	0.00	95.42
Cu195-04	46.97	0.01	36.24	0.21	0.01	0.70	0.02	0.14	9.26	0.01	0.26	0.00	0.00	93.83
Cu195-05	49.03	0.24	31.23	1.20	0.08	2.64	0.01	0.17	9.12	0.02	1.16	0.00	0.05	94.95
Cu207-01	50.23	0.13	31.62	0.20	0.18	2.88	0.00	0.04	8.67	0.00	0.53	0.04	0.03	94.56
Cu207-02	50.68	0.22	30.96	0.12	0.18	3.00	0.04	0.02	8.55	0.00	0.50	0.00	0.00	94.26
Cu207-03	50.46	0.16	31.76	0.20	0.11	2.84	0.10	0.20	8.79	0.00	0.51	0.00	0.00	95.13
Cu1141-2	48.38	0.05	31.95	1.47	0.00	1.96	0.08	0.88	9.81	0.00	1.10	0.00	0.09	95.751
Cu1141-6	47.27	0.00	35.18	0.75	0.16	0.91	0.01	0.35	10.73	0.01	0.71	0.00	0.01	96.0835
Cu1141-9	46.89	0.12	33.01	1.03	0.00	2.06	0.01	0.32	11.08	0.00	1.05	0.00	0.00	95.5708
Cu1138-8	50.87	0.10	30.74	0.29	0.21	2.92	0.03	0.03	8.82	0.00	1.58	0.09	0.06	95.7278
Cu1115-5	51.46	0.14	30.93	0.69	0.14	0.96	0.08	2.04	8.77	0.02	0.44	0.00	0.00	95.6727
Cu1129-1	47.55	0.37	29.73	1.11	0.07	3.26	0.09	0.37	10.72	0.01	1.55	0.02	0.00	94.8512
Cu1129-2	49.20	0.10	30.60	0.25	0.11	3.36	0.00	0.00	10.56	0.03	1.73	0.01	0.09	96.0325
Cu1129-3	47.59	0.09	29.66	1.50	0.00	3.27	0.00	0.23	10.49	0.00	1.57	0.00	0.06	94.4447
Cu1129-5	47.65	0.14	33.64	0.62	0.00	1.42	0.05	0.32	10.63	0.02	0.89	0.00	0.06	95.4354
Cu1129-6	47.78	0.00	32.93	0.50	0.00	1.45	0.00	0.42	10.41	0.00	0.92	0.05	0.09	94.5463
Cu101-1	46.93	0.16	34.00	0.80	0.00	0.98	0.00	0.24	10.64	0.04	1.04	0.00	0.00	94.8456
Cu101-3	47.86	0.06	35.51	0.30	0.10	0.65	0.00	0.11	9.65	0.00	0.82	0.00	0.16	95.21
Cu101-4	50.21	0.25	32.19	0.42	0.09	1.99	0.00	0.14	9.40	0.00	1.76	0.00	0.14	96.5978
Cu106-2	50.28	0.00	33.50	0.18	0.04	1.14	0.04	0.00	7.93	0.01	1.16	0.00	0.01	94.282
Cu106-3	48.60	0.08	35.56	0.03	0.07	0.75	0.00	0.16	8.75	0.00	0.84	0.13	0.03	94.9934
Cu091-1	47.33	0.33	34.90	1.38	0.12	0.95	0.00	0.16	10.07	0.00	0.79	0.04	0.00	96.0625
Cu091-2	45.44	0.16	35.35	1.01	0.00	0.75	0.00	0.33	10.96	0.00	0.86	0.06	0.16	95.0928
Cu091-4	47.30	0.03	35.06	0.45	0.00	0.99	0.00	0.22	10.76	0.00	0.90	0.00	0.06	95.7802

spot	SiO2	TiO2	Al2O3	FeO	MnO	MgO	CaO	Na2O	K2O	Cl	F	Cr2O3	BaO	SUM
Cu1132-2	49.67	0.18	30.69	0.95	0.03	3.00	0.00	0.13	9.71	0.01	1.84	0.00	0.06	96.2742
Cu1132-3	49.73	0.24	29.72	1.95	0.09	3.23	0.00	0.17	9.59	0.00	1.63	0.03	0.08	96.4545
Cu140-1	47.43	0.14	35.95	0.29	0.00	0.64	0.00	0.20	9.46	0.02	n/a	0.05	0.00	94.19
Cu140-2	48.19	0.13	35.08	0.12	0.00	0.59	0.06	0.09	9.05	0.00	n/a	0.00	0.00	93.32
Cu140-3	47.49	0.07	34.27	0.30	0.00	0.69	0.12	0.10	8.46	0.01	n/a	0.00	0.01	91.52
Cu140-6	47.58	0.03	34.01	0.34	0.00	0.81	0.09	0.15	8.52	0.02	n/a	0.02	0.00	91.57
Cu140-7	47.95	0.00	34.62	0.26	0.00	0.91	0.00	0.10	9.58	0.02	n/a	0.05	0.00	93.50
Cu140-8	48.30	0.16	35.47	0.17	0.12	0.79	0.02	0.10	8.75	0.01	n/a	0.00	0.00	93.90
Cu140-9	47.16	0.12	33.94	0.16	0.00	0.78	0.25	0.02	8.99	0.00	n/a	0.04	0.00	91.47
Cu140-12	48.14	0.00	34.98	0.33	0.07	0.71	0.05	0.04	9.55	0.01	n/a	0.02	0.10	94.00
Cu140-14	49.21	0.64	31.63	0.73	0.00	2.48	0.02	0.19	9.55	0.00	n/a	0.07	0.00	94.52
Cu140-16	48.06	0.23	33.56	0.53	0.02	1.46	0.00	0.28	9.93	0.02	n/a	0.00	0.04	94.14
Cu1115-5	45.96	0.04	37.41	0.48	0.00	0.97	0.17	0.73	0.14	0.09	n/a	0.06	0.00	86.04
Cu443-1	47.33	0.37	33.64	1.35	0.06	1.28	0.00	0.35	9.82	0.03	n/a	0.09	0.00	94.32
Cu443-2	50.31	0.06	30.72	1.40	0.00	3.10	0.00	0.31	9.90	0.00	n/a	0.04	0.00	95.84
Cu443-3	49.98	0.18	31.20	0.80	0.07	2.21	0.17	0.29	8.80	0.01	n/a	0.00	0.00	93.70

Point	SiO2	TiO2	Al2O3	FeO	MnO	MgO	CaO	V2O5	Cr2O3	NiO	Nb2O5	Ta2O5	ZnO	SO4	PbO	Sb2O3	UO3
769-13	30.00	36.42	1.03	1.64	0.00	0.00	27.90	n/a	0.00	0.00	n/a	n/a	n/a	n/a	n/a	n/a	n/a
769-14	29.82	36.07	1.16	1.27	0.00	0.00	28.13	n/a	0.00	0.00	n/a	n/a	n/a	n/a	n/a	n/a	n/a
769-35	29.29	35.89	0.97	1.49	0.00	0.00	27.63	n/a	0.00	0.00	n/a	n/a	n/a	n/a	n/a	n/a	n/a
cu746-g	29.24	36.48	0.64	1.34	n/a	n/a	26.61	n/a	n/a	n/a	n/a	n/a	n/a	n/a	n/a	n/a	n/a
cu746-j	29.05	35.99	0.64	1.39	n/a	n/a	26.41	n/a	n/a	n/a	n/a	n/a	n/a	n/a	n/a	n/a	n/a
Cu769-2	28.99	35.75	1.08	1.72	0.11	0.00	26.96	0.00	0.02	0.00	0.40	0.02	0.00	0.05	0.00	0.85	0.00
Cu769-3	29.36	35.88	0.98	1.70	0.30	0.08	26.86	0.00	0.00	0.20	0.70	0.06	0.00	0.00	0.27	0.10	0.00
Cu769-4	28.01	31.86	1.31	2.74	0.20	0.04	26.52	0.00	0.10	0.07	1.42	0.23	0.00	0.00	0.00	0.59	0.08
Cu769-5	28.76	34.74	1.36	2.26	0.24	0.02	26.88	0.00	0.04	0.04	0.29	0.00	0.00	0.00	0.00	0.51	0.08
Cu769-6	30.78	36.88	1.35	1.30	0.16	0.00	28.36	0.08	0.11	0.00	0.11	0.02	0.22	0.00	0.00	0.63	0.02
Cu769-7	29.71	36.78	1.23	1.31	0.15	0.04	28.39	0.00	0.15	0.02	0.18	0.00	0.23	0.00	0.05	0.26	0.25
Cu769-8	30.12	37.06	1.18	1.17	0.05	0.06	28.40	0.00	0.09	0.00	0.24	0.00	0.00	0.08	0.00	0.16	0.00
Cu769-9	30.02	37.28	1.20	1.08	0.00	0.00	28.44	0.00	0.13	0.00	0.35	0.01	0.00	0.00	0.05	0.43	0.08
Cu769-10	29.09	35.87	1.07	1.71	0.22	0.05	26.54	0.00	0.15	0.00	0.29	0.11	0.00	0.00	0.08	0.17	0.09
Cu769-11	29.25	35.56	1.05	1.70	0.03	0.02	26.82	0.11	0.15	0.00	0.56	0.06	0.09	0.00	0.02	0.44	0.00
Cu769-12	29.24	36.16	1.10	1.60	0.07	0.00	27.29	0.00	0.00	0.00	0.19	0.04	0.14	0.00	0.00	0.57	0.06
Cu769-13	28.70	35.65	1.25	1.85	0.12	0.12	26.63	0.00	0.00	0.05	0.23	0.07	0.07	0.00	0.03	0.69	0.00
Cu769-14	29.54	35.94	1.09	1.62	0.24	0.05	26.57	0.00	0.11	0.03	0.36	0.09	0.00	0.00	0.08	0.30	0.05
Cu769-15	29.94	36.42	1.16	1.60	0.20	0.02	27.36	0.19	0.00	0.00	0.13	0.00	0.03	0.00	0.00	0.22	0.03
Cu769-16	30.04	36.99	1.41	1.25	0.20	0.00	28.51	0.02	0.21	0.00	0.24	0.00	0.00	0.00	0.05	0.29	0.00
Cu769-17	29.45	36.53	1.23	1.71	0.11	0.05	27.64	0.00	0.17	0.04	0.09	0.02	0.16	0.00	0.00	0.36	0.00
Cu769-18	28.69	36.91	1.01	1.05	0.07	0.00	26.35	0.00	0.09	0.14	0.31	0.00	0.08	0.26	0.00	0.62	0.00
Cu046-1	29.88	37.68	1.10	1.29	0.12	0.00	28.95	0.08	0.00	0.04	0.23	0.00	0.14	0.00	0.11	0.14	0.00
Cu046-2	30.86	37.66	1.19	1.43	0.00	0.07	29.18	0.00	0.06	0.18	0.17	0.00	0.29	0.03	0.06	0.44	0.00
Cu046-3	30.29	37.65	1.13	1.30	0.14	0.04	29.07	0.00	0.20	0.02	0.17	0.00	0.16	0.05	0.08	0.15	0.05

Point	SiO2	TiO2	Al2O3	FeO	MnO	MgO	CaO	V2O5	Cr2O3	NiO	Nb2O5	Ta2O5	ZnO	SO4	PbO	Sb2O3	UO3
Cu046-4	30.04	37.32	1.07	1.24	0.18	0.00	28.58	0.00	0.00	0.03	0.12	0.05	0.00	0.00	0.14	0.22	0.08
Cu769*-1	29.98	36.29	1.26	1.49	0.28	0.05	28.01	0.00	0.11	0.11	0.23	0.02	0.15	0.00	0.00	0.45	0.00
Cu769*-2	28.96	37.07	1.11	1.21	0.16	0.03	27.74	0.03	0.07	0.00	0.11	0.01	0.16	0.00	0.00	0.29	0.00
Cu769*-3	30.06	36.11	1.05	1.69	0.19	0.08	27.48	0.02	0.00	0.02	0.47	0.00	0.06	0.00	0.12	0.46	0.00
Cu746-2t	22.00	20.28	2.26	5.01	0.00	0.24	16.70	0.00	0.00	0.00	0.01	1.32	0.05	0.64	14.81	n/a	0.00
Cu746-3t	29.63	36.72	1.17	1.63	0.10	0.04	27.78	0.00	0.04	0.00	0.27	0.90	0.10	0.01	0.09	n/a	0.03
Cu746-t5	28.94	38.09	0.76	1.09	0.00	0.00	27.97	0.20	0.00	0.00	0.10	2.29	0.28	0.03	0.00	n/a	0.00
Cu746-6t	28.96	36.40	1.27	1.72	0.16	0.00	28.08	0.07	0.02	0.05	0.21	1.80	0.06	0.00	0.16	n/a	0.00
Cu746-8t	29.63	37.00	0.92	1.15	0.19	0.00	28.03	0.22	0.01	0.00	0.41	0.91	0.02	0.00	0.03	n/a	0.00
Cu746-9t	28.79	36.30	0.90	1.49	0.15	0.00	26.90	0.00	0.15	0.00	0.55	1.07	0.20	0.04	0.07	n/a	0.01

Point	ThO2	La2O3	Ce2O3	Nd2O3	Y2O3	P2O5	Co2O	BaO	SnO2	Sum
769-13	n/a	n/a	n/a	n/a	n/a	0.00	n/a	0.37	n/a	97.36
769-14	n/a	n/a	n/a	n/a	n/a	0.00	n/a	0.57	n/a	97.03
769-35	n/a	n/a	n/a	n/a	n/a	0.00	n/a	0.64	n/a	95.91
cu746-g	n/a	n/a	n/a	n/a	n/a	0.91	n/a	n/a	n/a	95.21
cu746-j	n/a	n/a	n/a	n/a	n/a	0.82	n/a	n/a	n/a	94.31
Cu769-2	0.02	0.28	1.06	0.94	0.57	0.10	0.08	n/a	n/a	99.01
Cu769-3	0.00	0.42	1.05	0.62	0.69	0.09	0.00	n/a	n/a	99.36
Cu769-4	0.43	0.37	1.19	0.42	0.00	0.89	0.00	n/a	n/a	96.48
Cu769-5	0.00	0.09	0.95	0.93	0.47	0.18	0.02	n/a	n/a	97.86
Cu769-6	0.16	0.00	0.13	0.27	0.35	0.11	0.00	n/a	n/a	101.06
Cu769-7	0.00	0.00	0.28	0.42	0.07	0.16	0.00	n/a	n/a	99.69
Cu769-8	0.09	0.00	0.00	0.45	0.36	0.00	0.00	n/a	n/a	99.49
Cu769-9	0.00	0.15	0.53	0.21	0.04	0.11	0.16	n/a	n/a	100.26
Cu769-10	0.12	0.26	1.04	0.76	0.55	0.01	0.05	n/a	n/a	98.23
Cu769-11	0.00	0.46	1.03	1.09	0.58	0.29	0.00	n/a	n/a	99.32
Cu769-12	0.11	0.01	0.58	1.06	0.55	0.11	0.16	n/a	n/a	99.04
Cu769-13	0.00	0.41	1.04	1.11	0.55	0.08	0.08	n/a	n/a	98.75
Cu769-14	0.00	0.40	1.21	0.67	0.51	0.08	0.12	n/a	n/a	99.09
Cu769-15	0.00	0.19	0.62	0.72	0.17	0.15	0.00	n/a	n/a	99.15
Cu769-16	0.01	0.00	0.21	0.38	0.04	0.15	0.00	n/a	n/a	100.01
Cu769-17	0.14	0.06	0.48	0.69	0.32	0.01	0.00	n/a	n/a	99.26
Cu769-18	0.28	0.13	0.28	0.44	0.16	0.20	0.00	n/a	n/a	97.07
Cu046-1	0.16	0.00	0.15	0.28	0.22	0.11	0.00	n/a	n/a	100.68
Cu046-2	0.04	0.00	0.00	0.26	0.14	0.12	0.03	n/a	n/a	102.20
Cu046-3	0.10	0.13	0.17	0.31	0.30	0.05	0.00	n/a	n/a	101.57

Point	ThO2	La2O3	Ce2O3	Nd2O3	Y2O3	P2O5	Co2O	BaO	SnO2	Sum
Cu046-4	0.26	0.05	0.30	0.25	0.00	0.35	0.02	n/a	n/a	100.30
Cu769*-1	0.07	0.24	0.72	0.65	0.38	0.06	0.00	n/a	n/a	100.54
Cu769*-2	0.00	0.09	0.45	0.42	0.12	0.00	0.00	n/a	n/a	98.03
Cu769*-3	0.12	0.24	0.62	0.61	0.29	0.03	0.00	n/a	n/a	99.74
Cu746-2t	0.18	0.19	0.39	0.26	0.04	0.32	0.00	n/a	0.00	84.71
Cu746-3t	0.00	0.49	0.97	0.46	0.35	0.16	0.08	n/a	0.15	101.15
Cu746-t5	0.08	0.00	0.25	0.72	0.36	0.00	0.00	n/a	0.07	101.22
Cu746-6t	0.05	0.09	0.38	0.48	0.30	0.15	0.11	n/a	0.00	100.51
Cu746-8t	0.00	0.45	0.56	0.64	0.12	0.17	0.00	n/a	0.08	100.54
Cu746-9t	0.15	0.61	1.19	0.66	0.26	0.27	0.06	n/a	0.13	99.97

Point	mineral	SiO2	TiO2	Al2O3	FeO	MnO	MgO	CaO	Na2O	K2O	Cr2O3
cu524-1	amphibole	51.46	0.49	2.65	10.32	0.47	16.82	12.14	0.75	0.28	0.07
cu524-2	rim amphibole	48.48	0.69	4.49	11.58	0.40	15.18	11.95	0.82	0.51	0.10
cu524-3	amphibole core	51.36	0.38	3.09	10.71	0.52	16.87	12.25	0.77	0.29	0.00
cu524-4	apatite	0.16	0.00	0.04	0.37	0.00	0.00	57.14	0.02	0.00	0.00
cu524-5	amph rim	48.09	0.90	5.25	11.60	0.47	15.47	12.02	1.09	0.53	0.04
cu524-7	plag low tot	58.74	0.00	23.77	0.44	0.00	0.16	6.33	7.83	0.25	0.03
cu524-8	plag rim	59.80	0.12	23.71	0.31	0.00	0.15	5.99	8.27	0.27	0.06
cu524-9	amph rim	47.77	0.85	5.24	12.34	0.61	14.86	12.10	0.97	0.63	0.04
cu524-10	amph rim	50.07	0.65	3.95	10.19	0.45	16.47	12.19	0.88	0.37	0.06
cu524-11	amph core	49.74	0.52	4.00	10.87	0.53	16.23	12.22	0.87	0.37	0.11
cu524-12	plag	59.76	0.07	23.59	0.14	0.10	0.00	5.94	8.15	0.23	0.00
cu791-6	biotite	36.82	4.15	14.64	14.59	0.37	14.23	0.02	0.26	8.23	0.00
cu046-1	core amph	50.52	0.58	3.90	10.51	0.68	16.56	12.21	0.86	0.30	0.03
cu046-2	rim plag	60.10	0.09	23.81	0.24	0.05	0.00	5.87	7.48	0.31	0.08
cu046-3	rim amphibole	55.74	0.80	5.38	11.13	0.31	15.13	10.73	0.50	0.72	0.06
cu046-4	amph rim	48.11	0.87	5.19	11.82	0.52	15.32	12.10	0.94	0.45	0.01
cu046-5	plag rim	59.46	0.00	24.72	0.22	0.00	0.19	6.73	7.39	0.21	0.00
cu046-6	core amph	49.11	0.89	4.76	10.88	0.45	16.00	12.05	0.96	0.33	0.16
cu046-7	rim amphibole	48.94	0.95	4.79	11.37	0.55	15.67	11.82	0.83	0.48	0.00
cu046-8	rim amphibole	49.43	0.70	4.64	10.85	0.59	15.97	12.38	0.79	0.45	0.00
cu046-9	plag rim	59.95	0.05	23.83	0.27	0.06	0.00	6.08	7.70	0.17	0.00
cu789-1	plag rim	59.74	0.03	21.25	0.18	0.03	0.17	3.79	7.69	0.29	0.13
cu789-2	core amph	48.07	1.21	5.42	10.96	0.67	15.80	11.79	1.22	0.37	0.00
cu789-4	rim amphibole	48.48	1.24	5.69	10.93	0.52	15.90	12.04	1.08	0.38	0.09
cu789-5	rim amphibole	54.07	0.06	9.45	5.12	0.35	8.21	9.34	0.54	0.04	0.00
cu789-6	rim amphibole	53.64	0.47	3.76	9.32	0.51	17.12	11.73	0.56	0.25	0.11
cu789-7	core amph	48.42	1.23	5.64	10.99	0.63	15.77	11.96	1.35	0.40	0.04

Point	mineral	NiO	P2O5	Cl	SrO	ZrO2	La2O3	BaO	Total
cu524-1	amphibole	0.00	0.00	0.05	0.00	0.00	0.00	0.00	95.49
cu524-2	rim amphibole	0.00	0.00	0.05	0.00	0.00	0.02	0.00	94.27
cu524-3	amphibole core	0.00	0.00	0.06	0.00	0.00	0.15	0.31	96.77
cu524-4	apatite	0.03	42.08	0.24	0.00	0.00	0.00	0.00	100.10
cu524-5	amph rim	0.00	0.00	0.12	0.00	0.03	0.08	0.00	95.69
cu524-7	plag low tot	0.12	0.00	0.00	0.00	0.00	0.00	0.05	97.72
cu524-8	plag rim	0.02	0.00	0.00	0.00	0.00	0.00	0.00	98.70
cu524-9	amph rim	0.00	0.00	0.10	0.00	0.00	0.01	0.00	95.53
cu524-10	amph rim	0.02	0.00	0.09	0.00	0.02	0.12	0.29	95.82
cu524-11	amph core	0.00	0.00	0.07	0.00	0.00	0.00	0.28	95.79
cu524-12	plag	0.07	0.00	0.00	0.00	0.00	0.00	0.00	98.04
cu791-6	biotite	0.00	0.00	0.15	0.00	0.00	0.00	0.22	93.66
cu046-1	core amph	0.00	0.00	0.08	0.00	0.00	0.11	0.14	96.49
cu046-2	rim plag	0.01	0.00	0.04	0.00	0.08	0.19	0.07	98.42
cu046-3	rim amphibole	0.04	0.00	0.09	0.00	0.00	0.00	0.00	100.63
cu046-4	amph rim	0.00	0.00	0.08	0.00	0.11	0.08	0.00	95.60
cu046-5	plag rim	0.05	0.00	0.00	0.00	0.00	0.15	0.05	99.17
cu046-6	core amph	0.01	0.00	0.08	0.00	0.00	0.00	0.00	95.70
cu046-7	rim amphibole	0.09	0.00	0.10	0.00	0.07	0.03	0.00	95.67
cu046-8	rim amphibole	0.08	0.00	0.08	0.00	0.00	0.09	0.18	96.23
cu046-9	plag rim	0.00	0.00	0.00	0.00	0.03	0.02	0.00	98.16
cu789-1	plag rim	0.00	0.01	0.04	0.00	0.00	0.00	0.00	93.35
cu789-2	core amph	0.00	0.00	0.08	0.00	0.00	0.13	0.18	95.91
cu789-4	rim amphibole	0.00	0.00	0.05	0.00	0.13	0.00	0.05	96.59
cu789-5	rim amphibole	0.00	0.00	0.00	0.00	0.00	0.18	0.11	87.47
cu789-6	rim amphibole	0.00	0.00	0.04	0.00	0.16	0.02	0.04	97.73
cu789-7	core amph	0.00	0.00	0.11	0.00	0.01	0.00	0.02	96.56

Point	mineral	SiO2	TiO2	Al2O3	FeO	MnO	MgO	CaO	Na2O	K2O	Cr2O3
cu789-8a	rim	48.99	1.04	5.09	10.73	0.74	16.40	11.60	1.39	0.34	0.11
cu789-9	rim amphibole	53.03	0.15	2.83	9.78	0.53	17.76	12.38	0.47	0.13	0.08
cu789-10	rim plag	62.26	0.01	22.29	0.24	0.00	0.00	4.14	8.47	0.13	0.05
cu789-11	core plag	61.61	0.04	22.60	0.21	0.00	0.14	4.67	7.92	0.32	0.02
cu789-12	rim amphibole	51.79	0.30	4.85	8.21	0.51	14.08	10.64	1.23	0.15	0.00
cu789-13	rim amphibole	50.21	0.78	4.21	10.10	0.76	17.00	12.15	0.78	0.35	0.05
cu789-14	core amph	49.28	0.99	4.87	10.62	0.63	16.47	12.19	1.02	0.43	0.02

Point	mineral	NiO	P2O5	Cl	SrO	ZrO2	La2O3	BaO	Total
cu789-8a	rim	0.00	0.00	0.07	0.00	0.01	0.09	0.00	96.59
cu789-9	rim amphibole	0.09	0.00	0.02	0.00	0.00	0.00	0.00	97.25
cu789-10	rim plag	0.05	0.00	0.01	0.00	0.00	0.00	0.03	97.70
cu789-11	core plag	0.14	0.00	0.00	0.00	0.00	0.00	0.00	97.67
cu789-12	rim amphibole	0.21	0.00	0.03	0.00	0.15	0.00	0.00	92.13
cu789-13	rim amphibole	0.01	0.00	0.03	0.00	0.00	0.00	0.00	96.43
cu789-14	core amph	0.07	0.00	0.03	0.00	0.00	0.02	0.00	96.63

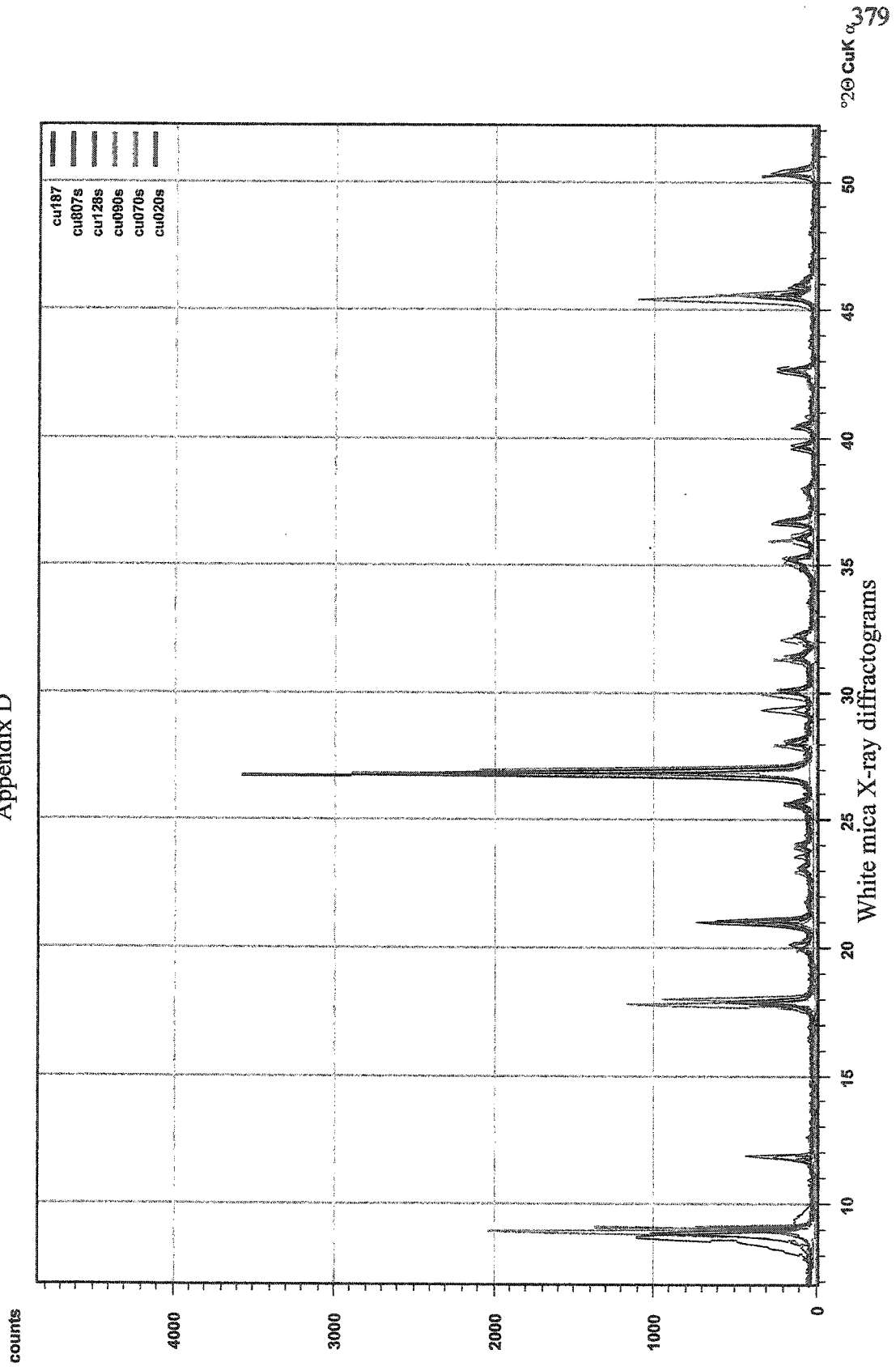
Sample	SiO2	Al2O3	CaO	Na2O	K2O	BaO	Total
Cu1333-1	61.87	23.36	4.79	9.28	0.14	0.00	99.44
Cu1333-2	64.11	21.5	2.91	10.31	0.12	0.00	98.95
Cu514-f	62.5	23.5	4.97	8.55	0.26	0.00	99.78
Cu514-g	62.7	23.19	4.41	9.19	0.2	0.00	99.69
Cu514-h	61.35	23.89	5.26	8.49	0	0.00	98.99
Cu512-3	62.61	22.67	4.36	9.08	0.19	0.00	98.91
Cu512-4	64.77	21.92	3.11	9.26	0.11	0.10	99.27
Cu769-z2	60.55	24.72	6.54	7.39	0.15	0.08	99.43
Cu769-z3	62.05	24.06	5.52	8.53	0.19	0.00	100.35
Cu769-z7	61.86	24.02	5.52	8.02	0.32	0.11	99.85
Cu769-a	61.42	23.25	5.16	8.50	0.65	0.00	98.98
Cu769-b	60.72	24.00	5.93	8.30	0.49	0.00	99.45
Cu769-2	63.79	22.51	3.89	9.12	0.35	0.00	99.65
Cu769-4	61.27	24.38	6.23	8.03	0.52	0.23	100.67
Cu769-5	61.16	24.58	6.41	8.34	0.17	0.00	100.67
Cu769-7	61.56	24.06	5.71	8.33	0.25	0.20	100.11
Cu769-8	62.29	23.63	5.29	8.90	0.18	0.12	100.41
Cu046-1	59.17	24.36	6.73	7.36	0.43	0.08	98.14
Cu046-4	58.79	25.42	7.62	6.25	0.62	0.00	98.69
Cu046-5	61.02	23.44	5.62	7.87	0.35	0.10	98.40
Cu046-6	60.22	24.22	6.07	7.62	0.35	0.17	98.65
Cu046-7	55.36	26.70	9.26	6.45	0.32	0.06	98.16
Cu046-8	56.95	26.98	9.13	6.27	0.22	0.07	99.62
Cu046-9	57.02	26.58	8.96	6.28	0.22	0.17	99.24
Cu046-10	53.48	28.54	11.40	5.11	0.16	0.00	98.68
Cu791-1	60.64	24.40	6.25	7.71	0.69	0.00	99.69
Cu791-2	61.34	24.14	5.49	8.35	0.33	0.39	100.04
Cu791-3	60.44	24.26	5.95	7.41	0.64	0.14	98.85
Cu791-4	59.91	24.39	6.11	7.76	0.41	0.00	98.59
Cu790-2	62.53	22.54	4.35	9.00	0.25	0.03	98.71
Cu790-3	63.90	22.11	3.66	9.10	0.17	0.00	98.93

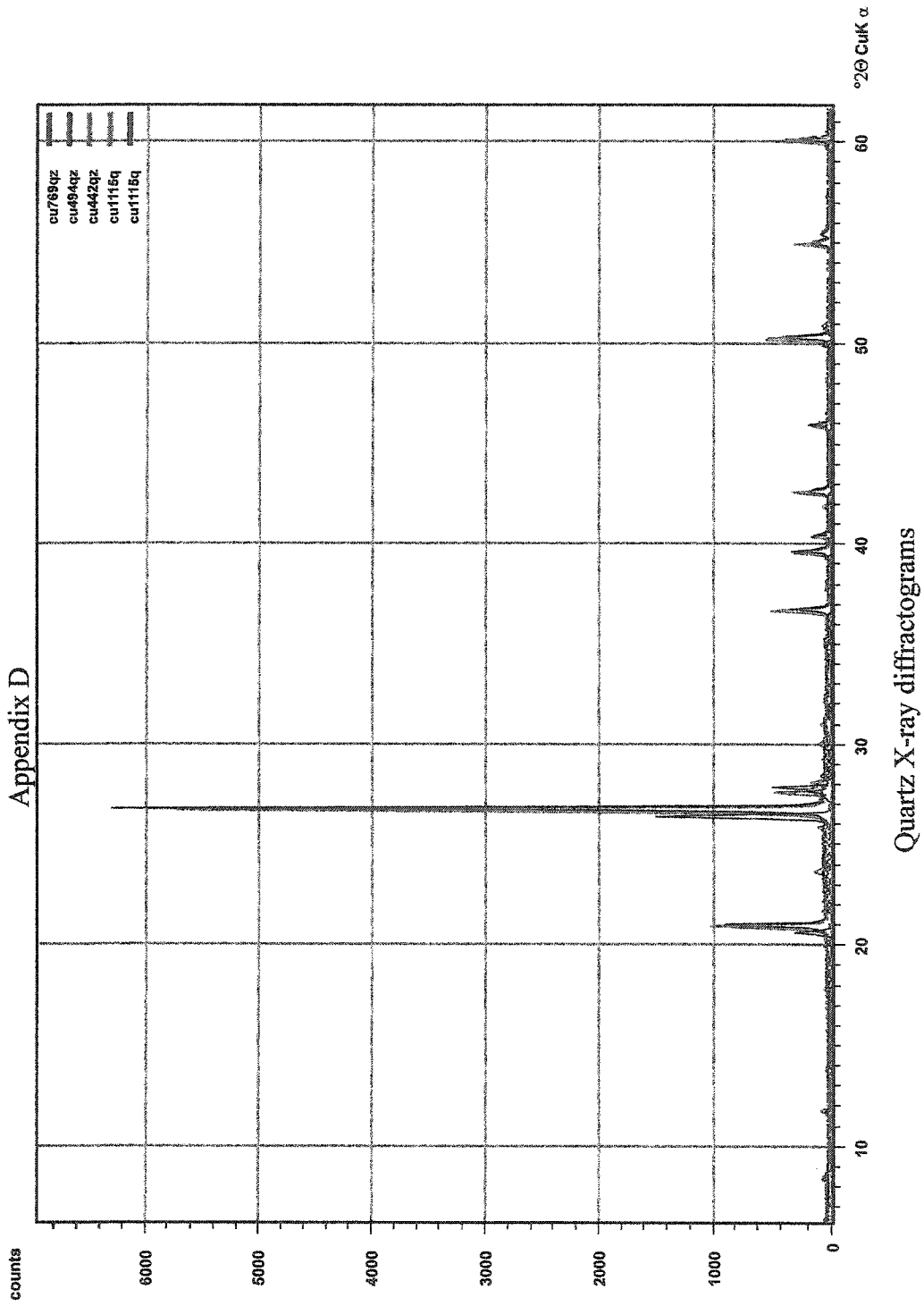
	molecular weight	a	b	c	Z	Density g/cm3	angstroms Volume -unit cell	volume -molecule
K-feldspar	278.34	8.59	12.966	7.223	4	2.57	719.22	179.81
Albite	262.24	8.138	12.785	7.158	4	2.62	664.69	166.17
Anorthite	278.22	8.18	12.88	14.17	8	2.76	1,338.84	167.36
Quartz	60.09	4.913	-	5.404	3	2.65	112.94	37.65
Muscovite-OH	796.6	~5.2	~9.0	~20.0	1	2.83	467.32	467.32
Biotite-OH	897.62	~5.3	~9.2	~10.3	1	3	496.74	496.74
Biotite-F	905.62	~5.3	~9.2	~10.3	1	3	501.17	501.17
Titanite	180.07	7.057	8.707	6.555	4	3.54	337.80	84.45
Rutile	79.9	4.593	-	2.959	2	4.865	54.53	27.27
Pyrite	119.97	5.417	-	-	4	4.99	159.66	39.91
Anhydrite	136.14	6.99	7	6.24	4	3	301.36	75.34
Gypsum	172.14	5.68	15.18	6.29	4	2.34	488.52	122.13

$V=(Z*M)/(N*D)$

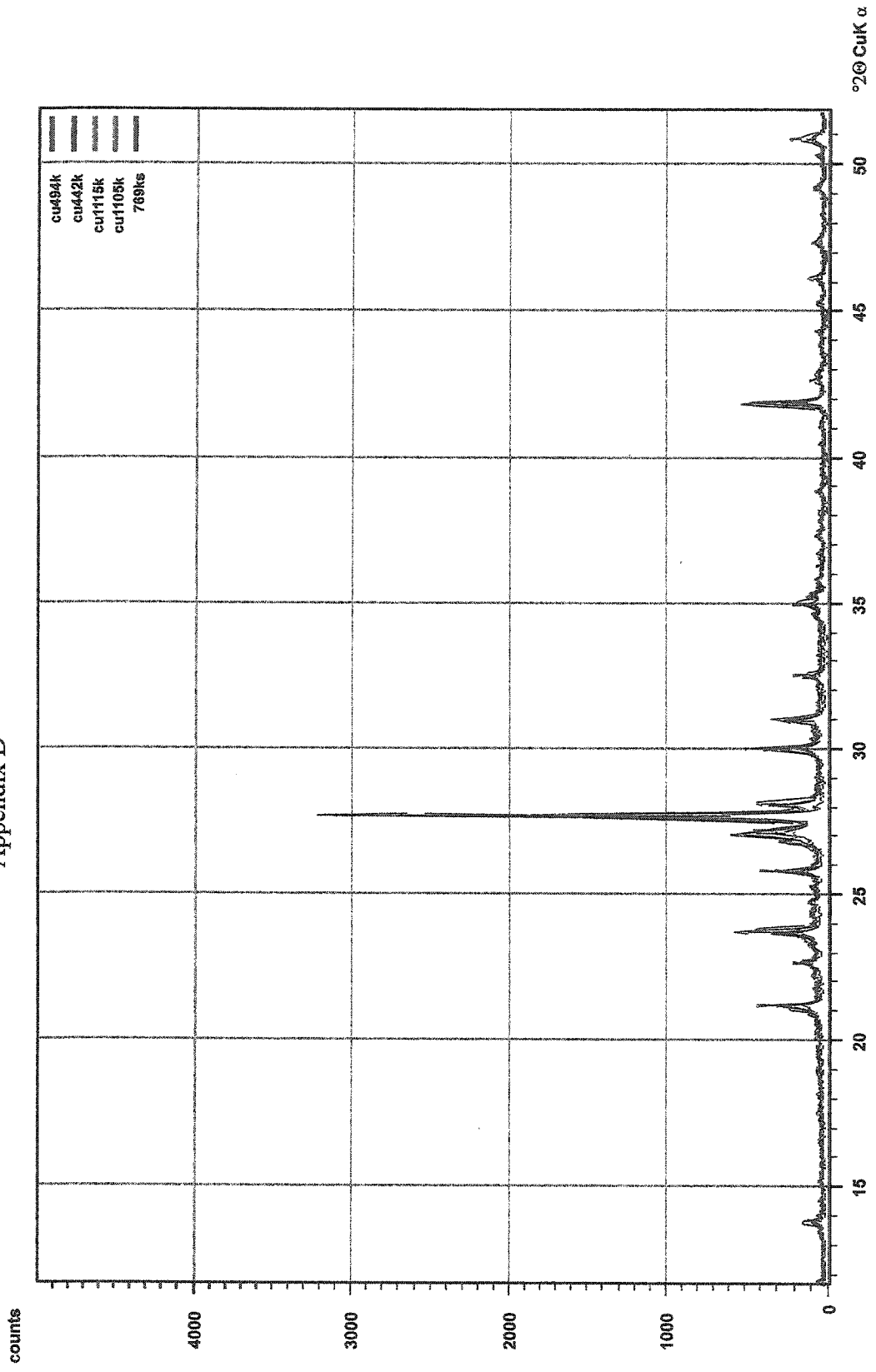
Appendix D
X-ray Diffraction

Appendix D

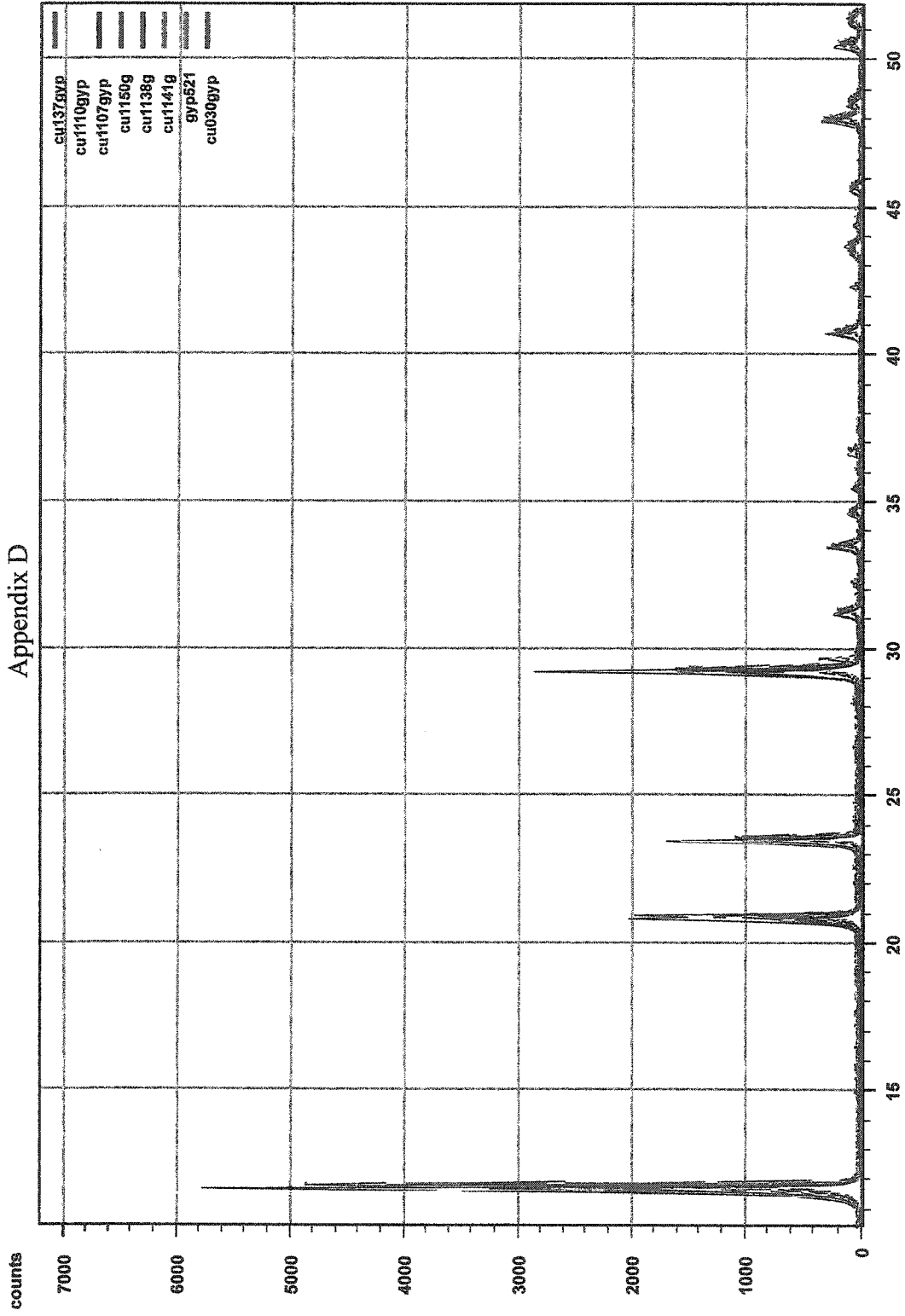




Appendix D



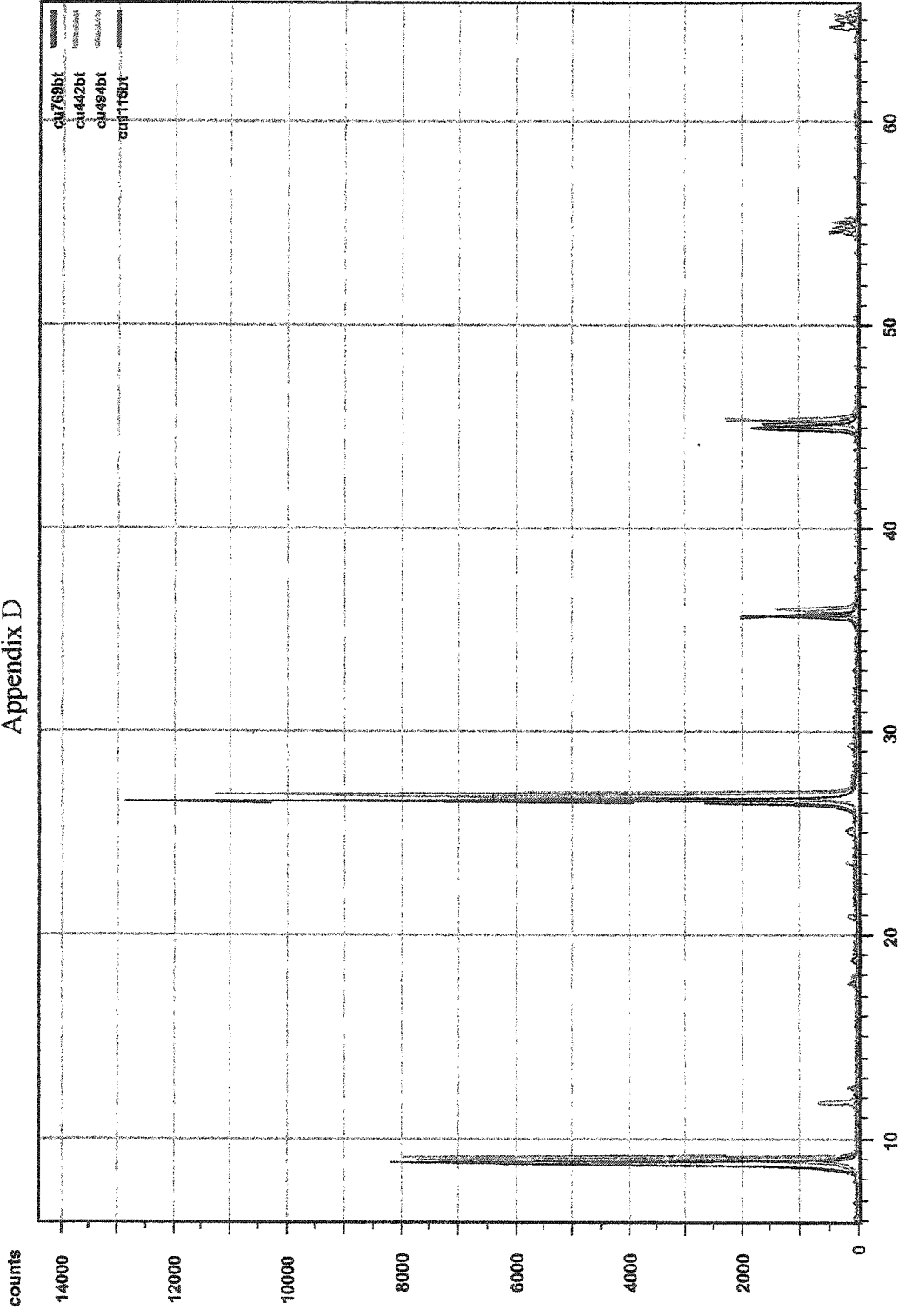
K-feldspar X-ray diffractogram



Appendix D

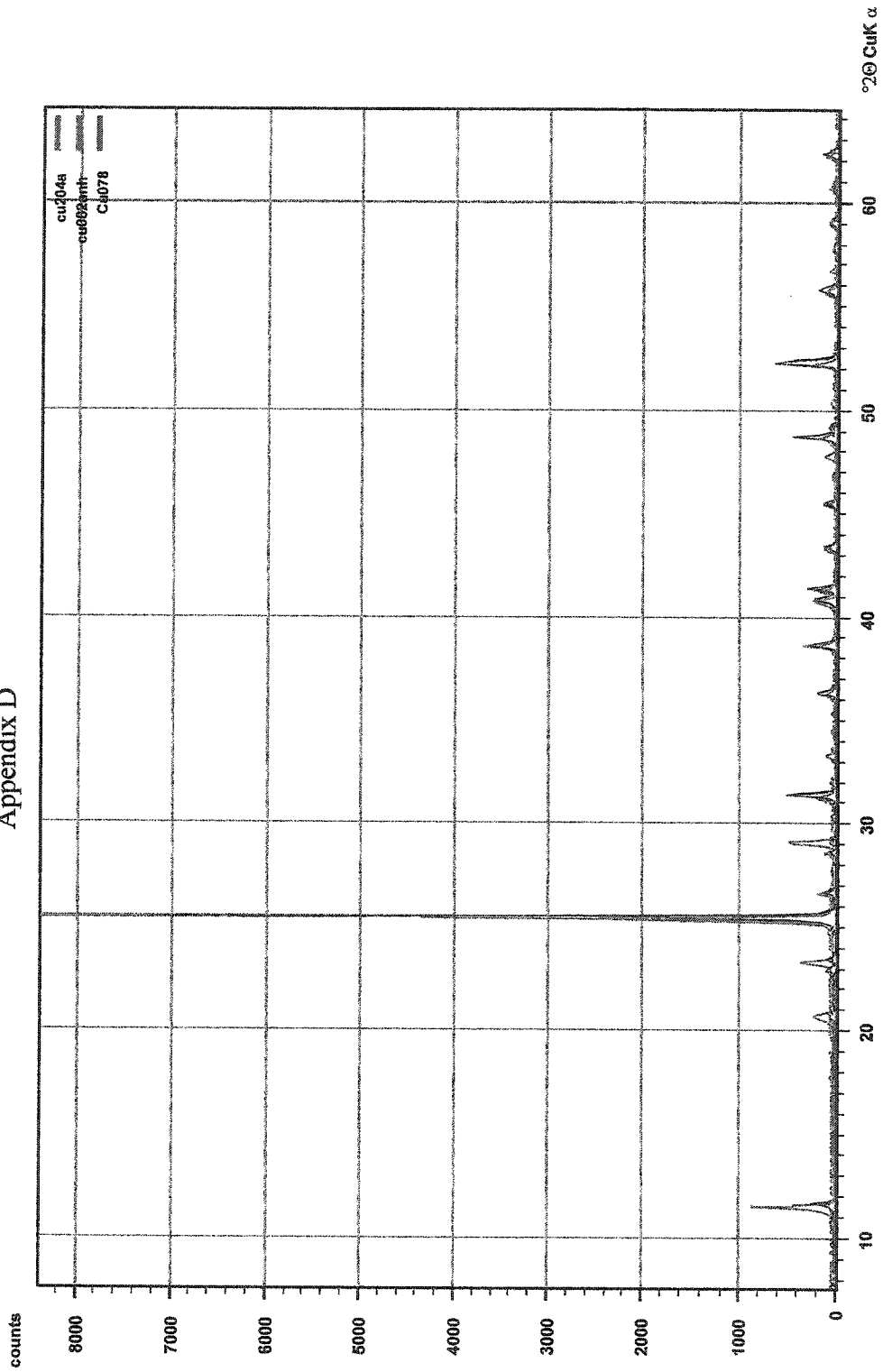
Gypsum X-ray Diffractogram

Appendix D



Biotite X-ray Diffractogram

Appendix D



Appendix E

Geochemistry

Appendix E: Geochemistry

11 samples were analyzed by Chemex Laboratory in Vancouver for whole-rock major, minor, and some trace-elements using X-ray fluorescence spectrometry (XRF) and titration. XRF is ideal for the measurement of major and minor elements (Chemex web site).

11 samples were also analyzed at the Chemex Laboratories for trace-elements and rare- earths elements, using inductively coupled plasma-mass spectrometry (ICP-MS). ICP-MS is used as a multi-element analytical technique capable of determining a wide range of elements to very low detection limits.

		Method	Detection	
SiO ₂	%	XRF	0.01	
TiO ₂	%	XRF	0.01	
Al ₂ O ₃	%	XRF	0.01	
FeO	%	titration	0.01	
Fe ₂ O ₃	%	XRF	0.01	
MgO	%	XRF	0.01	
MnO	%	XRF	0.01	
CaO	%	XRF	0.01	
K ₂ O	%	XRF	0.01	
Na ₂ O	%	XRF	0.01	
P ₂ O ₅	%	XRF	0.01	
Cr ₂ O ₃	%	XRF	0.01	
Total	%	calculated		
+H ₂ O	%	Leco RCM100	0.01	
-H ₂ O	%	Leco RCM100	0.01	
S	%	Leco-IR detector	0.001	
Ba	ppm	XRF	2	
Rb	ppm	XRF	2	
Sr	ppm	XRF	2	
Nb	ppm	XRF	2	
Zr	ppm	XRF	3	
Y	ppm	XRF	2	
				chondrite concentration
Ce	ppm	ICP-MS	2	0.865
Dy	ppm	ICP-MS	0.5	0.343
Er	ppm	ICP-MS	0.5	0.225
Eu	ppm	ICP-MS	0.2	0.077
Gd	ppm	ICP-MS	0.2	0.276
Ho	ppm	ICP-MS	0.2	0.078
La	ppm	ICP-MS	1	0.328
Lu	ppm	ICP-MS	0.1	0.034
Nd	ppm	ICP-MS	1	0.63
Pr	ppm	ICP-MS	0.2	0.123
Sm	ppm	ICP-MS	0.5	0.203
Tb	ppm	ICP-MS	0.1	0.052
Tm	ppm	ICP-MS	0.1	0.034
Yb	ppm	ICP-MS	0.1	0.22

		Method	Detection
Th	ppm	ICP-MS	1
U	ppm	ICP-MS	0.5
Cs	ppm	ICP-MS	0.1
Co	ppm	ICP-MS	0.5
Cu	ppm	ICP-MS	5
Ga	ppm	ICP-MS	1
Hf	ppm	ICP-MS	1
Pb	ppm	ICP-MS	5
Ni	ppm	ICP-MS	5
Ag	ppm	ICP-MS	1
Ta	ppm	ICP-MS	0.5
Tb	ppm	ICP-MS	0.1
Tl	ppm	ICP-MS	0.5
Sn	ppm	ICP-MS	1
W	ppm	ICP-MS	1
V	ppm	ICP-MS	5
Y	ppm	ICP-MS	0.5
Zn	ppm	ICP-MS	5

Sample	SiO2	TiO2	Al2O3	Fe2O3tot	MnO	MgO	CaO	Na2O	K2O	P2O5	LOI	TOTAL	FeO	S%
Cu-769	70.2	0.32	16.88	2.43	0.04	0.7	3.03	4.1	1.72	0.11	0.44	99.97	0.82	n/a
Cu-1333	68.06	0.3	17.36	1.36	0.01	0.37	1.01	3.71	4.06	0.08	2.41	98.73	n/a	n/a
Cu-1333	68.02	0.29	17.88	1.13	0.01	0.47	0.94	3.58	4.15	0.05	2.82	99.48	n/a	0.31
CU93-514	69.2	0.29	16.9	2.26	0.04	0.63	1.81	5.29	3.17	0.04	0.8	100.4	0.73	n/a
CU93-516	71	0.2	15.5	0.74	0.02	0.12	0.31	5.17	4.03	0.06	1.7	98.8	0.28	n/a
Cu-1112	70.64	0.32	15.74	0.76	0.01	0.46	0.32	5.77	4.09	0.06	0.42	98.59	n/a	n/a
CU-1115	69.94	0.24	14.95	2.02	0.04	0.76	0.21	4.1	4.79	0.08	1.19	98.32	n/a	n/a
Cu-020	68.26	0.26	11.1	2.63	b/d	0.29	3.51	b/d	3.43	0.08	8.97	98.56	n/a	3.68
Cu-070	83.6	0.1	6.42	1.17	0.01	0.49	1.92	b/d	1.95	0.03	3.77	99.56	n/a	1.03
Cu-093	86.52	0.07	4.84	1.03	b/d	0.08	1.56	b/d	1.46	0.07	3.3	99.03	n/a	1.67
Cu-102	80.87	0.19	11.74	0.89	b/d	0.22	0.05	b/d	3.58	0.09	1.99	99.67	n/a	0.74
Cu-1144	65.56	0.18	15.53	0.53	0.23	0.28	1.69	0	10.43	0.13	4.08	98.64	n/a	n/a
Cu-746	69.01	0.31	16.06	1.52	0.09	0.82	1.94	4.99	2.83	0.15	1.09	98.81	n/a	n/a
Cu-1334	68.96	0.23	15.19	0.5	0.01	0.49	1.42	3.92	5.79	0.09	2.94	99.64	n/a	0.94
Cu-524	64.4	0.56	14.9	3.18	0.07	1.52	3.69	3.55	3.87	0.16	0.85	96.75	n/a	n/a
Cu-526	64.6	0.43	16.6	3.61	0.08	1.31	4.13	2.48	4.41	0.21	1.97	99.83	n/a	n/a

Sample #	Ba	Rb	Sr	Y	Zr	Nb	Th	Pb	Ga	Zn	Ni
Cu 769	855	65	709	7	125	7	2	5	20	30	0
Cu 1333	799	107	400	9	188	5	3	15	22	435	20
Cu 512	712	158	346	4	108	9	n/a	n/a	n/a	n/a	n/a
Cu 524	649	177	367	27	315	4	n/a	n/a	n/a	n/a	n/a
Cu 526	704	75	638	9	156	5	n/a	n/a	n/a	n/a	n/a
Cu 1112	415	98	158	12	108	18	6	n/a	n/a	n/a	n/a
Cu 1115	625	154	116	14	102	12	n/a	n/a	n/a	n/a	n/a
Cu 020	129.5	90.4	108	4	207	7	4	20	23	145	35
Cu 070	80	44.8	94.4	2.5	48	6	1	15	14	15	110
Cu 093	203	32.6	212	2.5	46	1	7	35	12	20	60
Cu 102	234	91	72.9	2	138.5	6	2	20	26	15	30

Sample #	V	Hf	Cs	Ta	Co	U	W	Sn	Ag	Cu
Cu 769	35	4	1.4	1	3	2	0	0	0	410
Cu 1333	25	4	2.4	0	3	3	17	7	2	5410
Cu 512	n/a	n/a	n/a	n/a	n/a	n/a	n/a	n/a	n/a	n/a
Cu 524	n/a	n/a	n/a	n/a	n/a	n/a	n/a	n/a	n/a	n/a
Cu 526	n/a	n/a	n/a	n/a	n/a	n/a	n/a	n/a	n/a	n/a
Cu 1112	n/a	n/a	n/a	n/a	n/a	2	n/a	n/a	n/a	n/a
Cu 1115	n/a	n/a	n/a	n/a	n/a	n/a	n/a	n/a	n/a	n/a
Cu 020	60	4	1.3	<0.5	4	1.5	28	14	<1	844
Cu 070	60	1	0.6	<0.5	3.5	<0.5	12	7	1	347
Cu 093	30	<1	0.3	<0.5	3	0.5	9	6	11	1.66%
Cu 102	70	3	0.8	<0.5	1.5	0.5	21	13	6	1.82%

Sample #	La	Ce	Pr	Nd	Pm	Sm	Eu	Gd	Tb	Dy	Ho
Cu 769	24	43.5	5.1	19		2.6	0.8	2.4	0.3	1.2	0.2
Cu 1333	12	24	2.6	9		1.5	0.4	1.7	0.2	1.3	0.3
Cu 510	18	36	3.3	12		2	0.7	1.3	0.2	0.9	0.2
Cu 524	28	64	6.9	26		4.5	1	4.3	0.6	3.4	0.8
Cu 526	22	47	4.8	16		3.2	1.1	1.9	0.3	1.4	0.4
Cu 1112	15.5	30	3.5	12		2.1	0.4	1.4	0.1	0.7	<0.1
Cu 020	15.5	30.5	3.2	11		1.6	0.4	1.1	0.1	0.7	0.1
Cu 070	4.5	8.5	1	3.5		0.6	0.1	0.5	<0.1	0.3	<0.1
Cu 093	21.5	35	3	9		1.2	0.3	0.9	0.1	0.5	<0.1
Cu 102	7.5	15.5	1.6	5.5		0.9	0.1	0.6	<0.1	0.3	<0.1

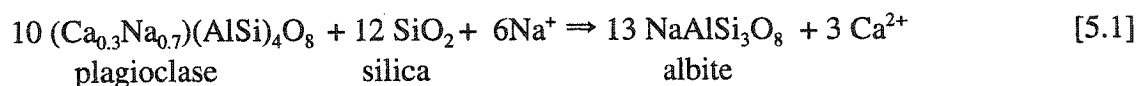
Sample #	Er	Tm	Yb	Lu
Cu 769	0.8	0.1	0.8	0.1
Cu 1333	0.9	0.1	0.9	0.1
Cu 510	0.3	0.1	0.5	0.1
Cu 524	1.7	0.3	1.9	0.3
Cu 526	0.7	0.1	0.7	0.1
Cu 1112	0.3	<0.1	0.3	<0.1
Cu 020	0.4	<0.1	0.4	<0.1
Cu 070	0.2	<0.1	0.2	<0.1
Cu 093	0.3	<0.1	0.2	<0.1
Cu 102	0.2	<0.1	0.1	<0.1

Sample #	Sp. Grav.
Cu086	2.73
Cu510	2.64
Cu511	2.61
Cu512	2.58
Cu513	2.56
Cu514	2.58
Cu516	2.53
Cu524	2.68
Cu526	2.59
Cu746	2.58
Cu769	2.65
Cu1112	2.6
Cu1115	2.55
Cu1132	2.53
CU1142	2.58
Cu1144	2.54
Cu070	2.63
Cu020	2.64
Cu102	2.73
Cu093	2.82

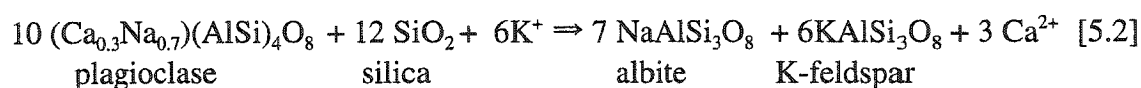
Mass balance calculation for the fresh versus potassic zones Appendix E

Petrographically, there is evidence of alteration from a fresh assemblage, represented by Cu 769, to a potassic assemblage, represented by Cu 1112. In the fresh rocks, amphibole has been partly altered to biotite along cleavage planes and grain boundaries. Rutile in the potassic zone has pseudomorphed titanite grains. Volumetrically, plagioclase is the most abundant mineral in the fresh and potassic rocks, although the composition has changed. Patches of K-feldspar in the plagioclase of the potassic K-feldspar are the result of replacement. K-feldspar megacrysts are more abundant in the potassic than the fresh rock.

The abundance of plagioclase remains relatively constant between the fresh and the potassic samples. The composition of plagioclase in the fresh rocks are andesine-oligoclase (An_{20-40}) and those of the potassic are albite ($An_{<6}$). Locally, the plagioclase of the potassic sample have antiperthitic lamellae. The addition of sodium and silica and the removal of calcium would result in the replacement of andesine-oligoclase by albite which can be expressed as:



K-feldspar of the fresh and potassic samples have the same composition. The potassic samples have more megacrystic phenocrysts of K-feldspar than the fresh sample. It would seem that there has been an increase in the amount of K-feldspar in the potassic zone compared to the fresh sample. This increase in K-feldspar and the presence of antiperthitic plagioclase in the potassic zone suggest that some of the plagioclase in the fresh rock may have been altered to K-feldspar, rather than to albite, by the addition of potassium and silica, such as:



The formula for biotite is highly variable and can be complex. Formula were determined (Table 2) using the basic formula for biotite $K_2[Mg,Fe]_{6-4}[Fe^{3+},Al,Ti]_{0-2}[Si_{6-5}Al_{2-3}O_{20}]_2O_{20}(F,OH)_4$ (Deer et al. 1992) and the calculated cations from microprobe data for biotite (Table 1).

Table 1. The calculated cation values from two electron microprobe analyses, one from the fresh and one from the potassic.

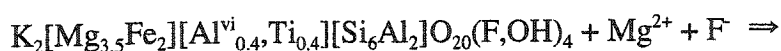
	Cu 769 (Fresh)	Cu 1112 (Potassic)	Site
Si	5.959	5.975	Z
Aliv	2.041	2.025	Z
Alvi	0.433	0.462	Y
Ti	0.417	0.446	Y
Fe2	2.065	0.833	Y
Mg	3.416	4.541	Y
Na	0.067	0.14	X
K	1.938	1.963	X
CF	0.648	4.119	
CCl	0.075	0.092	
OH	0	0	
O	24	24	

Since the amount of Na is negligible relative to the amount of K, the X site is assigned to K. The Z site is filled with 6 Si and 2 Al^{iv} and 20 O. The Al_{vi} and Ti remain relatively constant from the fresh to the potassic biotite. The variation in the Mg:Fe ratio is what differentiates the biotite in the fresh versus the potassic samples. There is a increase in the Mg and an equivalent decrease in the Fe from the fresh to the potassic.

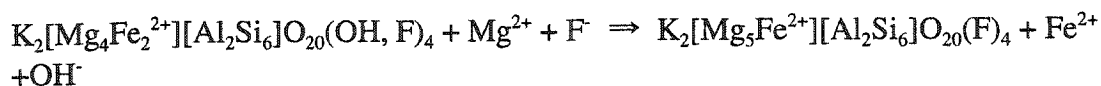
The hydroxyl site of the biotite is filled mainly with fluorine in the potassic sample while it is relatively OH-rich in the fresh sample (the value for OH is calculated to be zero in the table because there is no way to measure directly the amount of H in the electron microprobe analyses. There is only minor chlorine in the hydroxyl sites of both the fresh and potassic samples.

Table 2. Estimated biotite formula for the fresh and potassically altered Este Porphyry.

Basic Formula	$K_2[Mg,Fe]_{6.4}[Fe^{3+},Al,Ti]_{0.2}[Si_{6.5}Al_{2.3}]O_{20}(F,OH)_4$
Fresh	$K_2[Mg_{3.4}Fe_2][Al^{vi}_{0.4}Ti_{0.4}][Si_6Al_2]O_{20}(F,OH)_4$
Potassic	$K_2[Mg_{4.5}Fe_{0.8}][Al^{vi}_{0.4}Ti_{0.4}][Si_6Al_2]O_{20}(F)_4$



The charge on the biotites is not neutral, as is required for all minerals; they both have a charge of (+1.76). Since the Al and Ti remain constant in the transition from fresh to potassic biotites, Al and Ti are removed from the formula and added to the Mg and Fe^{2+} in the Y-site, and rounded off. As biotite is a minor phase in both the fresh and potassic zones, the change in the formula is negligible. This neutralizes the formulae and balances both equations and gives the following equation:



The values for the cations in the amphibole were calculated using microprobe analyses and Minpet; the results are given in Table 3.

Table 3. Predicted formula for amphibole in the fresh Este Porphyry.

Basic Formula	$(Na,K)_{0.1}Ca_2[Mg,Fe,Al]_5[Si_{6.7.5}Al_{2.0.5}O_{22}](F,OH)_2$
Fresh	$(Na_{0.1}K_{0.1})[Ca_{1.8}Mn_{0.1}Na_{0.1}]$ $[Mg_{3.6}Fe^{2+}_{0.9}Fe^{3+}_{0.3}Ti_{0.1}Mn_{0.1}][Si_{7.4}Al_{0.6}O_{22}](F,OH)_2$
Simplified	$Ca_2[Mg_{3.6}Fe_{1.2}Ti_{0.1}Mn_{0.1}][Si_{7.4}Al_{0.6}O_{22}](F,OH)_2$

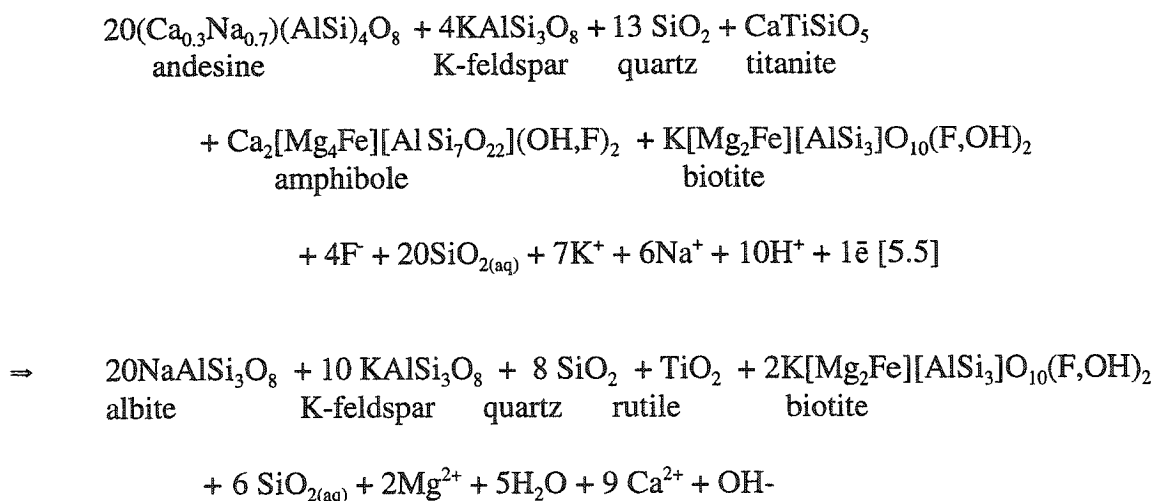
Table 4. Relative abundance of tectosilicates in the fresh Este Porphyry.
Cu 769- fresh

CIPW normative minerals	calculated CIPW values	based on 20 plagioclase
Quartz	31	13
Orthoclase	10	4
Plagioclase (Ab+An)	49	20

Table 5. Relative abundance of tectosilicates in the potassically altered Este Porphyry.
Cu 1112-potassic

CIPW normative minerals	calculated CIPW values	based on 20 plagioclase
Quartz	20	8
Orthoclase	25	10
Plagioclase (Ab+An)	51	20

Note the decrease in normative quartz and increase in normative K-feldspar. Biotite, amphibole and titanite are relatively minor phases in both the fresh and potassic samples and so were given values of 1 each. The formulae of biotite and amphibole have been simplified, as shown above. Minor elements such as titanium and manganese were not incorporated for simplicity of the calculations. The calculated values were then used to represent the units for the following equation:



Appendix F
Stable Isotope Data

Sample	mineral	Yield	$\delta^{18}\text{O}(\text{SMOW})$	Wt % H_2O	H/D
CU070S	illite	15	8.6	4.62	-58
CU070Q	quartz	16.4	11.2		
CU020	illite/mus+quartz	13.3	9.2	2.92	-50
CU090	illite/mus+quartz	14.8	9.6	5.73	-54
CU128	illite/mus+quartz	14.6	9.7	4.08	-53
CU807	quartz+illite	14.8	9.7	2.78	-52
CU442K	k-feldspar	14.7	9.2		
CU442Q	quartz	16.7	11.1		
CU442B	biotite	13.6	7.9		
CU494K	k-feldspar	14.6	8.9		
CU494Q	quartz	16.8	10.4		
CU494B	biotite	13.2	6.6		
CU769K	k-feldspar	14.8	8.2		
CU769Q	quartz	16.2	9.4		
CU769B	biotite	13.5	5.0	3.7	-85
CU769P	plagioclase	15.3	8.2		
CU1105	k-feldspar	14.7	11.0		
CU1115K	k-feldspar	14.5	9.8		
CU1115Q	quartz	16.8	10.6		
CU1115B	biotite	13.2	7.9		

	Quartz-K-feldspar Bottinga and Javoy 1973	Quartz-Biotite Bottinga and Javoy 1975	K-feldspar-Biotite Bottinga and Javoy 1973
CU442			926
CU442	445		
CU442		716	
CU494			697.2
CU494	535		
CU494		646	
CU769			574.6
CU769	626		
CU769		586	
CU1115	833		771
CU1115			
CU1115		788	

Calculation of range of $\delta^{18}\text{O}$ equilibrium for muscovite and quartz at 350°C.

Sample	Mineral	$\delta^{18}\text{O}$ Muscovite- O'Neil and Taylor 1967	$\delta^{18}\text{O}$ Quartz- Matsuhisa et al. 1979
Cu 070	Muscovite	6.36	N/A
Cu 070	Quartz	N/A	5.9
Cu 020	Muscovite-Quartz	6.96	3.9
Cu 090	Muscovite-Quartz	7.36	4.3
Cu 128	Muscovite-Quartz	7.46	4.4
Cu 807	Muscovite-Quartz	7.46	4.4

Calculation of range of δD in equilibrium for muscovite at 350°C.

Sample	measured δD	calculated δD Suzuoki and Epstein 1976
Cu 070	-58	-20.2
Cu 020	-50	-12.2
Cu 090	-54	-16.2
Cu 128	-53	-15.2
Cu 807	-52	-14.2

Calculated deuterium isotopes of fluid equilibrium.

Calculated temperature	Reference	valid for temperature range
421°C	Eslinger et al. 1979	350-500°C
334°C	O'Neil and Taylor 1969	400-650°C
569°C	Bottinga and Javoy 1975	500-800°C

Appendix G
Geochronology

K-feldspar, biotite, hornblende and sericite were dated using the high precision, stepwise degassing $^{40}\text{Ar}/^{39}\text{Ar}$ method available at the laboratory of Dr. P.H. Reynolds of Dalhousie University. Samples from fresh and altered rocks were dated. The samples were first crushed and then separated manually using a binocular picking microscope to ensure the separates were as pure and free as possible from other potassium-bearing minerals. The mineral separates were individually wrapped in aluminum foil and stacked in aluminum canister with between five and seven interspersed flux monitors. The flux monitor was the hornblende standard MMHb-1. This standard has an apparent K-Ar age of 520 ± 2 Ma (Samson and Alexander 1987). The canister was irradiated with fast neutrons in the nuclear reactor at McMaster University in Hamilton, Ontario. Isotopic analyses at Dalhousie University were made with a VG3600 mass spectrometer attached to a double -vacuum tantalum resistance furnace. Errors are reported at the 2-sigma level. These errors include the uncertainty in the irradiation parameter, J, but do not incorporate the assumed age of the flux monitor. An age plateau is defined where adjacent steps containing 50% or more of the total gas evolved exhibit no difference in apparent age beyond the ones expected from experimental uncertainties.

CU-070 SERICITE ARGON SUMMARY

T°C	mV 39	39%	AGE (Ma)±1σ	% ATM	37/39	36/40	39/40	% IIC
500	15.5	0.6	-36.6 ± 38.4	103	0.4	0.003496	0.003889	0.33
550	8.8	0.3	-45.4 ± 127	107	0.21	0.003648	0.007367	0.13
575	18.4	0.7	28.8 ± 12.6	89.1	0.01	0.003022	0.016032	0.02
600	21.6	0.8	30.1 ± 8.7	76	0.01	0.002582	0.0339	0.01
625	34.3	1.3	30.5 ± 5.6	68.4	0.01	0.002322	0.044156	0.01
650	52.3	2	30.8 ± 3.4	51.3	0.01	0.001742	0.067275	0.01
675	76.1	3	31.5 ± 2.3	37.8	0.01	0.001282	0.084192	0.01
700	102.9	4.1	31 ± 1.7	27.8	0	0.000945	0.099235	0
725	150.7	6	30.8 ± 1	11.6	0	0.000396	0.122073	0
750	173.4	6.9	31.3 ± .8	4.3	0	0.000148	0.130183	0
775	160.5	6.4	30.8 ± .9	5.5	0	0.000188	0.130414	0
800	172.5	6.8	31.2 ± .9	7.6	0	0.00026	0.126092	0
850	270.4	10.8	31 ± .5	4.1	0	0.000141	0.131561	0
900	312.3	12.4	31 ± .5	6.3	0	0.000213	0.12846	0
950	337	13.4	31.1 ± .4	3.8	0	0.000129	0.131516	0
1050	449	17.9	31.1 ± .4	6.7	0	0.000228	0.127423	0.01
1250	144.5	5.7	30.3 ± 1.7	56	0.01	0.0019	0.061717	0.01
1450	2.2	0	-99.4 ± 426	101	-0.04	0.003432	0.000614	0

MEAN AGE(900°C-1250°C)= 31 ± .6 Ma (2σ UNCERTAINTY, INCLUDING ERROR IN J)

J = .002382 ± .000012 (.5 %)

37/39,36/40 AND 39/40 Ar RATIOS ARE CORRECTED FOR MASS SPECTROMETER DISCRIMINATION, INTERFERING ISOTOPES AND SYSTEM BLANKS

% IIC - INTERFERING ISOTOPES CORRECTION

CU-082 SERICITE ARGON SUMMARY

T°C	mV 39	39%	AGE (Ma)±1σ	% ATM	37/39	36/40	39/40	% IIC
500	67.1	1.4	33.3 ± 1.6	66.8	0.03	0.002262	0.041046	0.03
550	108.7	2.3	29.9 ± 1.6	32.4	0.02	0.001099	0.093075	0.02
600	280.9	6.1	32.2 ± 1.3	12.9	0.01	0.000439	0.111651	0.01
650	609.1	13.3	32.2 ± 1.2	7.2	0	0.000244	0.118694	0.01
675	537.9	11.8	31.7 ± 1.1	3.3	0	0.000112	0.125932	0
700	520.5	11.4	31.4 ± 1.1	2.4	0	0.000081	0.128117	0
725	480.4	10.5	31.4 ± 1.1	1.3	0	0.000046	0.129615	0
750	420.8	9.2	31.1 ± 1.1	1	0	0.000035	0.13118	0
775	342.1	7.5	31 ± 1.2	1	0	0.000034	0.131777	0
800	267.5	5.8	30.7 ± 1.2	1.9	0	0.000064	0.131911	0
825	206.3	4.5	30.8 ± 1.2	1.3	0.01	0.000046	0.132029	0.01
850	160.6	3.5	30.7 ± 1.3	2.4	0.01	0.000084	0.131064	0.01
900	183	4	30.6 ± 1.3	5.6	0.02	0.00019	0.127359	0.02
950	169.6	3.7	30.8 ± 1.3	5.3	0.03	0.000181	0.127028	0.03
1000	109.6	2.4	30.9 ± 1.4	8.4	0.07	0.000286	0.122325	0.07
1100	79.7	1.7	31.4 ± 1.7	24.4	0.33	0.000829	0.099304	0.35
1200	4.8	0.1	45.5 ± 16.5	85.4	1.34	0.002892	0.013111	1
1450	2.4	0	92.2 ± 98.8	95.9	0.62	0.003245	0.001802	0.24

MEAN AGE(750°C-1000°C)= 30.9 ± 1.3 Ma (2σ UNCERTAINTY, INCLUDING ERROR IN J)

J = .002312 ± .0000185 (.8 %)

37/39, 36/40 AND 39/40 Ar RATIOS ARE CORRECTED FOR MASS SPECTROMETER DISCRIMINATION, INTERFERING ISOTOPES AND SYSTEM BLANKS
% IIC - INTERFERING ISOTOPES CORRECTION

CU-093 SERICITE ARGON SUMMARY

T°C	mV 39	39%	AGE (Ma)±1σ	% ATM	37/39	36/40	39/40	% IIC
500	53.8	1.2	30.1 ± 2.4	77.4	0.08	0.002619	0.030971	0.09
550	87.7	2	31.6 ± 1.1	53.3	0.06	0.001804	0.061043	0.07
600	197	4.4	31 ± .5	36.1	0.06	0.001223	0.085126	0.06
650	365.6	8.3	31.7 ± .3	18.1	0.04	0.000614	0.106526	0.04
675	336.4	7.6	31.5 ± .2	8.4	0.03	0.000284	0.119918	0.03
700	385.3	8.7	31.2 ± .2	4.8	0.02	0.000165	0.125769	0.02
725	448.2	10.2	31.2 ± .2	2.9	0.02	0.000099	0.12839	0.02
750	570.6	13	30.7 ± .1	4	0.02	0.000137	0.129101	0.02
775	463.1	10.5	31 ± .3	21.2	0.02	0.00072	0.104898	0.03
800	388.8	8.8	31 ± .2	1.6	0.03	0.000057	0.130947	0.03
825	380.2	8.6	31.3 ± .2	3.4	0.04	0.000115	0.127501	0.04
850	199.4	4.5	-	-	-	-	-	-
900	133.1	3	30.9 ± .3	1.1	0.13	0.000042	0.132047	0.14
950	104.3	2.3	30.6 ± .4	1.5	0.18	0.000057	0.132795	0.2
1000	98.9	2.2	31 ± .5	4.7	0.41	0.000169	0.126426	0.43
1100	151.9	3.4	31.1 ± .4	17	0.7	0.000581	0.109877	0.74
1200	21.8	0.4	37.8 ± 7	88.5	0.77	0.002997	0.012429	0.68

MEAN AGE(550°C-1000°C)= 31.1 ± .3 Ma (2σ UNCERTAINTY, INCLUDING ERROR IN J)
 J = .002312 ± .0000185 (.8%)
 37/39, 36/40 AND 39/40 Ar RATIOS ARE CORRECTED FOR MASS SPECTROMETER
 DISCRIMINATION, INTERFERING ISOTOPES AND SYSTEM BLANKS
 % IIC - INTERFERING ISOTOPES CORRECTION

CU-203 SERICITE ARGON SUMMARY

T°C	mV 39	39%	AGE (Ma)±1σ	% ATM	37/39	36/40	39/40	% IIC
500	1.6	0	5.2 ± 2.4	65.9	0.2	0.002157	0.258865	1.25
550	15.3	0.4	28.4 ± 1.8	15.4	0.17	0.000525	0.122647	0.2
600	123.1	3.4	37.3 ± 4	2.7	0.17	0.000096	0.107316	0.15
650	350.3	9.7	32.3 ± 2	12.1	0.17	0.000413	0.112201	0.17
675	312.2	8.7	31.4 ± 2	9.5	0.14	0.000324	0.118836	0.14
700	311.1	8.6	31 ± 2	7.2	0.12	0.000248	0.123482	0.13
725	465.5	13	31.3 ± 2	5.2	0.1	0.000179	0.124924	0.11
750	226.2	6.3	30.8 ± 2	3	0.11	0.000107	0.129804	0.12
775	233.6	6.5	30.8 ± 2	3.4	0.14	0.00012	0.129204	0.15
800	216.8	6	30.6 ± 2	4.2	0.17	0.000148	0.128793	0.18
825	187.6	5.2	30.5 ± 3	4.4	0.22	0.000153	0.129305	0.24
850	164.5	4.5	30.2 ± 3	6.2	0.3	0.000215	0.128167	0.33
900	209.6	5.8	29.5 ± 3	11.9	0.42	0.000409	0.123166	0.47
950	163.3	4.5	29.9 ± 4	13.5	0.52	0.000462	0.119328	0.57
1000	98.8	2.7	28.5 ± 7	28	1.51	0.000959	0.103922	1.74
1100	167.3	4.6	31 ± 5	33.5	1.7	0.00114	0.088359	1.81
1200	257.1	7.1	31.5 ± 4	34.3	0.02	0.001162	0.086113	0.02
1400	73.1	2	33.6 ± 1.9	73.3	0.04	0.00248	0.032776	0.04

MEAN AGE(725°C-1200°C)= 30.6 ± .3 Ma (2σ UNCERTAINTY, INCLUDING ERROR IN J)

J = .002312 ± .0000185 (.8 %)

37/39, 36/40 AND 39/40 Ar RATIOS ARE CORRECTED FOR MASS SPECTROMETER

DISCRIMINATION, INTERFERING ISOTOPES AND SYSTEM BLANKS

% IIC - INTERFERING ISOTOPES CORRECTION

CU-519 SERICITE ARGON SUMMARY

T°C	mV 39	39%	AGE (Ma)±1σ	% ATM	37/39	36/40	39/40	% IIC
500	150	3	32.8 ± .8	51.4	0.03	0.001739	0.061101	0.03
550	330.1	6.7	25.9 ± .3	26.1	0.03	0.000884	0.117826	0.04
600	519.4	10.5	31.1 ± .2	14.8	0.02	0.000502	0.112955	0.02
650	810.3	16.5	32.7 ± .2	7.1	0.02	0.000241	0.117101	0.02
675	665.5	13.5	32.6 ± .1	3.1	0.01	0.000106	0.122629	0.01
700	603.6	12.3	32.5 ± .1	1.4	0.01	0.00005	0.125107	0.01
725	573.3	11.6	32.1 ± .1	2.2	0.01	0.000077	0.125813	0.01
750	499.1	10.1	31.7 ± .1	1.9	0.01	0.000067	0.127565	0.01
775	316.9	6.4	31.3 ± .2	2.1	0.01	0.000073	0.129182	0.01
800	197	4	30.9 ± .3	2.6	0.01	0.000088	0.130133	0.01
825	109.9	2.2	30.1 ± .4	5.4	0.02	0.000184	0.129693	0.02
850	60	1.2	28.6 ± .8	12.8	0.03	0.000435	0.125826	0.04
900	39.3	0.8	31 ± 1.2	19.9	0.06	0.000675	0.106471	0.06
950	14.2	0.2	16.9 ± 2.9	60.8	0.13	0.002055	0.095909	0.25
1000	6.3	0.1	1.2 ± 6.4	98	0.31	0.00331	0.066152	8.03
1100	5.3	0.1	26.7 ± 10.9	76.2	0.36	0.002576	0.036724	0.45
1200	5.9	0.1	45.7 ± 35.7	95.6	0.25	0.003238	0.003866	0.19

MEAN AGE(650°C-825°C)= 32.1 ± .3 Ma (2σ UNCERTAINTY, INCLUDING ERROR IN J)

J = .002312 ± .0000185 (.8 %)

37/39, 36/40 AND 39/40 Ar RATIOS ARE CORRECTED FOR MASS SPECTROMETER DISCRIMINATION, INTERFERING ISOTOPES AND SYSTEM BLANKS
% IIC - INTERFERING ISOTOPES CORRECTION

CU-046 HORNBLLENDE ARGON SUMMARY

T°C	mV 39	39%	AGE (Ma)±1σ	% ATM	37/39	36/40	39/40	% IIC
700	17	2.7	28.2 ± 6.5	81.6	0.41	0.00276	0.026944	0.48
800	30.5	4.9	34.8 ± 2.5	45.5	0.26	0.001538	0.064729	0.25
900	29.8	4.8	-	-	-	-	-	-
950	12.4	2	41.6 ± 4.9	47.7	1.29	0.001611	0.051771	1.04
975	19.2	3	33.2 ± 3.2	49.9	4.72	0.001685	0.062349	4.72
1000	25.1	4	31.4 ± 4	41.4	8.88	0.001428	0.076188	9.36
1025	100.1	16.1	35.7 ± 9	30.5	10.47	0.001051	0.079777	9.76
1050	118.6	19.1	37.5 ± 8	21	9.66	0.000736	0.086383	8.62
1075	66.8	10.7	36.1 ± 1.4	19.3	9.04	0.000696	0.091224	8.37
1100	33.5	5.4	36.9 ± 2	20.5	7.01	0.000741	0.087607	6.35
1125	26.9	4.3	36.6 ± 2.7	30.2	7.55	0.001057	0.077702	6.88
1150	19.5	3.1	37.9 ± 4.5	27.9	10.15	0.001005	0.076771	8.96
1175	19.6	3.1	37.3 ± 4	45.1	11.83	0.001553	0.060017	10.61
1225	19	3	38.5 ± 4.2	46.7	11.92	0.001604	0.056507	10.38
1300	73.1	11.7	38.7 ± 1.4	37	11.97	0.001268	0.066855	10.38
1350	8.4	1.3	42.6 ± 12.8	83.8	11.84	0.002836	0.015623	9.38

MEAN AGE(1025°C- 1300°C)= 37.1 ± 1.1 Ma (2σ UNCERTAINTY, INCLUDING ERROR IN J)

J = .002317 ± .000023 (.9 %)

37/39,36/40 AND 39/40 Ar RATIOS ARE CORRECTED FOR MASS SPECTROMETER

DISCRIMINATION, INTERFERING ISOTOPES AND SYSTEM BLANKS

% IIC - INTERFERING ISOTOPES CORRECTION

CU-46 BIOTITE ARGON SUMMARY

T°C	mV 39	39%	AGE (Ma)±1σ	% ATM	37/39	36/40	39/40	% IIC
600	12	0.4	19.2 ± 9.1	80.3	0.04	0.002707	0.042306	0.08
650	16.1	0.6	33.4 ± 6.6	68.8	0.06	0.002325	0.038402	0.06
700	62.1	2.4	34.9 ± 1.8	52.1	0.01	0.001764	0.056545	0.01
750	200.2	7.9	36.3 ± .5	22.6	0	0.000766	0.088011	0
800	269.7	10.6	36.3 ± .3	7.9	0	0.000269	0.104719	0
850	164.9	6.5	36.3 ± .5	6.4	0	0.000219	0.106317	0
900	145.8	5.7	36.9 ± .5	6.6	0	0.000225	0.104453	0
950	121.9	4.8	36.9 ± .6	7.5	0	0.000253	0.103391	0
1000	219.2	8.6	36.8 ± .4	6.8	0	0.000233	0.104566	0
1050	619.8	24.4	36.3 ± .2	5	0	0.00017	0.108046	0
1100	676.8	26.7	36.4 ± .2	5	0	0.00017	0.107846	0
1150	18.3	0.7	37.6 ± 4.7	47.6	0.15	0.001607	0.057389	0.14
1300	3.4	0.1	104 ± 57.2	83.6	1.39	0.002826	0.006348	0.49

MEAN AGE(750°C- 1100°C)= 36.4 ± .4 Ma (2σ UNCERTAINTY, INCLUDING ERROR IN J)

J = .002318 ± .000023 (.9 %)

37/39,36/40 AND 39/40 Ar RATIOS ARE CORRECTED FOR MASS SPECTROMETER
DISCRIMINATION, INTERFERING ISOTOPES AND SYSTEM BLANKS
% IIC - INTERFERING ISOTOPES CORRECTION

CU-046 K-FELDSPAR ARGON SUMMARY

T°C	mV 39	39%	AGE (Ma)±1σ	% ATM	37/39	36/40	39/40	% IIC
550	2.4	0.1	52 ± 56.9	78.9	-0.81	0.002668	0.016616	0.52
650	19.9	0.9	38.5 ± 4.7	55.4	0.06	0.001874	0.047778	0.05
700	24.6	1.1	39 ± 2.9	17	0.09	0.000575	0.087841	0.08
750	43.3	2	37.7 ± 2	25.1	0.11	0.000852	0.081961	0.09
800	59.6	2.8	36.2 ± 1.2	11.9	0.07	0.000404	0.100484	0.06
850	63.8	3	36.5 ± 1.2	13.7	0.04	0.000465	0.097703	0.04
900	47.8	2.2	36.5 ± 1.6	12.6	0.01	0.000426	0.099042	0.01
950	109.4	5.1	35.2 ± .8	20.8	0.01	0.000704	0.092908	0.01
990	123	5.8	35.4 ± .8	24.7	0.01	0.000835	0.087967	0.01
1025	218.1	10.3	35.4 ± .5	26	0.02	0.00088	0.086526	0.01
1045	184.1	8.7	35.2 ± .6	30.6	0.02	0.001038	0.081298	0.02
1070	272.4	12.9	35.5 ± .5	27.4	0.02	0.000928	0.084463	0.02
1100	153.4	7.2	35.8 ± .7	29.1	0.02	0.000985	0.081844	0.02
1150	164.3	7.7	35.7 ± .7	27.4	0.04	0.000928	0.084105	0.04
1200	359.6	17	35.7 ± .4	24.1	0.01	0.000817	0.087906	0.01
1250	168	7.9	35.9 ± .7	31.3	0.02	0.00106	0.079	0.02
1300	84.1	3.9	38.5 ± 1.1	28.9	0.02	0.00098	0.076199	0.02
1350	9.3	0.4	103.3 ± 18.8	68.9	0.12	0.002334	0.012181	0.04

MEAN AGE(950°C- 1300°C)= 35.7 ± .5 Ma (2σ UNCERTAINTY, INCLUDING ERROR IN J)

J = .002318 ± .0000232 (1 %)

37/39,36/40 AND 39/40 Ar RATIOS ARE CORRECTED FOR MASS SPECTROMETER

DISCRIMINATION, INTERFERING ISOTOPES AND SYSTEM BLANKS

% IIC - INTERFERING ISOTOPES CORRECTION

CU-407 BIOTITE ARGON SUMMARY

T°C	mV 39	39%	AGE (Ma)±1σ	% ATM	37/39	36/40	39/40	% IIC
600	57.4	2.7	5.8 ± 2.2	89.1	0.22	0.003014	0.076831	1.22
650	44.2	2.1	16.1 ± 2.9	78.6	0.11	0.002658	0.055112	0.23
700	60.8	2.9	30 ± 2	50.9	0.01	0.001722	0.067792	0.02
750	158.9	7.6	34.9 ± 7	17	0.01	0.000577	0.098433	0.01
800	157.2	7.5	36.3 ± 6	6.9	0.02	0.000233	0.106105	0.01
850	198.9	9.5	37.4 ± 5	7.2	0.01	0.000243	0.102496	0
900	176.1	8.4	37.5 ± 5	6	0.01	0.000205	0.103501	0.01
950	202.2	9.6	38.2 ± 5	8.5	0.04	0.000288	0.09913	0.04
1000	240.3	11.5	38.5 ± 4	4.3	0.03	0.000147	0.102644	0.03
1050	280.3	13.4	37.5 ± 4	4.7	0.04	0.00016	0.105223	0.04
1100	349.6	16.7	36.8 ± 3	4.2	0.04	0.000144	0.10779	0.04
1150	132.9	6.3	36.1 ± 8	13.7	0.15	0.000464	0.098746	0.14
1200	12.6	0.6	47.8 ± 8	50.2	0.67	0.001697	0.042822	0.48
1300	15.2	0.7	35.8 ± 10.7	79.7	0.37	0.002696	0.023355	0.34

MEAN AGE(700°C- 1150°C)= 36.9 ± .5 Ma (2σ UNCERTAINTY,INCLUDING ERROR IN J)

J = .002321 ± .000023 (.9 %)

37/39,36/40 AND 39/40 Ar RATIOS ARE CORRECTED FOR MASS SPECTROMETER DISCRIMINATION,INTERFERING ISOTOPES AND SYSTEM BLANKS

% IIC - INTERFERING ISOTOPES CORRECTION

T°C	mV 39	39%	AGE (Ma)±1σ	% ATM	37/39	36/40	39/40	% IIC
600	27.1	0.6	31.2 ± 3.2	25.7	0.05	0.000871	0.098521	0.05
650	19.1	0.4	36.8 ± 4.4	16.7	0.01	0.000566	0.093564	0.01
700	57.3	1.2	35.2 ± 1.6	17.8	0.01	0.000605	0.096671	0.01
750	62.2	1.3	34 ± 1.5	21.3	0.02	0.000721	0.095861	0.02
800	58.5	1.3	34.2 ± 1.6	18.9	0.01	0.000641	0.098082	0.01
850	60.6	1.3	34.3 ± 1.8	30	0.03	0.001016	0.084376	0.03
900	41	0.9	34.6 ± 2.6	31.8	0.01	0.001079	0.081433	0.01
950	54.4	1.2	33.7 ± 1.9	33	0.01	0.001119	0.082158	0.01
980	42.3	0.9	34 ± 2.5	31.9	0.01	0.001082	0.082927	0.01
1010	65.9	1.4	34.8 ± 1.6	33.8	0	0.001144	0.078737	0
1040	82.7	1.8	34 ± 1.3	35.2	0	0.001193	0.078761	0
1070	159.6	3.5	34.1 ± .8	35.7	0	0.001211	0.078015	0
1100	239.4	5.3	35.1 ± .6	31.9	0	0.001079	0.08043	0
1140	385.2	8.6	34.8 ± .4	28.3	0	0.000958	0.085321	0
1170	947.7	21.1	34.8 ± .3	23.4	0	0.000792	0.091149	0
1200	941.6	21	35.2 ± .2	18.4	0	0.000625	0.09598	0
1230	461.1	10.3	34.9 ± .3	17.4	0	0.000589	0.097982	0
1280	149.4	3.3	35.3 ± .8	28.8	0	0.000975	0.083501	0
1350	75.6	1.6	35 ± 1.8	54.6	0.01	0.00185	0.053624	0.01
1450	471	10.5	35.4 ± .5	41.5	0	0.001407	0.068371	0
1500	27.3	0.6	25.8 ± 13.2	95.8	0.03	0.003242	0.006728	0.04
1550	43.1	0.9	32.2 ± 7.9	91.4	0.01	0.003096	0.010947	0.01

MEAN AGE(1100°C- 1450°C)= 35 ± .4 Ma (2σ UNCERTAINTY,INCLUDING ERROR IN J)

J = .002322 ± .000023 (.9 %)

37/39,36/40 AND 39/40 Ar RATIOS ARE CORRECTED FOR MASS SPECTROMETER
DISCRIMINATION,INTERFERING ISOTOPES AND SYSTEM BLANKS

% IIC - INTERFERING ISOTOPES CORRECTION

CU-524 HORNBLLENDE ARGON SUMMARY

T°C	mV 39	39%	AGE (Ma)±1σ	% ATM	37/39	36/40	39/40	% IIC
700	3.3	1	42.1 ± 3.2	86	8.36	0.002905	0.013695	6.7
800	7.3	2.4	37.2 ± 13.1	67	0.41	0.002253	0.036487	0.37
900	9.5	3.1	30 ± 9.4	66.8	0.14	0.002256	0.045734	0.15
950	17.6	5.8	36.8 ± 4.4	55.4	1.37	0.001868	0.049927	1.24
975	5.4	1.8	36 ± 6.7	24.8	3.55	0.000863	0.083299	3.29
1000	11.9	3.9	22.5 ± 6.3	59.5	6.48	0.002018	0.073188	9.41
1025	26.4	8.7	37.4 ± 2.5	25.4	9.19	0.00091	0.080694	8.23
1050	53.1	17.5	38 ± 1.4	14.7	9.38	0.000558	0.090809	8.26
1075	59.2	19.6	38.3 ± 1.5	10.4	9.56	0.000425	0.094538	8.37
1100	29.4	9.7	37.2 ± 3.3	20.2	8.89	0.000744	0.086718	7.99
1125	12.3	4	28.4 ± 4.9	42.7	9.1	0.001485	0.080892	10.55
1175	11.6	3.8	34.1 ± 4.7	31.2	9.73	0.00112	0.080416	9.49
1225	19.8	6.5	35.6 ± 4.4	57.1	10.44	0.001939	0.049341	9.79
1275	10.8	3.5	34.2 ± 8.8	75.9	10.56	0.002564	0.028925	10.29
1400	19.8	6.5	37.7 ± 6.6	82.8	9.98	0.002799	0.018782	8.86
1450	3.7	1.2	35.7 ± 57.8	97.2	0.93	0.003288	0.003128	0.87

MEAN AGE(1025°C- 1100°C)= 37.9 ± 2 Ma (2σ UNCERTAINTY, INCLUDING ERROR IN J)

J = .002319 ± .000023 (.9 %)

37/39,36/40 AND 39/40 Ar RATIOS ARE CORRECTED FOR MASS SPECTROMETER

DISCRIMINATION, INTERFERING ISOTOPES AND SYSTEM BLANKS

% IIC - INTERFERING ISOTOPES CORRECTION

CU-524 BIOTITE ARGON SUMMARY

T°C	mV 39	39%	AGE (Ma)±1σ	% ATM	37/39	36/40	39/40	% IIC
600	25.5	2.2	19.7 ± 4.2	71	0.02	0.0024	0.060951	0.04
650	10.2	0.9	34.5 ± 8.7	58.8	0.01	0.001992	0.049315	0.01
700	37.8	3.3	33.6 ± 2.6	37.5	0.03	0.001268	0.076843	0.03
750	63.8	5.6	37.2 ± 1.4	9.7	0.02	0.000328	0.100289	0.01
800	131.8	11.6	36.8 ± 7	7.2	0	0.000246	0.104025	0
850	53.2	4.7	37 ± 1.5	5	0	0.000171	0.106154	0
900	62.4	5.5	36.4 ± 1.2	3.7	0.01	0.000127	0.109261	0.01
950	103.5	9.1	36.8 ± .8	6.1	0.02	0.000207	0.105519	0.01
1000	173.2	15.3	36.2 ± .5	5.2	0	0.000176	0.108336	0
1050	322.6	28.5	36 ± .3	2.8	0.01	0.000097	0.111655	0.01
1100	133.5	11.8	36 ± .6	4.2	0	0.000144	0.110004	0
1150	11	0.9	36.2 ± 8.5	49.6	0.02	0.001676	0.057447	0.02

MEAN AGE(750°C- 1100°C)= 36.4 ± .6 Ma (2σ UNCERTAINTY, INCLUDING ERROR IN J)

J = .00232 ± .000023 (.9 %)

37/39, 36/40 AND 39/40 Ar RATIOS ARE CORRECTED FOR MASS SPECTROMETER DISCRIMINATION, INTERFERING ISOTOPES AND SYSTEM BLANKS

% IIC - INTERFERING ISOTOPES CORRECTION

T°C	mV 39	39%	AGE (Ma) $\pm 1\sigma$	% ATM	37/39	36/40	39/40	% IIC
550	9.6	0.9	-137.9 \pm 8.8	1617	73.78	0.042931	0.369391	12.6
600	9.5	0.9	-48.6 \pm 7.1	259	38.48	0.008303	0.128985	22.65
650	12.5	1.2	1.5 \pm 4.2	95.2	17.68	0.003158	0.118584	348.75
700	18.4	1.8	21.8 \pm 2.5	47.3	7.51	0.001591	0.097454	11.18
750	26.1	2.6	27.8 \pm 1.7	31.5	3.72	0.001059	0.100346	4.39
800	34.1	3.4	31.9 \pm 1	13.3	2.08	0.000456	0.110534	2.15
850	35.3	3.5	32.8 \pm .9	10	1.78	0.000348	0.111515	1.79
900	32.6	3.2	32.4 \pm 1	11.6	1.74	0.000397	0.111052	1.77
950	29.2	2.9	32.6 \pm 1	11.8	1.56	0.000402	0.109885	1.58
1000	34	3.4	33.1 \pm 1	12.2	1.29	0.000409	0.108154	1.29
1050	88.9	8.9	35.4 \pm .5	10.9	0.42	0.000362	0.103396	0.4
1100	162.5	16.3	35.7 \pm .3	10.1	0.23	0.000337	0.10381	0.22
1125	101.9	10.2	35.4 \pm .5	9.3	0.35	0.00031	0.105286	0.32
1150	49.7	5	34.6 \pm .7	9.3	0.5	0.000308	0.107303	0.48
1175	67.8	6.8	35.4 \pm .6	8.4	0.19	0.000274	0.106379	0.17
1200	112.9	11.3	35.9 \pm .4	6.3	0.01	0.000207	0.107372	0.01
1250	70.9	7.1	35.9 \pm .5	7.6	0.13	0.000248	0.105841	0.12
1275	23.8	2.4	36.8 \pm .9	7.1	0.14	0.000229	0.102891	0.12
1350	28.3	2.8	35.1 \pm 5.4	62.8	2.68	0.002081	0.043257	2.54
1450	14.3	1.4	35.6 \pm 3.1	41.6	0.42	0.001359	0.066907	0.39
1550	29.3	2.9	38.7 \pm 2.3	52.6	0.96	0.001759	0.050305	0.83

MEAN AGE(1050°C-1250°C)= 35.5 \pm .5 Ma (2 σ UNCERTAINTY,INCLUDING ERROR IN J)

J = .002312 \pm .0000232 (1 %)

37/39,36/40 AND 39/40 Ar RATIOS ARE CORRECTED FOR MASS SPECTROMETER
DISCRIMINATION,INTERFERING ISOTOPES AND SYSTEM BLANKS

% IIC - INTERFERING ISOTOPES CORRECTION

CU-790 K-FELDSPAR ARGON SUMMARY

T°C	mV 39	39%	AGE (Ma)±1σ	% ATM	37/39	36/40	39/40	% IIC
600	6.4	0.3	21.2 ± 4.5	46.5	0.44	0.001567	0.103021	0.68
650	16.6	1	34.7 ± 1.6	10.3	0.13	0.000352	0.10622	0.13
700	28.2	1.7	34.2 ± 1.2	14.8	0.06	0.000501	0.102398	0.06
750	39.6	2.4	34.7 ± .8	9.9	0.04	0.000337	0.106783	0.03
800	48.1	2.9	35.3 ± .7	8	0.03	0.000271	0.107309	0.03
850	46.2	2.8	34.8 ± .7	8	0.03	0.000271	0.108707	0.03
900	46.9	2.8	35.1 ± .8	14.2	0.03	0.000481	0.100496	0.03
950	45	2.7	34.9 ± .9	16	0.02	0.000543	0.099175	0.02
1000	107.1	6.5	35.1 ± .5	17.4	0.02	0.000591	0.09687	0.01
1050	201.1	12.2	35.6 ± .3	17.7	0.01	0.000598	0.095335	0.01
1100	252.5	15.3	35.7 ± .3	17	0.01	0.000576	0.095854	0.01
1150	221.6	13.5	35.5 ± .3	15.3	0.01	0.000517	0.098318	0.01
1250	469.5	28.6	35.5 ± .2	12.2	0	0.000413	0.101962	0
1350	68.7	4.1	35.1 ± .7	17.2	0.02	0.000584	0.097093	0.02
1450	42.2	2.5	31.7 ± 1.3	36.7	0	0.001243	0.082126	0

MEAN AGE(1000°C-1350°C)= 35.5 ± .4 Ma (2σ UNCERTAINTY, INCLUDING ERROR IN J)

J = .002312 ± .0000232 (1 %)

37/39, 36/40 AND 39/40 Ar RATIOS ARE CORRECTED FOR MASS SPECTROMETER DISCRIMINATION, INTERFERING ISOTOPES AND SYSTEM BLANKS
% IIC - INTERFERING ISOTOPES CORRECTION

CU-791 HORNBLLENDE ARGON SUMMARY

T°C	mV 39	39%	AGE (Ma)±1σ	% ATM	37/39	36/40	39/40	% IIC
650	233.1	19	12.3 ± .8	78	0.86	0.002641	0.073623	2.24
750	188	15.3	45.4 ± .5	27.8	0.66	0.000943	0.065349	0.49
850	143	11.6	41 ± .6	25.2	0.31	0.000853	0.075096	0.25
900	76.1	6.2	41.6 ± .8	16.1	0.35	0.000549	0.082865	0.28
950	112.1	9.1	50.4 ± .6	14.6	0.44	0.000495	0.069492	0.3
975	126.3	10.3	46.3 ± .5	11.7	0.63	0.000401	0.078209	0.46
1000	124.1	10.1	41.3 ± .5	11.2	1.92	0.00039	0.088261	1.56
1025	83.2	6.8	38.4 ± .7	9.7	4.24	0.000361	0.096177	3.69
1050	41	3.3	37.3 ± 1.1	10.9	4.27	0.000417	0.097173	3.82
1075	22.6	1.8	36.2 ± 1.9	19.1	5.01	0.000697	0.09072	4.61
1100	17.7	1.4	39 ± 2.4	18.8	6.68	0.000704	0.084088	5.74
1125	17.4	1.4	38.9 ± 2.7	25.3	8.77	0.00092	0.077481	7.53
1150	13.9	1.1	38.7 ± 3.5	32.9	11.79	0.001181	0.069867	10.19
1200	13.9	1.1	36.9 ± 4.7	61	8.39	0.002069	0.043146	7.58
1250	5.9	0.4	38.2 ± 10.1	71	5.95	0.002392	0.030986	5.21
1350	1.9	0.1	32.4 ± 36.5	90.5	8.76	0.00304	0.011853	8.95
1450	2.2	0.1	34.2 ± 53.2	96.2	2.59	0.003246	0.004532	2.51

TOTAL GAS AGE = 37.2 ± .5 Ma

J = .002312 ± 1.156E-05 (.5 %)

37/39,36/40 AND 39/40 Ar RATIOS ARE CORRECTED FOR MASS SPECTROMETER
DISCRIMINATION, INTERFERING ISOTOPES AND SYSTEM BLANKS
% IIC - INTERFERING ISOTOPES CORRECTION

T°C	mV 39	39%	AGE (Ma) $\pm 1\sigma$	% ATM	37/39	36/40	39/40	% IIC
550	16.3	0.9	-25.3 \pm 4.7	180	27.99	0.005994	0.129059	33.14
600	23.4	1.3	15.7 \pm 2.5	57.8	9.75	0.00196	0.109505	19.98
650	35.8	2.1	28.4 \pm 1.5	24.4	4.25	0.000839	0.108812	4.92
700	60.9	3.5	33 \pm .9	16.6	1.48	0.000558	0.103842	1.48
750	38.4	2.2	32 \pm 1.1	12.1	2.02	0.000422	0.112041	2.08
800	43.1	2.5	33.6 \pm .9	6.2	1.4	0.000223	0.113974	1.38
850	36.3	2.1	32.8 \pm 1	8.2	1.41	0.000288	0.114279	1.42
900	29.9	1.7	33.4 \pm 1.2	10.1	1.49	0.000348	0.10979	1.48
950	27.9	1.6	32.4 \pm 1.4	14.2	1.61	0.000482	0.108105	1.64
975	21.6	1.2	31.8 \pm 1.6	11.7	2.28	0.000414	0.1128	2.37
1000	21.7	1.2	32.5 \pm 1.6	12.2	1.92	0.000422	0.109768	1.96
1025	25.5	1.4	33.8 \pm 1.4	10.9	0.93	0.000365	0.107541	0.92
1050	36.1	2.1	35.8 \pm 1.1	10.7	0.36	0.000351	0.102205	0.33
1075	35.5	2	35.1 \pm 1.2	12.7	0.32	0.000415	0.102109	0.3
1100	35.5	2	35.6 \pm 1.1	10.2	0.22	0.000333	0.103444	0.2
1125	45.8	2.6	35.7 \pm 1	12	0.23	0.000395	0.101092	0.21
1150	69.6	4	35.1 \pm .8	14.9	0.15	0.000494	0.099793	0.14
1175	109.1	6.4	35.4 \pm .6	16.4	0.1	0.000548	0.097261	0.1
1200	107.5	6.3	35.4 \pm .6	16.9	0.1	0.000564	0.096537	0.1
1250	511.9	30	35.8 \pm .2	15.3	0.09	0.000517	0.097518	0.08
1350	175.1	10.2	36.8 \pm .4	15.7	0.18	0.000528	0.094197	0.16
1450	110.3	6.4	36.3 \pm .6	22.5	0.37	0.000754	0.087777	0.34
1550	85.1	4.9	58.6 \pm 1.5	46.6	12.08	0.00151	0.037055	7.13

MEAN AGE(1050°C-1450°C)= 35.8 \pm .5 Ma (2 σ UNCERTAINTY,INCLUDING ERROR IN J)

J = .002312 \pm .000023 (.9 %)

37/39,36/40 AND 39/40 Ar RATIOS ARE CORRECTED FOR MASS SPECTROMETER
DISCRIMINATION,INTERFERING ISOTOPES AND SYSTEM BLANKS

% IIC - INTERFERING ISOTOPES CORRECTION

CU-494 K-FELDSPAR ARGON SUMMARY

T°C	mV 39	39%	AGE (Ma)±1σ	% ATM	37/39	36/40	39/40	% IIC
550	13.1	0.3	26.9 ± 5.8	45.1	0.1	0.001542	0.087399	0.13
600	61.2	1.6	29.6 ± 2.2	56.5	0.06	0.001915	0.062504	0.07
650	124.4	3.2	30.3 ± 1.1	41	0.04	0.001391	0.082855	0.05
700	164.2	4.3	30.5 ± .9	30.8	0.03	0.001046	0.096492	0.03
750	206.9	5.4	30.3 ± .6	23.8	0.01	0.000805	0.107045	0.02
775	108.7	2.8	30.7 ± .9	13.6	0.01	0.000463	0.119907	0.01
800	73.5	1.9	30.1 ± 1.3	18	0.02	0.000611	0.116187	0.02
825	62.5	1.6	30.6 ± 1.5	15.5	0.02	0.000526	0.117514	0.02
850	59	1.5	30.3 ± 1.6	15	0.03	0.000512	0.119494	0.03
875	60.2	1.5	30.7 ± 1.5	13.6	0.03	0.000464	0.119691	0.03
900	61.4	1.6	31 ± 1.4	10.4	0.02	0.000354	0.123228	0.03
950	91.4	2.3	30.2 ± 1.1	14.8	0.02	0.000503	0.120047	0.02
1000	113.2	2.9	30.6 ± .9	13.3	0.01	0.000451	0.120717	0.01
1050	208.7	5.4	30.9 ± .6	22.7	0	0.000771	0.106266	0
1100	224.7	5.8	30.6 ± .6	23.1	0	0.000785	0.106805	0
1150	273.9	7.1	31.1 ± .5	25.2	0	0.000855	0.102403	0
1250	1157.6	30.3	30.8 ± .5	34.7	0	0.001178	0.090187	0
1450	745.3	19.5	31.7 ± .5	45.2	0	0.00153	0.073568	0

MEAN AGE(1150°C-1450°C)= 31.1 ± .7 Ma (2σ UNCERTAINTY, INCLUDING ERROR IN J)

J = .002382 ± .000012 (.5 %)

37/39, 36/40 AND 39/40 Ar RATIOS ARE CORRECTED FOR MASS SPECTROMETER
DISCRIMINATION, INTERFERING ISOTOPES AND SYSTEM BLANKS
% IIC - INTERFERING ISOTOPES CORRECTION

CU-442 BIOTITE ARGON SUMMARY

T°C	mV 39	39%	AGE (Ma)±1σ	% ATM	37/39	36/40	39/40	% IIC
550	12.7	0.4	-9.6 ±6.3	115	0.4	0.003948	0.072329	1.32
600	21	0.7	35 ±2.7	33.9	0.06	0.001153	0.080665	0.06
650	68.4	2.3	31.9 ±1.1	29.6	0.07	0.001006	0.093811	0.08
700	196.1	6.7	31.5 ±.4	17.3	0.01	0.000587	0.111561	0.01
750	408.4	13.9	31.5 ±.2	6.2	0	0.000211	0.126695	0
800	497.8	17	31.2 ±.2	5.3	0	0.000179	0.129031	0
850	287.6	9.8	30.9 ±.3	7.8	0	0.000264	0.12682	0
900	155.2	5.3	30.8 ±.4	11.8	0.01	0.000399	0.121905	0.01
925	86.9	2.9	30.7 ±.7	12.5	0.01	0.000426	0.121354	0.01
950	67.7	2.3	30.5 ±.8	12.6	0.02	0.000428	0.122166	0.03
975	57.8	1.9	30.2 ±.8	12.9	0.03	0.00044	0.12271	0.03
1000	56	1.9	30.2 ±.8	11.4	0.04	0.000388	0.124952	0.04
1025	64.5	2.2	30.3 ±.7	10.1	0.04	0.000344	0.126473	0.04
1050	80.5	2.7	30.3 ±.6	8.8	0.04	0.000299	0.12845	0.04
1075	98.3	3.3	30.5 ±.5	7.5	0.04	0.000255	0.129064	0.05
1100	119.1	4	30.8 ±.4	6.5	0.04	0.000224	0.129264	0.05
1250	546	18.6	31.3 ±.2	13.5	0.12	0.00046	0.117392	0.13
1450	97.6	3.3	27.6 ±2.1	79.3	0.02	0.002685	0.031885	0.02

MEAN AGE(650°C-1250°C)= 31.1 ±.2 Ma (2σ UNCERTAINTY, INCLUDING ERROR IN J)

J = .002383 ± .000012 (.5 %)

37/39,36/40 AND 39/40 Ar RATIOS ARE CORRECTED FOR MASS SPECTROMETER

DISCRIMINATION, INTERFERING ISOTOPES AND SYSTEM BLANKS

% IIC - INTERFERING ISOTOPES CORRECTION

CU-494 BIOTITE ARGON SUMMARY

T°C	mV 39	39%	AGE (Ma)±1σ	% ATM	37/39	36/40	39/40	% IIC
550	16.4	0.7	14.6 ± 4.4	68.6	0.37	0.00234	0.092256	0.84
600	45.3	2	30.4 ± 1.7	30.3	0.18	0.00103	0.097607	0.2
650	135.2	5.9	31.8 ± .6	19.4	0.11	0.000659	0.107718	0.12
700	263.1	11.6	31.7 ± .3	12.8	0.05	0.000434	0.116919	0.05
750	392	17.3	31.8 ± .2	6.3	0.04	0.000214	0.125192	0.04
800	451.7	20	31.7 ± .2	5.9	0.03	0.000202	0.126288	0.03
850	240.8	10.6	31.4 ± .4	10.4	0.04	0.000354	0.12128	0.04
900	70.2	3.1	30.5 ± 1.1	23.9	0.11	0.000812	0.106101	0.12
950	41.8	1.8	28.9 ± 1.8	30.2	0.14	0.001026	0.102818	0.17
1000	39.5	1.7	30.4 ± 1.5	24.3	0.14	0.000827	0.106019	0.16
1050	62.9	2.7	30.4 ± 1	16.8	0.09	0.000571	0.116587	0.1
1100	149	6.6	31.3 ± .5	9.5	0.05	0.000324	0.123077	0.06
1150	134.4	5.9	31 ± .6	14.9	0.11	0.000506	0.116659	0.12
1200	76.4	3.3	29.9 ± 1.2	35.5	0.26	0.001206	0.091591	0.29
1300	113.9	5	29.8 ± 1.1	50.5	0.12	0.001711	0.070698	0.14
1450	21.4	0.9	6.8 ± 11.8	98.6	0.08	0.003341	0.008259	0.39

MEAN AGE(650°C-1300°C)= 31.3 ± .3 Ma (2σ UNCERTAINTY, INCLUDING ERROR IN J)

J = .002381 ± .000012 (.5 %)

37/39, 36/40 AND 39/40 Ar RATIOS ARE CORRECTED FOR MASS SPECTROMETER
DISCRIMINATION, INTERFERING ISOTOPES AND SYSTEM BLANKS
% IIC - INTERFERING ISOTOPES CORRECTION

T°C	mV 39	39%	AGE (Ma) $\pm 1\sigma$	% ATM	37/39	36/40	39/40	% IIC
550	21.7	0.5	17.4 \pm 4	77.8	0.13	0.00264	0.054356	0.25
600	27.1	0.7	28.9 \pm 2.8	54.1	0.04	0.001837	0.067609	0.05
650	69.7	1.8	32.1 \pm 1.3	39.8	0.01	0.00135	0.079887	0.01
700	90.1	2.3	30.2 \pm .9	26.2	0	0.000888	0.103972	0
725	70.7	1.8	29.9 \pm .9	20.7	0	0.000702	0.112852	0
750	71.9	1.8	29.9 \pm .8	15.5	0	0.000527	0.120379	0
775	69.3	1.8	30.4 \pm .8	13	0	0.00044	0.12201	0
800	67.1	1.7	30.7 \pm .7	11.4	0	0.000387	0.123129	0
825	63.5	1.6	30.9 \pm .8	12	0	0.000407	0.121246	0
850	65.1	1.7	30.5 \pm .9	15.4	0	0.000525	0.118046	0
875	63.4	1.6	31.5 \pm .9	17.1	0	0.000582	0.112156	0
900	55.3	1.4	32.1 \pm .9	12.5	0	0.000426	0.116188	0
925	54.8	1.4	32.5 \pm .9	11.5	0	0.000393	0.11611	0
950	58.8	1.5	31.1 \pm .9	12	0	0.000407	0.120814	0
975	66.2	1.7	30.4 \pm .8	13.5	0	0.00046	0.121398	0
1000	78.8	2	30.5 \pm .7	13.5	0	0.00046	0.120704	0
1025	96.5	2.5	30.4 \pm .6	14.6	0	0.000496	0.119556	0
1050	148.4	3.8	30.9 \pm .5	15.3	0	0.000519	0.116832	0
1075	119.3	3.1	30.8 \pm .6	16.8	0	0.000569	0.115187	0
1100	119	3.1	30.6 \pm .6	19	0	0.000646	0.112612	0
1150	256.3	6.7	31.2 \pm .4	17.5	0	0.000595	0.112584	0
1200	525.7	13.8	31.6 \pm .2	13.8	0	0.000467	0.11599	0
1300	1074.5	28.2	32.1 \pm .2	11.7	0	0.000397	0.116954	0
1450	468.5	12.3	31.3 \pm .4	37.4	0	0.001268	0.085035	0
1500	5	0.1	-68.3 \pm -82.2	102	0.01	0.003481	0.001829	0

MEAN AGE(1200°C-1450°C)= 31.8 \pm .3 Ma (2 σ UNCERTAINTY,INCLUDING ERROR IN J)

J = .002383 \pm .000012 (.5 %)

37/39,36/40 AND 39/40 Ar RATIOS ARE CORRECTED FOR MASS SPECTROMETER
DISCRIMINATION,INTERFERING ISOTOPES AND SYSTEM BLANKS

% IIC - INTERFERING ISOTOPES CORRECTION

CU-1115 BIOTITE ARGON SUMMARY

T°C	mV 39	39%	AGE (Ma)±1σ	% ATM	37/39	36/40	39/40	% IIC
550	10.8	0.1	23.3 ± 4.4	48	0.16	0.001646	0.096035	0.23
600	57.2	0.9	33.2 ± 1.8	49.6	0.08	0.001683	0.064466	0.08
650	164.4	2.6	32.2 ± .7	33	0.06	0.001118	0.08837	0.07
700	311.7	5	31.7 ± .4	20.7	0.03	0.000703	0.106363	0.03
750	493.9	7.9	31.9 ± .2	13.9	0	0.000472	0.114707	0
800	537	8.6	31.8 ± .2	9.4	0	0.000319	0.121037	0
850	331.3	5.3	31.6 ± .3	10.4	0	0.000355	0.120677	0
900	206.9	3.3	31.1 ± .4	11.1	0.01	0.000376	0.121654	0.01
950	171.4	2.7	31 ± .5	11.3	0.02	0.000383	0.121684	0.02
1000	221.6	3.5	31.3 ± .4	12	0.02	0.000408	0.119712	0.02
1050	369	5.9	31.4 ± .3	11.8	0.01	0.000399	0.119327	0.01
1100	674.7	10.8	31.9 ± .2	8.6	0.01	0.000292	0.121605	0.01
1150	958.7	15.4	32.3 ± .2	8.3	0.01	0.000282	0.120808	0.01
1250	1297.7	20.9	31.3 ± .3	15	0.02	0.000508	0.115416	0.02
1450	381.5	6.1	31.1 ± .6	50	0.01	0.001695	0.068263	0.01
1500	6.2	0.1	-44.7 ± 76.7	102	0.02	0.003457	0.002064	0.01

MEAN AGE(1100°C-1450°C)= 31.7 ± .4 Ma (2σ UNCERTAINTY, INCLUDING ERROR IN J)

J = .002382 ± .000012 (.5 %)

37/39, 36/40 AND 39/40 Ar RATIOS ARE CORRECTED FOR MASS SPECTROMETER

DISCRIMINATION, INTERFERING ISOTOPES AND SYSTEM BLANKS

% IIC - INTERFERING ISOTOPES CORRECTION

T°C	mV 39	39%	AGE (Ma) $\pm 1\sigma$	% ATM	37/39	36/40	39/40	% IIC
700	34.5	1.7	29.6 \pm 3.2	45.4	0	0.001543	0.078501	0
725	44.1	2.2	30.8 \pm 2.3	31.2	0.01	0.001059	0.095222	0.01
750	45	2.2	30.3 \pm 2.1	25.6	0	0.000869	0.10459	0
775	37.7	1.9	30.4 \pm 2.4	24.6	0	0.000838	0.105628	0
800	31.9	1.6	31.1 \pm 3.1	35.4	0.01	0.001205	0.088629	0.01
825	27.5	1.4	31.2 \pm 3.5	37.8	0	0.001285	0.085173	0
850	22.1	1.1	28.7 \pm 3.9	37.5	0	0.001277	0.092903	0.01
875	22.4	1.1	31.1 \pm 4.3	41.7	0	0.001418	0.079986	0
900	21.8	1.1	30.6 \pm 3.8	33.2	0.01	0.001132	0.093335	0.01
925	25.5	1.2	30.5 \pm 3.3	28.8	0.01	0.00098	0.099869	0.01
950	34.6	1.7	29.6 \pm 2.7	31	0.01	0.001054	0.099282	0.01
975	45.7	2.3	30.2 \pm 2.2	28.8	0	0.000979	0.100625	0.01
1000	74	3.7	30.7 \pm 1.4	23.5	0	0.000799	0.105903	0
1025	160.9	8.1	30.9 \pm .7	19.6	0	0.000665	0.110738	0
1050	150.2	7.6	30.7 \pm .8	19.3	0	0.000655	0.111858	0
1075	110.9	5.6	30.8 \pm 1	24.2	0	0.00082	0.104739	0
1100	114	5.7	31 \pm 1	26.1	0	0.000885	0.101603	0
1150	253.3	12.8	31.3 \pm .5	22.3	0	0.000756	0.105689	0
1200	372.1	18.9	31.6 \pm .4	19.8	0	0.000671	0.107784	0
1250	232.5	11.8	31.7 \pm .6	26.4	0	0.000894	0.098731	0
1350	65.6	3.3	28.9 \pm 2.7	72.4	0	0.002454	0.040561	0
1450	39.2	1.9	23.3 \pm 6.7	92	0	0.003116	0.014511	0.01
1500	0.8	0	-815.8 \pm 3040.8	103	0.34	0.003515	0.000252	0

MEAN AGE(1150°C-1250°C)= 31.5 \pm .6 Ma (2 σ UNCERTAINTY,INCLUDING ERROR IN J)

J = .002382 \pm .000012 (.5 %)

37/39,36/40 AND 39/40 Ar RATIOS ARE CORRECTED FOR MASS SPECTROMETER
DISCRIMINATION,INTERFERING ISOTOPES AND SYSTEM BLANKS

% IIC - INTERFERING ISOTOPES CORRECTION

T°C	(39Ar/40Ar)*100 ± %	(36Ar/40Ar)*1000 ± %
650	6.727579 ± 6.28606	1.742246 ± 6.95483
675	8.419281 ± 5.451768	1.28267 ± 8.488431
700	9.923531 ± 4.753276	0.9457159 ± 10.60712
725	12.20732 ± 4.01975	0.3962496 ± 24.09885
750	13.01835 ± 3.715512	0.1486795 ± 63.39255
775	13.04145 ± 4.113228	0.1886688 ± 55.14728
800	12.60926 ± 3.639646	0.2606236 ± 34.46273
850	13.15615 ± 2.439483	0.1416271 ± 43.24482
900	12.84603 ± 2.087433	0.2139815 ± 23.8225
950	13.15161 ± 1.979026	0.1290985 ± 38.20044
1050	12.74237 ± 1.486221	0.2284974 ± 15.30239

ITERATIONS = 2

XBAR = 12.31495

YBAR = .3411868

SUM S = .1427531

SLOPE = -.2485765 ± 2.58455E-03 INCLUDING SUMS

X = 13.68751 ± 1.442146E-02
(Y=0)

Y = 3.402393 ± 3.208453E-02 (40Ar/36Ar INITIAL= 2.939108E-04 ± 3.208453E-02)
(X=0)

J = .002382 ± 2.382E-05 %

ISOCHRON AGE = 31.12 ± .34 Ma (2σ UNCERTAINTY INCLUDING ERROR IN J)

T°C	(39Ar/40Ar)*100 ± %	(36Ar/40Ar)*1000 ± %
750	13.11808 ± .7165542	3.574727E-02 ± 41.03806
775	13.17774 ± .8095611	3.489341E-02 ± 53.28365
800	13.1911 ± .9326825	6.493923E-02 ± 34.30751
825	13.20296 ± 1.137022	4.673361E-02 ± 62.50512
850	13.10644 ± 1.411826	8.482273E-02 ± 44.75647
900	12.736 ± 1.201685	0.1905059 ± 15.76043
950	12.70288 ± 1.298243	0.181445 ± 18.42283
1000	12.23253 ± 1.833541	0.286932 ± 16.50563

ITERATIONS = 3

XBAR = 13.04439

YBAR = 8.009592E-02

SUM S = 1.453082

SLOPE = -.298094 ± 3.454361E-02 INCLUDING SUMS

X = 13.31309 ± 3.521729E-02
(Y=0)

Y = 3.968552 ± .4506747 (40Ar/36Ar INITIAL= 2.519811E-04 ± .4506747)
(X=0)

J = .002312 ± 2.312E-05 %

ISOCHRON AGE = 31.05 ± .39 Ma (2σ UNCERTAINTY INCLUDING ERROR IN J)

T°C	(39Ar/40Ar)*100 ± %	(36Ar/40Ar)*1000 ± %
550	6.10436 ± 1.345521	1.804415 ± 2.181848
600	8.512614 ± .9244576	1.223137 ± 2.130883
650	10.65263 ± .7296968	0.6149234 ± 2.569394
675	11.99182 ± .8270795	0.2847038 ± 6.106147
700	12.57698 ± .7884355	0.1655738 ± 9.788392
725	12.83905 ± .7421295	0.09937713 ± 15.03424
750	12.9102 ± .6568976	0.1377588 ± 8.28139
775	10.48983 ± .6518371	0.7201963 ± 2.112489
800	13.0947 ± .8015861	0.05756828 ± 27.97806
825	12.7502 ± .8048855	0.1159544 ± 13.96492
900	13.20474 ± 1.914941	0.04287561 ± 119.3498
950	13.27955 ± 2.418155	0.05755871 ± 112.7036
1000	12.64263 ± 2.418519	0.1699351 ± 37.58241
1100	10.98771 ± 1.374421	0.5817062 ± 5.378174

ITERATIONS = 2

XBAR = 11.52894

YBAR = .4401313

SUM S = 10.72461

SLOPE = -.2516211 ± 4.817774E-03 INCLUDING SUMS

X = 13.27812 ± 3.414536E-02
(Y=0)

Y = 3.341056 ± 5.616397E-02 (40Ar/36Ar INITIAL= 2.993066E-04 ± 5.616396E-02
(X=0)

J = .002312 ± 2.312E-05 %

ISOCHRON AGE = 31.13 ± .39 Ma (2σ UNCERTAINTY INCLUDING ERROR IN J)

T°C	(³⁹ Ar/ ⁴⁰ Ar)*100 ± %	(³⁶ Ar/ ⁴⁰ Ar)*1000 ± %
725	12.49245 ± .6846207	0.1790467 ± 6.981828
750	12.98045 ± 1.085666	0.1072628 ± 23.67342
775	12.92042 ± 1.092247	0.120362 ± 22.09118
800	12.8794 ± 1.133602	0.1482373 ± 18.43149
825	12.93058 ± 1.275377	0.1538366 ± 20.45084
850	12.81672 ± 1.426316	0.215644 ± 16.50867
900	12.31664 ± 1.112446	0.4091512 ± 6.324344
950	11.93285 ± 1.322184	0.4627229 ± 6.772463
1000	10.39229 ± 1.80909	0.959052 ± 4.355785
1100	8.835993 ± 1.003099	1.14084 ± 2.346908
1200	8.611379 ± .7610011	1.16219 ± 1.974851

ITERATIONS = 3

XBAR = 11.3946

YBAR = 0.5137189

SUM S = 30.9536

SLOPE = -.2472161 ± .0121612 INCLUDING SUMS

X = 13.47261 ± .1075125
(Y=0)

Y = 3.330647 ± .1402878 (40Ar/36Ar INITIAL= 3.00242E-04 ± .1402878)
(X=0)

J = .002312 ± 2.312E-05 %

ISOCRON AGE = 30.69 ± .54 Ma (2σ UNCERTAINTY INCLUDING ERROR IN J)

T°C	(39Ar/40Ar)*100 ± %	(36Ar/40Ar)*1000 ± %
650	11.7101 ± .5660803	0.2410249 ± 3.268341
675	12.26291 ± .604574	0.1067814 ± 8.668516
700	12.51079 ± .6340265	0.05079545 ± 21.16461
725	12.58133 ± .6414945	0.07725783 ± 14.22099
750	12.75658 ± .6797671	0.0674713 ± 18.62954
775	12.91829 ± .8937424	0.0738253 ± 28.19697
800	13.01335 ± 1.288824	0.08869695 ± 37.57363
825	12.9693 ± 2.177126	0.1848201 ± 31.51384

ITERATIONS = 3

XBAR = 12.34101

YBAR = .1204759

SUM S = 22.10867

SLOPE = -.1771409 ± 3.287888E-02 INCLUDING SUMS

X = 13.02113 ± .1550055
(Y=0)

Y = 2.306574 ± .405991 (40Ar/36Ar INITIAL= 4.335436E-04 ± .405991)
(X=0)

J = .002312 ± 2.312E-05 %

ISOCHRON AGE = 31.74 ± .68 Ma (2σ UNCERTAINTY INCLUDING ERROR IN J)

References

- Alvarez, O., Miranda, J., and Guzman, P., 1980, Geología del complejo Chuquicamata, in *Minera des cobres porfídicos*: Instituto de Ingenieros de Minas de Chile, Santiago, v.2, p. 314-363.
- Ambrus, J., 1977, Geology of the El Abra porphyry copper deposit, Chile, *Economic Geology*, v. 72, p. 1062-1085.
- Ambrus, J., 1979, Emplazamiento y mineralización de porfidos cupríferos de Chile, Unpublished Ph.D., Universidad de Salamanca, 313p.
- American Geological Institute, 1984. *Dictionary of Geologic Terms*, 3rd edition.
- Applegate, B., 1966, Compilation map of the distribution of the lithologic units of the Chuquicamata deposit, Archives of the Superintendencia de Geología, CODELCO-Chuquicamata, Chuquicamata, Chile.
- Arnott, A.M., Zentilli, M., Graves, M.C., and Reynold, P., 1996, Constraints on the emplacement of the Fortuna Granodiorite, Chuquicamata, Chile, Abstract, Atlantic Geoscience Society Meeting, February 2-4, 1996, Bathurst, N.B.
- Avalos, C., 1899, Mineral de Chuquicamata, Department of Geology Chile Exploration Co., Informe Interno, CGN-1, 12p.
- Bandy, M.C., 1938, Mineralogy of three sulphate deposits of northern Chile, *American Mineralogist*, v. 23, p. 669-760.
- Bai, T.B., and van Groos, A.F.K., 1999, The distribution of Na, K, Rb, Sr, Al, Ge, Cu, W, Mo, La, and Ce between granitic melts and coexisting aqueous fluids, *Geochimica et Cosmochimica Acta*, v. 63, p. 1117-1131.
- Ballard, J.R., 2001, A comparative study between the geochemistry of ore-bearing and barren calc-alkaline intrusions, Unpublished Ph.D. thesis, Australian National University, 255p.
- Ballard, J.R., Palin, J.M., Williams, I.S., Campbell, I.H., and Faunes, A., 2001, Two ages of porphyry intrusion resolved for the super-giant Chuquicamata copper deposit of northern Chile by ELA-ICP-MS and SHRIMP, *Geology*, v. 29, p. 383-386.
- Barnes H.L., 1979, Solubility of ore minerals, in *Geochemistry of Hydrothermal Ore Deposits*, Barnes, H.L., ed., New York: Wiley-Interscience Publications, p. 404-460.

- Beane, R.E., 1974, Biotite Stability in the porphyry copper environment, *Economic Geology*, v. 69, p. 241-256.
- Beane, R.E., 1982, Hydrothermal alteration in silicate rocks, southwestern North America, *in* *Advances in Geology of the Porphyry Copper Deposit, Southwestern North America*, Titley, S., ed., University of Arizona Press, Tuscon, Arizona, p. 117-137.
- Bird, D.K., and Helgeson, H.C., 1981, Chemical interaction of aqueous solutions with epidote-feldspar mineral assemblages in geologic systems, II, Equilibrium constraints in metamorphic/geothermal processes, *American Journal of Science*, v. 281, p. 576-614.
- Blount, C.W., and Dickson, F.W., 1969, The solubility of anhydrite (CaSO_4) in $\text{NaCl-H}_2\text{O}$ from 100 to 450°C and 1 to 1000 bars, *Geochimica et Cosmochimica Acta*, v. 33, p. 227-245.
- Blount, C.W., and Dickson, F.W., 1973, Gypsum-anhydrite equilibria in systems $\text{CaSO}_4\text{-H}_2\text{O}$ and $\text{CaCO}_4\text{-NaCl-H}_2\text{O}$, *American Mineralogist*, v. 58, p. 323-331.
- Bodnar, R.J., Burnham, C.W., and Sterner, S.M., 1985, Synthetic fluid inclusions in natural quartz, III, Determination of phase equilibrium properties in the system $\text{H}_2\text{O-NaCl}$ to 1000°C and 1500 bars, *Geochimica et Cosmochimica Acta*, v. 49, p. 1861-1873.
- Boles, J.R., 1982, Active albitization of plagioclase, Gulf Coast Tertiary, *American Journal of Science*, v. 282, p. 165-180.
- Bottinga Y., and Javoy, M., 1973, Comments on oxygen isotopic geothermometry, *Earth and Planetary Science Letters*, v. 20, p. 250-265.
- Bottinga, Y., and Javoy, M., 1975, Oxygen isotope partitioning among the minerals in igneous and metamorphic rocks, *Review of Geophysics and Space Physics*, v. 13, p. 401-418.
- Bowen, N.L., and Tuttle, O.F., 1950, The system $\text{NaAlSi}_3\text{O}_8\text{-KAlSi}_3\text{O}_8\text{-H}_2\text{O}$, *Geological Society of American Bulletin*, v. 58, p. 498-511 *from* *Petrography to petrogenesis*, Hibbard, M.J., ed., 1995, New Jersey: Prentice Hall, 587p.
- Brimhall, G.H., Agee, C., and Stoffregen, R., 1985, The hydrothermal conversion of hornblende to biotite, *Canadian Mineralogist*, v. 23, p. 369-379.
- Brown, W.L., and Parsons, I., 1984, Exsolution and coarsening mechanisms and kinetics in ordered cryptoperthite series, *Contributions to Mineralogy and Petrology*, v. 86, p. 3-18.

- Brown, W.L., and Parsons, I., 1984, The nature of potassium feldspar exsolution microtextures and the development of dislocations as a function of composition in perthitic alkali feldspars, *Contributions to Mineralogy and Petrology*, v. 86, p. 335-341.
- Burnham, C.W., 1967, Hydrothermal fluids at the magmatic stage, *in* *Geochemistry of Hydrothermal Ore Deposits*, Barnes, H.L., ed., Holt, Rinehart and Winston, Inc., New York, p. 34-76.
- Burnham, C.W., 1979, Magmas and hydrothermal fluids, *in* *Geochemistry of hydrothermal ore deposits*, Barnes, H.L., ed., Hole, Rinehart and Winston, Inc. New York, p. 71-136.
- Burnham, C.W., 1997, Magmas and hydrothermal fluids, *in* *Geochemistry of Hydrothermal Ore Deposits*, Barnes, H.L., ed., John Wiley and Sons, Inc., New York, p. 63-123.
- Burnham, C.W., and Ohmoto, H., 1980, Late stage processes of felsic magmatism, *in* *Granitic Magmatism and Related Mineralization*, *Mining Geology Special Issue*, No. 8, p. 1-11.
- Butler, B.S., 1919, Primary (hypogene) sulphate minerals in ore deposits, *Economic Geology*, v. 14, p. 581-609.
- Callegari, E., and De Pieri, R., 1967, Crystallographic observations on some chess-board albites. *Schweiz Min. Petr. Mitt.*, v. 47, p. 99-110, *from* *Framework silicates: feldspars*, 2nd ed.; *Rock-forming Minerals*, Deer, W.A., Howie, R.A. and Zussman, J., eds., 2001, Geological Society of London, 972p.
- Candela, P.A., 1990, Theoretical constraints on the chemistry of the magmatic aqueous phase, *in* Stein, H.J., and Hannah, J.L., eds., *Ore-bearing granite systems; Petrogenesis and Mineralizing processes: Geological Society of America Special Paper 246*, p. 11-20.
- Candela, P.A., and Holland, H.D., 1984, The partitioning of copper and molybdenum between silicate melts and aqueous fluids, *Geochimica et Cosmochimica Acta*, v. 48, p. 373-380.
- Chappell, B.W., and White, A.J.R., 1974, Two contrasting granite types, *Pacific Geology*, v. 8, p. 173-174.
- Chou, I.M., and Frantz, J.D. 1977, Recalibration of Ag and AgCl acid buffer at elevated pressures and temperatures, *American Journal of Science*, v. 277, p. 1067-1072.

Clark, A.H. 1993. Are outsize porphyry copper deposits either anatomically or environmentally distinctive? in *Giant Ore Deposits*, Whiting, B.H., Hodgson, C.J., and Mason, R., eds., Society of Economic Geologists, Special Publication 2, p. 213-283.

Cline, J.S., and Bodnar, R.J., 1991, Can economic porphyry copper mineralization be generated by a typical calc-alkaline melt? *Journal of Geophysical Research*, v. 96, p. 8113-8126.

Cloos, M., 2001, Bubbling magma chambers, cupolas, and porphyry copper deposits, *International Geology Review*, v. 43, p. 285-311.

Collao, S., 1987, Inclusiones fluidas en el porfido cuprifero de Chuquicamata, Confidential Unpublished Report for Codelco Chuquicamata, 24p.

Craig, H., 1963, The isotopic geochemistry of water and carbon in geothermal areas, in *Nuclear Geology on Geothermal Areas*, Tongiorgio, E., ed., Consiglio Nazionale della Ricerca Laboratorio de Geologica Nucleare, Spoleto, Pisa, p. 17-53 *from* Ohmoto, H., 1986, Stable isotope geochemistry of ore deposits, in *Stable isotopes in high temperature geological processes*; Review in *Mineralogy*, Valley, J.W., Taylor, H.P., and O'Neil, J.R., eds. v. 16, p. 491-559.

Deer, W.A., Howie, R.A., and Zussman, J., 1966, An introduction to the rock-forming minerals, Longman Group Ltd. Essex.

Deer, W.A., Howie, R.A., and Zussman, J., 1992, An introduction to the rock-forming minerals, 2nd edition. Longman Group Ltd. Essex, 696p.

Deer, W.A., Howie, R.A., and Zussman, J. 2001, Framework silicates: feldspars, 2nd ed.; *Rock-forming Minerals*, Geologic Society of London, 972p.

Dilles, J.H., Farmer, G.L., and Field, C.W., 1995, Sodium-calcium alteration by non-magmatic saline fluids in porphyry copper deposits: Results from Yerington, Nevada, Mineralogical Association of Canada, Short Course Series, Volume 23: Magmas, fluids, and ore deposits, Thompson, J.F.H., ed., Victoria, BC.

Dilles, J., Tomlinson, A.J., Martin, M.W., and Blanco, N., 1997, El Abra and Fortuna Complexes: A porphyry copper batholith sinistrally displaced by the Falla Oeste [ext. abs.]: Congreso Geológico Chileno, 8th, Antofagasta, 1997, Actas, v. 3, p. 1883-1887.

- Dingwell, D.B., 1985, The structure and properties of fluorine-rich magmas: a review of experimental studies, in *Recent Advances in the Geology of Granite-Related Mineral Deposits*, Taylor, R.P., and Strong, D.F., eds., Canadian Institute of Mining and Metallurgy, p. 1-12.
- Eslinger, E.V., Savin, S.M., and Yeh, H., 1979, Oxygen isotope geothermometry of diagenetically altered shales, *SEPM Special Publication No. 26*, p. 113-124.
- Faure, G., 1977, *Principles of isotope geology*, John Wiley and Sons, New York, 464p.
- Fleck, R.D., Sutter, J.F., and Elliot, D., 1977, Interpretation of the discordant $^{40}\text{Ar}/^{39}\text{Ar}$ age-spectra of Mesozoic tholeiites from Antarctica, *Geochimica et Cosmochimica Acta*, v. 41, p. 15-32.
- Fournier, R.O., 1983, A method of calculating quartz solubilities in aqueous sodium chloride solution, *Geochimica et Cosmochimica Acta*, v. 47, p. 579-586.
- Fournier, R.O., 1983, Active hydrothermal systems as analogues of fossil systems, in *The Role of Heat in the Development of Energy and Mineral Resources in the Northern Basin and Range Province*, Geothermal Resources Council, v. 13, p. 263-284.
- Garrido, I., Cembrano, J., Siña, A., Stedman, P. and Yáñez, G., 2002, High magma oxidation state and bulk crustal shortening: key factors in the genesis of Andean porphyry copper deposits, central Chile (31-34°S), *Revista Geologica de Chile*, v. 29, p. 43-54.
- Giggenbach, W.F., 1997, The origin and evolution of fluids in magmatic-hydrothermal systems, in *Geochemistry of Hydrothermal Ore Deposits*, Barnes, H.L., ed., New York: Wiley-Interscience Publications, p. 737-796.
- Graves, M.C., Zentilli, M., and Lewis, M., 1997, Sulphur isotope study: Sulphide-sulphate veins associated with quartz-sericite alteration Chuquicamata porphyry copper deposit, Chile, Internal report, CODELCO, Division Chuquicamata, 16p.
- Graves, M.C., and Zentilli, M., 1995, Characterization of Zn in sulphide minerals: geological report and results of electron microprobe analyses of thirteen samples from Chuquicamata, Cuesta Research Ltd. Confidential Report for Codelco, 57p.
- Guilbert, J.M., 1963, Petrographic descriptions of selected rock specimens from Chuquicamata, Chile, Internal report, 45p.
- Guilbert, J.M., and Park, C.F., Jr., 1986, *The Geology of Ore Deposits*. W.H. Freeman and Company, New York, 985p.

- Gunow, A.J., Ludington, S., and Munoz, J.L., 1980, Fluorine in micas from the Henderson Molybdenite Deposit, Colorado, *Economic Geology*, v. 75, p. 1127-1137.
- Gustafson, L.B., and Hunt, J.P., 1975, The porphyry copper deposit at El Salvador, Chile, *Economic Geology*, v. 70, p. 875-912.
- Hammarstrom, J.M., and Zen, E., 1986, Aluminum in hornblende: An empirical igneous geobarometer, *American Mineralogist*, v. 71, p. 1297-1313.
- Hanor, J.S., 1979, The sedimentary genesis of hydrothermal fluids, *in* *Geochemistry of Hydrothermal Ore Deposits*, Barnes, H.L., ed., New York: Wiley-Interscience Publications, p. 137-172.
- Haselton, Jr. H.T., Hovis, G.L., Hemingway, B.S., and Robie, R.A., 1983, Calorimetric investigation of the excess entropy of mixing in analbite-sanidine solid solutions: lack of evidence for Na, K short range order and implication for two-feldspar thermometry, *American Mineralogist*, v. 68, p. 398-413.
- Hedenquist, J.W., and Lowenstern, J.B., 1994, The role of magmas in the formation of hydrothermal ore deposits, *Nature*, v. 370, p. 519-527.
- Hedenquist, J.W., and Richards, J.P., 1998, The influence of geochemical techniques on the development of genetic models for porphyry copper deposits *in* *Reviews in Economic Geology*, v. 10: Techniques in hydrothermal ore deposits geology, Richards, J.P. and Larson, P.B., eds., p. 235-256.
- Helgeson, H.C., 1964, *Complexing and hydrothermal ore deposition*, MacMillan, New York, 128 p.
- Hemley, J.J., Cygan, G.L., Fein, J.B., Robinson, G.R., and d'Angelo, W.M., 1992, Hydrothermal ore-forming processes in the light of studies in rock-buffered systems: I. Iron-copper-zinc-lead sulphide solubility relations, *Economic Geology*, v. 87, p. 1-22.
- Hibbard, M.J. 1995, *Petrography to petrogenesis*, New Jersey: Prentice Hall 587p.
- Higgins, M.D., 1999, Origin of megacrysts in granitoids by textural coarsening: a crystal size distribution (CSD) study of microcline in the Cathedral Peak Granodiorite, Sierra Nevada, California, *in* *Understanding granites: integrating new and classical techniques*, Castro, A., Fernandez C., and Vigneresse, J.L., eds., Geological Society Special Publication, No. 168.
- Hoefs, J., 1987, *Stable Isotope Geochemistry*, 3rd edition, Springer-Verlag, Berlin-Heidelberg, 241p.

Hollister, L.S., Grissom, G.C., Peters, E.K., Stowell, H.H., and Sisson, V.B., 1987, Confirmation of the empirical correlation of Al in hornblende with pressure of solidification of calc-alkaline plutons, *American Mineralogist*, v.72, p.231-239.

Hunt, J., 1963, Rock types at Chuquicamata. Memorandum to Mr. W.H Swayne. 23p.

Ishihara, S., 1977, The magnetite-series and ilmenite-series granitic rocks, *Mining Geology*, v. 27, p. 293-305.

Jacobs, D.C., and Parry, W.T., 1979, Geochemistry of biotite in the Santa Rita Porphyry copper deposit, New Mexico, *Economic Geology*, v. 74, p. 860-887.

Jacobs, D.C., and Parry, W.T., 1976, A comparison of the geochemistry of biotite from some basin and range stocks, *Economic Geology*, v.71, p.1029-1035.

Jensen, M.L., and Bateman, A.M., 1979, *Economic mineral deposits*, John Wiley and Sons, Inc. New York, 593 p.

Kay, S.M., and Mpodozis, C., 2001, Central Andean ore deposits linked to evolving shallow subduction systems and thickening crust, *GSA Today*, v. 11, p. 4-9.

Keppler, H., and Wyllie, P.J., 1991, Partitioning of Cu, Sn, Mo, W, U, and Th between melt and aqueous fluid in the systems haplogranite-H₂O-HCl and haplogranite-H₂O-HF, *Contributions to Mineralogy and Petrology*, v. 109, p. 139-150

Kirkham, R.V., 1972, Geology of copper and molybdenum deposits, Geological Survey of Canada, Paper 72-1A, p. 82-87.

Kusakabe, M., Hori, M., and Matsuhisa, Y., 1986, Primary mineralization-alteration of the El Teniente and Rio Blanco porphyry copper deposits, Chile, Technical Report of ISEI, serial A, no.5, 40p.

Langerfeldt, H., 1964, Preliminary survey of rock problems at Chuquicamata. Internal Report, 48p.

Leake, B.E., 1978, Nomenclature of amphiboles, *Mineralogical Magazine*, 42, p. 553-563.

Lehmann, B., Dietrich, Wallianos, A., 2000, From rocks to ore, *International Journal of Earth Sciences*, v. 89, p. 284-294.

- Lewis, M., 1996, Characterisation of hypogene covellite assemblages at the Chuquicamata porphyry copper deposit, Chile, section 4500N, Unpublished MSc. Thesis, Dalhousie University, Halifax, Canada, 223p.
- Lindgren, W., 1910, Anhydrite as a gangue mineral, *Economic Geology*, v. 5, p. 522-527.
- Lindgren, W., 1917, Report on the Chuquicamata lode, Internal Report, 55p.
- Lindsay, D.D., Zentilli, M., and Rojas de la Rivera, J., 1995, Evolution of an active ductile to brittle shear system controlling mineralization at the Chuquicamata porphyry copper deposit, northern Chile, *International Geology Review*, v. 37, p. 945-958.
- Lindsay, D.D., Godfrey-Smith, D., and Zentilli, M., 1996, Age determinations of the West Fissure, Chuquicamata, Chile: Integration of FT, TL, ESR with conventional K/Ar and $^{40}\text{Ar}/^{39}\text{Ar}$ dating techniques, Abstract, IGCP 342, Brazil, Age and Isotopes of South American Ore Deposits.
- Lindsay, D.D., 1998, Structural control and anisotropy of mineralization within the Chuquicamata porphyry copper deposit, northern Chile: Unpublished Ph.D. Thesis, Dalhousie University, Halifax, NS, 381p.
- Long, P.E., and Luth, W.C., 1986, Origin of K-feldspar megacrysts in granitic rocks: Implications of a partitioning model for barium, *American Mineralogist*, v. 71, p. 367-375.
- Lopez, V.M., 1939, The primary mineralization at Chuquicamata, Chile, S.A., *Economic Geology*, v. 34, p. 674-711.
- Lowell, J.D., and Guilbert, J.M., 1970, Lateral and vertical alteration-mineralization zoning in porphyry ore deposits, *Economic Geology*, v. 65, p. 373-408.
- Lowenstern, J.B., Mahood, G.A., Rivers, M.L., and Sutton, S.R., 1991, Evidence for extreme partitioning of copper into a magmatic vapor phase, *Nature*, v. 252, p. 1405-1409.
- Luhr, J.F., Carmichael, I.S.E., and Varekamp, J.C., 1984, The eruptions of El Chichón Volcano, Chiapas, Mexico: mineralogy and petrology of the anhydrite-bearing pumices, *Journal of Volcanology and Geothermal Research*, v. 23, p. 69-108.
- Maksaev, V., 1990, Metallogeny, geological evolution, and thermochronology of the Chilean Andes between latitudes 21° and 26° south, and the origin of major porphyry copper deposits, Unpublished Ph.D. Thesis, Dalhousie University, 554p.

Maksaev, V., and Zentilli, M., 1999, Fission track thermochronology of the Domeyko Cordillera, northern Chile: Implications for Andean tectonics and porphyry copper metallogenesis, *Exploration Mining Geology*, v. 8, p. 65-89.

Manning, D.A.C., 1982, An experimental study of the effects of fluorine on the crystallization of granitic melts, in *Metallization Associated with Acid Magmatism*, Evans, A.M., ed., John Wiley and Sons, Ltd., p. 191-203.

Mason, B., and Moore, C.B., 1982, *Principles of geochemistry*, 4th edition, John Wiley and Sons, Inc. New York, 344p.

Mason, R., 1992, Models of order and iron-fluorine avoidance in biotite, *Canadian Mineralogist*, v. 30, p. 343-354.

Mathur, R., Ruiz, J., and Munizaga, F., 2000, Relationship between copper tonnage of Chilean base-metal porphyry deposits and Os isotope ratios, *Geology*, v. 28, p. 555-558.

Mathur, R., Ruiz, J., Munizaga, F., and Zentilli, M. 2001, Reply: Relationship between copper tonnage of Chilean base-metal porphyry deposits and Os isotope ratios, *Geology*, v. 29, p. 468.

Matsuhisa, Y., Goldsmith, J.R. and Clayton, R.N., 1979, Oxygen isotope fractionation in the system quartz-albite-anorthite-water, *Geochimica et Cosmochimica Acta*, v. 43, p. 1131-1140.

Matthews, S., Sparks, S. and Gardeweg, M., 1995, The relationships between magma mixing and volatile behaviour at Lascar Volcano (23°22'S-67°44'W), northern Chile: significance for the formation of copper sulphide and magnetite-apatite orebodies, *Giant Ore Deposits II*. Queens University, Kingston, Canada, p. 146-181.

Mayne-Nicholls, A., Reyes, S., M., and Vicencio, G., S., 1995, *Chuquicamata Modelamiento Geologico*, Internal Report, CODELCO, Chuquicamata Division.

McBride, J.S., McInnes, B.I.A., and Keays, R.R., 2001, Comment: Relationship between copper tonnage of Chilean base-metal porphyry deposits and Os isotope ratios, *Geology*, v. 29, p. 467-468.

McGuire, A.V., Dyar, M.D., and Ward, K.A., 1989, Neglected Fe³⁺/Fe²⁺ ratios- a study of megacrysts from alkali basalts, *Geology*, v. 17, p. 687-690.

- McInnes, B.I.A., Farley, K.A., Sillitoe, R.H., and Kohn, B.P., 1999, Application of apatite (U-Th)/He thermochronometry to the determination of the sense and amount of vertical fault displacement at the Chuquicamata porphyry copper deposit, Chile, *Economic Geology*, v. 94, p. 937-948.
- McInnes, B.I.A., Farley, K.A., Sillitoe, R.H., and Kohn, B.P., 2001, Application of apatite (U-Th)/He thermochronometry to the determination of the sense and amount of vertical fault displacement at the Chuquicamata porphyry copper deposit, Chile-A reply, *Economic Geology*, v. 96, p. 1310.
- McMillan, W.J., and Panteleyev, A., 1988, Porphyry copper deposits. *In Ore Deposit Models*, R.G. Roberts and P.A. Sheahan (eds). Geoscience Canada reprint series 3. p. 45-58.
- Meyer, C., and Hemley, J.J., 1967, Chapter 6: Wall rock alteration in *Geochemistry of hydrothermal ore deposits*, Barnes, H.L., ed., Hole, Rinehart and Winston, Inc. New York, Chicago, San Francisco, Atlanta, Dallas, Montreal, Toronto, London.
- Miller, C.F., Stoddard, E.F., Bradfish, L.J. and Dollase, W.A., 1981, Composition of plutonic muscovite: genetic implications, *Canadian Mineralogist*, v. 19, p. 25-34.
- Moody, J.B., Jenkins, J.J., and Meyer, D., 1982, An experimental investigation of the albitization of plagioclase, *Canadian Mineralogist*, v. 23, p. 583-596.
- Moore, W.J. and Czamanske, G.K., 1973, Compositions of biotites from unaltered and altered monzonitic rocks in the Bingham Mining district, Utah, *Economic Geology*, v. 68, p. 269-280.
- Morse, S.A., 1969, Syenites *in Carnegie Institute Washington Yearbook*, 1967-8, p. 112-120, *from Petrography to petrogenesis*, Hibbard, M.J., ed., 1995, New Jersey: Prentice Hall, 587p.
- Munoz, J.L., 1984, F-OH and Cl-OH exchange in micas with application to hydrothermal ore deposits, *in Mineralogical Society of America, Reviews in Mineralogy*, v.13, ed. S.W. Bailey, p.469-494.
- Munoz, J.L. and Ludington, S.D., 1974, Fluorine-hydroxyl exchange in biotite, *American Journal of Science*, v. 274, p. 396-413.
- Naumov, G.B., Ryzhenko, B.N., and Khodakovsky, I.L., 1971, *Handbook of thermodynamic data*, Translation by G.J. Soleimani (1974), National Technological Information Service, PB-226-772.

- Nedachi, M., 1980, Chlorine and fluorine contents of rock-forming minerals of Neogene granitic rocks in Kyushu, Japan, *Mining Geology Special Issue*, No. 8, p. 39-48.
- Norton, D., 1982, Fluid and heat transport phenomena typical of copper-bearing pluton environment: Southeastern Arizona, *in* *Advances in the Geology of Porphyry Copper Deposits, Southwestern North America*, Titley, S.R., ed., University of Arizona Press, Tucson, p. 59-72.
- Ohmoto, H., 1986, Stable isotope geochemistry of ore deposits, *in* *Stable isotopes in high temperature geological processes; Review in Mineralogy*, Valley, J.W., Taylor, H.P., and O'Neil, J.R., eds. v. 16, p. 491-559.
- Ohmoto, H., and Oskvarek, J.D., 1985, An experimental study of oxygen isotope exchange reactions in the system muscovite-Co₂-H₂O-KCl-NaCl at T = 400°C and P = 5 kbar (abstract), *in* *Program with abstracts, 2nd International Symposium on Hydrothermal Reactions*, Pennsylvania State University, p. 47, from Ohmoto, H., 1986, Stable isotope geochemistry of ore deposits, *in* *Stable isotopes in high temperature geological processes; Review in Mineralogy*, Valley, J.W., Taylor, H.P., and O'Neil, J.R., eds. v. 16, p. 491-559.
- O'Neil, J.R., 1986, Theoretical and experimental aspects of isotopic fractionation, *in*: *Stable isotopes in high temperature geological processes, Review in Mineralogy*, Valley, J.W., Taylor, H.P., and O'Neil, J.R., eds., v. 16, p. 1-40.
- O'Neil, J.R., and Taylor, H.P., 1967, The oxygen isotope and cation exchange chemistry of feldspars, *American Mineralogist*, v. 52, p. 1414-1437.
- O'Neil, J.R., and Taylor, H.P., 1969, Oxygen isotope equilibrium between muscovite and water, *Journal of Geophysical Research*, v. 74, p. 6012-6022.
- Ossandon, C., G., and Zentilli, M., 1997, El distrito de Chuquicamata; una concentración de cobre de clase mundial, *Congreso Geológico Chileno, VIII, Antofagasta*, v. III, p. 1888-1892.
- Ossandón, G., Fréaut, R., Gustafson, L.B., Lindsay, D.D., and Zentilli, M., 2001, Geology of the Chuquicamata Mine: A Progress Report, *Economic Geology*, v. 96, p. 249-270.
- Oyarzun, R., Marquez, A., Lillo, J., Lopez, I. and Rivera, S. 2001, Giant versus small porphyry copper deposits of Cenozoic age in northern Chile: adakitic versus normal calc-alkaline magmatism, *Mineralium Deposita*, v. 36, p. 794-798.

- Parada, M.A., Aracena, I., and Tanaka, H., 1987, The petrology of Chuquicamata plutonic complex, Chile, *Journal Japanese Association of Mineralogy and Petrology*, v. 82, p. 177-188.
- Parry, W.T., 1972, Chlorine in biotite from Basin and Range plutons, *Economic Geology*, v. 67, p. 972-975.
- Parry, W.T., Ballantyne, G.H., and Wilson, J.C., 1978, Chemistry of biotite and apatite from a vesicular quartz latite porphyry plug at Bingham, Utah, *Economic Geology*, v. 73, p.1308-1314.
- Parsons, I., and Brown, W.L., 1984, Feldspars and the thermal history of igneous rocks, *in* Feldspars and Feldspathoids, Brown, W.L., ed., D.Reidel Publishing Company, p. 317-371.
- Pearce, J.A., and Cann, J.R., 1973, Tectonic setting of basic and volcanic rocks determined using trace element analysis, *Earth and Planetary Science Letters*, v. 19, p. 290-300.
- Pearce, J.A., Harris, N.B.W., and Tindle, A.G., 1984, Trace element discrimination diagrams for the tectonic interpretation of granitic rocks, *Journal of Petrology*, v. 25, p. 956-983.
- Phillips, W.J., 1985, Hydraulic fracturing effects in the formation of mineral deposits, *Trans. Institution Mining and Metallurgy*, v. 95, p.
- Porter, T.M., 1998, An overview of the world's porphyry and other hydrothermal copper and gold deposits and their distribution. *in* Porphyry and hydrothermal copper and gold deposits- a global perspective, Conference proceedings, AMF, Adelaide, 232p.
- Preece, III, R.K., and Beane, R.E., 1982, Contrasting evolutions of hydrothermal alteration in quartz monzonite and quartz diorite wall rocks at the Sierrita porphyry copper deposit, Arizona, *Economic Geology*, v.77, p.1621-1641.
- Pryer, L.L. and Robin, P-Y.F., 1995, Retrograde metamorphic reactions in deforming granites and the origin of flame perthite, *Journal of Metamorphic Geology*, v.13, p. 645-658.
- Pryer, L.L., and Robin, P-Y.F., 1996, Differential stress control on the growth and orientation of flame perthite: a palaeostress-direction indicator, *Journal of Structural Geology*, v. 18, p. 1151-1166.

Quirt, G.S., 1972, A potassium-argon geochronological investigation of the Andean mobile belt of north central Chile, Unpublished Ph.D. Thesis, Kingston, Canada, Queens University, 240p.

Ramberg, H., 1952, Chemical bonds and the distribution of cations in silicates, *Journal of Geology*, v. 60, p.331-355 *from* Mason, R., 1992, Models of order and iron-fluorine avoidance in biotite, *Canadian Mineralogist*, v. 30, p. 343-354.

Ramseyer, K., Boles, J.R., and Lichtner, P.C., 1992, Mechanism of plagioclase albitization, *Journal of Sedimentary Petrology*, v. 62, p. 349-356.

Reed, M.H., 1997, Chapter 7: Hydrothermal alteration and its relationship to ore fluid composition. In: *Geochemistry of hydrothermal ore deposits*, Barnes, H.L., ed., New York: Wiley-Interscience Publications, p. 303-366.

Renzetti, B.L., 1957, Geology and petrogenesis at Chuquicamata, Chile: Ph.D. thesis, Indiana University, 71p.

Reynolds, P., Ravenhurst, C., Zentilli, M., and Lindsay, D., 1998, High-precision $^{40}\text{Ar}/^{39}\text{Ar}$ dating of two consecutive hydrothermal events in the Chuquicamata porphyry copper system, Chile. *Chemical Geology*, v. 148, p. 45-60.

Rimstidt, J.D., 1997, Chapter 10: Gangue mineral transport and deposition. In: *Geochemistry of hydrothermal ore deposits*, Barnes, H.L., ed., New York: Wiley-Interscience Publications, p. 487-516.

Roedder, E., 1979, Fluid inclusions as samples of ore fluids, in *Geochemistry of Hydrothermal Ore Deposits*, Barnes, H.L., ed., New York: Wiley-Interscience Publications, p. 684-737.

Roedder, E., 1984, Fluid Inclusions, *Reviews in Mineralogy*, Ed. P.H. Ribbe. Mineralogical Society of America, v. 12, p.646.

Rogers, G., and Hawkesworth, C.J., 1989, A geochemical traverse across the North Chilean Andes: evidence for crust generation from mantle wedge, *Earth and Planetary Science Letters*, v. 91, p. 271-285.

Rollinson, H., 1993, *Using geochemical data: evaluation, presentation, interpretation*, Addison Wesley Longman Limited, Essex, 352p.

Rose, A.W., 1970, Zonal relations of wall rock alteration and sulfide distribution in porphyry copper deposits, *Economic Geology*, v. 65, p. 920-936.

- Rose, A.W., and Burt, D.M., 1979, Chapter 5: Hydrothermal alteration. *in*: *Geochemistry of hydrothermal ore deposits*, ed. H.L. Barnes (ed.). New York: Wiley-Interscience Publications, p. 173-235.
- Samson, S.D., and Alexander, E.G. Jr., 1987, Calibration of the interlaboratory $^{40}\text{Ar}/^{39}\text{Ar}$ dating standard, MMhb-1, in *New Developments and Applications in Isotope Geoscience*, Faure, G., ed. *Chemical Geology, Isotope Geoscience Section*, v. 66, p. 27-34.
- Sasaki, A., and Ishihara, S., 1979, Sulfur isotopic compositions of the magnetite-series and ilmenite-series granitoids in Japan, *Contributions to Mineralogy and Petrology*, v. 68, p. 107-115.
- Schmidt, M.W., 1992, Amphibole composition in tonalite as a function of pressure an experimental calibration of the Al-in-hornblende barometer, *Contributions to Mineralogy and Petrology*, v. 110, p. 304-310.
- Seward, T.M., 1991, The hydrothermal geochemistry of gold, in *Gold Metallogeny and Exploration*, Foster, R.P. ed, Blackie and Son, Glasgow, UK, p. 37-62.
- Seward, T.M., and Barnes, H.L., 1997, Chapter 9: Metal transport by hydrothermal ore fluids, *in* *Geochemistry of hydrothermal ore deposits*, Barnes, H.L., ed., New York: Wiley-Interscience Publications, p. 435-486.
- Sheppard, S.M.F., Nielsen, R.L. and Taylor, H.P., 1969, Oxygen and hydrogen isotope ratios of clay minerals from porphyry copper deposits, *Economic Geology*, v. 64, p. 755-777.
- Sheppard, S.M.F., 1986, Characterization and isotopic variations in natural waters, in. *Stable Isotopes in High Temperature Geological Processes*, Valley, J.W., Taylor, H.P., O'Neil, J.R., eds. *Reviews in Mineralogy*, v.16, p. 165-183.
- Sheppard, S.M.F., Nielsen, R.L. and Taylor, H.P., 1971, Hydrogen and oxygen isotope ratios in minerals from porphyry copper deposits, *Economic Geology*, v. 66, p. 515-542.
- Sheppard, S.M.F., and Gustafson, L.B., 1976, Oxygen and hydrogen isotopes in the porphyry copper deposit at El Salvador, Chile, *Economic Geology*, v. 71, p. 1549-1559.
- Sillitoe, R., 1973, Tops and bottoms of porphyry copper deposits, *Economic Geology*, v. 68, p. 799-815.
- Sillitoe, R., 1988, Ores in volcanoes. *Proceedings of the 7th Quadrennial IAGOD Symposium*; E. Schweizerbatt's Verlagsbuchhandlung, D-7000 Stuttgart I. 10p.

Sillitoe, R., 1993, Epithermal models: Genetic types, geometrical controls and shallow features, *in* Mineral Deposit Modeling: Geological Association of Canada, Kirkham, R.V., Sinclair, W.D., and Duke, J.M., eds., Special Paper 40, p. 403-417.

Sillitoe, R., 1996, Granites and metal deposits, *Episodes*, v. 19, p. 126-133.

Smith, J.V., and Brown, W.L., 1988, Feldspar minerals; Volume 1: Crystal structures, physical, chemical, and microtextural properties, 2nd ed. Springer-Verlag, Berlin, Heidelberg, New York, 828p.

Soto, H.M., 1979, Alteracion y mineralizacion primaria en Chuquicamata, Unpublished PhD. thesis, Universidad de Salamanca, 243p.

Speer, J.A., 1984, Micas in igneous rocks *in* Mineralogical Society of America, *Reviews in Mineralogy*, v.13, Bailey, S.W., ed., p. 299-356.

Streckeisen, A., 1976, To each plutonic rock its proper name, *Earth Science Reviews*, v. 12, p. 1-33.

Suzuoki, T., and Epstein, S., 1976, Hydrogen isotope fractionation between OH-bearing minerals and water, *Geochimica et Cosmochimica Acta*, v. 40, p. 1229-1240.

Tagaki, T., and Tsukimura, K., 1997, Genesis of oxidized- and reduced-type granites, *Economic Geology*, v. 92, p.81-86.

Taylor, H.P., 1967, Oxygen Isotope Studies of hydrothermal mineral deposits, *in* *Geochemistry of Hydrothermal Ore Deposits*, Barnes, H.L., ed.. New York: Holt, Rinehart and Winston, Inc., p. 109-142.

Taylor, H.P., 1968, The oxygen isotope geochemistry of igneous rocks, *Contributions to Mineralogy and Petrology*, v. 19, p. 1-71.

Taylor, H.P., 1971, Oxygen isotope evidence for large-scale interaction between meteoric ground waters and Tertiary granodiorite intrusion, western Cascade range, Oregon, *Journal of Geophysical Research*, v. 76, p. 843-883.

Taylor, H.P., 1997, Oxygen and hydrogen isotope relationships in hydrothermal mineral deposits, *in* *Geochemistry of Hydrothermal Ore Deposits*, 3rd ed. Barnes, H.L., New York: John Wiley and Sons, Inc. p. 229-302.

Taylor, R.P., and Fryer, B.J., 1982, Rare earth element geochemistry as an aid to interpreting hydrothermal ore deposits, *in* *Metallization Associated with Acid Magmatism*, Evans, A.M., ed. John Wiley and Sons, Ltd., p. 357-365.

Thompson, B., 1964, Summary of Activities, Chuquicamata Open Copper Mine, 43p.

Tomlinson, A.J., and Blanco, N., 1997, Structural evolution and displacement history of the West Fault system, Precordillera, Chile: Part 2, Postmineral history [ext. abs.]: Congreso Geológico Chileno, 8th, Antofagasta, 1997, Actas, v.3, p. 1878-1882.

Tosdal, R.M., and Richards, J.P., 2001, Magmatic and structural controls on the development of porphyry Cu \pm Mo \pm Au deposits, Society of Economic Geologists, Reviews, v. 14, p. 157-181.

Turintzev, J., Charron, D., Reyes, M., Soto, C., Pallauta, J., Nunez, A., and Leitz, C., 1973, Estabilidad de taludes en mina Chuquicamata, CODELCO Report, 18p.

Tuttle, O.F., and Bowen, N.L., 1958, Origin of granite in the light of experimental studies in the system, Geological Society of America Memoir, 74p., *from* Petrography to petrogenesis, Hibbard, M.J., ed., 1995, New Jersey: Prentice Hall, 587p.

Vega, M., 1989, Estudio y caracterizacion de vetas de cuarzo en un sector del yacimiento Chuquicamata, Unpublished Bsc. Thesis, Antofagasta, Chile, Universidad de Norte, 77p.

Vernon, R.H., 1986, K-feldspar megacrysts in granites- phenocrysts, not porphyroblasts, Earth Science Reviews, v. 23, p. 1-63.

Webster, J.D., 1997, Exsolution of magmatic volatile phases from Cl-enriched mineralizing granitic magmas and implications for ore metal transport, Geochimica et Cosmochimica Acta, v. 61, p. 1017-1029.

Webster, J.D., and Holloway, J.R., 1990, Partitioning of F and Cl between magmatic hydrothermal fluids and highly evolved granitic melts, in Ore-bearing Granitic Systems; Petrogenesis and Mineralizing Processes, Geological Society of America, Special Paper 246, p. 21-34.

Weidner, J.R., and Martin, R.F., 1987, Phase equilibria of a fluorine-rich leucogranite from the St. Austell pluton, Cornwall, Geochimica et Cosmochimica Acta, v. 51, p. 1591-1597.

Whitton, D.G.A., 1972, The Penguin dictionary of geology, Penguin Books, London. 495p.

Wigger, P.J., Schmitz, M., Arandeda, M., Asch, G., Baldzuhn, S., Giese, P., Heinsohn, W.-D., Martinez, E., Ricaldi, E., Rower, P., and Viramonte, J., 1994, Variation in the crustal structure of the southern central Andes deduced from seismic refraction investigations, in *Tectonics of the Southern Central Andes: Structure and Evolution of an Active Continental Margin*, Reutter, K.-J., Scheuber, E., and Wigger, P.J., eds., Springer-Verlag, Berlin, Heidelberg, 333p.

Winchester, J.A., and Floyd, P.A., 1977, Geochemical discrimination of different magma series and their differentiation products using immobile elements, *Chemical Geology*, v. 20, p. 325-343.

Winter, J.D., 2001, *An introduction to igneous and metamorphic petrology*, Prentice Hall, New Jersey, 697p.

Wood, S.A., 1998, Calculation of activity-activity and $\log f_{O_2}$ -pH diagrams, from *Techniques in hydrothermal ore deposits geology*, *Reviews in Economic Geology*, v. 10, p. 81-96.

Wood, S.A., and Samson, I.M., 1998, Solubility of ore minerals and complexation of ore metals in hydrothermal solutions, in *Techniques in hydrothermal ore deposits geology*, *Reviews in Economic Geology*, v. 10, p. 33-80.

Yoder, H.S., Stewart, D.B., and Smith, J.R., 1957, Ternary feldspars, *Carnegie Institute Geophysical Laboratory Yearbook*, v. 56, p. 206-214 *from* *Petrography to petrogenesis*, Hibbard, M.J., ed., 1995, New Jersey: Prentice Hall, 587p.

Zentilli, M., Doe, B.R., Hedge, C.E., Alvarez, O., Tidy, E., and Daroca, J.A., 1988, Isotopos de plomo en yacimientos de tipo cuprifero comparados con otros depositos metaliferos en los Andes del norte Chile y Argentina, *V Congreso Geologico Chileno*, p. B331-369.

Zentilli, M., Graves, M.C., Lindsay, D., Ossandón, G., and Camus, F., 1995, Recurrent mineralization in the Chuquicamata porphyry copper system: Restrictions on genesis from mineralogical, geochronological and isotopic studies, *Proceedings, Giant Ore Deposits II* (A.H. Clark), editor, April 25-27, Queens University, Kingston, Ontario. p. 86-100K.

Zentilli, M., Graves, M., and Lindsay, D., 1994a, Mineralogical, geochemical and structural study of Chuquicamata, Internal Report, CODELCO, Chuquicamata Division, Chile.

Zentilli, M., Leiva Q., G., Rojas de la R., J., and Graves, M.C., 1994b, The Chuquicamata porphyry copper system revisited, 7th Congreso Geológico Chileno, Actas volumen II, p. 1647-1651.

Zentilli, M., Aracena, I., Graves, M., 1997, Reconnaissance trace element study of Chuquicamata, mansa Mina, and Radomiro Tomic porphyry copper deposits, Chile. SEG Symposium on the Chuquicamata Porphyry Copper System, Actas, 8th Chilean Geological Congress, Antofagasta, v. 3, p. 1913-1917.

Zheng, Y., 1993a, Calculation of oxygen isotope fractionation in anhydrous silicate minerals, *Geochimica et Cosmochimica Acta*, v. 57, p. 1079-1091.

Zheng, Y., 1993b, Calculation of oxygen isotope fractionation in hydroxyl-bearing silicates, *Earth and Planetary Letters*, v.120, p. 247-263.